Optimizing Nitrogen-Vacancy Diamond Magnetic Sensors and Imagers for Broadband Sensitivity

by

Jennifer May Schloss

B.A., Oberlin College (2011)

Submitted to the Department of Physics
in partial fulfillment of the requirements for the degree of

Doctor of Philosophy in Physics

at the

MASSACHUSETTS INSTITUTE OF TECHNOLOGY

June 2019

Author .....
Department of Physics
May 24, 2019

Certified by .....
Ronald L. Walsworth
Senior Physicist, Harvard-Smithsonian Astrophysical Observatory
Thesis Supervisor

Certified by .....
Isaac L. Chuang
Professor of Physics
Thesis Co-Supervisor

Accepted by .....
Nergis Mavalvala
Associate Department Head of Physics

Optimizing Nitrogen-Vacancy Diamond Magnetic Sensors and Imagers for Broadband Sensitivity

by

Jennifer May Schloss

Submitted to the Department of Physics
on May 24, 2019, in partial fulfillment of the
requirements for the degree of
Doctor of Philosophy in Physics

Abstract

Solid-state spin systems form an increasingly impactful quantum sensing platform. Atomic-scale defects in diamond called nitrogen-vacancy (NV) centers offer high-resolution magnetic sensing and imaging under ambient conditions. NV-based magnetometers have found broad utility thanks to long spin lifetimes at room temperature, coherent microwave spin manipulation, and optical spin-state initialization and readout. Their applications span pure and applied sciences, including condensed matter physics, neuroscience and living systems biology, nuclear magnetic resonance, Earth and planetary science, and industrial vector magnetometry.

In this work, we employ ensembles of NV centers for high-sensitivity, broadband magnetic sensing and imaging. We present three experiments, which share a common principal application of time-resolved magnetic field detection from firing neurons. For each experiment, we implement novel techniques to improve magnetometer performance, optimizing a different variant of the DC magnetic field sensitivity. Among solid-state spin-based sensors, these devices demonstrate record sensitivities to broadband magnetic signals. Nonetheless, the achieved sensitivities remain orders of magnitude away from theoretical limits. Primary obstacles include optical readout fidelities far from unity and typical NV-ensemble dephasing times T_2^* thousands of times shorter than spin lifetimes T_1. We therefore investigate techniques for improving these key parameters to enable considerable sensitivity enhancements. We develop a strategy for extending T_2^* in NV-rich diamonds, which could in turn make exotic techniques to increase readout fidelity more practical. Moreover, we identify methods to optimize diamond fabrication and treatment, and we highlight where further materials science research is warranted. In short, this work demonstrates advances in NV-ensemble magnetic sensing and establishes a basis for further sensitivity improvements, perhaps even inspiring new innovations to approach fundamental limits.

Thesis Supervisor: Ronald L. Walsworth
Title: Senior Physicist, Harvard-Smithsonian Astrophysical Observatory

Thesis Co-Supervisor: Isaac L. Chuang
Title: Professor of Physics

Acknowledgments

I am sincerely grateful to the many people who contributed to my Ph.D. experience and made this work possible. I would like to begin by thanking my research advisor, Dr. Ronald Walsworth, for his guidance over the past four years. From the day I walked into his office, looking to take on a new research direction for the remainder of my Ph.D., Ron trusted my abilities and believed in my drive. Ron taught me many lessons, from the technical to the strategic, and entrusted me with the freedom to pursue my scientific interests and goals. He always sincerely engaged with my research, and his broad knowledge and perspective elevated this work in numerous ways. Ron not only cared about my success and well-being as a student, but he also regularly treated me as a colleague, honestly valuing my insights and contributions to the group.

I also owe a debt of gratitude to my thesis co-supervisor, Professor Isaac Chuang. Even before I joined the Walsworth group, Ike served me as a mentor and a role model, making time to share advice with me and challenge me to expand my thinking. Ike's perspective has been tremendously valuable to me, especially as I endeavored to unify the work and themes contained in this thesis. He has simultaneously given me confidence in myself and pushed me to grow as a scientist.

Professor Wolfgang Ketterle, my thesis committee member, my academic advisor, my general oral exam committee chair, and the professor who taught me atomic physics, served as a foundation of my education and my growth into a physicist. I am grateful for Wolfgang's shrewd advice and keen physical insights, which will serve me for many years. His own winding journey to the field that earned him a Nobel Prize and became his life's work gave me the courage to change research directions and discover an area that I am passionate about.

I also wish to thank my final thesis committee member, Professor Nikta Fakhri, for enhancing my thesis work with her fresh perspective and thoughtful comments, and for serving as a scientific role model for me.

I am tremendously grateful for my research team, the "T_2^* task force": John Barry,

Matthew Turner, Erik Bauch, and Connor Hart. I can only hope that someday in the future I'll get the opportunity again to be part of a team as fantastic as this one. John in many ways models the kind of scientist I strive to become, in particular through his drive, his care for his work, and his scientific philosophy. Matthew has been a consistent research partner, always giving of his time and technical expertise. His broad skill set complements my own capabilities, and his creativity and diligence continue to inspire me. Erik has enriched my Ph.D. through his deep knowledge and wise insights, and by improving my writing. The model of a team player, Erik has been a pleasure to work with. Finally, I am lucky to have gotten to work with the multi-skilled, dedicated, and genuinely kind Connor. His many contributions have accelerated my progress on experimental projects, and he's been a reliable co-lead on our external collaborations. This thesis would not have been possible without the hard work, clever insights, and collaborative spirit of John, Matthew, Erik, and Connor.

I am fortunate to been part of an engaging, talented, creative, and friendly research group. I have benefited from the knowledge and expertise of Keigo Arai, Nithya Arunkumar, Mikael Backlund, Oren Ben Dor, Dominik Bucher, Francesco Casola, David Glenn, J.C. Jaskula, Pauli Kehayias, Mark Ku, Nick Langellier, Junghyun Paul Lee, Rebecca Li, Tim Milbourne, David Phillips, Diana Prado Lopes Aude Craik, Aakash Ravi, Emma Rosenfeld, Patrick Scheidegger, Raisa Trubko, Huiliang Zhang, Yuan Zhu, and others. Furthermore, the diamond research community in and around Cambridge has been an invaluable resource to me. In particular, Ashok Ajoy, Danielle Braje, Alexei Bylinskii, Colin Connolly, Alexandre Cooper-Roy, Andy Greenspon, Linh Pham, Ziwei Qui, Alex Xingyu Zhang, Professor Mikhail Lukin, Professor Hongkun Park, Professor Evelyn Hu, and others in the Cappellaro, Hu, Loncar, Lukin, Park, and MIT Lincoln Lab groups have enriched my Ph.D.

I gratefully acknowledge my fellowship support from the National Science Foundation Graduate Research Fellowship Program, the Clare Booth Luce Program, and the Fannie and John Hertz Foundation. I have been fortunate to have received continuous support over my entire Ph.D., which has allowed me to pursue my research interests

free from worry about funding. I am particularly grateful to the Hertz Foundation for fostering a vibrant community of current and former fellows, who have inspired me, mentored me, and enriched my life.

Next, I must thank the MIT Physics Department for stewarding me through my graduate education. In particular, I am grateful to Cathy Modica for selflessly sharing her time and compassion, especially during the most difficult parts of my Ph.D. experience. I am also thankful to Professor Nergis Mavalvala, who, like Cathy, went out of her way to make me feel valued and respected when I needed that support the most. I am also grateful to my classmates and friends from the physics graduate student council, the graduate women in physics, the physics REFS, and the broader MIT REFS program, including the one and only Libby Mahaffy.

I am fortunate to have matriculated with a superb group of MIT physics graduate students and to have developed close friendships with many of them, as well as other science and engineering folks. This journey has been not only endurable, but incredibly enjoyable, thanks to Alex, Maxine, Nancy, Cody, Janos, Lina, Gabriel, Mukund, Alex, Alex, John, Tom, Matt, Murphy, Ian, Kristi, Arolyn, Jacob, Ben, Gizem, Zoe, and others. I am also grateful for my non-physics friends, including Amanda, Louisa, Jocelyn, my other old hometown friends, my Oberlin College friends, and my Brooklyn Boulders gym buddies, all of whom have kept me grounded and balanced over these past years.

Everything I've accomplished up to this point traces back to my loving family. My parents always encouraged me to follow my curiosity and supported me through every step of my journey to today. I strive to live by their example of diligence, humility, generosity, and perseverance, and my Ph.D. is better for that. I am so grateful to my sister Heather and brother David for being in my court during their whole lives, for teaching me how to collaborate, and for helping me gain the courage to change course toward the new and unknown. I am also fortunate to have the best in-laws. I am thankful for my kind and supportive brother-in-law, Alex, and I am so lucky to have been welcomed into the fantastic Mahony/Stromberg clan, who have shown me more love and support than I ever could have imagined.

Finally, I owe everything to my husband and best friend, Tom Mahony. His contributions to this thesis are mostly invisible, but they are considerable. Throughout my Ph.D., Tom was a sounding board and a source of valuable technical advice. His constant belief in me sustained me through the most difficult parts of my Ph.D., and his joy in my achievements made those successes sweeter. I am a better scientist and a better person thanks to Tom. He made the last seven years more wonderful than I could ever have hoped for, and I am so excited to share all my future years with him.

Contents

List of Figures

List of Tables

Chapter 1

Introduction

1.1 Magnetometry with ensemble NV-diamond

Quantum sensors encompass a diverse class of devices that exploit quantum coherence to detect weak or nanoscale signals. As their behavior is tied to physical constants, quantum devices can achieve accuracy, repeatability, and precision approaching fundamental limits [1]. As a result, these sensors have shown utility in a wide range of applications spanning both pure and applied science [2]. A rapidly emerging quantum sensing platform employs atomic-scale defects in crystals. In particular, magnetometry using nitrogen vacancy (NV) color centers in diamond has garnered increasing interest.

The use of NV centers as magnetic field sensors was first proposed [3, 4] and demonstrated with single NVs [5, 6] and NV ensembles [7] circa 2008. In the decade following, both single- and ensemble-NV-diamond magnetometers [8, 9] have found use in applications spanning condensed matter physics [10], neuroscience and living systems biology [11, 12], nuclear magnetic resonance (NMR) [12], Earth and planetary science [13], and industrial vector magnetometry [14].

Solid-state defects such as NV centers exhibit quantum properties similar to traditional atomic systems yet confer technical and logistical advantages for sensing applications. NVs are point defects composed of a substitutional nitrogen fixed adjacent to a vacancy within the rigid carbon lattice (see Figure 1.1.1a). Each NV

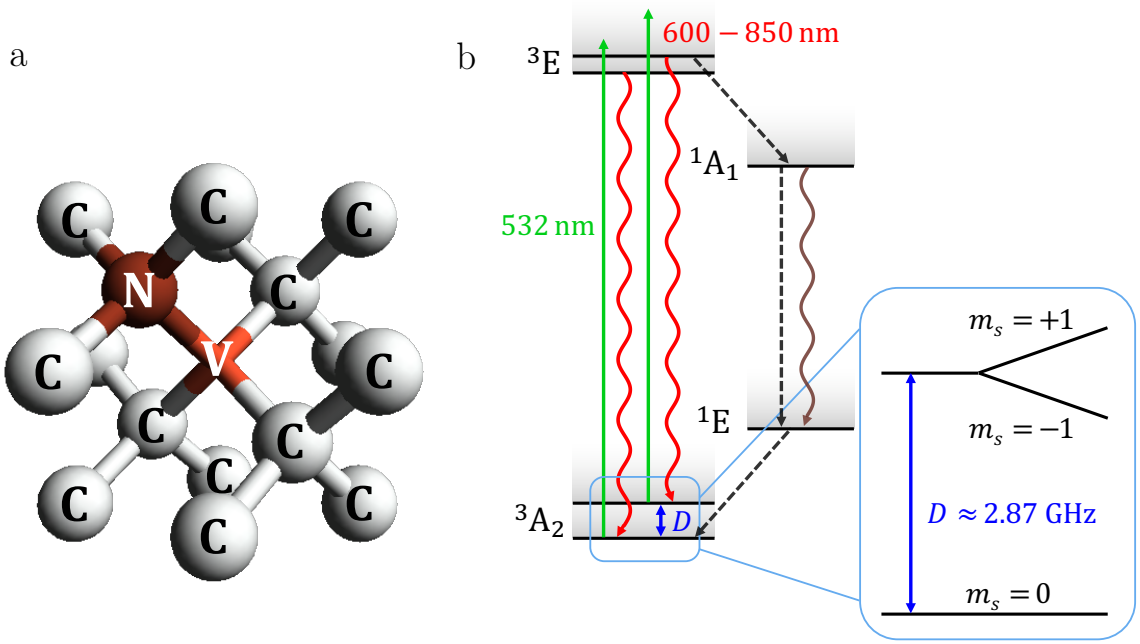

Figure 1.1.1: Overview of the NV$^-$ center quantum system. a) Diagram of diamond's carbon lattice containing a nitrogen vacancy (NV) center, which consists of a substitutional nitrogen adjacent to a lattice vacancy. b) Energy level diagram for the negatively charged NV$^-$ center in diamond, with zero-field splitting D between the ground-state electronic spin levels $m_s = 0$ and $m_s = \pm 1$. The $m_s = \pm 1$ energy levels experience a Zeeman shift in the presence of a magnetic field $\vec{B}$, which forms the basis for NV$^-$ magnetometry.

center's symmetry axis is constrained to lie along one of the four [111] crystallographic directions. While NVs are observed to exist in three charge states (NV^-, NV^0 and NV^+), the negatively charged NV^- center is favored for quantum sensing and quantum information applications [8]. The NV^- defect exhibits a spin-1 triplet electronic ground state with long spin lifetimes at room temperature: longitudinal relaxation times $T_1 \approx 6$ ms [15, 16] are typical and coherence times T_2 up to a few ms are achievable [17]. The defect's spin energy levels are sensitive to magnetic fields, electric fields, strain, and temperature variations [8], allowing NV^- to operate as a multi-modal sensor. Coherent spin control is achieved by application of resonant microwaves (MWs) near 2.87 GHz. Upon optical excitation, a spin-state-dependent intersystem crossing [18, 19] combined with decay through a primarily non-radiative pathway allows for both spin-state-dependent fluorescence contrast and optical spin initialization into the NV^- center's $m_s = 0$ ground state (see Figure 1.1.1b).

Relative to alternative technologies [14], sensors employing NV^- centers excel in technical simplicity and spatial resolution [20, 21, 22]. Such devices may operate as broadband sensors with bandwidths up to ~ 100 kHz [23, 24, 25] or as high frequency detectors for signals up to $\sim$ GHz [26, 27, 28, 29, 30, 31, 32, 33, 34, 35, 36, 37, 10, 38, 39, 40]. Importantly, effective optical initialization and readout of NV^- spins does not require narrow-linewidth lasers; rather, a single free-running 532 nm solid-state laser is sufficient. NV-diamond sensors operate at ambient temperatures, pressures, and magnetic fields, and thus require no cryogenics, vacuum systems, or large applied bias fields. Furthermore, diamond is chemically inert, making NV^- devices biocompatible. These properties allow sensors to be placed within ~ 1 nm of field sources [33], which enables magnetic field imaging with nanometer-scale spatial resolution [20, 21, 22]. NV-diamond sensors are also operationally robust and may function at pressures up to 60 GPa [41, 42, 43] and temperatures from cryogenic to 700 K [44, 45, 46].

Although single NV^- centers find numerous applications in ultra-high-resolution sensing due to their angstrom-scale size [6, 5, 10], sensors employing ensembles of NV^- centers provide improved signal-to-noise ratio (SNR) at the cost of spatial resolution by virtue of statistical averaging over multiple spins [3, 7]. Diamonds may be

engineered to contain concentrations of NV^- centers as high as 10^{19} cm^{-3} [47], which facilitates high-sensitivity measurements from single-channel bulk detectors as well as wide-field parallel magnetic imaging [3, 48, 49, 31, 50, 51, 52, 53]. These engineered diamonds typically contain NV^- centers with symmetry axes distributed along all four crystallographic orientations, each sensitive to a different magnetic field component; thus, ensemble-NV^- devices provide full vector magnetic field sensing without heading errors or dead zones [54, 48, 49, 50, 25]. NV^- centers have also been employed for high-sensitivity imaging of temperature [55], strain, and electric fields [56, 57]. Recent examples of ensemble-NV^- sensing applications include optical magnetic detection of single-neuron action potentials [24]; magnetic imaging of living cells [50, 31], malarial hemozoin [53], and biological tissue with subcellular resolution [52]; nanoscale thermometry [55, 58]; single protein detection [59, 32]; nanoscale and micron-scale NMR [60, 61, 62, 63, 64, 65, 66, 67]; and the study of meteorite composition [68] and paleomagnetism [13, 69].

Despite demonstrated utility in a number of applications, the present performance of ensemble-NV^- sensors remains far from theoretical limits. Even the best demonstrated ensemble-based devices exhibit readout fidelities of $\sim$ 0.01 [70], $\sim 100\times$ worse than the spin projection limit. Additionally, reported dephasing times T_2^* in NV-rich diamonds remain 100 to $1000\times$ shorter than the theoretical maximum of $2T_1$ [71, 72]. As a result, whereas present state-of-the-art ensemble-NV^- magnetometers exhibit $\mathrm{pT}/\sqrt{\mathrm{Hz}}$-level sensitivities, competing technologies such as superconducting quantum interference devices (SQUIDs) and spin-exchange relaxation-free (SERF) magnetometers exhibit sensitivities at the $\mathrm{fT}/\sqrt{\mathrm{Hz}}$-level and below [73]. This $\sim 1000\times$ sensitivity discrepancy corresponds to a $\sim 10^6\times$ increase in required averaging time, which precludes many envisioned applications. For example, the sensing times required to detect weak static signals with an NV-diamond sensor may be unacceptably long; e.g., biological systems may have only short-term viability. In addition, many applications, such as spontaneous event detection and time-resolved sensing of dynamic processes [74, 34], are incompatible with signal averaging. Realizing NV-diamond magnetometers with improved sensitivity could enable a new

class of scientific and industrial applications poorly matched to bulkier SQUID and vapor-cell technologies. Examples include noninvasive, real-time magnetic imaging of neuronal circuit dynamics [24], high throughput nanoscale and micron-scale NMR spectroscopy [75, 61, 65], nuclear quadrupole resonance (NQR) [76], human magnetoencephalography (MEG) [77], subcellular magnetic resonance imaging (MRI) of dynamic processes, precision metrology, and tests of fundamental physics [78, 79].

This dissertation accordingly focuses on optimization of the sensitivity and performance of broadband magnetic sensors and imagers based on ensembles of NV^- centers in diamond. We identify biocurrent detection and imaging in neurons and other electrically active cells as a primary application of NV^--based sensors and we demonstrate the first optical magnetic detection of single-neuron action potentials using a record-sensitivity broadband magnetometer. We introduce full vector magnetic field detection as an important additional capability for ensemble NV^- devices and demonstrate a simultaneous vector magnetometry technique to enable fast time-resolved sensing of all vector field components. We then turn our focus to the chief bottleneck for applications of broadband ensemble-NV^- magnetometers: sensitivity. We identify existing sensitivity limitations and provide a broad literature review and in-depth analysis of present and proposed methods for optimizing magnetic field sensitivity. We analyze techniques to improve NV^- spin phase coherence and spin readout fidelity in existing diamonds as well as methods to improve the quality and consistency of the diamond material properties. We combine this updated understanding of sensitivity optimization with work developing a high-speed Ramsey magnetic imager to demonstrate steps toward realizing a next-generation device for neuroimaging and other broadband magnetic sensing applications.

1.2 This work

1.2.1 Organization of this dissertation

This chapter provides background on NV^- centers in diamond and gives particular focus to their use as sensors of static (DC) or broadband magnetic fields. The mathematical formalism governing spins in static and oscillating magnetic fields is introduced, and the sensitivity of a Ramsey-based magnetometer in the presence of quantum spin projection noise and photon shot noise is derived. Alternatives protocols to Ramsey magnetometry are introduced and their sensitivity limitations are highlighted. Finally, the parameters currently limiting the achievable sensitivity of Ramsey-based NV^- magnetic sensors are scrutinized.

Chapter 2 identifies the inhomogeneous dephasing time, T_2^*, as a key parameter limiting DC and broadband ensemble-NV^- magnetic sensitivity. The factors contributing to the value of T_2^* are examined. Furthermore, the particular contributions of various spin species in diamond to T_2^* (and also, where relevant, the coherence time T_2) are quantified.

Chapters 3-7 focus on optimizing NV-diamond magnetometer performance given different initial goals and constraints. Across all of these chapters, we assume applications require ambient-temperature magnetometer operation. In addition, signals are assumed to be low-magnitude magnetic fields containing broadband frequency information from DC up to several kHz (or at most 100 kHz). Therefore, high sensitivity and high bandwidth are primary goals for all of these chapters.

The techniques considered and implemented in the following chapters diverge, though, as different additional goals and constrains are applied in each. Chapter 3 describes a first experiment employing a high-sensitivity ensemble-NV^- magnetometer to the detection of the tiny and fleeting magnetic fields produced by the firing of individual neurons. In this work, our goal is time-resolved detection of single-neuron action potentials from giant axons. In this project, high magnetic field sensitivity from DC to $\sim$ kHz is desired. Because the goal is single-channel detection rather than magnetic field imaging, high spatial resolution is not required. Furthermore,

as the magnetic field source may be placed with a fixed orientation relative to the diamond, sensing of a single magnetic field component rather than the full field vector is sufficient. In this case, the relevant figure of merit is the signal-to-noise ratio (SNR) in a given measurement time for a pre-determined magnetic field component. In other words, we aim to optimize the magnetic field sensitivity η for the chosen field component. Considering the finite optical and MW power as well as additional constraints set by the diamond material and the signal source's spatial dimensions, we choose to implement a modulated variant of the NV$^-$ magnetometry protocol called continuous-wave optically detected magnetic resonance (CW-ODMR), and we achieve a record NV$^-$ magnetic field sensitivity of $\eta \approx 15$ pT$/\sqrt{\text{Hz}}$ from 80 Hz to ~ 3 kHz. The techniques employed to reach this nearly-shot-noise-limited sensitivity are discussed in detail.

Chapter 4 describes a second experimental work, demonstrating a novel technique for high-speed vector magnetometry employing the four NV$^-$ crystallographic orientation classes in diamond. Relative to the performance goals of the previous chapter, here an additional requirement is introduced that *all* components of the magnetic field vector be reconstructed with high SNR in a short period of time, to allow high-speed vector field sensing. In this case, the relevant figures of merit become the rate of full vector-field measurements and the SNR along the worst-sensitivity field direction. In other words, we aim to minimize $\max\{\eta_x, \eta_y, \eta_z\}$. We therefore experimentally implement a new technique to simultaneously record all Cartesian field components using a CW-ODMR variant combining multi-tone MW addressing of the four NV$^-$ orientations and multi-channel lock-in detection. We achieve a record NV$^-$ vector magnetic field sensitivity of $\max\{\eta_x, \eta_y, \eta_z\} = 57$ pT$/\sqrt{\text{Hz}}$ from 5 to 200 Hz, and we also demonstrate vector sensing with up to 12 kHz bandwidth. Finally, we describe a pulsed magnetometry extension of our scheme that could enable even higher broadband sensitivity at the cost of some experimental complexity.

Chapter 5 shifts focus to a broadband imaging goal, where spatial resolution is valued in addition to sensitivity. In this case, the relevant figure of merit is the magnetic field SNR in a given measurement time from a given volume of NV-diamond.

In other words, we seek to minimize the average volume-normalized magnetic field sensitivity $\eta^V = \eta\sqrt{V}$ over a moderate field of view (50 μm to 1 mm on a side). Depending on the application, η^V for field projections along a pre-determined axis can be minimized, or for full vector magnetic imaging $\max\{\eta_x, \eta_y, \eta_z\}$ can be minimized. In this chapter we concentrate on the former optimization goal. Not only should the average sensitivity over the image be high, but the sensitivity should be uniform to avoid dead zones in a magnetic field imager. Given these goals combined with finite optical power and diamond material constraints, we choose to employ a pulsed double-quantum Ramsey magnetometry technique. Pulsed magnetometry allows higher volume-normalized sensitivity than CW-ODMR (see Section 1.6.1), and double-quantum imaging allows uniform imaging sensitivity uncorrupted by intrinsic diamond strain. In this chapter we describe a new technique mitigating the effects of pulse errors on double-quantum Ramsey imaging, and we demonstrate broadband reconstruction of magnetic fields from currents in nontrivial structures. We then discuss next steps and future applications of ensemble-NV$^-$ magnetic imaging devices to imaging of biocurrents in neurons and cardiomyocytes.

Chapter 6 is based upon the recognition that, even in the experimental implementations described in this dissertation, where ensemble-NV$^-$ devices with record magnetic field sensitivity are demonstrated, the achieved sensitivities remain orders of magnitude away from theoretical limits. Therefore, this chapter explores strategies to extend spin dephasing times toward relaxation times $T_1 \sim$ ms and to overcome the poor spin readout fidelities so far achieved for NV$^-$ ensembles. We present a broad literature review of methods proposed and demonstrated in the literature for enhancing sensitivity of broadband ensemble-NV$^-$ magnetometers. In particular, we analyze and evaluate experimental techniques from the past decade in the context of broadband ensemble-NV$^-$ devices. The methods considered are divided into three general categories: techniques that endeavor to extend spin phase coherence (T_2^* and/or T_2); those that aim to improve the spin readout fidelity, i.e., reduce the factor σ_R above spin-projection-noise-limited sensitivity; and miscellaneous other enhanced sensing techniques. We note that many of these techniques require engineering advances or

a high degree of experimental complexity. When realistic technical constraints are applied, such as low optical power or low bias field strength, even the most promising of these techniques can become impractical. However, many of the methods analyzed here represent the best ideas so far proposed or demonstrated in the NV^- magnetometry field to enable orders-of-magnitude improvements in magnetic field sensitivity, approaching fundamental limits.

While the majority of chapters in this dissertation consider the case where the diamond material itself is a magnetometer design constraint, Chapter 7 investigates strategies to optimize the fabrication and treatment of host diamond material in order to produce NV^--rich diamonds more suitable for high-sensitivity ensemble-based magnetometry. We identify key parameters to be optimized, including the nitrogen-to-NV conversion efficiency and the charge state efficiency, (i.e, the fraction of NV centers in the useful negative charge state NV^-). We examine methods to increase these efficiencies and also to reduce unwanted paramagnetic defect concentrations and gradients in diamond crystal strain. We provide a brief history of the development of well-accepted methods for diamond growth and treatment, and we identify areas in diamond engineering and diamond materials science where further study is needed.

Chapter 8 combines the insights gleaned in the previous chapters and synthesizes a general strategy for designing and implementing ensemble-NV^- magnetometers with sensitivities approaching theoretical limits. In addition, an outlook is provided on areas where further study and development is merited. The appendices contain additional experimental details and analysis.

In summary, this dissertation aims to establish foundational principles and a clear reasoning strategy for those seeking to develop optimized magnetic field sensors based on ensembles of NV^- centers in diamond geared toward a range of applications. By laying this groundwork, we hope to stimulate development of new techniques that could further enhance solid-state sensor performance.

1.2.2 Publications

Much of the work presented in this dissertation has been previously published or submitted for publication.

Main works contributing to this thesis:

- [24]: J. F. Barry, M. J. Turner, **J. M. Schloss**, D. R. Glenn, Y. Song, M. D. Lukin, H. Park, and R. L. Walsworth, "Optical magnetic detection of single-neuron action potentials using quantum defects in diamond," *Proc. Natl. Acad. Sci.*, vol. 113, no. 49, pp. 14133 - 14138, Dec 2016.

- [25]: **J. M. Schloss**[*], J. F. Barry[*], M. J. Turner, and R. L. Walsworth, "Simultaneous broadband vector magnetometry using solid-state spins," *Phys. Rev. Applied*, vol. 10, p. 034044, Sep 2018[†].

- [80]: J. F. Barry[*], **J. M. Schloss**[*], E. Bauch[*], M. J. Turner, C. A. Hart, L. M. Pham, and R. L. Walsworth, "Sensitivity Optimization for NV-Diamond Magnetometry," *ArXiv e-prints*, Mar 2019.

Works contributing in smaller part to this thesis:

- [81]: E. Bauch[*], C. A. Hart[*], **J. M. Schloss**, M. J. Turner, J. F. Barry, P. Kehayias, S. Singh, and R. L. Walsworth, "Ultralong dephasing times in solid-state spin ensembles via quantum control," *Phys. Rev. X*, vol. 8, p. 031025, Jul 2018[†].

- [82]: S. T. Alsid, J. F. Barry, L. M. Pham, **J. M. Schloss**, M. F. O'Keeffe, P. Cappellaro, and D. A. Braje, "Photoluminescence decomposition analysis: A technique to characterize N-V creation in diamond," submitted to Phys. Rev. Applied, Mar 2019.

Chapters 1, 2, 6, 7, and 8 reproduce and adapt material from the review article Ref. [80] and references contained therein. Chapter 3 is adapted from Ref. [24], and Chapter 4 is adapted from Ref. [25]. In addition, Sections 6.1.2 and 6.1.3, reproduced from Ref. [80], report on results from Ref. [81], and Section 7.4.2 contains material from the Appendix of Ref. [82].

[*]Equal contribution

[†]

1.2.3 Co-worker contributions

The work comprising this thesis is strengthened by collaboration. Just as I have contributed to additional projects not presented in this dissertation [83, 84, 85], my research colleagues have made valuable contributions to my thesis work. Needless to say, my advisor Ron Walsworth oversaw all the projects contained in this dissertation. My co-workers' contributions are summarized below.

The single-neuron sensing work presented in Chapter 3 [24] was undertaken jointly with John Barry and Matthew Turner. John led design and implementation of the magnetometer, and Matthew led the biology preparation and electrophysiology, with assistance from Yuyu Song. John, Matthew, and I participated equally in performing experiments, analyzing the data, and writing the paper. David Glenn contributed to conception of the experiment, and all co-authors commented on the manuscript. While Chapter 3 focuses mainly on my particular contributions to this project, the work could not have existed without John and Matthew.

John, Matthew, and I also participated equally in conceiving the idea for the simultaneous vector magnetometry technique presented in Chapter 4 [25]. John led the initial experimental implementation. Matthew developed the back-end analysis code for converting detected ODMR line shifts to Cartesian magnetic field components, adapting a framework originally established by David Glenn. I designed and performed the experiments and wrote the paper, with considerable input from both John and Matthew.

While I led the project presented in Chapter 5, Connor Hart, Matthew Turner, Patrick Scheidegger, Yuan Zhu, John Barry, Erik Bauch, and Linh Pham all made substantial contributions. John researched and obtained most of the equipment for the experiment, including the lock-in camera. Linh and Erik developed the original MATLAB codebase that controls the experiment. Connor and Patrick expanded the codebase and added capabilities for imaging with the lock-in camera. I designed and implemented the apparatus with considerable assistance from Matthew Turner. Matthew and Yuan designed the MW delivery structure, and Matthew originally

conceived the idea for a gold fabricated phantom. I designed the phantom with input from Matthew and Connor. Matthew fabricated the phantom and MW delivery structure. Connor and I jointly performed experiments. I analyzed the data and characterized the magnetometer performance.

The review and analysis from Ref. [80] presented in Chapters 1, 2, 6, 7, and 8 was jointly led by John Barry and myself with significant editing performed by Erik Bauch. John and I discussed nearly every aspect of the review at length and co-wrote nearly all the sections. Erik provided organizational vision and led writing of the sections on double quantum coherence magnetometry, spin bath driving, and spin-to-charge conversion readout. Connor Hart and I researched and wrote the section on techniques for the strong NV^--NV^- interaction regime. Matthew and I researched and wrote the section on photoelectric readout. Linh Pham led writing of the dynamical decoupling section and provided substantial feedback on the introduction. Erik, Matthew, and Connor read and commented on every section of the manuscript, and John and I prepared the final versions of all sections.

1.3 Nitrogen-vacancy center physics

The negatively charged NV^- center is a localized atomic-scale defect consisting of a substitutional nitrogen adjacent to a vacancy in the carbon lattice. The negatively-charged NV^- center's electronic ground state has spin $S = 1$ with the lower-energy $m_s = 0$ level separated from the $m_s = \pm 1$ levels by a zero-field splitting $D \approx 2.87\,\mathrm{GHz}$ (see Figure 1.1.1a).

Crucially, the NV^- electronic spin state can be initialized and read out optically. Illumination at wavelengths shorter than the NV^- center's 637 nm zero-phonon line (532 nm radiation is commonly employed) excites the NV^- center electronically to the excited triplet state, which is accompanied mainly by spin-conserving fluorescent decay to the ground state [8]. However, the electron may also decay through inter-system crossing to an excited singlet state, through a cascade to a lower metastable single state [86], and finally back to the triplet ground state in a spin-state-dependent

process that preferentially populates the $|m_s=0\rangle$ ground spin state [18, 19, 87]. This alternate decay pathway enables both spin polarization and spin state detection, as population originally in the $|m_s=\pm1\rangle$ states are more likely to pass through the singlet cascade and not emit photons in the 600 - 850 nm band, resulting in higher photoluminescence (PL) from the $|m_s=0\rangle$ than from the $|m_s=\pm1\rangle$ states [18, 19].

In a bias magnetic field $\vec{B}_0$, the NV$^-$ $m_s=\pm1$ energy levels are Zeeman-shifted in opposite directions away from 2.87 GHz by an amount approximately equal to $g_e\mu_B$ times the projection of $\vec{B}_0$ along the NV$^-$ center's symmetry axis, where $g_e \approx 2.003$ is the NV$^-$ electron g-factor [8] and μ_B is the Bohr magneton. By application of coherent microwave (MW) fields resonant with the transition between the $|m_s=0\rangle$ and either of the $|m_s=\pm1\rangle$ states, magnetic fields may be sensed through optically detected magnetic resonance (ODMR). The NV$^-$ center's ground state spin states exhibit substructure arising from hyperfine coupling to the NV$^-$ center's nitrogen nuclear spin ($I=1$ for ^{14}N and $I=1/2$ for ^{15}N) and, for ^{14}N, the nuclear quadrupolar interaction [88, 89]. An NV$^-$ center's symmetry axis may lie along one of four orientations set by the tetrahedral symmetry of the diamond lattice (see Figure 1.1.1b), which enables determination of a vector magnetic field's magnitude and direction from detection of the Zeeman shifts associated with each NV$^-$ orientation.

NV$^-$ centers are also sensitive to strain, electric fields, and temperature. The Hamiltonian for the NV$^-$ ground state spin in the presence of a bias magnetic field $\vec{B}_0$, an electric field $\vec{E}$, and intrinsic crystal strain to is given by [90, 8]

$$\begin{aligned} H/h = &\left(D + \mathcal{M}_z + d_\parallel E_z\right) S_z^2 \\ &+ \frac{g_e\mu_B}{h}\left(B_{0,z}S_z + B_{0,x}S_x + B_{0,y}S_y\right) \\ &+ \left(\frac{d_\perp E_x}{h} + \mathcal{M}_x\right)\left(S_y^2 - S_x^2\right) \\ &+ \left(\frac{d_\perp E_y}{h} + \mathcal{M}_y\right)\left(S_xS_y + S_yS_x\right) \\ &+ \mathcal{N}_x\left(S_xS_z + S_zS_x\right) + \mathcal{N}_y\left(S_yS_z + S_zS_y\right). \end{aligned} \tag{1.1}$$

Here S_i with $i = x, y, z$ are the dimensionless spin-1 projection operators in the frame

of the NV$^-$ symmetry axis; D is the NV$^-$ zero field splitting ($\approx$ 2.87 GHz at room temperature with dependence $dD/dT = -74$ kHz/K [91]); $d_\parallel = 3.5 \times 10^{-3}$ Hz/(V/m) and $d_\perp = 0.17$ Hz/(V/m) are the axial and transverse electric dipole moments [92, 56, 93]; and $\mathcal{M}_z$, $\mathcal{M}_x$, $\mathcal{M}_y$, $\mathcal{N}_x$, and $\mathcal{N}_y$ are spin-strain coupling parameters. The Hamiltonian and its eigenstates may be simplified when D is large compared to all other coupling terms, i.e., in the regime of low magnetic field, electric field, and strain. In particular, energy level shifts associated with transverse magnetic field components $B_{0,x}$ and $B_{0,y}$ [94], and with spin-strain coupling parameters $\mathcal{N}_x$ and $\mathcal{N}_y$, are suppressed by D [85]. Furthermore, as discussed in Section 6.1.4 and Appendix B, when the applied bias magnetic field is nonzero, its projection along the NV$^-$ symmetry axis suppresses the contribution of transverse electric fields and spin-strain coupling parameters $E_x, E_y, \mathcal{M}_x$, and $\mathcal{M}_y$ to the spin eigenstates, enabling these terms to be ignored from the Hamiltonian at bias fields larger than a few gauss typically [94]. The spin resonances between the $|m_s = 0\rangle$ and the $|m_s = \pm 1\rangle$ eigenstates of this simplified Hamiltonian are given by

$$\nu_\pm = \left(D + \mathcal{M}_z + d_\parallel E_z\right) \pm \frac{g_e \mu_B}{h} B_{0,z}. \tag{1.2}$$

By tuning the MW frequency to near resonance with $\nu_\pm$ and either monitoring changes in the ODMR signal or applying pulsed magnetometry sequences, changes in the magnetic field $\delta B_z = \frac{h}{g_e \mu_B} \delta \nu_\pm$ can be detected, and thus NV^- centers may serve as quantum sensors for magnetic fields. Monitoring both the upper and lower resonance allows magnetic field changes to be distinguished from changes in D, $\mathcal{M}_z$ or E_z.

1.4 Magnetic sensing

1.4.1 DC and AC sensing

Quantum sensing approaches may be divided into two broad categories based on the spectral characteristics of the fields to be detected, summarized in Table 1.4.1. In particular, DC sensing protocols are sensitive to static, slowly-varying, or broadband

signals, whereas AC sensing protocols typically detect narrowband, time-varying signals at frequencies up to $\sim$ 10 MHz [26, 27, 28, 29, 30, 31, 33, 34, 35, 36], although AC sensing experiments of $\sim$ 100 MHz signals have also been demonstrated for niche applications [37]. Both DC and AC sensors employing NV^- ensembles exhibit sensitivities limited, in part, by the relevant NV^- spin relaxation times. DC sensitivity is limited by the ensemble's inhomogeneous dephasing time T_2^*, which is of order 1 μs in most present implementations. AC sensitivity is limited by the coherence time T_2, which is typically one to two orders of magnitude longer than T_2^* [95, 84], and which can be extended through use of dynamical decoupling protocols to approach the longitudinal spin relaxation time T_1 (see Section 6.1.1). Additionally, alternative forms of T_1-limited AC sensing such as T_1 relaxometry allow phase-insensitive detection of signals at frequencies in the $\sim$ GHz regime [38, 40, 10, 34, 39]. In general, the enhanced field sensitivities afforded by longer AC sensor coherence times coincide with reduced sensing bandwidth as well as insensitivity to static fields, restricting the application space of AC sensors (see Table 1.4.1). This dissertation concentrates primarily on DC sensing protocols with particular focus applied to sensors designed to detect broadband time-varying magnetic fields from DC to $\sim$ 100 kHz.

1.4.2 Vector magnetic field measurement

In contrast to scalar magnetometers, (such as vapor cell magnetometers, proton precession magnetometers, and Overhauser effect magnetometers), which measure magnitude but not direction of a magnetic field, vector magnetometers measure the magnetic field projection onto a fixed axis of the sensing device [1]. Scalar magnetometers have the property that the sensing element tends to align along the magnetic field, and thus the sensor can sense only the magnitude and not the direction. In contrast, SQUIDS, Hall probes, fluxgate magnetometers, and NV-diamond magnetometers are vector magnetometers, sometimes called vector projection magnetometers, since the sensing element is fixed in space and does not align along the direction of the magnetic field. An NV^- spin is quantized along one of four crystallographic NV^- symmetry axes in the diamond crystal; and therefore a single NV^- center senses not the magnitude

	Broadband DC sensing	AC sensing
Common techniques	Ramsey, CW-ODMR, pulsed ODMR	Hahn echo, dynamical decoupling
Sensitivity	Limited by inhomogeneous spin dephasing (T_2^*)	Limited by homogeneous spin decoherence (T_2) and longitudinal relaxation (T_1)
Frequency/ bandwidth	0 to $\sim$100 kHz (pulsed), 0 to $\sim$10 kHz (CW)	Center freq: $\sim$1 kHz to $\sim$10 MHz; bandwidth: $\lesssim$100 kHz
Example magnetic sensing applications	Biocurrent detection; magnetic particle tracking; magnetic imaging of rocks and meteorites, magnetic nanoparticles in biological systems, and electrical current flow in materials; magnetic anomaly detection, navigation	Single biomolecule and protein detection; nanoscale nuclear magnetic resonance and electron spin resonance; magnetic resonant phenomena in materials, noise spectroscopy

Table 1.4.1: Performance metrics and selected applications of broadband DC and AC sensing protocols employing NV^- ensembles in diamond. T_1 relaxometry methods are not considered.

of the magnetic field but rather the field projection along its own symmetry axis, defined by the line connecting the nitrogen and the vacancy. In a typical NV^- ensemble with no preferential orientation [96], the four crystallographic NV^- symmetry axes are equally populated [3]. An ensemble NV-diamond magnetometer can be set up to be sensitive to the magnetic field projection along a single NV^- axis or along a vector that equally projects onto two or more of the NV^- axes. Because the four NV^- axes form a basis set that spans three-dimensional space, a local magnetic field's magnitude and direction can be reconstructed from its measured projections onto the NV^- axes [49, 50]. We distinguish magnetometers that measure a single magnetic field projection from vectors that reconstruct both the fields magnitude and direction as vector projection magnetometers and full vector magnetometers, respectively.

An example demonstration of vector projection magnetometry is shown in Figure 1.4.1. Here, a wire-like magnetic field source oriented at angle α with respect to the direction of maximum magnetic field sensitivity (in this case the x-direction), generating a field with magnitude $B(t)$ and direction transverse to its orientation direction,

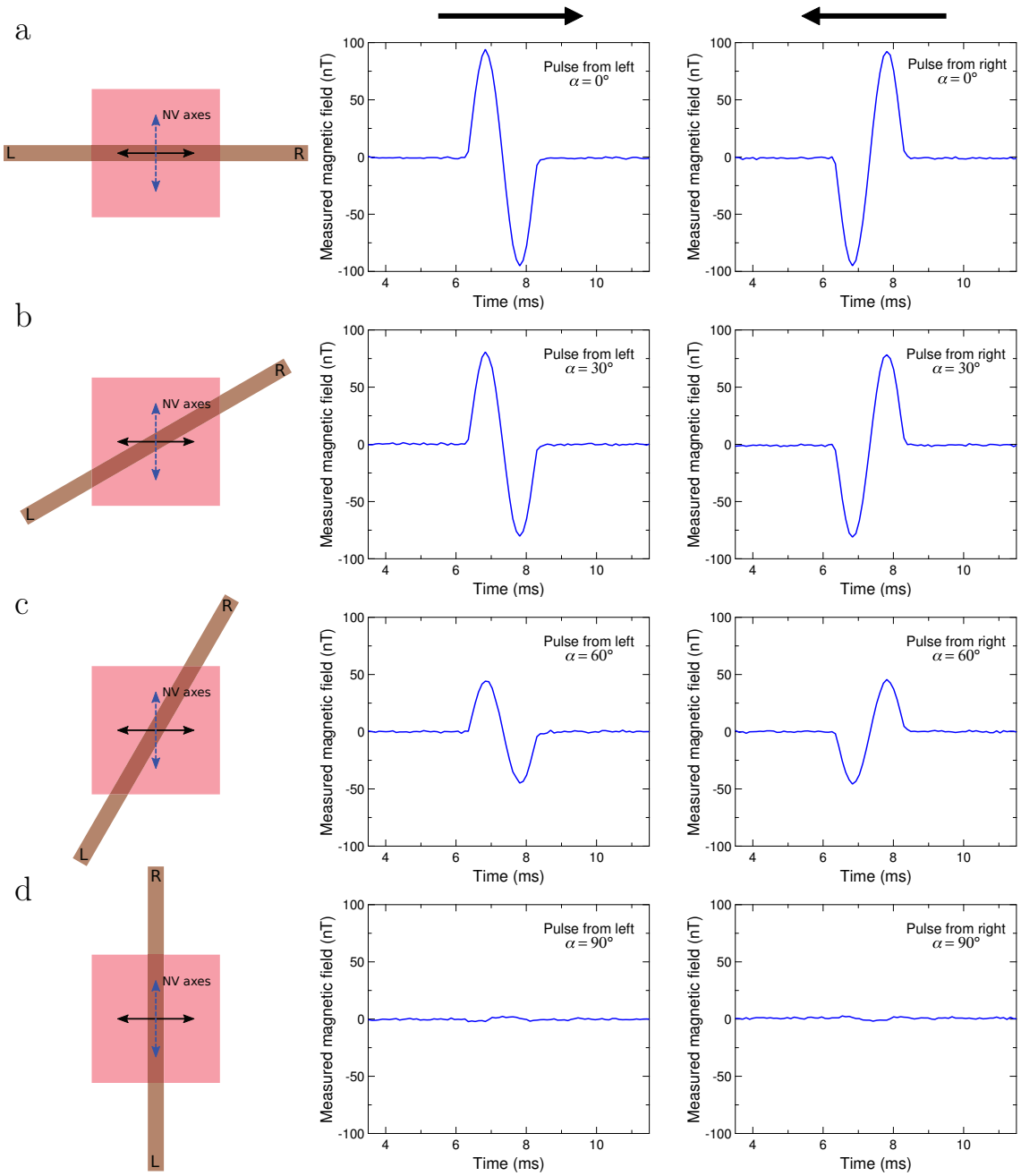

Figure 1.4.1: Vector projection magnetometry demonstration. Measured magnetic fields from biphasic current pulses (with positive polarity first) sent through copper wire positioned on surface of NV-diamond magnetic sensor employed in Ref. [24] (see Chapter 3) at angles (a), $\alpha = 0$ °, (b) $\alpha = 30$ °, (c) $\alpha = 60$ °, and (d) $\alpha = 90$ ° with respect to the maximum sensitivity angle (defined to be $\alpha = 0$ °). For each angle: cartoons (left column) give orientation of wire on diamond surface, where blue dashed lines indicate two NV^- axes used for sensing; and data is shown for current pulses initiated from left (middle column) and right (right column). For a current pulse producing a magnetic field $B(t) = 94$ nT perpendicular to the wire at the NV^- layer, detected signal depends on α as $B_x(t) = B(t)\cos(\alpha)$. Projected pulse propagation direction along x-axis (indicated by black arrows in left column cartoons) can be determined from the polarity of the magnetic signal for all α except 90°, where $B_x(t)$ goes to zero. Each magnetic trace is an average of $N_{\text{avg}} = 32$ trials.

results in a detected magnetic field reduced by a factor $\cos(\alpha)$: $B_x(t) = B(t)\cos(\alpha)$.

For the demonstration in Figure 1.4.1, a current-carrying copper wire is oriented at a variety of angles α, and for each measurement a single-period pulse of a sine wave with frequency 512 Hz is sent through the wire, resulting in a 94 nT peak amplitude magnetic field at the NV$^-$ sensing layer (the same diamond sample and magnetometry setup employed in Ref. [24] and described in Chapter 3). For any orientation in the plane except for $\alpha = 90°$, the magnetic field projection along the x-axis of the magnetometer is nonzero. If the expected signal size for $\alpha = 0°$ is known *a priori*, the angle α can be determined from a measurement of $B_x(t)$.

For full vector magnetometry, the magnetic field's magnitude and angle are determined, often by performing a series of projective field measurements along multiple axes. In Chapter 4 we introduce a technique to perform these projective field measurements simultaneously using a single NV-diamond sensor and a single optical detector.

1.5 Magnetic field measurement and sensitivity

The spin-projection-noise-limited sensitivity of an ensemble magnetometer consisting of N non-interacting $S = 1/2$ spins is approximately given by [1, 3]

$$\eta_{\mathrm{sp}}^{\mathrm{ensemble}} \approx \frac{\hbar}{g_e \mu_B} \frac{1}{\sqrt{N\tau}}, \tag{1.3}$$

where $g_e \approx 2.003$ is the NV$^-$ center's electronic g-factor [8], μ_B is the Bohr magneton, $\hbar$ is the reduced Planck constant, and τ is the free precession (i.e., interrogation) time per measurement. To generalize to higher-multiplicity spins ($S \geqslant 1$) where the m_s states used for the interferometry measurement differ by $\Delta m_s \geqslant 2$, the expression for $\eta_{\mathrm{sp}}^{\mathrm{ensemble}}$ is multiplied by the factor $1/\Delta m_s$.

To achieve projection-noise-limited sensitivity, the tools for manipulating and measuring the spins (MW fields and optical photons in the case of NV$^-$ centers) must not interfere with the magnetic field interrogation. This requires use of pulsed magne-

tometry schemes such as Ramsey's separated oscillatory field method [97], henceforth called Ramsey magnetometry. In this method, which is depicted schematically in Figure 1.5.3a, the spins interrogate the magnetic field for a free precession interval during which no external electromagnetic fields are applied. The free precession time is chosen for optimal sensitivity at a value close to the characteristic decay time T_2^* of the Ramsey fringes (see Figure 1.5.3b and Section 2.1.7). Here we derive the state evolution and projection-noise-limited sensitivity for a Ramsey magnetometry measurement.

1.5.1 Ramsey DC magnetic field measurement

The following is a derivation of a Ramsey-type pulsed magnetometry sequence (see Figure 1.5.3) using a magnetic dipole moment. Here the magnetic moment is taken to be an NV$^-$ center's ground-state electronic spin, although this discussion applies to any two-level system sensitive to magnetic fields, including atomic vapors and other solid state defects. Although the NV$^-$ ground state spin is a triplet with $S = 1$, a bias magnetic field B_0 can be applied along the NV$^-$ symmetry axis to split the $m_s = +1$ and $m_s = -1$ energy levels so that resonant MWs may selectively drive the $m_s = 0$ to $m_s = +1$ (or $m_s = 0$ to $m_s = -1$) transition. Any off-axis magnetic field component $B_\perp$ can be ignored so long as $(\gamma_e B_\perp)^2/[(2\pi D)^2 \pm (\gamma_e B_0)^2] \ll 1$, where $D = 2.87$ GHz is the zero-field splitting and $\gamma_e = g_e \mu_B/\hbar$ is the gyromagnetic ratio of the NV$^-$ electronic spin. Here the NV$^-$ center's nuclear spin is also ignored as well as static electric or strain fields. This two-level subspace can be described as a pseudo-spin-$\frac{1}{2}$ system with $|m_s = +1\rangle = |\uparrow\rangle$ and $|m_s = 0\rangle = |\downarrow\rangle$ and Hamiltonian

$$\begin{aligned} H &= (2\pi D + \gamma_e B) S_z \\ &= \frac{\hbar}{2} \begin{pmatrix} 2\pi D + \gamma_e B & 0 \\ 0 & -2\pi D - \gamma_e B \end{pmatrix}, \end{aligned} \tag{1.4}$$

where S_z is the operator for the z-projection of the pseudo-spin; and $B = B_0 + B_{\text{sense}}$ is the total magnetic field projection along the NV$^-$ symmetry axis, taken here to be

the z-axis, which is the sum of the applied bias field and an unknown DC field to be sensed. Here terms in the Hamiltonian proportional to the identity matrix have been dropped, as they introduce only a global phase to the states' time evolution. In the bias field B_0 the spin resonance frequency is $\omega_0 = 2\pi D + \gamma_e B_0$. Spin operators are expressed in the S_z basis in terms of the Pauli matrices $\vec{S} = \frac{\hbar}{2}\vec{\sigma}$, yielding

$$H = \frac{\hbar\omega_0}{2}\sigma_z + \frac{\hbar}{2}\gamma_e B_{\text{sense}}\sigma_z. \tag{1.5}$$

As described herein, a Ramsey sequence consists of two $\pi/2$-pulses of an oscillating magnetic field resonant with the transition between $|\downarrow\rangle$ and $|\uparrow\rangle$, which are separated by a free precession time τ. The spin state evolution on the Bloch sphere is shown in Figure 1.5.1. The sequence begins at time $t = 0$, with the spin polarized to $|\psi(0)\rangle = |\downarrow\rangle$. An oscillating magnetic field oriented perpendicular to the NV$^-$ symmetry axis $\vec{B}_1(t) = B_1\cos(\omega t)\hat{y}$ with angular frequency $\omega \approx \omega_0$ is turned on abruptly. Without loss of generality $\vec{B}$ is assumed to be polarized along the y-axis. For $B_1 \gg B_{\text{sense}}$, the second term in H can be dropped, thereby ignoring effects of the unknown DC sensing field while the oscillating field is on. The Hamiltonian for the system driven by this oscillating field, denoted H_{driv}, becomes

$$H_{\text{driv}} = \frac{\hbar\omega_0}{2}\sigma_z + \frac{\hbar}{2}\gamma_e B_1\cos(\omega t)\sigma_y. \tag{1.6}$$

We proceed in the interaction picture, with $H_0 = \frac{\hbar\omega_0}{2}\sigma_z$ and $H_1 = \frac{\hbar}{2}\gamma_e B_1\cos(\omega t)\sigma_y$. This step is equivalent to transforming into a rotating frame with angular frequency ω_0. The interaction-picture state vector $|\tilde{\psi}(t)\rangle$ is defined in terms of the Schrödinger-picture state vector $|\psi(t)\rangle$ as $|\tilde{\psi}(t)\rangle = U_0^\dagger(t)|\psi(t)\rangle$ with $U_0(t) = e^{-iH_0 t/\hbar}$. This state evolves according to $|\tilde{\psi}(t)\rangle = \tilde{U}_1(t)|\tilde{\psi}(0)\rangle$ where $\tilde{U}_1(t) = e^{-i\tilde{H}_1 t/\hbar}$, with

$$\begin{aligned}\tilde{H}_1 &= U_0^\dagger(t)H_1U_0(t)\\ &= \frac{\hbar}{4}\,\gamma_e B_1\begin{pmatrix} 0 & -i(e^{-i(\omega_0+\omega)t}+e^{-i(\omega_0-\omega)t}) \\ i(e^{i(\omega_0-\omega)t}+e^{i(\omega_0+\omega)t}) & 0\end{pmatrix}.\end{aligned} \tag{1.7}$$

The transformed interaction Hamiltonian $\tilde{H}_1$ is simplified by assuming resonant driving of the spin with $\omega = \omega_0$ and by making the rotating wave approximation, dropping off-resonant terms rotating at $2\omega_0$, to yield

$$\tilde{H}_1 \approx \frac{\hbar}{4}\gamma_e B_1 \sigma_y. \tag{1.8}$$

This Hamiltonian causes the spin system to undergo Rabi oscillations at angular frequency $\Omega = \gamma_e B_1/2$. The oscillating field $\vec{B}_1(t)$ is turned off abruptly after a duration $\tau_{\frac{\pi}{2}} = \frac{\pi}{2\Omega} = \frac{\pi}{\gamma_e B_1}$, so that

$$\begin{aligned}
|\tilde{\psi}(\tau_{\frac{\pi}{2}})\rangle &= \exp\left(-i\frac{\gamma_e B_1 \sigma_y \tau_{\frac{\pi}{2}}}{4}\right)|\tilde{\psi}(0)\rangle \\
&= \exp\left(-i\frac{\pi}{4}\sigma_y\right)|\downarrow\rangle \\
&= \frac{1}{\sqrt{2}}\begin{pmatrix} 1 & -1 \\ 1 & 1 \end{pmatrix}\begin{pmatrix} 0 \\ 1 \end{pmatrix} \\
&= \frac{1}{\sqrt{2}}\left(-|\uparrow\rangle + |\downarrow\rangle\right),
\end{aligned} \tag{1.9}$$

which uses the identity $e^{-i\theta\hat{n}\cdot\vec{\sigma}} = \cos(\theta)\, I - i\sin(\theta)\,(\hat{n}\cdot\vec{\sigma})$ where $\hat{n}$ is a unit vector on the Bloch sphere. This constitutes a $\pi/2$-pulse on the spin.

Next, the magnetic moment undergoes free precession in the absence of $\vec{B}_1(t)$ for a sensing time τ. During this time the system Hamiltonian returns to H from Equation 1.4. We continue to use the interaction picture with $H_0 = \frac{\hbar\omega_0}{2}\sigma_z$, and with new interaction Hamiltonian H_1' determined by $\vec{B}_{\text{sense}} = B_{\text{sense}}\hat{z}$ as

$$H_1' = \frac{\hbar}{2}\gamma_e B_{\text{sense}}\sigma_z. \tag{1.10}$$

Recognizing that H_1' commutes with H_0, the transformed interaction Hamiltonian $\tilde{H}_1' \equiv U_0^\dagger(t) H_1' U_0(t) = H_1'$, and thus the interaction-picture state vector $|\tilde{\psi}(t)\rangle$ evolves

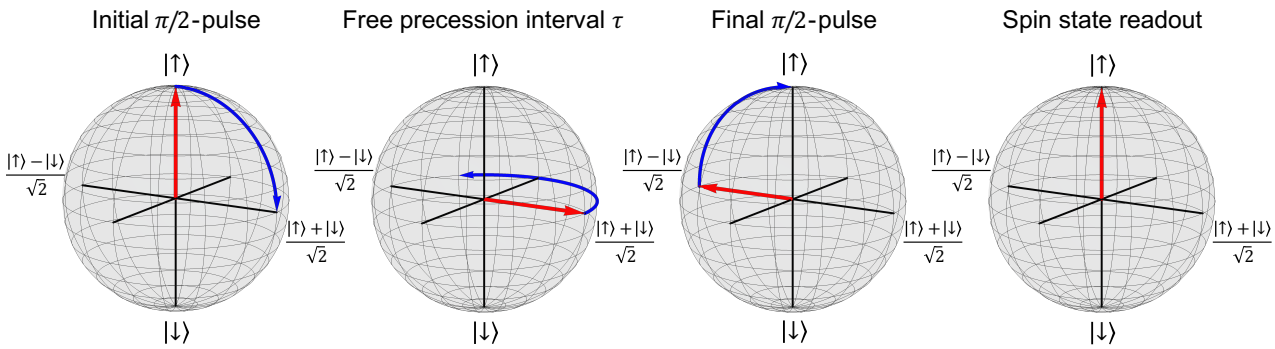

Figure 1.5.1: Bloch sphere depiction of Ramsey sequence. After initialization to the spin state $|\uparrow\rangle$, an oscillating magnetic field applies a $\pi/2$-pulse, causing the Bloch vector to undergo 1/4 of a Rabi oscillation and preparing a superposition of $|\uparrow\rangle$ and $|\downarrow\rangle$ spin states. Next, the Bloch vector undergoes free precession for duration τ, accumulating a phase ϕ proportional to the static magnetic field being sensed. After time τ, a second $\pi/2$-pulse maps the accumulated phase onto a population difference between the $|\uparrow\rangle$ and $|\downarrow\rangle$ states. Here, a $\phi = \pi$ phase accumulation is shown, which maps back to the state $|\uparrow\rangle$ when the relative angle α between the oscillating magnetic field vectors for the initial and final $\pi/2$ pulses is chosen to be 0 (see text). Finally, a projective spin state measurement detects the population difference, allowing determination of the static magnetic field sensed by the spin.

under H_1' into

$$\begin{aligned} |\tilde{\psi}(\tau_{\pi/2}+\tau)\rangle &= e^{-iH_1'\tau/\hbar}|\tilde{\psi}(\tau_{\pi/2})\rangle \\ &= \frac{1}{\sqrt{2}}(-e^{-i\phi/2}|\uparrow\rangle + e^{i\phi/2}|\downarrow\rangle), \end{aligned} \tag{1.11}$$

where $\phi = \gamma_e B_{\text{sense}}\tau$ is the phase accumulated due to B_{sense}. (If $B_{\text{sense}} = 0$, the state vector $|\tilde{\psi}(t)\rangle$ accumulates no phase, as H_1' vanishes and the entire Hamiltonian $H = H_0$.)

To complete the sequence, a second oscillating field $\vec{B_2}(t) = \vec{B_2}\cos(\omega_0 t)$, is applied for a $\pi/2$-pulse. As with the first $\pi/2$-pulse, $B_{\text{sense}} \ll B_2$ is assumed so that additional spin state evolution due to B_{sense} can be ignored. The polarization of $\vec{B_2}(t)$ is chosen to be along $\hat{n}$ in the x-y plane at an angle ϑ with respect $\hat{y}$, the polarization direction of the first $\pi/2$-pulse $\vec{B_1}(t)$. After again making the rotating wave approximation, the

transformed interaction Hamiltonian, $\tilde{H}_1''$ is given by

$$\tilde{H}_1'' \approx \frac{\hbar}{4}\gamma_e B_2 \left(\cos\left(\vartheta\right)\sigma_y - \sin\left(\vartheta\right)\sigma_x\right) \tag{1.12}$$

and

$$\begin{aligned}
&|\tilde{\psi}(\tau_{\frac{\pi}{2}} + \tau + \tau_{\frac{\pi}{2}})\rangle \\
&= e^{-i\tilde{H}_1''\tau_{\frac{\pi}{2}}/\hbar}|\tilde{\psi}(\tau_{\frac{\pi}{2}} + \tau)\rangle \\
&= \frac{1}{\sqrt{2}}\begin{pmatrix} 1 & -e^{-i\vartheta} \\ e^{i\vartheta} & 1 \end{pmatrix}\cdot\frac{1}{\sqrt{2}}\begin{pmatrix} -e^{-i\phi/2} \\ e^{i\phi/2} \end{pmatrix},
\end{aligned} \tag{1.13}$$

which, up to a global phase, is equal to

$$|\tilde{\psi}\rangle = \cos\left(\frac{\phi-\vartheta}{2}\right)|\uparrow\rangle - ie^{i\vartheta}\sin\left(\frac{\phi-\vartheta}{2}\right)|\downarrow\rangle. \tag{1.14}$$

The phase accumulated during τ is thus mapped on to a population difference between the $|\uparrow\rangle$ and $|\downarrow\rangle$ states. The value of B_{sense} is determined by measuring the observable $\tilde{S}_z = S_z$ and relating that to ϕ.

$$\begin{aligned}
\langle\tilde{S}_z\rangle &= \frac{\hbar}{2}\langle\tilde{\psi}|\sigma_z|\tilde{\psi}\rangle \\
&= \frac{\hbar}{2}\left(\cos^2\left(\frac{\phi-\vartheta}{2}\right) - \sin^2\left(\frac{\phi-\vartheta}{2}\right)\right) \\
&= \frac{\hbar}{2}\cos(\phi-\vartheta) \\
&= \frac{\hbar}{2}\cos(\gamma_e B_{\text{sense}}\tau - \vartheta).
\end{aligned} \tag{1.15}$$

The cosinusoidal fluctuations in $\langle\tilde{S}_z\rangle$ are termed Ramsey fringes. Common choices of ϑ are 0 and $\pi/2$. The case where $\vartheta = 0$ (respectively, $\vartheta = \pi/2$) is commonly called cosine (sine) magnetometry, as the observable $\langle\tilde{S}_z\rangle$ varies as the cosine (sine) of B_{sense} for fixed τ. For ensembles of NV$^-$ centers, $\langle\tilde{S}_z\rangle$ is measured by reading out the spin-state-dependent fluorescence over a predetermined readout window of several hundred nanoseconds (see Figure 1.5.2).

For small B_{sense} such that $\phi \ll 2\pi$, Equation 1.15 can be linearized about $\phi = 0$ for any value of ϑ except $\vartheta = 0$. The values of B_{sense} and ϕ can then be related to a small change in the observable $\delta\langle S_z\rangle = \langle S_z\rangle|_\phi - \langle S_z\rangle|_0$ as follows:

$$\begin{aligned} B_{\text{sense}} = \frac{\phi}{\gamma_e \tau} &\approx \frac{1}{\gamma_e \tau} \frac{\delta\langle S_z\rangle}{\frac{d\langle S_z\rangle}{d\phi}|_0} \\ &\approx \frac{1}{\gamma_e \tau} \frac{\frac{2}{\hbar}\langle S_z\rangle|_\phi - \cos(\vartheta)}{\sin(\vartheta)}. \end{aligned} \tag{1.16}$$

For $\vartheta = 0$ the linear term $\delta\langle S_z\rangle$ vanishes, as the slope of the Ramsey fringe goes to zero; a small B_{sense} produces to lowest order a quadratic change in $\langle \tilde{S}_z\rangle$. For $\vartheta = \pi/2$, the slope of the Ramsey fringe is maximized, and Equation 1.16 reduces to

$$B_{\text{sense}} \approx \frac{2}{\hbar \gamma_e \tau} \langle S_z\rangle. \tag{1.17}$$

1.5.2 Spin-projection-noise-limited sensitivity

The spin-projection-noise-limited magnetic field sensitivity is defined as the field δB at which the size of the signal $\delta\langle S_z\rangle$ due to δB is equal to the uncertainty in the signal, i.e., when $\delta\langle S_z\rangle = \Delta S_z$, where $\Delta S_z = \sqrt{\langle S_z^2\rangle - \langle S_z\rangle^2}$ is the standard deviation of a series of identical measurements of δB. For a precession time τ, this minimum field is

$$\delta B_{\text{sp}} = \frac{1}{\gamma_e \tau} \frac{\Delta S_z}{|\frac{d\langle S_z\rangle}{d\phi}|}. \tag{1.18}$$

When M uncorrelated consecutive measurements are taken, each with precession time τ over a total measurement time t_{meas}, the minimum field is reduced by the factor $\sqrt{1/M} = \sqrt{\tau/t_{\text{meas}}}$, yielding

$$\delta B_{\text{sp}} = \frac{1}{\gamma_e} \frac{1}{\sqrt{\tau t_{\text{meas}}}} \frac{\Delta S_z}{|\frac{d\langle S_z\rangle}{d\phi}|}. \tag{1.19}$$

The spin-projection-noise-limited sensitivity of a Ramsey magnetometry measure-

ment is then

$$\eta_{\rm sp} = \delta B_{\rm sp}\sqrt{t_{\rm meas}} = \frac{1}{\gamma_e\sqrt{\tau}}\frac{\Delta S_z}{|\frac{d\langle S_z\rangle}{d\phi}|}. \tag{1.20}$$

The quotient $\frac{\Delta S_z}{|\frac{d\langle S_z\rangle}{d\phi}|}$ is calculated:

$$\langle S_z\rangle = \frac{\hbar}{2}\cos(\phi-\vartheta), \tag{1.21}$$

$$\frac{d\langle S_z\rangle}{d\phi} = -\frac{\hbar}{2}\sin(\phi-\vartheta), \tag{1.22}$$

$$\begin{aligned}\langle S_z^2\rangle &= \frac{\hbar^2}{4}\langle\psi|\sigma_z^2|\psi\rangle \\ &= \frac{\hbar^2}{4}\left(\cos^2\left(\frac{\phi-\vartheta}{2}\right)+\sin^2\left(\frac{\phi-\vartheta}{2}\right)\right) \\ &= \frac{\hbar^2}{4},\end{aligned} \tag{1.23}$$

$$\begin{aligned}\Delta S_z &= \sqrt{\langle S_z^2\rangle - \langle S_z\rangle^2} \\ &= \sqrt{\frac{\hbar^2}{4}\left(1-\cos^2(\phi-\vartheta)\right)} \\ &= \frac{\hbar}{2}|\sin(\phi-\vartheta)|,\end{aligned} \tag{1.24}$$

$$\frac{\Delta S_z}{|\frac{d\langle S_z\rangle}{d\phi}|} = 1. \tag{1.25}$$

This result is independent of the value of ϕ or ϑ. The projection noise is always equal to the slope of the Ramsey fringe. That is, a magnetometer limited by spin projection noise has the same signal-to-noise ratio regardless of where on the Ramsey fringe the measurement is taken. The sensitivity at the spin projection noise limit, (also called the standard quantum limit) is simply

$$\eta_{\rm sp} = \delta B_{sp}\sqrt{t_{\rm meas}} = \frac{1}{\gamma_e\sqrt{\tau}}. \tag{1.26}$$

For sensing with an ensemble of N independent spins, the sensitivity $\eta_{\mathrm{sp}}^{\mathrm{ensemble}} = \eta_{\mathrm{sp}}/\sqrt{N}$ such that

$$\eta_{\mathrm{sp}}^{\mathrm{ensemble}} = \frac{1}{\gamma_e \sqrt{N\tau}}. \tag{1.27}$$

1.5.3 Photon-shot-noise-limited sensitivity

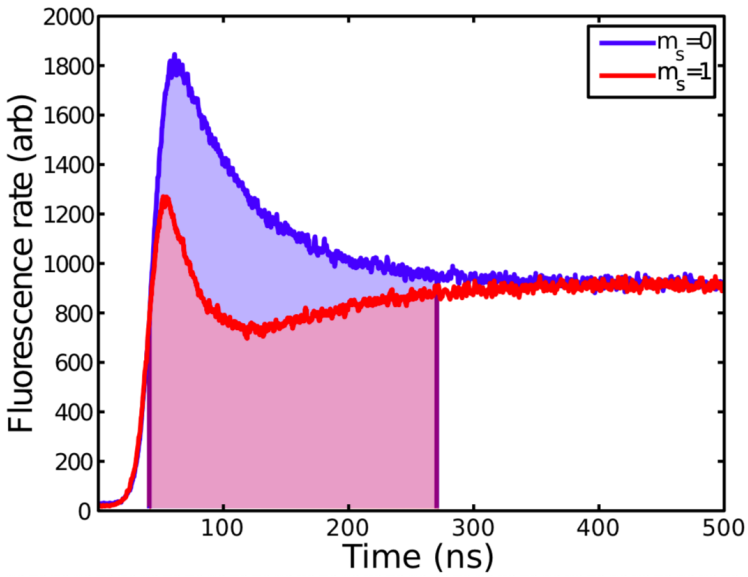

Figure 1.5.2: Fluorescence of the NV$^-$ spin states. NV$^-$ centers prepared in the $m_s = 0$ state emit more photons than centers prepared in the $m_s = \pm 1$ states. This spin-dependent fluorescence forms the basis of conventional NV$^-$ readout. Data courtesy of Brendan Shields.

Magnetic field sensors based on ensembles of NV$^-$ centers ensemble magnetometers suffer from an major experimental non-ideality that deteriorates the achievable magnetic field sensitivity. Namely, while the above discussion considered a direct measurement of S_z, the measurement technique for NV$^-$ spins - optical readout - indirectly probes the spin through measuring the spin-state-dependent PL in the 600 - 850 nm band. This conventional optical readout does not allow single-shot determination of the NV$^-$ spin state to the spin projection limit. Therefore, shot noise on the collected PL photons must be incorporated into the measurement uncertainty and sensitivity.

As described previously in Section 1.3 Conventional NV$^-$ optical readout exploits the $m_s = \pm 1$ states' higher likelihood to enter the singlet-state cascade relative to the $m_s = 0$ state (see Table 1.7.1). An NV$^-$ center that enters the singlet state cascade

does not fluoresce in the 600 - 850 nm band, whereas an NV^- center decaying directly to the spin-triplet ground state can continue cycling between the ground and excited triplet states, producing PL in the 600 - 850 nm band. Thus, population originally in the $m_s = \pm 1$ states may be distinguished from the $m_s = 0$ states by relative lower PL in the 600 - 850 nm band, as shown in Figure 1.5.2.

To phenomenologically introduce Poisson fluctuations from the PL photons into the sensitivity, the optical readout procedure is treated as a mapping of the spin eigenstates onto two light field modes: $|m_s = +1\rangle = |\uparrow\rangle \rightarrow |\beta\rangle$ and $|m_s = 0\rangle = |\downarrow\rangle \rightarrow |\alpha\rangle$, where $|\alpha\rangle$ and $|\beta\rangle$ are coherent states defined by $\hat{a}|\alpha\rangle = \alpha|\alpha\rangle$ and $\hat{b}|\beta\rangle = \beta|\beta\rangle$. We define $a = |\alpha|^2$ as the mean number of photons in $|\alpha\rangle$ and $b = |\beta|^2$ as the mean number of photons in $|\beta\rangle$. Since the $|m_s = 0\rangle$ state produces more fluorescent photons during readout than the $|m_s = +1\rangle$ state, $a > b$. The final spin state $|\tilde{\psi}\rangle$ from Equation 1.14 is mapped onto the photon field state

$$|\psi_{\text{ph}}\rangle = \cos\left(\frac{\phi - \vartheta}{2}\right)|\beta\rangle - ie^{i\vartheta}\sin\left(\frac{\phi - \vartheta}{2}\right)|\alpha\rangle. \tag{1.28}$$

A measurement of the spin state has become a measurement of the number of photons collected from the two light fields $\hat{N} = \hat{a}^\dagger\hat{a} + \hat{b}^\dagger\hat{b}$. Defining $\varphi = \phi - \vartheta$,

$$\begin{aligned}\langle\hat{N}\rangle &= \langle\psi_{\text{ph}}|(\hat{a}^\dagger\hat{a} + \hat{b}^\dagger\hat{b})|\psi_{\text{ph}}\rangle = b\cos^2\left(\frac{\varphi}{2}\right) + a\sin^2\left(\frac{\varphi}{2}\right) \\ &= b\left(\frac{1 + \cos(\varphi)}{2}\right) + a\left(\frac{1 - \cos(\varphi)}{2}\right).\end{aligned} \tag{1.29}$$

where the two light fields are assumed to be noninterfering so that $\hat{a}|\beta\rangle = \hat{b}|\alpha\rangle = 0$ and $\langle\alpha|\beta\rangle = \langle\beta|\alpha\rangle = 0$.

The sensitivity of a magnetometer employing optical readout is written in the same way as the spin-projection-noise-limited sensitivity given in Equation 1.20, but with the observable S_z replaced by $\hat{N}$:

$$\eta_{\text{opt}} = \delta B_{\text{opt}}\sqrt{t_{\text{meas}}} = \frac{1}{\gamma_e\sqrt{\tau}}\frac{\Delta\hat{N}}{\left|\frac{d\langle\hat{N}\rangle}{d\phi}\right|}, \tag{1.30}$$

where $\Delta\hat{N} = \sqrt{\langle\hat{N}^2\rangle - \langle\hat{N}\rangle^2}$. The derivative of $\langle\hat{N}\rangle$ with respect to ϕ is

$$\frac{d\langle\hat{N}\rangle}{d\phi} = \frac{d\langle\hat{N}\rangle}{d\varphi} = \frac{(a-b)}{2}\sin(\varphi). \tag{1.31}$$

Recalling the operator commutation relation $[\hat{a}, \hat{a}^\dagger] = 1$, $\Delta\hat{N}$ is calculated:

$$\begin{aligned}
\langle\hat{N}^2\rangle &= \langle(\hat{a}^\dagger\hat{a} + \hat{b}^\dagger\hat{b})(\hat{a}^\dagger\hat{a} + \hat{b}^\dagger\hat{b})\rangle \\
&= \langle\psi_{\text{ph}}|(\hat{a}^\dagger\hat{a}\hat{a}^\dagger\hat{a} + \hat{b}^\dagger\hat{b}\hat{b}^\dagger\hat{b})|\psi_{\text{ph}}\rangle \\
&= \langle\psi_{\text{ph}}|(\hat{a}^\dagger(\hat{a}^\dagger\hat{a} + 1)\hat{a} + \hat{b}^\dagger(\hat{b}^\dagger\hat{b} + 1)\hat{b})|\psi_{\text{ph}}\rangle \\
&= b(b+1)\left(\frac{1+\cos(\varphi)}{2}\right) + a(a+1)\left(\frac{1-\cos(\varphi)}{2}\right),
\end{aligned} \tag{1.32}$$

$$\begin{aligned}
\langle\hat{N}\rangle^2 = b^2\left(\frac{1/2+\cos(\varphi)}{2}\right) + a^2\left(\frac{1/2-\cos(\varphi)}{2}\right) \\
+ \left(\frac{b^2}{4} + \frac{a^2}{4}\right)\cos^2(\varphi) + \frac{ba}{2}\sin^2(\varphi),
\end{aligned} \tag{1.33}$$

$$\begin{aligned}
\Delta\hat{N} &= \sqrt{\langle\hat{N}^2\rangle - \langle\hat{N}\rangle^2} \\
&= \sqrt{\left(\frac{b^2}{4} - \frac{ba}{2} + \frac{a^2}{4}\right)\sin^2(\varphi) + b\left(\frac{1+\cos(\varphi)}{2}\right) + a\left(\frac{1-\cos(\varphi)}{2}\right)} \\
&= \sqrt{\frac{(a-b)^2}{4}\sin^2(\varphi) + b\cos^2\left(\frac{\varphi}{2}\right) + a\sin^2\left(\frac{\varphi}{2}\right)}.
\end{aligned} \tag{1.34}$$

Using Equations 1.34 and 1.31, the sensitivity reduces to

$$\frac{\Delta\hat{N}}{|\frac{d\langle N\rangle}{d\phi}|} = \sqrt{\frac{\frac{(a-b)^2}{4}\sin^2(\varphi) + b\cos^2\left(\frac{\varphi}{2}\right) + a\sin^2\left(\frac{\varphi}{2}\right)}{\frac{(a-b)^2}{4}\sin^2(\varphi)}}. \tag{1.35}$$

Note that in the case of very strong coherent states, such that $a(a+1) \approx a^2$ and $b(b+1) \approx b^2$, Equation 1.35 approaches the spin-projection noise limit of $\frac{\Delta\hat{N}}{|\frac{d\langle\hat{N}\rangle}{d\phi}|} = 1$.

For the case $\varphi = \pi/2$, the sensitivity is optimized, yielding

$$\frac{\Delta\hat{N}}{|\frac{d\langle\hat{N}\rangle}{d\phi}|} = \sqrt{\frac{\frac{(a-b)^2}{4} + \frac{a+b}{2}}{\frac{(a-b)^2}{4}}} = \sqrt{1 + \frac{2(a+b)}{(a-b)^2}}. \tag{1.36}$$

We identify $C = \frac{a-b}{a+b}$ as the measurement contrast, (i.e., the fringe visibility), and $n_{\text{avg}} = \frac{a+b}{2}$ as the average number of photons collected per measurement (per spin, if the measurement is on an ensemble). The contrast C depends on the degree of initial polarization of the spin state and the readout duration. Although sub-optimal NV$^-$ spin initialization and readout times t_I and t_R can degrade the value of C, it is henceforth assumed that t_I and t_R are optimized to avoid this effect.

Neglecting contrast degradation due to loss of spin coherence, the sensitivity for a Ramsey measurement on a single spin with both photon shot noise and spin-projection noise is given by

$$\eta_{\text{opt}} = \delta B_{\text{opt}}\sqrt{t_{\text{meas}}} = \frac{1}{\gamma_e\sqrt{\tau}}\sqrt{1 + \frac{1}{C^2 n_{\text{avg}}}}. \tag{1.37}$$

When sensing with an ensemble of N independent spins, the sensitivity is given by

$$\eta_{\text{opt}}^{\text{ensemble}} = \frac{\eta_{\text{opt}}}{\sqrt{N}}. \tag{1.38}$$

In conventional NV$^-$ optical readout, the $\sim 140 - 200$ ns [98, 99, 23] spin-singlet cascade lifetime and limited differences in $m_s = \pm 1$ and $m_s = 0$ decay behavior ensures that contrast is low ($\lesssim 15\%$). Moreover, the number of photons n_{avg} collected per spin is limited by the ratio of the optical cycling rate to the singlet-state decay rate to be $\lesssim 15$ [3, 100], and is often much less due to imperfect collection efficiency. Thus, $C^2 n_{\text{avg}} \ll 1$, and shot noise becomes the dominant contribution to the magnetic field sensitivity, with

$$\eta_{\text{shot}} \approx \frac{1}{\gamma_e}\frac{1}{C\sqrt{n_{\text{avg}}\tau}}. \tag{1.39}$$

and

$$\eta_{\text{shot}}^{\text{ensemble}} \approx \frac{1}{\gamma_e} \frac{1}{C\sqrt{N n_{\text{avg}} \tau}}. \tag{1.40}$$

In general, we quantify the added noise to a magnetic field measurement from photon shot noise or other imperfect readout with the parameter σ_R [101], such that $\sigma_R = 1$ corresponds to readout at the spin projection limit. This parameter is the inverse of the measurement fidelity: $\mathcal{F} \equiv 1/\sigma_R$. For readout in the presence of photon shot noise as described above, the value of σ_R is given by [3, 101]

$$\sigma_R = \sqrt{1 + \frac{2(a+b)}{(a-b)^2}} \tag{1.41}$$

$$= \sqrt{1 + \frac{1}{C^2 n_{\text{avg}}}}, . \tag{1.42}$$

This is a useful parameter to consider when seeking to improve magnetic field sensitivity, as it quantifies how far the sensitivity is from the standard quantum limit.

1.5.4 Sensitivity accounting for overhead time

The sensitivity equations above have neglected any optical initialization or readout time t_I and t_R, as well as the finite duration of the two $\pi/2$-pulses of the Ramsey sequence. Grouping all of these factors into an experimental dead time t_O, we find the sensitivity factor for M measurements each with sensing time τ over a total time t_{meas} is $\sqrt{1/M} = \sqrt{(\tau + t_O)/t_{\text{meas}}}$, yielding a sensitivity limited by shot noise and spin-projection noise of

$$\eta_{\text{opt}} = \delta B_{\text{opt}} \sqrt{t_{\text{meas}}} = \frac{\sigma_R}{\gamma_e} \frac{\sqrt{\tau + t_O}}{\tau}. \tag{1.43}$$

1.5.5 Sensitivity accounting for loss of phase coherence

A third factor that degrades the sensitivity and limits the optimal free-precession time τ of a measurement sequence is loss of spin phase coherence. For Ramsey-type pulsed magnetometry, (i.e., with no spin echo), the dephasing occurs with characteristic time

T_2^* (see Chapter 2) so that η is deteriorated by the factor

$$\frac{1}{e^{-(\tau/T_2^*)^p}}, \tag{1.44}$$

where the value of the stretched exponential parameter p depends on the origin of the dephasing (see Section 2.1.6). NV$^-$ spin resonance lineshapes with exactly Lorentzian profiles correspond to dephasing with $p = 1$, and spin resonance lineshapes with Gaussian profiles correspond to $p = 2$ (see Section 2.1.4).

We note that this factor degrades both the shot-noise and spin-projection-noise terms in the measurement sensitivity η_{opt}, an thus it must be included explicitly rather than incorporated into C. Thus, we should modify the Equations 1.37 - 1.43 by the expression in Equation 1.44, while noting that the value of T_2^* typically differs for measurements on single NV$^-$ centers compared to ensembles.

Finally, substituting $g_e\mu_B/\hbar$ for the NV$^-$ electron spin gyromagnetic ratio γ_e and generalizing to account for the possible use of the full spin-1 nature of the NV$^-$ center, where the m_s states used for the interferometry measurement can differ by $\Delta m_s = 2$ at most, the sensitivity for a Ramsey-type NV$^-$ broadband ensemble magnetometer [102] is written as

$$\eta_{\text{Ramsey}}^{\text{ensemble}} \approx \frac{\hbar}{g_e\mu_B} \times \frac{1}{\Delta m_s} \times \frac{\sigma_R}{\sqrt{N}} \times \frac{1}{e^{-(\tau/T_2^*)^p}} \times \frac{\sqrt{\tau + t_O}}{\tau}, \tag{1.45}$$

.

Again, in the limit of measurement contrast $C \ll 1$ and when the number of photons collected per NV$^-$ center per optical readout is much less than 1, σ_R is dominated by photon shot noise and can be approximated as $\sigma_R \approx \frac{1}{C\sqrt{n_{\text{avg}}}}$. Defining $\mathcal{N} = N n_{\text{avg}}$ to be the average number of photons detected per measurement from the ensemble of N NV$^-$ centers yields the following shot-noise-limited sensitivity equation for a Ramsey scheme [103]:

$$\eta_{\text{Ramsey}}^{\text{ensemble,shot}} \approx \frac{\hbar}{g_e\mu_B} \frac{1}{\Delta m_s} \frac{1}{C e^{-(\tau/T_2^*)^p} \sqrt{\mathcal{N}}} \frac{\sqrt{\tau + t_O}}{\tau}. \tag{1.46}$$

Henceforth we assume broadening mechanisms produce Lorentzian lineshapes, so that $p = 1$. For negligible t_O, the optimal measurement time is $\tau = T_2^*/2$, whereas for $t_O \gg T_2^*$, the optimal τ approaches T_2^* (see Section 2.1.7). Equation 1.46 illustrates the benefits attained by increasing the dephasing time T_2^*, the measurement contrast C, the number of NV$^-$ spin sensors N, and the average number of photons detected per NV$^-$ per measurement n_{avg}. Table 1.5.1 depicts example values of σ_R and $\mathcal{N}$ achieved using conventional optical readout in pulsed and CW magnetometry measurements, with both single NV$^-$ centers and ensembles. At present, conventional optical readout is insufficient to reach the spin projection limit for both single- and ensemble-NV$^-$ sensors.

In addition to Ramsey-type methods, other protocols allow measurement of DC magnetic fields. These alternative methods, including continuous-wave and pulsed optically detected magnetic resonance, offer reduced sensitivity compared to Ramsey-type sequences (for a fixed number of NV$^-$ centers addressed), as discussed in the following sections.

1.5.6 Readout SNR analysis from NV$^-$ rate equations

Here we numerically solve a system of equations approximating the NV$^-$ dynamics under optical excitation. We investigate the effect of excitation intensity on peak readout SNR and optimal readout pulse duration for Ramsey magnetometry sequences. As depicted in Figure 1.5.4, we describe the NV$^-$ electronic and spin energy levels and their transition dynamics by a simplified 5-level system, where Levels 1 and 2 represent the $m_s = 0$ and $m_s = \pm 1$ ground states (^{3}A$_2$), Levels 3 and 4 represent the $m_s = 0$ and $m_s = \pm 1$ electronic excited states (^{3}E), and Level 5 represents the singlet state manifold (^{1}A$_1 \rightarrow {}^1$E). We assume decay rates consistent with those measured in Refs. [111, 98, 99], which are reproduced in Table 1.7.1. The triplet excited state decay rates from Level 4 to 2 and from 3 to 1 are taken to be $\Gamma = 67\ \mu\mathrm{s}^{-1}$. We assume no direct decay from Level 4 to 1 or from 3 to 2. Decay rates to and from Level 5 are expressed in terms of Γ by pre-factors $\kappa_{i,j}$, where $\kappa_{4,5} = 1$, $\kappa_{3,5} = 1/7$, $\kappa_{5,2} = 1/50$, and $\kappa_{5,1} = 1/25$ based on approximate averages of the rates reported in Table 1.7.1.

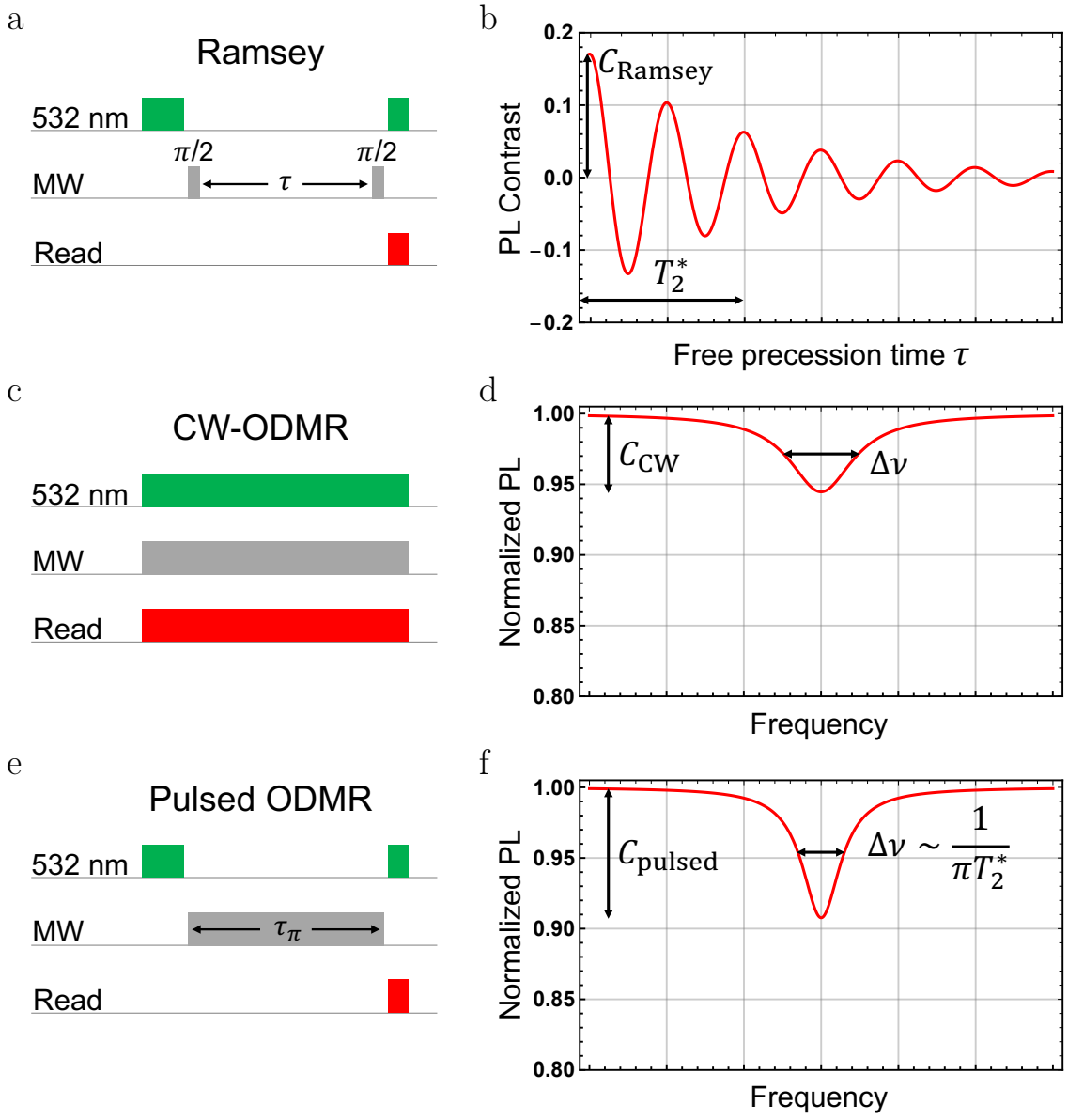

Figure 1.5.3: Overview of Ramsey, CW-ODMR, and pulsed ODMR magnetometry protocols. a) Schematic of Ramsey magnetometry protocol. b) Cartoon of free induction decay associated with a Ramsey protocol versus free precession time τ. Fringes exhibit contrast C_{Ramsey} and decay exponentially with dephasing time T_2^*. c) Schematic of CW-ODMR sensing protocol. d) Cartoon of CW-ODMR spectrum with contrast C_{CW} and linewidth $\Delta\nu$. e) Schematic of pulsed ODMR sensing protocol with MW π-pulse time $\tau_\pi \sim T_2^*$. f) Cartoon of pulsed ODMR spectrum with contrast C_{pulsed} and linewidth $\Delta\nu \sim 1/(\pi T_2^*)$.

Ref.	Readout method	No. NV$^-$ centers	σ_R	$\mathcal{N}$ [cts/measurement]
[101]	conventional	single	10.6	9.45×10^5 cps $\times\, t_R$
[101]	spin-to-charge conversion	single	2.76	-
[32]	conventional	single	35	$\sim 10^5$ cps $\times\, t_R$
[32]	ancilla-assisted	single	5	-
[104]	conventional	single	80	0.01
[105]	conventional	single	48	0.04
[105]	spin-to-charge conversion	single	3	-
[106]	conventional	single	54	0.022
[106]	spin-to-charge conversion	single	5	-
[107]	ancilla-assisted	single	1.1	-
[108]	conventional	ensemble	67	2×10^8
[109]	conventional	ensemble	~ 1000	10^{12}
[110]	NIR absorption†	ensemble	65	-
[24]	conventional†	ensemble	$\sim$ 5000	-
[25]	conventional†	ensemble	$\sim$ 5000	-

Table 1.5.1: Example literature values for readout schemes employing conventional optical readout or alternative techniques. The parameter σ_R characterizes the factor above spin projection noise and $\mathcal{N}$ is the average number of photons collected per measurement. Conventional NV$^-$ readout is unable to reach the spin projection limit ($\sigma_R = 1$), whereas alternative schemes can allow readout to approach this limit. The best demonstrated pulsed readout methods with ensembles are presently $\sim 100\times$ away from the spin projection limit. The symbol † denotes non-pulsed schemes for comparison, and dashed lines (-) indicate values not reported (or not applicable to non-pulsed schemes).

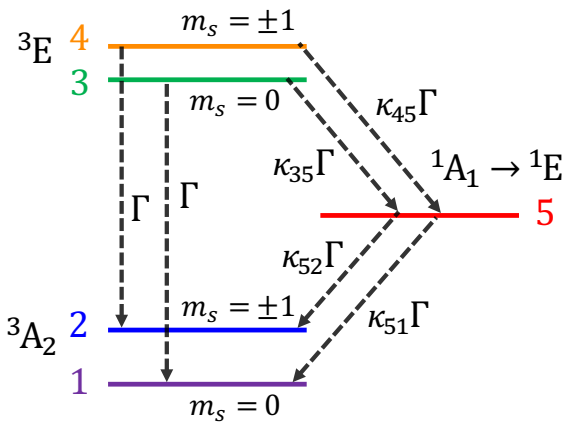

Figure 1.5.4: Five-level energy diagram for NV$^-$ rate equations

We solve the following system of first-order differential equations:

$$n_1'(t)/\Gamma = -s\, n_1(t) + n_3(t) + \kappa_{51}\, n_5(t) \tag{1.47}$$

$$n_2'(t)/\Gamma = -s\, n_2(t) + n_4(t) + \kappa_{52}\, n_5(t) \tag{1.48}$$

$$n_3'(t)/\Gamma = s\, n_1(t) - (1 + \kappa_{35})\, n_3(t) \tag{1.49}$$

$$n_4'(t)/\Gamma = s\, n_2(t) - (1 + \kappa_{45})\, n_4(t) \tag{1.50}$$

$$n_5'(t)/\Gamma = \kappa_{35}\, n_3(t) + \kappa_{45}\, n_4(t) - (\kappa_{51} + \kappa_{52})\, n_5(t), \tag{1.51}$$

assuming population originates entirely in either Level 1 or Level 2. Here $n_i(t)$ is the population in Level $i = 1 : 5$ at time t, and $s = I/I_{\text{sat}}$ is the saturation parameter with I_{sat} determined by Γ and the NV$^-$ absorption cross section at 532 nm [112]. We solve the equations for a range of saturation parameters from $s = 10^{-4}$ to $s = 10^2$. For each of the two initial conditions, we find the PL emission rate $R(t)$ as

$$R(t) = \Gamma\left[n3(t) + n4(t)\right]. \tag{1.52}$$

Defining $R_1(t)$ and $R_2(t)$ as the PL rate with the initial population in Levels 1 and 2 respectively, we extract the integrated shot-noise-limited readout SNR as a function of t:

$$\text{SNR}(t) = \frac{\int_0^t \left(R_1(t) - R_2(t)\right) dt'}{\sqrt{\int_0^t \frac{1}{2}\left(R_1(t) + R_2(t)\right) dt'}}. \tag{1.53}$$

Then, normalizing by the peak SNR for $s = 1$, we display the results for the investigated range of s in Figure 1.5.5.

Several trends are apparent. For each value of s there is an optimal readout duration, when PL contrast exists between the two solutions, before the spin state is repolarized. The optimal readout duration changes very little above $s = 1$ and then increases nearly inverse-linearly as s decreases. The peak SNR increases substantially between $s = 0.1$ and $s = 10$ and very little for higher intensities, as is expected from saturation. At $s < 0.1$, the peak SNR levels off.

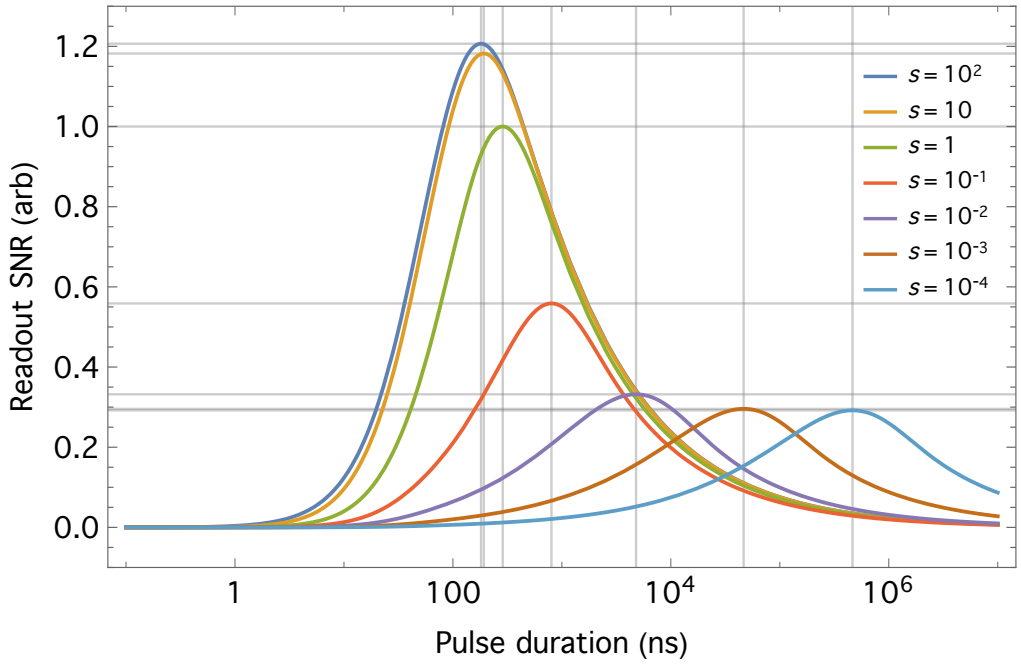

Figure 1.5.5: Simulated photon-shot-noise-limited SNR versus readout duration for varying optical excitation intensity. SNR is calculated from Equation 1.53 and normalized by the peak value for $s = 1$.

Here we present an intuitive picture to describe these observations. For high-intensity, short-duration readout pulses, the time required for the NV$^-$ population to decay through the singlet state manifold limits the readout SNR. Higher laser power allows more photons to be collected from the cycling between the $m_s = 0$ ground and excited states, while the population initially in the $m_s = \pm 1$ states is shelved in the singlet manifold. More precisely, in the limit of high s, the maximum achievable SNR is limited by the ratio of the triplet optical cycling rate to singlet state decay rate. Meanwhile, at low excitation intensity, the SNR is not limited by this ratio but instead by the upper branching ratios into the singlet state manifold. For $s \ll 1$, each NV$^-$ center essentially never emits more than one photon from the $m_s = 0$ excited state during the singlet state lifetime, so a change in optical cycling rate (set by s) does not affect the peak readout SNR.

The implications for selecting a target value of s when designing an ensemble-NV$^-$ magnetometer depends on which version of sensitivity is being optimized. Figure 1.5.6

shows the measurement-time-normalized SNR (proportional to the inverse magnetic field sensitivity) as a function of s. The calculation assumes an optimal readout time t_R is chosen for each value of s and accounts for overhead time t_O. We determine the total measurement time $\tau + t_O = +\tau + t_I + t_R$ by assuming optical initialization time $t_I = 3t_R$ and precession time $\tau = 1$ μs. We also divide all points by the time-normalized SNR for $s = 1$. In Figure 1.5.6a, the interrogation volume (i.e., the number of addressed NV$^-$ centers in the ensemble) is held fixed. Here, like in Figure 1.5.5, the time-normalized SNR improves most between $s = 0.1$ and $s = 10$. This suggests that for fixed interrogation volume, or when volume-normalized sensitivity $\eta^V = \eta\sqrt{V}$ is to be optimized, operating with $s \gtrsim 1$ is optimal. By contrast, in Figure 1.5.6b the interrogation volume is not held fixed for each value of s; it is made to vary as $V \propto 1/s$ in order to model the case where optical power is held constant. For simplicity we assume uniform optical intensity over the interrogation volume for all values of s. In this case, the optimal time-normalized SNR occurs at $s \approx 0.1$, suggesting that when the sensitivity η rather than η^V is to be optimized and laser power is fixed, operating below optical saturation with a larger interrogation volume is preferable to operating with $s \gtrsim 1$.

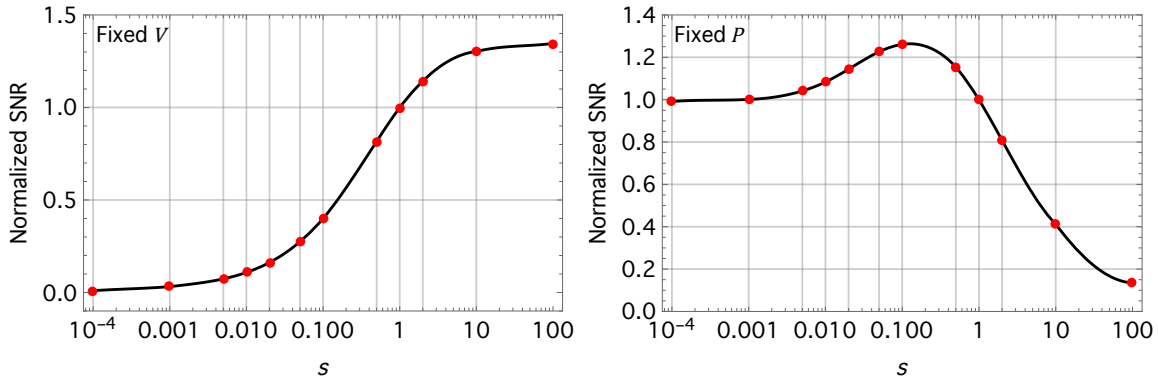

Figure 1.5.6: Measurement-time-normalized SNR for fixed interrogation volume and fixed optical power. a) Simulated time-normalized SNR versus saturation parameter s assuming sequence measurement time $\tau + 4t_R$ with the optimal value of t_R from Figure 1.5.5 chosen for each value of s. b) Simulated time-normalized SNR for the same conditions as in (a) except allowing interrogation volume to increase as $1/s$, as would be possible with fixed optical power. Red dots mark calculated SNR values for investigated values of s, and black lines are interpolations intended to guide the eye.

1.6 Alternatives to Ramsey magnetometry

1.6.1 CW-ODMR

Continuous-wave optically detected magnetic resonance (CW-ODMR) is a simple and widely employed magnetometry method [113, 7, 100, 114, 111, 24, 25] wherein the MW driving and the optical polarization and readout occur simultaneously (see Figure 1.5.3c). Laser excitation continuously polarizes NV^- centers into the more fluorescent $m_s = 0$ ground state while MWs tuned near resonance with one of the $m_s = 0 \leftrightarrow m_s = \pm 1$ transitions drive NV^- population into the less fluorescent $m_s = \pm 1$ state, reducing the emitted light. A change in the local magnetic field shifts the ODMR feature with respect to the MW drive frequency, causing a change in the detected fluorescence, as illustrated in Figure 1.5.3d.

The shot-noise-limited sensitivity of an NV^- magnetometer employing CW-ODMR is given by [100, 24]

$$\eta_{\mathrm{CW}} = \frac{4}{3\sqrt{3}} \frac{h}{g_e \mu_B} \frac{\Delta\nu}{C_{\mathrm{CW}}\sqrt{R}} \tag{1.54}$$

with photon detection rate R, linewidth $\Delta\nu$ and CW-ODMR contrast C_{CW}. The prefactor $4/(3\sqrt{3})$ originates from the steepest slope of the ODMR lineshape when assuming a Lorentzian resonance profile, and is achieved for a detuning of $\frac{\Delta\nu}{2\sqrt{3}}$ from the linecenter [115].

CW-ODMR is technically easier to implement than pulsed measurement schemes such as Ramsey and may yield sensitivities similar to Ramsey when a larger number of sensors are interrogated with the same optical excitation power [24]. However, CW-ODMR is not envisioned for many high-sensitivity applications for multiple reasons. First, CW-ODMR precludes use of pulsed methods to improve sensitivity, such as double-quantum coherence magnetometry (see Section 6.1.2), and many readout-fidelity enhancement techniques. Second, CW-ODMR methods suffer from MW and optical power broadening, degrading both $\Delta\nu$ and C_{CW} compared to optimized Ramsey sequences. Optimal CW-ODMR sensitivity is achieved approximately when opti-

cal excitation, MW drive, and T_2^* dephasing contribute roughly equally to the ODMR linewidth [100]. In this low-optical-intensity regime, the detected fluorescence rate per interrogated NV$^-$ center is significantly lower than for an optimized Ramsey scheme, which results in readout fidelities $\sim 10^3$ below the spin projection limit [24]. This low optical intensity requirement becomes more stringent as T_2^* increases, meaning that CW-ODMR sensitivity largely does not benefit from techniques to extend T_2^*.

1.6.2 Pulsed ODMR

Pulsed ODMR is an alternative magnetometry method first demonstrated for NV$^-$ centers by Dréau *et al.* in Ref. [100]. Similar to Ramsey and in contrast to CW-ODMR, this technique avoids optical and MW power broadening of the spin resonances, enabling nearly T_2^*-limited measurements. In contrast to Ramsey magnetometry, however, pulsed ODMR is linearly sensitive to spatial and temporal variations in MW Rabi frequency. When such variations are minimal, pulsed ODMR sensitivity may approach that of Ramsey magnetometry without requiring high Rabi frequency [100], making the method attractive when high MW field strengths are not available.

In the pulsed ODMR protocol, depicted schematically in Figure 1.5.3e, the NV$^-$ spin state is first optically initialized to $m_s = 0$. Then, during the sensing time τ, a resonant MW π-pulse is applied with duration equal to the sensing time, $\tau_\pi = \tau$, where the Rabi frequency $\Omega_R = \pi/\tau_\pi$. Finally, the population is read out optically. A change in the magnetic field detunes the spin resonance with respect to the MW frequency, resulting in an incomplete π-pulse and a change in the population transferred to the $m_s = \pm 1$ state prior to optical readout.

For a Lorentzian ODMR lineshape (see Sections 2.1.4 and 2.1.5), the expected shot-noise-limited sensitivity may be calculated starting from the shot-noise-limited CW-ODMR sensitivity given by Equation 1.54. For pulsed ODMR, the resonance profile is given by a convolution of the natural T_2^*-limited line profile and additional broadening from the NV$^-$ spin's response to a fixed-duration, detuned MW π-pulse, as shown in Figure 1.6.1. When the sensing time τ_π is set to $\approx T_2^*$, these two broad-

ening mechanisms contribute approximately equally to the resonance linewidth [100]. Assuming $\tau_\pi \approx T_2^*$, we write the pulsed ODMR linewidth $\Delta\nu$ as $\Delta\nu \approx \Gamma = 1/(\pi T_2^*)$ (see Figure 1.5.3f), while noting that this approximation likely underestimates the linewidth by $\lesssim 2\times$.

Choosing initialization and readout times t_I and t_R and sensing time $\tau_\pi = T_2^*$ reduces the time-averaged photon collection rate R by the readout duty cycle $t_R/(t_I + T_2^* + t_R)$. Then, defining $\mathcal{N} = Rt_R$ to be the mean number of photons collected per optical readout cycle, defining the measurement overhead time as $t_O = t_I + t_R$, and replacing C_{CW} with the pulsed-ODMR contrast C_{pulsed} yields the pulsed-ODMR sensitivity

$$\eta_{\mathrm{pulsed}} \approx \frac{8}{3\sqrt{3}} \frac{\hbar}{g_e \mu_B} \frac{1}{C_{\mathrm{pulsed}}\sqrt{\mathcal{N}}} \frac{\sqrt{T_2^* + t_O}}{T_2^*}. \tag{1.55}$$

The value of C_{pulsed} under optimized conditions is expected to be higher than C_{CW} (for the same number of interrogated NV$^-$ centers and same mean photon collection rate R) because pulsed ODMR enables use of high optical intensities that would degrade C_{CW} [100]. Although C_{pulsed} may approach the Ramsey contrast C_{Ramsey} (see Figure 1.5.3a,b), $C_{\mathrm{pulsed}} < C_{\mathrm{Ramsey}}$ is expected in practice for several reasons: First, because the technique requires Rabi frequencies to be of the same order as the NV$^-$ natural linewidth, the MW drive may be too weak to effectively address the entire inhomogeneously-broadened NV$^-$ ensemble. Second, while the high Rabi frequencies $\sim 2\pi \times 10$ MHz commonly employed in Ramsey sequences effectively drive all hyperfine-split NV$^-$ transitions of ^{14}NV$^-$ or ^{15}NV$^-$ [7], the weaker π-pulses required for pulsed ODMR cannot effectively drive all hyperfine transitions with a single tone. Pulsed ODMR operation at the excited state level anticrossing [100] or utilizing multi-tone MW pulses [116, 24, 117] could allow more effective driving of the entire NV$^-$ population and more optimal values of C_{pulsed}. However, when multi-tone pulses are employed, care should be taken to avoid degradation of C_{pulsed} due to off-resonant MW cross-excitation, which may be especially pernicious when the natural linewidth (and thus MW Rabi frequency) is similar to the hyperfine splitting.

Although pulsed ODMR may sometimes be preferable to Ramsey, the technique

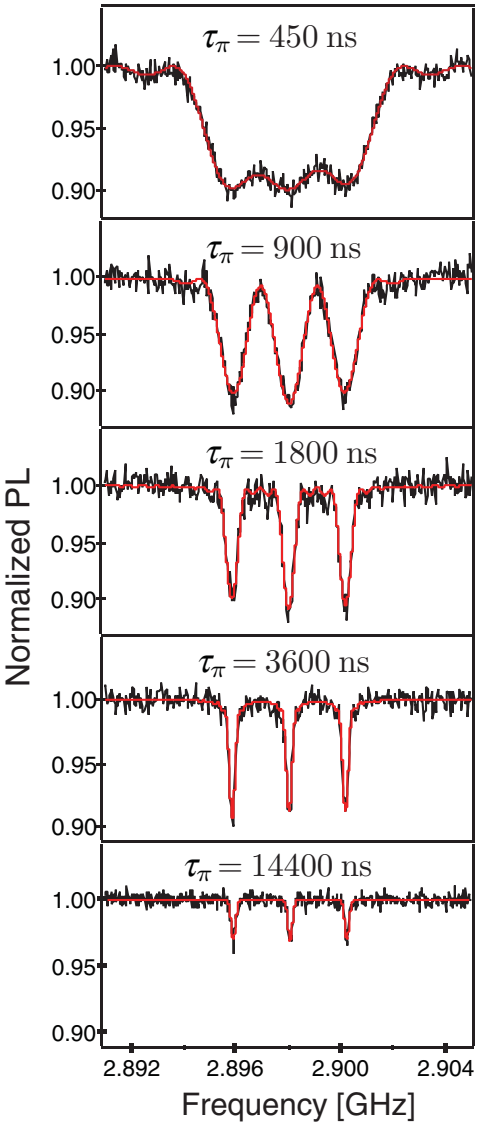

Figure 1.6.1: Pulsed ODMR spectra for various π-pulse durations τ_π. When $\tau_\pi \ll T_2^*$, the ODMR lineshape is Fourier-broadened beyond the natural linewidth. When $\tau_\pi \gg T_2^*$ the photoluminescence (PL) contrast is diminished due to spin dephasing. Choice of $\tau_\pi \sim T_2^*$ (≈ 3 μs here) allows nearly-T_2^*-limited linewidths while preserving PL contrast. From Ref. [100].

ultimately provides inferior sensitivity. Several factors of order $\sqrt{2}$, (which arise from a lineshape-dependent numerical prefactor [100], MW Fourier broadening, nonuniform ensemble driving, and hyperfine driving inefficiencies), combine to degrade the pulsed ODMR sensitivity with respect to that of Ramsey. Furthermore, unlike double-quantum Ramsey magnetometry (see Section 6.1.2), pulsed ODMR has not been experimentally demonstrated to mitigate line broadening from temperature fluctuations or other common-mode dephasing mechanisms. Hypothetical double-quantum analogs to pulsed ODMR [3, 104] might likely require, in addition to the sensing π-pulse, high-Rabi-frequency MW pulses to initialize the $|\pm 1\rangle$ superposition states similar to those employed for double-quantum Ramsey, which would negate pulsed ODMR's otherwise attractive low MW Rabi frequency requirements.

A generalization of pulsed ODMR is Rabi beat sensing [118, 119], wherein the spins are driven through multiple Rabi oscillations during the field interrogation time. Under optimal conditions, Rabi beat magnetometry, like the specific case of pulsed ODMR, may exhibit sensitivity approaching that of Ramsey magnetometry. For the regime wherein the Rabi frequency Ω_R is large compared to the ODMR linewidth ($\sim 1/T_2^*$), sensitivity is optimized when the detuning is chosen to be similar to the Rabi frequency, ($\Delta \sim \Omega_R$), when the interrogation time is similar to the dephasing time, ($\tau \sim T_2^*$, see Section 2.1.7), and when τ is chosen to ensure operation at a point of maximum slope of the Rabi magnetometry curve. However, Rabi beat magnetometry is sensitive to spatial and temporal variations in the MW Rabi frequency Ω_R [97]. For high values of Ω_R, MW field variations may limit the Rabi measurement's effective T_2^*. Hence, practical implementations of Rabi beat magnetometry on NV$^-$ ensembles likely perform best when $\Omega_R \sim 1/T_2^*$, i.e., when pulsed ODMR is employed.

1.7 Parameters limiting sensitivity

Examination of Equation 1.45 reveals the relevant parameters limiting magnetic field sensitivity $\eta_{\text{Ramsey}}^{\text{ensemble}}$: (i) the dephasing time T_2^*; (ii) the readout fidelity $\mathcal{F} = 1/\sigma_R$; (iii) the sensor concentration [NV$^-$] and the interrogated diamond volume V, which to-

gether set the total number of sensors $N = [\mathrm{NV^-}] \times V$; (iv) the measurement overhead time $t_O \approx t_I + t_R$; and (v) the relative precession rates of the two states comprising the interferometry measurement. Sensitivity enhancement requires improving one or more of these parameters. As we will discuss, parameters (i) and (ii) are particularly far from physical limits and therefore warrant special focus. In contrast, we believe prospects are modest for improving sensitivity by engineering parameters (iii), (iv), and (v). We note that the derivation of Equation 1.45 makes certain assumptions (e.g., the N sensors are independent) that neglect additional elaborate approaches such as exploiting strong $\mathrm{NV^-}$-$\mathrm{NV^-}$ interactions via Floquet techniques and harnessing entanglement for sensing (see Section 6.3.4) [120].

1.7.1 Dephasing time T_2^*

In current realizations, dephasing times in application-focused broadband $\mathrm{NV^-}$ ensemble magnetometers [24, 110, 55, 121] are typically $T_2^* \lesssim 1$ µs. Considering the physical limit $T_2^* \leqslant 2T_1$ [71, 72] where the longitudinal relaxation time is $T_1 \approx 6$ ms for $\mathrm{NV^-}$ ensembles [15], a maximum $T_2^* \approx 12$ ms is theoretically achievable, corresponding to a sensitivity enhancement of $\approx 100\times$. Although the feasibility of realizing T_2^* values approaching $2T_1$ remains unknown, general improvement of T_2^* is believed to be an effective approach to enhancing sensitivity (see Section 2.1.1). While the stretched exponential parameter p can provide information regarding the dephasing source limiting T_2^*, its value (typically between 1 and 2 for ensembles) does not strongly affect achievable sensitivity [81].

1.7.2 Readout fidelity

Increasing readout fidelity $\mathcal{F} = 1/\sigma_R$ is another effective method to enhance sensitivity, as fractional fidelity improvements result in equal fractional improvements in sensitivity. With conventional 532 nm fluorescence readout, current $\mathrm{NV^-}$ ensemble readout fidelities $\mathcal{F}$ are a factor $\gtrsim 67\times$ removed from the spin projection limit $\sigma_R = 1$ [108], indicating large improvements might be possible. For comparison, mul-

tiple readout methods employing single NV$^-$ centers achieve $\mathcal{F}$ within 5× of the spin projection limit, i.e., $\sigma_R < 5$ [32, 101, 106, 105, 122, 123] with Ref. [107] achieving $\sigma_R = 1.1$.

1.7.3 Overhead time

Although measurement overhead time can likely be decreased to ~ 1 µs, in the regime where $T_2^* \sim t_I + t_R$, maximum sensitivity enhancement is expected to be limited to order unity, e.g., $\lesssim 3\times$. See Section 2.1.1 for a more detailed discussion.

1.7.4 Precession rate

Use of the NV$^-$ center's full $S = 1$ spin can allow $\Delta m_s = 2$ in Equations 1.45 and 1.46, i.e., a 2× increase in the relative precession rate of the states comprising the interferometry measurement compared to use of the standard $S = 1/2$ sub-basis (see Section 6.1.2) [104, 81]. However, further improvement is unlikely, as the NV$^-$ spin dynamics are fixed.

1.7.5 Sensor number, sensor concentration, and interrogation volume

Increasing the number N of interrogated NV$^-$ centers by increasing either the interrogation volume or the NV$^-$ concentration may be partially effective to improve magnetic field sensitivity. In this instance, the number of photons detected per measurement $\mathcal{N}$ increases with the number of sensors N. However, a series of practical factors may hinder this strategy. Sensitivity enhancement exhibits sublinear scaling with N and the associated number of photons detected per measurement $\mathcal{N}$, i.e., $\eta \propto \frac{1}{\sqrt{\mathcal{N}}}$, making significant sensitivity improvements from increasing N difficult. To date no demonstrated high sensitivity bulk NV-diamond magnetometer [24, 109, 110, 121] has utilized more than a few percent of the available NV$^-$ in the diamond, suggesting limited utility for increasing sensor number N in current devices. We expect increases

in N to enable only modest sensitivity enhancements (e.g., $\lesssim 5\times$) over standard methods given the associated technical difficulties described herein.

Increasing N necessarily also increases the minimum number of photons required for optical initialization. Assuming that each interrogated NV$^-$ center requires m photons for optical initialization, each measurement is expected to require an energy of

$$E_{\text{init}} = Nm\frac{hc}{\lambda}, \tag{1.56}$$

where h is Planck's constant, c is the speed of light and λ is the excitation wavelength. If measurements are performed every T_2^*, the required mean power is

$$P_{\text{init}} = \frac{Nm}{T_2^*}\frac{hc}{\lambda}. \tag{1.57}$$

For example, initialization of all 1.76×10^{14} NV$^-$ centers in a 1 mm^3 diamond with 1 ppm [NV$^-$] would require $E_{\text{init}} = 200$ μJ, using a crude guess of $m = 3$ (see Table 1.7.1). Assuming $T_2^* = 1$ μs, the required power is $P_{\text{init}} = 200$ W. Equation 1.57 illustrates that achieving a sensitivity improvement by increasing the NV$^-$ ensemble size will increase P_{init} unless T_2^* is increased as well. For experimental approaches employing an acousto-optic modulator to gate a CW laser, the required CW laser power will be higher, as many photons are wasted.

Another difficulty encountered when increasing the number of interrogated NV$^-$ centers N (and thus detected photon number $\mathcal{N}$) is that reaching the shot noise limit can become challenging for large values of $\mathcal{N}$. For example, the absolute noise contributed by some systematic (not stochastic) noise sources scales linearly with the number of photons detected, i.e., $\propto k_1\mathcal{N}$, where $k_1 \ll 1$. In comparably proportional units, shot noise scales as $\propto\sqrt{\mathcal{N}}$. For $\mathcal{N} > \frac{1}{k_1^2}$, the systematic noise will be larger than shot noise. Primary examples of such noise sources include laser intensity noise in all implementations, timing jitter in the readout pulse length for Ramsey and pulsed ODMR, and MW amplitude noise in CW-ODMR.

While larger N can be achieved either by increasing the NV$^-$ concentration or increasing the interrogation volume, both approaches exhibit distinct difficulties. In-

Reference	[111]	[98]	[99]	[23]	
NV^- centers probed	4	3	2	ensemble	units
Values reported	avg. (max, min)	avg. (max, min)	avg.		
$^3E(m_s = 0) \rightarrow {}^3A_2(m_s = 0)$	67.9 (63.2, 69.1)	66.16 (66.08, 66.43)	64.2	-	μs^{-1}
$^3E(m_s = \pm 1) \rightarrow {}^3A_2(m_s = \pm 1)$	67.9 (63.2, 69.1)	66.16 (66.08, 66.43)	64.9	-	μs^{-1}
$^3E(m_s = 0) \rightarrow {}^1A_1$	5.7 (5.2, 10.8)	11.1 (10.9, 11.2)	11.2	-	μs^{-1}
$^3E(m_s = \pm 1) \rightarrow {}^1A_1$	49.9 (48.6, 60.7)	91.8 (89.3, 92.9)	80.0	-	μs^{-1}
$^1E \rightarrow {}^3A_2(m_s = 0)$	1.0 (0.7, 1.5)	4.87 (4.75, 4.90)	3.0	-	μs^{-1}
$^1E \rightarrow {}^3A_2(m_s = \pm 1)$	0.75 (0.4, 1.4)	2.04 (2.03, 2.13)	2.6	-	μs^{-1}
$^1A_1$ lifetime	-	144.5 (144.3, 145.3)	178 ± 6	219 ± 3	ns

Table 1.7.1: NV^- decay rates measured at room temperature. Averages over measured NV^- centers are weighted by reported uncertainties. Dashed lines (-) indicate values not reported. Branching ratios can be derived from the given data.

creasing N by increasing the interrogation volume with fixed [NV^-] may increase the diamond cost and creates more stringent uniformity requirements for both the bias magnetic field (to avoid degrading the dephasing time T_2^*) and the MW field (to ensure uniform spin manipulation over the sensing volume) [124, 125]. Furthermore, increasing interrogation volume is incompatible with high-spatial-resolution sensing and imaging modalities [50, 49, 48, 51, 126, 127, 13, 68].

Alternatively, increasing NV^- concentration necessarily positions NV^- spins (and all other nitrogen-related paramagnetic spins) closer together, which results in increased dipolar dephasing rates and shorter associated T_2^* values. Mitigation of the dipolar dephasing requires employment of additional techniques (e.g., spin bath driving - see Section 6.1.3), adding experimental complexity. Otherwise, attempts to enhance sensitivity by increasing the NV^- spins may in practice result in equal or reduced sensitivity.

1.8 Conclusion

This chapter introduces broadband magnetic sensing with ensembles of NV^- centers in diamond. Importantly, existing ensemble NV^- quantum sensors exhibit sensitivities far from theoretical limits. We argue that pulsed Ramsey-type magnetometry protocols are superior to CW- and pulsed ODMR for improving sensitivity toward these limits. For CW-ODMR, the technique employed in Chapters 3 and 4, improving the magnetic field sensitivity is primarily accomplished through increasing the interrogation volume and associated number of sensor spins. Magnetometers pursuing this strategy quickly encounter technical constraints such as excitation power availability and photon-handling limits of electronics. Furthermore, as CW-ODMR requires lower excitation intensity than pulsed magnetometry, it does not allow high volume-normalized sensitivity. Meanwhile, Ramsey magnetometry can harness of additional strategies to improve both volume-normalized sensitivity and overall sensitivity, including extensions of the spin dephasing time T_2^* and the spin readout fidelity. Nonetheless, CW-ODMR magnetometry is employed for the experiments in Chapters 3 and 4, as its implementation is technically simpler than pulsed magnetometry and it can yield reasonable sensitivity for fixed optical and microwave (MW) power in combination with high [NV^-] and large interrogation volume.

Overall, the following chapters are all motivated by efforts to improve the magnetic field sensitivity of sensing and imaging devices based on ensembles of NV^- centers in diamond. Chapter 2 examines the dephasing time T_2^* and the mechanisms that limit its value and the associated achievable sensitivity. Chapters 3, 4, and 5 describe experiments where broadband magnetic sensitivity is both desired and demonstrated. Chapters 6 and 7 provide near-comprehensive surveys of methods for improving broadband magnetometry from DC to $\sim$ 100 kHz. Finally, Chapter 8 synthesizes the findings from the previous chapters into an overarching strategy for optimizing broadband sensitivity of ensemble-NV^- magnetometers.

Chapter 2

Inhomogeneous spin dephasing time T_2^*

This chapter examines the NV$^-$ spin ensemble dephasing time T_2^* and, to a lesser extent, the coherence time T_2. In particular, Section 2.1 defines T_2^* and discusses its connections to and differences from other parameters of interest for quantum sensing. In particular, Section 2.1.1 motivates efforts to extend T_2^* for improved magnetometer sensitivity; Section 2.1.2 distinguishes T_2^* from the spin-echo coherence time T_2; Section 2.1.3 describes differences between T_2^* for ensembles and for single spins; Sections 2.1.4 and 2.1.5, and 2.1.6 highlight connections between T_2^* and the resonance linewidth for different common lineshapes, pointing out T_2^* for NV$^-$ ensembles can be estimated from electron paramagnetic resonance (EPR) measurements of other spin defects; Section 2.1.6 connects the resonance lineshape to the stretched exponential parameter that characterizes the free-induction decay (FID) envelope; and Section 2.1.7 determines how the value of T_2^* sets the optimal field interrogation time τ for a pulsed magnetometry measurement in the presence of overhead time t_O. Next, Section 2.2 characterizes various mechanisms contributing to NV$^-$ ensemble T_2^*, with Sections 2.2.1-2.2.4 investigating limits to T_2^* and T_2 from dipolar interactions with specific paramagnetic species within the diamond. A majority of this chapter is adapted from Ref. [80].

2.1 What is T_2^*?

The parameter T_2^* characterizes the decay of spin coherence associated with static or slowly varying inhomogeneities in a spin system. T_2^* is commonly measured as the $1/e$ envelope decay time of a free induction decay (FID) experiment, measured by performing a series of Ramsey sequences with varying free precession time τ and tracing out the decay of the Ramsey fringes as τ is increased. The name T_2^* originates from the NMR field, where the "star" is intended to distinguish it from the coherence time T_2, also called the transverse or spin-spin relaxation time, which can exceed T_2^* by orders of magnitude [95, 81, 84]. Whereas T_2 decay characterizes loss of quantum coherence to the surrounding environment, the dephasing characterized by T_2^* is not a true loss of quantum coherence but rather a more classical dephasing, either of constituent spins within an ensemble due to static field inhomogeneity, or of repeated measurements of the same spin, due to temporal environmental fluctuations over the course of an FID experiment. These distinctions are discussed in more detail in Sections 2.1.2 and 2.1.3.

2.1.1 Why investigate and extend T_2^*?

A promising approach to enhance DC sensitivity focuses on extending the dephasing time T_2^* [81]. The effectiveness of this approach may be illustrated by close examination of Equations 1.45, 1.46. First, optimal sensitivity is obtained when the precession time τ is similar to the dephasing time T_2^* (see Section 2.1.7), so that the approximation $\tau \sim T_2^*$ is valid for an optimized system. Therefore, for the simple arguments presented in this section, we assume that T_2^* extensions translate to proportional extensions of the optimal τ. When the dephasing time T_2^* is similar to or shorter than the measurement overhead time ($T_2^* \lesssim t_O \equiv t_I + t_R$), which may be typical for Ramsey magnetometers employing ensembles of NV$^-$ centers in [N$^{\mathrm{T}}$] = 1-20 ppm diamonds, the sensitivity enhancement may then be nearly linear in T_2^*, as shown in Figure 2.1.1.

The above outlined sensitivity scaling can be intuitively understood as follows:

when the free precession time is small relative to the overhead time, i.e., $\tau \sim T_2^* \ll t_O$, doubling T_2^* (thus doubling τ) results in twice the phase accumulation per measurement sequence and only a slight increase in the total sequence duration; in this limit, magnetometer sensitivity is enhanced by nearly $2\times$. This favorable sensitivity scaling positions T_2^* as an important parameter to optimize when $T_2^* \lesssim t_O$.

Typical NV$^-$ ensemble T_2^* values are $\sim$ 500 ns in $[\mathrm{N}^\mathrm{T}] \approx 20\,\mathrm{ppm}$ chemical-vapor-deposition-grown diamonds from Element Six, a popular supplier of scientific diamonds. Even when employing maximally optimistic values of $t_I = 1$ µs and $t_R = 300$ ns in Ramsey sequences performed on such ensembles, only roughly one quarter of the total measurement time is allocated to free precession. In this regime, as discussed above, the sensitivity scales as $\sim 1/T_2^*$. Although values of t_I and t_R vary in the literature (see Table 2.1.1), the use of longer t_I and t_R, which may achieve better spin polarization and higher readout fidelity, will only increase the relative sensitivity improvement from extending T_2^*. Notably, initialization times are typically longer for NV$^-$ ensembles than for single NV$^-$ defects, as spatial non-uniformity in the optical intensity applied to the ensemble (e.g., with a Gaussian illumination profile) can be compensated for by increasing the initialization time [109].

Longer dephasing times T_2^* offer additional benefits beyond direct sensitivity improvement. For example, higher T_2^* values, leading to lower duty cycles for specific experimental protocol steps, may relax certain technical requirements. In a standard Ramsey-type experiment, the optical initialization and optical readout occur once per measurement sequence. Assuming a fixed mean number of photons are required to both spin polarize and read out the NV$^-$ ensemble, the time-averaged optical power and resulting heat load are expected to scale as $1/T_2^*$. Reducing heat loads is prudent for minimizing temperature variation of the diamond, which couples to individual NV$^-$ resonances like a spurious magnetic signal and may require correction (see Section 6.1.2). Minimizing heat load is also important for many NV-diamond sensing applications, particularly in the life sciences. Assuming a fixed overhead time t_O, the realization of higher values of T_2^*, and thus τ, necessitates processing fewer photons per unit time, which may relax design requirements for the photodetector front end

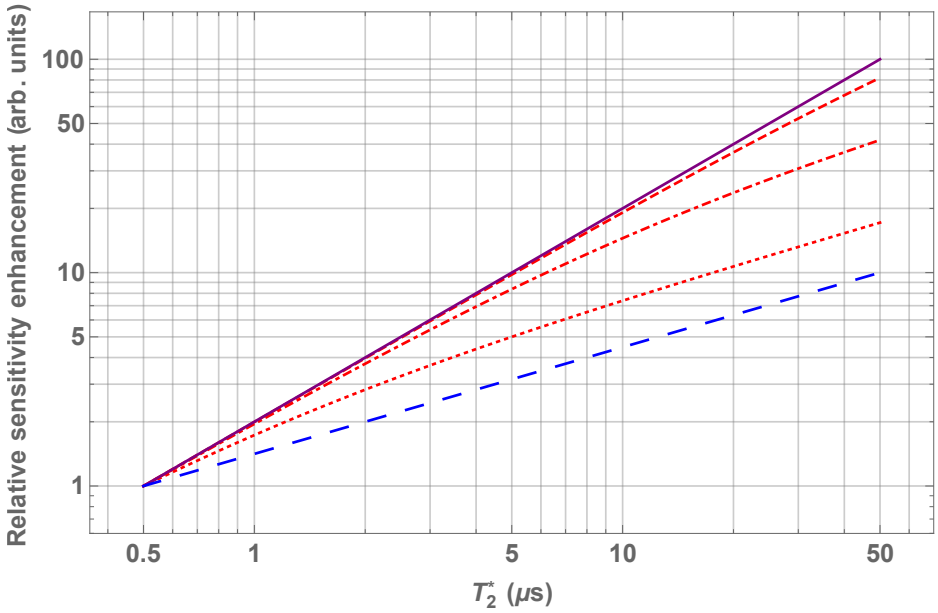

Figure 2.1.1: Sensitivity enhancement scaling with dephasing time T_2^* for a Ramsey-type magnetometer normalized to the same device with $T_2^* = 500$ ns. The different curves assume overhead times ($t_O = t_I + t_R$) of 1 µs (···), 10 µs (-·-), and 100 µs (- - -). The sensitivity enhancement is bounded by either the fractional T_2^* improvement (—) or the square root (– – –) of the fractional T_2^* improvement. For simplicity the precession time τ is set to T_2^*. See Section 2.1.7 for details on determining the optimal precession time.

and associated electronics [128].

Extended T_2^* times can provide similar benefits to the MW-related aspects of the measurement. A standard Ramsey-type measurement protocol employs a MW $\pi/2$-pulse before and after every free precession interval. If the length of each $\pi/2$-pulse is held fixed, the time-averaged MW power and resulting heat load will scale as $1/T_2^*$. Additionally, higher T_2^* values can allow for more involved, longer-duration MW pulse sequences in place of simple $\pi/2$-pulses to mitigate the effects of Rabi frequency inhomogeneities [129, 130, 116] or allow for other spin-manipulation protocols. Finally, higher T_2^* values could make exotic readout schemes that tend to have fixed time penalties experimentally feasible, such as spin to charge conversion readout [101] (see Section 6.2.1) and ancilla-assisted repetitive readout [131, 32] (see Section 6.2.3).

Reference	No. NV^- probed	t_I	t_R
[101]	single	150 ns	-
[132]	single	600 ns	600 ns
[105]	single	1 µs	200 ns
[104]	single	2 µs	300 ns
[5]	single	2 µs	324 ns
[133]	single	3 µs	-
[108]	ensemble	600 ns	300 ns
[81]	ensemble	20 µs	-
[109]	ensemble	100 µs	10 µs
[134]	ensemble	1 ms	-
[15]	ensemble	1 ms	-

Table 2.1.1: Initialization and readout times in the literature used for conventional optical readout of NV^- defects. In general, NV^- ensembles require longer initialization times than single NV^- defects, in part to account for the often non-uniform optical excitation intensity applied to the ensemble [109]. Dashed lines (-) indicate values not reported.

2.1.2 T_2^* versus T_2

Static and slowly-varying inhomogeneities limit T_2^* by causing different spins within an ensemble to precess at different rates. After a free precession interval of $\sim T_2^*$ or longer, the spins have gone out of phase with one another. This dephasing, which is depicted in the second Bloch sphere in Figure 2.1.2, degrades the contrast of a measurement from the spin ensemble. However, if the dephasing results from fields that are static over the course of the measurement, it can be reversed by application of a π-pulse halfway through the free precession interval. In this protocol, called a spin echo or Hahn echo sequence [135], the π-pulse changes the direction of spin precession, such the phase accumulated due to static fields during the second half of the sequence cancels the phase from the first half. At the end of the sequence, the net phase accumulated by each NV^- spin due to static fields vanishes. Thus, spins in inhomogeneous fields rephase, producing a recovered signal termed a "spin echo" (Figure 2.1.2) The decay of this spin echo signal, which is characterized by the coherence time T_2, occurs over timescales typically one to two orders of magnitude longer

than T_2^* dephasing in diamond [95, 81, 84]. T_2 decay is caused by inhomogeneous fields that fluctuate over the course of a Hahn echo sequence, leading to phase accumulation not canceled by the central π-pulse. By design, the Hahn echo sequence and its numerous extensions [136, 137, 138] are insensitive to DC magnetic field signals and thus are typically employed for sensing AC signals, as discussed in Section 1.4.1. Meanwhile, the dephasing time T_2^* is the relevant decay decay time for most DC sensing experiments.

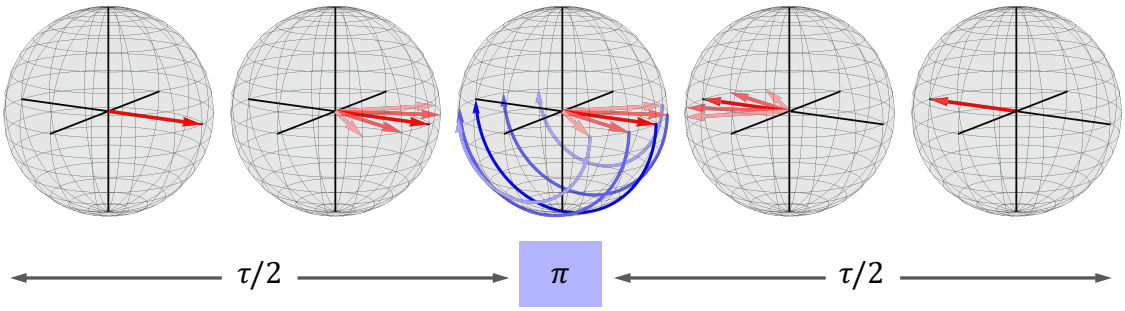

Figure 2.1.2: Recovery of spin phase coherence with central π-pulse. Bloch sphere depiction of spin dephasing due to static field inhomogeneities (characterized by T_2^*) followed by application of a π pulse at time $\tau/2$ and then spin rephasing at time τ. The π-pulse cancels T_2^* dephasing as well as sensitivity to static signal fields.

2.1.3 Ensemble and single-spin T_2^*

The dephasing time T_2^* is defined differently for a single spin than for a spin ensemble. While an ensemble's T_2^* characterizes relative dephasing of the constituent spins, a single spin's T_2^* characterizes dephasing of the spin with itself, i.e., the distribution of phase accumulation from repeated measurements on the spin over time [139, 140]. Since this work focuses on ensemble-based sensing, single-spin dephasing times are herein denoted $T_2^{*\{\text{single}\}}$, while the term T_2^* is reserved for ensemble dephasing times.

Values of $T_2^{*\{\text{single}\}}$ are affected by slow magnetic, electric, strain, and temperature fluctuations. Variations in the magnetic environment may arise from dipolar interactions with an electronic or nuclear spin bath. The strength of these fluctuations can vary spatially throughout a sample due to the microscopically nonuniform distribution of bath spins. As a result, different NV^- centers in the same sample display

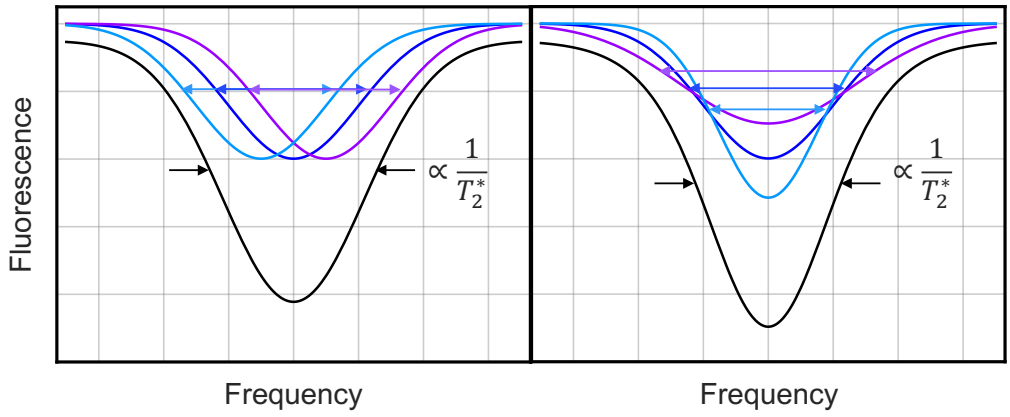

Figure 2.1.3: Contributions of individual spin resonances to the spin ensemble lineshape. The ensemble resonance lineshape (—) is broadened both by the distribution of line centers (left) and the distribution of linewidths (right) of the constituent spins (—, —, —).

different $T_2^{*\{\text{single}\}}$ values [141, 142, 143, 140]. For example, an NV$^-$ spin in close proximity to several bath spins will experience faster dephasing than an NV$^-$ spin many lattice sites away from the nearest bath spin.

Although ensemble T_2^* values are also influenced by spin-bath fluctuations, as discussed in Sections 2.2.1 and 2.2.3, an ensemble T_2^* value is not equal to the most common value of $T_2^{*\{\text{single}\}}$ within the ensemble. For one, the latter is limited by sources of zero-frequency noise that do not contribute to $T_2^{*\{\text{single}\}}$, such as spatially inhomogeneous magnetic fields, electric fields, strain, or g-factors [139]. These inhomogeneities cause a spatially-dependent distribution of the single-NV$^-$ resonance line centers, which broadens the ensemble resonance line and thus degrades T_2^*. Figure 2.1.3 depicts broadening contributions to T_2^* from both varying single-NV$^-$ line centers and varying single-NV$^-$ linewidths ($\propto 1/T_2^{*\{\text{single}\}}$). The relative contribution to an ensemble's T_2^* value from these two types of broadening is expected to be sample-dependent. Although measurements in Ref. [140] on a collection of single NV$^-$ centers in a sparse sample found the distribution of line centers to be narrower than the median single-NV$^-$ linewidth, such findings are not expected to hold generally.

However, even in the absence of static field inhomogeneities, the spin-bath-noise-limited T_2^* value of an ensemble is expected to be shorter than the most likely $T_2^{*\{\text{single}\}}$ value, as the ensemble value is strongly influenced by the small minority of NV$^-$ cen-

ters with bath spins on nearby lattice sites [141]. In fact, theoretical calculations in Refs. [141, 144] reveal that single spins and ensembles interacting with surrounding spin baths exhibit free-induction-decay (FID) envelopes with different functional forms (see Sections 2.1.4 and 2.1.6), a result borne out by experiments [145, 84, 81]. In general, the ensemble T_2^* value cannot be predicted from $T_2^{*\{\text{single}\}}$ of any constituent spin [141], and application of single-spin measurements or theory to ensembles, or vice versa, should be done with great care.

2.1.4 Spin resonance linewidth and T_2^*

The quantity T_2^*, which characterizes the time scale of the free induction decay (FID), is inversely proportional to the natural spin resonance linewidth in the absence of power broadening. Exact conversion between T_2^* and linewidth requires knowledge of the functional form of the FID or the resonance lineshape [146, 147]. Ramsey fringes decaying with an FID envelope $\propto e^{-t/T_2^*}$ indicate a Lorentzian spin resonance profile with full width at half maximum (FWHM) $\Gamma = \frac{1}{\pi T_2^*}$, as shown by the Fourier transform pair:

$$\begin{aligned}\mathcal{F}_t[e^{2\pi i f_0 t} e^{-t/T_2^*}](f) &= \frac{1}{\pi} \frac{\frac{1}{2\pi T_2^*}}{\left(\frac{1}{2\pi T_2^*}\right)^2 + (f - f_0)^2} \\ &= \frac{1}{\pi} \frac{\Gamma/2}{(\Gamma/2)^2 + (f - f_0)^2},\end{aligned} \tag{2.1}$$

valid for $t \geqslant 0$, where f_0 is the Ramsey fringe frequency.

A Gaussian decay envelope $\propto e^{-(t/T_2^*)^2}$ corresponds to a resonance with a Gaussian profile, with standard deviation $\sigma = \frac{1}{\sqrt{2}\pi T_2^*}$ as shown by the Fourier transform pair:

$$\begin{aligned}\mathcal{F}_t[e^{2\pi i f_0 t} e^{-(t/T_2^*)^2}](f) &= \sqrt{\pi} T_2^* e^{-(\pi T_2^* (f - f_0))^2} \\ &= \frac{1}{\sigma\sqrt{2\pi}} e^{-(f-f_0)^2/(2\sigma^2)}.\end{aligned} \tag{2.2}$$

2.1.5 Estimating T_2^* from resonance linewidths of other spin defects

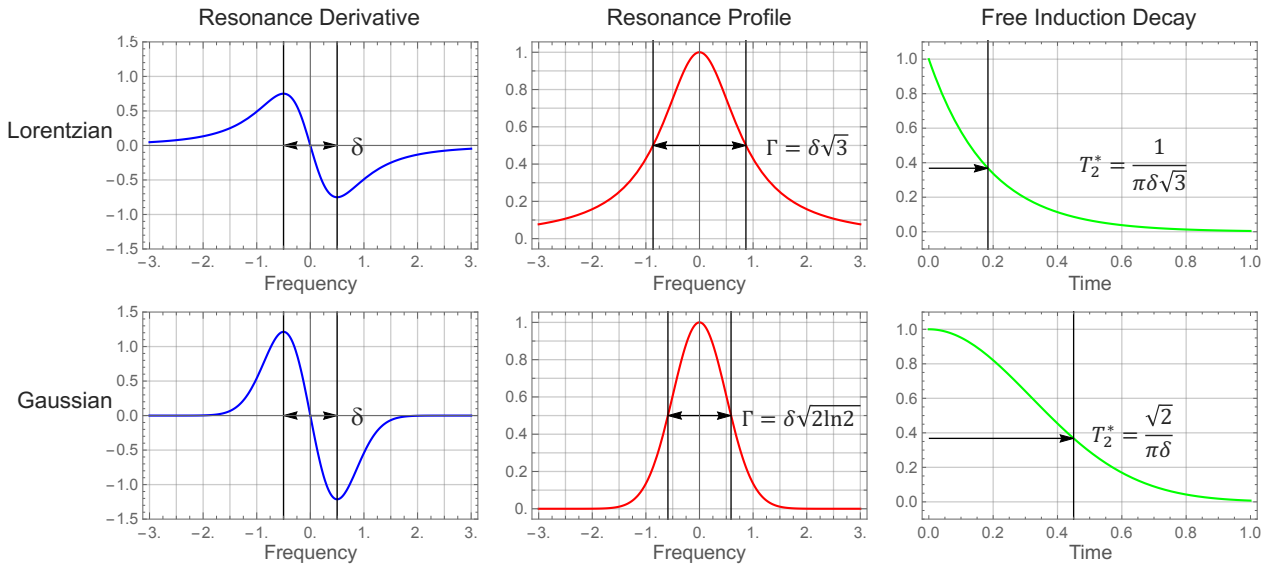

Figure 2.1.4: Relation between resonance width and free induction decay (FID) time for different lineshapes. Resonance derivatives (—), resonance profiles (—), and FID envelopes (—) for Lorentzian and Gaussian lineshape profiles with the same peak-to-peak widths δ. Full-width-at-half-max linewidths Γ and FID decay envelope times T_2^* are indicated and expressed in terms of the peak-to-peak width δ, a commonly reported parameter characterizing linewidth in electron paramagnetic resonance (EPR) data.

Although sensor performance is dictated by T_2^* of the NV$^-$ ensemble, T_2^* values of other paramagnetic defects within the diamond, such as substitutional nitrogen defects, can provide useful information on sources of NV$^-$ spin dephasing. Such T_2^* values can be extracted from linewidth measurements, for example from electron paramagnetic resonance (EPR). Accurate conversion from EPR linewidth to paramagnetic-defect T_2^* enables leveraging of existing diamond EPR data [148] to better understand the contributions of different noise sources to NV$^-$ ensemble T_2^* values.

EPR linewidths are commonly tabulated by their peak-to-peak widths ΔB, where ΔB denotes the magnetic field spacing between extrema of the resonance line first derivative [149]. In (linear) frequency units, this peak-to-peak width is $\delta = \frac{g\mu_B}{h}\Delta B$. Accurately relating δ and T_2^* requires the resonance lineshape to be known [147]. For

example, a Lorentzian profile with full width at half maximum (FWHM) Γ, expressed in frequency units, has $\delta = \Gamma/\sqrt{3}$ and $\Gamma = \frac{1}{\pi T_2^*}$ (see Section 2.1.4). Combining these relations yields $T_{2\,\mathrm{Lor}}^* = \frac{1}{\sqrt{3}\pi\delta}$. A Gaussian lineshape with the same measured peak-to-peak linewidth δ has standard deviation $\sigma = \delta/2$ and $\sigma = \frac{1}{\sqrt{2}\pi T_2^*}$ (see Section 2.1.4). Thus, $T_{2\,\mathrm{Gau}}^* = \frac{\sqrt{2}}{\pi\delta}$, which is $\sqrt{6}\times$ longer than $T_{2\,\mathrm{Lor}}^*$. A visual comparison of these relationships is displayed in Figure 2.1.4.

Diamond EPR literature results may report values of δ without giving the associated resonance lineshape, preventing accurate determination of T_2^* from δ. For example, linewidth measurements in Ref. [148] on substitutional nitrogen defects $\mathrm{N_S^0}$ in diamond indicate an inverse linear scaling of $T_2^*\{\mathrm{N_S^0}\}$ with varying nitrogen concentration $[\mathrm{N_S^0}]$, but the scaling factor relating the two quantities cannot be accurately determined without knowledge of the lineshape.

Theoretical and experimental results on dipolar-coupled spin systems suggest a Lorentzian resonance lineshape when spin-bath interactions are the dominant source of line-broadening [150, 146, 141, 144]. Furthermore, Ramsey measurements with $\mathrm{NV^-}$ spin ensembles show FID envelopes well fit by $e^{-(t/T_2^*)^p}$ with $p \sim 1$, corresponding to a Lorentzian lineshape (see Section 2.1.6, Figure 2.1.4 and Ref. [81]) when T_2^* is expected to be spin-bath limited.

2.1.6 Stretched exponential parameter

Ramsey T_2^* decay	p	Reference (experiment)	Reference (theory)
Single $\mathrm{NV^-}$	2	[145]	[141, 139, 144]
$\mathrm{NV^-}$ ensemble	1	[151, 81]	[141, 144]

Table 2.1.2: Stretched exponential parameters p associated with free induction decay envelopes for single $\mathrm{NV^-}$ centers and $\mathrm{NV^-}$ ensembles in dipolar-coupled spin baths

Equations 2.1 and 2.2 show that the spin resonance lineshape can be parameterized by the stretched exponential parameter p of the free induction decay (FID) envelope $e^{-(t/T_2^*)^p}$. We note that for the idealized case of a purely Lorentzian lineshape, $p = 1$, and for a purely Gaussian lineshape, $p = 2$. The exact ODMR lineshape

and value of p are well characterized for single spins under a variety of environmental conditions [139, 143, 141, 145, 144]. For example, a single spin experiencing dipolar coupling to a surrounding bath of spins displays an FID envelope with stretched exponential parameter $p = 2$ [139, 141, 145, 144] (Gaussian ODMR lineshape, see Table 2.1.2 and Figure 2.1.4). Meanwhile, NV$^-$ ensembles with linewidth limited by dipolar coupling to a spin bath are predicted [141, 144] and measured [151, 81] to exhibit FID envelopes with $p = 1$ (Lorentzian ODMR lineshape, see Table 2.1.2 and Figure 2.1.4). However, experimental Ramsey measurements on NV$^-$ ensembles may sometimes exhibit decay envelopes with $p \neq 1$, suggesting the presence of other broadening mechanisms such as strain gradients, magnetic field gradients, or temperature fluctuations [81]. A noninteger p for an ensemble may also indicate the presence of more complex dephasing and decoherence dynamics, including spatial inhomogeneity, than can be encompassed by a single decay time constant. In some cases the decay may be better described by a sum [152] or a product of multiple decay curves with different values of T_2^* and p. For example, a product of two FID decays, one with $p = 1$ and one with and $p = 2$, corresponds to a Voigt profile lineshape. Allowing p to vary when fitting FID envelopes crudely accounts for these sorts of lineshape variations while only requiring a single additional fit parameter. Therefore, Ramsey FID measurements exhibiting $1 \leqslant p \leqslant 2$ for some NV$^-$ ensembles may suggest contributions to the ODMR lines from both Lorentzian and Gaussian broadening mechanisms [81].

Hahn echo T_2 decays of single NV$^-$ spins have been predicted [139] and measured [95] to exhibit a stretched exponential parameter $p = 3$ when T_2 is limited by spin-bath noise. In contrast, Hahn echo decay envelopes for ensembles of NV$^-$ spins have been seen to exhibit p varying from ~ 0.5 to 3, depending on the dominant contributors to the spin bath and the bias magnetic field angle [153, 84].

2.1.7 Optimal precession time

The optimal precession time τ to achieve best Ramsey magnetometry sensitivity (Equation 1.46) depends on the value of the stretched exponential parameter p, the initialization time t_I, and the readout time t_R. By defining the overhead time per

measurement as $t_O = t_I + t_R$, Equation 1.46 reduces to

$$\eta \propto \frac{1}{e^{-(\tau/T_2^*)^p}} \frac{\sqrt{t_O + \tau}}{\tau}. \tag{2.3}$$

For $t_O \ll T_2^*$, sensitivity is optimized when $\tau \approx T_2^*/2$ for $1 \leqslant p \leqslant 2$. Particularly, for $t_O = 0$ and $p = 1$ or $p = 2$ (see Section 2.1.6), sensitivity is exactly optimized for $\tau = T_2^*/2$. As t_O increases from zero, the optimal precession time increases as well, asymptotically approaching $\tau = T_2^*$ when $t_O \gg T_2^*$ for $p = 1$. Figure 2.1.5 shows the optimal precession time τ for various combinations of p and t_O. For clarity the optimal precession time is normalized to the dephasing time in the employed measurement basis (single or double quantum). Equation 2.3, and thus Figure 2.1.5, also apply for Hahn echo (Equation 6.1) with T_2^* replaced by T_2 (see Section 6.1.1).

In practice, additional experimental factors warrant consideration when choosing the Ramsey free precession time τ. For example, because time-varying electric and magnetic fields and temperature may mask as dephasing mechanisms, the measured value of T_2^* depends on the measurement duration. Thus, if the time required to measure the value of T_2^* is significantly longer than the duration of a magnetic field measurement, field fluctuations may artificially reduce the measured value of T_2^* compared to the value relevant for sensing. This spoiled T_2^* measurement could lead to a suboptimal choice of τ [81]. Therefore, care should be taken when choosing the appropriate free precession time τ for a magnetometry experiment.

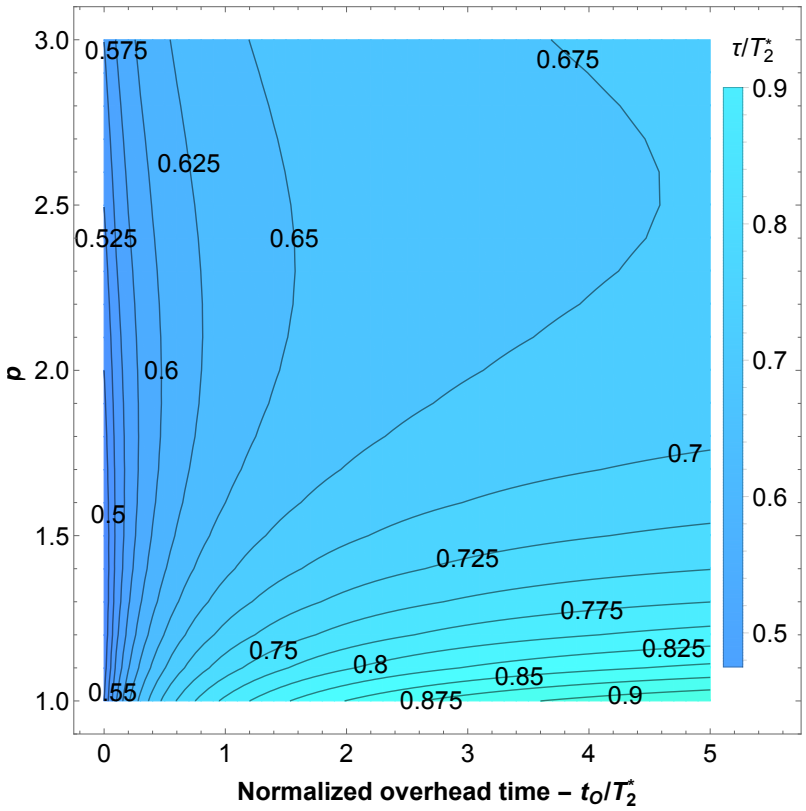

Figure 2.1.5: Optimal precession time τ for a pulsed magnetometry protocol. Contour plot shows precession time τ to achieved optimal sensitivity, in units of T_2^*, for different stretched exponential parameters p and different overhead times t_O.

2.2 Dephasing mechanisms and their limits to T_2^*

An NV$^-$ ensemble's spin dephasing time T_2^* can be qualitatively expressed as

$$\begin{aligned}\frac{1}{T_2^*} \approx \frac{1}{T_2^*\{\text{electronic spin bath}\}} + \frac{1}{T_2^*\{\text{nuclear spin bath}\}} \\ + \frac{1}{T_2^*\{\text{strain gradients}\}} + \frac{1}{T_2^*\{\text{electric field noise}\}} \\ + \frac{1}{T_2^*\{\text{magnetic field gradients}\}} + \frac{1}{T_2^*\{\text{temperature variation}\}} \\ + \frac{1}{T_2^*\{\text{unknown}\}} + \frac{1}{2T_1},\end{aligned} \tag{2.4}$$

where the symbol notation $T_2^*\{\text{X}\}$ denotes the limit to T_2^* solely due to mechanism X. Equation 2.4 assumes all mechanisms are independent and the associated dephasing rates add linearly. The second assumption is strictly only valid when all dephasing mechanisms lead to single-exponential free-induction-decay envelopes, (i.e., Lorentzian lineshapes); see Sections 2.1.4, 2.1.5, and 2.1.6. Here we briefly discuss each of these contributions to NV$^-$ ensemble dephasing, and in later sections we examine their scaling, and how each mechanism may be mitigated.

The electronic spin bath consists of paramagnetic impurity defects in the diamond lattice, which couple to NV$^-$ spins via magnetic dipolar interactions. The inhomogeneous spatial distribution and random instantaneous orientation of these bath spins cause dephasing of the NV$^-$ spin ensemble [143, 141, 81, 84]. Electronic spin bath dephasing can be broken down into contributions from individual constituent defect populations,

$$\begin{aligned}\frac{1}{T_2^*\{\text{electronic spin bath}\}} = \frac{1}{T_2^*\{\text{N}_\text{S}^0\}} + \frac{1}{T_2^*\{\text{NV}^-\}} \\ + \frac{1}{T_2^*\{\text{NV}^0\}} + \frac{1}{T_2^*\{\text{other electronic spins}\}}.\end{aligned} \tag{2.5}$$

Here $T_2^*\{\text{N}_\text{S}^0\}$ denotes the T_2^* limit from dephasing by paramagnetic substitutional nitrogen defects N_S^0 ($S = 1/2$), also called P1 centers, with concentration $[\text{N}_\text{S}^0]$ [154, 155, 156]. As substitutional nitrogen is a necessary ingredient for creation of NV$^-$ centers,

N_S^0 defects typically persist at concentrations similar to or exceeding NV^- (and NV^0) concentrations, and may account for the majority of electronic spin bath dephasing [81]. Section 2.2.1 examines $T_2^*\{N_S^0\}$ scaling with $[N_S^0]$. For NV-rich diamonds, dipolar interactions among NV^- spins may also cause dephasing of the ensemble, with associated limit $T_2^*\{NV^-\}$. Section 2.2.4 examines the $T_2^*\{NV^-\}$ scaling with $[NV^-]$ and other experimental parameters. In NV-rich diamonds, the neutral charge state NV^0 ($S = 1/2$) is also present at concentrations similar to $[NV^-]$ [157], and may also contribute to dephasing, with limit $T_2^*\{NV^0\}$. The quantity $T_2^*\{\text{other electronic spins}\}$ encompasses dephasing from the remaining defects in the electronic spin bath, such as negatively charged single vacancies [158], vacancy clusters [159, 160] and hydrogen-containing defects [161].

The quantity $T_2^*\{\text{nuclear spin bath}\}$ in Equation 2.4 describes NV^- ensemble dephasing from nuclear spins in the diamond lattice. In samples with natural isotopic abundance of carbon, the dominant contributor to nuclear spin bath dephasing is the ^{13}C isotope ($I = 1/2$), with concentration $[^{13}C] = 10700 \pm 800$ ppm [162], so that $T_2^*\{\text{nuclear spin bath}\} \approx T_2^*\{^{13}C\}$ [163, 17, 164, 144]. Other nuclear spin impurities exist at much lower concentrations and thus have a negligible effect on dephasing. The $T_2^*\{^{13}C\}$ scaling with concentration $[^{13}C]$ is discussed in Section 2.2.3 and can be minimized through diamond isotope engineering [17, 165].

Another major source of NV^- ensemble dephasing is non-uniform strain across the diamond lattice. Because strain shifts the NV^- spin resonances [56, 94, 166], gradients and inhomogeneities in strain may dephase the ensemble, limiting T_2^*. Strain may vary by more than an order of magnitude within a diamond sample [81], and can depend on myriad diamond synthesis parameters [167, 168]. For a given NV^- orientation along any of the [111] diamond crystal axes, strain couples to the NV^- Hamiltonian approximately in the same way as an electric field (though with a different coupling strength) [56, 169, 57] (see Appendix B for further discussion). Thus, the quantity $T_2^*\{\text{strain gradients}\}$ may be separated into into terms accounting for strain coupling

along (||) and transverse to ($\perp$) the NV$^-$ symmetry axis,

$$\frac{1}{T_2^*\{\text{strain gradients}\}} = \frac{1}{T_2^*\{\text{strain}_{||}\}} + \frac{1}{T_2^*\{\text{strain}_{\perp}\}}. \tag{2.6}$$

Application of a sufficiently strong bias magnetic field mitigates the transverse strain contribution to dephasing [94], (see Section 6.1.4), while the longitudinal contribution may be canceled by employing double-quantum coherence magnetometry (see Section 6.1.2).

Inhomogeneous and fluctuating electric fields also cause NV$^-$ ensemble dephasing [94], with associated limit $T_2^*\{\text{electric field noise}\}$. This dephasing source may also be broken down into components longitudinal and transverse to the NV$^-$ symmetry axis, and the contributions can be suppressed by the same methods as for strain-related dephasing.

In addition, external magnetic field gradients may cause NV$^-$ spin dephasing by introducing spatially-varying shifts in the NV$^-$ energy levels across an ensemble volume, with associated limit $T_2^*\{\text{magnetic field gradients}\}$. Design of uniform bias magnetic fields minimizes this contribution to NV$^-$ ensemble dephasing, and is largely an engineering challenge given that modern NMR magnets can exhibit sub-ppb uniformities over their cm-scale sample volumes [116].

Even though T_2^* is considered the *inhomogeneous* dephasing time, homogeneous time-varying electric and magnetic fields may mask as dephasing mechanisms if these fields fluctuate over the course of multiple interrogation/readout sequences, in other words, if the fields are inhomogeneous in time. Such a scenario could result in the unfortunate situation where the measured value of T_2^* depends on the total measurement duration (see Section 2.1.7). By the same argument, temperature fluctuations and spatial gradients can also mask as dephasing mechanisms and can artificially limit the measured T_2^*. Temperature variations cause expansion and contraction of the diamond crystal lattice, altering the NV$^-$ center's zero-field splitting parameter D ($dD/dT = -74$ kHz/K [91]) and may also shift the bias magnetic field. Finally, we include a term in Equation 2.4 for as-of-yet unknown mechanisms limiting T_2^*, and

note that T_2^* is limited to a theoretical maximum value of $2T_1$ [71, 72].

Importantly, Equation 2.4 shows that the value of T_2^* is primarily set by the dominant dephasing mechanism. Therefore, when seeking to extend T_2^*, one should focus on reducing whichever mechanism is dominant until another mechanism becomes limiting. Reference [170] aptly expresses the proper strategy as a "shoot the alligator closest to the boat" approach. For example, if the dephasing due to substitutional nitrogen is decreased by $\sim 10\times$ in a physical experiment, the improvement in T_2^* may only be $2\times$ if, say, strain inhomogeneity becomes a limiting factor; at that point it becomes more fruitful to shift focus towards reducing strain-induced dephasing.

2.2.1 Substitutional nitrogen limit to T_2^*

In nitrogen-rich diamonds, the majority of electronic spins contributing to the spin bath originate from substitutional nitrogen defects, since N_S^0 may donate its unpaired electron to another defect X and become spinless N_S^+, e.g., via the process [171],

$$N_S^0 + X^0 \leftrightarrow N_S^+ + X^-. \tag{2.7}$$

In these samples, the electronic spin concentration is closely tied to the total concentration of substitutional nitrogen donors $[N_S^T]$, and thus $T_2^*\{\text{electronic spin bath}\}$ is primarily set by $[N_S^T]$. In unirradiated nitrogen-rich diamonds, however, N_S^0 serves as the primary contributor to the electronic spin bath [81]. The N_S^0 contribution to dephasing obeys

$$\frac{1}{T_2^*\{N_S^0\}} = A_{N_S^0}\,[N_S^0] \tag{2.8}$$

where $[N_S^0]$ is the concentration of neutral substitutional nitrogen, and $A_{N_S^0}$ characterizes the magnetic dipole interaction strength between NV^- spins and N_S^0 spins. The inverse linear scaling of $T_2^*\{N_S^0\}$ is supported by both theory [146, 3, 164, 172, 84], and experiment [81, 84, 148]. However, reported values of the scaling factor $A_{N_S^0}$ from theoretical spin-bath simulations vary widely; for example, Ref. [164] predicts $A_{N_S^0} = 56$ ms^{-1}ppm^{-1}, whereas Ref. [172] predicts $A_{N_S^0} = 560$ ms^{-1}ppm^{-1}, a $10\times$ dis-

crepancy. The authors of Ref. [81, 84] measure $T_2^*\{N_S^0\}$ on five samples in the range $[N_S^0] = 0.75 - 60$ ppm (see Figure 2.2.2) and determine $A_{N_S^0} = 101 \pm 12$ ms^{-1}ppm^{-1}, such that for a sample with $[N_S^0] = 1$ ppm, $T_2^*\{N_S^0\} = 9.9 \pm 1.2$ µs. The experimental value of $A_{N_S^0}$ is consistent with numerical simulations in the same work [84]. The authors calculate the second moment of the dipolar-broadened single NV$^-$ ODMR linewidth [146] for 10^4 random spin bath configurations and, by computing the ensemble average over the distribution of single-NV$^-$ linewidths [141], find good agreement with the experimental value $A_{N_S^0} = 101$ ms^{-1}ppm^{-1}.

Electron paramagnetic resonance (EPR) measurements of nitrogen N_S^0 defects in diamond [148] from 63 samples also confirm the scaling $1/T_2^* \propto [N_S^0]$ and the approximate scaling constant $A_{N_S^0}$. Assuming a Lorentzian profile when converting peak-to-peak widths δ from Ref. [148] to T_2^* values (as discussed in Section 2.1.5) yields $A_{N_S^0} \approx 130$ ms^{-1}ppm^{-1} for nitrogen spins in a nitrogen spin bath (see Figure 2.2.1). This calculated scaling factor is considered to be an upper bound because (i), a Gaussian or Voigt profile would result in a smaller value of $A_{N_S^0}$ than that calculated by assuming a Lorentzian profile, as $1/T_{2\,\mathrm{Gau}}^* = 1/(\sqrt{6} \times T_{2\,\mathrm{Lor}}^*)$; and (ii), other sources of broadening may contribute to the EPR linewidths observed in Ref. [148]. In the latter case the true contribution to dephasing from dipolar interactions between N_S^0 spins would be smaller than that estimated from the measured δ. Nitrogen-spin-bath induced dephasing of N_S^0 and of NV$^-$ are expected to be similar, as the dipolar coupling between two N_S^0 spins is similar to the dipolar coupling between a N_S^0 and an NV$^-$ for equivalent separation [143]. Thus, the spin-bath-limited linewidth of nitrogen defects in diamond measured via EPR can serve as a proxy for the spin-bath limited linewidth of NV$^-$ centers. The value of $A_{N_S^0} \approx 130$ ms^{-1}ppm^{-1} for N_S^0 from the data in Ref. [148] serves as an independent estimate of $A_{N_S^0}$ for NV$^-$ centers in a nitrogen spin bath. This value is in good agreement with the measured $A_{N_S^0} \approx 101$ ms^{-1}ppm^{-1} for NV$^-$ ensembles from Ref. [81].

In addition, the data in Ref. [148] suggest that dipolar dephasing contributions from ^{13}C at natural isotopic abundance (10700 ppm [162]) and from substitutional nitrogen are equal for $[N_S^0] = 10.8$ ppm. The measured values of $A_{N_S^0}$ [81] and $A_{^{13}C}$

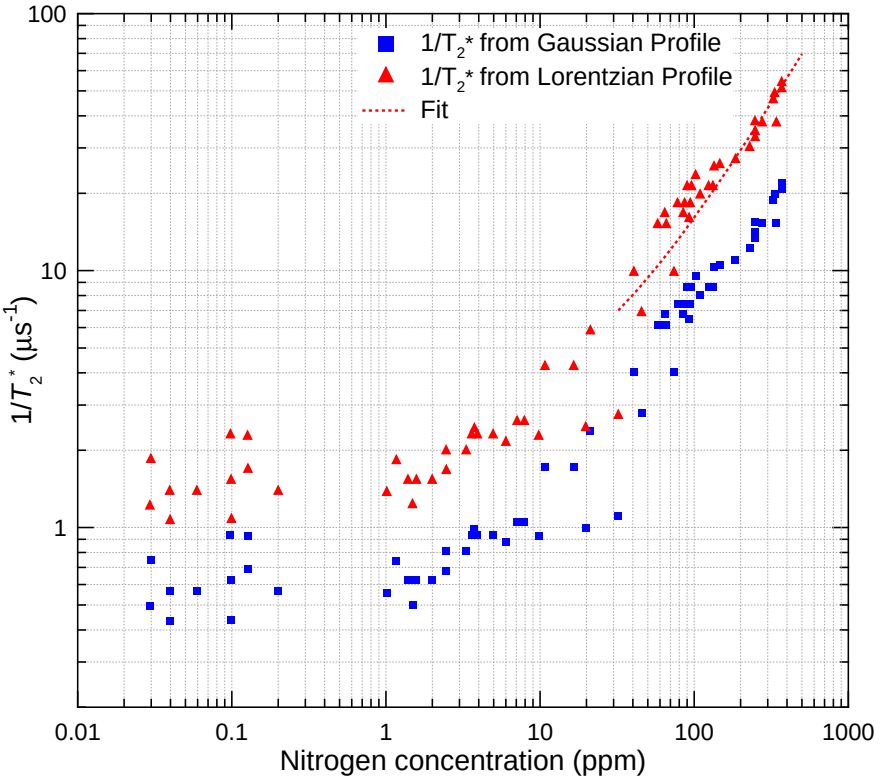

Figure 2.2.1: Bounds on $1/T_2^*$ associated with EPR linewidth measurements of N_S^0 defects (P1 centers) from Ref. [148] in diamonds with a range of nitrogen impurity concentrations, calculated assuming Gaussian (▪) and Lorentzian (▲) EPR lineshapes. A fit to the function $1/T_2^* = A_{N_S^0}[N_S^0] + b$ assuming a Lorentzian lineshape (····) yields $A_{N_S^0} \approx 130$ ms^{-1}ppm^{-1} for nitrogen spins in a nitrogen spin bath (see main text).

(see Section 2.2.3) for NV^- ensembles predict the two contributions to be equal at $N_S^0 = 10.3$ ppm, which is consistent to within experimental uncertainty.

When engineering diamond samples for broadband ensemble-NV^- magnetometry, the grown-in nitrogen concentration should be chosen to optimize achievable sensitivity. Here we present a simple toy model to aid in selecting a target nitrogen concentration in diamond for this goal. The following discussion parallels the clear analysis presented in Ref. [173], which the reader is encouraged to review. Equation 2.4 can be simplified by grouping all non-nitrogen-related broadening mechanisms together, yielding

$$\frac{1}{T_2^*} = \frac{1}{T_2^*\{N_S^0\}} + \frac{1}{T_2^*\{NV^-\}} + \frac{1}{T_2^*\{NV^0\}} + \frac{1}{T_2^*\{\text{other}\}}, \tag{2.9}$$

where we have ignored typically less common defects in fully treated diamond (i.e., irradiated, annealed, etc.) such as NVH^-, N_2V^-, etc. [157]; and $T_2^*\{\text{other}\}$ denotes the T_2^* limit from all non-nitrogen-related dephasing mechanisms. The above equation can be rewritten as

$$\begin{aligned}\frac{1}{T_2^*} = A_{N_S^0}[N^T][1 - E_{conv} - E_{conv}^0 - E_{conv}^{N_S^+}] + A_{NV^-}[N^T][E_{conv}] \\ + A_{NV^0}[N^T][E_{conv}^0] + \frac{1}{T_2^*\{\text{other}\}}\end{aligned} \tag{2.10}$$

where $E_{conv} \equiv [NV^-]/[N^T]$, $E_{conv}^0 \equiv [NV^0]/[N^T]$, and $E_{conv}^{N_S^+} \equiv [N_S^+]/[N^T]$ are the conversion efficiencies from the total nitrogen concentration $[N^T]$ to $[NV^-]$, $[NV^0]$, and $[N_S^+]$ respectively. The A_X coefficients characterize the magnetic dipole interaction strength between NV^- spins and spin species X. The value of $A_{N_S^0}$ is defined in Equation 2.8, the value of A_{NV^-} is defined in Section 2.2.4, and in this section for reasons of compactness we do not differentiate between $A_{NV_\parallel^-}$ and $A_{NV_\nparallel^-}$. The value of A_{NV^0} is defined so that the NV^- dephasing from NV^0 satisfies $\frac{1}{T_2^*\{NV^0\}} = A_{NV^0}[NV^0]$. Under the assumption that E_{conv}, E_{conv}^0, $E_{conv}^{N_S^+}$ are independent of $[N^T]$, consolidation yields

$$\frac{1}{T_2^*} = \kappa[N^T] + \frac{1}{T_2^*\{\text{other}\}}, \tag{2.11}$$

where $\kappa = A_{\mathrm{N_S^0}}[1 - \mathrm{E_{conv}} - \mathrm{E^0_{conv}} - \mathrm{E^{N_S^+}_{conv}}] + A_{\mathrm{NV^-}}[\mathrm{E_{conv}}] + A_{\mathrm{NV^0}}[\mathrm{E^0_{conv}}]$. The detected number of PL photons per measurement is $\mathcal{N} \propto [\mathrm{N^T}]\mathrm{E_{conv}} V n_{\mathrm{avg}}$ where V is the interrogation volume. For simplicity we consider the limit where initialization and readout times t_I and t_R are negligible, so that sensitivity is

$$\eta \propto \sqrt{\frac{1}{\mathcal{N} T_2^*}} = \sqrt{\frac{1}{\mathrm{E_{conv}} V n_{\mathrm{avg}}}} \times \sqrt{\kappa + \frac{1}{[\mathrm{N^T}] T_2^* \{\mathrm{other}\}}}, \tag{2.12}$$

which suggests that for $[\mathrm{N^T}] \gg \frac{1}{\kappa\, T_2^* \{\mathrm{other}\}}$, sensitivity is independent of $[\mathrm{N^T}]$. Qualitatively, this can be interpreted as follows: when T_2^* is limited by nitrogen-related dephasing mechanisms (i.e., $\mathrm{NV^-}$, $\mathrm{NV^0}$, $\mathrm{N_S^0}$), and again assuming $\mathrm{E_{conv}}$, $\mathrm{E^0_{conv}}$, and $\mathrm{E^{N_S^+}_{conv}}$ are independent of $[\mathrm{N^T}]$, decreasing $[\mathrm{N^T}]$ increases T_2^* by the same fractional quantity that the $\mathrm{NV^-}$ ensemble photoluminescence $\mathcal{N}$ is decreased. However, when T_2^* is limited by other broadening mechanisms unrelated to nitrogen, decreasing $[\mathrm{N^T}]$ decreases the collected fluorescence $\mathcal{N}$ without any corresponding T_2^* increase. The implications here are significant: this analysis suggests that while there is not a unique value of $[\mathrm{N^T}]$ for maximal sensitivity, there is a minimum value. In other words, if nitrogen-related broadening is a small contributor to T_2^*, the nitrogen content should be increased; the increased resulting PL will favorably offset the increase in T_2^*, resulting in overall enhanced sensitivity.

A few points are in order regarding the above analysis. Experimental considerations can also set an upper bound on the most desirable total nitrogen concentration $[\mathrm{N^T}]$. For example, the larger detected photon number $\mathcal{N}$ associated with higher values of $[\mathrm{N^T}]$ can present technical challenges (see Section 1.7.5). Moreover, the above analysis considers the simple limit where the initialization and readout times are negligible; accounting for this fixed overhead time (see Equations 1.43, 1.45, and 1.46) favors trading off nitrogen concentration density for longer values of T_2^*, in order to reduce the fractional overhead time devoted to initialization and readout. Overall, combined experimental and theoretical considerations suggest that for best sensitivity nitrogen concentration should be decreased until nitrogen-related broadening is similar to broadening unrelated to nitrogen, i.e., $\kappa[\mathrm{N^T}] \approx \frac{1}{T_2^* \{\mathrm{other}\}}$.

2.2.2 Substitutional nitrogen limit to T_2

Although this dissertation primarily focuses on T_2^*-limited broadband DC sensing, with only passing discussion of AC sensing protocols (Section 6.1.1), measuring and understanding the Hahn echo coherence time T_2 can provide useful insights for characterization and evaluation of NV-diamond samples. For example, the value of T_2 in a given diamond sets a rough bound on the achievable T_2^* for a ensemble-NV$^-$ sensor device employing that diamond. Therefore, here we discuss the limit to T_2 imposed by substitutional nitrogen spins in diamond.

Like the dephasing time T_2^*, the coherence time T_2 depends on the neutral substitutional nitrogen concentration $[\mathrm{N_S^0}]$, which sets both the average dipolar-coupling strength between NV$^-$ and nitrogen bath spins, (i.e., $A_{\mathrm{N_s^0}}[\mathrm{N_s^0}]$ from Equation 2.8), as well as the average coupling strength between nitrogen bath spins [139, 174]. Furthermore, it can be shown that when nitrogen is the dominant decoherence mechanism, $T_2\{\mathrm{N_S^0}\}$ depends inverse linearly on the nitrogen concentration $[\mathrm{N_S^0}]$ [84], revealing a close relationship to $T_2^*\{\mathrm{N_S^0}\}$. The dependence of $T_2\{\mathrm{N_S^0}\}$ on $[\mathrm{N_S^0}]$ was recently determined experimentally through NV$^-$ ensemble measurements on 25 diamond samples (see Figure 2.2.2b), yielding [84]

$$\frac{1}{T_2\{\mathrm{N_S^0}\}} = B_{\mathrm{N_S^0}}[\mathrm{N_S^0}]. \tag{2.13}$$

Here, $B_{\mathrm{N_S^0}} = 6.25 \pm 0.47$ ms^{-1}ppm^{-1}, such that an NV$^-$ ensemble in a 1-ppm-nitrogen sample is expected to exhibit $T_2 \simeq 160 \pm 12$ μs. The scaling in Equation 2.13 should also be compared to $T_2^*\{\mathrm{N_S^0}\}$ (Equation 2.8), with $T_2\{\mathrm{N_S^0}\}/T_2^*\{\mathrm{N_S^0}\} = B_{\mathrm{N_S^0}}/A_{\mathrm{N_S^0}} \approx 17$. A straightforward application of these results is the calibration of the total nitrogen spin concentration in diamond samples through T_2^* measurements, T_2 measurements, or both, provided that nitrogen remains the primary source of dephasing and decoherence in such samples. Here, T_2 measurements should be advantageous over T_2^* (or linewidth) measurement schemes, as the latter are more likely to be limited by non-nitrogen dephasing mechanisms [81].

Lastly, we note that the inverse linear scaling of $T_2^*\{\mathrm{N_S^0}\}$ and $T_2\{\mathrm{N_S^0}\}$ with $[\mathrm{N_S^0}]$, as

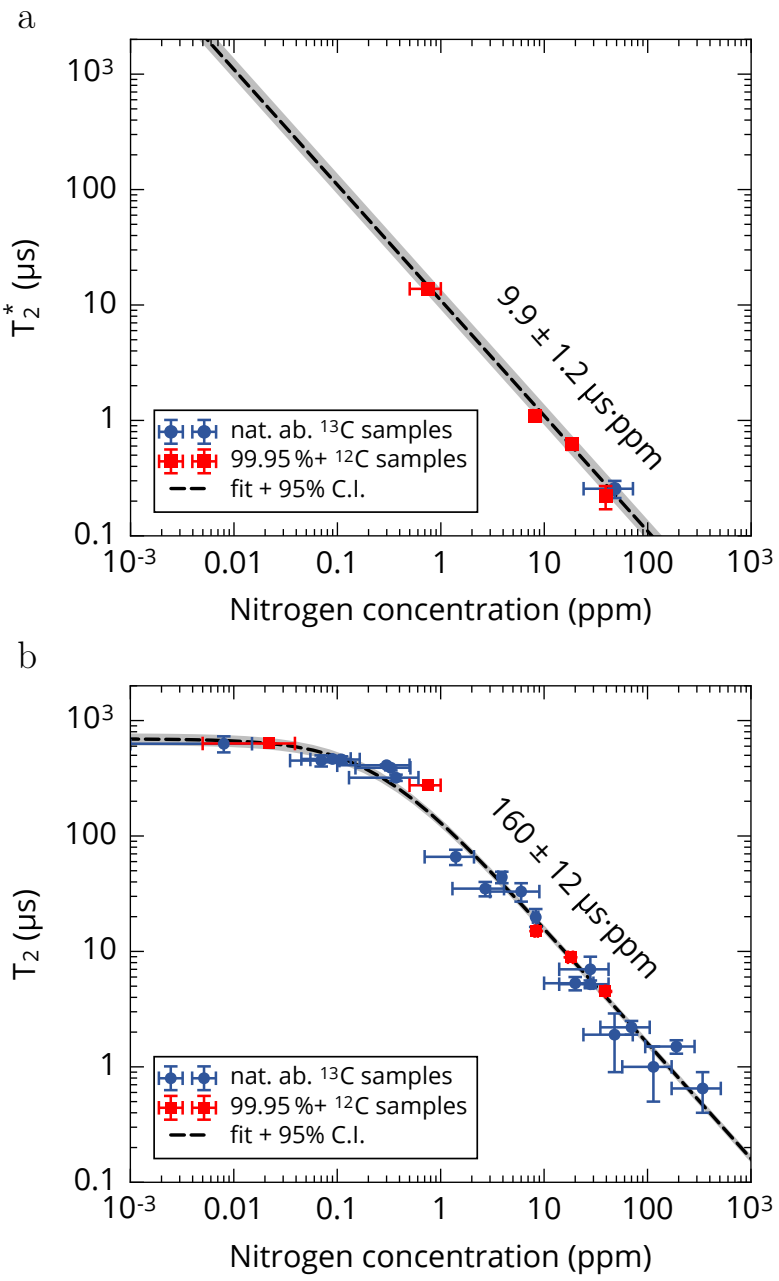

Figure 2.2.2: Substitutional nitrogen spin bath contribution to ensemble-NV$^-$ dephasing time T_2^* and coherence time T_2. a) Measured spin-bath contribution to T_2^* vs. nitrogen concentration measured by secondary ion mass spectrometry (SIMS) for five diamond samples. Fit yields $1/T_2^*\{\mathrm{N_S^0}\} = A_{\mathrm{N_S^0}}[\mathrm{N_S^0}]$ with $A_{\mathrm{N_S^0}} = 101 \pm 12$ ms^{-1}ppm^{-1}. b) Measured Hahn echo T_2 vs. nitrogen concentration for 25 diamond samples. Fit yields $1/T_2\{\mathrm{N_S^0}\} = B_{\mathrm{N_S^0}}[\mathrm{N_S^0}]$ with $B_{\mathrm{N_S^0}}[\mathrm{N_S^0}] = 6.25 \pm 0.47$ ms^{-1}ppm^{-1}. Adapted from Ref. [84].

well as the hierarchy $T_2 \gg T_2^*$, are consistent with earlier EPR studies of N_S^0 nitrogen defects in nitrogen-rich diamonds [148, 175] and other comparable spin systems in silicon [176, 177]. A direct comparison of T_2 between the different spin systems, however, cannot easily be made and would require accounting for specifics of the different experimental techniques.

2.2.3 ^{13}C limit to T_2^*

Dipolar coupling between NV$^-$ electronic and ^{13}C nuclear spins can also limit T_2^* [141, 17, 164, 144]. Reducing the ^{13}C content below the natural abundance concentration $[^{13}\mathrm{C}] = 10700 \pm 800$ ppm $\approx 1.1\%$ [162] through isotope engineering is the most direct way to mitigate this effect [17, 178, 81]. In the "dilute" spin limit where $[^{13}\mathrm{C}]/[^{12}\mathrm{C}] \ll 0.01$ [150], the ^{13}C dephasing contribution is well-approximated by

$$\frac{1}{T_2^*\{^{13}\mathrm{C}\}} = A_{^{13}\mathrm{C}}\,[^{13}\mathrm{C}], \tag{2.14}$$

where $A_{^{13}\mathrm{C}}$ is a constant characterizing the magnetic dipole interaction strength between NV$^-$ spins and ^{13}C nuclear spins, in accordance with theoretical predictions [141, 144, 146, 150]. Although experimental measurements relating T_2^* to $[^{13}\mathrm{C}]$ are only available for single NV$^-$ centers [17, 179] and not for NV$^-$ ensembles, the scaling in Equation 2.14 is consistent with experimental findings in a similar ensemble spin system; EPR linewidth measurements on substitutional phosphorus spin ensembles in a ^{28}Si crystal exhibit the same scaling for various dilute concentrations of ^{29}Si [176, 180]. Figure 4b in Ref. [176] suggests that Equation 2.14 is approximately valid for $[^{29}\mathrm{Si}]/[^{18}\mathrm{Si}] \lesssim 0.05$, so it is feasible that $A_{^{13}\mathrm{C}}$ can be inferred from measurements on diamonds with natural ^{13}C isotopic abundance where $[^{13}\mathrm{C}]/[^{12}\mathrm{C}] \approx 0.0107$. We make this approximation henceforth.

While the value of $A_{^{13}\mathrm{C}}$ is not known precisely for NV$^-$ ensembles, T_2^* measurements in diamond with natural ^{13}C abundance set an approximate upper bound on $A_{^{13}\mathrm{C}}$, since necessarily $1/T_2^* > 1/T_2^*\{^{13}\mathrm{C}\}$. Figure 2.2.3 shows a Ramsey FID for a diamond with natural ^{13}C abundance, which suggests $A_{^{13}\mathrm{C}} \approx 0.100$ ms^{-1}ppm^{-1}.

With this value for $A_{^{13}\mathrm{C}}$, the expected limit for a 99.999% ^{12}C isotopically enhanced diamond is $T_2^*\{^{13}\mathrm{C}\} \approx 1$ ms, making dephasing due to ^{13}C nuclear spins negligible compared to other dephasing mechanisms (see Equation 2.4). Comparing $A_{^{13}\mathrm{C}}$ with the measured $A_{\mathrm{N_S^0}} = 101$ ms^{-1}ppm^{-1} for dephasing of NV$^-$ ensembles by substitutional nitrogen (see section 2.2.1), dephasing from natural abundance $[^{13}\mathrm{C}] = 10700$ ppm and substitutional nitrogen with concentration $[\mathrm{N_S^0}] = 10.6$ ppm should be equivalent, in good agreement with Ref. [148], which observes equivalence for $[\mathrm{N_S^0}] \approx 10.8$ ppm. Conveniently, it is easy to remember that $T_2^*\{^{13}\mathrm{C}\}$ is 1 μs for natural abundance ^{13}C diamond to better than 10%.

The bound on $A_{^{13}\mathrm{C}}$ derived above can be crudely confirmed utilizing a mix of theoretical predictions from Ref. [144] and data from Ref. [145]. The authors of Ref. [145] find the most probable T_2^* for a single NV$^-$ center in natural isotopic diamond to be $T_2^{*\{\mathrm{single,mp}\}} = 1.8 \pm 0.6$ μs (measured in a 20 G bias field, Figure 4a in Ref. [145]). From relations in Ref. [144] we estimate $A_{^{13}\mathrm{C}} \approx 2.2\, A_{^{13}\mathrm{C}}^{\mathrm{single,mp}}$, which yields $A_{^{13}\mathrm{C}} = 0.11 \pm 0.04$ ms^{-1}ppm^{-1}.

Our measured value $A_{^{13}\mathrm{C}} \approx 0.100$ ms^{-1}ppm^{-1} is also in reasonable agreement with first-principles theoretical calculations by Ref. [144], suggesting $A_{^{13}\mathrm{C}} \approx 0.057$ ms^{-1}ppm^{-1} for NV$^-$ ensembles in natural isotopic diamond in tens-of-gauss bias fields. Note that the experimental determination of $A_{^{13}\mathrm{C}}$ outlined in this section represents an upper bound on the true value of $A_{^{13}\mathrm{C}}$ in the dilute (dipolar-broadened) limit; if substantial broadening arises from Fermi-contact contributions in addition to dipolar interactions in natural abundance ^{13}C samples, or if $[^{13}\mathrm{C}] = 10700$ ppm does not qualify as the dilute limit [150, 146], the value of $A_{^{13}\mathrm{C}}$ given here will be overestimated.

Engineering diamonds for low ^{13}C content may be challenging [181, 182, 165]. The isotopic purity of a diamond grown by plasma-enhanced chemical vapor deposition (PE-CVD) is expected to be limited by the purity of the carbon source gas, which is most commonly methane (CH_4). However, diamonds grown with isotopically enriched methane may exhibit higher fractional ^{13}C content than the source gas due to extraneous carbon sources in the CVD chamber [182]. Nonetheless, Teraji *et al.* achieve $[^{12}\mathrm{C}] = 99.998\%$ as measured by secondary ion mass spectrometry (SIMS) when using

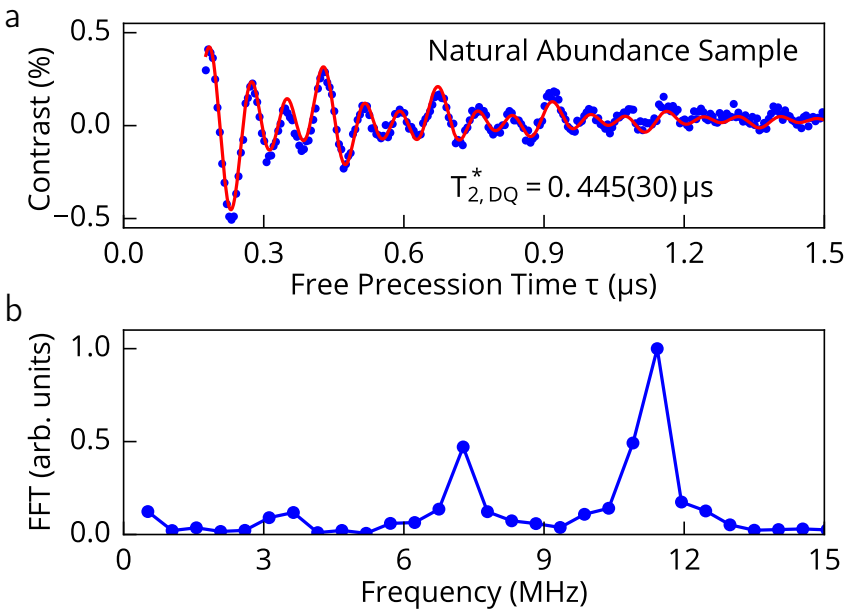

Figure 2.2.3: T_2^* measurement of a low-nitrogen-content diamond with natural abundance $[^{13}C]$ = 10700 ppm to assess the ^{13}C contribution to dephasing. a) Double quantum Ramsey free induction decay (FID) (•) and associated fit (—) suggest T_2^* is 445 ns in the double quantum basis. This data sets a bound $A_{^{13}C} < 0.105$ ms^{-1}ppm^{-1}. Correcting for the test diamond's approximately known $[N_S^0] \approx 0.5$ ppm content allows further refinement to $A_{^{13}C} \approx 0.100$ ms^{-1}ppm^{-1}. b) Fourier transform of the FID shown in the top panel. The three peaks arise from hyperfine interactions associated with the NV$^-$ center's ^{14}N nuclear spin $I = 1$ and exhibit intra-peak spacing double that of an equivalent single-quantum Ramsey measurement. The unbalanced peak heights are attributed to nuclear spin polarization induced by the 150 gauss bias magnetic field.

isotopically-enhanced methane with 99.999% ^{12}C (i.e., [^{13}C] $\leqslant$ 10 ppm) [165, 183]. Although such isotopically enhanced methane is currently 10^3 - 10^4 times more expensive than natural abundance CH_4, order unity conversion of the methane's carbon content into diamond is attainable [165].

2.2.4 NV$^-$ limit to T_2^*

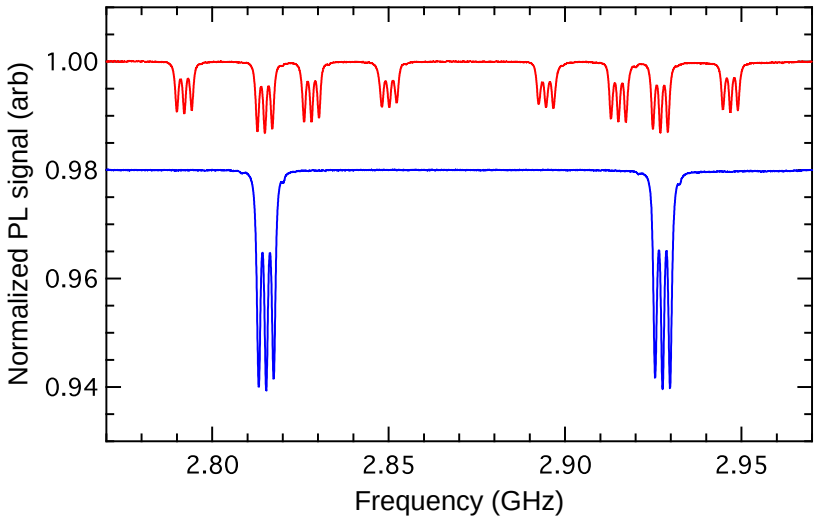

Figure 2.2.4: Experimental ODMR spectra from the same NV$^-$ ensemble in different applied bias magnetic fields. The data shown here are recorded from an ensemble of $\sim 10^{12}$ ^{14}NV$^-$ centers in the NV$^-$-rich diamond sample employed in Chapter 3. A bias field with a different projection on each of the four NV$^-$ crystallographic orientations separates the $m_s = 0 \leftrightarrow m_s = \pm 1$ spin resonances into distinct groups (—). A bias field that projects equally onto all four orientations overlaps the spin resonances (—, offset for clarity).

Dipolar interactions among negatively-charged NV$^-$ centers may also limit the dephasing time T_2^*. Dephasing from NV$^-$-NV$^-$ interactions arises from NV$^-$ spins in both the same and different groups as the NV$^-$ centers used for sensing, where groups are defined as follows: NV$^-$ centers with approximately the same spin resonance frequency are considered to be in the same group, whereas spins with different resonance frequencies are in different groups [184]. Depending on the strength and angle of the applied bias field, the spin resonances of the four NV$^-$ orientations may be spectrally separated, or two or more may be overlapped, changing the fraction of NV$^-$ spins in

the same group (see Figure 2.2.4). The NV^--NV^- dipolar contribution to T_2^* is then given by

$$\begin{aligned}\frac{1}{T_2^*\{NV^-\}} &= \frac{1}{T_2^*\{NV^-\}_{\parallel}} + \frac{1}{T_2^*\{NV^-\}_{\nparallel}} \\ &= \varsigma_{\parallel} A_{NV^-_{\parallel}} [NV^-_{\parallel}] + \varsigma_{\nparallel} A_{NV^-_{\nparallel}} [NV^-_{\nparallel}].\end{aligned} \tag{2.15}$$

Here the constants $A_{NV^-_{\parallel}}$ and $A_{NV^-_{\nparallel}}$ characterize the dipolar interaction strength for pairs of NV^- centers in the same group and different groups respectively; $[NV^-_{\parallel}]$ is the concentration of NV^- spins in the group being used for sensing and $[NV^-_{\nparallel}]$ is the concentration of NV^- spins in other groups, with $[NV^-_{\parallel}] + [NV^-_{\nparallel}] = [NV^-_{\text{total}}]$; and $\varsigma_{\parallel}$ and $\varsigma_{\nparallel}$ are dimensionless factors of order unity accounting for (imperfect) initialization of NV^- centers [8]. For example, off-resonant NV^- populations polarized into the spinless $m_s = 0$ state during initialization should not contribute to dephasing of the NV^- centers used for sensing, giving $\varsigma_{\nparallel} \simeq 0$.

Flip-flop interactions between NV^- spins in different groups are off-resonant and are thus suppressed, whereas flip-flop interactions can occur resonantly between spins in the same group. The extra interaction terms in the dipole-dipole Hamiltonian for spins in the same group result in a slightly increased dephasing rate [146, 184]. Following Ref. [146], it is expected that $A_{NV_{\parallel}} = 3/2\, A_{NV_{\nparallel}}$.

The lack of published data at present for $T_2^*\{NV^-\}$ in samples with varying NV^- concentration prevents definitive determination of $A_{NV_{\parallel}}$ and $A_{NV_{\nparallel}}$. However, both terms can be estimated from the experimentally determined value of $A_{N_S^0} = 101 \pm 12$ $ms^{-1}ppm^{-1}$ [84], which describes the scaling of NV^- ensemble T_2^* with substitutional nitrogen concentration (see Section 2.2.1). Assuming an NV^- electronic spin bath couples to NV^- sensor spins with approximately the same strength as a substitutional nitrogen spin bath [143], and accounting for the higher spin multiplicity of NV^- centers

($S_{\mathrm{NV^-}} = 1$) compared to substitutional nitrogen spins ($S_{\mathrm{N_S^0}} = 1/2$), we calculate [146]

$$\begin{aligned} A_{\mathrm{NV^-_{\nparallel}}} &\simeq \sqrt{\frac{S_{\mathrm{NV^-}}(S_{\mathrm{NV^-}}+1)}{S_{\mathrm{N_S^0}}(S_{\mathrm{N_S^0}}+1)}} A_{\mathrm{N_S^0}} \\ &\simeq \sqrt{8/3} A_{\mathrm{N_S^0}} \\ &\simeq 165 \text{ ms}^{-1}\text{ppm}^{-1} \end{aligned} \tag{2.16}$$

and find $A_{\mathrm{NV^-_{\parallel}}} = 3/2\, A_{\mathrm{NV^-_{\nparallel}}} \simeq 247$ ms^{-1}ppm^{-1}. Although the value of $T_2^*\{\mathrm{NV^-}\}$ depends on experimental conditions including optical initialization fraction (determining $\varsigma_{\parallel}$ and $\varsigma_{\nparallel}$) and bias magnetic field orientation (setting the ratio $[\mathrm{NV^-_{\parallel}}]/[\mathrm{NV^-_{\nparallel}}]$), the value of $T_2^*\{\mathrm{NV^-}\}$ for a given NV$^-$ concentration is well approximated (up to a factor of order unity) by the dephasing time $T_2^*\{\mathrm{N_S^0}\}$ for the same concentration of $\mathrm{N_S^0}$ spins.

Magnetometer operation in the NV$^-$-NV$^-$ interaction limit may occur as the N-to-NV$^-$ conversion efficiency $\mathrm{E_{conv}}$ approaches its theoretical limit of 50% [49, 185] (see Section 7.1). Under these circumstances, and when other sources of dephasing can be neglected - such as magnetic, electric, and strain gradients as well as ^{13}C nuclear spins (see Section 2.2.3) and other paramagnetic defects (see Section 7.6) - the interaction among NV$^-$ spins becomes the dominant source of dephasing. However, maximal N-to-NV$^-$ conversion efficiency is not necessarily required to operate in the NV$^-$-NV$^-$ interaction limit. When $\mathrm{E_{conv}} < 50\%$, dephasing due to other paramagnetic impurities may be reduced through spin bath driving techniques described in Section 6.1.3. Spin bath driving can also decouple the NV$^-$ centers in different groups from the NV$^-$ centers in the group used for sensing [81], mitigating the second term in Equation 2.15 ($1/T_2^*\{\mathrm{NV^-}\}_{\nparallel}$), and leaving only the first term ($1/T_2^*\{\mathrm{NV^-}\}_{\parallel}$) as a fundamental limit to NV$^-$ ensemble T_2^*.

While this section has focused on the negatively charged NV$^-$ center, NV centers are also present in the neutral charge state NV^0 ($S = 1/2$) (see Section 7.1). As NV^0 has not been observed in its ground state in EPR, an effect tentatively attributed to resonance line broadening from dynamic Jahn-Teller distortion [186], magnetic noise created by NV^0 may be reduced by a motional-narrowing-type effect to less than otherwise expected for a $S = 1/2$ defect (see Section 6.1.3). Consequently, the contri-

bution of NV^0 spins to dephasing of NV^- spins, may be smaller than expected. What little, if any, NV^+ present in the sample is expected to be spinless (see Table 7.6.1) and should not contribute substantially to dephasing.

Recently, several protocols have been theoretically proposed to mitigate strong NV^--NV^- dipolar interactions and extend T_2^* [170] or T_2 [187] while retaining magnetic field sensitivity. In addition, it has been proposed that under certain circumstances the NV^--NV^- dipolar interaction could enhance magnetometry sensitivity through enabling entanglement of multiple NV^- centers [120] (see Section 6.3.4). Harnessing entanglement could enable superior scaling of measurement SNR with number of spins addressed N, exceeding the standard quantum limit SNR$\propto\sqrt{N}$ and approaching the Heisenberg limit, SNR$\propto N$. Controlled coupling of NV^- spin pairs [188, 189, 190, 191, 192, 193] has been demonstrated; however, applying entanglement-enhanced techniques to larger ensembles is expected to be challenging.

2.3 Conclusion

Pulsed Ramsey-type magnetometers with NV^- ensembles exhibit sensitivities limited by the spin dephasing time T_2^*, which presently remains orders of magnitude shorter than the physical limit of $2T_1$. The Ramsey magnetic field sensitivity improves nearly linearly with T_2^* extension when the measurement overhead time is significant ($t_O \gtrsim T_2^*$), as is common for present-day ensemble-NV^- magnetometers. Therefore, the understanding presented in this Chapter on limitations to T_2^* in NV-rich diamonds lays important groundwork for improving magnetic field sensitivity. Not only does extending T_2^* directly improve achievable sensitivity of conventional fluorescence-based readout, but it also allows readout-fidelity-enhancement techniques that require long overhead times to offer sensitivity improvements. (Chapter 6).

Among the factors limiting T_2^* are magnetic-field, electric-field, and strain gradients. Ensemble-NV^- T_2^* values may also be limited by dipolar interactions with the diamond's inhomogeneous paramagnetic spin bath. We determine the individual contributions to T_2^* from substitutional nitrogen N_S^0 electronic spins (Section 2.2.1), ^{13}C

nuclear spins (Section 2.2.3), and NV^- spins (Section 2.2.4). Recent experiments determine T_2- and T_2^*-dependencies on nitrogen concentration to better than 10% [81, 84]. Chapters 6 and 7 employ insights from this chapter to guide analysis of strategies to extend T_2^*, increase spin readout fidelity, and improve the host diamond material properties.

Chapter 3

Optical magnetic detection of single-neuron action potentials using quantum defects in diamond

3.1 Introduction

A key challenge for neuroscience is noninvasive, label-free sensing of neuronal action potential (AP) dynamics with single-cell resolution. Magnetic field measurement provides a favorable alternative to existing electrical and optical neurosensing and neuroimaging methods, as neuronal APs pass largely unperturbed through biological tissue, allowing magnetic measurements of AP dynamics to be performed extracellularly or even outside intact organisms. To date, however, magnetic techniques for sensing neuronal activity have either operated at the macroscale with coarse spatial and/or temporal resolution - e.g., magnetic resonance imaging methods and magnetoencephalography [77] - or been restricted to biophysics studies of excised neurons probed with cryogenic or bulky detectors that do not provide single-cell spatial resolution and are not scalable to functional networks or intact organisms [194].

This chapter describes our demonstration of AP magnetic sensing with both single-neuron sensitivity and intact organism applicability using negatively-charged

nitrogen-vacancy (NV^-) quantum defects in diamond, optically probed under ambient conditions and with the NV-diamond sensor in close proximity ($\sim$ 10 μm) to the biological sample. High-resolution magnetic field sensing [21] and imaging employing NV^- centers has shown broad applicability to both physical [68] and biological [55, 50, 51, 32] systems under ambient conditions. For example, NV-diamond optically detected magnetic resonance (ODMR) has been used to image patterns of static magnetic fields produced by populations of living magnetotactic bacteria [50] and by immunomagnetically labeled tumor cells [51], with $\sim$ 1 μm resolution and $\sim$ 1 mm field of view.

Our technique applying NV^- ensembles for neuronal current detection exhibits a unique combination of features: (i) it is noninvasive, as the light that probes the NV^- sensors stays within the biocompatible diamond chip and does not enter the organism, enabling activity monitoring over extended periods; (ii) it is label-free and should be widely applicable to most organisms; (iii) it provides high spatial and temporal resolution, allowing precise measurement of the AP waveforms and magnetic field correlates of the conduction velocities of individual neurons; (iv) it directly determines AP propagation direction through the inherent sensitivity of NVs to the associated AP magnetic field vector; (v) it is applicable to neurons located within optically opaque tissue or whole organisms; and (vi) it is scalable and can be integrated with existing techniques such as wide-field and superresolution imaging.

We achieve a magnetic field sensitivity of 15 $pT/\sqrt{Hz}$ from 80 Hz to $\sim$ 3 kHz, which represents a 20× improvement over previous broadband NV-diamond magnetometers [121], and we also demonstrate operation with temporal resolution down to $\sim$ 32μs. We utilize this device to measure the time-dependent magnetic fields produced by single-neuron APs with signal-to-noise ratio (SNR) above 1 for a single event when using matched filtering. We demonstrate this method for excised single neurons from marine worm and squid, and then exterior to intact, optically opaque marine worms over extended periods and with no observed adverse effect on the animal. For each biological specimen, we typically acquire repeated AP magnetic field measurements, often over extended periods of time (hours). Multiple synchronized,

consecutive AP measurements (N_{avg}) can also be averaged together to increase the measurement SNR.

This chapter begins by introducing the NV-diamond magnetometer apparatus, next describes our single-neuron action potential measurements, and then discusses future projections for a next-generation NV-diamond magnetic imager capable of resolving magnetic fields from currents in mammalian neurons. Much of this chapter is adapted from Ref. [24].

3.2 The NV-diamond magnetic sensor

The work described in this chapter employs a simple, robust apparatus (Figure 3.2.1) with a magnetic field sensor consisting of a macroscopic, single-crystal diamond with a uniform 13 μm layer containing a high concentration ($\sim 3\times10^{17}$ cm^{-3}) of NV$^-$ centers at the top surface. Biological specimens may be placed on or directly above the NV-enriched surface (Figure 3.2.1a), providing micron-scale proximity between the layer of NV$^-$ centers and the sources of magnetic field signals, in contrast to macroscale sensors used to sense neuronal magnetic fields or activity [194, 77, 195]. Microwaves (MWs) are applied to the NV$^-$ centers via a wire loop positioned above the diamond, with minimal observed perturbation to the specimen studied, 12 [196, 197, 24]). Laser radiation at 532 nm enters the diamond through its side facet at a sufficiently shallow angle as to undergo total internal reflection within the diamond crystal and avoid irradiating any living sample placed above the diamond (Figure 3.2.1b). The light excites the NV$^-$ centers, causing emission of photoluminescence (PL), which is imaged onto a photodiode. Continuous-wave ODMR magnetometry [100, 26] is used to detect the magnetic field of a propagating action potential (AP) as a time-varying shift in the center of the ODMR line, as described further in Section 3.2.2.

3.2.1 Device details

The diamond is an electronic grade ([N] < 5 ppb) single crystal chip, with rectangular dimensions 4 mm × 4 mm × 500 μm, grown using chemical vapor deposition

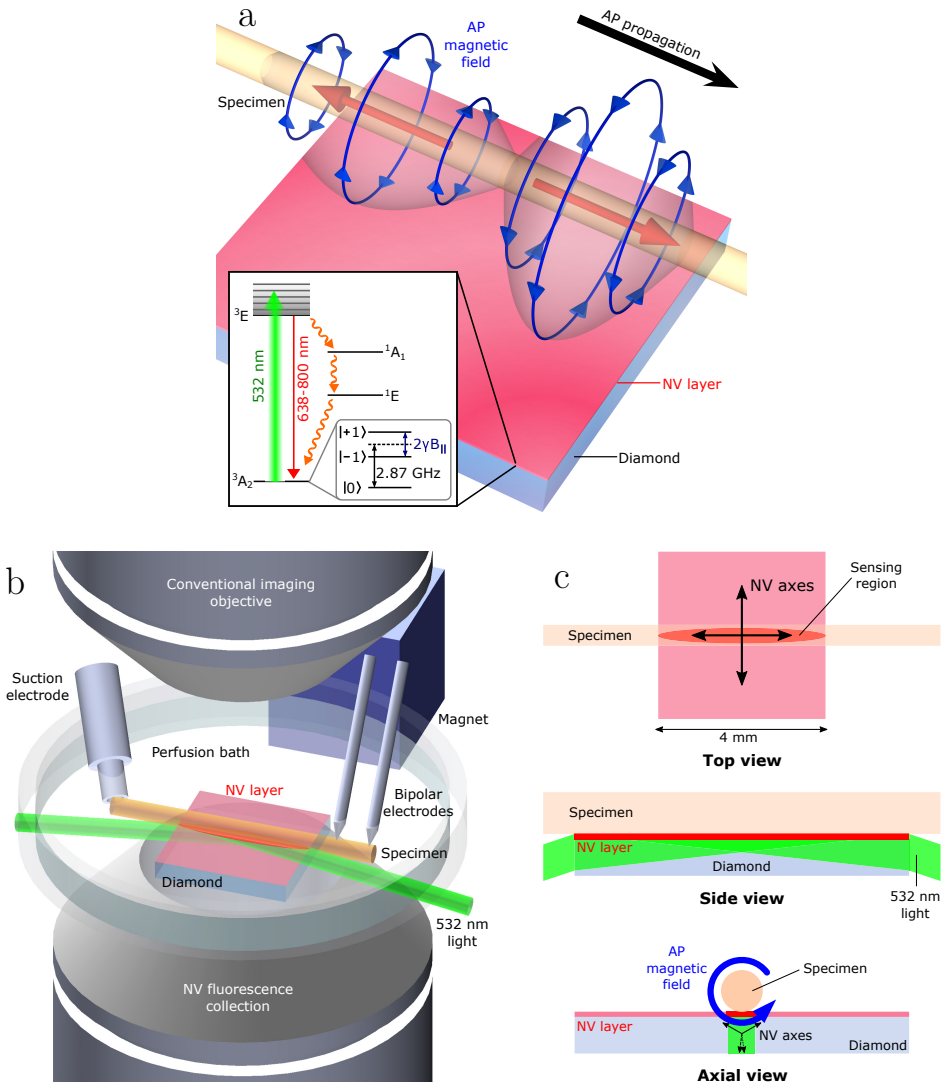

Figure 3.2.1: Experimental overview. a) Schematic image depicting bipolar azimuthal magnetic field associated with AP propagating from left to right. Red arrows indicate axial current through axon. Magnetic field (blue arrows) projection is detected by 13 µm-thick NV^--rich layer on diamond substrate. (Inset) NV^- center energy level diagram. b) Custom-built microscope for simultaneous magnetic sensing and conventional imaging of specimens. NV^- centers are excited by 532-nm laser light oriented at grazing incidence to diamond top surface. Inverted aspheric condenser objective collects NV^- PL. Magnet applies uniform 7-G bias field at diamond. Specimens are placed on top of diamond, and individual APs are stimulated by suction electrode and detected downstream via a pair of bipolar recording electrodes. For clarity, wire loop for MW delivery and axon clamp are not shown. c) Top, side, and axial views of NV-diamond sensor and specimen. Top view shows sensing region from which LIF is collected, as well as top-down projection of the four crystallographic NV^- axes. AP magnetic field projects onto two NV axes perpendicular to specimen axis. Side view shows 532-nm laser light entering diamond at grazing angle and exciting NV^--rich layer. Blue arrow depicts AP magnetic field; black arrows depict NV^- axes.

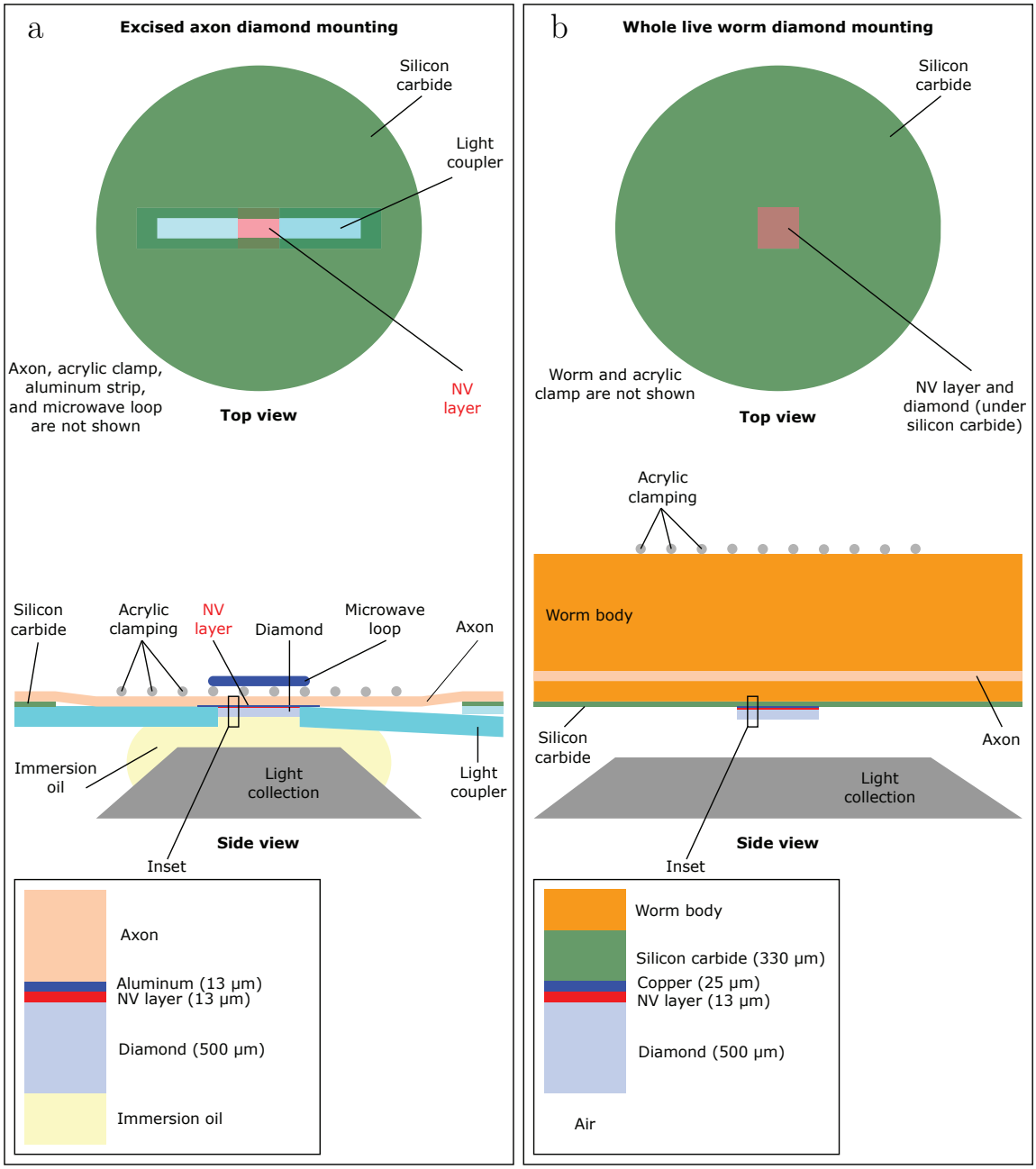

Figure 3.2.2: Diamond mounting. a) Diamond mounting for excised axon experiments, as described in the text. b) Diamond mounting for live, intact worm experiments, as described in the text. MWs are applied through the 25 μm thick copper layer.

(CVD) by Element Six. The 13 μm thick top-surface NV^- sensing layer consists of 99.999% ^{12}C with 27 ppm ^{14}N as evaluated by secondary ion mass spectroscopy, which is irradiated with 4.6 MeV electrons with 1.3×10^{14} $cm^{-2}s^{-1}$ flux for 5 hours and subsequently annealed in vacuum at 800 °C for 12 hours. The measured nitrogen-to-NV^- conversion efficiency is $\sim 6\%$. The diamond is cut so that the 500 μm × 4 mm faces are perpendicular to the [110] crystal axis. The sides are mechanically ground to an optical-quality polish. The diamond is mounted to a 2" diameter, 330 μm thick silicon carbide (SiC) heat spreader via thermal epoxy (Epotek H20E) as shown in Figure 3.2.2a. A 2 mm × 25 mm slot in the SiC provides access to the diamond surface for the dissected axon studies.

For NV^- magnetometry, the diamond sensor is illuminated by 2.75 - 4.5 W of 532 nm laser light (Coherent Verdi V-5) as shown in Figure 3.2.3b. Laser light is guided into the diamond via an in-house fabricated UV fused silica coupler, making a $\sim 3^\circ$ angle to the NV^- layer. A 13 μm thick and 1 mm wide reflective aluminum layer on the diamond surface blocks both excitation light scattered by surface defects and PL from impinging upon the specimen. A rare earth magnet ($1'' \times 1'' \times 1''$ N42 K&J Magnetics) with south pole facing the diamond creates a bias magnetic field B_0 with equal projections of 7 gauss (0.7 mT) along the two NV^- axes perpendicular to the axon axis, shifting the MW resonance between the $m_s = 0$ and $m_s = +1$ sublevels to ≈ 2.89 GHz.

Figure 3.2.3a shows a schematic of the MW setup. A commercial MW source (Agilent E8257D) outputs a single near-resonant frequency, which is square-wave modulated with frequency deviation $\omega_{\text{dev}} = 2\pi \times 360$ kHz at frequency $f_{\text{mod}} = 18$ kHz (Rigol DG1022U). The modulated MWs pass through an isolator (Teledyne Microwave T-2S73T-II) and a −10 dB coupler before mixing via a double balanced mixer (RELCOM M1G) with a 2.16 MHz sinusoidal waveform (Stanford Research Systems DS345). The coupled port of the −10 dB coupler is further attenuated by 6 dB and combined (Mini-Circuits ZX-10-2-42-S+) with the mixer output and then sent through a second -10 dB coupler. The coupled output is sent to a spectrum analyzer (Agilent E4405B) while the transmitted output is amplified (Mini-Circuits

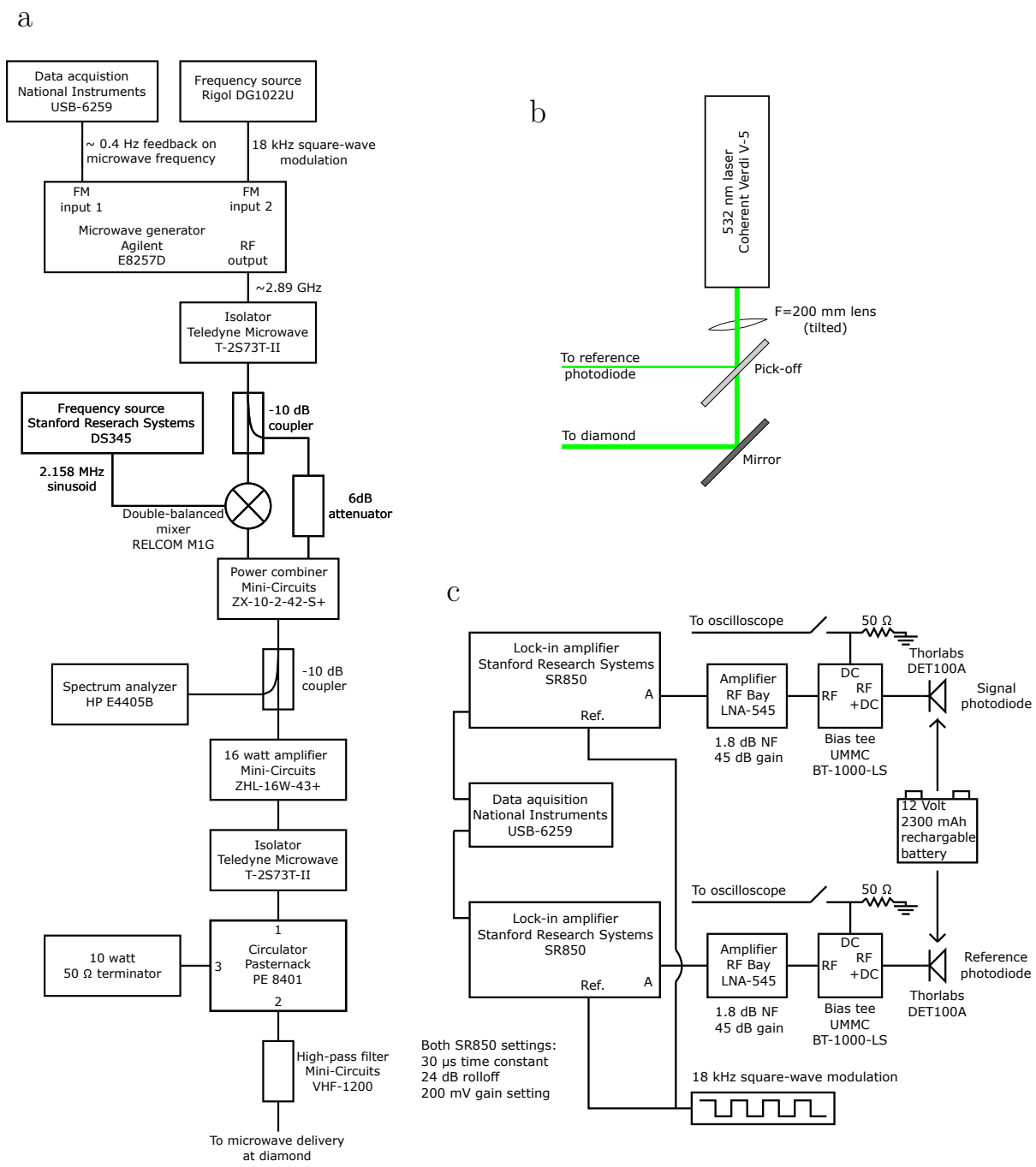

Figure 3.2.3: Microwave, laser, and light collection setup. a) MW generation, modulation, and delivery setup as described in the text. b) Laser setup as described in SI Appendix. c) Signal photodiode, reference photodiode, and downstream electronics and LIAs as described in the text.

ZHL-16W-43+), passed through another isolator (Teledyne Microwave T-2S73T-II), a circulator (Pasternack, PE 8401), and a high-pass filter (Mini-Circuits VHF-1200), before delivery to a square 5 mm × 5 mm × 5 mm loop located ≈ 2 mm above the diamond sensor. Slow variations in the NV$^-$ ODMR resonances, e.g., due to diamond temperature drift, are compensated with ≈ 0.4 Hz feedback to the MW frequency f_{MW}. The ODMR features can also be used to continuously monitor the diamond substrate temperature in real time.

Typically 17 mW (and up to 28 mW) of PL from the NV-diamond is collected by a 1.4 numerical aperture (NA) aspheric aplanatic oil condenser (Olympus), passed through a 633 nm longpass filter (Semrock LP02-633RU-25), and imaged onto a biased photodiode (Thorlabs DET100A). The photodiode (PD) is powered by a 12 V lithium ion rechargable battery and is terminated into the RF + DC port of a bias tee (Universial Microwave Component Corporation BT-1000-LS) with bandwidth 10 kHz - 1 GHz. The bias tee DC port is terminated by 50 Ω during experiments; whereas during optical alignment the port is monitored on an oscilloscope to optimize PL collection. The RF output of the bias tee is amplified by a low noise amplifier (RF Bay LNA-545) and then sent into a LIA (Stanford Research Systems SR850). The LIA gain setting is 200 mV, and the nominal time constant is 30 µs with a 24 dB/octave roll-off, yielding a measured 3 dB cutoff frequency of f_c = 3.6 kHz and a measured equivalent noise bandwidth (ENBW) of f_{ENBW} = 4.0 kHz. The LIA voltage output is expanded by 5× using the LIA expand function, digitized (National Instruments USB-6259) at 250 kHz, and then subsequently divided by 5. The temporary LIA signal expansion is employed to mitigate digitization noise. A ∼ 1 nT magnetic field corresponds to a fractional change in the NV$^-$ PL of $\Delta F/F \sim 10^{-6}$.

To mitigate correlated magnetic noise from the lab environment, the following procedure is adopted. A lock-in amplifier (Stanford Research Systems, SR830) generates a 60 Hz transistor-transistor logic (TTL) signal phase-locked to the 60 Hz, 120 volt facility supply power. Each pair of AP stimulations consists of one AP stimulation triggered after a fixed delay T_{delay} relative to a TTL rising edge (following the nominally desired trigger time) and another AP stimulation triggered after the

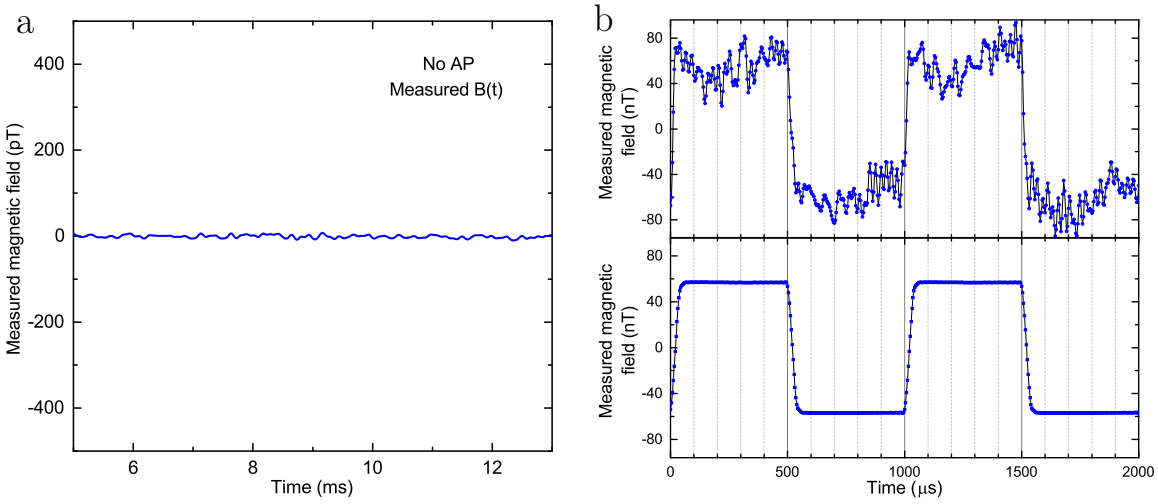

Figure 3.2.4: Magnetometer noise analysis and temporal resolution. a) Magnetometer signal $B(t)$ under experimental running conditions in the absence of a specimen, averaged for traces. No discernible pattern in the noise is present, suggesting that the magnetometer is free from correlated noise. b) Top: Measured real-time magnetic field time trace of 1 kHz square wave with 57 nT amplitude. Bottom: Same experimental setup as above, but highly averaged ($N_{\text{avg}} \sim 10^6$). Data analysis indicates a 10% - 90% rise time of $\tau_{10/90} = 32$ μs. For these data only, $f_{\text{mod}} = 60$ kHz, $\tau_{\text{LIA}} = 10$ μs nominally, and a 6 dB/octave roll-off is used, yielding a measured $f_{\text{ENBW}} = 33$ kHz. Data are FFT low-pass filtered at 45 kHz.

same fixed delay T_{delay} relative to a TTL falling edge (following the nominally desired trigger time). The value of T_{delay} for each pair of AP stimulations is randomly chosen without replacement from an even distribution from 0 to 1/60 seconds. Using this procedure, the magnetic noise is monitored and found to produce no discernible pattern after averaging for 75,000 stimulations under experimental conditions (except with no specimen), as shown in Figure 3.2.4a. Allan variance measurements of $B(t)$ taken up to a total measurement time of 100 seconds (with all $B(t)$ filtering off) are consistent with uncorrelated noise. Spurious magnetic signal from the current stimulation is typically well-separated in time from the AP magnetic signal, as shown in Figures 3.3.1d, and 3.3.5. Furthermore, as discussed below, the magnetometer operates within a factor of two of the predicted sensitivity limited by photon shot noise, which is itself an uncorrelated noise source.

To suppress laser intensity noise near f_{mod}, the 532 nm laser light is sampled and focused on a separate, reference PD (see Figure 3.2.3b, c). This PD and all

electronics (bias-tee, low-noise amplifier, LIA, input into data acquisition system) exactly duplicate the setup of the signal PD and accompanying electronics. The phase of the reference LIA is aligned with the phase of the signal LIA. We find that subtraction (rather than division) of the correlated noise is sufficient to reach the photon shot noise sensitivity limit in the absence of the MWs, in agreement with Ref. [109]. The detected signal is digitally filtered with an 80 Hz FFT high-pass filter, and with 1-Hz-wide notch stop filters at all 60 Hz harmonics through 660 Hz and at 30 other frequencies above 2 kHz. The experiment achieves sensitivity $\sim 50\%$ above the photon-shot-noise limit, which is discussed in the sensitivity section below.

For magnetic measurements of intact organisms, several changes are made to the experimental apparatus (see Figure 3.2.2b). An upgraded aluminum mount (larger than the mount for excised axons) is used to fit the large intact specimens (see Figure 3.3.2a). A SiC wafer with no slot is used as a heat spreader. The NV-diamond sensor is therefore offset from the worm exterior by a spacer of thickness 330 μm. MWs are delivered to a 25 μm thick copper foil layer directly on top of the diamond. The Olympus oil aspheric condenser is exchanged for a 0.79 NA air aspheric condenser (Thorlabs ACL25416U-B). Stained transverse sections in Figures 3.3.3a and b show a typical tissue thickness of $\sim$ 900 μm from the center of the axon to the worm exterior [24], consistent with the literature [198, 199], although this distance is also noted [198] to be highly variable among different specimens and along a single organism's length. The overall typical distance from the axon center to the diamond sensor is $\sim$ 1.2 mm, consistent with the measured roughly four-fold magnetic signal reduction compared to excised worm axons, where the distance from axon center to NV^- detector layer is typically $\sim$ 300 μm.

Excitation-laser-induced heating of the diamond is measured via NV^- ODMR frequency shifts to be 2.4 °C/watt. During magnetometry operation, the diamond temperature is 21 ± 3 °C. For studies of excised axons, which are placed directly against the diamond and thin aluminum layer, we estimate the sample temperature to be $\sim$ 21 °C. As the intact organisms measured in this work are separated from the diamond by the 330- μm-thick SiC heat spreader, their temperature during sensing is

lower, at ~ 10 °C.

3.2.2 Magnetometry method

The experiments detailed in this chapter measure the magnetic field projection along the vector that equally projects onto two NV$^-$ axes; hence the device operates as a vector projection magnetometer. AP magnetic fields are expected to encircle the axon and be directed perpendicular to the axon axis and also the direction of AP propagation. In the magnetometer configuration detailed in this work, the sensor records the component B_x the AP magnetic field parallel to the NV$^-$ layer surface, and is most sensitive to APs from axons oriented on the diamond surface perpendicular to the x-axis. In this work the axons are oriented roughly linearly on the diamond and perpendicular to two NV$^-$ axes, maximizing the projection of the AP magnetic field $B(t)$ onto those axes, as shown in Figure 3.2.1c, with the projection along the other two NV$^-$ axes expected to be near-zero.

In the present instrument, a modified continuous-wave optically detected magnetic resonance (CW-ODMR) technique is employed, wherein optical NV$^-$ spin polarization, MW drive, and spin-state readout via PL collection occur simultaneously. Continuous green laser excitation at 532 nm polarizes the NV$^-$ center into the $m_s = 0$ ground state. Applied MWs, when tuned to resonance with the transition between the optically bright $m_s = 0$ spin state and one of the less bright $m_s = +1$ or -1 states, cause NV$^-$ spin precession into a mixed state and a detectable reduction in PL. A change in the local magnetic field shifts the ODMR feature and, for near-resonant MW drive, is detected as a change in the fluorescence rate.

A single ODMR feature of Lorentzian lineshape with angular frequency ω_0 (where $\omega \equiv 2\pi f$), linewidth γ, and contrast $\mathcal{C}$ is detected in fluorescence as $F(\omega) = F_0(1 - \mathcal{C}\frac{(\Gamma/2)^2}{(\Gamma/2)^2+(\omega-\omega_0)^2})$ (see Figure 3.2.5a), where F_0 is the fluorescence detected in the absence of MWs, and optical and MW broadening are ignored for simplicity. As the majority of noise in the system has $1/f$ character, greater SNR is achieved by shifting the measurement bandwidth to higher frequency via a lock-in technique, which generates a dispersion-like signal with a characteristic zero-crossing feature: i.e., a rapid change

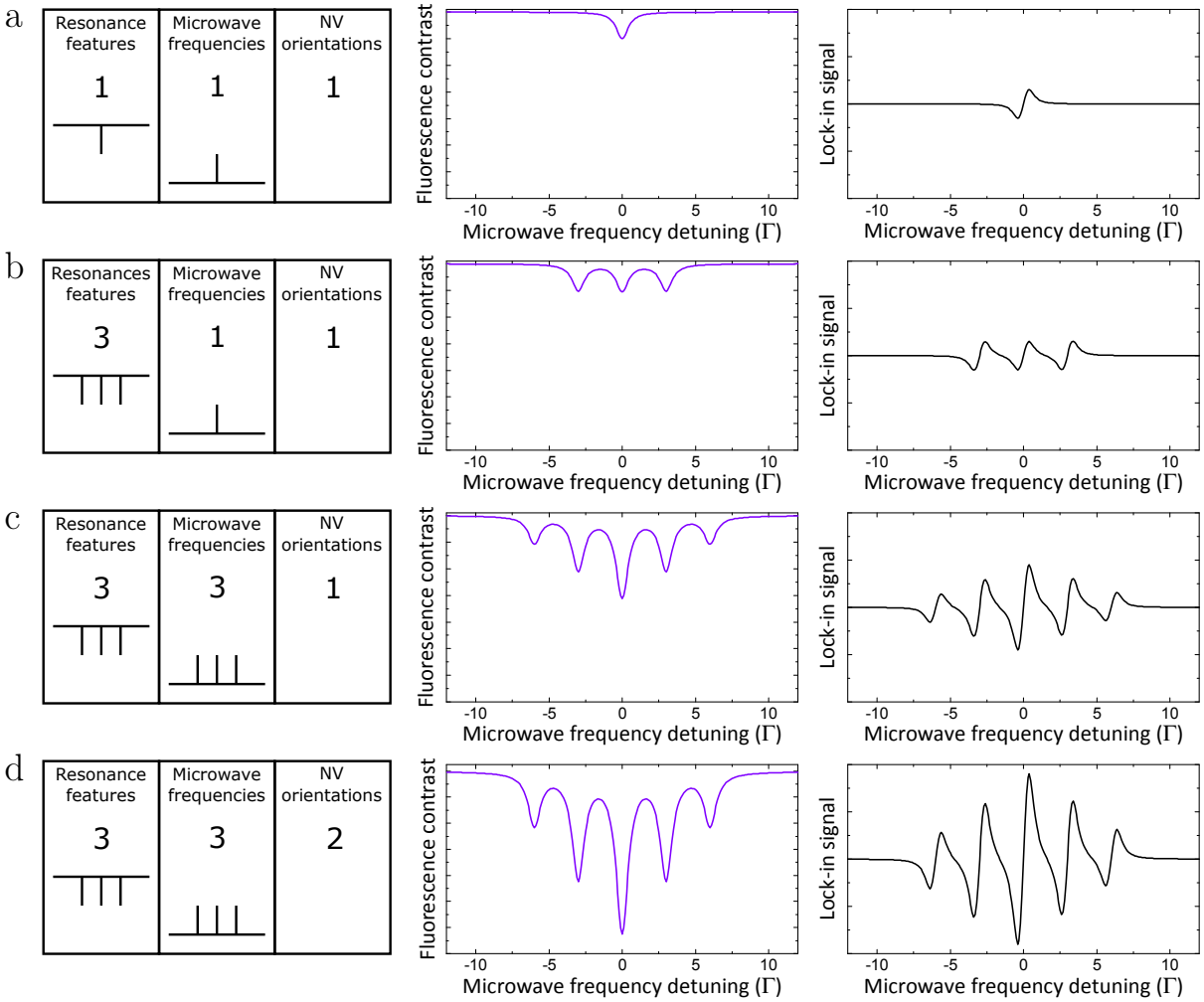

Figure 3.2.5: Illustration of magnetometry technique. Left column shows schematic diagrams illustrating number of ODMR features, number of MW frequencies applied, and number of NV$^-$ axes used for sensing; middle column shows calculated ODMR fluorescence profiles in units of the natural linewidth Γ, in the absence of power broadening; and right column shows associated dispersion-type lock-in amplifier (LIA) signals. Fluorescence and LIA signals are given in arbitrary units. a) Diagram, fluorescence signal, and LIA signal for a single ODMR feature addressed by a single (modulated) MW frequency, sensed along a single NV$^-$ axis. b) Diagram, fluorescence signal, and LIA signal for three ODMR features addressed by a single (modulated) MW frequency, sensed along a single NV$^-$ axis. c) Diagram, fluorescence signal, and LIA signal for three ODMR features addressed by three (modulated) MW frequencies with equivalent spacing, sensed along a single NV$^-$ axis. The central feature corresponds to all three applied frequencies resonantly addressing ODMR features. d) Diagram, fluorescence signal, and LIA signal for same scenario as in (c) but with B_0 oriented to have equal projection along two NV$^-$ axes, overlapping their ODMR features.

of the lock-in amplifier (LIA) voltage and sign with frequency. The applied MWs are square-wave frequency modulated at f_{mod} (typically 18 kHz) about the center frequency ω_c with frequency deviation ω_{dev}: i.e., $\omega_{\text{MW}}(t) = \omega_c + \omega_{\text{dev}}\text{square}(2\pi f_{\text{mod}} t)$. The collected fluorescence is then $F(\omega_{\text{MW}})$. After demodulation by the LIA with a reference signal $V(\text{ref} = \sin(2\pi f_{\text{mod}} t)$, the DC output is a dispersion-type signal with a zero-crossing at ω_0:

$$\begin{aligned} V_{\text{LIA}}(\omega_c, \omega_{\text{dev}}) &\propto \frac{F(\omega_c + \omega_{\text{dev}}) - F(\omega_c - \omega_{\text{dev}})}{2} \\ &= \frac{V_0 \mathcal{C}}{2}\left(-\frac{(\Gamma/2)^2}{(\Gamma/2)^2 + ((\omega_c + \omega_{\text{dev}}) - \omega_0)^2} + \frac{(\Gamma/2)^2}{(\Gamma/2)^2 + ((\omega_c - \omega_{\text{dev}}) - \omega_0)^2}\right), \end{aligned} \tag{3.1}$$

where V_0 is a prefactor voltage determined by F_0 and the output settings of the LIA. Setting $\omega_{\text{dev}} = \frac{\Gamma}{2\sqrt{3}}$ theoretically maximizes the slope of the zero-crossing $\frac{dV_{\text{LIA}}}{d\omega_c}|_{V_{\text{LIA}}=0}$ in the absence of power broadening [115]. Time-varying magnetic fields $B(t)$ are sensed by setting $\omega_c = \omega_0|_{t=0}$ and detecting resonance frequency shifts $\omega_0(t) = \omega_0 + \delta\omega(t)$, where $\delta\omega(t) = \frac{g_e \mu_B}{\hbar} B(t)$, as:

$$\begin{aligned} V_{\text{LIA}}(t) &= V_{\text{LIA}}\left(\omega_0 - \frac{g_e \mu_B}{\hbar} B(t)\right) \\ &= \frac{V_0 \mathcal{C}}{2}\left(-\frac{(\Gamma/2)^2}{(\Gamma/2)^2 + \left(\frac{\Gamma}{2\sqrt{3}} - \frac{g_e \mu_B}{\hbar} B(t)\right)^2} + \frac{(\Gamma/2)^2}{(\Gamma/2)^2 + \left(\frac{\Gamma}{2\sqrt{3}} + \frac{g_e \mu_B}{\hbar} B(t)\right)^2}\right) \\ &\approx -\frac{2\sqrt{3}}{4}\frac{V_0 \mathcal{C}}{\Gamma}\frac{g_e \mu_B}{\hbar} B(t). \end{aligned} \tag{3.2}$$

The NV$^-$ spin resonance has three features separated by the hyperfine (HF) splitting of $\Delta\omega_{\text{HF}} = 2\pi \times 2.16$ MHz, as shown in Figure 3.2.5b. For a single MW frequency sweeping across the features, and again ignoring MW power broadening, we find

$$F(\omega) = F_0\left(1 - \sum_{q=-1}^{1} \mathcal{C}\frac{(\Gamma/2)^2}{(\Gamma/2)^2 + (\omega - (\omega_0 + q\Delta\omega_{\text{HF}}))^2}\right). \tag{3.3}$$

Addressing all three NV$^-$ HF features simultaneously with three MW frequencies also separated by $\Delta\omega_{\mathrm{HF}}$ yields

$$F(\omega, \Delta\omega_{\mathrm{HF}}) = F_0 \left(1 - \sum_{p=-1}^{1} \sum_{q=-1}^{1} \mathcal{C} \frac{(\Gamma/2)^2}{(\Gamma/2)^2 + ((\omega + p\Delta\omega_{\mathrm{HF}}) - (\omega_0 + q\Delta\omega_{\mathrm{HF}}))^2}\right). \tag{3.4}$$

As displayed in Figure 3.2.5c, the observed NV$^-$ fluorescence signal shows five ODMR peaks. The outer two peaks correspond to one of the three MW frequencies on resonance; the second and fourth peaks correspond to two of the three frequencies tuned to resonance; and the innermost peak corresponds to all three MW frequencies resonantly addressing the HF features. The dispersion signal is then:

$$V_{\mathrm{LIA}}(\omega, \Delta\omega_{\mathrm{HF}}, \omega_{\mathrm{dev}}) = V_0 \sum_{p=-1}^{1} \sum_{q=-1}^{1} \left(-\mathcal{C} \frac{(\Gamma/2)^2}{(\Gamma/2)^2 + ((\omega + p\Delta\omega_{\mathrm{HF}} - \omega_{\mathrm{dev}}) - (\omega_0 + q\Delta\omega_{\mathrm{HF}}))^2} + \mathcal{C} \frac{(\Gamma/2)^2}{(\Gamma/2)^2 + ((\omega + p\Delta\omega_{\mathrm{HF}} + \omega_{\mathrm{dev}}) - (\omega_0 + q\Delta\omega_{\mathrm{HF}}))^2}\right). \tag{3.5}$$

In this simple treatment in which MW power broadening is ignored, our measurement technique increases the contrast of the central NV$^-$ HF feature by a factor of 3. In practice, a contrast improvement factor of ≈ 1.9 is achieved compared to the case of addressing a single HF feature.

The overall measurement contrast is further improved by orienting the bias field B_0 to have equal projection along two NV$^-$ axes. Projecting along two NV$^-$ axes doubles the contrast as shown by comparing Figure 3.2.5c and d, although the angle between the NV$^-$ axes and $B(t)$ causes the sensitivity improvement to be $2\sin[\theta_{\mathrm{tet}}/2] = 2\sqrt{2/3}$ where $\theta_{\mathrm{tet}} = 109.4712^\circ$ is the tetrahedral bond angle in the diamond lattice.

3.2.3 Magnetometer calibration

The measured magnetic field $B^{\mathrm{meas}}(t)$ is determined from the output voltage of the LIA, denoted V_{LIA}, by the relation $B^{\mathrm{meas}}(t) = C_{\mathrm{LIA}} V_{\mathrm{LIA}}$, where C_{LIA} is a voltage-to-

magnetic-field conversion factor given by

$$C_{\mathrm{LIA}} = \frac{h}{\frac{dV_{\mathrm{LIA}}}{df}|_{V_{\mathrm{LIA}}=0}\, g_e \mu_B \sin[\frac{\theta_{\mathrm{tet}}}{2}]}. \tag{3.6}$$

Here $\frac{dV_{\mathrm{LIA}}}{df}|_{V_{\mathrm{LIA}}=0}$ is the slope of the zero-crossing in V/Hz, g_e is the electron g-factor of the NV$^-$ ground state, $\sin[\theta_{\mathrm{tet}}/2] = \sqrt{2/3}$, and μ_B is the Bohr magneton.

Calibration of the NV-diamond magnetometer is independently verified by applying a known test magnetic field $B_{\mathrm{test}}(t) = B_{\mathrm{test}}\mathrm{square}[2\pi f_{\mathrm{test}} t]$ with square wave amplitude B_{test} and frequency f_{test}, and confirming the magnetometer records the correct value for B^{meas}. The test magnetic field is produced by a multi-turn circular current loop (coil) with $N_{\mathrm{turns}} = 7$ and radius $r_{\mathrm{coil}} = 0.0235$ m, located at a distance $z_{\mathrm{coil}} = 0.103$ m from the diamond chip center. The coil is connected in series with an $R_{\mathrm{series}} = 50\ \Omega$ resistor. The value of B_{test} is calculated using the formula

$$B_{\mathrm{test}} = \frac{\mu_0 N_{\mathrm{turns}} I_{\mathrm{coil}} r_{\mathrm{coil}}^2}{2[z_{\mathrm{coil}}^2 + r_{\mathrm{coil}}^2]^{3/2}}, \tag{3.7}$$

where I_{coil} is the current in the coil generated by driving a voltage $V_{\mathrm{coil}}(t)$ across the circuit. A 44 mV amplitude square wave yields $B_{\mathrm{test}} = 1.8$ nT, with RMS magnetic field $B_{\mathrm{test}}^{\mathrm{rms}} = B_{\mathrm{test}}$ When this value of B_{test} is applied at frequency $f_{\mathrm{test}} = 110$ Hz, the measured value of $B(t)$ consistent with the value of B_{test} to better than 5% as shown in Figure 3.2.6a. A calibration without harmonics is also performed by applying a 62 mV amplitude sine wave yielding a consistent value of $B_{\mathrm{test}}^{\mathrm{rms}} = B_{\mathrm{test}}/\sqrt{2} = 1.8$ nT.

3.2.4 Magnetic field sensitivity

A magnetometer's sensitivity is defined as $\eta = \delta B\sqrt{T}$ where δB is the magnetic field signal that is as large as the noise, i.e., at SNR = 1, after measurement time T [114]. The sensitivity of our NV-diamond magnetometer is evaluated using three methods. In method 1, a test magnetic field $B_{\mathrm{test}} = B_{\mathrm{test}} \sin[2\pi f_{\mathrm{test}} t]$ is applied for $N_{\mathrm{trials}} = 150$, each of time $T_{\mathrm{trial}} = 1$ s, and the measured magnetic field $B^{\mathrm{meas}}(t)$ is recorded. For

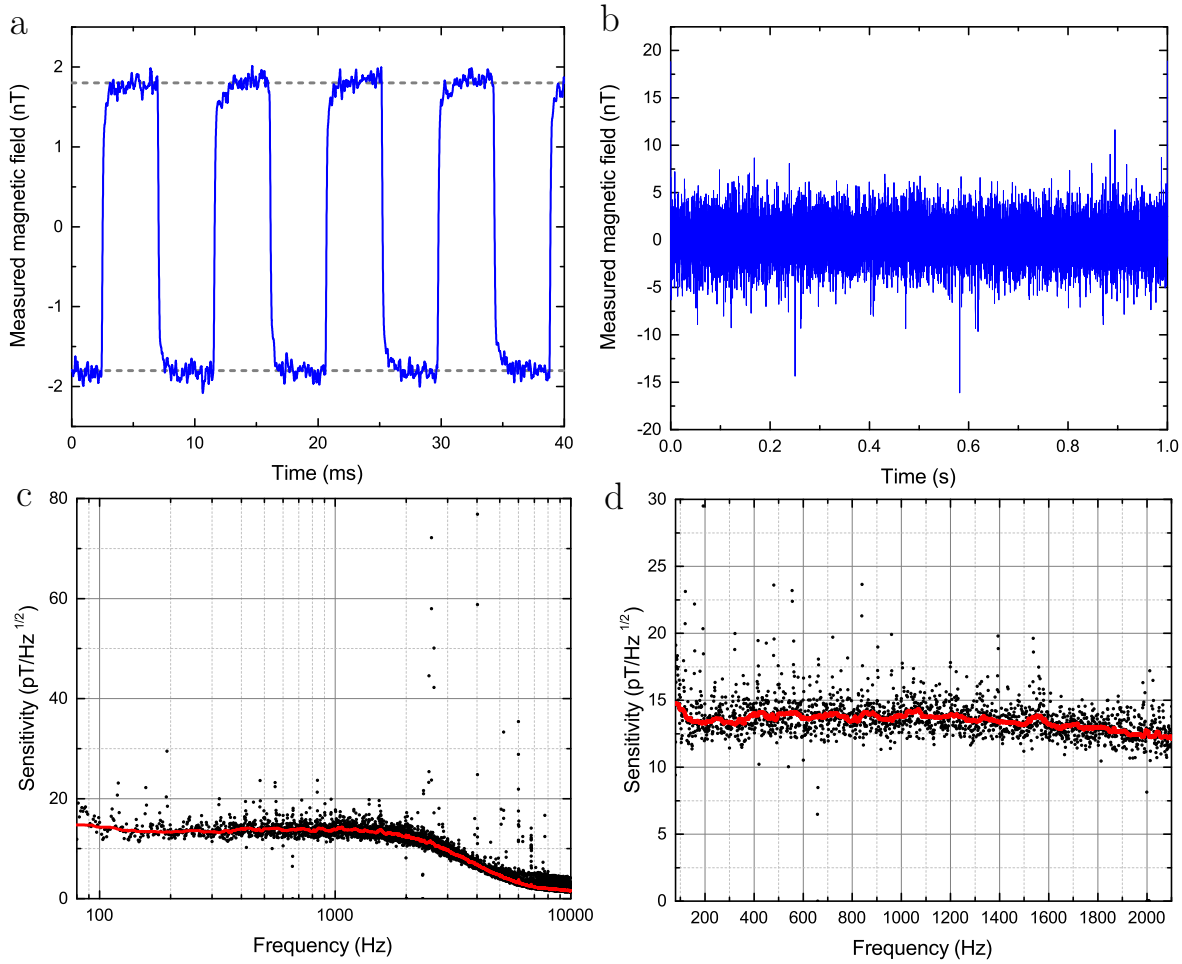

Figure 3.2.6: Magnetometer calibration and sensitivity measurement. a) Calibration verification. A 110 Hz square wave with 1.8 nT amplitude (calculated from coil geometry, coil distance to diamond sensor, and current through coil only) is averaged for $N_{\text{avg}} = 1000$ trials. The measured magnetic field, calibrated only from the value of C_{LIA} and the lock-in amplifier voltage time trace $V_{\text{LIA}}(t)$ is consistent with a 1.8 nT amplitude square wave to better than 5%. Gray dashed lines depict -1.8 nT and $+1.8$ nT levels. The slight rounding of the square wave's corners results from coil non-idealities rather than the magnetometer. b) Measured real-time magnetic field time trace of measured magnetic field $B^{\text{meas}}(t)$ with no external time-varying magnetic field applied. c) Fourier transform (black points) of $N_{\text{avg}} = 150$ traces of (b) is smoothed (red line) for clarity and is consistent with an overall sensitivity of 15 pT/$\sqrt{\text{Hz}}$. d) Reproduction of (c) with linear scale over approximate neuron signal bandwidth (80 Hz to 2 kHz). All data are taken for standard conditions ($f_{\text{mod}} = 18$ kHz, nominal $\tau_{\text{LIA}} = 30$ µs, with 24 dB/octave roll-off).

each trial i the quantity

$$x_i = \frac{1}{T_{\text{trial}}} \int_0^{T_{\text{trial}}} B^{\text{meas}}(t) B_{\text{test}}(t) dt \tag{3.8}$$

is computed. The method 1 sensitivity η_1 is

$$\eta_1 = \frac{B_{\text{test}}^{\text{rms}}\sqrt{2}}{\mu} \sqrt{\frac{1}{N_{\text{trials}}} \sum_{i=0}^{N_{\text{trials}}} (x_i - \mu)^2} \times \sqrt{T_{\text{trial}}}, \tag{3.9}$$

where the factor of $\sqrt{2}$ accounts for quadrature noise, $B_{\text{test}}^{\text{rms}} = B_{\text{test}}/\sqrt{2}$, and typically $f_{\text{test}} = 250$ Hz. In method 2, $B_{\text{test}}(t)$ is applied for $N_{\text{trials}} = 150$, each of time $T_{\text{trial}} = 1$ s, and $B^{\text{meas}}(t)$ is recorded. The single-sided root-mean-square (RMS) spectral frequency profile of $B^{\text{meas}}(t)$ is defined to be $\tilde{B}^{\text{meas}}(f)$. The method 2 sensitivity η_2 is

$$\eta_2 = B_{\text{test}}^{\text{rms}} \left\langle \frac{\frac{1}{f_{\text{stop}} - f_{\text{start}}} \int_{f_{\text{start}}}^{f_{\text{stop}}} \tilde{B}^{\text{meas}}(f) df}{\frac{1}{\Delta f} \int_{f_{\text{test}} - \Delta f/2}^{f_{\text{test}} + \Delta f/2} \tilde{B}^{\text{meas}}(f) df} \right\rangle_{N_{\text{trials}}} \times \sqrt{T_{\text{trial}}}, \tag{3.10}$$

where $\Delta f = 1/T_{\text{trial}}$, the expected value is taken over N_{trials}, and typically $f_{\text{start}} = 300$ Hz, $f_{\text{stop}} = 600$ Hz, and $f_{\text{test}} = 250$ Hz. In method 3, no test magnetic field is applied and $B^{\text{meas}}(t)$ is recorded for $N_{\text{trials}} = 150$, each of time $T_{\text{trial}} = 1$ s; an example trace is shown in Figure 3.2.6b. The sensitivity is then calculated as

$$\eta_3 = \sqrt{\frac{1}{T_{\text{trial}}} \int_0^{T_{\text{trial}}} [B^{\text{meas}}(t)]^2 dt} \times \frac{1}{\sqrt{2 f_{\text{ENBW}}}}, \tag{3.11}$$

with $f_{\text{ENBW}} = 4.0$ kHz. In all evaluations of the instrument's magnetic field sensitivity, $\eta_1 \sim \eta_2 \sim eta_3$ is found, although η_1 converges most slowly and is therefore of limited use. Over 150 trials, η_3 ranges from 15.0 to 15.8 pT/$\sqrt{\text{Hz}}$, while η_2 is 15 ± 1 pT/$\sqrt{\text{Hz}}$. The two values are consistent. We thus conclude the NV-diamond magnetometer sensitivity is 15 ± 1 pT/$\sqrt{\text{Hz}}$, also consistent with a noise floor measurement of $|\tilde{B}^{\text{meas}}(2\pi f)|$ for $T_{\text{trial}} = 1$ s averaged over $N_{\text{trials}} = 150$, as shown in Figure 3.2.6c, d.

This realized magnetic field sensitivity agrees with the expected sensitivity for our NV$^-$ CW-ODMR technique limited by photon shot noise and added MW and amplifier noise, as estimated herein. In the limit of low contrast $\mathcal{C}$ of the ODMR feature, defined for CW-ODMR as the fractional dip on resonance of collected PL [100], the photon-shot-noise-limited sensitivity for CW-ODMR magnetometry using NV$^-$ centers is given by [100]

$$\eta_{\mathrm{CW}} = \frac{4}{3\sqrt{3}} \frac{h}{g_e \mu_B} \frac{\Delta f}{\mathcal{C}\sqrt{\mathcal{R}}}, \tag{3.12}$$

where $\mathcal{R}$ is the photon detection rate (away from resonance, corrected for detector quantum efficiency), Δf is the power-broadened full-width-half-maximum (FWHM) resonance linewidth, and the factor $\frac{4}{3\sqrt{3}}$ comes from a Lorentzian feature's steepest slope. The CW-ODMR method employed with the present NV-diamond magnetometer detects along two NV$^-$ axes as described above, doubling the contrast while reducing the magnetic field sensitivity by the angle factor $\sin[\theta_{\mathrm{tet}}/2] = \sqrt{2/3}$. The shot-noise-limited sensitivity of our magnetometer is given nominally by

$$\eta_{\mathrm{CW}}^{\mathrm{shot}} = \frac{4}{3\sqrt{3}} \frac{h}{g_e \mu_B} \frac{\Delta f}{\mathcal{C}_2 \sin\left[\frac{\theta_{\mathrm{tet}}}{2}\right] \sqrt{\mathcal{R}}}, \tag{3.13}$$

where $\Delta f = 1.1 \pm 0.1$ MHz is the measured linewidth; and $\mathcal{C}_2 = 5.3 \pm 0.1\%$ is the CW-ODMR contrast when sensing along two NV$^-$ axes, which is measured in the absence of modulation while addressing all three hyperfine features. The detected photon rate $\mathcal{R}$ is defined in terms of the photoelectron current $q\mathcal{R} = V_{\mathrm{sig}}/R_L$, where q is the elementary charge and $V_{\mathrm{sig}} = 400$ mV is the typical signal PD voltage after $R_L = 50\ \Omega$ termination. This idealized shot-noise-limited CW-ODMR sensitivity is found to be 3.1 pT/$\sqrt{\mathrm{HZ}}$.

In practice, several factors diminish the sensitivity: first, the reference PD adds in quadrature an equivalent amount of shot noise, increasing the sensitivity by a factor $\mathcal{P}_{\mathrm{ref}} = \sqrt{2}$; second, the slope is reduced with respect to the steepest slope of a Lorentzian due to the other nearby power-broadened hyperfine features, resulting in a sensitivity cost of $\mathcal{P}_{\mathrm{slope}} = 1.19$. Taking these factors into account yields a shot-noise-limited CW-ODMR sensitivity of 5.2 pT/$\sqrt{\mathrm{Hz}}$. Furthermore, in our square-

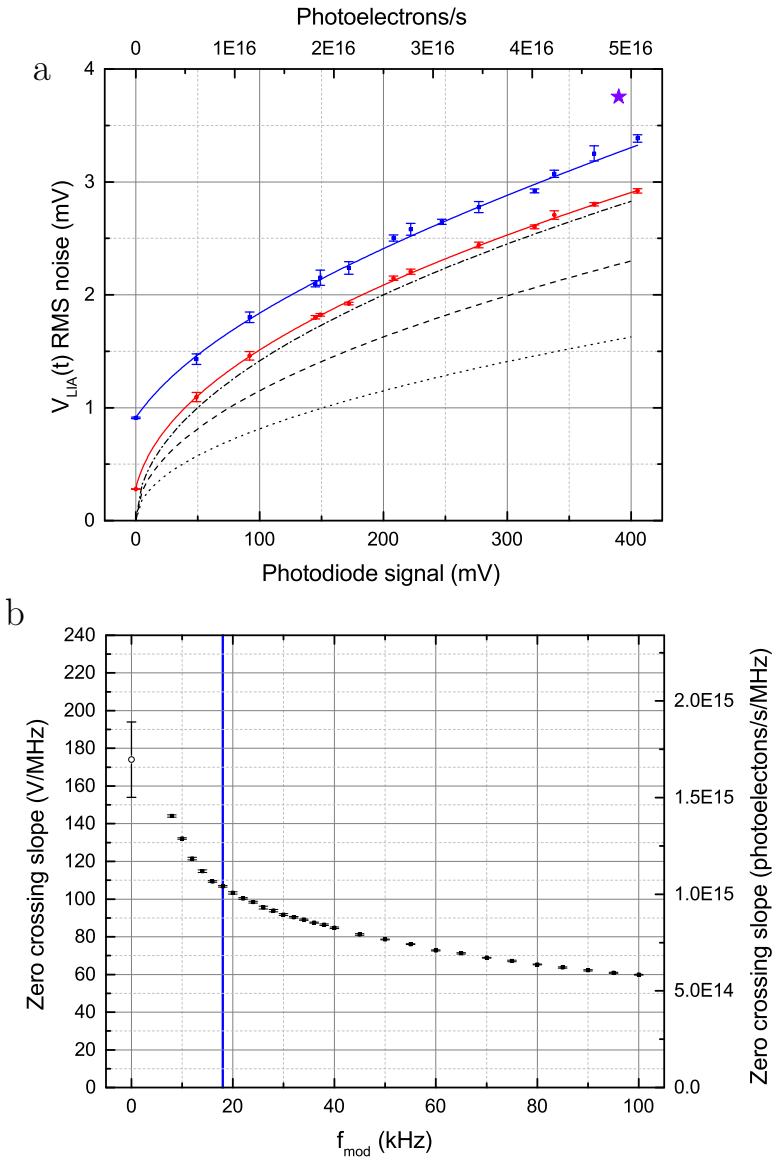

Figure 3.2.7: Magnetometer sensitivity analysis. a) Measured and calculated RMS noise on V_{LIA} versus signal photodiode voltage. Data shown by blue squares (red dots) are taken without applied MWs at $f_{\mathrm{mod}} = 18$ (90) kHz. Error bars denote standard deviation (SD). Blue and red curves are fits to the respective data sets, demonstrating the square-root dependence of the measured noise. Purple star marks measured noise during typical operating conditions in the presence of applied MWs. Black curves indicate calculated theoretical noise for shot noise from only the signal channel (dotted), shot noise including both the signal and reference channels (dashed), and expected noise level including shot noise from both channels and the LNA-545 amplifier noise figure of 1.8 (dot-dashed). b) Measured slope of zero-crossing $\frac{dV_{\mathrm{LIA}}}{df}|_{V_{\mathrm{LIA}}=0}$ with modulation frequency f_{mod}. Blue line denotes $f_{\mathrm{mod}} = 18$ kHz. Error bars denote SD. Open circle marks the slope in the absence of modulation, calculated from the measured DC photodiode signal and the LNA-545 amplifier and LIA gains.

wave modulated CW-ODMR implementation, the contrast is reduced by an empirical factor $\mathcal{P}_{\text{mod}} \approx 1.6$, as shown in Figure 3.2.7b, due to the finite cycling time of the NV$^-$ center quantum states [200, 26], and the loss of signal in higher harmonics resulting from demodulation with a sinusoidal lock-in frequency waveform [115]. The LNA-545 amplifier's noise figure of 1.8 increases the noise level by $\mathcal{P}_{\text{ampl}} \approx 1.23$. Excess noise at the 18 kHz modulation frequency increases the noise by $\mathcal{P}_{\text{excess}} \approx 1.16$, while application of MWs further increases the measured noise level by $\mathcal{P}_{\text{MW}} \approx 1.16$, as shown in Figure 3.2.7a. These factors raise (i.e., worsen) the expected magnetic field sensitivity to $\eta \approx \mathcal{P}_{\text{MW}}\mathcal{P}_{\text{excess}}\mathcal{P}_{\text{ampl}}\mathcal{P}_{\text{mod}}\mathcal{P}_{\text{slope}}\mathcal{P}_{\text{ref}}\,\eta_{\text{shot}} \approx 13.8$ pT/$\sqrt{\text{Hz}}$, which agrees to within 8% of the measured 15 ± 1 pT/$\sqrt{\text{Hz}}$ for the data shown in Figures 3.2.6b-d and 3.2.7a.

To confirm the NV$^-$ magnetometer sensitivity near the photon shot noise limit in the absence of applied MWs, we measure the RMS noise in V_{LIA} for a range of power incident on the PD, at both 18 kHz and 90 kHz modulation frequencies, as shown in Figure 3.2.7a. Data are fit to the function $y = \sqrt{a + bx + cx^2}$. For 90 kHz modulation, the fit parameters are $a = (7.9 \pm 0.1) \times 10^{-2}$, $b = (2.2 \pm 0.02) \times 10^{-2}$, and $c = (-3.0 \pm 0.8) \times 10^{-6}$; for 18 kHz modulation the fit parameters are $a = (8.3 \pm 0.2) \times 10^{-1}$, $b = (2.4 \pm 0.1) \times 10^{-2}$, and $c = (0.5 \pm 3.6) \times 10^{-6}$. The fits for both cases suggest the measured noise is dominated by the bx term, as expected for a shot-noise-limited measurement. The measured noise agrees with expected photoelectron shot noise from signal and reference channels plus LNA-545 amplifier noise for equivalent noise bandwidth $f_{\text{ENBW}} = 4.0$ kHz.

The fundamental sensitivity limit for spin-based magnetometers is given by the noise intrinsic to quantum projection. For a sample of N electronic spins with characteristic dephasing time T_2^*, the spin-projection-noise-limited sensitivity is [1]:

$$\eta_q = \frac{\hbar}{g_e \mu_B} \frac{1}{\sqrt{N T_2^*}}. \tag{3.14}$$

The sample used in this work has a total NV$^-$ density $\sim 3 \times 10^{17}$ cm^{-3} and no preferential orientation [96]. The density of NVs used to sense AP magnetic fields

is reduced by a factor of two, as the AP magnetic field projects along only two NV$^-$ axes. The illumination volume is $\sim 13\ \mu\text{m} \times 200\ \mu\text{m} \times 2\ \text{mm} \approx 5 \times 10^{-6}\ \text{cm}^3$, so the number of probed NV$^-$ spins is $N \sim 8 \times 10^{11}$ with $T_2^* \approx 450$ ns. Using these values along with the NV$^-$ electron's gyromagnetic ratio $\gamma = g_e \mu_B / \hbar = 1 \times 10^{11}\ \text{s}^{-1}\text{T}^{-1}$ gives a spin projection noise estimate for our sample volume of $\sim 10\ \text{fT}/\sqrt{\text{Hz}}$. At ~ 1500 times better than the present nearly photon-shot-noise-limited sensitivity, there is much promise for significant gains in magnetometer sensitivity through use of pulsed magnetometry, optimized NV-diamond samples, and quantum-assisted techniques, as discussed below.

3.2.5 Temporal resolution

Temporal resolution of the NV-diamond magnetometer is tested by applying a test magnetic field $B_{\text{test}}(t) = B_{\text{test}}\text{square}[2\pi f_{\text{test}} t]$ with $B_{\text{test}} \approx 57$ nT and $f_{\text{test}} = 1$ kHz, and measuring the $10\% - 90\%$ rise time of $B^{\text{meas}}(t)$ denoted by $\tau_{10/90}$. Using $f_{\text{mod}} =$ 60 kHz, τ_{LIA}10 μs, and 6 dB/octave rolloff (yielding a measured $f_{\text{ENBW}} = 33$ kHz), $\tau_{10/90} = 32$ μs is observed as shown in Figure 3.2.4b, which displays both real-time and averaged $B^{\text{meas}}(t)$ traces that are FFT low-pass filtered at 45 kHz. All AP data presented in this paper are acquired using $f_{\text{mod}} = 18$ kHz $V_{\text{LIA}} = 30$ μs, and 24 dB/octave rolloff, which gives $\tau_{10/90} = 100$ μs. Note that higher values of f_{mod} reduce NV$^-$ spin-state contrast, an effect previously observed in Refs. [114, 200, 26] and shown here in Figure 3.2.7b. When operating with a temporal resolution higher than 40 μs, the magnetic field sensitivity of the present instrument is reduced by a factor of ~ 1.6 with respect to standard running conditions. With pulsed Ramsey-type schemes [102], to be employed in a next-generation NV-diamond magnetic imaging system, the time resolution is expected to be significantly enhanced without loss of NV$^-$ contrast. The temporal resolution of a Ramsey scheme is in practice limited by the repetition rate of the pulse sequence. For typical initialization and readout times of 1 μs and 300 ns respectively, and for a 450 ns T_2^*-limited spin precession time, we anticipate a temporal resolution of ~ 2 μs. Temporal resolution can be further increased at the expense of sensitivity by reducing the initialization and spin

precession times, down to a theoretical limit given by the $\sim$ 200 ns NV^- singlet state lifetime [23].

3.3 Results

3.3.1 Magnetic measurements of single-neuron action potentials

We first performed magnetic sensing of propagating single-neuron APs from excised invertebrate giant axons, together with simultaneous electrophysiology measurements on the axons as a comparison and check on the magnetic data. We studied two species, with consistent results: the marine fanworm *Myxicola infundibulum* and the North Atlantic longfin inshore squid *Loligo pealeii* - a model organism for neuroscience. Details of specimen preparation, axonal AP stimulation, and electrophysiology measurements and simulations are described in the Methods and SI Appendix of Ref. [24]. Figure 3.3.1a shows a representative measured intracellular axonal AP voltage time trace $\Phi_{\text{in}}^{\text{meas}}(t)$ from *M. infundibulum*. In a simple model of the electromagnetic dynamics of axonal propagating APs [201, 202, 203] (see the SI Appendix of Ref. [24]), the magnetic field $B(t)$ is proportional to the temporal derivative of the intracellular voltage $\Phi_{\text{in}}(t)$: $B(t) = s\partial\Phi/\partial t$, where s is a scaling constant dependent on geometrical parameters (axon radius r_a, radial distance of the field point to the axon center ρ) and electrophysiological axon parameters (AP conduction velocity v_c, axoplasm electrical conductivity σ). As shown in Figure 3.3.1b and c, we find good agreement between (i) $B^{\text{calc}}(t)$, the AP magnetic field calculated from $\Phi_{\text{in}}^{\text{meas}}(t)$ for a typical value of s for *M. infundibulum*, and (ii) a representative measured AP magnetic field time trace $B^{\text{meas}}(t)$. This correspondence demonstrates the consistency of NV-diamond magnetic AP measurements with standard electrophysiology techniques and theory. Note that the example $B^{\text{meas}}(t)$ in Figure 3.3.1c has a peak-to-peak amplitude = 4.1 ± 0.2 nT (mean $\pm$ standard deviation (SD.) for four measurements on the same specimen each with $N_{\text{avg}} = 150$), corresponding to an SNR of 1.2 ± 0.1 for a single AP firing, i.e.,

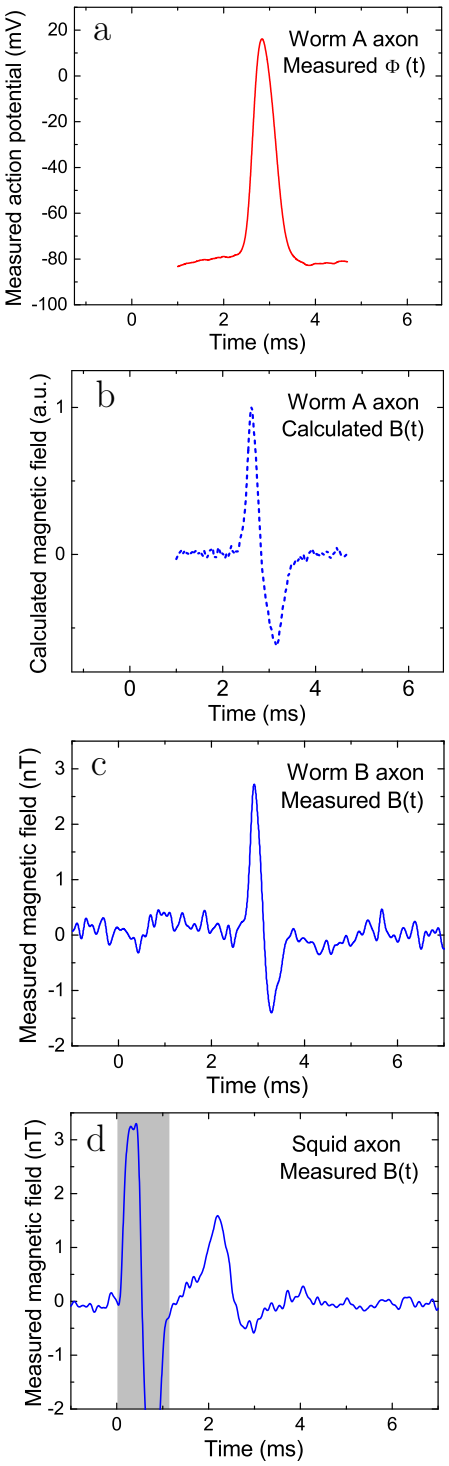

Figure 3.3.1: Measured AP voltage and magnetic field from excised single neurons. a) Measured time trace of AP voltage $\Phi_{\text{in}}^{\text{meas}}(t)$ for giant axon from *M. infundibulum* (worm). b) Calculated time trace of AP magnetic field $B^{\text{calc}}(t)$ for *M. infundibulum* extracted from data in (a). c) Measured time trace of AP magnetic field $B^{\text{meas}}(t)$ for *M. infundibulum* giant axon with $N_{\text{avg}} = 600$. d) Measured time trace of AP magnetic field $B^{\text{meas}}(t)$ for *L. pealeii* (squid) giant axon with $N_{\text{avg}} = 375$. Gray box indicates magnetic artifact from stimulation current.

$N_{\text{avg}} = 1$. Here SNR is defined as the ratio of the mean signal peak-to-peak amplitude to the root mean square (RMS) noise after matched filtering is applied (see the SI Appendix of Ref. [24] for SNR calculation and SNR analysis in terms of spike detection probabilities using a next-generation neuron magnetic sensor). Furthermore, we demonstrated that our method has multispecies capability via magnetic sensing of axonal APs from the squid *L. pealeii* (Figure 3.3.1d). No change to the apparatus or magnetic sensing protocol is required upon switching organisms, and good reproducibility is found for both the excised worm and squid axon AP magnetic field measurements, on the same and different specimens (see the SI Appendix of Ref. [24]).

We next demonstrated single-neuron AP magnetic sensing exterior to a live, intact, opaque organism - an undissected specimen of *M. infundibulum* (Figure 3.3.2a) - for extended periods, with minimal adverse effect on the animal. Figure 3.3.2b shows an example measured axonal AP magnetic field time trace $B^{\text{meas}}(t)$ for a live intact specimen, which also serves as a demonstration of single-neuron magnetoencephalography (MEG) from the exterior of an intact animal. The measured AP waveform in Figure 3.3.2b is similar to that of an excised axon (Figure 3.3.1c), with roughly 4 times smaller peak-to-peak amplitude ($\sim$ 1 nT), which is consistent with the separation of $\sim$ 1.2 mm from the center of the axon inside the animal to the NV^- sensing layer (see transverse sections and diagrams in Figure 3.3.3a-d). In addition, we recorded $B^{\text{meas}}(t)$ from a live intact worm after $>$ 24 h of continuous exposure to the experimental conditions, including applied MWs and optical illumination of the diamond sensor. We observed little to no change in the magnetic AP signal or in the animal behavior (compare Figure 3.3.3e and 3.3.4). Physical stimulus applied to the specimen after $>$ 24 h hours further confirmed its responsiveness and health.

We also used live intact worms to demonstrate the capability of NV-diamond magnetic sensing to determine the AP propagation direction and sense magnetic signal amplitude differences correlated with differences in conduction velocity v_c, all from a single-channel measurement. NV-diamond allows for vector magnetometry [1] by sensing the magnetic field projection along one or more of the four NV^- center orientations within the diamond crystal lattice (see Figures 3.3.1c and 1.4.1). An axonal

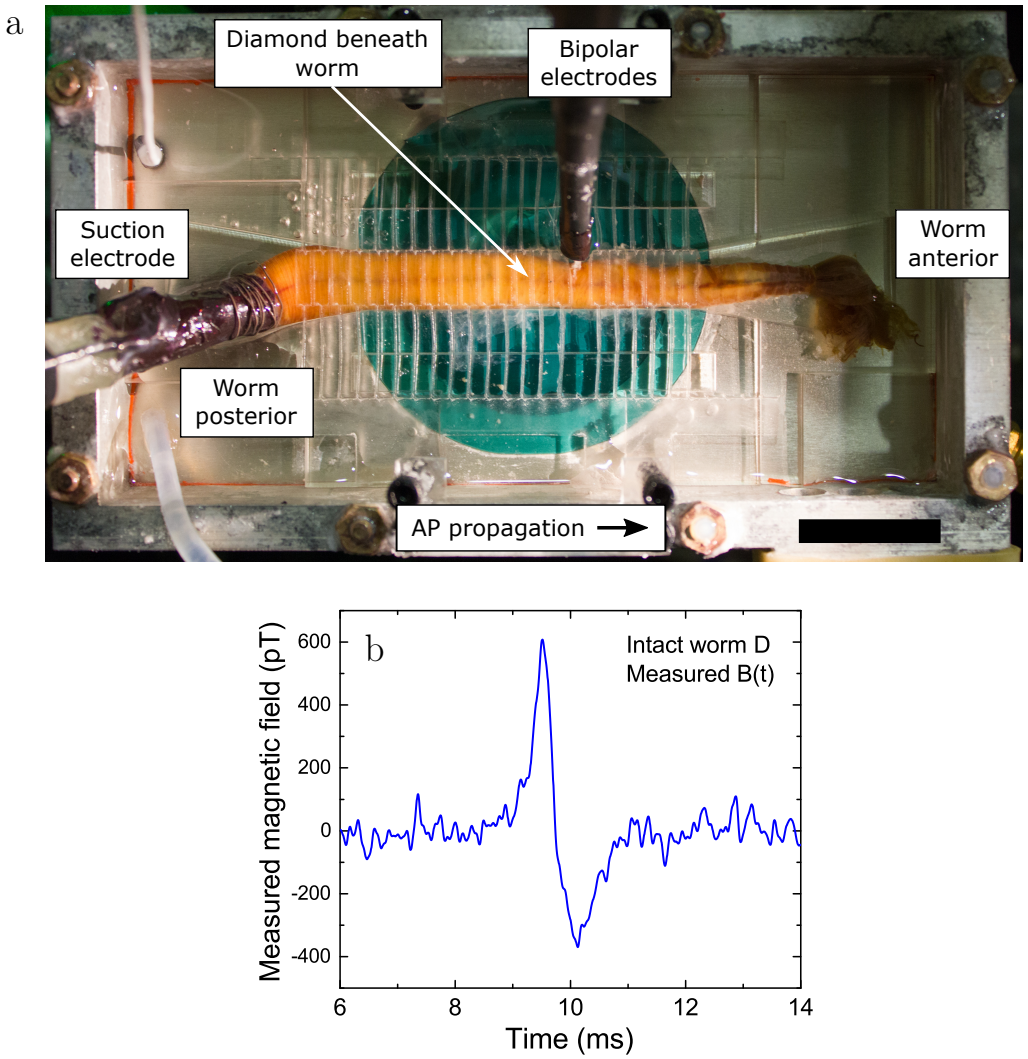

Figure 3.3.2: Single-neuron AP magnetic sensing exterior to live, intact organism. a) Overhead view of intact living specimen of *M. infundibulum* (worm) on top of NV-diamond sensor. In configuration shown, animal is stimulated from posterior end by suction electrode, APs propagate toward worm's anterior end, and bipolar electrodes confirm AP stimulation and propagation. (Scale bar, 20 mm.) b) Recorded time trace of single-neuron AP magnetic field $B_{\text{meas}}(t)$ from live intact specimen of *M. infundibulum* for $N_{\text{avg}} = 1,650$ events.

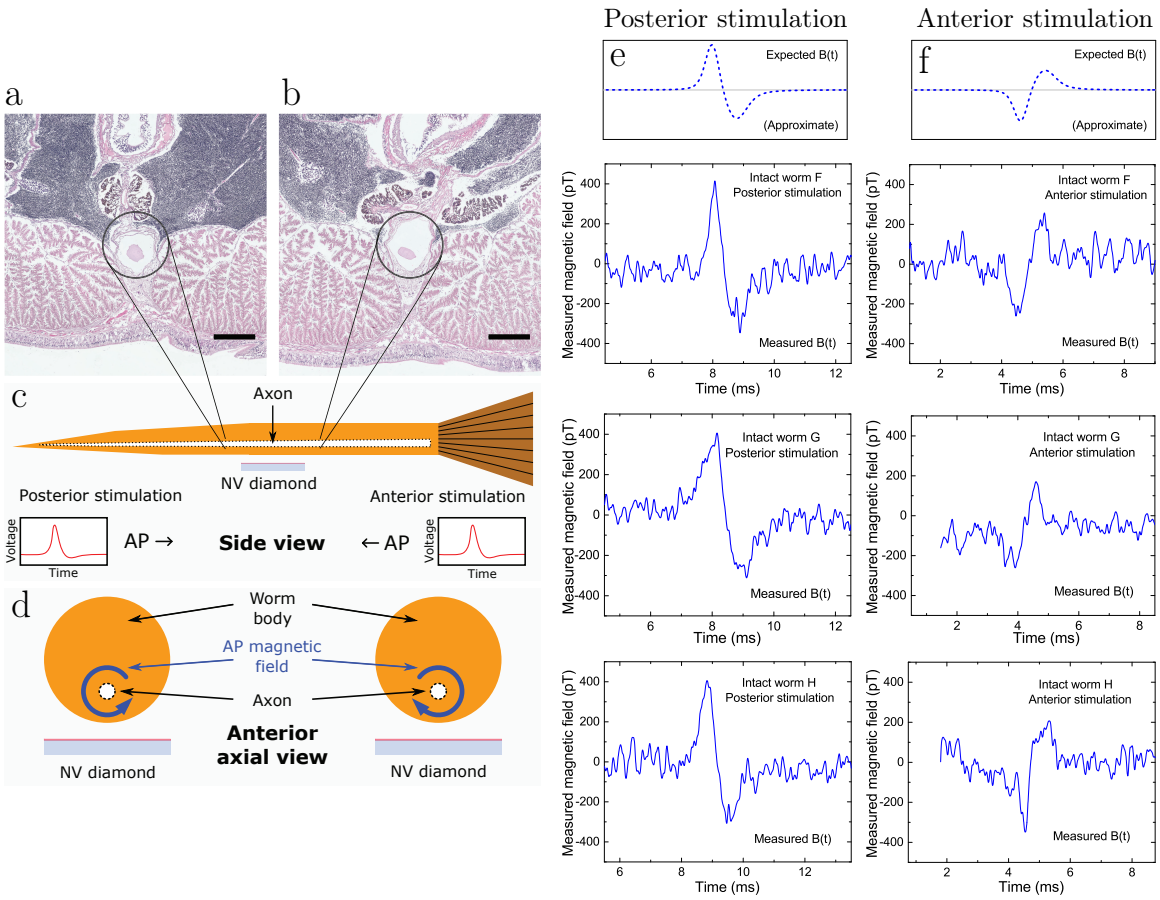

Figure 3.3.3: Single-channel magnetic sensing of AP propagation exterior to live, intact organism. Transverse sections of *M. infundibulum* near worm's midpoint illustrate giant axon radius tapering from (a) smaller near posterior to (b) larger near anterior. Sections were taken ~ 1 cm apart. Encircled white structure is giant axon. (Scale bars, 400 μm.) c) Cartoon cross-section side view of live, intact worm and NV diamond sensor. Black dashed lines indicate tapered giant axon. Cartoon time traces of AP voltage indicate typical qualitative indistinguishability for posterior stimulation (right-propagating AP) and anterior stimulation (left-propagating AP). d) Cartoon cross-section axial view from anterior end. Blue arrows encircling axon indicate opposite azimuthal AP magnetic field vectors for oppositely propagating APs. e) (Top) Expected AP magnetic field time trace for posterior stimulation of *M. infundibulum*, indicating effect of AP propagation direction and conduction velocity on sign of bipolar magnetic field waveform and field amplitude. (Bottom) Recorded time trace of AP magnetic field $B^{\text{meas}}(t)$ from three live intact specimens of *M. infundibulum* for posterior stimulation and $N_{\text{avg}} = 1,650$ events each. f) (Top) Expected AP magnetic field time trace for anterior stimulation. (Bottom) Recorded time trace of AP magnetic field $B^{\text{meas}}(t)$ from same three intact live specimens of *M. infundibulum* as in (e) for anterior stimulation and $N_{\text{avg}} = 1,650$ events each. Observed sign of $B^{\text{meas}}(t)$ is reversed depending on AP propagation direction, and average ratio of magnetic signal amplitude for posterior-stimulated APs (B_p) and anterior-stimulated APs (B_a) from three specimens shown (worms F, G, and H) is $B_p/B_a = 1.41 \pm 0.22$ (mean $\pm$ SD for three samples, each with $N_{\text{avg}} = 1,650$), consistent with two-point electrophysiology measurements of lower AP conduction velocity for posterior stimulation (see SI Appendix of Ref. [24]).

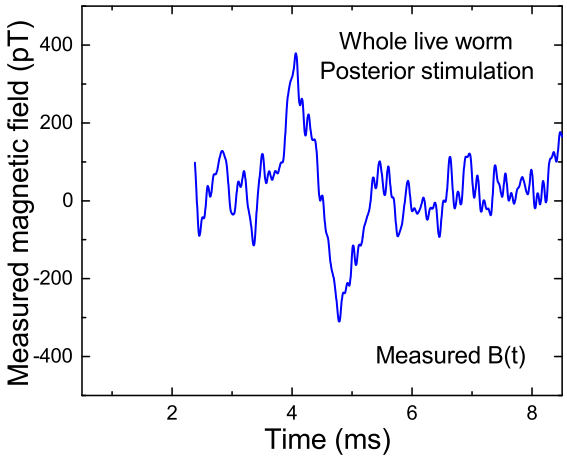

Figure 3.3.4: Extended duration sensing. Measured time trace of AP magnetic field $B^{\text{meas}}(t)$ for *M. infundibulum* giant axon (worm E) with $N_{\text{avg}} = 1200$ following continuous magnetic monitoring of this worm with full laser and MW power for the preceding 24 hours. Peak-to-peak value of $B^{\text{meas}}(t)$ for worm E is not statistically different from values for worms D, F, G, or H with posterior stimulation, indicating little if any negative effects from NV-diamond magnetic sensing over long time periods.

AP produces a bipolar azimuthal magnetic field waveform, with the time-varying field orientation set by the direction of AP propagation (Figures 3.2.1a and 3.3.3d). Thus, the measured AP magnetic field time trace $B^{\text{meas}}(t)$ from an intact worm has an inverted waveform for anterior versus posterior AP stimulation, demonstrating clear distinguishability between oppositely propagating APs, as shown in Figure 3.3.3e and f, for three intact specimens (denoted worms F, G, and H) with both posterior and anterior stimulation, each with $N_{\text{avg}} = 1,650$ trials.

In addition to inversion of the $B^{\text{meas}}(t)$ waveform upon reversal of the AP propagation direction, an asymmetry is observed in the peak-to-peak amplitude of the magnetic signal. As shown in Figure 3.3.3e and f, larger peak-to-peak values of $B^{\text{meas}}(t)$ are found for posterior stimulation (denoted B_p) than for anterior stimulation (B_a) for each of the three worms tested: $B_p/B_a = 1.66 \pm 0.12$ for worm F, 1.28 ± 0.09 for worm G, and 1.27 ± 0.10 for worm H (mean $\pm$ SD for 1,650 trials for each sample). The asymmetry is found to be statistically significant, with P-values reported in Ref. [24]. The average asymmetry is $B_p/B_a = 1.41 \pm 0.22$ (mean $\pm$ SD for three samples). The asymmetry is independent of which point of stimulation (pos-

terior or anterior) is tested first, and the effect is robust under multiple switches of stimulation (e.g., posterior, anterior, then posterior again).

We understand the origin of the observed $B^{\text{meas}}(t)$ asymmetry as a difference in AP conduction velocity v_c dependent on the AP propagation direction. As described in Ref. [24], we performed traditional electrophysiology measurements of $\Phi_{\text{in}}(t)$ v_c with both posterior and anterior stimulation, we related the magnetic data to the electrophysiology data via the simple magnetic model described above, and we performed numerical simulations of APs using a model of the *M. infundibulum* giant axon. Our electrophysiology measurements show a significant difference between the conduction velocities upon anterior and posterior stimulation, consistent with the ratio of B_p/B_a measured with NV-diamond magnetometry. We identify the origin of the conduction velocity difference to be a tapered axon morphology. When APs originate from the posterior end, where the axon radius is more narrow, the APs propagate more slowly through the axon, resulting in a larger magnetic field B_p compared to B_a measured at the same point along the axon from APs originating at the larger-radius anterior end. Simulations based on cable theory [204] in a model tapered axon with geometrical and electrophysiological properties consistent with typical values for *M. infundibulum*, showed consistent results [24]. These results demonstrate the capability of the ensemble-NV^- diamond magnetic sensor to measure small differences in magnetic signal waveforms correlated with differences in conduction velocity, which, in the present study, have contributions from differences in axon morphology.

3.3.2 Systematic checks

We performed multiple tests to verify that the observed $B^{\text{meas}}(t)$ arises solely from an axon AP (i.e., intracellular axial current). The tests and results are summarized in Table 3.3.2 and discussed here: (i) observation of a nonzero $B^{\text{meas}}(t)$ signal requires successful AP stimulation and propagation as determined by electrophysiology measurements of the extracellular action potential $\Phi_{\text{ex}}(z, \rho, t)$, and the observed $B^{\text{meas}}(t)$ is synchronized with $\Phi_{\text{ex}}(z, \rho, t)$ to within experimental error; (ii) crosstalk ('pickup artifacts') during data acquisition between the recorded $\Phi_{\text{ex}}(z, \rho, t)$ and $V_{\text{LIA}}(t)$ is ruled

Reversal	**Result**	**Systematic ruled out**
Axon firing $\rightarrow$ Axon not firing	$B^{\text{meas}}(t) \rightarrow 0$	Any non-AP signal, including stimulation artifacts
$\Phi_{\text{ex}}(z_1, \rho_1, t) \rightarrow \Phi_{\text{ex}}(z_2, \rho_2, t)$	$B^{\text{meas}}(t) \rightarrow B^{\text{meas}}(t)$	Cross-talk of $B^{\text{meas}}(t)$ with $\Phi_{\text{ex}}(z, \rho, t)$
$\text{sgn}[\frac{dV_{\text{LIA}}}{df}] = 1 \rightarrow -1$	$B^{\text{meas}}(t) \rightarrow -B^{\text{meas}}(t)$	Any non-magnetic artifact including cross-talk of $B^{\text{meas}}(t)$ with $\Phi_{\text{ex}}(z, \rho, t)$
$\phi_{\text{LIA}} \rightarrow \phi_{\text{LIA}} + 180^\circ$	$B^{\text{meas}}(t) \rightarrow -B^{\text{meas}}(t)$	Cross-talk of $B^{\text{meas}}(t)$ with $\Phi_{\text{ex}}(z, \rho, t)$
$B_0 \rightarrow -B_0$	$B^{\text{meas}}(t) \rightarrow -B^{\text{meas}}(t)$	Magnetic artifact from motional coupling to small $\frac{\partial B_0}{\partial x}$ across diamond

Table 3.3.1: Systematic checks

out through varying the recording electrode placement and observing no change in $B^{\text{meas}}(t)$; (iii) the origin of the NV-observed $B^{\text{meas}}(t)$ signal is demonstrated to be magnetic by switching to an LIA voltage zero-crossing with slope $\frac{dV_{\text{LIA}}}{df}$ of opposite sign (see Figure 3.2.5), and observing inversion of $B^{\text{meas}}(t)$; (iv) similarly, inverting the phase of the LIA reference signal ϕ_{LIA} by 180° produces the same result, also confirming the magnetic origin of the signal sensed by the NV$^-$ ensemble; and (v) time-varying magnetic fields from motional artifacts, e.g., specimen-induced instrument motion in the presence of a gradient in the bias field B_0 are ruled out by reversing the orientation of the permanent magnet and observing inversion of $B^{\text{meas}}(t)$. In addition, an investigation of whether the presence of muscle action accompanying axonal APs affects the observed $B^{\text{meas}}(t)$ in intact worm studies is described in Ref. [24]. Muscle action was seen to be temporally separated from AP propagation in electrophysiology measurements. Furthermore, the electrical signal associated with muscle action was found to decrease and eventually disappear with consecutive AP stimulations, an effect attributed to muscle fatigue and consistent with independent observations in the literature [205].

3.3.3 Action potential signal-to-noise ratio

The SNR of an AP magnetic field data set is calculated using (i) the peak-to-peak detected AP signal from an averaged set of N_{avg} measurements and (ii) the standard deviation of the time trace in a section of the same data set in which no AP is present. The single-shot SNR is calculated by dividing the SNR of the averaged data by $\sqrt{N_{\text{avg}}}$ For excised axon studies, $t = 0$ corresponds to the beginning of the stimulation pulse. For averaging data in intact organism studies, traces are aligned in time using a digital trigger set on either the maximum or minimum of the extracellular AP voltage signal $\Phi_{\text{ex}}(t)$; this alignment compensates for specimen contractions resulting in variable propagation delays and thus prevents smearing out of the averaged signal. The SNR is further quantified for the specimens studied in Figure 3.3.1c, d (worm B axon and squid A axon) with a series of technical replicates, displayed in Figure 3.3.5.

To maximally improve the SNR of a known expected signal in the presence of white noise, a matched filter can be shown to be the optimal linear filter 21. For a detected signal $x(t)$ containing an expected signal and additive noise, the matched filtered signal $y(t)$ is given by the convolution

$$y(t) = \int_0^t h(t - t')x(t')dt' \tag{3.15}$$

where $h(t)$ is the time-reversed trace of the expected signal. The matched filter is constructed from the data shown in Figure 3.3.1c with $N_{\text{avg}} = 600$. This trace is high-pass FFT filtered at 80 Hz to prevent non-DC values due to drift from being interpreted as signal. The trace is then zeroed for all times except a 1.4 ms window that includes the full detected AP signal, time-reversed, and then taken as the expected signal $h(t)$ for the matched filter. This filter is applied to the four consecutive sets of 150 averages contained in the larger data set (shown in Figure 3.3.511). The SNR of each of these filtered traces is improved to be between 14.5 and 16, indicating that the SNR of a single AP event after filtering is 1.2 ± 0.1 (mean $\pm$ SD for four magnetic measurements, each with $N_{\text{avg}} = 150$).

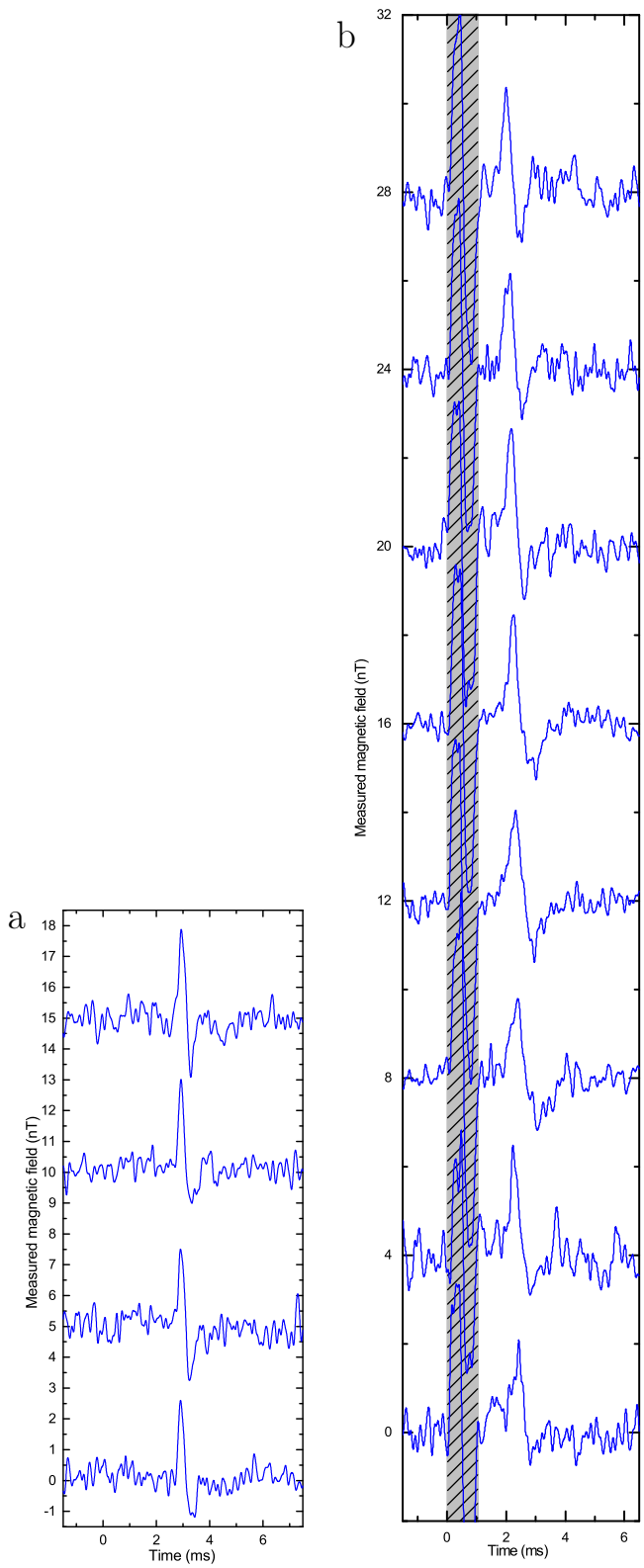

Figure 3.3.5: Technical replicates. a) Four traces of $B^{\text{meas}}(t)$ for worm B axon, each with $N_{\text{avg}} = 150$, which are combined to make the data shown in Figure 3.3.1c. Traces are offset for clarity with 5 nT spacing. b) Eight additional technical replicates of the data in Figure 3.3.1d. Traces are offset for clarity with 4 nT spacing.

3.4 Discussion and future projections

In the present work, we exploit two key advantages of NV-diamond for magnetic sensing of living biological systems - ability to bring the NV^- ensemble into close proximity of the signal source and operation under ambient conditions (biocompatibility) - to demonstrate single-neuron axonal AP magnetic sensing within ~ 10 μm of the specimens. By comparison, sensitive superconducting quantum interference devices (SQUIDs) [194] and atomic magnetometers [206] used for MEG [77] and neuron biophysics studies typically operate with standoff distances of several millimeters or more from the biological sample, as they function under extreme temperature conditions (cryogenic and heated, respectively) and have extended sensor geometries. Although SQUIDS can operate with sensitivity of ~ 1 fT/$\sqrt{\text{Hz}}$ [207], the much closer proximity of the NV-diamond sensor to the neuronal signal source boosts the measurement SNR by several orders of magnitude for a given magnetic field sensitivity and, additionally, for a given SNR, enables a higher quality reconstruction of source currents from a magnetic field map [208]. Furthermore, operation of an ensemble-NV^- magnetometer at a distance much closer than the AP wavelength λ_{AP} (of order ~ 1 mm for unmyelinated mammalian axons) [209, 210] can provide a more accurate determination of AP currents due to the reduced contribution from extracellular return currents [210], which significantly attenuate AP signals at standoff distances λ_{AP}. A third key advantage of NV-diamond technology is straightforward parallelization of optically detected NV^- sensors to provide wide-field magnetic imaging with micrometer-scale spatial resolution, e.g., by imaging fluorescence from the NV^- sensing layer onto a camera [50]. In combination with close proximity, the high spatial resolution provided by NV-diamond magnetic imaging enables sensitivity to magnetic fields generated by currents on small length scales [49], which tend to cancel at the typical standoff distances of other magnetometers. With both source-to-sensor standoff distance and spatial resolution at the micrometer scale, a wide variety of neuronal current sources and sinks could be resolvable with NV-diamond magnetic imaging.

Key technical challenges to realize a next-generation NV-diamond magnetic im-

ager suitable for neuroscience applications include (i) improving the magnetic field sensitivity [109, 200] to enable real-time, single-cell AP event detection from individual mammalian neurons, which are expected to generate peak AP magnetic fields up to $\sim$ 1 nT at the NV$^-$ sensor layer (see the SI Appendix of Ref. [24]); and (ii) incorporating wide-field imaging of transient AP magnetic fields with micron-scale resolution. The imaging challenge can be met by adapting established NV$^-$ techniques for wide-field imaging of static magnetic fields in biological samples [50, 51] to be able to acquire repeated, fast (< 0.1 ms) images. This capability can then be integrated with tomographic methods similar to those used in MEG [77, 211, 212], such as spatial filtering [208, 213], to confront the inverse problem [214] of assigning measured magnetic waveforms from axonal APs, soma, and other neuronal processes to individual cells within a crowded field of neurons. Prior knowledge about the neuronal sample, such as the cell network geometry, axon morphology, and degree of myelination, could aid magnetic signal localization as well as determination of the physiological origin of signal differences between individual neurons, e.g., arising from variations in AP conduction velocity.

The sensitivity challenge can be addressed through a series of methods analysed in detail in Chapters 4-6. In short, combining engineering of optimized diamonds [96] with higher N-to-NV$^-$ conversion efficiency and longer NV$^-$ ensemble spin dephasing times T_2^* [141], and implementing pulsed double-quantum Ramsey [102, 104, 215] measurement protocols is estimated to enable an enhancement of the volume-normalized sensitivity by nearly 300$\times$-fold from the demonstrated 34 nT μm$^{-3/2}$ Hz$^{-1/2}$ to $\sim$ 118 pT μm$^{-3/2}$ Hz$^{-1/2}$. Along with the anticipated sensitivity improvement, the smaller sensing volume V of a next-generation instrument should allow a $\sim 6,000$-fold gain in the figure of merit $1/(\eta V)$ relevant for fields containing spatial information, such as is expected from dense neuronal networks (see Section 3.4.3). To realize further sensitivity enhancements, quantum-assisted techniques [104, 215, 131, 188] could enable measurements approaching fundamental quantum limits (see Chapter 5). Our present NV-diamond instrument has a photon shot-noise-limited magnetic field sensitivity $\sim 1,500\times$ worse than the quantum spin projection limit (see Section 3.4.2),

highlighting the potential for large sensitivity gains. For example, spin-to-charge-state readout for single NV^- centers was demonstrated to provide enhanced magnetic field sensitivity with readout fidelity only a factor of 3 away from the spin projection limit [101].

3.4.1 Expected magnetic field sensitivity in next-generation instrument

In this section we estimate the magnetic field sensitivity of a next-generation magnetic imaging instrument based on existing demonstrated magnetometry techniques and anticipated advances in diamond growth. A next-generation instrument will likely employ pulsed magnetic field sensing schemes, such as Ramsey-type sequences, which do not suffer from laser and MW power broadening of the NV-diamond ODMR features and thus allow for higher contrast and enhanced sensitivity per volume than CW-ODMR [102]. A Ramsey scheme with free precession time τ, and optical and MW initialization and readout times t_I and t_R, has shot-noise-limited sensitivity [3, 103, 101] of

$$\eta_{\text{Ramsey}} = \frac{\hbar}{g_e \mu_B} \frac{\sqrt{t_I + \tau + t_R}}{\tau} \frac{1}{\mathcal{C}' e^{-(\tau/T_2^*)^p} \sqrt{\beta}}, \tag{3.16}$$

where $\beta = \mathcal{R}t$ is the average number of photons collected per measurement, $\mathcal{C}'$ is the fluorescence contrast at $\tau = 0$, and the exponential factor $e^{-(\tau/T_2^*)^p}$ accounts for contrast degradation due to NV^- spin dephasing with characteristic time T_2^*. For broadening mechanisms that produce Lorentzian lineshapes, $p = 1$; and for Gaussian lineshapes, $p = 2$. For typical measurements on large ensembles, we may assume $p = 1$ [141]. We note that $\mathcal{C}'$ is defined as the difference in collected PL between the maximum and minimum of a Ramsey fringe divided by the sum of the maximum and minimum collected PL [3]. This definition differs from the earlier definition of contrast $\mathcal{C}$ used for CW-ODMR as $\mathcal{C}' = \frac{\mathcal{C}}{2-\mathcal{C}}$. Depending upon the values of t_I and t_R, the sensitivity is typically optimized for $T_2^*/2 \leqslant \tau < T_2^*$.

Here we calculate the sensitivity improvement for both the diamond used in the present work and a future anticipated diamond chip with improved sensing parame-

ters. For both estimates we assume a fluorescence contrast per NV$^-$ axis of $\mathcal{C}' = 3.9\%$, a collection efficiency of CE = 0.2 (corresponding to the collection efficiency of a lossless 1.49 NA oil objective [108] and including a reflective layer on the NV$^-$ diamond surface to further double the collected PL), and an excitation intensity near saturation leading to a time-averaged photon emission rate of $\Gamma_{\mathrm{ph}} = 1/(200\ \mathrm{ns})$ per NV. Employing double-quantum magnetometry [104, 215] increases the magnetic precession rate by 2×, which effectively reduces T_2^* from its native value by 2×, so that $T_{2\,\mathrm{DQ}}^* = T_2^*/2$. Double-quantum magnetometry can also provide common-mode rejection of noise due to strain and temperature inhomogeneities, promising a further sensitivity enhancement, which is not explicitly accounted for here. Both estimates also presume simultaneous interrogation of all four NV$^-$ axes, which provides a sensitivity enhancement of $2\sqrt{4/3}$ ($= 4\cos[\theta_{\mathrm{tet}}/2]$). Combining these enhancement factors into Equation 3.16 yields

$$\eta_{\mathrm{DQ,4\text{-}axis}} = \frac{1}{2}\frac{1}{2\sqrt{4/3}}\frac{\hbar}{g_e\mu_B}\frac{\sqrt{t_I+\tau+t_R}}{\tau}\frac{1}{\mathcal{C}'e^{-\tau/T_{2\,\mathrm{DQ}}^*}\sqrt{\beta}}. \tag{3.17}$$

The diamond used in the present work has native $T_2^* = 450$ ns, [N] = 27 ppm, and ∼ 6% conversion efficiency from [N] to [NV$^-$]. In an illumination volume of 1 μm^3, $n_{\mathrm{NV}} = 3.0 \times 10^5$ NV$^-$ spins are addressed. For simplicity these estimates assume negligible light losses in the optical system so that the photon collection rate from a 1 μm^3 volume is $\mathcal{R} = 3.0 \times 10^{11}$ photons per second. We assume typical values of $t_I = 1$ μs and $t_R = 300$ ns. Using these parameters in Equation 3.17 with $\tau = T_{2\,\mathrm{DQ}}^* = T_2^*/2 = 225$ ns, the expected volume-normalized sensitivity of an enhanced sensitivity magnetometer using the present diamond chip is 1.57 nT μm$^{3/2}$Hz$^{-1/2}$. This represents more than 20-fold improvement over the present instrument, with bulk sensitivity 15 pT/$\sqrt{\mathrm{Hz}}$ over a 13 μm × 200 μm × 2000 μm = 5×10^6 μm^3 volume, leading to a volume-normalized sensitivity of 34 nT μm$^{3/2}$Hz$^{-1/2}$.

For a next-generation diamond chip, we assume the following parameters: $T_2^* = 21$ μs, $t_I = 2$ μs, $t_R = 300$ ns, [N] = 2 ppm, and 50% conversion efficiency from [N] to [NV$^-$], such that in an illumination volume of 1 μm^3, $n_{\mathrm{NV}} = 1.76 \times 10^5$ and

$\mathcal{R} = 1.76\times10^{11}$ photons per second. Using these parameter estimates in Equation 3.17 and using $\tau = T^*_{2\,\mathrm{DQ}} = T^*_2/2 = 5.25$ μs, the expected volume-normalized sensitivity is 118 pT μm$^{3/2}$Hz$^{-1/2}$, representing a nearly 300× improvement over the present instrument. Further sensitivity enhancements may be possible through quantum-assisted techniques [101, 131, 188] or even using other solid-state color defects [216].

3.4.2 Trade-off between signal-to-noise ratio, spatial resolution, and temporal resolution in next-generation magnetic imager

The challenges to improve sensitivity and implement high-resolution imaging resolution are related, as there exist trade-offs between magnetic field sensitivity and both spatial and temporal resolution for a given NV$^-$ density in the NV$^-$-rich layer [3]. To assess these trade-offs to inform future studies, we calculate the expected spatial resolution and SNR of a next-generation NV-diamond magnetic imager with a projected volume-normalized sensitivity of 118 pT μm$^{-3/2}$ Hz$^{-1/2}$ in the context of sensing propagating APs from mammalian neurons (see Figure 3.4.1).

In the idealized case of uniform optical intensity, MW intensity, and NV$^-$ density, the shot-noise-limited magnetometer sensitivity scales as $\eta \propto 1/\sqrt{V}$ where V is the total sensing volume. We denote the volume-normalized sensitivity $\eta^V \equiv \eta\sqrt{V}$. As discussed above, the present NV-diamond magnetometer has $\eta^V = 34$ nT μm$^{3/2}$Hz$^{-1/2}$; whereas a next-generation magnetic sensor is expected to achieve $\eta^V = 118$ pT μm$^{3/2}$Hz$^{-1/2}$, nearly 300 times better than the present system.

The sensing volume V consists of the NV$^-$ layer at the diamond chip surface, with area A and depth d such that $V = Ad$. The sensing surface may be divided into a square grid of M pixels, with each pixel forming the top surface of a voxel of volume $v = l^2 d$, where $l = \sqrt{A/M}$ is the pixel side-length. The sensitivity for a pixel is then $\eta_{\mathrm{pixel}} = \frac{\eta^V}{l\sqrt{d}}$. The scaling relation between η_{pixel} and l is illustrated in Figure 3.4.1a.

For a shot-noise-limited magnetometer, higher temporal resolution requires increased magnetometer bandwidth BW. The SNR for a fixed amplitude magnetic

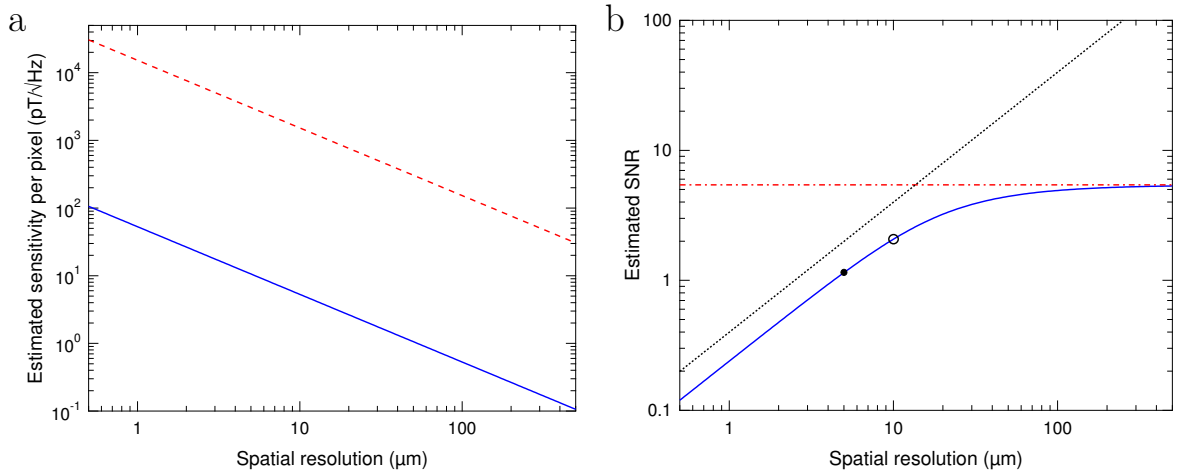

Figure 3.4.1: Estimated sensitivity and signal-to-noise ratio versus spatial resolution. a) Scaling with spatial resolution l of the expected sensitivity of a magnetometer with volume-normalized sensitivity 34 nTμm$^{3/2}$Hz$^{-1/2}$ of the present instrument (red dashed line) and of a next-generation NV-diamond magnetic imager (blue solid line) with volume-normalized sensitivity 118 pTμm$^{3/2}$Hz$^{-1/2}$. Here l is defined in terms of the volume v of NV-diamond directly below the axon from which the NV$^-$ fluorescence is imaged onto a single pixel, $v = l^2 d$, for an NV$^-$ layer thickness $d = 5$ μm. b) Magnetic signal-to-noise ratio (SNR) for a single pixel of a next-generation instrument with sensitivity 118 pTμm$^{3/2}$Hz$^{-1/2}$ versus spatial resolution l for NV$^-$ layer thickness $d = 5$ μm and area $l \times l$. Blue trace shows scaling of estimated SNR from an axon of radius $r_a = 5$ μm with an estimated magnetic field of 1 nT at the axon surface, using Equation 3.18. Red dot-dashed trace denotes the asymptotic limit of the expected SNR arising from the inverse scaling of the magnetic field with distance ρ from the source: $B \propto 1/\rho$. Black dashed trace shows the expected SNR of a uniform 1 nT field versus l for $d = 5$ μm. Solid black dot marks expected SNR at $l = d = r_a = 5$ μm, and open circle marks expected SNR at $l = 10$ μm, the approximate crossover point between the two limiting regimes for $d = r_a = 5$ μm. The SNR of the same system using an identical magnetometer but with volume normalized sensitivity 34 nTμm$^{3/2}$Hz$^{-1/2}$ would provide signals with SNR reduced by a factor of 288.

signal varies as SNR$\propto 1/\sqrt{\text{BW}}$. For this exercise, the desired bandwidth is assumed to be from DC to BW. The rise time, a measure of the temporal resolution, is related to the bandwidth by BW(Hz)$= 0.35/\tau_{10/90}$(s). By substitution, SNR$\propto\sqrt{\tau_{10/90}}$. Moreover, since $\eta_{\text{pixel}} = \frac{\eta^V}{l\sqrt{d}}$, the SNR for a single pixel also scales as SNR$\propto l$. Thus the SNR for a pixel remains constant when the quantity $\tau_{10/90}l^2$ is held constant. For example, to gain a factor of 4× in temporal resolution while maintaining fixed SNR, the spatial resolution of the magnetic field map would have to be made 2× worse. This illustrates the inherent trade-off between spatial resolution and temporal resolution if a given SNR is desired.

For signal fields containing spatial information, however, the SNR may level off or even decrease as l increases, as discussed in more detail below, which can also affect the trade-off between $\tau_{10/90}$ and and l for fixed SNR. See Figure 3.4.1b for an example estimated SNR scaling for a typical mammalian axon ($r_a = 5$ μm) with spatial resolution l, for fixed NV$^-$ layer depth ($d = 5$ μm). In such cases, smaller sensing volumes are often preferable, even for fixed η^V. The quantity $1/(\eta V)$ is a useful figure of merit for imaging non-uniform fields from mammalian neurons, as this quantity encompasses the trade-off between SNR and spatial resolution for magnetic fields that fall off as $1/\sqrt{V}$, (i.e., as $1/l$ for fixed d). In a next-generation NV-diamond magnetometer with $V \approx 50\ \mu\text{m} \times 50\ \mu\text{m} \times 5\ \mu\text{m} = 1.25 \times 10^4\ \mu\text{m}^3$, the value of $1/(\eta V)$ is expected to be enhanced by ~ 6000 compared to the present instrument.

Optimization may be performed to find the ideal sensing volume per pixel for a given bulk sensitivity by considering the spatial information of the fields being sensed. At sensor-to-source standoff distances much less than the AP wavelength λ_{AP} (~ 1 mm for unmyelinated mammalian axons [209, 210]), external return currents do not attenuate the magnetic signal appreciably and axon AP magnetic fields fall off with radial distance from the neuron center ρ as $1/\rho$ [201]. Let the average field at the location of an NV$^-$ center positioned at the neuron surface directly beneath the neuron (i.e., $\rho = r_a$) be $B(r_a, t) = B_0(t)$. The average field sensed by a layer of NVs of thickness d directly below the neuron surface ranging from $\rho = r_a$ to $\rho = r_a + d$ is then $B_{\text{avg}}(t) = B_0(t)\frac{r_a}{d}\int_{r_a}^{r_a+d}\frac{d\rho}{\rho} = B_0(t)\frac{r_a}{d}\ln\left(\frac{r_a+d}{r_a}\right)$. For example, for an AP signal

that reaches a peak value of 1 nT at the surface of an axon, where $r_a = 5$ μm, the average magnetic field detected by an NV^- layer of thickness $d = 5$ μm below the axon is 0.69 nT.

In addition, the detected signal falls off in the lateral dimensions for NVs not positioned directly under the center of the axon. Taking the positive z-direction to be the propagation direction of the AP, and transforming from cylindrical to Cartesian coordinates ($\rho^2 = x^2 + y^2$, $\tan(\theta) = y/x$), the magnitude of the AP magnetic field scales as $B(x,y,t) = B_0(t)\frac{r_a}{\sqrt{x^2+y^2}}$ with x- and y-components $B_x(x,y,t) = \frac{-y}{x^2+y^2}r_a$ and $B_y(x,y,t) = \frac{x}{x^2+y^2}r_a$, and z-component $B_z = 0$. The average field over a square layer of area $l \times l$ in the x-z plane and thickness of d in y is thus

$$\begin{aligned} B_{x,\text{avg}}(t) &= -B_0(t)\frac{r_a}{l^2 d}\int_{-l/2}^{l/2} dz \int_{-l/2}^{l/2} dx \int_{-r_a}^{-(r_a+d)} dy \frac{y}{x^2+y^2} \\ &= B_0(t)\left[\frac{r_a}{2d}\ln\left(\frac{(r_a+d)^2+(l/2)^2}{r_a^2+(l/2)^2}\right) + \frac{r_a^2}{(l/2)d}\tan^{-1}\left(\frac{r_a}{l/2}\right)\right. \\ &\qquad \left. -\frac{r_a(r_a+d)}{(l/2)d}\tan^{-1}\left(\frac{r_a+d}{l/2}\right) + \frac{\pi r_a}{l}\right]. \end{aligned} \tag{3.18}$$

A similar equation exists for $B_{x,\text{avg}}(t)$. Here we have made the valid assumption that the layer dimension along z is small compared to the characteristic AP length scale, $l \ll \lambda_{\text{AP}}$, such that the magnetic signal is not attenuated when averaged over this dimension. Again, for $r_a = 5$ μm and $d = 5$ μm, and with $l = 5$ μm, the expected magnetic field averaged over the sensing region is reduced only slightly further to 0.66 nT.

As described above, the spatially averaged AP magnetic field from an axon of radius r_a, placed on a sensing layer of area $a = l \times l$ and thickness d, and oriented along the z-axis, is given by Equation 3.18. In the limit where $d, l \ll r_a$, the signal approaches $B_0(t)$. For $l \gg r_a, d$, the signal falls as $1/l$, and for $d \gg r_a, l$, the signal falls off as $1/d$. As shown in Fig.S13B, there is a trade-off between spatial resolution and SNR for a fixed sized axon. Determination of the optimal spatial resolution requires evaluating when the marginal resolution cost of increasing l is no longer justified by increased SNR, as shown in Figure 3.4.1b. For a signal field that approximates the

field from a current-carrying wire (from the axon model [201, 202]), and for pixel sensing volumes much larger than the wire radius but still smaller than the wire length, such that the above equation for $B_{x,\mathrm{avg}}(t)$ continues to apply, the average magnetic field over a sensing volume $v = l^2 d$ falls off as roughly $1/l$ for fixed d, and the shot-noise limited SNR is independent of l. In this flat asymptotic limit shown in Figure 3.4.1b, enhancing the spatial resolution has negligible cost to the SNR. In contrast, when l becomes small compared to r_a, the signal field becomes roughly uniform over each sensing volume. At this point, the SNR per pixel falls off with decreasing l, as shown in Figure 3.4.1b, and the additional spatial information gained from the enhanced resolution diminishes. However, in the absence of camera read noise, more pixels - each corresponding to smaller sensing regions - may be used and later binned together in post-processing to recover larger SNR values.

Based on this analysis, where for simplicity we have ignored camera read noise, we conclude that the optimal regime in which to operate an NV-diamond neuron magnetic imager with fixed η^V (in the absence of image post-processing) is when both d and l are $\approx r_a$. For the example of a neuron with $r_a = 5$ μm, (and choosing $d = r_a$), Figure 3.4.1b marks with an open circle the approximate crossover between the two limiting regimes at $l = 10$ μm. Use of non-square sensing regions ($a = l \times w, l \neq w$) matched roughly to the dimensions of the sources being imaged can lead to significant improvements in expected SNR, as discussed below.

We next estimate the SNR of a detected mammalian neuron AP magnetic signal using a next-generation NV-diamond magnetometer, which, as discussed above, has an anticipated volume-independent sensitivity of 118 pT $\mu\mathrm{m}^{3/2}\mathrm{Hz}^{-1/2}$. For a sensing volume of 5 μm × 12.5 μm × 200 μm, and a 5 μm-radius mammalian axon centered on and oriented along the long axis of the sensing region with a 1 nT peak AP magnetic field at the surface of the axon, the spatially-averaged magnetic field detected by the NV-diamond sensor is 564 pT. The RMS noise of a time trace of magnetic data taken over that sensing volume with sampling rate 3 kS/s is 57.9 pT. The expected SNR from this estimate is thus 9.73, prior to any SNR-enhancing temporal filtering techniques.

3.4.3 Extension of technique to resolving currents from mammalian neuron systems

In a next-generation NV-diamond instrument for magnetic imaging of networks of neurons oriented arbitrarily on the diamond surface, the component of $B(t)$ perpendicular to the NV^- layer at each point on the diamond surface can be sensed, as shown in Figure 3.4.2. The azimuthal AP magnetic field projections would then have opposite sign for measurement points on different sides of the axon, and $B(t)$ would in general have nonzero projection on each of the four NV^- axes, allowing mapping of AP propagation in the network.

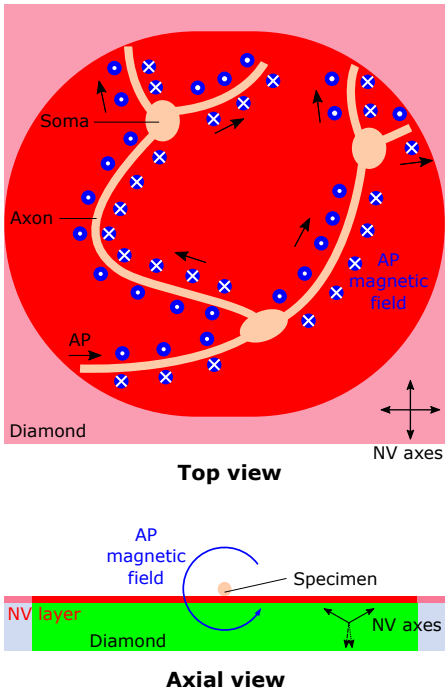

Figure 3.4.2: Proposed method for magnetic imaging of AP dynamics from networks of smaller neurons with arbitrary orientation. Here the NV^- sensor layer detects the magnetic field component normal to the diamond surface, which has opposite sign on different sides of the specimen.

Realization of sufficient magnetometer sensitivity is anticipated to be the primary challenge to extending NV-diamond magnetic imaging to mammalian neurons and from single neurons to networks of neurons. In contrast, implementation of magnetic imaging with micron-scale spatial resolution and ~ 100 μm field of view is expected

to be relatively straightforward, as it mainly requires applying previously developed wide-field NV-diamond magnetic imaging technology demonstrated with biological systems [217] to the present and anticipated enhanced-sensitivity magnetometer. Sensitivity rather than spatial resolution is thus the chief limit to reconstructing neuronal currents from acquired magnetic field maps using an NV-diamond magnetic imager.

However, both the optimal resolution and the achievable SNR for a given sensitivity depend on the nature, number, and spacing of current sources being measured. In the absence of noise, the biomagnetic inverse problem [211] can be uniquely solved for 2D networks close [213] to the diamond sensing layer. 3D networks are more problematic: not only are magnetic signals smaller due to greater source-sensor standoff distance, but the problem is under-constrained, meaning that multiple reconstructions of current sources are possible from an observed magnetic field map. In all cases, *a priori* information about the network structure under study, as could be obtained with a bright field confocal microscope or other traditional optical methods, may be used to further constrain solutions, thereby increasing reconstruction accuracy and decreasing magnetometer sensitivity requirements. Similarly, prior information about axon morphology, the presence or absence of myelin, and other physiological and geometrical features could inform determination of the origins of imaged magnetic signal differences and associated individual neuronal currents, e.g., due to differences in AP conduction velocity [218]. To resolve signals from networks of neurons and non-axonal processes, we envision a staged approach outlined in more detail below. For this discussion we define the mean neuron-to-neuron spacing as w and the mean neuron-to-sensor-plane standoff distance as q. Note also that each stage of this effort will be aided by studies of model physical systems (e.g., fabricated wire arrays placed on the NV-diamond sensor surface) to characterize system performance and current source reconstruction algorithms for well-controlled systems.

The first stage consists of imaging sparse ($w > q$), where ($q \sim 10$ μm), 2D arrays of neurons and reconstructing the axonal currents. As an example, we show simulations of expected magnetic field maps of AP signals from four overlapping mammalian axons combined with added fluctuations due to magnetometer shot noise, both with and

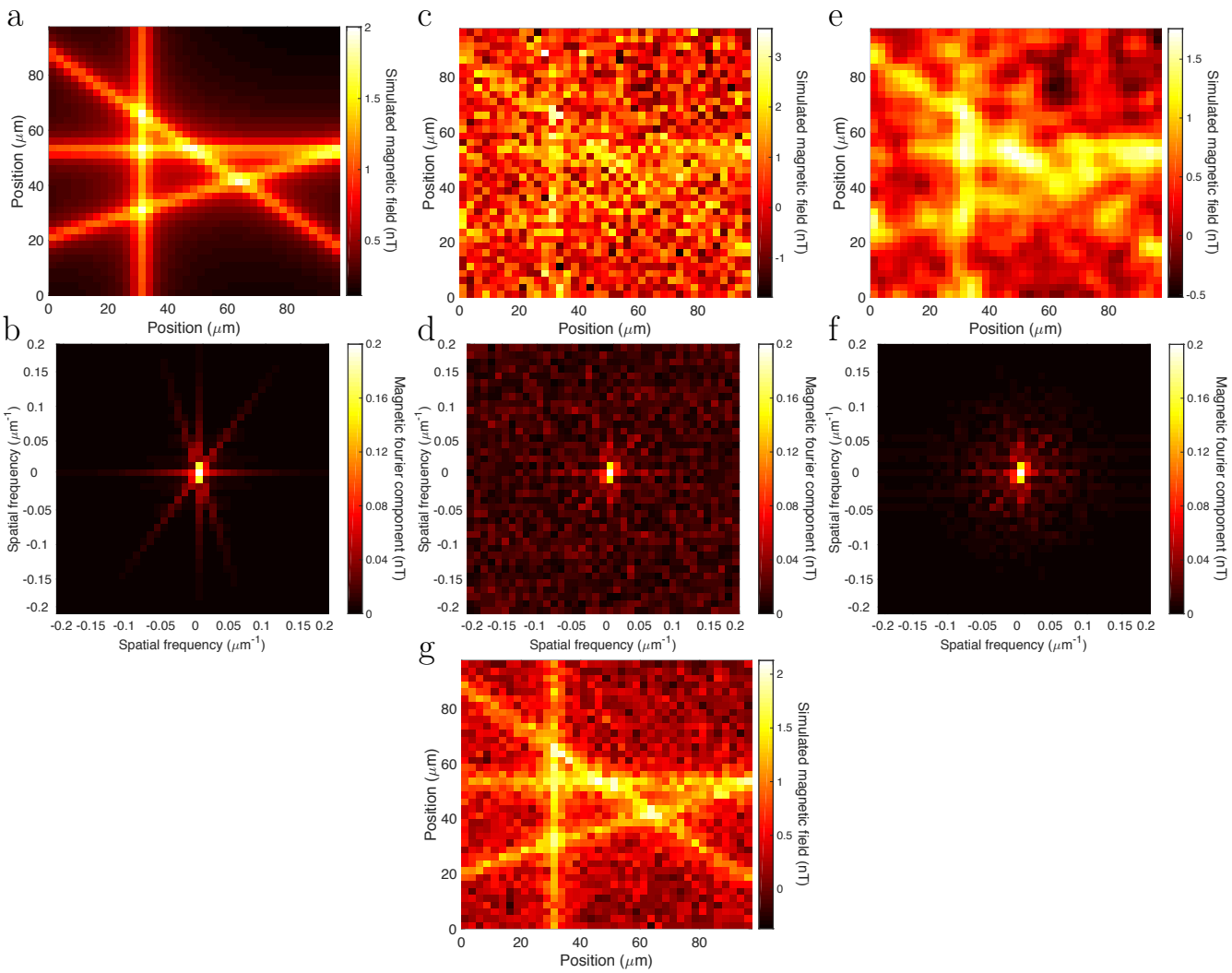

Figure 3.4.3: Simulated magnetic field maps from multiple neurons. a) Calculated map of average magnetic field magnitude over NV$^-$ layer from four firing wire-like axons with $r = 5$ μm each producing a maximum field amplitude of 1 nT at the axon surface. Axons are placed directly on the NV$^-$ sensing layer of thickness $d = 5$ μm. Field of view is $100\,\mu\text{m} \times 100\,\mu\text{m}$ and pixel area is $l \times l = 2.5\,\mu\text{m} \times 2.5\,\mu\text{m}$. b) Spatial Fourier transform of image in (a). Signal information is concentrated at low spatial frequencies. c) Simulated raw image of magnetic field map from (a) in the presence of Gaussian noise of 1.2 nT RMS deviation per pixel, as expected from a shot-noise-limited NV-diamond magnetic imager with sensitivity 118 $\text{pT}\,\mu\text{m}^{3/2}\text{Hz}^{-1/2}$ and sampling rate 3 kS/s. A magnetic imager with volume-normalized sensitivity 34 $\text{nT}\,\mu\text{m}^{3/2}\,\text{Hz}^{-1/2}$ of the present instrument would require $N_{\text{avg}} = 83000$ averaged trials to yield an image with the same SNR. d) Spatial Fourier transform of field map in (c). e) Magnetic map from (c) after processing with spatial low-pass filter applied via convolution with Gaussian kernel of 1-pixel (2.5 μm) s.d. f) Spatial Fourier transform of field map in (e), displaying reduced contribution from noise at high spatial frequencies and preserved low-frequency signal information. Displayed color scale in (b), (d), and (f) saturates the center pixel, which has value ~ 0.53 nT in all three images. g) Magnetic field map from (a) simulated in the presence of $1/\sqrt{10}$ the noise in (c), demonstrating SNR enhancement from averaging $N_{\text{avg}} = 10$ trials.

without modest spatial filtering of the simulated data to demonstrate the capability for enhanced SNR with image processing (see Figure 3.4.3).The simulation assumes a shot-noise-limited sensitivity of 118 pT $\mu m^{3/2} Hz^{-1/2}$, as outlined above. The field-of-view of the simulation is 100 μm $\times$ 100 μm and the NV^- layer depth is $d = 5$ μm. The pixel size is set to 2.5μm $\times$ 2.5 μm. Axons are modeled as straight wire-like sources according to the axon (volume conductor) model [210, 201] with $r_a = 5$ μm placed in contact with the diamond NV^- layer; and fired simultaneously, each with action current set to produce a peak field of 1.0 nT at the axon surface. For the sensing volume corresponding to each pixel, the expected magnitude of the magnetic field vector is calculated (Figure 3.4.3a). A noise profile of 1.2 nT RMS deviation per pixel, calculated from expected performance of the next-generation device, is added on top of this profile to achieve the realistic profile of an image taken in a single shot with a sampling rate 3 kS/s (Figure 3.4.3c).

Without substantial loss of spatial information, the SNR of the image can be improved through use of low-pass spatial filtering, as shown in Figure 3.4.3e, where a simple Gaussian convolution is applied to the image in Figure 3.4.3c. This spatial filter takes advantage only of the knowledge that shot-noise fluctuations have a higher spatial frequency bandwidth than the magnetic signal, as shown in Figure 3.4.3b, d, f. By filtering out high spatial frequency components of the image, a Gaussian spatial filter eliminates more noise than signal from the image. This and other straightforward spatial filters are able to enhance image SNR without knowledge of the propagation direction or conduction velocity of APs. When the temporal profile of expected magnetic signals is known, temporal matched filtering can improve image SNR even in the absence of information on the spatial distribution or propagation directions of current sources. The temporal profile of an axonal AP magnetic signal waveform is independent of axon orientation, even when only a single component of the magnetic field is measured. Further improved performance can be achieved using prior information about the spatial locations of the neuronal current sources (i.e., spatial matched filtering), through combining spatial information with the known temporal profile of the action current, and through use of similar image-processing methods [219].

Where possible, synchronizing multiple AP firings and averaging traces together, as is done in the present studies, can significantly improve image SNR. To represent the effect of modest ($N_{\text{avg}} = 10$ trials) averaging, the noise level is decreased to 1.2 nT/$\sqrt{10}$ = 0.35 nT in Figure 3.4.3g to demonstrate the distinguishability of the four axons in the image, even from the raw unprocessed magnetometer output.

Furthermore, methods of spatial filtering can be used to solve the biomagnetic inverse problem - i.e., relate magnetic field maps back to current distributions - even in the absence of prior knowledge about the nature of the sources. Substantial work in the literature, (particularly by Wikswo and collaborators) demonstrates the ability to reconstruct arbitrary 1D and 2D current distributions from magnetic field images recorded some distance from the sources in the presence of noise [213, 203, 208]. Additionally, spatial filtering introduces a trade-off between required SNR to determine the current distribution and standoff distance q from the imaging plane to the source plane, favoring small q. For example, Ref. [213] shows that two magnetic imagers - one with 100× the noise and 1/5 the SNR of the other, but positioned 3× closer to the source - can reconstruct a 2D current distribution equally well. Growth of 2D cultures of neurons directly on the diamond sensor alongside use of a sufficiently thin NV^- sensor layer ($d \sim 5$ μm) will ensure that q is always small compared to both w and λ_{AP}. Thus, we envision assigning magnetic fields to particular cells in sparse networks, without prior knowledge of the nature of the signals, based on magnetic field maps with limited SNR.

The next stage involves magnetic imaging of currents from dense 2D neuronal networks comprising overlapping neurons with mean neuron-neuron spacing $w \lesssim 10$ μm. To avoid aliasing of high spatial frequencies when using spatial filtering methods, $w \gtrsim l, d$ is generally required [213, 212]. Fortunately, the sensing surface of an ensemble-based NV^- imager is continuous, with imaging resolution adjustable external to the sensor (e.g., by changing imaging magnification), with the restriction that the ultimate resolution will be limited to approximately the sensor layer thickness d. With sufficient magnetometer sensitivity, spatial filtering techniques are also expected to allow effective reconstruction of currents in non-axonal processes in 2D,

even without *a priori* knowledge of the currents within such structures. Furthermore, super-resolution imaging techniques could be applied to the diamond sensor to enhance spatial resolution below the optical diffraction limit [21]. Therefore, the principal challenge in magnetic imaging of dense 2D neuronal networks reduces to improving magnetometer sensitivity.

Assuming successful implementation of the above, we next foresee reconstruction of sparse neural networks in 3D space, e.g., cultures or tissue slices with nonnegligible thickness ($\sim$ 100 µm) placed on the diamond surface. We expect to maintain a proximity of $\sim$ 10 µm from the sensor layer to the tissue slice, although the standoff distance q to a given current source within the slice will naturally be larger (up to $\sim$ 100 µm) reducing magnetic signal amplitudes and limiting the effective spatial resolution to $\sim q$ in the absence of additional known structural information localizing specific current sources within the tissue.

Solving the inverse problem in 3D requires *a priori* assumptions about the nature of the expected sources in order to determine a unique solution [213]. For example, schemes used in present-generation MEG typically employ a dipole model of currents in the brain generating detectable magnetic fields [77]. While this simplification sufficiently constrains the inverse problem and allows for physical solutions to be found, it largely neglects the complex physiological activity generating the fields - effects that often cannot be observed at distances far from the sources such as outside the skull. Furthermore, in some cases dipole models are physiologically unrealistic [208].

Where possible, it is preferable to use a model that retains information on individual neurons. For example, the axon (volume conductor) model [210, 201], which constitutes the basis for the simple magnetic model used in the present work, treats individual neurons as cylindrically symmetric wire-like current sources. In order to resolve currents from individual neurons and justify use of this model, magnetic field measurements must be made at distances sufficiently close to the neurons, such that $q \leqslant w$ [208]. For SQUID and atomic magnetometers, both of which are bulky and typically cannot meet this requirement, the method of downward continuation [214] may be used to reconstruct the field distribution in the near-field [208]. However,

downward continuation requires a much improved SNR and places additional restrictions on both acceptable values of w and the nature of the sources [214]. The close proximity to sources afforded by the NV-diamond sensor greatly alleviates these restrictions [213]. In the near-field regime, ($q < \lambda_{AP} \approx 1$ mm), magnetic fields from simultaneous currents at different locations will neither partially nor completely cancel as they would at a location ~ 1 cm or more away [208]. The ability of NV-diamond to perform magnetic field measurements in the near-field, where return-currents can largely be ignored, allows for the application of more physically detailed, physiologically realistic models to sufficiently constrain the inverse problem without ignoring physiologically relevant information about the neuronal dynamics. Furthermore, the high temporal resolution of NV^- magnetometry can allow for nearly-overlapping current sources to be resolved as long as their signals are separated in time. To further aid in simplifying the substantial inverse problem posed by dense 2D and sparse 3D networks, cultures may be encouraged to grow in controlled patterns [220, 221].

Resolving activity from non-axonal processes in dense 3D networks with both high spatial and high temporal resolution is a significant challenge in neuroscience [74], which we regard as a longer-term goal that may realistically require additional structural knowledge of the network, such as provided by a confocal scan, along with further sensitivity enhancements of the magnetic imaging technique. We regard the task of achieving the necessary sensitivity to map neuronal network dynamics as a practical challenge, albeit a difficult one, which is limited more by a need for engineering advances in NV-diamond magnetometry than by fundamental constraints.

Chapter 4

Simultaneous broadband vector magnetometry using solid-state spins

This chapter describes a novel technique for high-speed NV-diamond vector magnetometry and its experimental implementation. The chief performance goal for vector magnetometry is that all components of a magnetic field vector be reconstructed with high SNR in a short period of time, meaning that the sensitivity along all field directions, η_x, η_y, and η_z, must be minimized. Toward this goal, we demonstrate a vector magnetometer that simultaneously measures all Cartesian components of a dynamic magnetic field using multi-channel lock-in detection to extract the magnetic-field-dependent spin-resonance shifts of NVs oriented along all four tetrahedral diamond axes from the optical signal measured on a single detector. The sensor operates from near DC (5 Hz) up to a 12.5-kHz measurement bandwidth and simultaneously achieves $\sim$ 50 pT/$\sqrt{\text{Hz}}$ magnetic-field sensitivity for each Cartesian component, which is, to date, the highest demonstrated sensitivity of a full vector magnetometer employing solid-state spins. Compared to optimized devices interrogating the four NV orientations sequentially, the simultaneous vector magnetometer enables a 4$\times$ measurement speedup. The technique can be extended to pulsed-type sensing protocols and parallel wide-field magnetic imaging. The majority of this chapter is adapted from Ref. [25].

4.1 Introduction

A wide range of magnetometry applications require real-time sensing of a dynamic vector magnetic field, including magnetic navigation [222, 223, 224, 225], magnetic anomaly detection [223, 224], surveying [226], current and position sensing [223, 224, 227], and biomagnetic field detection and imaging [194, 77, 228, 50, 51, 24, 229, 52]. Scalar magnetometers, such as vapor cell, proton precession, and Overhauser effect magnetometers, measure only the magnetic field magnitude [227]. Vector projection magnetometers, including SQUIDs, fluxgates, and Hall probes, measure the magnetic field projection along a specified axis in space; the determination of all three Cartesian field components then requires multiple sensors aligned along different axes. Uncertainty or drifts in the relative orientations or gains of these multiple sensors can result in heading errors, which limit the vector field reconstruction accuracy [230, 231, 232]. In contrast, the fixed crystallographic axes inherent to solid-state spin-based sensors allow complete vector field sensing while mitigating systematic errors from sensor axis misalignment and drifting gains [54, 49, 50, 233, 234, 225].

In particular, negatively charged nitrogen-vacancy (NV^-) centers in single-crystal diamond provide high-sensitivity broadband magnetic sensing and imaging under ambient or extreme physical conditions [3]. As described in Chapter 1, the NV^- center's electronic ground state has spin $S = 1$ with the lower-energy $m_s = 0$ level separated from the $m_s = \pm 1$ levels by a zero-field splitting $D \approx 2.87\,\mathrm{GHz}$ (see Figure 4.1.1a). NV^- centers have symmetry axes aligned along one of four crystallographic orientations set by the diamond lattice's tetrahedral symmetry (see Figures 4.1.1b and 4.1.1c). A bias magnetic field $\vec{B}_0$, the $m_s = \pm 1$ Zeeman-shifts the NV^- spin energy levels by $\approx \pm\hbar\gamma_e \vec{B}_0 \cdot \hat{n}$ for fields $\gamma_e B_0 \ll 2\pi D$, where $\gamma_e = g_e \mu_B/\hbar = 2\pi \times 28.03\,\mathrm{GHz/T}$ is the NV^- electron gyromagnetic ratio and $\hat{n}$ is the NV^- symmetry axis. Optical preparation and readout of the NV^- spin state is mediated by an intersystem crossing through a set of singlet states with preferential decay to the $|m_s = 0\rangle$ state, which results in higher photoluminescence (PL) from the $|m_s = 0\rangle$ than from the $|m_s = \pm 1\rangle$ states [18, 19]. By measuring the optically detected magnetic resonance (ODMR)

features of an *ensemble* of NV^- centers, with NV^- symmetry axes distributed along all four crystallographic orientations (Figure 4.1.1d), the three Cartesian components of a vector magnetic field signal can be sensed using a monolithic diamond crystal [49]. Furthermore, the fixed crystallographic axes inherent to this solid-state system enable vector sensing free from heading errors.

To date, ensemble NV^- vector magnetometers measure the three Cartesian magnetic field components either by sweeping a microwave (MW) tone across the full ODMR spectrum [54, 48, 235] or by interrogating multiple ODMR features, either individually [3, 49, 50, 236, 237, 238] or in parallel [239, 240, 241], with near-resonant MWs. Although at least three ODMR features must be interrogated to determine the magnetic field vector, four or more are often probed to mitigate systematic errors from strain, electric fields, or temperature variation [169, 56, 91, 8]. Regardless of implementation, these existing methods all reconstruct the three Cartesian magnetic field components from a series of field projection measurements along at least three predetermined axes (see Section 1.4.2).

In existing implementations, the projective field measurements are performed sequentially, and such magnetometers have so far only demonstrated sensing of static or slowly varying fields [54, 48, 49, 242, 50, 240, 241]. A sequential vector magnetometer inherently exhibits suboptimal sensitivity, however, as the sensor is temporarily blind to magnetic field components *transverse* to the chosen axis during each projective measurement. In addition, any dead time associated with the vector field measurement, including time spent switching the MW frequency or driving far off resonance, reduces the measurement speed and bandwidth as well as the achievable sensitivity of a shot-noise-limited device.

To overcome these drawbacks, we demonstrate simultaneous measurement of all Cartesian components of a dynamic magnetic field components using parallel addressing and readout from all four NV^- orientations in a single-crystal diamond. We implement this technique using multi-channel lock-in detection to extract the four magnetic-field-dependent spin-resonance shifts from the optical signal measured on a single detector. By performing four projective field measurements simultaneously,

our technique enables high-sensitivity, broadband vector magnetometry without the inefficiency inherent to sequential projective measurement techniques. This method can decrease the time required to reconstruct a magnetic field vector with a given signal-to-noise ratio (SNR) by at least $4\times$ compared to optimized sequential addressing of the NV$^-$ orientations, resulting in at least $\sqrt{4} = 2\times$ higher sensitivity for shot-noise-limited magnetometers.

The present device operates from near dc (5 Hz) up to a 12.5-kHz measurement bandwidth and simultaneously achieves ~ 50 pT/$\sqrt{\text{Hz}}$ magnetic-field sensitivity for each Cartesian component, which is, to date, the highest demonstrated sensitivity of a full vector magnetometer employing solid-state spins. In this chapter we introduce the simultaneous vector magnetometry method, we describe the implementation of the magnetometer, and we discuss sensor calibration and signal processing. We then show a vector sensing demonstration, wherein we reconstruct all three Cartesian components of an applied dynamic vector magnetic field with high sensitivity and bandwidth. Finally, we discuss extensions of this technique to pulsed-type sensing protocols and parallel wide-field magnetic imaging.

4.2 Simultaneous vector magnetometry method

In many high-sensitivity measurements, technical noise such as $1/f$ noise is mitigated by moving the sensing bandwidth away from DC via up-modulation. One method, common in NV-diamond magnetometry experiments, applies frequency [26, 24, 244, 241] or phase modulation [49, 245, 33, 81] to the MWs addressing a spin transition, which causes the magnetic field information to be encoded in a band around the modulation frequency. Here we demonstrate a multiplexed [246, 247, 248, 249] extension of this scheme, where information from multiple NV$^-$ orientations is encoded in separate frequency bands and measured on a single optical detector. Lock-in demodulation and filtering then extracts the signal associated with each NV$^-$ orientation, enabling concurrent measurement of all components of a dynamic magnetic field.

In this technique, four dedicated MW tones, each dithered at a unique modula-

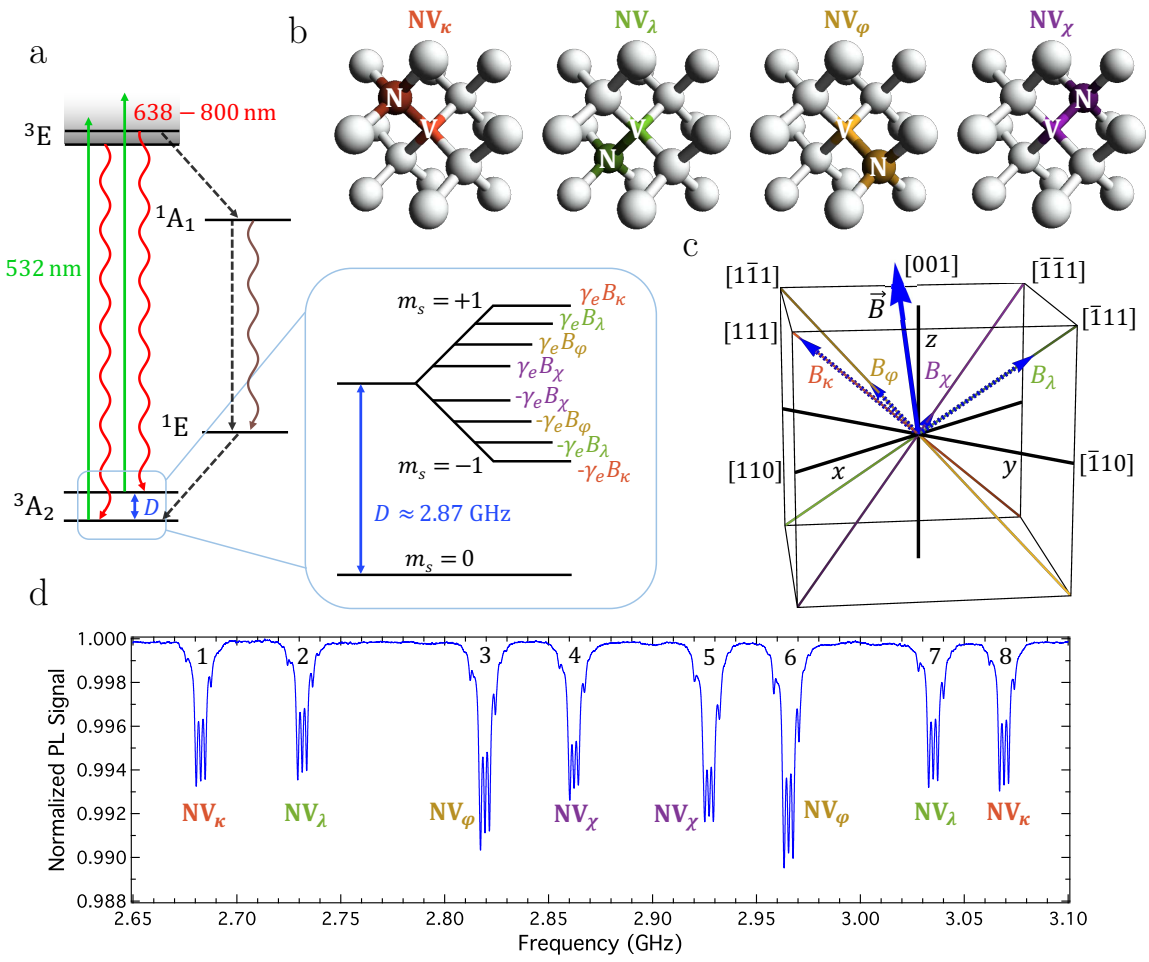

Figure 4.1.1: NV$^-$ ensembles for vector field sensing. a) Energy level diagram for the nitrogen-vacancy (NV) center in diamond, with zero-field splitting D between the ground-state electronic spin levels $m_s = 0$ and $m_s = \pm 1$. Expanded view shows Zeeman shifts of the $m_s = \pm 1$ energy levels in the presence of a magnetic field $\vec{B}$ for different projections along the NV$^-$ symmetry axis. b) Four crystallographic orientations of the NV$^-$ center in diamond. For an ensemble of NV$^-$ centers within a single crystal diamond, the NV$^-$ symmetry axes are equally distributed along the four orientations. c) NV$^-$ symmetry axes and lab-frame directions ($\hat{x}$, $\hat{y}$, $\hat{z}$), defined in terms of diamond lattice vectors. A magnetic field $\vec{B}$ projects onto the four NV$^-$ orientations, causing the Zeeman shifts shown in (a). Shifts associated with off-axis magnetic fields are ignored for simplicity. d) Optically detected magnetic resonance (ODMR) spectrum displaying photoluminescence (PL) signal from an ensemble of NV$^-$ centers in a bias magnetic field $\vec{B} = \vec{B}_0 = (3.54, 1.73, 6.95)$ mT, $|\vec{B}_0| = 7.99$ mT. Resonance features numbered 1 - 4 (5 - 8) correspond to $|m_s = 0\rangle \rightarrow |m_s = -1\rangle$ ($|m_s = 0\rangle \rightarrow |m_s = +1\rangle$) spin transitions, and subfeatures arise from NV$^-$ hyperfine structure [169, 243, 7] (see Figure D.1.1).

tion frequency, address a subset of four of the eight ODMR features shown in Figure 4.1.1d. The implementation here uses modulated continuous-wave (CW) ODMR, where the MWs are frequency modulated and the PL from all NV$^-$ orientations is detected continuously on a single optical detector. Multi-channel demodulation and filtering in software reveal the ODMR line center shifts in response to a change in the magnetic field vector. The Cartesian components of the dynamic magnetic field are reconstructed in real time utilizing an approximated linear transformation derived from the NV$^-$ ground state spin Hamiltonian (see Section 4.5.2). This simultaneous magnetometry method generalizes to addressing any number of ODMR features.

4.3 Sensitivity and bandwidth in vector magnetometry

4.3.1 Sensitivity definition

The sensitivity of a vector projection magnetometer (see Section 1.4.2) is defined as

$$\eta \equiv \delta B \sqrt{T}, \tag{4.1}$$

where T is the duration of a magnetic field measurement and δB is the "minimum detectable" field projection along the magnetometer sensing axis, that is, the field projection giving a signal-to-noise ratio (SNR) of 1 [3, 114, 250, 108]. (Note that in practice an SNR several times greater than 1 is required to distinguish a signal from the noise.) The magnetic field sensitivity of a particular magnetic sensor device is calculated from a measurement of magnetometer noise and the magnetometer's equivalent noise bandwidth as follows (see also the SI Appendix of Ref. [24]).

A magnetic field measurement of duration T (with sampling rate $F_s = 1/T$) has a Nyquist-limited single-sided bandwidth $\Delta f = F_s/2 = 1/(2T)$. When the measurement bandwidth is sampling-rate limited, (and when the noise is white, as is approximately true for photon shot noise), then the noise level of the magnetometer, denoted

σ_B, is given by the standard deviation of a series of such measurements. Therefore, the minimum detectable field δB (SNR = 1) is equal to σ_B, and the magnetic field sensitivity is given by

$$\eta = \sigma_B \sqrt{T} = \frac{\sigma_B}{\sqrt{2\Delta f}}. \tag{4.2}$$

However, if the data are filtered to a reduced equivalent noise bandwidth $f_{\mathrm{ENBW}} < \Delta f$, the sensitivity should remain unchanged, as sensitivity is a bandwidth-normalized quantity. In this case, the measured standard deviation is reduced to $\sigma'_B = \sigma_B \sqrt{f_{\mathrm{ENBW}}/\Delta f}$, and the magnetic field sensitivity is

$$\eta = \frac{\sigma'_B}{\sqrt{2 f_{\mathrm{ENBW}}}}. \tag{4.3}$$

Thus, the factor of $\sqrt{2}$ appearing in Equation 4.3 arises from the definition of magnetometer sensitivity (Equation 4.1).

4.3.2 Bandwidth and signal-to-noise ratio

For a nitrogen-vacancy (NV) ensemble-based magnetometer that interrogates NV$^-$ orientations sequentially, a measurement of the full vector magnetic field exhibits a reduced maximum bandwidth relative to a measurement of a single magnetic field component on the same device. The bandwidth difference arises because the full magnetic field vector must be deduced from multiple measurements interrogating different NV$^-$ orientations. If a measurement using a single NV$^-$ orientation requires time T, a sequential measurement utilizing all four NV$^-$ orientations will require time $4T$ to sense the full vector magnetic field. Thus, the maximum bandwidth of a full vector magnetic field measurement utilizing all four NV$^-$ orientations is $4\times$ lower than for a magnetic field measurement utilizing a single NV$^-$ orientation.

In contrast, for a simultaneous vector magnetometry measurement, each NV$^-$ orientation is interrogated for the full measurement time. Because the measurement signal-to-noise ratio (SNR) scales as $\sqrt{T}$ for statistically uncorrelated noise, a magnetometry simultaneous technique achieves $2\times$ the SNR of the sequential measurement

for each NV$^-$ orientation. In practice, the relative SNR enhancement may be higher than 2×, as a sequential measurement using a single microwave (MW) generator may suffer from dead time when the MW carrier frequency is switched between the optically detected magnetic resonance (ODMR) features from different NV$^-$ orientations.

4.3.3 Anisotropic vector sensitivity

For a vector magnetometer that measures field projections along multiple fixed axes in space, the response to a magnetic field's magnitude may vary with the field's direction. As a result, the device sensitivity may be anisotropic, in that higher-precision estimation of a magnetic field's magnitude may be possible when the field is oriented along certain directions relative to other directions. Consider for example a two-dimensional vector projection magnetometer with sensing axes oriented along $\hat{n}_1 = \hat{x}$ and $\hat{n}_2 = \hat{y}$. A field $\vec{B}_{\text{sens}}$ will produce a different net signal on the vector magnetometer depending on the field's angular orientation. If $\vec{B}_{\text{sens}}$ projects equally on $\hat{x}$ and $\hat{y}$, e.g., $\vec{B}_{\text{sens}} = (B_{\text{sens}}/\sqrt{2})\hat{x} + (B_{\text{sens}}/\sqrt{2})\hat{y}$, then the total detected signal S_{net} is given by

$$\begin{aligned} S_{\text{net}} &= |S_1| + |S_2| \\ &\propto |\vec{B}_{\text{sens}} \cdot \hat{x}| + |\vec{B}_{\text{sens}} \cdot \hat{y}| \\ &\propto B_{\text{sens}}/\sqrt{2} + B_{\text{sens}}/\sqrt{2} \\ &\propto B_{\text{sens}}\sqrt{2}, \end{aligned} \tag{4.4}$$

whereas if $\vec{B}_{\text{sens}}$ is oriented along $\hat{x}$, then the total detected signal is instead only $S_{\text{net}} \propto B_{\text{sens}}$.

For an NV-diamond-based four-axis vector magnetometer operating in the low-field regime (where the approximation that the ODMR line shifts are proportional to the on-axis magnetic field projections is valid), the net signal is

$$S_{\text{net}} \propto |\vec{B}_{\text{sens}} \cdot \hat{n}_\lambda| + |\vec{B}_{\text{sens}} \cdot \hat{n}_\chi| + |\vec{B}_{\text{sens}} \cdot \hat{n}_\varphi| + |\vec{B}_{\text{sens}} \cdot \hat{n}_\kappa|. \tag{4.5}$$

Figures 4.3.1a and 4.3.1b show the expected net signal on a four-axis NV$^-$ vector projection magnetometer from a unit-magnitude magnetic field as a function of field direction. In this simplified case, magnetic fields oriented along the crystal lattice vectors [100], [010], and [001], produce the largest net signal of any field orientation. We note that fields with these orientations project equally on all four NV$^-$ symmetry axes. In contrast, the net signal is minimized for fields oriented along the crystal lattice vectors [110] and [$\bar{1}$10].

For an NV-diamond-based four-axis vector magnetometer operating in the general regime (where magnetic field projections both parallel and transverse to the NV$^-$ symmetry axes may cause ODMR line shifts), the net signal for small $\vec{B}_{\text{sens}}$ is

$$S_{\text{net}} \propto |\mathbf{A}_1 \cdot \vec{B}_{\text{sens}}| + |\mathbf{A}_2 \cdot \vec{B}_{\text{sens}}| + |\mathbf{A}_3 \cdot \vec{B}_{\text{sens}}| + |\mathbf{A}_4 \cdot \vec{B}_{\text{sens}}|, \tag{4.6}$$

where $\mathbf{A}_i$ is the i^{th} row of the linearized matrix $\mathbf{A}$. Equation 4.6 can be used to determine the angular dependence of the net signal from a fixed-magnitude magnetic field on the present device in the bias field $\vec{B}_0 = (3.54, 1.73, 6.95)\,\text{mT}$, as depicted in Figure 4.3.1c. As shown in Figure 4.3.1d, the more generalized treatment (Equation 4.6) introduces a non-negligible shift in the anisotropy compared to that predicted by the simple projection-based treatment (Equation 4.5).

4.4 Technique implementation

Figure 4.4.1 depicts the experimental setup, including laser excitation, MW generation, and magnetic field detection. The diamond crystal is a $4\,\text{mm} \times 4\,\text{mm} \times 0.5\,\text{mm}$ chip with $\langle 110 \rangle$ edges and a $\{100\}$ front facet, grown by Element Six Ltd. The diamond contains a bulk density of grown-in nitrogen $[^{14}\text{N}] \approx 4.9 \times 10^{18}\,\text{cm}^{-3}$ and an estimated N-to-NV$^-$ conversion efficiency of $\sim 10\%$ after irradiation and annealing.

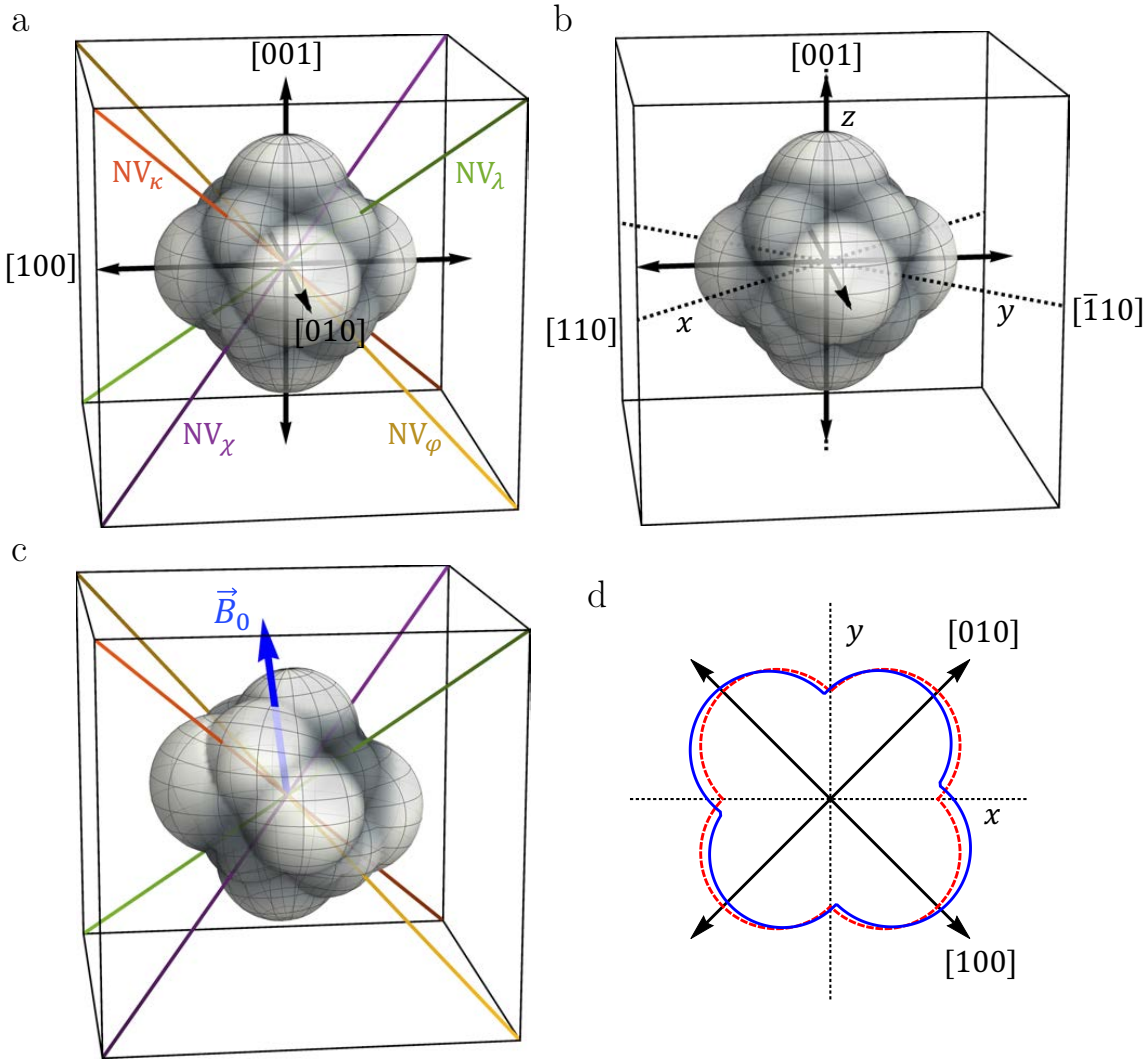

Figure 4.3.1: Anisotropy of four-axis vector magnetometer response. a) Net signal on a four-axis projection-based NV-diamond magnetometer versus direction for a fixed-magnitude magnetic field $\vec{B}_{\text{sens}}$. The response is largest for magnetic fields oriented parallel or antiparallel to the diamond crystal lattice vectors ([100], [010], [001]). b) Same as (a) but with lab-frame x-, y-, and z-axes. Net signal is minimized for magnetic fields along $\hat{x}$ and $\hat{y}$ ([110] and [$\bar{1}$10]). c) Net signal on the present NV-diamond vector magnetometer in the bias field $\vec{B}_0 = (3.54, 1.73, 6.95)\,\text{mT}$, including contributions from field components both parallel and transverse to the NV$^-$ symmetry axes. A slight shift of the signal anisotropy compared to a is apparent. d) Slices of the surface plots in (a) and (c) for $z = 0$. Red dashed (- -) and blue solid (—) curves respectively mark the net signal from the simplified projection-based magnetometer, and from the present magnetometer.

4.4.1 Diamond mounting

The diamond is adhered to a 2" diameter, 330 µm thick wafer of semi-insulating 6H silicon carbide (SiC) from PAM-XIAMAN to provide both thermal and mechanical stability to the diamond crystal (see Figure 4.4.1a). The SiC wafer is in turn affixed to a 0.04" thick tungsten sheet for additional mechanical stability, which is attached to an aluminum breadboard. The breadboard is mounted vertically so that the SiC and diamond surface ({100} facet) make a 90° angle with the optical table. A 1.5" hole cut in the center of the tungsten sheet and a 2" aperture in the center of the breadboard enable the SiC and diamond to be accessed from both sides. The axis normal to the diamond surface, aligned with the [001] crystal lattice vector, is defined to be the lab-frame z-axis; the vertical axis normal to the optical table and along crystal lattice vector $[\bar{1}10]$ is the lab-frame y-axis, and the horizontal axis perpendicular to both the z- and y-axes, along [110], is the x-axis (see Figure 4.1.1c).

4.4.2 Optical setup

The excitation laser source is a 532 nm Verdi V-5 outputting 4.3 W during typical operating conditions. The laser output passes through a Glan-Thompson polarizer, a half waveplate, and an $f = 400$ mm focusing lens. A silver mirror (Thorlabs PF10-03-P01) then directs the beam through a beam sampler (Thorlabs BSF10-A), after which 3.3 W impinges on the {100} diamond surface at an oblique angle $\approx 73°$ to the normal with a 400 µm Gaussian $1/e^2$ width. Reflections and scattered excitation light are reflected back toward the diamond using an aluminized mylar sheet opposite the excitation light entry side. The PL from the diamond is collected by an aspheric, aplanatic condenser (Olympus 204431), is long-pass filtered at 633 nm (Semrock LP02-633RU-25), and ~ 52 mW is imaged onto a silicon photodiode (Thorlabs FDS1010), termed the *signal photodiode*. Given the photodiode's 0.46 A/W responsivity at $\sim$ 700 nm, the $\sim$ 52 mW PL generates a 24.1 mA photocurrent. This photodiode is reversed biased at 25 volts with a voltage regulator (Texas Instruments TPS7A49) followed by two capacitance multipliers in series [128]. The photocurrent is terminated

into $R_{\text{sig}} = 300\,\Omega$. Before the diamond, the beam sampler picks off and directs $\sim$ 135 mW of the excitation light through a beam diffuser and onto a second identical photodiode, termed the *reference photodiode* (see Figure 4.4.1b). This photodiode is powered from the same voltage source as the signal photodiode, and its photocurrent (30.1 mA, given the 0.24 A/W photodiode responsivity at 532 nm) is terminated into $R_{\text{ref}} = 270\,\Omega$.

Each photodiode voltage signal is simultaneously digitized by three analog-to-digital converters (ADCs), two of which are AC-coupled channels of an NI PXI-4462 digitizer. The signals from the AC-coupled channels are averaged in software to reduce digitization noise. Each photodiode voltage signal is also digitized by third ADC, which is a DC-coupled channel of an NI PXI-4461 digitizer. The signals from the DC-coupled channels are used to implement laser noise cancellation, which is discussed in the following section. For the vector sensing demonstration described in Sections 4.4.5-4.6.5, all channels operate at sampling rate $F_s = 202.8$ kSa/s.

4.4.3 Laser noise cancellation

Laser intensity noise is canceled by scaling and subtracting the green reference signal from the diamond PL signal. The digitized AC voltage from the reference photodiode, sampled over a 1-second-long interval, is scaled and subtracted from the AC voltage from the signal photodiode. The scaling factor for each interval is the ratio of the signal photodiode's mean DC value to the reference photodiode's mean DC value from that interval. This cancellation reduces the experimental noise in the 2-6 kHz frequency band by $\sim 30\times$, achieving a noise level (in the absence of MW noise) that is $\sim 1.5\times$ above the expected level due to shot noise from both the signal and reference photocurrents (see Section 4.6.4). Under operating conditions with all modulated MWs in use, the experimental noise floor is 2.5 - 3$\times$ above this same expected shot-noise level. See Section 4.6.5 for noise analysis.

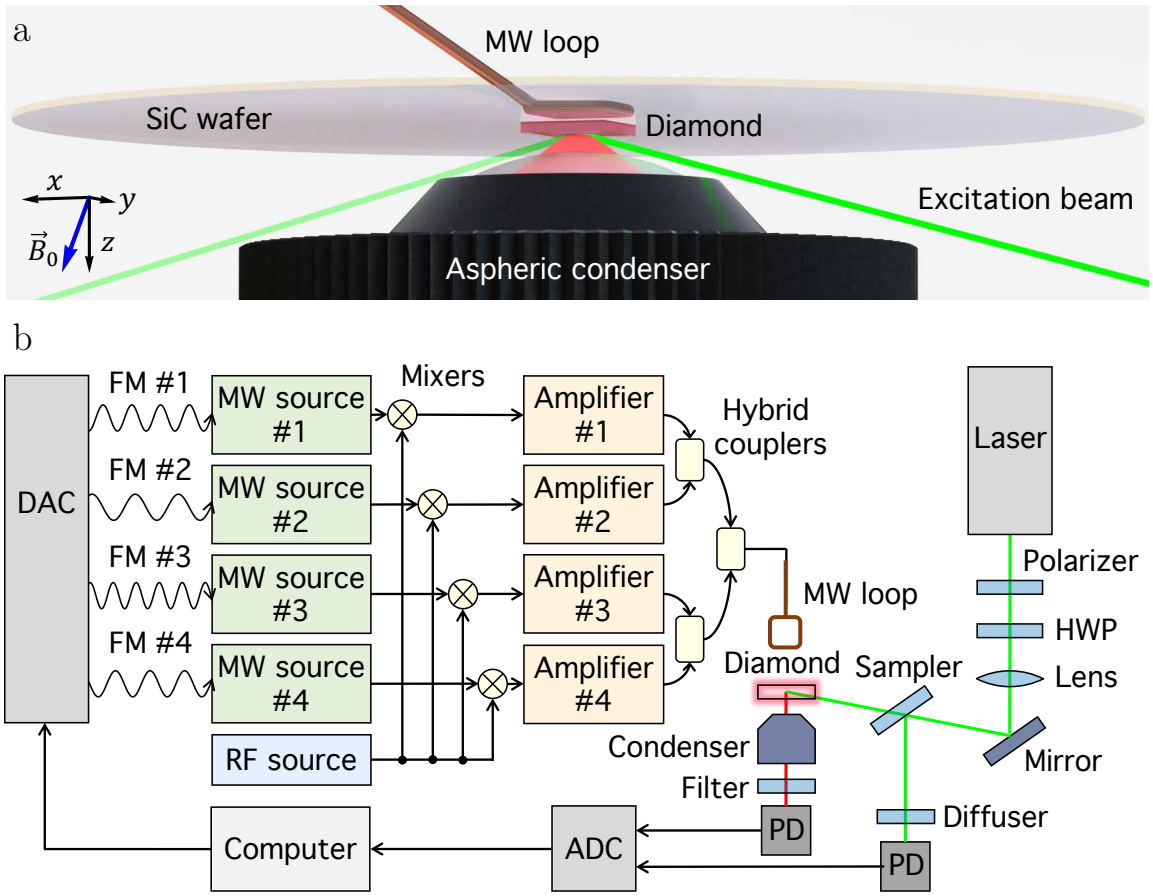

Figure 4.4.1: Experimental setup for simultaneous vector magnetometer. a) Laser and microwave (MW) excitation of NV^- centers in diamond sensor crystal and photoluminescence (PL) collection scheme. Diamond is affixed to one side of silicon carbide (SiC) wafer for stabilization and heat sinking. MW loop on reverse side of SiC provides modulated MW drive to NV^- ensemble. Excitation light at 532 nm enters diamond at $\approx 73^\circ$ to the normal and PL is collected by aspheric aplanatic condenser shown below diamond. From this perspective, the y-axis points primarily into the page. b) Schematic of setup. Digital-to-analog converter (DAC) outputs MW frequency modulation (FM) waveforms. MWs are generated by four sources and mixed with radiofrequency (RF) signal at 2.158 MHz to produce modulated carriers plus sidebands, which are amplified, combined, and radiated by the MW loop. Separate MW amplifiers are used to avoid intermodulation (see Section 4.7.2). Excitation laser beam passes through polarizer, half waveplate (HWP), and focusing lens. After a mirror, the beam passes through a beam sampler, where a fraction is imaged onto a photodiode and digitized at the analog-to-digital converter (ADC); and the rest of the beam impinges on the diamond. The diamond PL is collected by the aspheric condenser, long-pass filtered at 633 nm, imaged onto a photodiode, and digitized. See Figure 4.4.2 for a detailed electronics schematic.

4.4.4 Microwave signals and delivery

Figures 4.4.1b and 4.4.2 show schematic diagrams of the experimental setup. Four carrier signals at frequencies $\nu_\lambda, \nu_\chi, \nu_\varphi$, and ν_κ are generated by Agilent E8257D, E4421B, E4421B, and E4422B MW synthesizers. The MW signals are resonant with the ODMR features respectively numbered 2, 4, 6, and 8 in Figure 4.1.1d. These MW tones are sinusoidally frequency modulated at corresponding modulation frequencies $f_\lambda, f_\chi, f_\varphi$, and f_κ and frequency deviations $\delta\nu_\lambda, \delta\nu_\chi, \delta\nu_\varphi$, and $\delta\nu_\kappa$, all of which are tabulated in Table 4.4.1 and described further in Section 4.5.3. The modulation signals are generated from the two analog outputs of each of two National Instruments (NI) PXI 4461 cards within an NI PXIe-1062Q chassis. The chassis also contains another NI PXI-4461 card used to trigger MW sweeps on the Agilent E8275D and for digitizing the detected optical signals, and an NI PXI-4462 card also for digitizing optical signals. All cards within the chassis and all MW and RF sources are synchronized to the Agilent E8257D's 10 MHz clock using a distribution amplifier (Stanford Research Systems FS735).

Along with the MW carrier signals, MW sidebands - which are generated by mixing an RF source at 2.158 MHz with the MW carrier frequencies - address the NV^- hyperfine subfeatures [24]. The RF source is an Agilent E4430B synthesizer. A power divider (TRM DL402) splits the 2.158 MHz signal four ways. Each of the split signals passes through a Mini-Circuits SLP-19+ low-pass filter and then is mixed with one of the four modulated carrier MW signals using a Relcom double-balanced mixer, either M1J or M1K. Before the mixer, each carrier signal passes through a Teledyne 2-4.5 GHz isolator and a 10 dB directional coupler. The coupled portion of the carrier signal passes through a 3 dB attenuator and is then combined (Mini-Circuits ZX10-2-42-S+) with the sideband frequencies after the mixer to generate a MW signal resonant with all three hyperfine-split spin resonances for a given ODMR feature [169, 24].

The four sets of modulated MWs are amplified using four separate Mini-Circuits ZHL-16W-43-S+ amplifiers to avoid intermodulation (see Section 4.7.2). The ampli-

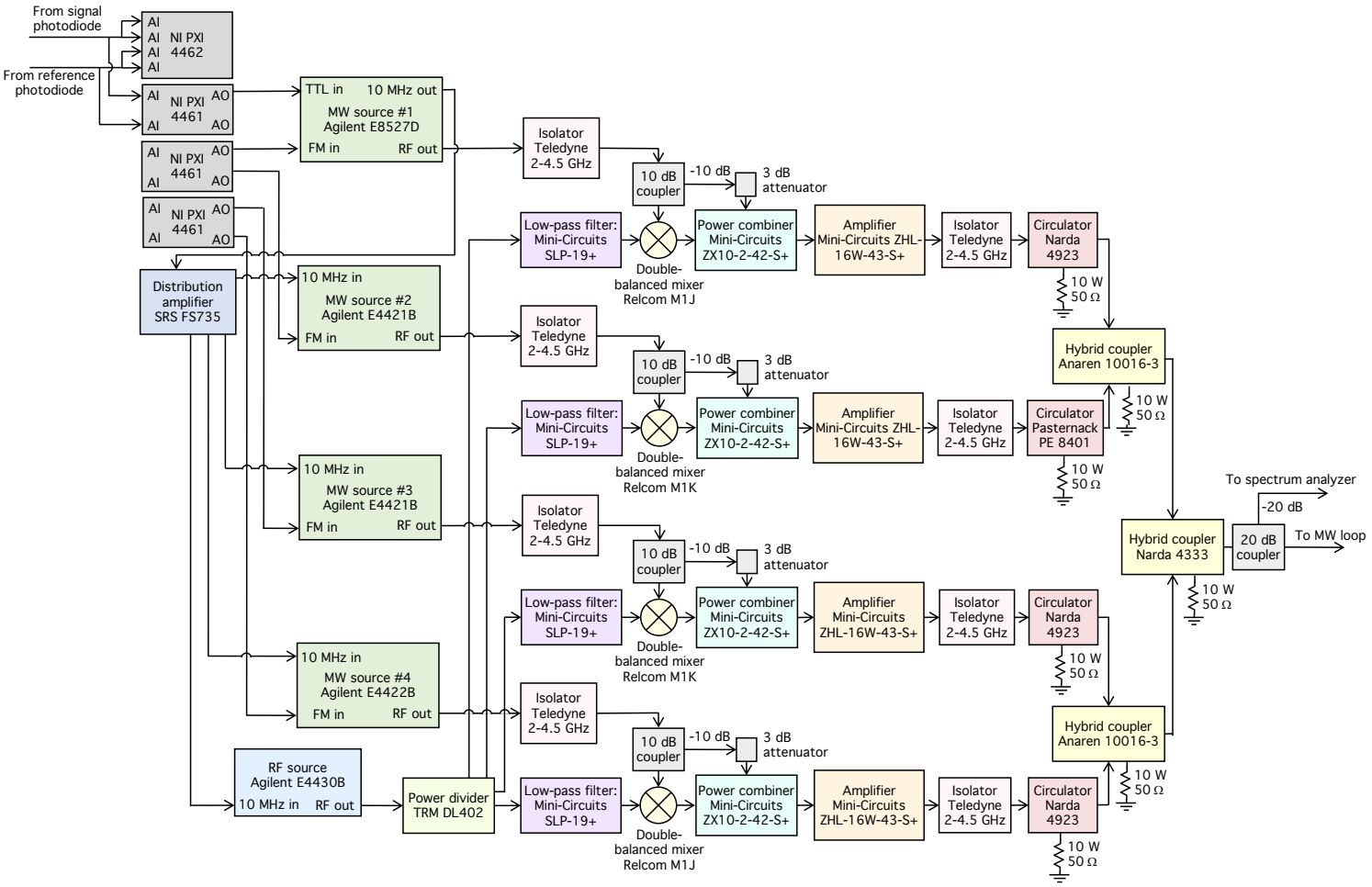

Figure 4.4.2: Electronic equipment used to generate MW tones to drive four NV$^-$ orientations in the simultaneous vector magnetometer. Analog inputs and outputs are abbreviated AI and AO.

NV$^-$ axis	$\hat{n}_\lambda \parallel [\bar{1}11]$	$\hat{n}_\chi \parallel [\bar{1}\bar{1}1]$	$\hat{n}_\varphi \parallel [1\bar{1}1]$	$\hat{n}_\kappa \parallel [111]$
MW source	1	2	3	4
Carrier freq.	$\nu_\lambda = 2.731\,\text{GHz}$	$\nu_\chi = 2.862\,\text{GHz}$	$\nu_\varphi = 2.966\,\text{GHz}$	$\nu_\kappa = 3.069\,\text{GHz}$
Transition	$\|0\rangle \leftrightarrow \|-1\rangle$	$\|0\rangle \leftrightarrow \|-1\rangle$	$\|0\rangle \leftrightarrow \|+1\rangle$	$\|0\rangle \leftrightarrow \|+1\rangle$
Mod. freq.	$f_\lambda = 4056\,\text{Hz}$	$f_\chi = 2704\,\text{Hz}$	$f_\varphi = 5070\,\text{Hz}$	$f_\kappa = 3380\,\text{Hz}$
Deviation	$\delta\nu_\lambda = 832\,\text{kHz}$	$\delta\nu_\chi = 828\,\text{kHz}$	$\delta\nu_\varphi = 775\,\text{kHz}$	$\delta\nu_\kappa = 1178\,\text{kHz}$
Lock-in signal slope	$dS_\lambda/d\Delta\nu_\lambda =$ $39.5\,\mu\text{V/kHz}$	$dS_\chi/d\Delta\nu_\chi =$ $42.0\,\mu\text{V/kHz}$	$dS_\varphi/d\Delta\nu_\varphi =$ $53.4\,\mu\text{V/kHz}$	$dS_\kappa/d\Delta\nu_\kappa =$ $41.6\,\mu\text{V/kHz}$

Table 4.4.1: Parameters detailing the four-axis simultaneous vector magnetometry implementation, as discussed in the text.

fier outputs pass through Teledyne 2-4.5 GHz isolators and then circulators (either Pasternack PE 8401 or Narda 4923, each terminated with a 10 W 50 Ω terminator), before being combined with each other using three hybrid couplers (two Anaren 10016-3 and one Narda 4333, each terminated with a 10 W 50 Ω terminator). The combined MWs pass through a 20 dB directional coupler, which picks off a portion of the signal for monitoring on a spectrum analyzer, and the rest is sent to a copper wire loop placed in close proximity to the diamond to drive the NV$^-$ spin resonances. The loop, which is depicted in Figure 4.4.1a, is made from a shorted end of semi-rigid nonmagnetic coaxial cable. The loop orientation is chosen for delivery of MWs polarized approximately along the lab-frame $\hat{z}$ so that the four NV$^-$ orientations are addressed roughly equally.

4.4.5 Bias magnetic field

The NV-diamond sensor is placed in a bias magnetic field $|\vec{B}_0| = 7.99\,\text{mT}$, $\vec{B}_0 = (3.54, 1.73, 6.95)\,\text{mT}$, where the lab-frame coordinates (x, y, z) are defined with respect to the normal faces of the mounted diamond crystal, with unit vectors $\hat{x}$, $\hat{y}$, and $\hat{z}$ lying along [110], [$\bar{1}$10], and [001], respectively, as depicted in Figure 4.1.1c. In this coordinate system, the unit vectors parallel to the NV$^-$ symmetry axes are $\hat{n}_\kappa = \left(\sqrt{2/3}, 0, \sqrt{1/3}\right) \parallel [111]$, $\hat{n}_\lambda = \left(0, -\sqrt{2/3}, -\sqrt{1/3}\right) \parallel [\bar{1}11]$, $\hat{n}_\varphi = \left(0, \sqrt{2/3}, -\sqrt{1/3}\right) \parallel [1\bar{1}1]$,

and $\hat{n}_\chi = \left(-\sqrt{2/3}, 0, \sqrt{1/3}\right) \parallel [\bar{1}\bar{1}1]$. The bias field $\vec{B}_0$ is applied via a pair of 50 mm diameter, 30 mm thick N52 NdFeB neodymium magnets (Sunkee).

4.5 Sensor calibration

4.5.1 Bias field parameter determination

Magnetometer calibration requires determination of the bias magnetic field $\vec{B}_0$, the zero-field splitting D, and strain/electric field coupling parameters $\vec{\mathcal{M}}_z$. This calibration procedure is separate from high-sensitivity measurements of small vector magnetic fields $\vec{B}_{\text{sens}}(t)$. The bias magnetic field is determined using the NV-diamond magnetometer in a measurement consistent with a Hall probe measurement of $|\vec{B}_0| = 8.4\,\text{mT}$. (The latter measurement is limited by the Hall probe's precision and $\sim$ cm standoff distance from the diamond.)

By numerically fitting the NV$^-$ ground-state Hamiltonian to the eight measured resonance line centers, the bias field $\vec{B}_0$ is determined, along with the value of D and the longitudinal strain/electric field coupling parameters $\vec{\mathcal{M}}_z \equiv [\mathcal{M}_z^\lambda, \mathcal{M}_z^\chi, \mathcal{M}_z^\varphi, \mathcal{M}_z^\varphi]$. From the fit, we obtain $D = 2.8692\,\text{GHz}$, $\vec{\mathcal{M}}_z = [-20, -60,\ 50,\ 30]\,\text{kHz}$, and $\vec{B}_0$ as reported above.

The NV-diamond magnetometer measures the bias field parameters by sweeping a single MW tone from 2.65 to 3.10 GHz, and monitoring the PL from the diamond; this yields an ODMR spectrum as shown in Figure 4.1.1d. Using a least-squares fit, we determine the line center of the middle hyperfine subfeature of each of the eight m_s spin transitions. Averaging 10^3 sweeps yields the following set of line centers, which are used to fit for the static field parameters $\vec{B} = \vec{B}_0$, D, and $\vec{\mathcal{M}}_z \equiv [\mathcal{M}_z^\lambda, \mathcal{M}_z^\chi, \mathcal{M}_z^\varphi, \mathcal{M}_z^\varphi]$:

$$\vec{\nu}_{\mathrm{ODMR}} = \begin{bmatrix} \nu_{\kappa^-} \\ \nu_{\lambda^-} \\ \nu_{\varphi^-} \\ \nu_{\chi^-} \\ \nu_{\chi^+} \\ \nu_{\varphi^+} \\ \nu_{\lambda^+} \\ \nu_{\kappa^+} \end{bmatrix} = \begin{bmatrix} 2.6825 \\ 2.7314 \\ 2.8193 \\ 2.8622 \\ 2.9272 \\ 2.9655 \\ 3.0351 \\ 3.0692 \end{bmatrix} \text{GHz.} \tag{4.7}$$

A nonlinear least-squares (Levenberg-Marquardt) numerical minimization method is used to fit the differences between eigenvalues of the NV$^-$ ground state spin Hamiltonian

$$\hat{\mathcal{H}}^i = h(D + \mathcal{M}_z^i)(S_z^i)^2 + g_e \mu_B \vec{B} \cdot \vec{S}^i \tag{4.8}$$

to the measured line centers for the four NV$^-$ orientations $i = \lambda, \chi, \varphi, \kappa$, as described in the Supporting Information of Ref. [13]. Here the dimensionless spin-1 operator of the NV$^-$ triplet ground state $\vec{S}^i$ is defined in the NV$^-$ body frame with $\hat{z} \equiv \hat{n}_i$; D is the temperature- and strain-dependent zero-field splitting, defined specifically to be the coupling component $\propto (S_z^i)^2$ that is common to all four NV$^-$ orientations [169]; and $\mathcal{M}_z^i$ is the additional anisotropic coupling, which differs between the four orientations and is attributed to longitudinal strain and electric fields [57, 13, 251]. Coupling of transverse strain and electric fields $\mathcal{M}_x^i$ and $\mathcal{M}_y^i$ to the NV$^-$ spin is suppressed by the on-axis component of the bias field, ($\frac{g_e \mu_B}{h} B_{0,z}^i \gg \mathcal{M}_x^i, \mathcal{M}_y^i$), and is therefore neglected [81, 94]. In contrast, the components of $\vec{B}_0$ transverse to the NV$^-$ symmetry axes, ($B_{0,x}^i$ and $B_{0,y}^i$), contribute non-negligible shifts to the observed ODMR line centers.

Statistical uncertainties in the bias field parameters are estimated to be $\sim 100\,\mathrm{nT}$ for each component of $\vec{B}_0$ and $\sim 2\,\mathrm{kHz}$ for each of the electric/strain field coupling parameters $\vec{\mathcal{M}}_z$ and D. The uncertainties are determined by extracting $\vec{B}_0$, $\vec{\mathcal{M}}_z$, and

D from each of the 10^3 measurements of the ODMR line centers, and then calculating the standard deviation of each extracted parameter. The uncertainties are found to be weakly correlated; for example, Pearson correlation coefficients between bias magnetic field components and strain coupling parameters range in magnitude from 0.01 to 0.15. Accounting for possible systematic offsets such as diamond lattice distortion (see Section 4.7.3 for additional discussion) [156, 252, 253, 254], we estimate systematic errors of $\sim 1\,\mu\text{T}$ in the components of $\vec{B}_0$, $\sim 8\,\text{kHz}$ in D, and $\sim 10\,\text{Hz}$ in the entries of $\vec{\mathcal{M}}_z$. Although higher-precision measurements of $\vec{B}_0$, D, and $\vec{\mathcal{M}}_z$ are possible, the reported uncertainties in these parameters do not limit the present device's sensitivity to small dynamic magnetic fields $\vec{B}_{\text{sens}}$, as described in the following section.

4.5.2 Dynamic vector field measurement protocol

A flowchart in Figure 4.5.1 summarizes the magnetometer calibration and measurement protocol. After determination of $\vec{B}_0$, D, and $\vec{\mathcal{M}}_z \equiv [\mathcal{M}_z^{\lambda}, \mathcal{M}_z^{\chi}, \mathcal{M}_z^{\varphi}, \mathcal{M}_z^{\varphi}]$ from the measured ODMR line centers, a subset of the detected ODMR line centers from Equation 4.7 are selected for MW addressing $\vec{\nu}_{\text{MW}} = \vec{\nu}_{\text{ODMR}}\{2,4,6,8\} = [\nu_{\lambda^-}, \nu_{\chi^-}, \nu_{\varphi^+}, \nu_{\kappa^+}]$. The $+$ and $-$ subscripts are dropped herein. Next, the Hamiltonian from Equation 4.8 is linearized about $\vec{B}_0$, D, and $\vec{\mathcal{M}}_z$ to calibrate the expected frequency shifts of the four addressed NV$^-$ resonance line centers in the presence of an additional small field $\vec{B}_{\text{sens}}$ to be sensed. The result of the numerical linearization is a 4×3 matrix $\mathbf{A}$, where

$$\begin{bmatrix} \Delta\nu_{\lambda} \\ \Delta\nu_{\chi} \\ \Delta\nu_{\varphi} \\ \Delta\nu_{\kappa} \end{bmatrix}_{\text{sens}} = \mathbf{A} \begin{bmatrix} B_x \\ B_y \\ B_z \end{bmatrix}_{\text{sens}} . \tag{4.9}$$

The matrix $\mathbf{A}$ is defined as

$$\mathbf{A} = \begin{bmatrix} \frac{\partial \nu_\lambda}{\partial B_x} & \frac{\partial \nu_\lambda}{\partial B_y} & \frac{\partial \nu_\lambda}{\partial B_z} \\ \frac{\partial \nu_\chi}{\partial B_x} & \frac{\partial \nu_\chi}{\partial B_y} & \frac{\partial \nu_\chi}{\partial B_z} \\ \frac{\partial \nu_\varphi}{\partial B_x} & \frac{\partial \nu_\varphi}{\partial B_y} & \frac{\partial \nu_\varphi}{\partial B_z} \\ \frac{\partial \nu_\kappa}{\partial B_x} & \frac{\partial \nu_\kappa}{\partial B_y} & \frac{\partial \nu_\kappa}{\partial B_z} \end{bmatrix}_{\vec{B}_0, D, \vec{\mathcal{M}}_z}, \tag{4.10}$$

where B_x, B_y, and B_z are the lab-frame components of the total magnetic field. The values of D and $\vec{\mathcal{M}}_z$ are taken here to be constant during measurements, such that changes in the ODMR line centers are entirely attributed to magnetic field variations.

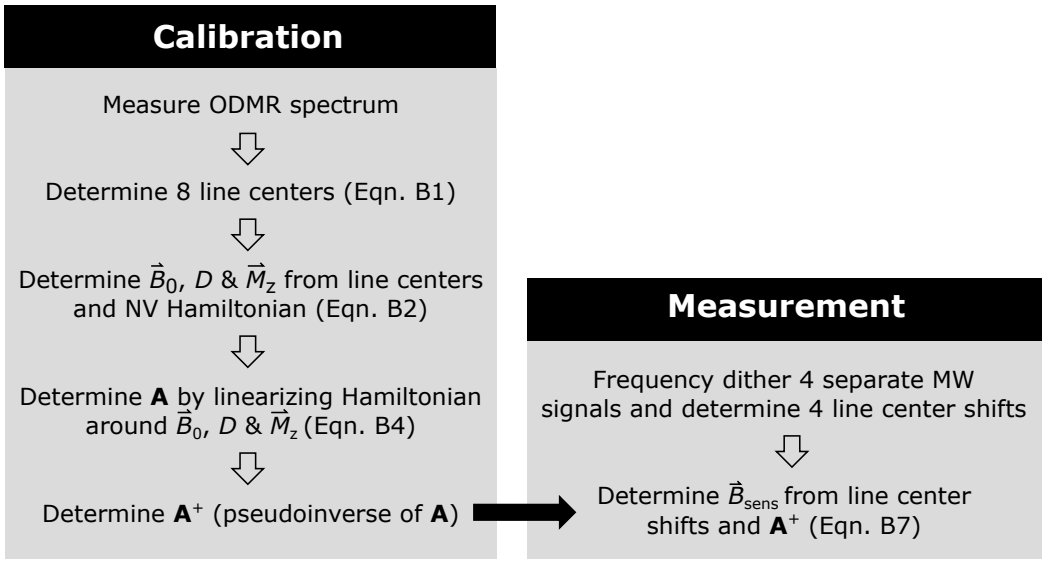

Figure 4.5.1: Magnetometer calibration and measurement protocol flowchart

The assumption of constant $\vec{\mathcal{M}}_z$ is valid in the present device because strain in the diamond is static and electric fields couple only very weakly to the NV^- energy levels at typical values of the bias magnetic field $\vec{B}_0$ [92, 94]. Although temperature drifts couple to D with $dD/dT = -74\,\mathrm{kHz/K}$ [91], these drifts occur on timescales of seconds to hours, and the associated changes in D are therefore outside the 5 Hz to 210 Hz measurement bandwidth of the present device. Furthermore, use of a SiC heat spreader attached to the diamond mitigates laser-induced temperature fluctuations [24]. In a vector magnetometer optimized for sensing lower-frequency magnetic

fields ($\lesssim$ Hz), a changing zero-field splitting D_{sens} could also be determined along with $\vec{B}_{\text{sens}}$ from the four measured ODMR line shifts. To additionally sense any dynamic changes in $\vec{\mathcal{M}}_z$ would require MW addressing of more than four ODMR features. See Section 4.7.3 for additional discussion of the systematic offsets and drifts.

In the simple limiting case where, for each NV$^-$ orientation $i = \lambda, \chi, \varphi, \kappa$, the transverse components of the bias magnetic field are much smaller than the zero-field splitting, ($B_x^i, B_y^i \ll \frac{h}{g\mu_B} D$), and strain coupling is negligible, ($\mathcal{M}_x^i, \mathcal{M}_y^i, \mathcal{M}_z^i \ll \frac{g\mu_B}{h} B_z^i$), the marginal shifts $\Delta\nu_i$, are linearly proportional to the magnetic field projections B_z^i along the respective NV$^-$ symmetry axes. In this linear Zeeman regime, the rows of the matrix $\mathbf{A}$ are given, up to a sign, by the NV$^-$ symmetry axis unit vectors $\hat{n}_i$:

$$\mathbf{A}_{\text{L.Z.}} = \frac{g_e \mu_B}{h} \begin{bmatrix} \hat{n}_\lambda \\ -\hat{n}_\chi \\ -\hat{n}_\varphi \\ \hat{n}_\kappa \end{bmatrix} = \frac{g_e \mu_B}{h} \begin{bmatrix} 0 & -\sqrt{2/3} & -\sqrt{1/3} \\ \sqrt{2/3} & 0 & -\sqrt{1/3} \\ 0 & -\sqrt{2/3} & \sqrt{1/3} \\ \sqrt{2/3} & 0 & \sqrt{1/3} \end{bmatrix}. \tag{4.11}$$

Whether the unit vector is multiplied by $+1$ or -1 depends on the sign of $B_z^i \equiv \vec{B}_0 \cdot \hat{n}_i$ and on whether the addressed transition couples the $|m_s = 0\rangle$ state to the $|m_s = +1\rangle$ or $|m_s = -1\rangle$ state.

Because the bias field $\vec{B}_0$ has non-negligible components transverse to each NV$^-$ symmetry axis, the present experiment does not satisfy the requirement that only magnetic field projections on the NV$^-$ symmetry axes contribute to the measured ODMR frequency shifts, and consequently $\mathbf{A}$ differs from $\mathbf{A}_{\text{L.Z.}}$. We determine $\mathbf{A}$ numerically by evaluating the partial derivatives using a step size of $\delta B_x = \delta B_y =$

$\delta B_z = \frac{h}{g_e \mu_B} \cdot 10\,\text{Hz}$. The matrix $\mathbf{A}$ is calculated to be

$$\mathbf{A} = \frac{g_e \mu_B}{h} \begin{bmatrix} 0.10388 & -0.89383 & -0.46341 \\ 0.90435 & 0.04596 & -0.38836 \\ 0.10524 & -0.69511 & 0.73528 \\ 0.75551 & 0.04984 & 0.66268 \end{bmatrix}. \tag{4.12}$$

The left Moore-Penrose pseudoinverse $\mathbf{A}^+$ is then numerically calculated from $\mathbf{A}$ via

$$\begin{bmatrix} B_x \\ B_y \\ B_z \end{bmatrix}_{\text{sens}} = \mathbf{A}^+ \begin{bmatrix} \Delta\nu_\lambda \\ \Delta\nu_\chi \\ \Delta\nu_\varphi \\ \Delta\nu_\kappa \end{bmatrix}_{\text{sens}} \tag{4.13}$$

at the measured $\vec{B}_0$, D, and $\vec{\mathcal{M}}_z$ using the MATLAB function `pinv`. The matrix is found to be

$$\mathbf{A}^+ = \frac{h}{g_e \mu_B} \begin{bmatrix} 0.08016 & 0.69252 & -0.02239 & 0.48676 \\ -0.71456 & 0.05848 & -0.50880 & 0.09912 \\ -0.39850 & -0.37710 & 0.51861 & 0.43394 \end{bmatrix}. \tag{4.14}$$

and is used to transform detected frequency shifts $\Delta\nu_i(t)$, $i = \lambda, \chi, \varphi, \kappa$ (displayed in Figures 4.6.1c-4.6.1f) into a measured vector field $\vec{B}_{\text{sens}}(t)$, shown in Figure 4.6.3.

The entries of $\mathbf{A}^+$ are robust to small variation in the bias magnetic field and other Hamiltonian parameters. A 10 μT change in any component of the bias magnetic field $\vec{B}_0$ changes no entry of $\mathbf{A}^+$ by more than 1% and some by less than 0.01%. Doubling the strain parameters $\vec{\mathcal{M}}_z$ also affects the entries of $\mathbf{A}^+$ by less (and for most entries much less) than 1%. A 150 kHz change in D (corresponding to a temperature change of 2 K [91]) affects the entries of $\mathbf{A}^+$ by 0.01% or less. Thus, drifts in temperature or in the bias electric, strain, or magnetic fields affect the reconstruction accuracy of

$\vec{B}_{\text{sens}}$ by $<1\%$ and are ignored in the present study.

This linearized matrix method was compared against a numerical least-squares Hamiltonian fit, which is identical to the eight-frequency minimization method for ν_{ODMR} described in Section 4.5.1 except that D and $\vec{M}_z$ are held constant and $\vec{B} = \vec{B}_0 + \vec{B}_{\text{sens}}$ is determined from only the four frequencies ν_{MW}. The methods were compared for a range of simulated fields $\vec{B}_{\text{sens}}$ ranging from 1 nT to 100 µT. The linear transformation using $\mathbf{A}^+$ from Equation 4.14 agreed with the Hamiltonian fit to better than 0.001% for $|\vec{B}_{\text{sens}}| \lesssim 100$ nT and to better than 0.3% for $|\vec{B}_{\text{sens}}| \lesssim 100$ µT. When run on the same desktop computer, the linearized matrix method determines $\vec{B}_{\text{sens}}$ from $\vec{\nu}_{\text{MW}}$ with ~ 20 µs per measurement, whereas the least-squares Hamiltonian fit requires ~ 500 ms per field measurement. This $\sim 25{,}000\times$ speedup enables real-time vector magnetic field reconstruction from sensed frequency shifts in the present device.

4.5.3 Modulation, demodulation, and filtering

The modulation frequencies f_i, $i = \lambda, \chi, \varphi, \kappa$ are selected to balance measurement bandwidth and contrast [26, 24] while ensuring that no frequency is an integer multiple of any other. The latter choice avoids cross-talk from the NV$^-$ centers responding nonlinearly to the modulated MWs at harmonics of f_i. All f_i are chosen to divide evenly into the overall sampling rate $F_s = 202.800$ kSa/s. For the main sensing demonstration performed in this work, these frequencies are chosen for a vector sensing bandwidth ≈ 200 Hz, whereas higher modulation frequencies are employed for a second higher-bandwidth (≈ 12.5 kHz) demonstration (see Section 4.6.6). Deviations $\delta\nu_\lambda$, $\delta\nu_\chi$, $\delta\nu_\varphi$, and $\delta\nu_\kappa$ are empirically optimized for maximal demodulated signal contrast. The optimal $\delta\nu_i$ depends on ODMR linewidth, which varies among the addressed NV$^-$ resonances, as shown in Figure 4.1.1d. The linewidth variations are the result of varying degrees of optical and MW power broadening, which arise from different laser and MW polarization angles with respect to the optical and magnetic transition dipole moments of the four NV$^-$ orientations [255, 256, 251].

Lock-in demodulation is performed in software in the present implementation,

although the technique is also compatible with hardware demodulation. The noise-canceled PL signal is first high-pass filtered at 1690 Hz with a 10th-order Butterworth filter, then separately mixed with sinusoidal waveforms at the four modulation frequencies given in Table 4.4.1. The four demodulated traces are band-pass filtered (5 Hz to 210 Hz 10th-order Butterworth filter), which eliminates cross-talk from the other channels, upmodulated signal at $2f_i$, and environmental noise outside the sensing band. The filtered traces are then downsampled (decimated without averaging) by 75× from 202.8 kSa/s to 2.704 kSa/s. Finally, spurious signals at 49 Hz, 50 Hz, and 60 Hz and remaining cross-talk at 338 Hz not completely eliminated by the band-pass filter are removed with 1-Hz-wide FFT notch-stop filters. The resulting signals each have single-sided equivalent noise bandwidth $f_{\mathrm{ENBW}} = 203$ Hz [257, 258].

4.5.4 Lock-in signal slope measurement

The demodulated lock-in signals S_i for channels $i = \lambda, \chi, \varphi, \kappa$ are converted to ODMR line shifts $\Delta\nu_i$ via measured lock-in signal slopes $dS_i/d\Delta\nu_i$. These slope values are determined by (sequentially) sweeping the modulated MW carrier frequencies by 20 kHz about the operation frequency. The PL voltage signal is measured, demodulated, and filtered; the resulting signal is plotted vs. MW frequency and fit to a linear function, from which the slope is extracted [24, 200, 110]). The slope for each channel in μV/kHz is averaged over ∼ 25 seconds. For the dynamic magnetic field measurements reported in Sections 4.4.5-4.6.5, the measured slopes for the four channels are tabulated in Table 4.4.1.

4.6 Vector sensing demonstration

4.6.1 Applied dynamic magnetic fields

Three orthogonal coils create the time-varying magnetic field $\vec{B}_{\mathrm{sens}}(t)$ to be sensed by the NV-diamond magnetometer. The magnetic field coils are displaced from the diamond along the x-, y-, and z-axes by 28 cm, −26.5 cm, and 28.5 cm respectively. The

coils respectively contain 129, 130, and 142 turns and have diameters of 25 cm, 32 cm, and 25 cm. Sinusoidally varying currents with root-mean-square (RMS) amplitudes of 0.24 mA, 0.13 mA, and 0.28 mA are applied to the respective coils, generating the dynamic vector magnetic field $\vec{B}_{\text{sens}}(t) = (B_x(t), B_y(t), B_z(t))$ at the diamond sensor, where $B_j(t) = \sqrt{2}B_{j,\text{RMS}} \cdot \sin(2\pi f_j \cdot t + \phi_j)$ for $j = x, y, z$. Here $f_x = 67$ Hz, $f_y = 32$ Hz, $f_z = 18$ Hz, and the phases ϕ_x, ϕ_y, ϕ_z are chosen arbitrarily. The applied field amplitudes $B_{x,\text{RMS}} = 8.12$ nT, $B_{y,\text{RMS}} = 9.56$ nT, and $B_{z,\text{RMS}} = 9.86$ nT are calibrated by conventional sequential NV$^-$ magnetometry methods and are consistent with *a priori* calculations from the known coil geometries and applied currents. See Section 4.7.1 for discussion of off-axis field nulling.)

4.6.2 Simultaneous vector magnetometry measurement

Figure 4.6.1b shows the voltage spectral density of the digitized, noise-canceled PL signal from 1 second of data acquisition; Figure 4.6.2 displays semi-log plots of the same data over different frequency ranges. The raw PL signal is high-pass filtered at 1690 Hz and demodulated at the four modulation frequencies f_i, $i = \chi, \kappa, \lambda, \varphi$, by mixing the PL signal with a normalized sinusoidal waveform at each f_i. The four demodulated time traces are then band-pass filtered, notch-stop filtered, and downsampled to 2.704 kSa/s, producing the data shown in Figures 4.6.1c-4.6.1f, as described in Section 4.5.3. The single-sided equivalent noise bandwidth of each of the resulting time traces is $f_{\text{ENBW}} = 203$ Hz. For applications requiring sensing at higher frequencies, measurement bandwidth can be greatly increased for a small (order unity) loss in sensitivity, as demonstrated in Section 4.6.6.

Figure 4.6.3 displays the vector field components B_x, B_y, B_z extracted from the measured frequency shifts of Figures 4.6.1c-4.6.1f.

Because the optical table used in the present experiment is made from ferromagnetic steel, the magnetic fields detected at the diamond sensor differ from the fields naively expected based on knowledge of the coil and diamond geometries (see Section 4.7.1) [24, 110]. For this reason, the accuracy of the simultaneous vector magnetic field measurements is determined by comparison with conventional sequential vector

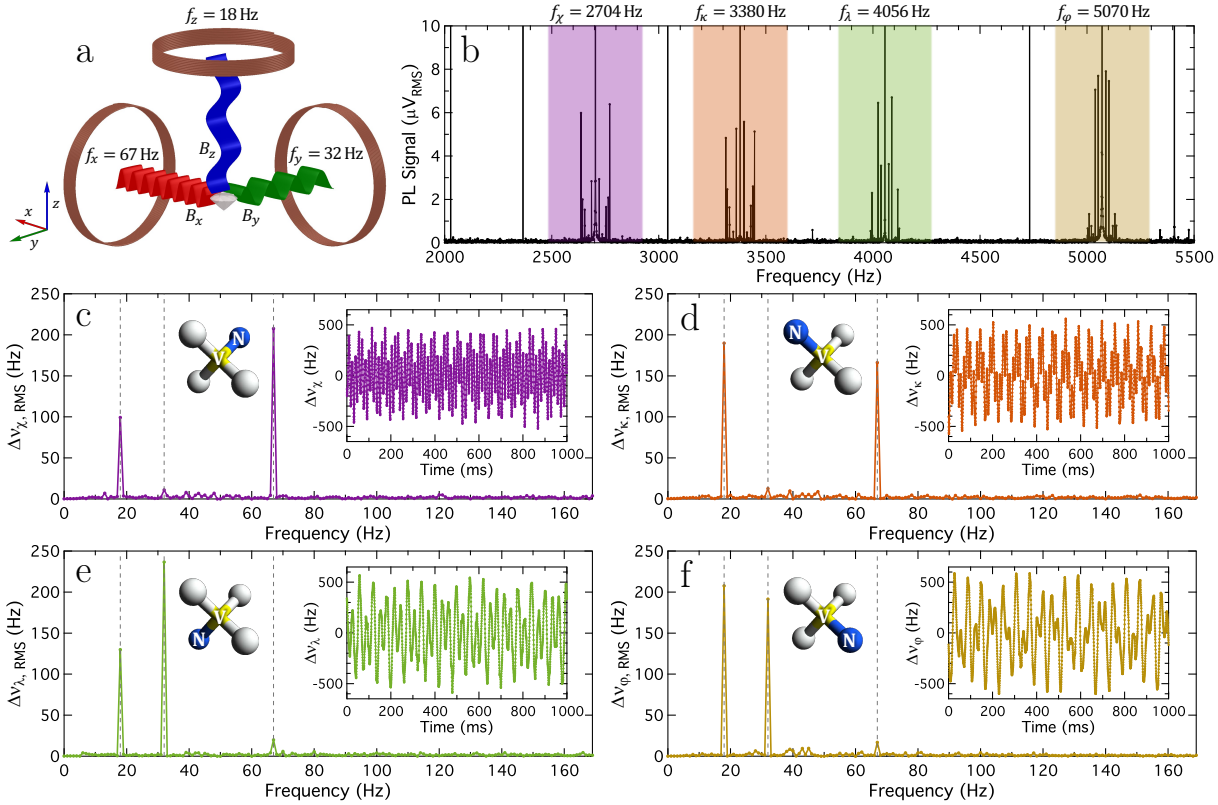

Figure 4.6.1: Applied magnetic fields and simultaneous vector magnetometry data. a) Three coils generate magnetic field signals $B_x(t), B_y(t)$, and $B_z(t)$ at $f_x = 67$ Hz, $f_y = 32$ Hz, and $f_z = 18$ Hz with root-mean-square (RMS) amplitudes $B_{x,\mathrm{RMS}} = 8.12$ nT, $B_{y,\mathrm{RMS}} = 9.56$ nT, and $B_{z,\mathrm{RMS}} = 9.86$ nT. b) Spectral density of detected PL signal from 1 second of continuous acquisition. Shaded regions mark frequency bands containing four modulation frequencies f_i, where $i = \lambda, \chi, \varphi, \kappa$ (see Table 4.4.1), and encoded magnetic field signal around each f_i. Third-order intermodulation products at 2028 Hz, 2366 Hz, 3042 Hz, and 4732 Hz, and the second harmonic of f_χ at 5408 Hz arise due to the nonlinear response of the NV$^-$ PL to frequency-modulated MW driving [259] (see Section 4.7.2). c-f) Spectral densities of magnetic-field-dependent frequency shifts $\Delta\nu_{i,\mathrm{RMS}}$ of each addressed NV$^-$ ODMR feature from 1 second of PL detection, after demodulating at f_i and filtering; (inset), time series of same demodulated and filtered data, showing magnetic-field-dependent shifts $\Delta\nu_i$, and cartoons depicting the NV$^-$ orientation corresponding to each measured $\Delta\nu_i$ trace.

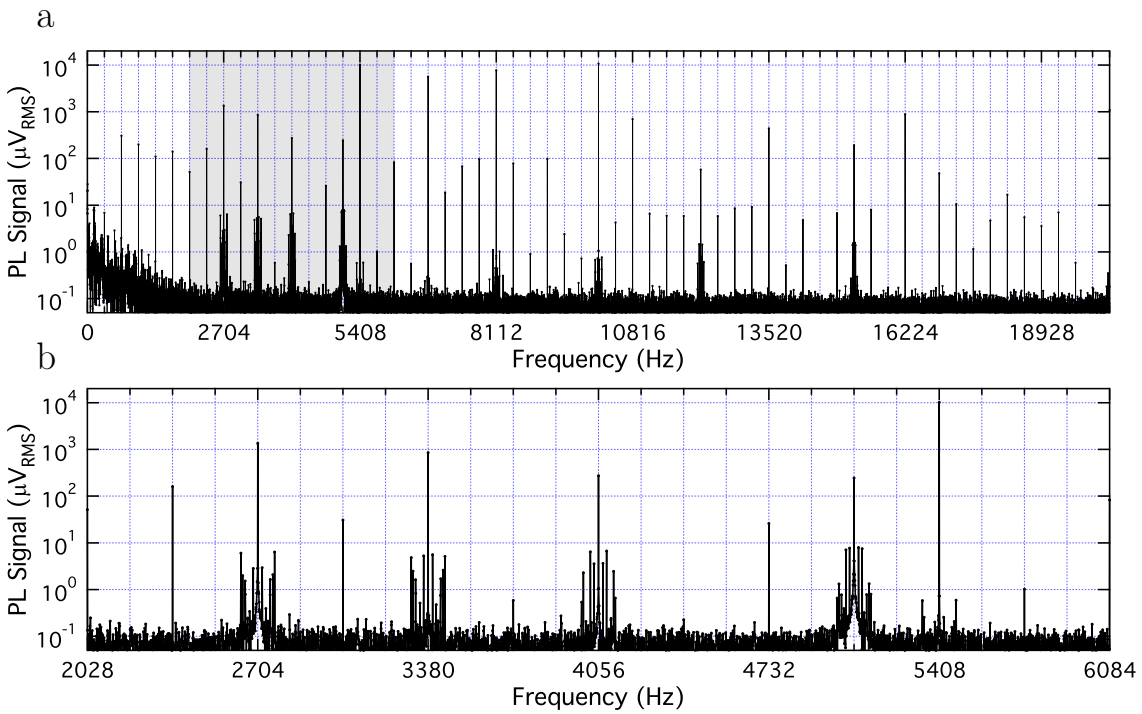

Figure 4.6.2: a) Spectral density from vector magnetometry demonstration after laser noise cancellation. Low-frequency noise is apparent, revealing the utility of modulated ODMR to approach shot-noise-limited magnetometry. Harmonics and intermodulation products of the modulation frequencies f_i are also visible. Magnetic signals encoded around the harmonics are reduced by $\sim 10\times$ compared to signals around the fundamental f_i, and signals around the intermodulation products are below the noise floor. b) Zoomed-in plot of gray box in (a). Magnetic signals encoded around the modulation frequencies f_i are visible, along with intermodulation products of f_i and the harmonic at $2f_\chi = 5408\,\mathrm{Hz}$.

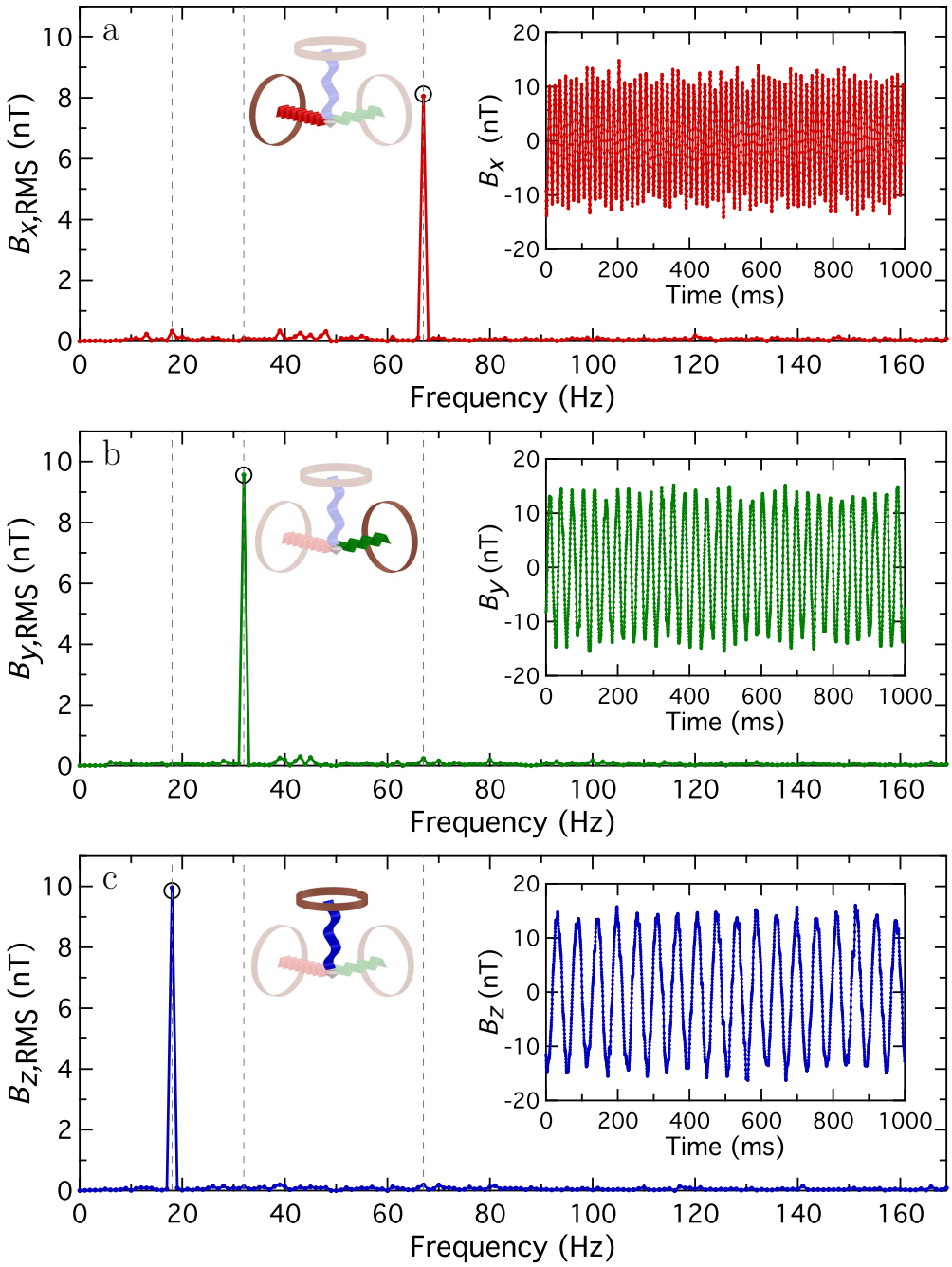

Figure 4.6.3: Detected magnetic fields using simultaneous vector magnetometer, extracted from data in Figure 4.6.1. a) B_x time trace (inset) and spectral density showing detected signal at $f_x = 67\,\text{Hz}$. b) B_y time trace (inset) and spectral density showing detected signal at $f_y = 32\,\text{Hz}$. c) B_z time trace (inset) and spectral density showing detected signal at $f_z = 18\,\text{Hz}$. Dashed lines mark applied signal frequencies f_x, f_y, f_z, and circles center on expected applied field amplitudes determined by sequential NV^- vector magnetometry. Cartoon recreations of Figure 4.6.1a illustrate isolated detected components of dynamic vector magnetic field $B_x(t)$, $B_y(t)$, $B_z(t)$.

magnetic field measurements using the same experimental setup. The extracted field components show good agreement with the amplitudes determined by sequential NV$^-$ vector magnetometry, with differences at the 1% level or better.

We investigated the remaining discrepancy between the sequential and simultaneous magnetic field measurements in our system. We found that sequentially addressing the NV$^-$ ODMR lines yields lock-in signal slopes $dS_i/d\Delta\nu_i$ that differ from the simultaneous measurement lock-in signal slopes by up to 1%. This difference is consistent with a $\sim 1\%$ increase in the ODMR linewidth of the probed NV$^-$ orientation when the other NV$^-$ orientations are driven with near-resonant modulated MWs. The linewidth increase is observed by comparing the PL signal measured by sweeping a MW tone over one ODMR feature both with and without application of resonant MWs to ODMR features from the other NV$^-$ orientations. We hypothesize that the broadening is caused by driving NV$^-$ spins from other orientations out of the $m_s = 0$ state into the $m_s = \pm 1$ states, thereby increasing NV$^-$-NV$^-$ dipolar interactions.

4.6.3 Magnetic field sensitivity

Sensitivities η_x, η_y, and η_z to magnetic field components along $\hat{x}$, $\hat{y}$, and $\hat{z}$ are determined using Equation 4.3 from a series of magnetometry measurements with no applied magnetic signal made over a 1-second duration. After multi-channel demodulation and filtering of these zero-signal traces ($f_{\mathrm{ENBW}} = 203\,\mathrm{Hz}$), the detected frequency shifts $\Delta\nu_\lambda, \Delta\nu_\chi, \Delta\nu_\varphi, \Delta\nu_\kappa$ are extracted. These shifts are then transformed to B_x, B_y, and B_z using the matrix $\mathbf{A}^+$, yielding the data displayed in Figure 4.6.4.

The sensitivity η_j to fields along the j direction is given by

$$\eta_j = \frac{\sigma_{B_j}}{\sqrt{2 f_{\mathrm{ENBW}}}} \tag{4.15}$$

for $j = x, y, z$, where σ_{B_j} is the standard deviation of the zero-signal magnetic field time trace B_j. We measure sensitivities $\eta_x = 57\,\mathrm{pT}/\sqrt{\mathrm{Hz}}$, $\eta_y = 46\,\mathrm{pT}/\sqrt{\mathrm{Hz}}$, and $\eta_z = 45\,\mathrm{pT}/\sqrt{\mathrm{Hz}}$ based on the data in Figure 4.6.4. Photon shot-noise-limited sensitivities are calculated in the following section to be $\eta_x^{\mathrm{shot}} = 18.1\,\mathrm{pT}/\sqrt{\mathrm{Hz}}$, $\eta_y^{\mathrm{shot}} = 18.4\,\mathrm{pT}/\sqrt{\mathrm{Hz}}$,

and $\eta_z^{\text{shot}} = 17.5\,\text{pT}/\sqrt{\text{Hz}}$. The 2.5 - 3× factor above shot noise is attributed to uncanceled MW and laser intensity noise (see Section 4.6.5). The reported sensitivities are the highest demonstrated to date for any solid-state spin-based magnetometer performing broadband sensing of all magnetic field vector components.

4.6.4 Shot-noise-limited vector field sensitivity

The photon-shot-noise-limited sensitivities to magnetic fields oriented along $\hat{x}$, $\hat{y}$, and $\hat{z}$ are calculated herein [260, 261, 262]. First we consider only photon shot noise on the detected PL signal from the diamond. The smallest detectable ODMR line shift (SNR = 1) due to a magnetic field in the presence of shot noise from photoelectrons on the signal photocurrent alone, $\Delta\nu_{i,\text{min}}^{I_{\text{sig}}}$, is given by

$$\Delta\nu_{i,\text{min}}^{I_{\text{sig}}} = \sigma_i^{I_{\text{sig}}} = \frac{R_{\text{sig}}}{\frac{dS_i}{d\Delta\nu_i}}\sqrt{2\,q\,I_{\text{sig}}\Delta f}, \tag{4.16}$$

where $\sigma_i^{I_{\text{sig}}}$ is the standard deviation of the frequency shifts (in Hz) on channel i due to shot noise on the PL photocurrent, R_{sig} is the signal photodiode's termination in ohms, $\frac{dS_i}{d\Delta\nu_i}$ is the PL lock-in signal slope in V/Hz, q is the elementary charge, and Δf is the single-sided measurement bandwidth.

When limited by photon shot noise, fluctuations on each of the four lock-in detection channels are uncorrelated, and the covariance matrix of ODMR frequency fluctuations is given by

$$\mathbf{\Sigma}_{\Delta\nu} = \begin{bmatrix} (\sigma_\lambda^{I_{\text{sig}}})^2 & 0 & 0 & 0 \\ 0 & (\sigma_\chi^{I_{\text{sig}}})^2 & 0 & 0 \\ 0 & 0 & (\sigma_\varphi^{I_{\text{sig}}})^2 & 0 \\ 0 & 0 & 0 & (\sigma_\kappa^{I_{\text{sig}}})^2 \end{bmatrix}. \tag{4.17}$$

The sensitivities to fields along $\hat{x}$, $\hat{y}$, and $\hat{z}$ are found by transforming $\mathbf{\Sigma}_{\Delta\nu}$ into a

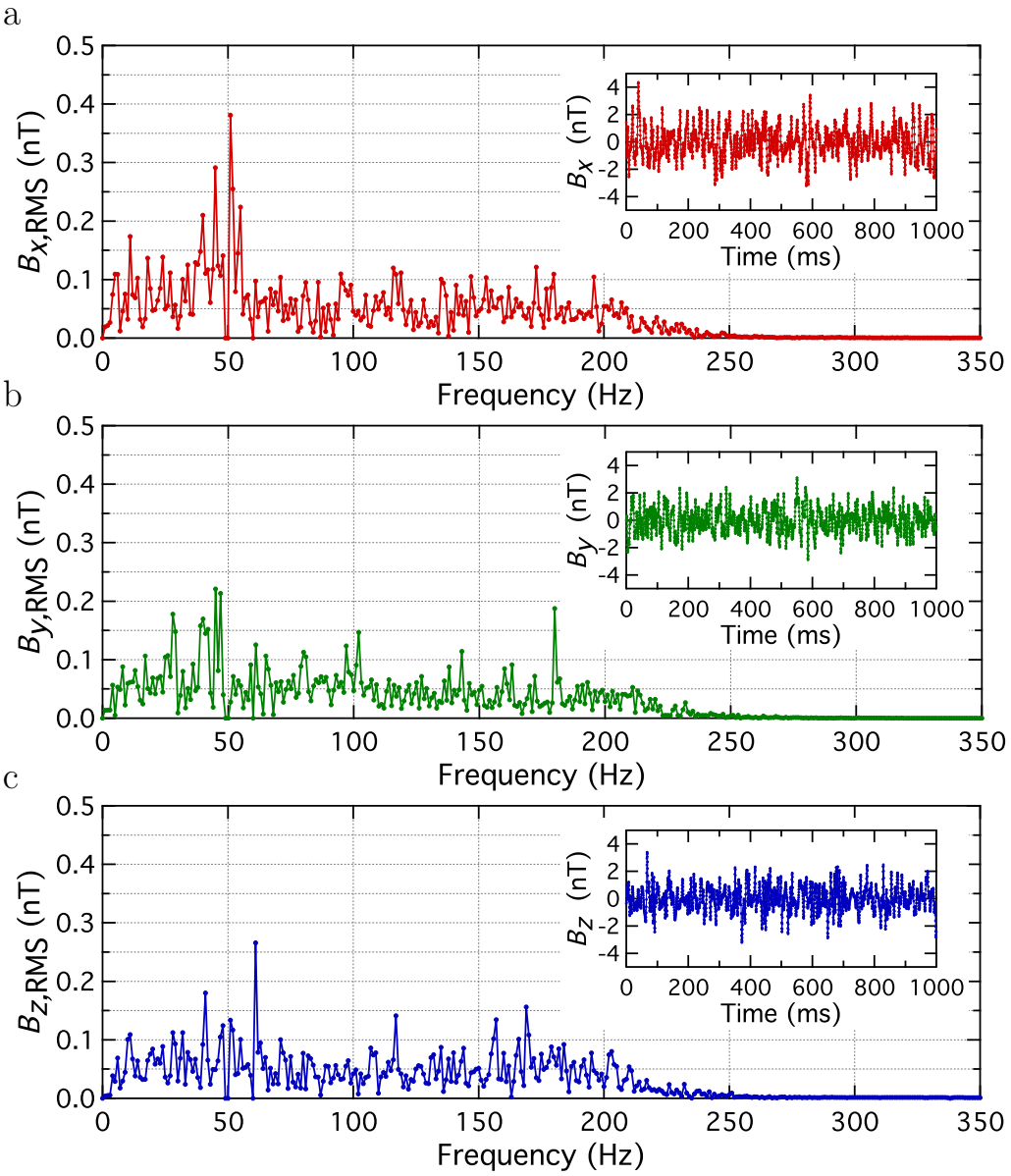

Figure 4.6.4: Magnetometer noise in the absence of applied magnetic fields. All data are band-pass filtered from 5 Hz to 210 Hz and notch-stop filtered at 49, 50, 60, and 338 Hz. a) B_x spectral density from a 1-second measurement and corresponding time trace (inset). b) B_y spectral density and time trace (inset). c) B_z spectral density and time trace (inset). The sensitivity to magnetic fields along x, y, or z may be determined by (i), squaring the measured root-mean-square (RMS) spectral density to obtain the power spectral density; (ii), integrating over the sensing bandwidth to obtain the variance $\sigma^2_{B_x}$, $\sigma^2_{B_y}$, or $\sigma^2_{B_z}$; (iii), dividing the variance by the double-sided bandwidth $2f_{\mathrm{ENBW}}$; and (iv), taking the square root (see Equations 4.1 and 4.15). These data are consistent with sensitivities $\eta_x = 57\,\mathrm{pT}/\sqrt{\mathrm{Hz}}$, $\eta_y = 46\,\mathrm{pT}/\sqrt{\mathrm{Hz}}$, and $\eta_z = 45\,\mathrm{pT}/\sqrt{\mathrm{Hz}}$.

covariance matrix of lab-frame magnetic field shifts:

$$\mathbf{\Sigma}_B = \mathbf{A}^+ \mathbf{\Sigma}_{\Delta\nu} \left(\mathbf{A}^+\right)^{\mathrm{T}}, \tag{4.18}$$

where $\left(\mathbf{A}^+\right)^{\mathrm{T}}$ is the transpose of the matrix $\mathbf{A}^+$. The diagonal elements of $\mathbf{\Sigma}_B$ are the variances $(\sigma_x^{I_{\mathrm{sig}}})^2$, $(\sigma_y^{I_{\mathrm{sig}}})^2$, and $(\sigma_z^{I_{\mathrm{sig}}})^2$, which have dimensions of tesla^2. Off-diagonal elements of $\mathbf{\Sigma}_B$ represent noise correlations; for diagonal $\mathbf{\Sigma}_{\Delta\nu}$, these correlations arise from mixing of the $|m_s = \pm 1\rangle$ states with the $|m_s = 0\rangle$ state due to the bias magnetic field's non-negligible projections transverse to the NV$^-$ symmetry axes.

The sensitivity $\eta_x^{I_{\mathrm{sig}}}$ is given by

$$\eta_x^{I_{\mathrm{sig}}} = \sigma_x^{I_{\mathrm{sig}}} \sqrt{T}, \tag{4.19}$$

where, for continuous readout as in CW-ODMR, the measurement time is $T = 1/(2\Delta f)$. Note this definition matches Equation 4.15, where $\Delta f = f_{\mathrm{ENBW}}$, and with $\sigma_x^{I_{\mathrm{sig}}}$ here replacing the measured standard deviation σ_x. The y- and z-sensitivities $\eta_y^{I_{\mathrm{sig}}}$ and $\eta_z^{I_{\mathrm{sig}}}$ are defined equivalently.

As described in Section 4.4.3, the present experiment approaches shot-noise-limited sensing by canceling laser intensity fluctuations using a reference photodetector and a software-based noise cancellation protocol. Here we consider the limit wherein this method completely cancels laser intensity fluctuations. In this limit, shot noise from the reference photocurrent also contributes to the estimated sensitivity. Including this contribution as a separate uncorrelated noise source increases the minimum detectable ODMR line shift by a term $\mathcal{F}_{\mathrm{ref}} = \sqrt{1 + \frac{I_{\mathrm{sig}}}{I_{\mathrm{ref}}}}$ to $\Delta\nu_{i,\mathrm{min}}^{I_{\mathrm{sig}},I_{\mathrm{ref}}} = \mathcal{F}_{\mathrm{ref}} \Delta\nu_{i,\mathrm{min}}^{I_{\mathrm{sig}}}$. In the limit of high reference photocurrent, $\mathcal{F}_{\mathrm{ref}}$ approaches 1; when $I_{\mathrm{sig}} = I_{\mathrm{ref}}$, $\mathcal{F}_{\mathrm{ref}} = \sqrt{2}$. The term $\mathcal{F}_{\mathrm{ref}}$ enters Equations 4.17-4.19 in the form of a constant prefactor, such that the photon-noise-limited sensitivity, modified by the reference detection, is given by $\eta_x^{I_{\mathrm{sig}},I_{\mathrm{ref}}} = \mathcal{F}_{\mathrm{ref}} \sigma_x^{I_{\mathrm{sig}}} \sqrt{T}$.

In the present experiment, the reference photodiode collects an average photocurrent $I_{\mathrm{ref}} = 30.1\,\mathrm{mA}$ from the picked-off 532 nm beam, and the signal photodiode collects an average photocurrent $I_{\mathrm{sig}} = 24.1\,\mathrm{mA}$ from the diamond PL. Inserting these

values into Equation 4.16 along with $R_{\text{sig}} = 300\,\Omega$ and the slopes $\frac{dS_i}{d\Delta\nu_i}$ given in Table 4.4.1 yields, for a 1-second measurement (i.e., $\Delta f = 0.5\,\text{Hz}$): $\Delta\nu_{\lambda,\text{min}}^{I_{\text{sig}},I_{\text{ref}}} = 0.632\,\text{Hz}$, $\Delta\nu_{\chi,\text{min}}^{I_{\text{sig}},I_{\text{ref}}} = 0.594\,\text{Hz}$, $\Delta\nu_{\varphi,\text{min}}^{I_{\text{sig}},I_{\text{ref}}} = 0.468\,\text{Hz}$, and $\Delta\nu_{\kappa,\text{min}}^{I_{\text{sig}},I_{\text{ref}}} = 0.600\,\text{Hz}$. Using Equations 4.17-4.19 with $T = 1\,\text{s}$ to calculate the photon-noise-limited sensitivities along $\hat{x}$, $\hat{y}$, and $\hat{z}$, we find $\eta_x^{I_{\text{sig}},I_{\text{ref}}} = 18.1\,\text{pT}/\sqrt{\text{Hz}}$, $\eta_y^{I_{\text{sig}},I_{\text{ref}}} = 18.4\,\text{pT}/\sqrt{\text{Hz}}$, and $\eta_z^{I_{\text{sig}},I_{\text{ref}}} = 17.5\,\text{pT}/\sqrt{\text{Hz}}$, which are 2.5 - 3× better than the realized sensitivities of the present device.

4.6.5 Noise analysis

Uncompensated MW and laser noise are found to be the dominant contributors to the present instrument's noise floor being 2.5 - 3× above the shot noise limit. This determination is based on the following observations: First, we measure uncompensated laser noise by recording magnetometer data with the MW sources turned off, removing the device's sensitivity to magnetic fields or MW noise, and we observe a noise floor $\sim 1.5\times$ above shot noise. Second, under typical experimental conditions (with MWs applied to the sensor), the lock-in amplifier phase for each demodulation frequency is chosen to maximize magnetic signal in the in-phase channel and minimize magnetic signal in the quadrature channel. The quadrature channel is thus insensitive to magnetic fields while still being sensitive to MW and laser intensity fluctuations. We observe approximately the same noise level for both the in-phase and quadrature channels, 2.5 - 3× above shot noise. This observation suggests that uncompensated laser and MW amplitude noise, not magnetic noise, limit the present device's sensitivity.

We also investigated possible magnetic noise sources and determined that these sources are unlikely to limit the sensitivity of the present device. Ferromagnetic objects exhibit thermal magnetization noise, whereby the thermal energy of the material at non-zero temperatures results in random but probabilistic flips of the individual magnetic domains [263]. The thermal magnetization noise amplitude varies with frequency f as $1/\sqrt{f}$ [264]. As the device's noise level is frequency-independent over the device's frequency encoding bands (see Figure 4.6.2), thermal magnetization noise

can be ruled out as the dominant noise source. The flat noise spectrum also suggests that resonant mechanical vibration of the bias magnets does not limit the device's noise level; this motion would likely generate narrow-band noise in the $\sim 10\,\mathrm{Hz}$ to $\sim 1\,\mathrm{kHz}$ range.

In addition, objects fabricated from electrically conductive materials (including NdFeB rare earth magnets) generate magnetic noise from Johnson-Nyquist currents flowing within the volume or over the surface. This noise source was evaluated for the optics table, the aluminum breadboard, and the copper microwave delivery loop. Rough calculations suggest that, due to its $\sim$ mm proximity to the diamond, the MW delivery loop is the dominant contributor. Nonetheless, the MW loop was estimated to generate magnetic noise $\sim 500\,\mathrm{fT}/\sqrt{\mathrm{Hz}}$ or less, well below the present device's noise floor.

4.6.6 High bandwidth vector sensing demonstration

Figure 4.6.5 shows simultaneous sensing of all Cartesian components of high-frequency vector magnetic fields, achieved by operating the present device with higher modulation frequencies than employed in the previous sections to achieve $\approx 12.5\,\mathrm{kHz}$ measurement bandwidth. Test magnetic fields at 1 kHz and 10 kHz were generated by applying sinusoidal currents to the coils aligned along $\hat{x}$ and $\hat{z}$, respectively. The magnetic field vector was reconstructed from the frequency shifts detected from three NV$^-$ orientations: λ, χ, and φ. Modulation frequencies $f_\lambda = 40.896\,\mathrm{kHz}$, $f_\chi = 12.780\,\mathrm{kHz}$, and $f_\varphi = 68.160\,\mathrm{kHz}$ were used, with carrier frequencies and frequency deviations identical to those employed in the previous lower-bandwidth sensing demonstration, reported in Table 4.4.1. The PL was digitized at $F_s = 204.480\,\mathrm{kSa/s}$ and converted to ODMR line center frequency shifts via measured lock-in signal slopes: $dS_\lambda/d\Delta\nu_\lambda = 9.2\,\mu\mathrm{V/kHz}$, $dS_\chi/d\Delta\nu_\chi = 16.6\,\mu\mathrm{V/kHz}$, and $dS_\varphi/d\Delta\nu_\varphi = 7.0\,\mu\mathrm{V/kHz}$. The observed reductions in signal slope are consistent with reduced ODMR contrast at higher modulation frequencies due to the finite cycling time of the NV$^-$ quantum states [26, 200, 24].

Recorded PL data were digitally demodulated and band-pass filtered from 80 Hz to 12.5 kHz. The maximum sampling rate $F_s^{\max} = 204.8\,\mathrm{kSa/s}$ of the digitizers used in

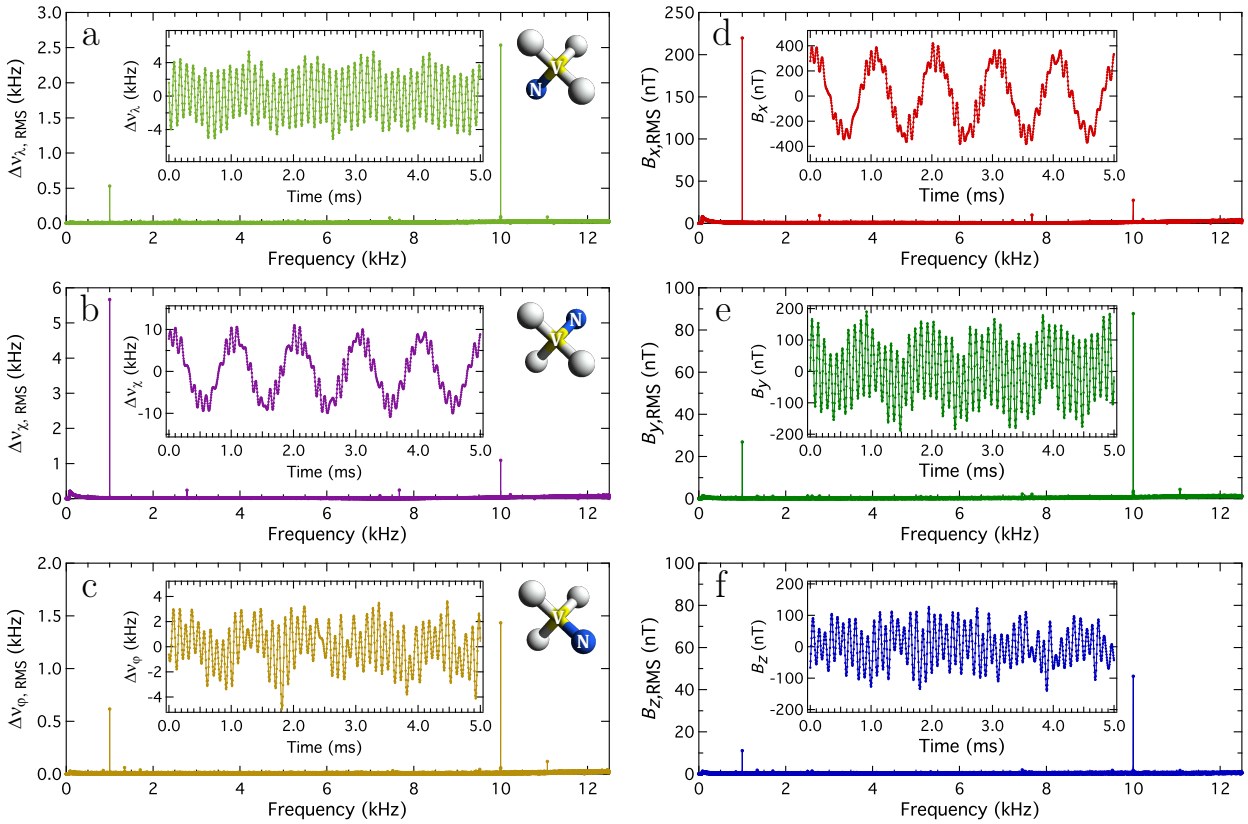

Figure 4.6.5: Simultaneous vector magnetic sensing of high-frequency fields with $\approx 12.5\,\mathrm{kHz}$ measurement bandwidth. Sinusoidal magnetic fields were applied at 1 kHz and 10 kHz. a-c) Frequency shifts of ODMR line centers detected from three NV$^-$ orientations: λ, χ, and φ. d-f) Cartesian field components reconstructed from detected frequency shifts. Modulation frequencies $f_\lambda = 40.896\,\mathrm{kHz}$, $f_\chi = 12.780\,\mathrm{kHz}$, and $f_\varphi = 68.160\,\mathrm{kHz}$ were employed, and PL was sampled at $F_s = 204.480\,\mathrm{kSa/s}$. Several notch-stop filters removed cross-talk from harmonics and intermodulation products of the modulation and signal frequencies. As discussed in Section 4.6.6, achieving cross-talk-free sensing (see Figures 4.6.1 and 4.6.3) with $\approx 12.5\,\mathrm{kHz}$ measurement bandwidth requires modest technical upgrades to the device.

the present device limited this demonstration to modulation frequencies $< F_s^{\max}/2 =$ 102.4 kHz. In addition, the modulation frequencies were chosen to divide evenly into the sampling rate to avoid aliasing effects, which limited the highest modulation frequency to $F_s/3$. Meeting these requirements for $\approx$ 12.5 kHz measurement bandwidth resulted in several harmonics and intermodulation products of the modulation frequencies being located in the frequency encoding bands of the measurement channels. Therefore, 1-Hz-wide FFT filters were employed to remove harmonics and intermodulation products of the modulation and signal frequencies. Optimal high bandwidth sensing with this method would require use of higher modulation frequencies (and thus higher signal sampling rate) than employed here to ensure that harmonics and intermodulation products fall outside the encoding bands of the measurement channels.

The detected ODMR line shifts were transformed into Cartesian magnetic field components via the linearized method discussed in Section 4.5.2, using in place of $\mathbf{A}$ the 3×3 submatrix $\mathbf{A}'$ consisting of the first three rows of $\mathbf{A}$, and using its inverse $(\mathbf{A}')^{-1}$ in place of $\mathbf{A}^{+}$. Because of the ferromagnetic optical table and $\sim$ 20 mH inductances in the magnetic field coils, pick-up of the 10 kHz signals by coils aligned along the other two axes is expected, along with interference from other metallic elements in the setup, resulting in non-negligible 10 kHz magnetic field components detected along $\hat{x}$, $\hat{y}$, and $\hat{z}$. No field-nulling currents (see Section 4.7.1) were applied to the coils in this demonstration.

4.7 Consideration and mitigation of sensor system nonidealities

This section describes (i) the compensation of nonidealities in the applied dynamic magnetic fields for the vector sensing demonstration described above, and (ii) a series of factors that can complicate the performance of a simultaneous ensemble-NV^- vector magnetometer or the accurate reconstruction of dynamic vector magnetic fields.

These factors include crosstalk between channels in the multiplexed measurement and possible systematic offsets and drifts.

4.7.1 Off-axis field nulling

Although the coils used for generating dynamic magnetic fields are intended to generate fields exactly along the directions $\hat{x}$ $\hat{y}$, and $\hat{z}$, we found that the magnetizable steel optical table employed in the present experiment distorts the resultant magnetic field at the diamond sensor, both in magnitude and direction. We performed numerical simulations (using Radia [265, 266]) of the distortion of coil fields due to a ferromagnetic optical table and found good agreement with experiments.

First we discuss the observed distortion in the measured coils field strengths at the diamond sensor. The expected coil fields at the diamond may be naively estimated based on the coil geometries and placement (reported in Section 4.6.1) and the assumptions that there is no distortion of the fields by the optical table or any other magnetizable material in the vicinity of the coils or diamond. From the applied currents to the x-, y-, and z-coils with RMS amplitudes of 0.24 mA, 0.13 mA, and 0.28 mA respectively, this simple calculation yields expected fields at the diamond sensor of $B^{\text{calc}}_{x,\text{RMS}} = 10.51\,\text{nT}$, $B^{\text{calc}}_{y,\text{RMS}} = 8.71\,\text{nT}$, and $B^{\text{calc}}_{z,\text{RMS}} = 12.86\,\text{nT}$. However, these estimated fields disagree with the magnetic fields measured via conventional sequential NV^- vector magnetometry, which found $B_{x,\text{RMS}} = 8.12\,\text{nT}$, $B_{y,\text{RMS}} = 9.56\,\text{nT}$, and $B_{z,\text{RMS}} = 9.86\,\text{nT}$, as marked by the open circles in Figure 4.6.3.

In addition to discrepancies in measured field amplitudes, the magnetic fields from the coils oriented along the two horizontal directions $\hat{x}$ and $\hat{z}$ also exhibit distortions in direction, due to the ferromagnetic optical table, resulting in nonzero magnetic field components along the vertical $\hat{y}$ direction. The off-axis components are approximately $\sim 20\,\%$ of the total field produced by each coil. In contrast, components of x-coil's field along the z-axis and vice versa occur at the few-percent level and are attributed to error in coil alignment. Signal from the y-coil appearing along $\hat{x}$ and $\hat{z}$ is similarly negligible. The observed distortion of the x-coil and z-coil signals along $\hat{y}$ is consistent with numerical simulations of the coils and the ferromagnetic optical table using the

Radia package in *Mathematica* [265, 266], up to the uncertainty of the table's relative permeability. See Appendix D.2 for simulations and additional discussion.

To effectively null the off-axis fields, small currents at the frequencies $f_x = 67\,\text{Hz}$ and $f_z = 18\,\text{Hz}$ were applied to the y-oriented coil. The effectiveness of the field nulling was verified through standard NV$^-$ vector magnetometry using sequential addressing of the NV$^-$ resonances. Remaining non-idealities in the applied fields at the few-percent level, which can be seen in Figure 4.6.3, are attributed to imperfect off-axis field nulling and error in coil alignment.

4.7.2 Mitigation of cross-excitation and intermodulation

Here we discuss cross-talk issues that may degrade the performance of a simultaneous vector magnetometer. First, off-resonant excitation of one NV$^-$ orientation by MWs intended to drive another NV$^-$ orientation is a general concern for both simultaneous and sequential vector magnetic field sensing as well as single-axis sensing from NV$^-$ ensembles. This type of cross-talk is mitigated in this work by using a sufficiently strong bias magnetic field to spectrally separate the NV$^-$ ODMR features. Modulated ODMR [26] is less sensitive to off-resonant excitation than conventional continuous-wave (CW) ODMR because the MW frequency modulation and subsequent lock-in detection generates a dispersion-type signal, which is approximately proportional to the derivative of the ODMR lineshape [24, 115]. In an NV$^-$ ensemble, the ODMR features exhibit approximately Lorentzian lineshapes [7]; at large detunings Δ compared to the full width at half maximum Γ of a Lorentzian-type feature ($\Delta \gg \Gamma$), the Lorentzian wings decay as $\sim 1/\Delta^2$. As a result, the change in detected PL in response to a small magnetic field deviation, i.e., $d\text{PL}/dB_i(\Delta)$, falls off as $\sim 1/\Delta^3$. Meanwhile, the wings of the dispersion-type lock-in signal decay as $\sim 1/\Delta^3$ far off resonance. Therefore, response of the lock-in signal S_i to a small magnetic field deviation, $dS_i/dB_i(\Delta)$, scales as $\sim 1/\Delta^4$. This $\sim 1/\Delta^4$ fall-off was confirmed experimentally by applying an 18 Hz magnetic field along the lab-frame z-axis and detecting the signal on the channel corresponding to the highest-frequency ODMR line, centered at ν_{κ^+} (see Figure 4.1.1d and Section 4.5.1), using a MW drive with carrier frequency detun-

ing varied from +5 MHz to +15 MHz. At the applied $\vec{B}_0$, the nearest two hyperfine ODMR subfeatures from different NV$^-$ orientations are separated by 30 MHz, which is large compared to the $\sim$ MHz ODMR linewidths, so we conclude that off-resonant cross excitation during vector magnetometry measurements is negligible.

Second, if multiple MW tones ν_i pass through the same MW amplifier, the amplifier's nonlinear response near saturation may cause intermodulation. In particular, third-order products $2\nu_i - \nu_j$ may drive NV$^-$ spin transitions if they happen to coincide with any of the ODMR features. The present device mitigates this effect by using four MW amplifiers, one for each MW carrier frequency (see Figure 4.4.2). For particular values of the bias field $\vec{B}_0$, two amplifiers may be sufficient to avoid cross-excitation if the intermodulation products are far off resonance from all NV$^-$ ODMR features.

Third, intermodulation products of the modulation frequencies f_i may also appear in the detected PL due to insufficiently suppressed off-resonant MW cross-excitation or to NV$^-$-NV$^-$ dipolar interactions. This intermodulation may occur when NV$^-$ spins of a given crystallographic orientation are interrogated by two sets of modulated MWs ν_i and ν_j with different modulation frequencies f_i and f_j. Because of the NV center's nonlinear response to MW driving, the detected PL may be modulated not only at both f_i and f_j, but also at sums, differences, and higher-order products of f_i and f_j. The strong bias field $\vec{B}_0$, along with the use of four MW amplifiers, avoids accidental near-resonant excitation by multiple MW tones in the present experiment. As shown in Figure 4.6.2, a judicious choice of modulation frequencies f_i ensures that all remaining third-order intermodulation products lie outside each channel's measurement bandwidth, and thus the present device avoids complications from intermodulation.

Fourth, we note a possible complication that should be accounted for in envisioned applications. If magnetic field signals are present at frequencies above the measurement bandwidth, these signals may be aliased into the wrong measurement channel. For example, a high-frequency field causing shifts in the NV$_\chi$ ODMR line could be detected in the band corresponding to the NV$_\kappa$ ODMR line and be misinterpreted as a low-frequency field along the NV$_\kappa$ symmetry axis. However, such spurious signals could be rejected in postprocessing by requiring that sensed signals correspond to ge-

ometrically possible field vectors. Such a requirement would eliminate, for example, signal waveforms appearing in only a single measurement channel.

4.7.3 Systematic offsets and drifts

Factors limiting accurate determination of the bias field parameters ($\vec{B}_0$, D, and $\vec{\mathcal{M}}_z$) include, for example, uncertainty in the NV$^-$ g-tensor [8, 156, 243], which may lead to a $\sim 10^{-4}$ fractional error in the magnetic field magnitude in the absence of external calibration. In addition, angular errors in the bias field measurement may result from uncertainty in the diamond spatial orientation. The diamond is nominally cut to have $\langle 110 \rangle$ edges and $\{100\}$ front facets; however, angle deviations from these cuts typically vary by $\sim 1^\circ$. Additionally, we estimate a few-degree uncertainty in the orientation of the diamond crystal with respect to the magnetic field coils. For simplicity, in the present study, the lab frame is defined with respect to the diamond lattice vectors, and thus diamond orientation uncertainty is ignored. The angles between the diamond's cut facets and internal lattice vectors may be measured via X-ray diffraction, and external calibration methods may be employed to determine the orientation of the diamond lattice vectors with respect to an external reference frame [232].

Small diamond lattice distortions resulting from both external and internal stress may also limit accurate measurement of $\vec{B}_0$, D, and $\vec{\mathcal{M}}_z$. External stress on the diamond is expected to cause distortions of $\ll 1^\circ$. For example, applying a 1 N cantilever force on one side of a 4 mm $\times$ 4 mm $\times$ 0.5 mm diamond crystal is estimated to cause a $\lesssim 0.01^\circ$ deflection, based on the 1200 GPa Young's modulus of single-crystal diamond [252]. Strain within the diamond is also estimated to change the lattice angles by $\ll 1^\circ$. For example, considering a typical strain-dependent ODMR line-center shift of ~ 500 kHz [81] and longitudinal and transverse NV$^-$ strain coupling parameters of ~ 15 GHz/strain [253, 254], a distortion of $\sim 0.002^\circ$ is expected.

To estimate the effect of a 0.01° lattice distortion on the bias field parameters ($\vec{B}_0$, D, and $\vec{\mathcal{M}}_z$), the Hamiltonian fit model used to extract the bias field parameters from the 8 measured ODMR line centers was altered to introduce a change of magnitude 0.01° in each of the assumed NV$^-$ angles. For a set of 10^3 ODMR line center mea-

surements, the extracted field parameters with these altered angles were compared against the field parameters extracted assuming no distortion in the tetrahedral angles ($\theta_{\text{tet}} = 2\cos^{-1}(\sqrt{1/3})$). From this test, we estimate a 0.01° lattice distortion results in fractional errors of $\sim 10^{-4}$ in the components of the bias field $\vec{B}_0$ ($\sim 1\,\mu\text{T}$ at the measured bias field $|\vec{B}_0| = 7.99\,\text{mT}$), as well as a $\sim 3 \times 10^{-6}$ fractional error in D ($\sim 8\,\text{kHz}$), and $\sim 10^{-3}$ fractional errors in the entries of $\vec{\mathcal{M}}_z$ ($\sim 10\,\text{Hz}$).

However, because the present instrument is optimized to measure small magnetic fields $\vec{B}_{\text{sens}}$ at frequencies $> 5\,\text{Hz}$, systematic offsets in the bias field parameters only affect the measured components of $\vec{B}_{\text{sens}}$ by altering the entries of the linearized matrix $\mathbf{A}$ and its pseudoinverse $\mathbf{A}^+$. The estimated errors in the bias field parameters due to angle distortion change the entries of $\mathbf{A}$ and $\mathbf{A}^+$ by $\ll 0.1\%$, and thus change the reconstruction accuracy of small signal fields by $\ll 0.1\%$ (see Section 4.5.2).

Drifts in temperature, longitudinal strain, or diamond orientation may be compensated by periodically measuring the ODMR spectrum and recalculating $\mathbf{A}$ and $\mathbf{A}^+$. Assuming such magnetometer recalibration is performed on a time scale much shorter than drifts in diamond orientation, the sensed value of the scalar field $|\vec{B}_{\text{sens}}|$ is expected to be robust to these drifts to well within the uncertainty of the linearized field reconstruction method. For example, for simulated signal fields of magnitude ranging from 1 nT to $10\,\mu\text{T}$, simulated diamond rotations of up to 30° yield fractional changes of $\lesssim 10^{-6}$ in the reconstructed field magnitude.

4.8 Extensions and outlook

4.8.1 Proposed pulsed extension

This simultaneous vector magnetometry method should be extendable to pulsed-type measurement protocols, such as Ramsey [102], pulsed ODMR [100], and Hahn echo [267]. For example, Ramsey magnetometry typically employs MW phase modulation in a modified variant of the dual measurement scheme used in NV$^-$ sensing protocols to mitigate systematic noise sources [49, 245, 62]. In this dual measurement

scheme, otherwise identical pulse sequences alternately project the final spin state onto the $|m_s = \pm 1\rangle$ and $|m_s = 0\rangle$ basis states by varying the phase of the final $\pi/2$ pulse, as illustrated in Figure 4.8.1a. The magnetic field is then calculated using

$$\langle B \rangle = \frac{\alpha}{2\langle S \rangle} \Big[\, S_1 \, - \, S_2 \, \Big], \tag{4.20}$$

where S_i denotes the integrated PL signal resulting from the i^{th} measurement, α is a proportionality constant between the magnetic field and the integrated PL, $\langle S \rangle$ denotes the mean integrated PL averaged over projections on the $|m_s = \pm 1\rangle$ and $|m_s = 0\rangle$ basis states, and the gray box (no box) indicates that the given measurement S_i is projected onto the $|m_s = \pm 1\rangle$ ($|m_s = 0\rangle$) state. The dual measurement scheme effectively removes background PL offsets, mitigates laser intensity fluctuations, and protects against certain systematics causing long-term drifts of S_i.

For the proposed extension to pulsed vector magnetometry, simultaneous pulse sequences are applied to multiple spectrally-separated ODMR features, each with a separate near-resonant MW frequency and a distinct alternation pattern of final $\pi/2$-pulse phases. Use of orthogonal binary sequences such as Walsh-Hadamard codes [268, 269, 270, 271, 272] for the phase alternation patterns ensures the detected PL can be demodulated to separate out the magnetic field signal associated with each NV$^-$ orientation. For example, with the encoding scheme illustrated in Figure 4.8.1b, these magnetic signals are given by

$$\langle B_1 \rangle = \frac{\alpha_1}{8\langle S \rangle} \Big[\quad S_1 - S_2 + S_3 - S_4 + S_5 - S_6 + S_7 - S_8 \Big] \tag{4.21}$$

$$\langle B_2 \rangle = \frac{\alpha_2}{8\langle S \rangle} \Big[\quad S_1 + S_2 - S_3 - S_4 + S_5 + S_6 - S_7 - S_8 \Big] \tag{4.22}$$

$$\langle B_3 \rangle = \frac{\alpha_3}{8\langle S \rangle} \Big[-S_1 + S_2 + S_3 - S_4 - S_5 + S_6 + S_7 - S_8 \Big] \tag{4.23}$$

$$\langle B_4 \rangle = \frac{\alpha_4}{8\langle S \rangle} \Big[\quad S_1 + S_2 + S_3 + S_4 - S_5 - S_6 - S_7 - S_8 \Big]. \tag{4.24}$$

From the observed values of $\langle B_1 \rangle$, $\langle B_2 \rangle$, $\langle B_3 \rangle$, and $\langle B_4 \rangle$, the lab-frame magnetic field components B_x, B_y, and B_z can be determined utilizing a linearized matrix as

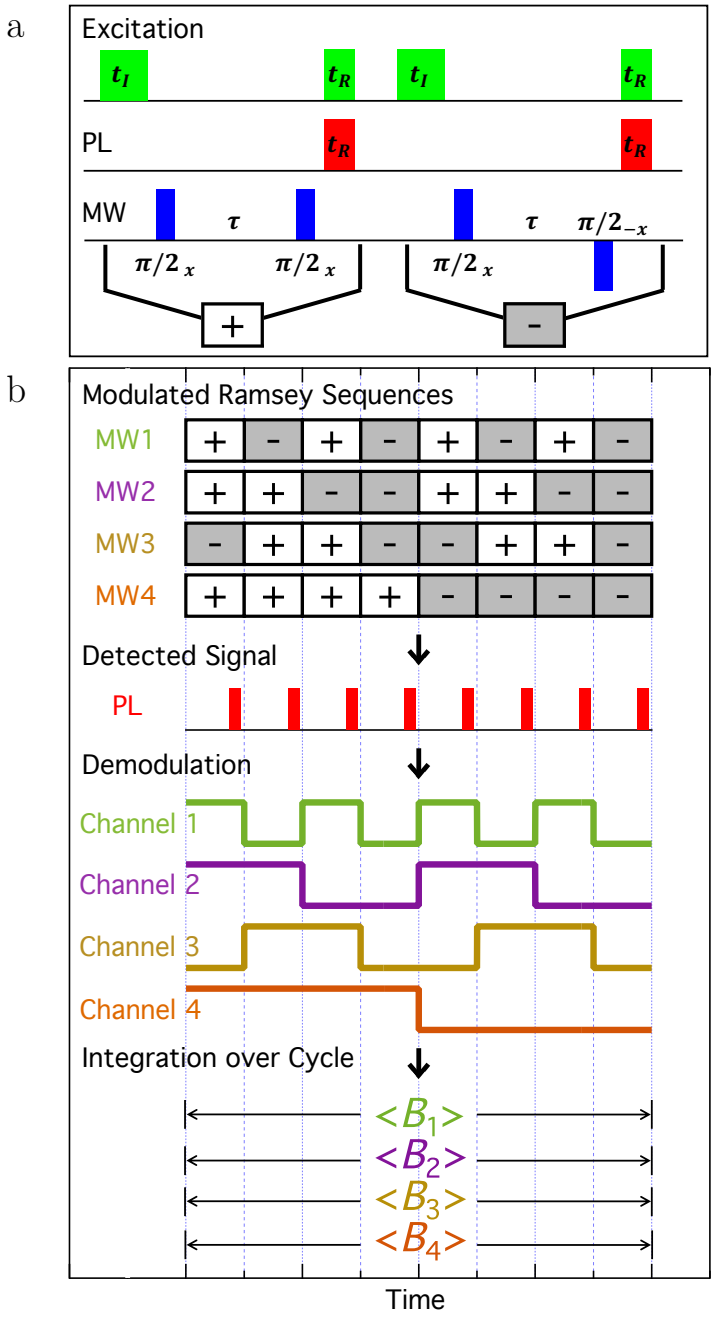

Figure 4.8.1: Proposed pulsed implementation of simultaneous vector magnetometry. a) Set of two Ramsey sequences with modulated MW phase. Green and red rectangles depict periods of 532 nm laser excitation and PL collection, respectively, with NV^--spin-state initialization time t_I and spin readout time t_R. After an initial $\pi/2$ pulse, the magnetic field is sensed for a duration τ followed by a final MW $\pi/2$ pulse of variable phase. Sequences denoted + and − differ in phase by 180° and yield equal and opposite PL contrast signals from a DC magnetic field [49, 245, 62]. b) Four-channel modulated Ramsey scheme. Final MW $\pi/2$ pulse phases from each sequence are modulated according to the a set of orthogonal Walsh-Hadamard codes [268]. Detected PL signal is demodulated according to same Walsh-Hadamard codes to separate and extract magnetic-field-dependent shifts of four addressed NV^- orientations.

described in Section 4.5.2. The simultaneous scheme (Equations 4.21-4.24) achieves the same bandwidth but a 2× higher SNR than the scheme in Equation 4.20 applied sequentially to the four NV$^-$ orientations, since both schemes require eight pulse sequences to reconstruct the magnetic field vector (see Section 4.3.2).

This pulsed implementation of simultaneous vector magnetometry is expected to allow improvements in both bandwidth and sensitivity compared to the demonstrated CW-ODMR implementation. In particular, sensing bandwidths up to $\sim 100\,\mathrm{kHz}$ are anticipated, based on arguments in Ref. [24]. The two main contributors to the expected sensitivity enhancement are (i) more effective noise rejection due to modulated pulsed-type protocols encoding magnetic information at higher frequencies than CW-ODMR, and (ii) the combination of enhanced PL contrast and reduced resonance linewidth from avoiding laser and MW power broadening [100, 24].

4.8.2 Imaging implementation

This simultaneous vector magnetometry method is expected to be compatible with camera-based wide-field magnetic imagers using NV-diamond [48, 49, 50, 273, 31, 274, 275, 166, 126, 13, 52], both for frequency-modulated CW-ODMR and for phase-modulated pulsed-type sensing schemes. We note that the demodulation and summation described in Section 4.8.1 and shown in Figure 4.8.1 is a time-domain picture of the demodulation and low-pass filtering lock-in scheme used in the CW-ODMR demonstration. The same approach is expected to apply to camera-based parallel imaging, where the PL detection S_n represents the n^{th} camera exposure, and the signals $\langle B_1\rangle, \langle B_2\rangle, \langle B_3\rangle, \langle B_4\rangle$ and reconstructed field components B_x, B_y, B_z represent magnetic field image frames.

For frequency-modulated CW-ODMR magnetic imaging, square-wave modulation may enable increased SNR compared to sinusoidal modulation, as the adding and subtracting of image exposures amounts to square-wave demodulation of the detected signal. In both imaging and single-channel detection modalities, square-wave modulation and demodulation is expected to slightly increase measurement SNR by ensuring that the MWs always interrogate NV$^-$ ODMR features at the points of steep-

est slope [115, 24, 244].

4.8.3 Conclusion

The method presented here allows simultaneous recording of all three Cartesian components of a dynamic vector magnetic field using a solid-state spin sensor. The technique is a straightforward extension of established methods for broadband magnetometry using ensembles of solid-state defects, and implementation in an existing system requires only additional MW components. The method offers at least a 2× improvement in shot-noise-limited sensitivity, corresponding to a 4× reduction in measurement time to achieve a target SNR when compared to sequential vector magnetic field sensing. While the technique is demonstrated here for a single optical detector employing CW-ODMR, it is expected to be compatible with CW and pulsed-type measurements in both single-channel detectors and camera-based magnetic field imagers.

This technique is expected to advance real-time magnetic sensing and imaging applications, such as detection of biocurrents from neurons placed in close proximity to the diamond [24]. With the ability to sense dynamic vector magnetic fields, this method could enable real-time imaging of spontaneous activity from multiple neurons with arbitrary orientations.

Chapter 5

High-speed strain-free NV-diamond biomagnetic imager

5.1 Introduction

This chapter describes an ongoing project to demonstrate high-sensitivity broadband magnetic field imaging using NV^- ensembles and double-quantum Ramsey magnetometry. Chief applications include imaging of magnetic fields produced by electrically-active biological cells such as neurons and cardiomyocytes.

In the previous chapters we presented high-sensitivity broadband bulk magnetometry demonstrations. Here, we combine these advances with parallel, wide-field imaging. For magnetic imaging applications, both sensitivity and spatial resolution are important parameters to optimize. Therefore, the relevant figure of merit for magnetic imaging is the SNR in a fixed measurement time from a fixed volume of NV-diamond. Since for shot-noise-limited operation, the SNR scales with square root of the interrogation volume and the measurement time, we seek to minimize the volume-normalized sensitivity $\eta^V = \eta\sqrt{V}$ (see Section 3.4). Previous uses of NV^- ensembles for imaging have focused on mapping DC fields using CW-ODMR [48, 50, 68, 51, 13, 69, 53, 52, 85], or on narrow-band AC magnetic imaging and noise spectroscopy using pulsed techniques [3, 49, 31]. Meanwhile, time-resolved broadband magnetic imaging would benefit many applications in biophysics

and neuroscience, as activity in electrically-active cells typically occurs on millisecond timescales. To date, no ambient-temperature magnetic imaging system capable of resolving currents from networks of electrically active cells with single-cell resolution has been demonstrated. Here, we present a wide-field, double-quantum Ramsey magnetic imager designed for this purpose. As discussed in Sections 1.6.1 and 3.4, Ramsey magnetometry enables higher volume normalized sensitivity than CW-ODMR, as the optical intensity can be increased toward saturation without degrading the measured PL contrast. We apply our device to high-speed imaging of magnetic fields from currents in neuron phantoms, which are fabricated wire structures designed to mimic certain spatial and temporal characteristics of mammalian neuron activity.

Our magnetic imager employs double-quantum (DQ) Ramsey sequences [81, 104, 215] with a novel phase alternation scheme designed to cancel the effects of pulse errors associated with strain gradients and temperature drifts over the interrogated NV^- ensemble. Combining this protocol, which we call DQ 4-Ramsey, with readout on a high-speed lock-in camera capable of handling high photon flux, we demonstrate high-sensitivity, strain-free magnetic imaging with $\lesssim 10$ μm resolution, and we reconstruct time-resolved magnetic signals from DC to $\sim$ kHz over a ~ 300 μm field of view. We discuss ongoing efforts toward optimizing the magnetic field sensitivity, implementing high-speed vector magnetic imaging [25], and mapping currents in phantoms fabricated from graphene - which has lower conductivity than gold or other metals, closer to that of neurons. In addition to enabling new neuroscience studies, we anticipate the advances embodied in this device could also be employed in condensed matter physics, such as for time-resolved imaging of skyrmion domain-wall hopping [276] or of dynamics in other topologically nontrivial materials.

5.2 Magnetometry protocol

As described in Section 6.1.2, double-quantum coherence magnetometry leverages the full spin-1 nature of the NV^- ground state to both increase sensitivity to magnetic fields and cancel effects of longitudinal strain and electric fields, and temperature vari-

ation. A DQ Ramsey protocol is similar in practice to a conventional single-quantum (SQ) Ramsey protocol (see Sec. 1.5.1). In both schemes, near-resonant MWs create a superposition of spin states, which accumulates a magnetic-field dependent phase during a free-precession time τ before being mapped onto a population difference and subsequently detected via a projective measurement. In the DQ case, however, the quantum states prepared for sensing differ from the states read out in the projective measurement. As depicted in Figure 5.2.1b and c, a dual-tone MW pulse prepares an equal superposition of the $|m_s = +1\rangle$ and $|m_s = -1\rangle$ states, with a phase relationship $(|+1\rangle + e^{i\Delta\phi}|-1\rangle)/\sqrt{2}$ determined by the relative phase $\Delta\phi$ of the two MW tones. This state which couples to the MW drive is commonly called the bright state, while the orthogonal superposition state blind to MWs is termed the dark state. In Figure 5.2.1c, $\Delta\phi = 0$ is chosen such that the bright state is $|+_{\mathrm{DQ}}\rangle = (|+1\rangle + |-1\rangle)/\sqrt{2}$ and the dark state is $|-_{\mathrm{DQ}}\rangle = (|+1\rangle - |-1\rangle)/\sqrt{2})$.

Considering the states $\{|0\rangle, |+_{\mathrm{DQ}}\rangle\}$ as a two-level system, the applied DQ pulse is a π-pulse, in contrast to the $\pi/2$-pulse employed for SQ Ramsey sequences. Consequently, if a conventional SQ Ramsey protocol employs MW Rabi frequency Ω_{SQ} on either the $|0\rangle \leftrightarrow |-1\rangle$ or $|0\rangle \leftrightarrow |+1\rangle$ transition with a $\pi/2$-pulse of duration $\tau_{\mathrm{SQ}} = \frac{\pi}{2\Omega_{\mathrm{SQ}}}$ (see Figure 5.2.1a), a two-tone DQ pulse with Rabi frequency Ω_{SQ} applied on each spin transition requires a π-pulse duration $\tau_{\mathrm{DQ}} = \sqrt{2}\tau_{\mathrm{SQ}}$ (see Figure 5.2.1c).

Because neither the bright nor the dark state is an energy eigenstate of the spin system, population is transferred between $|+_{\mathrm{DQ}}\rangle$ and $|-_{\mathrm{DQ}}\rangle$ during the free-precession interval τ, as the spin accumulates a magnetic-field-dependent phase. After time τ, whatever population remains in the bright state is transferred to $|m_s = 0\rangle$, allowing optical detection of the phase via the PL difference between the $|0\rangle$ and $|\pm 1\rangle$ states.

Like with conventional single-quantum Ramsey magnetometry, systematic noise sources may be mitigated through application of MW phase alternation patterns [49, 245, 62, 25]. In the standard SQ dual-measurement scheme, the phase of the final $\pi/2$ pulse is varied by 180° between otherwise identical Ramsey sequences, alternately rotating the spin-state Bloch vector toward the north and south poles, (i.e., toward $|0\rangle$ and either $|+1\rangle$ or $|-1\rangle$). By subtracting every second sequence's PL detection

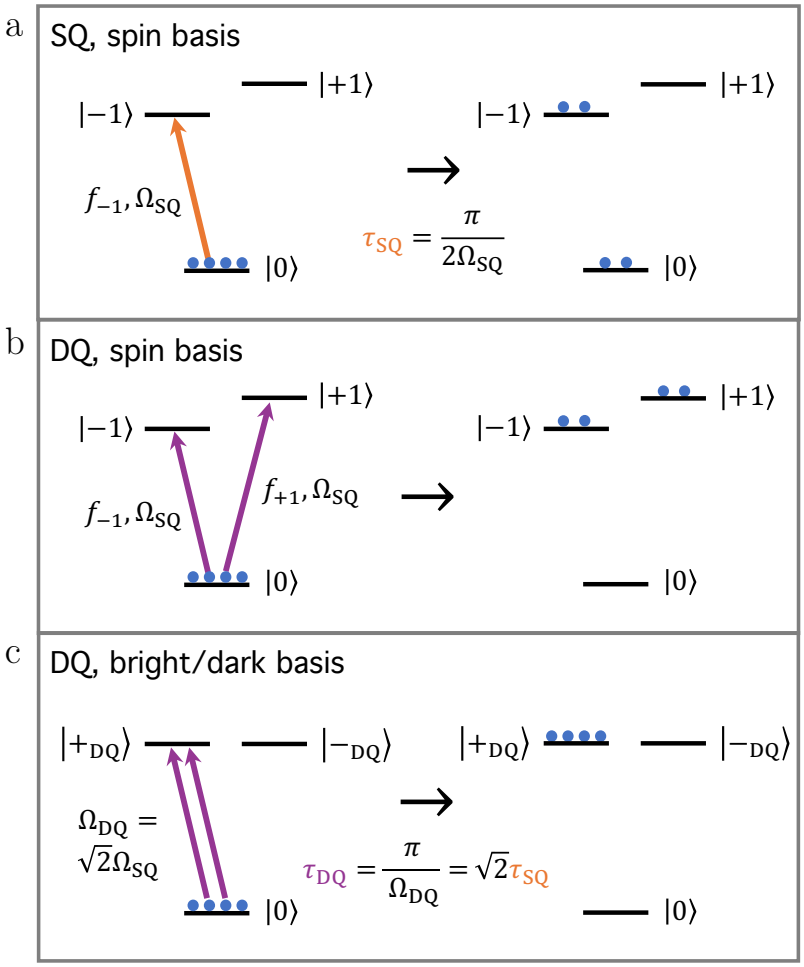

Figure 5.2.1: NV$^-$ ground state spin energy levels and MW pulses for single-quantum (SQ) and double-quantum (DQ) Ramsey magnetometry. a) SQ $\pi/2$-pulse, addressing the $|0\rangle \leftrightarrow |-1\rangle$ transition with frequency f_{-1}, Rabi frequency Ω_{SQ}, and duration $\tau_{SQ} = \frac{\pi}{2\Omega_{SQ}}$, generates an equal superposition of $|0\rangle$ and $|-1\rangle$. b) Analogous DQ two-tone pulse, addressing both the $|0\rangle \leftrightarrow |-1\rangle$ and $|0\rangle \leftrightarrow |+1\rangle$ transitions with frequencies f_{-1} and f_{+1}, respectively, and equal Rabi frequencies Ω_{SQ}, generates an equal superposition of $|+1\rangle$ and $|-1\rangle$. c) DQ pulse represented in the bright/dark basis, where the bright state (here $|+_{DQ}\rangle$) is defined as the state that couples to the MWs. The state $|+_{DQ}\rangle$ is prepared after a π-pulse, in this basis, of duration $\tau_{DQ} = \frac{\pi}{\Omega_{DQ}} = \sqrt{2}\tau_{SQ}$.

from the previous, and then dividing by the sum of both detections, the magnetic field signal is rectified, while systematic noise (varying over durations longer than two Ramsey sequences) is canceled. This scheme is particularly effective for mitigating laser intensity fluctuations.

In the DQ extension of this scheme, the final MW pulse alternately interrogates the $|0\rangle \leftrightarrow |+_{\mathrm{DQ}}\rangle$ and $|0\rangle \leftrightarrow |-_{\mathrm{DQ}}\rangle$ transitions in successive sequences. This alternation of the state coupled to the MWs is accomplished by varying the *relative* phase between the two MW tones by 180°. As in the single-quantum protocol, the change in PL signal associated with a magnetic field change has the opposite sign in every second sequence, such that subtraction of each second detection from the first results in a rectified, noise-canceled magnetic field signal.

An added challenge specific to DQ magnetometry is that pulse errors, which result in imperfect preparation of the $|+_{\mathrm{DQ}}\rangle$ state, cause residual population to be prepared in a single-quantum superposition of the $|0\rangle$ and $|\pm 1\rangle$ states. These states accumulate magnetic-field-dependent phase at half the rate of the DQ superposition state, degrading the contrast of a DQ Ramsey magnetic field measurement. Furthermore, the residual SQ coherence is sensitive to strain, electric fields, and temperature changes, meaning that a DQ measurement is not free from these spurious signals unless pulse errors are mitigated. For measurements employing ensembles of NV^- centers, it is typically impossible to completely eliminate MW pulse errors, as the finite T_2^* of the ensemble ensures that different NV^- centers experience different detunings of their spin resonances from the MW drive frequencies. Additionally, MW field inhomogeneity over an ensemble causes different NV^- centers to experience different MW Rabi frequencies.

To overcome this challenge, we develop and demonstrate a four-measurement extension of the DQ dual-measurement scheme. The phase alternation pattern used in this 4-Ramsey protocol cancels the magnetic signal from any residual single-quantum coherence and retains only the double-quantum magnetic signal. Here we describe our implementation of this scheme, which is depicted in Figure 5.2.2. First we report our particular choice of MW pulse phases and then outline more general phase

requirements.

We apply MW pulses on both spin transitions, each yielding a B_1 field that points along either the x-axis or the $-x$-axis in the rotating frame. The phase encoded in the bright superposition state $(|{+1}\rangle + e^{i\Delta\phi}|{-1}\rangle)/\sqrt{2}$ is given by the relative phase between these two B_1 field vectors. For all four Ramsey sequences, the first MW B_1 field points along x for both transitions, resulting in a DQ transition between the $|0\rangle$ and $|{+_{\mathrm{DQ}}}\rangle$ states. Then, in each of the four sequences, we choose a different combination of B_1 field directions for the final two-tone MW pulse. In the first sequence, the final-pulse B_1 fields align along x for both transitions. In the second sequence, the final-pulse fields align along $-x$ for the upper transition and x for the lower transition, resulting in DQ coupling to the $|{-_{\mathrm{DQ}}}\rangle$ state. In the third sequence, the final-pulse B_1 fields align along $-x$ for both transitions, causing DQ coupling to the $|{+_{\mathrm{DQ}}}\rangle$ state as in the first sequence. Then, in the fourth sequence, the fields align along x for the upper transition and $-x$ for the lower transition, connecting the $|0\rangle$ and $|{-_{\mathrm{DQ}}}\rangle$ states as in the second sequence. If the signal from each of the four sequences $i = 1-4$ is denoted S_i, the normalized signal from the 4-Ramsey sequence $S_{\text{4-Rams}}$ is given by

$$S_{\text{4-Rams}} = \frac{S_1 - S_2 + S_3 - S_4}{S_1 + S_2 + S_3 + S_4}. \tag{5.1}$$

This normalization preserves the double-quantum magnetic field signal, as Sequences 2 and 4 contain the opposite DQ magnetic signals to Sequences 1 and 3. Meanwhile, if there are pulse errors resulting in some residual single-quantum coherence, the normalization scheme from Equation 5.1 cancels the resultant SQ signal, as the same SQ signal is contained in the sum $S_2 + S_4$ as in $S_1 + S_3$.

The generalized implementation of this 4-Ramsey scheme allows more freedom in selection of MW pulse B_1-field directions. First, the order of the sequences may be permuted. For example, Sequences 1 and 3 may be swapped. Second, if we parametrize the direction of the MW B_1 field in the xy-plane by a phase ϕ, arbitrary phase differences may be selected for the MW fields driving the two transitions in the first sequence, so long as the phase differences for the subsequent sequences maintain

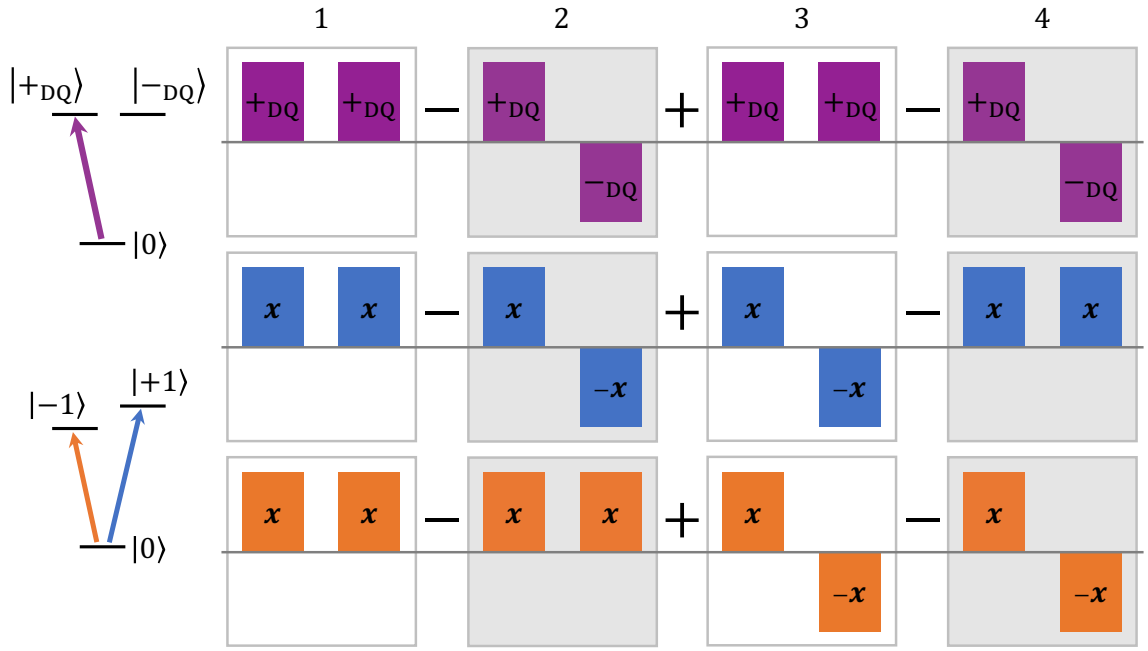

Figure 5.2.2: Schematic representation of MW phase alternation pattern chosen for double-quantum 4-Ramsey implementation. The protocol cancels residual single-quantum signals that result from MW pulse errors. The x and $-x$ designations refer to the direction of the B_1 field associated with a given MW drive in its rotating frame. The B_1 field direction in the xy-plane is more generally parametrized by a phase ϕ. When the relative phase $\Delta\phi$ between the MW drives addressing the $|0\rangle \leftrightarrow |+1\rangle$ and $|0\rangle \leftrightarrow |-1\rangle$ transitions changes by 180°, the double-quantum π-pulse accesses the orthogonal superposition state of $|+1\rangle$ and $|-1\rangle$. For example, in Sequence 2, the initial two-tone pulse along $\{x, x\}$ corresponds to a DQ π-pulse between $|0\rangle$ and $|+_{DQ}\rangle = (|+1\rangle + |-1\rangle)/\sqrt{2}$, while the final two-tone pulse along $\{-x, x\}$ corresponds to a DQ π-pulse between $|0\rangle$ and $|-_{DQ}\rangle = (|+1\rangle - |-1\rangle)/\sqrt{2}$. MW phases are chosen so that the DQ magnetic field signal from Sequences 2 and 4 (gray boxes) is the negative of that from Sequences 1 and 3 (white boxes). Meanwhile, any SQ Ramsey signal from Sequence 1 is canceled by Sequence 3 and that from Sequence 2 is canceled by Sequence 4. By adding and subtracting the four PL detections as shown and normalizing by their sum (see Equation 5.1), the DQ magnetic signal is retained while unwanted residual SQ signals are canceled, eliminating spurious effects of temperature variation, strain gradients, and electric field noise. Like the SQ dual-measurement scheme [49, 245, 62], this protocol also removes background PL and other systematic noise, such as laser intensity fluctuations.

a specific relationship to those of the first sequence. A generalized choice of MW phases for all 16 pulses is shown in Figure 5.2.3, where the phases α, β, ϕ_i, and θ_i with $i = 1 - 4$ may be chosen arbitrarily.

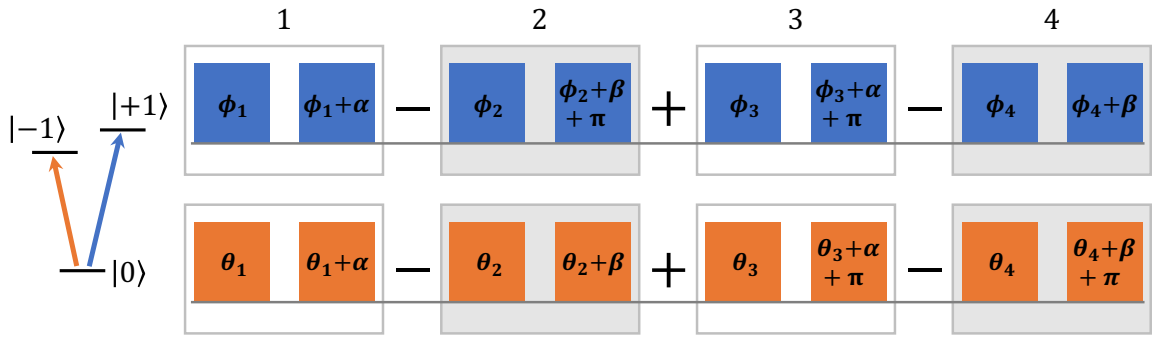

Figure 5.2.3: Generalized phase requirements for double-quantum 4-Ramsey protocol. The phases α, β, ϕ_i, and θ_i for $i = 1 - 4$ may be chosen arbitrarily. Sequences 2 and 4 (gray boxes) produce DQ magnetic signals that differ in sign from the signals from Sequences 1 and 3 (white boxes), whereas the four sequences combined as shown and normalized (see Equation 5.1) cancel residual SQ signal as well as background PL and systematic noise.

Figure 5.2.4 shows DQ-Ramsey free induction decay (FID) profiles taken when implementing a conventional 2-Ramsey dual-measurement scheme and our 4-Ramsey protocol. The measurements are performed on an as-grown diamond sample with [^{14}N] $\approx$ 0.75 ppm (Sample B from Reference [81]). The amplitude spectral density of the PL contrast from the 2-Ramsey measurement (Figure 5.2.4a) exhibits three primary features arising from double-quantum Ramsey fringes at the two-photon detunings of the three ^{14}NV$^-$ hyperfine resonances. The FID spectral density exhibits additional, broader features at approximately half the frequencies of the DQ peaks. These features arise from spurious SQ coherence prepared by imperfect DQ π-pulses. Implementation of the 4-Ramsey protocol (Figure 5.2.4b) eliminates the residual SQ signal, leaving a DQ signal insensitive to strain gradients, electric field noise, and temperature drifts.

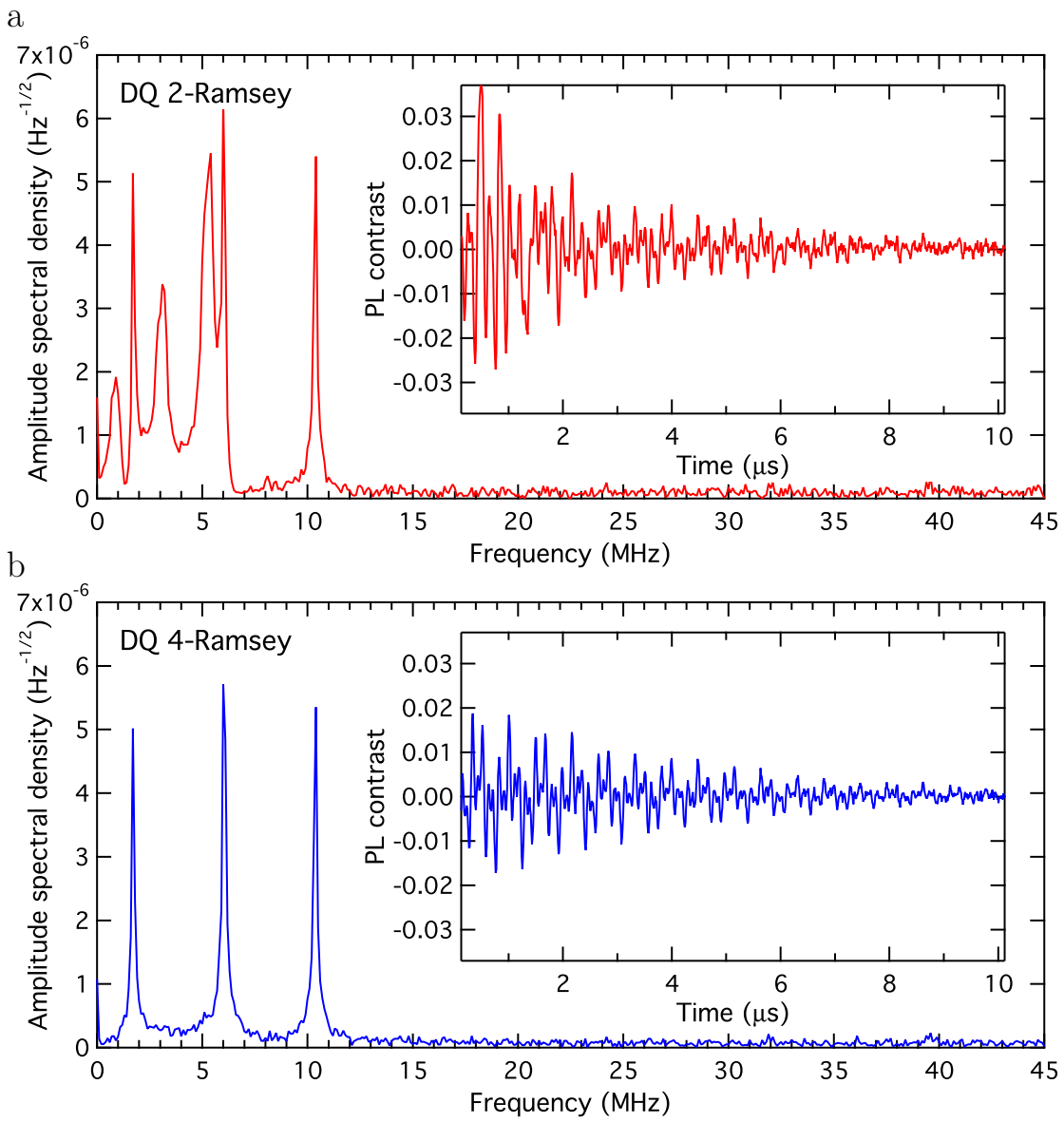

Figure 5.2.4: Experimental demonstration of DQ 4-Ramsey protocol compared to standard 2-Ramsey normalization scheme. a) Amplitude spectral density of PL contrast from DQ Ramsey FID (inset) utilizing conventional dual-measurement (2-Ramsey) scheme for eliminating background PL and canceling systematic noise. Narrow features at 1.7, 6.0, and 10.4 MHz arise from DQ coherence of the three ^{14}NV$^-$ hyperfine features of the interrogated diamond sample. Broader features centered at 0.8, 3.1, and 5.3 MHz arise from SQ coherence, prepared by imperfect DQ MW π-pulses. Diamond probed (Sample B from Ref. [81]) has [N] $\sim$ 0.75 ppm and high strain gradients over the field of view, which contribute both to broad SQ features and to large pulse errors, which cause substantial residual SQ coherence. b) Amplitude spectral density of PL contrast from DQ Ramsey FID (inset) utilizing 4-Ramsey protocol, which eliminates spurious SQ signal in addition to background PL and systematic noise.

5.3 Lock-in imaging

Lock-in detection is useful for ensemble-NV^- sensing experiments, as the detected signal from conventional optical readout is typically a small variation on top of a DC offset. By modulating the frequency [26, 24, 244, 241, 25] or phase [49, 245, 33, 81] of the MWs and then demodulating the detected signal, NV^- lock-in measurements both eliminate background PL offsets and cancel technical noise away from the modulation frequency. Application of such schemes to broadband imaging is limited by the exposure rate of the employed camera. Therefore, a camera with a high exposure rate is necessary for broadband ensemble-NV^- magnetic imaging. For fast lock-in DQ Ramsey imaging using the 4-Ramsey protocol described above, we utilize a CMOS lock-in camera with a maximum exposure rate of 1 MHz, the Heliotis heliCam C3 [277, 278], fabricated with microlenses for improved collection efficiency [279]. While the heliCam was designed for optical coherence tomography [280], it has also been proposed or employed for a variety of other applications including femtosecond pump-probe spectroscopy [281], optical frequency comb spectroscopy [282], holography [283], velocimetry [284], and ensemble-NV^- sensing [285].

The heliCam operates by subtracting alternate exposures in analog and then digitizing the resultant background-subtracted signal, enabling the detected magnetic field information to fill each pixel's 10-bit dynamic range. Although the camera's maximum output rate of 3800 frames per second (fps) limits the detection bandwidth to $\lesssim 1.9$ kHz, the imager is capable of canceling noise out to higher frequencies by operating at lock-in frequencies up to 250 kHz. Our device typically operates with a ~ 50 kHz lock-in frequency. Each demodulation cycle is broken into four quarters. The exposures from the first and third quarter subtract to generate an *in-phase* signal on the camera's I channel, while the exposures from the second and fourth quarter generate a *quadrature* signal on the camera's Q channel. Every output frame then consists of two images - an I image and a Q image - each composed of the sum of pairs of exposures from multiple demodulation cycles.

Each pixel's well depth is 3.5×10^5 photoelectrons, corresponding to 5.6 nA

at the maximum rate of 1M exposures per second [285]. However, activating an offset compensation circuit in the camera allows detection of photocurrents up to 500 nA [277, 278, 286]. Considering the $\sim$ 50% optical fill factor of the sensor with micro-lenses and the $\sim$ 60% quantum efficiency at 700 nm [279], (the approximate center wavelength of the NV^- emission), the heliCam with offset compensation is expected to handle up to 3 μW incident light per pixel, or at most 270 mW over the full sensor.

In this work we demonstrate a first implementation of pulsed light readout with the heliCam. Figure 5.3.1 schematically outlines the application of DQ Ramsey sequences synchronized with the camera's I and Q exposures. We interleave two 4-Ramsey protocols, one on the I channel and one on the Q channel. The MW pulse phases are chosen so that the Q channel contains the negative magnetic field signal of the I channel. After N demodulation cycles, an I image and a Q image are produced. The signal on a given pixel in the I image is then

$$\mathcal{S}_I = \sum_{j=1}^{N} \left(S_{I+}^j - S_{I-}^j \right). \tag{5.2}$$

Normalization is accomplished frame-by-frame through subtracting the Q image from the I image and dividing by their sum, such that for a given pixel, the normalized signal is

$$\mathcal{S}_{\text{norm}} = \frac{\mathcal{S}_I - \mathcal{S}_Q}{\mathcal{S}_I + \mathcal{S}_Q}. \tag{5.3}$$

While the lock-in demodulation of each channel already cancels noise that couples to the PL signal additively, this normalization procedure also largely mitigates multiplicative noise.

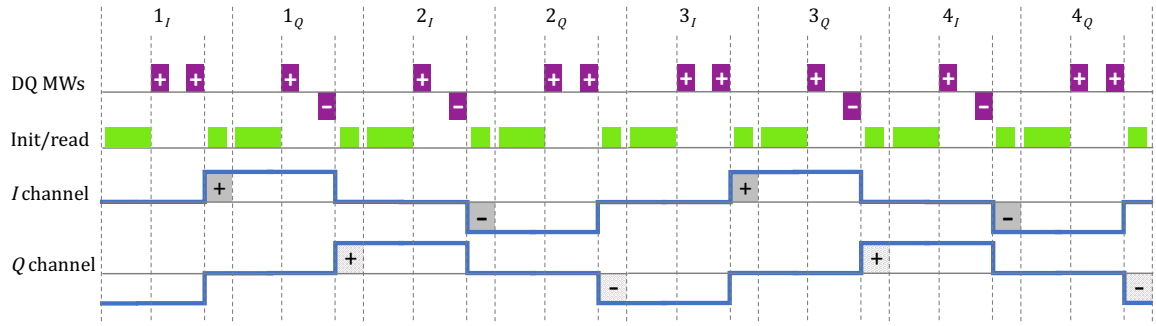

Figure 5.3.1: Schematic representation of DQ Ramsey magnetometry protocol synchronized with heliCam exposures. Shown here are two 4-Ramsey protocols, one on each of the in-phase (I) and quadrature (Q) channels of the heliCam, occurring over the course of two full demodulation cycles. The camera actively exposes only during the readout pulses and is blind to the fluorescence from the optical initialization periods. Chosen MW phases both cancel residual SQ coherence and ensure the Q channel contains the opposite magnetic field signal to the I channel. After N demodulation cycles, an I image and a Q image are produced. A noise-canceled magnetic field image is extracted by subtracting the Q image from the I image and dividing by their sum.

5.4 Experimental details

5.4.1 Diamond sample and bias field

The diamond employed in this work is an electronic grade ([N] $<$ 5 ppb) single crystal chip fabricated via chemical-vapor-deposition by Element Six Ltd. The crystal has rectangular dimensions 4.5 mm $\times$ 4.5 mm $\times$ 0.5 mm with $\langle 110 \rangle$ side facets and a $\{100\}$ top facet. The diamond side facets are mechanically polished to an optical quality. The top 10 µm of material is grown with an isotopically purified carbon source (99.99% ^{12}C) and isotopically purified nitrogen (99.97% ^{15}N) introduced, resulting in [^{15}N] $\approx$ 10 ppm and residual [^{14}N] $\approx$ 0.5 ppm in the 10 µm layer. A total ^{15}NV concentration of $\sim$ 3 ppm is present in the layer after electron irradiation with energy 4.6 MeV and dose $\sim 3 \times 10^{18}$ e$^-$/cm^2 followed by annealing in vacuum for 12 hours at 800 °C and 12 hours at 1000 °C.

The diamond is affixed to a 2”-diameter, 330-µm-thick semi-insulating silicon carbide (SiC) heat spreader. The SiC wafer is attached via mechanical pressure to a 0.04”-thick tungsten sheet, which is mounted to an aluminum breadboard on a three-

axis translation stage. A pair of temperature-compensated samarium cobalt ring magnets (SuperMagnetMan) produce a bias magnetic field at the diamond. The custom-designed magnets have 2.75" outer diameter, 2" inner diameter, and 0.5" thickness. The magnets are enclosed in custom 3D-printed holders and mounted along the vertical axis in the lab frame to produce a magnetic field of 6.45 mT along the diamond's [100] axis, herein called the diamond z-axis. The bias field overlaps the resonances from the four NV^- orientations in the diamond crystal, centering their ODMR features at 2.777 and 2.986 GHz. The ensemble-NV^- imager is sensitive primarily to magnetic fields along this same diamond z-axis.

5.4.2 Optical setup

The optical setup for the Ramsey imager is depicted in Figure 5.4.1. A Sprout-H diode-pumped solid state (DPSS) laser from Lighthouse Photonics outputs up to 10 W of 532 nm light. A 500 mm lens focuses the beam to a 74 μm waist ($1/e^2$ radius) at the position of a 250 MHz acousto-optic modulator (AOM, Gooch & Housego AOMO-3250-220). The first-order diffracted beam is then shaped to produce a roughly circular illumination spot at the diamond top surface, while the zeroth order beam is blocked by a beam block and an iris. The diffracted beam passes through a cylindrical lens (f_x = 130 mm, where x is the horizontal axis perpendicular to beam propagation) and is then reflected by a mirror (Thorlabs, E02-coated) toward the diamond at $\approx 20^\circ$ to its top surface. A 100 mm best-form lens (Thorlabs A-coated) focuses the beam toward the $\langle 110 \rangle$ side facet of the diamond, where it enters and undergoes total-internal reflection. The beam profile as a function of optical path length for the present design is shown in Figure 5.4.2a, simulated assuming Gaussian beam propagation in free space and the thin lens approximation. In Figure 5.4.2b the beam entrance angle, the angle inside the diamond, and the elliptical beam radii are shown. The beam's projection on the top diamond surface at the NV^--rich layer is designed to have an intensity profile along both horizontal directions with full-width at half maximum (FWHM) of 100 μm. In practice, we expand the excitation spot by translating the diamond away from the position of the beam focus. For the magnetic

images recorded in this chapter, the detected PL originates from an imaging spot with approximate FWHM dimensions 250 μm × 300 μm. The wider dimensions of the PL spot compared to the designed excitation spot could be due to a combination of lens positioning errors, deviation of lens behavior from the ideal thin lens approximation, and NV^- saturation effects.

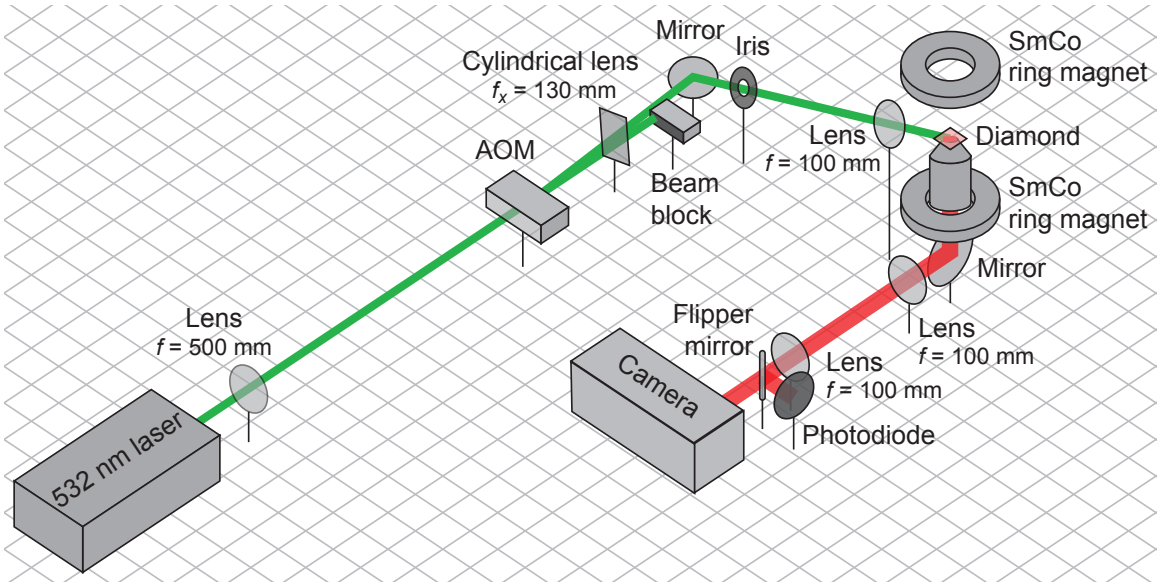

Figure 5.4.1: Ramsey imager optical setup. Up to 10 W of 532 nm CW light is generated by a Sprout-H DPSS laser (Lighthouse Photonics). After a 500 mm lens (Thorlabs, A-coated), the beam passes through a 250 MHz AOM (Gooch & Housego AOMO-3250-220). The zeroth order beam is blocked by a beam block and an iris, while the first-order diffracted beam passes through a cylindrical lens (Thorlabs, A-coated, $f_x = 130$ mm) to generate an elliptical beam at the diamond (see Figure 5.4.2). A mirror (Thorlabs, E02-coated), directs the beam toward the diamond at $\approx 20°$ to the diamond top surface. A 100 mm best-form lens (Thorlabs A-coated) focuses the beam at the diamond center. A pair of temperature-compensated samarium cobalt ring magnets (SuperMagnetMan) produce a 6.45 mT magnetic field along the vertical [100] direction. PL from the NV^--rich layer is collected by a 0.75 NA 20× air objective (Nikon), directed by a protected silver mirror (Thorlabs) through a telescope comprising a pair of 100 mm lenses (Thorlabs, B-coated), toward a flipper mirror (Thorlabs, protected silver), which determines whether the PL is directed toward a photodiode (Thorlabs DET-100A) or the lock-in camera (Heliotis heliCam C3). Long-pass filters (633 nm, Semrock) at the camera and the photodiode block any scattered 532 nm light from being detected.

PL from the NV^--rich layer is collected by a 0.75 NA 20× air objective (Nikon 0500-0087) and directed by a protected silver mirror (Thorlabs) through a telescope

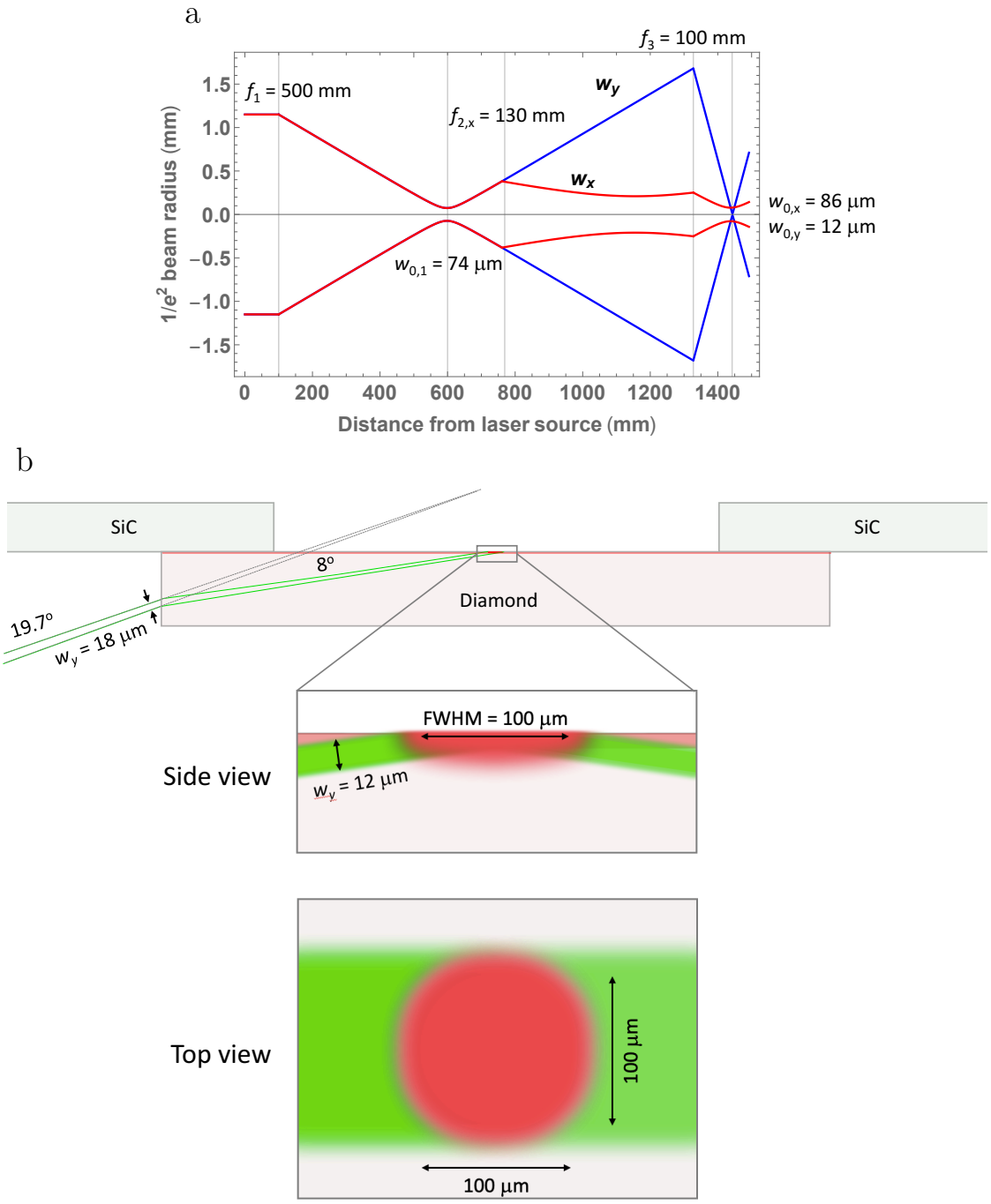

Figure 5.4.2: Excitation beam shaping for generating imaging spot on diamond. a) Simulated Gaussian profile of 532 nm excitation laser beam along x, the horizontal axis perpendicular to beam propagation, and y, the axis perpendicular to both beam propagation and x. The combination of three lenses produces a 74 µm beam waist at the position of the AOM (600 mm from the laser source), and an elliptical beam with waist $w_{0,x} = 86$ µm in x and $w_{0,y} = 12$ µm in y at the center of the diamond, $\approx$ 1440 mm from the laser source. b) Designed beam profile and propagation into diamond. Excitation laser travels within diamond at an angle of 8° from top surface and produces a spot at the NV$^-$-rich layer (zoomed-in side view and top view) with FWHM $\approx$ 100 µm in both horizontal dimensions.

comprising a pair of 100 mm lenses (Thorlabs, B-coated). The PL is then either incident on the lock-in camera, or reflected by a flipper mirror (Thorlabs, protected silver) toward a silicon biased photodiode (Thorlabs DET-100A). Two 633 nm long-pass filters (Semrock), one at the camera and one at the photodiode, ensure scattered 532 nm light is not detected. When PL is directed to the photodiode, the photocurrent is terminated into 50 Ω, producing a voltage digitized by a USB-6259 data acquisition (DAQ) module interfaced with the computer. PL detection on the photodiode from CW-ODMR, pulsed ODMR, and Ramsey sequences is used for system calibration and optimization, including magnet alignment, MW pulse duration calibration, and measurement of the NV$^-$ ensemble's T_2^* for selecting free precession intervals τ for SQ and DQ Ramsey protocols.

5.4.3 Electronic setup

Figure 5.4.3 shows the electronic equipment employed in the present work. A PulseBlaster (PBESR-PRO-500) generates logic pulses for controlling MW and RF switches, photodiode signal DAQ timing, and lock-in camera frame triggering and demodulation timing. One PulseBlaster channel triggers sets of heliCam frame acquisitions, and another channel determines the lock-in demodulation cycle timing. AOM readout and initialization pulses and MW pulses are synchronized with the camera cycles, as shown in Figure 5.3.1. An Agilent E4430B synthesizer generates a 250 MHz tone for driving the AOM. The RF tone is passed through two RF switches in series (Mini-Circuits ZASWA-2-50DR+), with gating controlled by a single PulseBlaster output channel. After amplification (Mini-Circuits ZHL-03-5WF), 6.6 W of RF power is sent to the AOM, which gates the optical beam path to the diamond.

Two MW synthesizers (Agilent E8257D and E4422B) generate MW tones near 2.986 and 2.777 GHz to address the upper and lower NV$^-$ spin resonances respectively. All synthesizers and the PulseBlaster are synchronized to the Agilent E8257D's 10 MHz clock via a distribution amplifier (Stanford Research Systems FS735). Each MW tone is sent through a Teledyne 2-4.5 GHz isolator and then a power splitter (Mini-Circuits ZX10-2-42-S+). The two splitter outputs pass through phase shifters

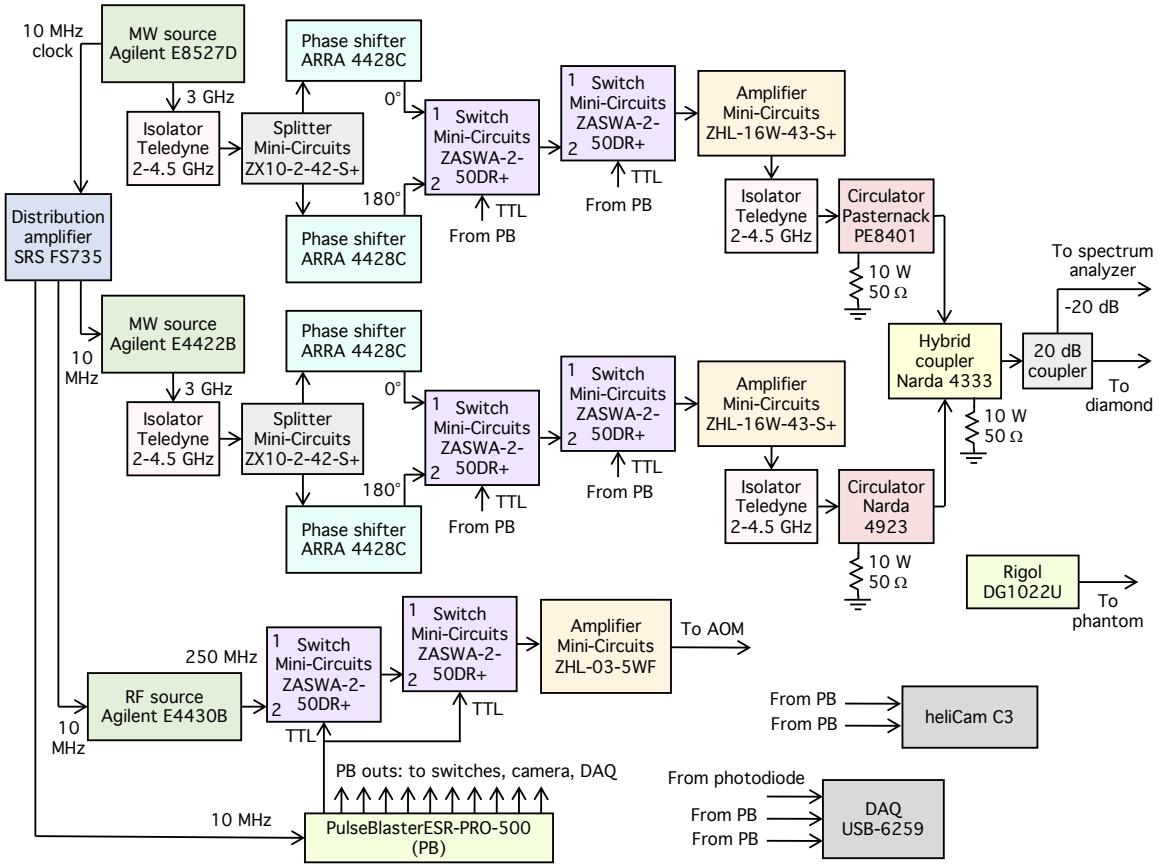

Figure 5.4.3: Electronic equipment for MW delivery, AOM gating, and signal detection in the broadband Ramsey imager. PulseBlaster (PB) outputs control MW gating, RF gating of the AOM, photodiode data acquisition (DAQ) timing, and heliCam triggering and demodulation timing.

(ARRA 4428C), which produce a 180° phase difference between the two signals. A switch (Mini-Circuits ZASWA-2-50DR+) controlled by a PulseBlaster channel passes either the 0° or the 180° signal to a second switch, where a second PulseBlaster channel gates the MWs. The passed MW signal is amplified (Mini-Circuits ZHL-16W-43-S+) and then sent through another Teledyne 2-4.5 GHz isolator followed by a circulator (Pasternack PE8401 or Narda 4923, see Figure 5.4.3), which is terminated into 50 Ω. A hybrid coupler (Narda 4333), also terminated into 50 Ω, combines the two amplified MW signals. The MWs then pass through a 20 dB directional coupler, which picks off a portion for monitoring on a spectrum analyzer, and the rest is sent to the MW delivery structure at the diamond to drive the NV^- spin resonances.

5.4.4 Microwave delivery

Efficient MW delivery to the diamond is achieved via a gold structure fabricated on the SiC heat-spreader wafer. After patterning via photolithography, an 8 nm chromium adhesion layer followed by a 300 nm layer of gold is evaporated onto the wafer. The pattern is displayed in Figure 5.4.4. The MW delivery structure combines a co-planar waveguide design (with a same-surface ground plane) for impedance matching with an omega loop design for uniform B_1 fields across the magnetic imaging spot. The gap inside the loop contains a gold wire phantom fabricated on the same wafer via evaporation of 30 nm of gold on top of an 8 nm chromium layer. Two SMA to ultra-miniature coaxial connector (UMCC) adapter cables (Taoglas CAB.721) bring MWs to and from the gold structure. The UMCC connector ends (Molex 0734120110) are attached to the gold with silver epoxy (EPO-TEK H20E). After passing through the gold structure, the MWs are terminated into 50 Ω. Another SMA-to-UMCC adapter, which is silver-epoxied to the phantom leads, enables currents to be sent through the phantom. A Rigol DG1022U signal generator applies sinusoidal or square-wave voltages to the gold phantom, generating currents within the phantom and associated magnetic fields to be imaged.

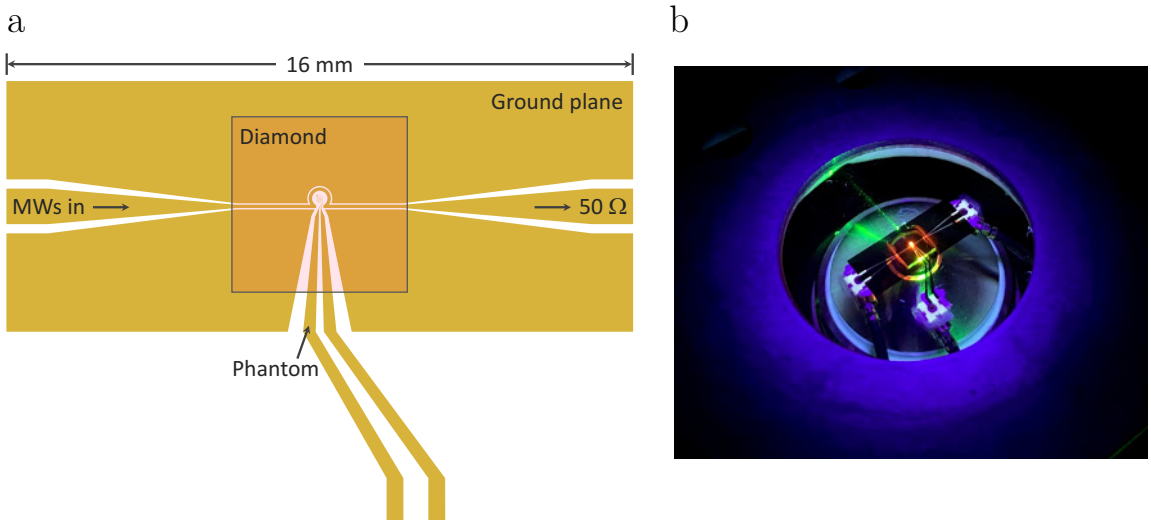

Figure 5.4.4: Microwave delivery structure and diamond for Ramsey imager. a) Fabricated gold MW delivery structure design, combining coplanar waveguide with omega loop. The gap inside the loop contains a fabricated gold wire phantom, which produces nontrivial magnetic fields at the NV^- sensing layer from applied currents. MW delivery structure is mounted to semi-insulating SiC wafer. b) Top-down image of diamond mounted to SiC wafer with MW delivery structure, which is affixed to tungsten mount. Diamond and mount are illuminated from above by blue LED. Green excitation laser (here shown at < 10 mW) enters from diamond side facet and focuses at center of gold omega loop, where phantom is located. PL from illuminated spot on NV^- sensing layer is collected by 0.75 NA air objective below. MWs are sent through omega loop to 50 Ω termination and currents are sent through phantom via SMA-to-UMCC adapter cables, with ends affixed to the gold leads via silver epoxy.

5.4.5 Phantom design and fabrication

Figure 5.4.5 shows the gold fabricated phantom. The phantom is designed in the shape of a cartoon snail in order to ensure that the magnetic fields produced by currents flowing through the phantom exhibit nontrivial spatial characteristics. A spiral pattern is chosen in particular because it is expected to generate fields along the diamond z-axis in the gaps between the gold traces that add constructively. In contrast, closed circular paths within the imaging spot are avoided, as they are expected to produce near-zero B_z fields in their center.

The phantom traces are 5 μm wide and 30 nm thick. The traces are designed to be 10× thinner than the MW structure in order to increase the phantom's resistance and minimize MW pickup. However, we observed that even this thin phantom interferes with MW delivery, causing nonuniform MW Rabi frequencies in its vicinity. Therefore, future iterations of the phantom will use an even more resistive material to produce neuron-like magnetic fields without interfering with MW delivery. We are presently investigating both palladium, which is $\approx 5\times$ more resistive than gold, and deposited graphene, which we estimate will result in a measured resistance $\sim 200\times$ higher than the present phantom.

5.5 Results

5.5.1 Lock-in camera characterization

We observe readout SNR on the heliCam consistent with shot noise, where the standard deviation (s.d.) of a set of images scales as the square root of the number of detected photons N per camera exposure. After confirming this scaling, we measure the conversion factor (CF) between photoelectrons and camera analog-digital units (ADU) as follows. For shot-noise-limited detection, the s.d. on each pixel in ADU scales as $\mathrm{CF}\sqrt{N}$, Because the heliCam is a lock-in camera, the signal scales not directly with the total number of detected photons N per exposure but rather the difference ΔN in detected photons between the positive and negative exposures in the

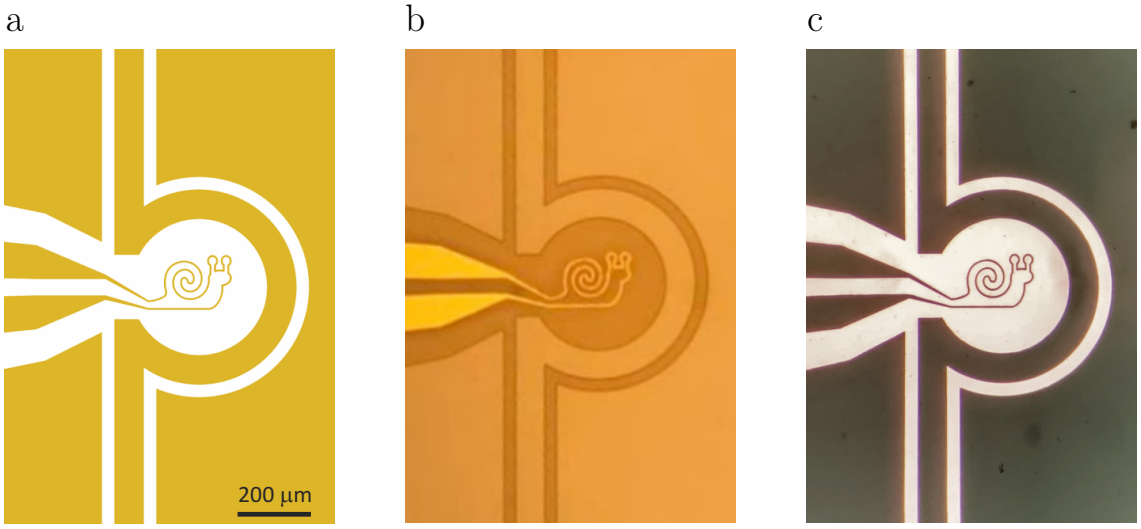

Figure 5.4.5: Fabricated wire phantom inside MW delivery structure. a) Phantom design drawing. Gold color represents where gold layers are deposited on SiC wafer. This phantom is shaped like a cartoon snail to ensure generation of fields with nontrivial spatial characteristics. Phantom wires taper to 5 µm width. b) Optical microscope image of phantom and photoresist patterned above it. After 30 nm of gold is evaporated and lifted off to reveal the phantom, a second photolithography step produces the pattern for the MW loop. The pattern covers the phantom and the darker regions in the image. c) After a 300 nm gold layer is evaporated onto the wafer, liftoff reveals the MW omega loop structure and the phantom, shown in this optical microscope image.

demodulation cycle, as CFΔN. Therefore, we perform two sets of measurements, one extracting the noise scaling constant and one extracting the signal scaling constant. For the noise measurement we vary N by varying the AOM readout pulse duration t, as $N \propto t$. We then record a characteristic pixel's s.d. for each value of t and find the slope A_{noise} of the linear relationship between $(\text{s.d.})^2$ and t. For the signal measurement, we vary the number of photons ΔN contributing to the signal on the I channel $\mathcal{S}_I$ by introducing a variable difference Δt in the AOM pulse duration on the positive and negative exposures. We find the slope A_{sig} of the linear relationship between $\mathcal{S}_I$ and Δt. By varying t for the noise measurement and Δt for the signal measurement and recognizing that $\Delta N/N = \Delta t/t$, we can deduce the conversion factor CF:

$$\begin{aligned} (\text{s.d.})^2 &= A_{\text{noise}}\, t = (\text{CF})^2 N \\ \mathcal{S}_I &= A_{\text{sig}}\, \Delta t = \text{CF}\Delta N \\ \text{CF} &= \frac{A_{\text{noise}}}{A_{\text{sig}}}. \end{aligned} \tag{5.4}$$

For typical operating conditions - 50 kHz lock-in frequency and 14 demodulation cycles per frame - we find $1/\text{CF} = 460 \pm 30$ photoelectrons per ADU at unity camera gain. Phantom magnetic images were recorded at the maximum camera gain of 3 in order to fill the camera's dynamic range, and thus for these images $1/\text{CF}_{\text{max}} = 153 \pm 10$ photoelectrons per ADU.

5.5.2 Strain-free double-quantum imaging

Double-quantum coherence magnetometry is particularly advantageous for magnetic field imaging when the NV-diamond material exhibits strain gradients over the field of view. As an example, Figure 5.5.1 shows an image of the dephasing time T_2^* from a strained region of diamond for both SQ and DQ Ramsey measurements. Not only is $T_{2\,\text{SQ}}^*$ shorter than $2T_{2\,\text{DQ}}^*$ (and even shorter than $T_{2\,\text{DQ}}^*$ in some regions), but the variation in $T_{2\,\text{SQ}}^*$ and associated variation in ODMR line centers limits the achievable imaging sensitivity [85]. The optimal precession time τ and detuning Δ

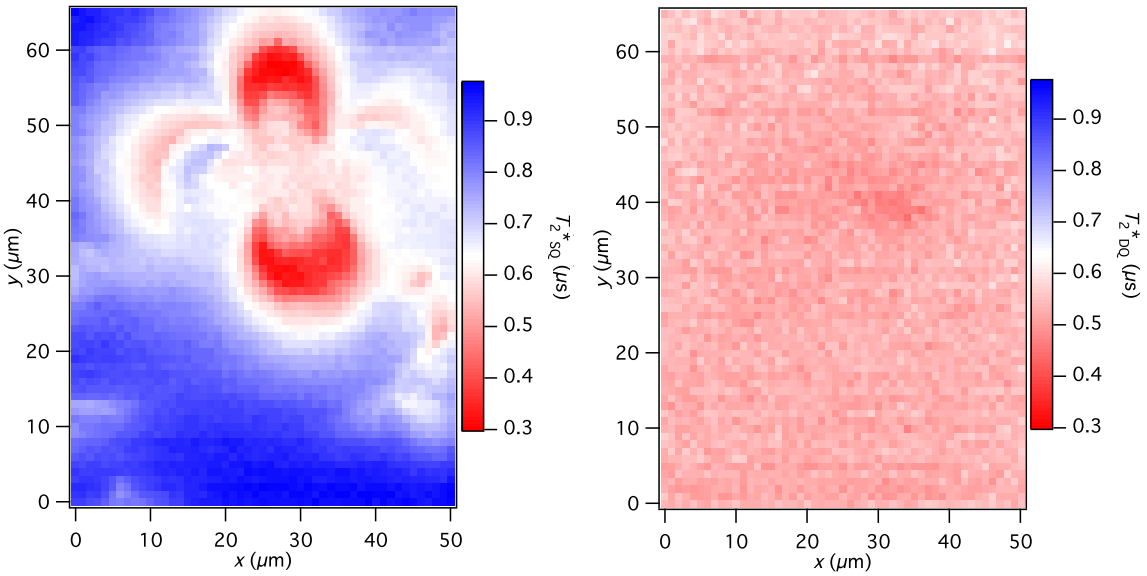

Figure 5.5.1: SQ and DQ T_2^* image in a strained region of diamond. $T_{2\,\mathrm{SQ}}^*$ values provide a measure of the ODMR line center shifts over the image, where higher gradients correspond to degraded magnetic field sensitivity. $T_{2\,\mathrm{DQ}}^*$ values are insensitive to strain (see Section 6.1.2), resulting in more uniform sensitivity over the field of view. Images here are taken with heliCam on a diamond sample similar to the sample employed for phantom magnetic imaging (see text).

from resonance varies across the SQ image, and yet only one choice of τ and Δ can be made for a parallel imaging measurement, meaning that most areas of the diamond will provide suboptimal sensitivity. Meanwhile, the DQ image is almost entirely insensitive to strain (see Section 6.1.2), which enables uniform-sensitivity magnetic imaging even over common diamond strain features [85]. The diamond probed here is similar to the sample employed for double-quantum Ramsey phantom current imaging: a $[^{15}\mathrm{N}] = 10$ ppm, 40 μm-thick layer CVD-grown on electronic grade diamond by Element Six, irradiated with 3×10^{18} $\mathrm{e}^-/\mathrm{cm}^2$ at 1 MeV and annealed for 12 hours at 800 °C and 12 hours at 1000 °C.

5.5.3 Phantom magnetic field imaging

By performing double-quantum 4-Ramsey magnetic imaging with the heliCam, we produce magnetic field images of currents in the gold snail-shaped phantom. The imaging excitation spot on the NV^- layer is measured, based on the known phantom

dimensions, to be roughly 250 μm × 300 μm (FWHM). With the 532 nm laser operating at output power 3 W, we estimate ≈ 2 W incident on the NV^- layer after the AOM, mirror, lenses, and reflection at the air-diamond interface. Accounting for the 8° beam propagation angle with respect to the diamond top surface, the average intensity over the imaging region is estimated to be ∼ 0.14 mW/μm^2. The PL is imaged onto the camera, where each pixel corresponds to 3 μm × 3 μm.

After matching the single-quantum Rabi frequencies for both transitions, we measure a double-quantum Rabi image. The DQ Rabi frequency is observed to be highly inhomogeneous over the image, with characteristic Rabi oscillation decay times ∼ 100 ns. The inhomogeneity is attributed to MW pickup by the conductive phantom, causing both gradients in the MW intensity and variations in the B_1-field direction over the image. For a characteristic DQ Rabi frequency of $2\pi \times 6$ MHz over the imaging region, we select 84 ns DQ π-pulse durations.

We choose a free-precession time $\tau = 504$ ns, which corresponds to DQ Ramsey fringe extremum when MWs address the upper and lower spin transitions at frequencies midway between each transition's ^{15}N hyperfine-split resonances. For finite overhead time, the optimal precession time is between $T_2^*/2$ and T_2^*, so this choice is near optimal for the present diamond's DQ dephasing time $T_{2\,\mathrm{DQ}}^* = 800$ ns. We then choose an optimal detuning at this value of τ by sweeping the two MW frequencies in opposite directions, generating a double-quantum DC magnetometry curve, and choosing the smallest two-photon detuning that produces a zero-crossing of the curve (a point of maximum sensitivity).

We empirically select an optical readout time $t_R \approx 1$ μs and additional initialization time $t_I \approx 2$ μs in order to sufficiently detect and repolarize the spins without introducing excessive measurement overhead time. Each Ramsey sequence is contained within the duration of a quarter period of the heliCam's demodulation cycle, which is chosen to be 5.3 μs to ensure that the readout pulses are contained within - and the initialization pulses are isolated from - the heliCam exposures. The camera's lock-in frequency is thus 47.2 kHz.

Figure 5.5.2 shows a DQ magnetic image of a 20 Hz sinusoidal 260 μA root-mean-

square (RMS) current in the phantom. The image is produced by taking the standard deviation (s.d.) of 400 frames recorded at 2.95 kHz, where each frame consists of a sum over $N = 16$ demodulation cycles of duration 21.2 μs. Every demodulation cycle contains four double-quantum Ramsey sequences, two on the I channel and two on the Q channel. Each of the 400 frames is made up of the normalized difference of an I image and a Q image (Equation 5.2). As a 4-Ramsey protocol performed on both channels occurs over two demodulation cycles (Figure 5.3.1), each frame contains signals from eight 4-Ramsey repetitions on each channel, i.e., 64 Ramsey sequences total.

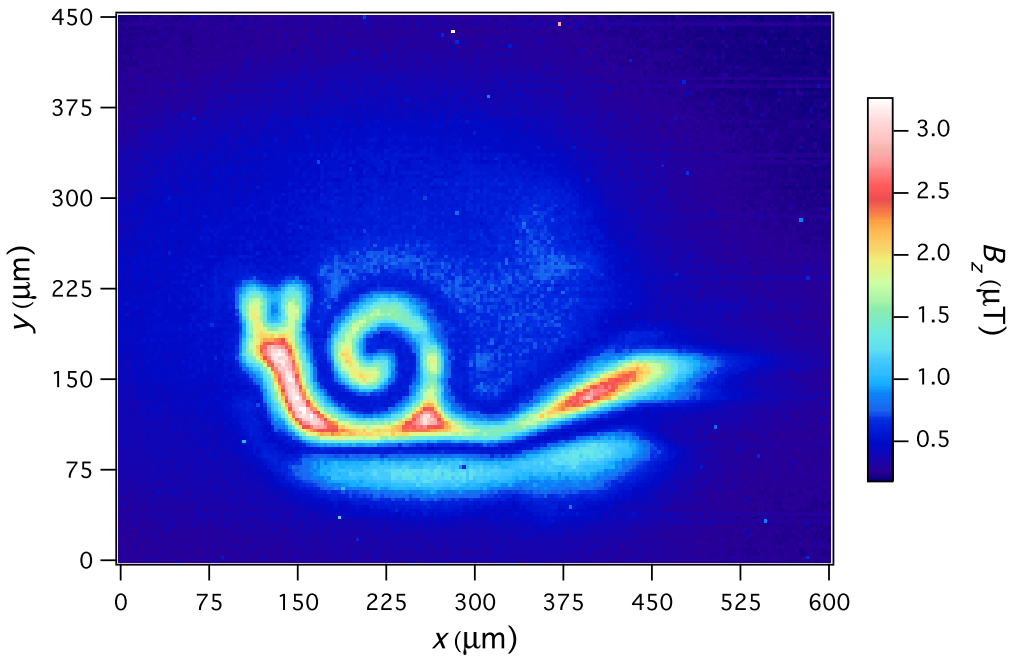

Figure 5.5.2: Double-quantum Ramsey magnetic field image of phantom. Standard deviation (s.d.) of 400 frames recorded over 136 ms at 2.95 kHz, where each frame comprises 64 double-quantum Ramsey sequences split between the I and Q channels over 14 demodulation cycles of duration 21.2 μs. A 260 μA-RMS 20 Hz sinusoidal current flows through the gold phantom, and RMS fields along the diamond z-axis of up to ≈ 3 μT are detected. The image is mirrored with respect to the phantom images in Figure 5.4.5 because the fields are imaged through the diamond. The s.d. is slightly increased in the center of the frame with respect to the edges due to photon shot noise on the detected PL. The volume-normalized magnetic field sensitivity [24] is ~ 100 nT $\mu m^{3/2} Hz^{1/2}$.

The image's spatial resolution is limited by the 10 μm sensing layer and possibly

also by collecting the PL through the 500 μ diamond substrate thickness [287]. For improved spatial resolution, a diamond with a thinner layer of NV^--rich material, and or a thinner diamond substrate, could be employed. Additional spatial field information could be obtained by reconfiguring the magnetic imager for full vector magnetometry. Although the heliCam is incompatible with simultaneous vector magnetometry [25], high-speed sequential addressing of the four NV^- crystallographic orientations should be straightforward to implement.

The measurement bandwidth is limited by the camera's frame rate. Although the image displayed here results from a 20 Hz signal, we observe signals at frequencies up to 1.5 kHz without significant attenuation. We measure signals from both sine waves and square waves, where the latter provides a test of the broad sensing bandwidth, and we intend in future experiments to apply pulsed currents to mimic the magnetic signals from neurons [24].

The s.d. image in Figure 5.5.2 shows the detected RMS amplitude, which lacks information about the phase of the magnetic field signal. For example, although not visible in the s.d. image, we observe that the detected B_z field in the image region below the snail phantom has the opposite sign of the field within the phantom, as expected from Biot-Savart's law. The s.d. is also observed to be increased where the PL intensity is higher, as expected from photon shot noise. As described previously, in the absence of applied phantom currents, we observe the s.d. exhibits square-root scaling with the PL intensity and with the readout duration, suggesting shot-noise-limited performance.

Based on the DQ Ramsey magnetometry curve slope for a characteristic pixel, the measured noise in that pixel in the absence of an applied magnetic field, and the volume (3 μm × 3 μm × 10μm) of NV-diamond corresponding to each pixel, we measure the volume-normalized sensitivity to magnetic fields along the diamond z-axis to be $\sim$ 100 nT $\mu m^{3/2} Hz^{1/2}$ [24, 25]. We expect the sensitivity can be increased by one to two orders of magnitude through (i) improving the Rabi frequency homogeneity to increase the Ramsey contrast, (ii) increasing the PL collection rate by operating at higher laser power and improving the collection efficiency, and (iii) mitigating any

remaining noise sources limiting sensitivity.

5.6 Next steps and outlook

Here we have demonstrated high-speed imaging of magnetic fields from currents in fabricated wire phantoms. This project remains a work in progress, though, and many steps are required to realize the full potential of the imaging system and apply it to visualising broadband magnetic activity within biological systems. Technical improvements include optimizing the magnetic field sensitivity, as discussed above, and iterating on the phantom design to better approximate neuronal systems.

Additional next steps include performing high-speed vector magnetic imaging of phantom currents in order to reconstruct all three Cartesian magnetic field components over the image and to investigate whether separating the resonances from the four NV^- orientations improves the field reconstruction accuracy and spatial resolution. In addition, we aim to simulate the fields from phantom currents to confirm agreement with measured images. We will also simulate the detected phantom fields as a function of NV^- layer thickness to check that our measured images exhibit spatial resolution in fact limited by the layer thickness.

Applications of this system in biology include resolving action potentials in cultured mammalian neuron systems [209, 219] as well as current flow through cultures of patterned, interconnected cardiomyocytes [288, 289, 290, 291]. Magnetic measurements from these systems could inform magnetic models of electrically active cells and cell networks, which would contribute to basic biophysical understanding and could also aid medical research into, e.g., neurodegenerative diseases or neural plasticity. Finally, we envision condensed matter physics as an alternative application of a high-speed DQ Ramsey magnetic imager. For example, our system could enable real-time imaging of the dynamics of certain topologically non-trivial materials [276].

Chapter 6

Review of strategies to improve ensemble-NV$^-$ magnetic sensitivity

This chapter examines methods to enhance NV-diamond magnetometer sensitivity, with a principal focus on broadband DC magnetometry employing ensembles of NV$^-$ centers. A majority of this chapter is reproduced with modifications from Ref. [80].

6.1 Strategies to extend T_2^* and T_2

6.1.1 Dynamical decoupling for AC magnetometry

While this review primarily addresses the broadband DC sensing modality of ensemble-NV$^-$ magnetometers, many of the sensitivity-improvement techniques described herein can also be applied to detecting narrowband AC magnetic fields. Here we provide a brief overview of standard AC sensing schemes; we discuss several approaches to improving AC magnetic field sensitivity; and we highlight challenges unique to the AC sensing modality.

The Hahn echo (alternatively referred to as the spin echo) protocol, shown in Figure 6.1.1, builds upon the Ramsey protocol with an additional central MW π-pulse, which refocuses dephasing of the NV$^-$ spin ensemble [135]. The decay of spin coherence measured with this pulse sequence is characterized by T_2, which is typically one to two

orders of magnitude longer than T_2^* in NV$^-$ ensemble measurements (see Sections 2.1.2 and 2.2). Furthermore, while the refocusing pulse decouples the NV$^-$ spin from DC magnetic fields, its presence makes Hahn echo measurements particularly sensitive to oscillating magnetic fields with period T_B matching the spin interrogation time τ of the pulse sequence. In the ideal case where the three MW pulses are commensurate with the nodes of the AC magnetic field, the shot-noise-limited sensitivity of a Hahn-echo-based measurement is given by [103]:

$$\eta_{\text{echo}}^{\text{shot}} \approx \frac{\pi}{2} \frac{\hbar}{g_e \mu_{\text{B}}} \frac{1}{C e^{-(\tau/T_2)^p} \sqrt{\mathcal{N}}} \frac{\sqrt{t_I + \tau + t_R}}{\tau}, \tag{6.1}$$

where C is the measurement contrast prior to precession (see Section 1.5), p is a stretched exponential parameter set by ensemble averaging of the local NV$^-$ spin environments (see Section 2.1.6), and t_I and t_R are the optical initialization and readout times, respectively. For more realistic measurements in which the pulse sequence cannot be phase-locked to the AC magnetic field, the magnetic sensitivity is degraded by $\sqrt{2}$.

The shot-noise-limited sensitivity given by Equation 6.1 has several key differences to that of a Ramsey-based DC sensing protocol (Equation 1.46). First, since typically $T_2 \gg T_2^*$, AC sensing schemes can achieve better sensitivity than DC sensing schemes. Second, choice of spin interrogation time τ is more straightforward for Ramsey schemes than for echo-based schemes. For Ramsey-based sensing of DC or quasi-static fields, $\tau \sim T_2^*$ is optimal (Section 2.1.7). In contrast, while $\tau \sim T_2$ is optimal for Hahn-echo-based protocols, τ should also be matched to the period T_B of the AC magnetic field to be measured. As a result the scheme is maximally sensitive to fields of period $T_B \sim T_2$, with a detection bandwidth set by the relevant filter function [293]. Finally, coherent interactions between the NV$^-$ spin and other spin impurities in the diamond can modulate the Hahn-echo coherence envelope. At best, these effects introduce collapses and revivals that do not affect T_2 and merely complicate the NV$^-$ magnetometer's ability to measure AC magnetic fields of arbitrary frequency. Collapse-and-revival dynamics occur for diamond samples containing a

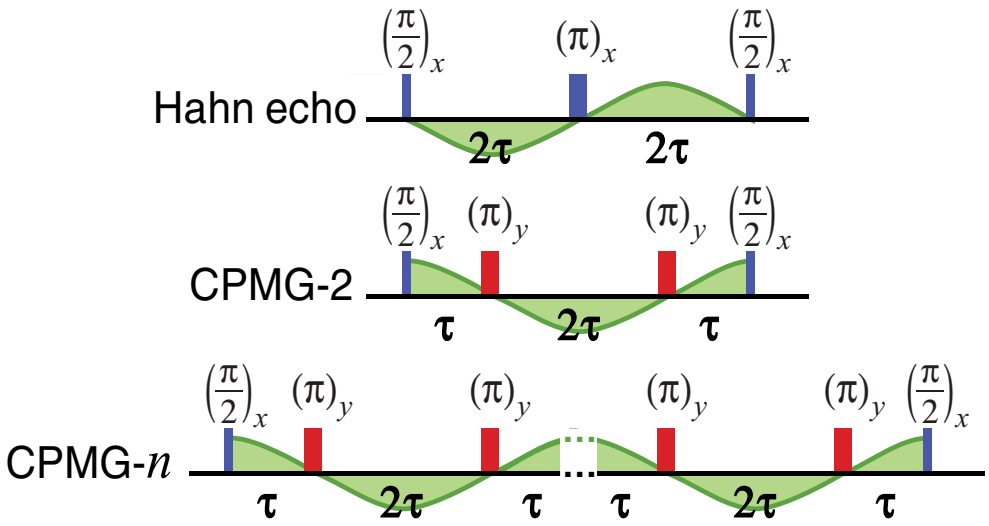

Figure 6.1.1: Select pulse sequences for AC magnetometry. The Hahn echo sequence includes a refocusing π-pulse midway through the spin interrogation time, allowing phase-sensitive lock-in-type measurements of AC magnetic fields (top). Hahn echo is maximally sensitive to AC fields with nodes coincident with the three MW pulses. Detection of AC fields with the quadrature phase can be achieved using the Carr-Purcell-Meiboom-Gill-2 (CPMG-2) sequence (middle). Employing additional π-pulses (CPMG-n) achieves more efficient decoupling of the NV^- from substitutional nitrogen and other paramagnetic defects in the diamond and provides sensitivity to higher-frequency AC magnetic fields (bottom). From Ref. [292].

natural abundance of ^{13}C, when the bias magnetic field is aligned to the NV$^-$ symmetry axis such that the ^{13}C Larmor precession sets the oscillation frequency. At worst, misalignment between the bias magnetic field and different NV$^-$ symmetry axes results in anisotropic hyperfine interactions, which can enhance the nuclear-spin Larmor precession rate for both ^{13}C (as a function of ^{13}C-NV$^-$ spacing) and ^{15}N (in ^{15}NV-diamonds) [294, 295]. These effects ensemble average to an effectively shorter coherence time T_2 [153], which degrades AC sensitivity.

Despite these differences, the Ramsey and spin-echo measurement schemes share many of the same components; consequently, many techniques for improving spin readout fidelity (analyzed in Section 6.2) apply to both DC and AC sensing modalities. For example, ancilla-assisted repetitive readout (Section 6.2.3), level-anticrossing-assisted readout (Section 6.2.4), and improved fluorescence collection methods (Section 6.2.5) increase the number of detected photons per measurement $\mathcal{N}$; preferential NV$^-$ orientation (Section 7.7) enhances the measurement contrast C; and spin-to-charge-conversion (SCC) readout (Section 6.2.1) and NV$^-$ charge state optimization (Section 7.2) increase both C and $\mathcal{N}$. We note that because typically $T_2 \gg T_2^*$, advanced readout techniques such as repetitive readout and SCC readout presently offer greater sensitivity improvement for AC schemes than for DC schemes, as their long-readout-time requirements introduce smaller fractional overhead in AC measurements with longer spin interrogation times.

Additionally, techniques to extend T_2^* for DC and broadband magnetometry may also improve AC magnetic field sensitivity. For example, double-quantum (DQ) coherence magnetometry (Section 6.1.2) is expected to improve AC sensitivity both by introducing a 2× increase in the NV$^-$ spin precession rate [104, 215] and, in certain cases, by extending the NV$^-$ coherence time T_2 [129]. Similarly, spin bath driving (Section 6.1.3) and operation at a sufficiently strong bias magnetic field (Section 6.1.4) may extend T_2 by suppressing magnetic and electric/strain noise, respectively.

Another technique for enhancing NV$^-$ magnetic sensitivity, unique to the AC sensing modality, is the application of multi-pulse sequences, whose timing is based on the Carr-Purcell-Meiboom-Gill (CPMG) family of pulse sequences well-known in

NMR [293, 103] (see Figure 6.1.1). By applying additional MW π-pulses at a rate of $\frac{1}{2T_B}$, these multi-pulse sequences (i) extend the NV$^-$ coherence time T_2 by more effectively decoupling the NV$^-$ spins from magnetic noise and (ii) increase the time during which the NV$^-$ spins interrogate the AC magnetic field. The coherence time has been found to scale with a power law s ($T_2 \rightarrow T_2^{(k)} = T_2 k^s$) as a function of the number of pulses k [292], where s is set by the noise spectrum of the decohering spin bath and is typically sub-linear. For example, a bath of electronic spins, such as N_S^0 defects in diamond, exhibits a Lorentzian noise spectrum and results in a power-law scaling of the coherence time with $s = 2/3$, when the electronic spin bath is the dominant decoherence source [139]. The shot-noise-limited multi-pulse sensitivity and the optimal number of pulses k_{opt} for an AC magnetic field with period T_B are given by

$$\eta_{\text{multi}}^{\text{shot}} \approx \frac{\pi\hbar}{2g_e\mu_B}\frac{1}{C\sqrt{\mathcal{N}}}\exp\left[\left(\frac{k^{(1-s)}T_B}{2T_2}\right)^p\right]\frac{1}{\sqrt{\frac{k}{2}T_B}}, \tag{6.2}$$

$$k_{\text{opt}} = \left[\frac{1}{2p(1-s)}\left(\frac{2T_2}{T_B}\right)^p\right]^{\frac{1}{p(1-s)}}, \tag{6.3}$$

assuming interrogation time $\tau = \frac{k}{2}T_B$, initialization and readout times $t_I, t_R \lesssim \tau$, and π-pulses commensurate with the nodes of the oscillating magnetic field. As before, the sensitivity is degraded by $\sqrt{2}$ when measuring AC magnetic fields with unknown or randomly fluctuating phase.

Equations 6.2 and 6.3 illustrate that multi-pulse measurement schemes improve sensitivity to magnetic fields with periods $T_B < T_2$ and enable sensing of higher frequencies than can be accessed with Hahn-echo-based measurements. For example, in Ref. [292], Pham *et al.* demonstrate a 10× improvement in ensemble AC sensitivity at 220 kHz by using a multi-pulse sequence, compared to Hahn echo. However, the increased number of control pulses, which are typically imperfect due to NV$^-$ hyperfine structure and inhomogeneities in the system, can result in cumulative pulse error and thus degraded AC sensitivity [138]. Compensating pulse sequences, including schemes in the XY-, concatenated, and BB-n families, may then be employed to restore AC field sensitivity [138, 137, 296, 297, 298].

A final consideration in the application of multi-pulse sequences for enhancing AC magnetometry with NV$^-$ centers is that extension of the T_2 coherence time (and thus enhancement of AC magnetic field sensitivity) is eventually limited by the T_1 spin-lattice relaxation time, beyond which increasing the number of π-pulses is ineffective. This limitation can be overcome by reducing the magnetometer operating temperature, thereby suppressing the two-phonon Raman process that dominates NV$^-$ spin-lattice relaxation near room temperature and extending T_1 [15]. Multi-pulse sequences performed at 77 K have demonstrated $> 100\times$ extensions in T_2 compared to room temperature measurements [245], and corresponding improvements to AC magnetic field sensitivity are expected.

6.1.2 Double-quantum coherence magnetometry

Standard NV$^-$ magnetometry techniques, such as CW-ODMR (Section 1.6.1), pulsed ODMR (Section 1.6.2), and pulsed Ramsey (Section 1.5.1) or echo-type schemes (Section 6.1.1), are typically performed in the pseudo-spin-$\frac{1}{2}$ *single-quantum* (SQ) subbasis of the NV$^-$ ground state, with the $m_s = 0$ and either the $m_s = +1$ or $m_s = -1$ spin state ($\Delta m_s = 1$) employed for sensing. In contrast, *double-quantum* (DQ) coherence magnetometry ($\Delta m_s = 2$) works as follows for a Ramsey-type implementation. First, a superposition of both $m_s = +1$ and $m_s = -1$ states (here termed the bright state $|B\rangle$) is prepared. Then, after a free precession interval, the final superposition state is projected onto a population difference between $|0\rangle$ and $|B\rangle$, and the population is read out optically.

Use of the full spin-1 nature of the NV$^-$ center and the double-quantum basis $\{-1, +1\}$ allows for several sensing advantages. First, at fixed magnetic field, an NV$^-$ spin prepared in a superposition of the $m_s = +1$ and $m_s = -1$ states precesses at twice the rate as in the standard $\{0, \pm 1\}$ basis, enabling enhanced magnetometer sensitivity. Moreover, measurements in the DQ basis are differential, in that noise sources perturbing the $|0\rangle \leftrightarrow |+1\rangle$ and $|0\rangle \leftrightarrow |-1\rangle$ transitions in common-mode are effectively rejected. Sources of common-mode noise may include temperature fluctuations, which enter the NV$^-$ Hamiltonian via the zero-field splitting parameter

D ($\frac{\partial D}{\partial T} \approx -74$ kHz/K) [91, 45, 55]; axial strain gradients; axial electric fields; and transverse magnetic fields. For a detailed discussion see Ref. [81].

If the spin bath environment is dominated by magnetic noise, as is common for high-nitrogen and natural ^{13}C abundance diamond samples, measurements in the DQ basis exhibit an increased linewidth and shortened associated dephasing time, as the 2× enhanced sensitivity to magnetic fields causes the spin ensemble to dephase twice as quickly as in the SQ basis, i.e., $T^*_{2,\mathrm{DQ}} \approx T^*_{2,\mathrm{SQ}}/2$. This increased dephasing and decoherence is confirmed experimentally for single NV$^-$ centers by the authors of Ref. [104], who observe a 2× decrease in T_2^*, and by the authors of Ref. [215], who observe a ≈2× decrease in the Hahn-echo coherence time T_2. Similar results are reported for NV$^-$ ensembles [184, 81].

Non-magnetic noise sources such as temperature fluctuations, electric field noise, and inhomogeneous strain may also contribute to spin dephasing (see Section 2.2). However, measurements in the DQ basis are insensitive to noise sources that shift the $|0\rangle \leftrightarrow |+1\rangle$ and $|0\rangle \leftrightarrow |-1\rangle$ spin transitions in common mode. When such noise sources dominate dephasing in the standard basis, the DQ dephasing time $T_{2,\mathrm{DQ}}$ may exceed $T_{2,\mathrm{SQ}}$, allowing for additional sensitivity improvement. For example, DQ measurements reported in Ref. [81] on NV$^-$ ensembles demonstrate a ∼ 6× increase in T_2^* (narrowing of linewidth) in an isotopically purified, low-nitrogen diamond, leading to an effective 13× enhancement in phase accumulation per measurement when considering the twice faster precession rate in the DQ basis. In Ref. [81], the standard SQ basis T_2^* is found to be limited by strain inhomogeneities, whereas the T_2^* value measured in the DQ basis is likely primarily limited by interactions with residual ^{13}C nuclear spins (∼ 100 ppm). This T_2^* limitation emphasizes the importance of isotopic purification when low-nitrogen samples are employed (see Section 2.2.3).

For AC magnetometry, dephasing due to strain inhomogeneities and temperature fluctuations can be largely alleviated by using Hahn echo or similar dynamical decoupling sequences (see Section 6.1.1) [103]. Nevertheless, double-quantum coherence magnetometry should still yield benefits. First, ensemble AC magnetometry benefits from the expected $\sqrt{2}$× sensitivity gain due to twice faster precession [104]. Sec-

ond, sensitivity may be further enhanced if $T_{2,\mathrm{DQ}}$ exceeds $T_{2,\mathrm{SQ}}/2$. For example, the authors of Ref. [129] observe $T_{2,\mathrm{SQ}} = 1.66 \pm 0.16$ ms and $T_{2,\mathrm{DQ}} = 2.36 \pm 0.09$ ms for single near-surface NV$^-$ center with $T_{2,\mathrm{SQ}}$ likely limited by electric field noise. In addition to magnetic sensing, measurements in the DQ basis can enhance sensitivity for temperature sensing [45] and noise spectroscopy applications [299, 72].

Implementation of double-quantum coherence magnetometry is a straightforward addition to standard pulsed magnetometry. The DQ technique requires applying MW pulses to drive transitions from the $m_s = 0$ state to both the $m_s = +1$ and $m_s = -1$ states. For sufficiently large magnetic fields, these two transitions must be addressed with separate and phase-locked MW frequencies [215, 129]. At low magnetic, electric, and strain fields, a single MW frequency is adequate [104]. In either case, care must be taken to ensure that both the upper and lower spin transitions are addressed with adequate MW pulses to achieve an equal superposition of the $m_s = +1$ and $m_s = -1$ states [215, 81]. While equal Rabi frequencies on the two transitions are desirable, the MW pulse durations may be adjusted to compensate for unequal Rabi frequencies. MW pulses for each spin transition may be applied sequentially [45] or simultaneously [104, 215, 81]. Due to the minimal increase in experimental complexity, the ability to suppress common-mode noise sources, and the increased spin precession rate, we expect DQ coherence magnetometry to become standard for high-performance pulsed-measurement DC magnetometers employing NV$^-$ ensembles.

6.1.3 Spin bath driving

Residual paramagnetic impurity spins in diamond contribute to NV$^-$ dephasing, thereby reducing T_2^*. This effect can be mitigated by directly driving the impurity spins, which is particularly useful when dynamical decoupling (see Section 6.1.1) of the NV$^-$ sensor spins is not applicable, such as in DC sensing protocols. This technique, termed spin bath driving, has been successfully demonstrated with substitutional nitrogen spins N_S^0 ($S = 1/2$) [132, 300, 81], and, due to the high typical concentrations of N_S^0 spins in NV-rich diamonds, we focus our discussion on this implementation.

In pulsed spin bath driving (see Figure 6.1.2a), a resonant π-pulse is applied to the N_S^0 spins halfway through the NV$^-$ Ramsey sequence, decoupling the N_S^0 spins from the NV$^-$ spins in analogy with a refocusing π-pulse in a spin echo sequence (see Figure 6.1.1) [132, 81]. Alternatively, the spin bath can be driven continuously (see Figure 6.1.2b) [132, 300, 81]. In the latter case, the driving Rabi frequency Ω_N must significantly exceed the NV$^-$-N_S^0 coupling rate γ_N, i.e., satisfy $\Omega_N/\gamma_N \gg 1$, to achieve effective decoupling. Under this condition, the nitrogen spins undergo many Rabi oscillations during the characteristic dipolar interaction time $1/\gamma_N$, where $\gamma_N \sim 2\pi \times (0.01 - 10)$ MHz for nitrogen concentrations in the $1 - 1000$ ppm range (see Section 2.2.1). As a result, the NV$^-$ ensemble is decoupled from the nitrogen spin bath and the NV$^-$ dephasing time is enhanced. This situation is similar to motional narrowing observed in many NMR and ESR systems, such as rotation- and diffusion-induced time-averaging of magnetic field imhomogeneities [146, 255].

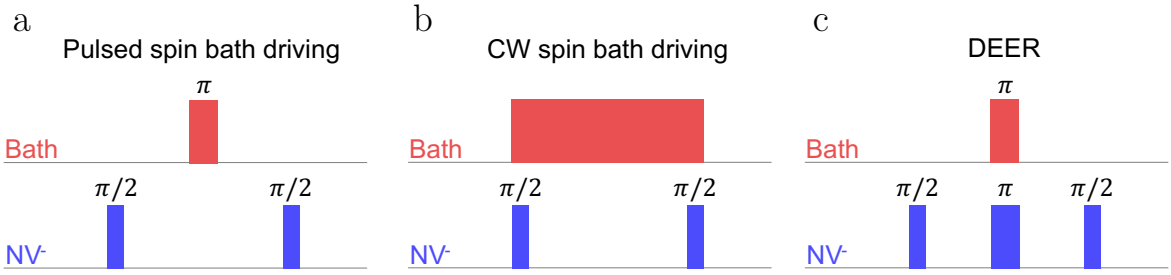

Figure 6.1.2: Selected pulse sequences for concurrent manipulation of NV$^-$ spins and the surrounding paramagnetic spin bath. a) Pulsed spin bath driving protocol combining a Ramsey sequence on the NV$^-$ center(s) with a central RF π-pulse on the spin bath. b) Continuous spin bath driving protocol combining a Ramsey sequence with continuous resonant RF spin bath drive. c) Double electron-electron resonance (DEER) protocol consisting of a Hahn echo sequence performed on the NV$^-$ center(s) combined with a resonant RF π-pulse performed on the spin bath. Recreated from Ref. [81].

The authors of Ref. [132] perform pulsed spin bath driving in a Type Ib diamond with $[N^T] \lesssim 200$ ppm and increase T_2^* for a single NV$^-$ 1.6×, from 278 ns to 450 ns. Similarly, in Ref. [300], T_2^* for an individual NV$^-$ is extended from 0.44 µs to 1.27 µs, a 2.9× improvement, using continuous spin bath driving in nanodiamonds with $[N] \lesssim 36$ ppm. An NV$^-$ ensemble study in Ref. [81] finds that if another mech-

anism, such as lattice strain or magnetic field gradients, is the dominant source of dephasing, spin bath driving becomes less effective, as shown in Figure 6.1.3 (see also Section 2.2). Nonetheless, at high nitrogen concentrations ($[N_S^T] \gtrsim 1$ ppm), NV$^-$ ensemble dephasing due to dipolar interaction with nitrogen spins can be greatly reduced by spin bath driving [81], in agreement with single-NV$^-$ results [132, 300].

To effectively suppress NV$^-$ dephasing, all nitrogen spin transitions must typically be driven. Elemental nitrogen occurs in two stable isotopes, ^{14}N with 99.6% natural isotopic abundance, and ^{15}N with 0.4% natural isotopic abundance. Diamonds may contain predominantly ^{14}N, where the 99.6% natural abundance purity is typically deemed sufficient, or ^{15}N, which requires isotopic purification. ^{14}N exhibits nuclear spin $I = 1$ while ^{15}N exhibits nuclear spin $I = 1/2$, resulting in 3 and 2 magnetic-dipole-allowed transitions for each isotope, respectively [154, 155, 156]. Like NV$^-$ centers, substitutional nitrogen defects possess a trigonal symmetry as a result of a Jahn-Teller distortion [301, 302, 303]. The Jahn-Teller distortion defines a symmetry axis along any of the 4 crystallographic [111] axes leading to 4 groups of N_S^0 spins. For a bias magnetic field B_0 larger than the substitutional nitrogen hyperfine interaction $A_{HF} \sim 100$ MHz, m_s and m_I are good quantum numbers, and the ^{14}N spectrum consequently exhibits up to 12 distinct resonances, which need to be driven [132, 304]. If B_0 is aligned with any of the diamond [111] axes, the 12 resonances reduce to 6 partially-degenerate groups with approximate amplitude ratio 1:3:1:3:3:1 (see Figure 6.1.4a). Similarly, the ^{15}N spectrum shows up to 8 distinct resonances, which reduce to 4 partially-degenerate groups with approximate amplitude ratio 1:3:3:1 in an aligned bias field B_0 (see Figure 6.1.4b). This technique is expected to be easiest to execute when the bias magnetic field B_0 and hyperfine coupling A_{HF} are not of the same order. When $\frac{g\mu_B}{h} B_0 \sim A_{HF}$, additional nuclear-spin-non-conserving transitions arise, resulting in reduced oscillator strength for the nuclear-spin-conserving transitions. Thus, given fixed RF power, the drive efficiency for each addressed transition decreases. Although spin bath driving has to date only been demonstrated in the regime $\frac{g\mu_B}{h} B_0 \gtrsim A_{HF}$ [132, 300, 81], driving in the $\frac{g\mu_B}{h} B_0 \ll A_{HF}$ regime is also expected to be effective.

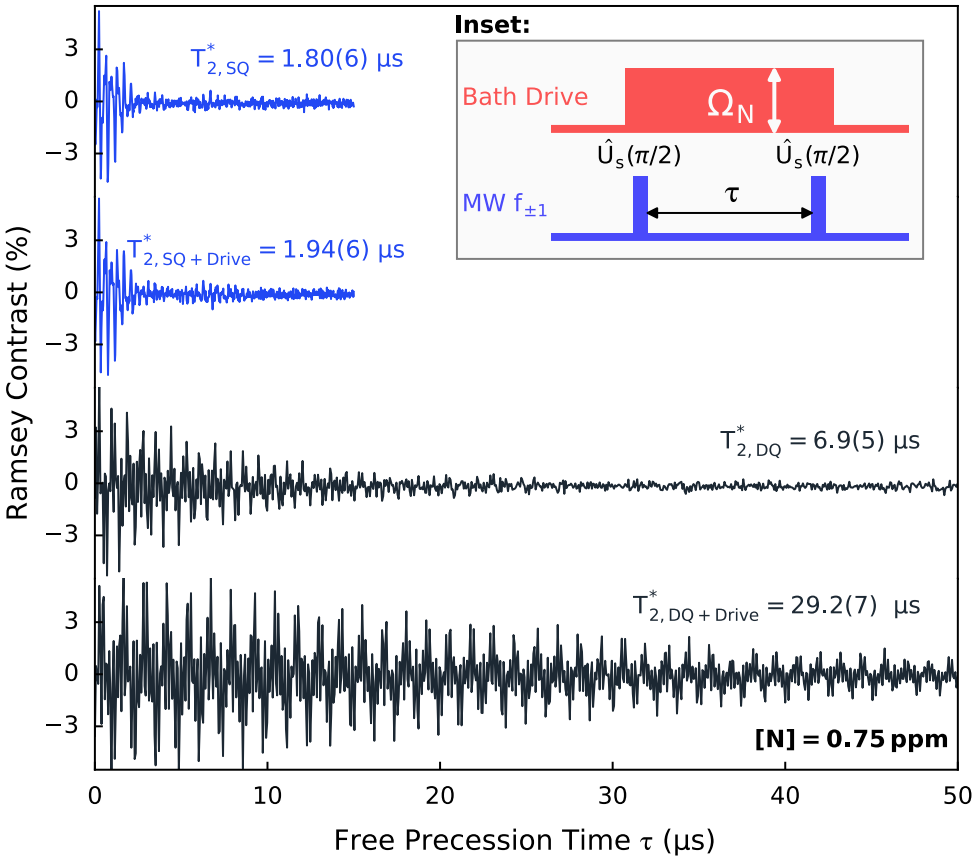

Figure 6.1.3: Ensemble free induction decay envelopes as measured using SQ and DQ Ramsey magnetometry, with and without continuous spin bath driving (inset). Measurements are shown for the following: in the SQ basis without spin bath driving (—, first from top); in the SQ basis with spin bath driving (—, second from top); in the DQ basis without spin bath driving (—, third from top); in the DQ basis with spin bath driving (—, fourth from top). Measurements in the DQ basis mitigate strain-induced dephasing while spin bath driving mitigates dipolar dephasing from the paramagnetic substitutional nitrogen in the diamond. The data illustrate the synergistic effect of combining DQ coherence magnetometry and spin bath driving; the aggregate approach vastly outperforms either technique employed independently. Even with twice faster precession, T_2^* is extended from 1.8 μs to 29 μs. From Ref. [81].

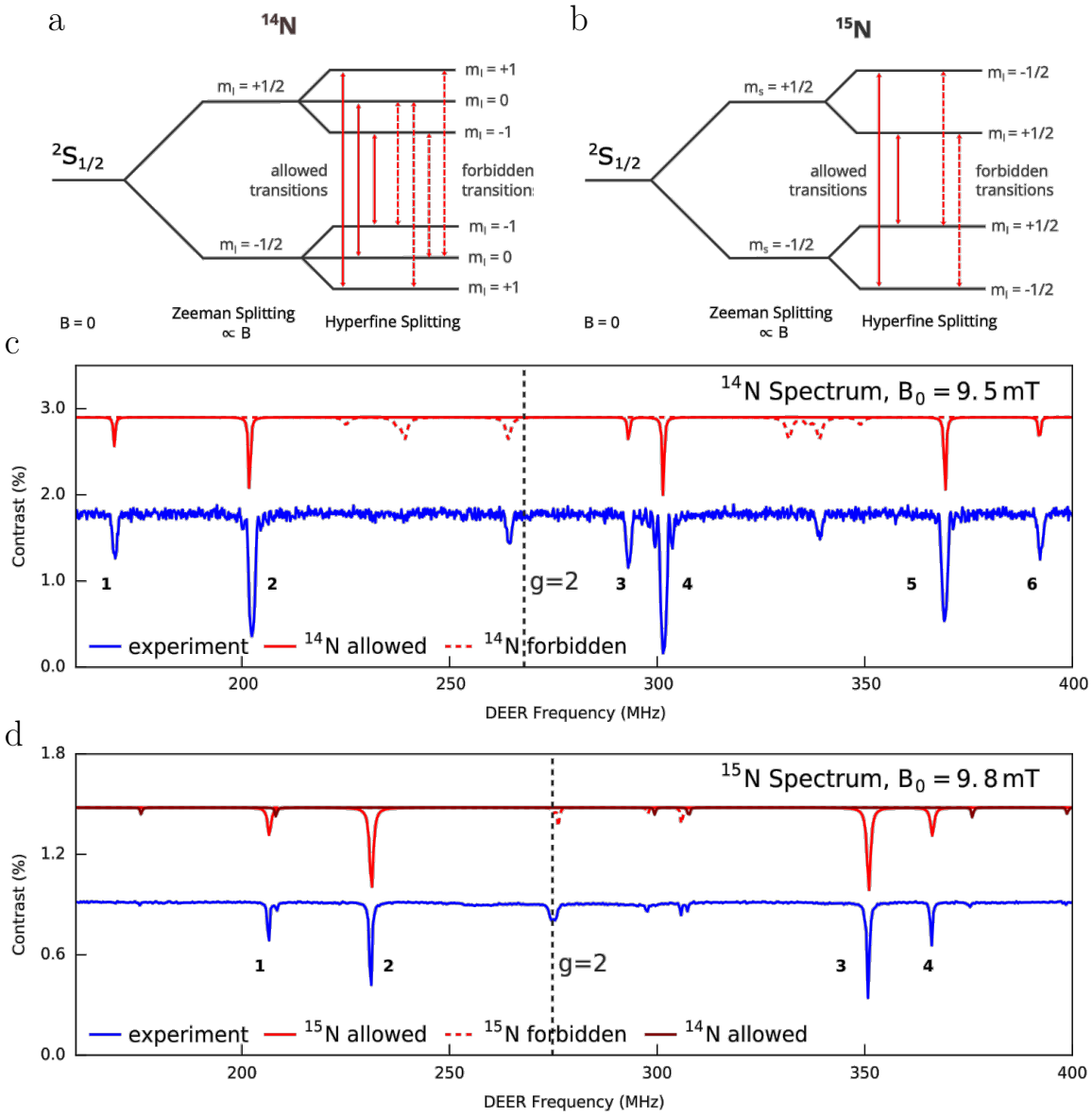

Figure 6.1.4: Substitutional nitrogen N_S^0 spin energy levels and associated double electron-electron resonance (DEER) spectra. a) Energy level diagram for $^{14}N_S^0$ spin showing allowed (—) and forbidden (---) transitions. b) Energy level diagram for $^{15}N_S^0$ spin showing allowed (—) and forbidden (---) transitions. c) Experimental $^{14}N_S^0$ DEER spectrum (—) and simulated $^{14}N_S^0$ DEER spectra showing allowed ($\Delta m_I = 0$) resonances (—) and forbidden ($\Delta m_I \neq 0$) resonances (---). d) Experimental DEER spectrum (—) in diamond with primarily $^{15}N_S^0$ and simulated DEER spectra showing $^{15}N_S^0$ allowed ($\Delta m_I = 0$) resonances (—), $^{15}N_S^0$ forbidden ($\Delta m_I \neq 0$) resonances (---), and allowed transitions residual $^{14}N_S^0$ impurities (—). In c and d the simulated resonance linewidths and amplitudes are chosen to approximately match the experimental data. Spectra are simulated for and experimentally measured in an external magnetic field aligned along the diamond crystallographic [111] axis. Adapted from Ref. [81].

The N_S^0 electron spin resonance spectra for ^{14}N and ^{15}N are readily observed in EPR experiments (see for example Ref. [154] and [305]). Alternatively, the nitrogen resonance spectra in a diamond can be characterized with NV^- centers using the double electron-electron resonance (DEER) technique [132, 81]. In this instance, the NV^- electronic spin is made sensitive to decoherence from N_S^0 target impurity spins via application of frequency-selective π-pulses at the targeted spins' resonance frequency. A schematic of the DEER pulse sequence is shown in Figure 6.1.2c, and the resulting DEER spectra for both nitrogen isotopes are compared in Figure 6.1.4. Extra resonance features associated with substitutional-nitrogen-related dipole-forbidden transitions and additional paramagnetic spins are also commonly observed, and may reveal additional sources of dephasing.

The experimental requirements for effective spin bath driving typically depend on the substitutional nitrogen concentration. At lower impurity concentrations, reduced spin bath drive strength (i.e., RF power) is needed to mitigate nitrogen-induced dephasing. However, dephasing mechanisms unrelated to nitrogen may exhibit larger relative contributions to T_2^* in this regime, limiting the achievable T_2^* increase from nitrogen spin bath driving. In particular, in samples with nitrogen content $[N_S^0] \lesssim 1$ ppm, lattice strain gradients may dominate the ensemble dephasing time, as is found in Ref. [81]. In this instance, strain-insensitive measurement techniques, such as double-quantum coherence magnetometry (see Section 6.1.2) must be employed for spin bath driving to extend T_2^*. In the intermediate regime ($[N_S^0] \sim 1$ ppm), where strain gradients and NV^- dipolar interactions with the nitrogen spin bath are of similar magnitude, neither spin bath driving nor DQ coherence magnetometry alone can achieve significant enhancement of the dephasing time. However, Ref. [81] demonstrates a $\sim 16\times$ improvement in T_2^* (effectively a $\sim 32\times$ improvement when considering the twice faster precession rate in the DQ basis) for a $[N_S^0] \simeq 0.75$ ppm diamond when both techniques are combined, as shown in Figure 6.1.5. In contrast, employing spin bath driving alone improves the dephasing time only by $\sim 1.1\times$ (see Figure 6.1.3), as strain-induced dephasing is left unmitigated.

In nitrogen-rich diamonds ($[N_S^0] \gtrsim 1$ ppm) achieving the motional narrowing con-

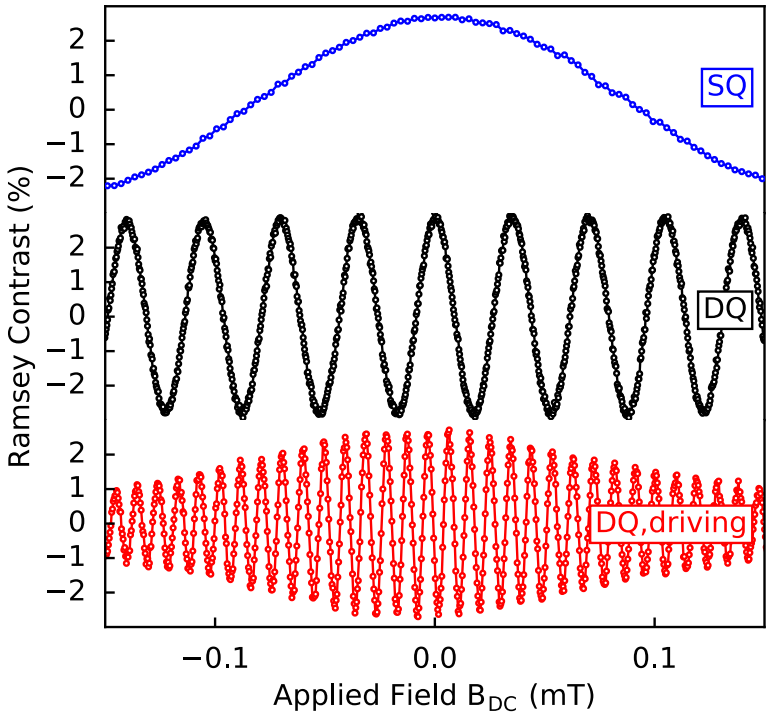

Figure 6.1.5: Ramsey interference fringes versus applied test magnetic field, measured in the SQ basis (—, top), DQ basis (—, middle), and DQ basis with N_S^0 spin bath driving (—, bottom). The longer dephasing times achieved when combining DQ coherence magnetometry and spin bath driving allow for denser Ramsey fringes and enhanced sensitivity. The decreased contrast for magnetic fields >0.05 mT in the bottom plot results from magnetic-field-induced detuning of the nitrogen spin resonances with respect to the RF drive frequencies. From Ref. [81].

dition $\Omega_N/\gamma_N \gg 1$ may be technically difficult; increases in $[N_S^0]$ necessitate linear proportional increases in Ω_N, which correspond to quadratic increases in the RF power required [81]. We expect both pulsed and continuous spin bath driving in nitrogen-rich samples to be ultimately limited by parasitic effects. These effects include induced AC Zeeman shifts, strain gradients, and sample heating due to the strong applied RF fields [300].

We note that spin bath driving should be applicable to any paramagnetic spin species in diamond, such as electronic dark spins, NV^- centers, or even nuclear spins. The effectiveness of the driving for dilute bath spins (fractional concentration $\ll 0.01$) is expected to depend on the target spin's concentration but not its gyromagnetic ratio, as both Ω_N and γ_N vary linearly with the target spin's gyromagnetic ratio. In other words, species with small gyromagnetic ratios are difficult to drive but also do not contribute much to dephasing for a given concentration [81]. Therefore, spin bath driving of the ^{13}C in a natural abundance diamond ($[^{13}C]$= 10700 ppm) is expected to be quite challenging [84]. Lastly, as the nitrogen spin bath contributes to T_2 decoherence [292, 174], nitrogen spin bath driving would be expected to extend the Hahn echo T_2, and, to a lesser extent, coherence times achieved with dynamical decoupling sequences [81], although neither application has been demonstrated at present.

6.1.4 Transverse strain and electric field suppression

Spatial and temporal variations in electric fields or in diamond crystal strain can degrade T_2^*, as described in Sections 2.2 and 6.1.2. Measurements performed in the NV^- spin's double-quantum basis are insensitive to variations in the *axial* components of the electric field E_z and spin-strain coupling $\mathcal{M}_z$, as these terms cause common-mode shifts in the spin resonance frequencies [57, 13]. In contrast, broadening due to *transverse* electric fields E_x, E_y and transverse spin-strain couplings $\mathcal{M}_x$ and $\mathcal{M}_y$ may remain in DQ measurements [57, 90]. However, by operating at a sufficiently strong axial bias magnetic field $B_{0,z}$, the resonance line broadening from E_x, E_y, $\mathcal{M}_x$, and $\mathcal{M}_y$ can be mitigated [94, 25], as illustrated in Figure 6.1.6 and discussed further in

Appendix B.

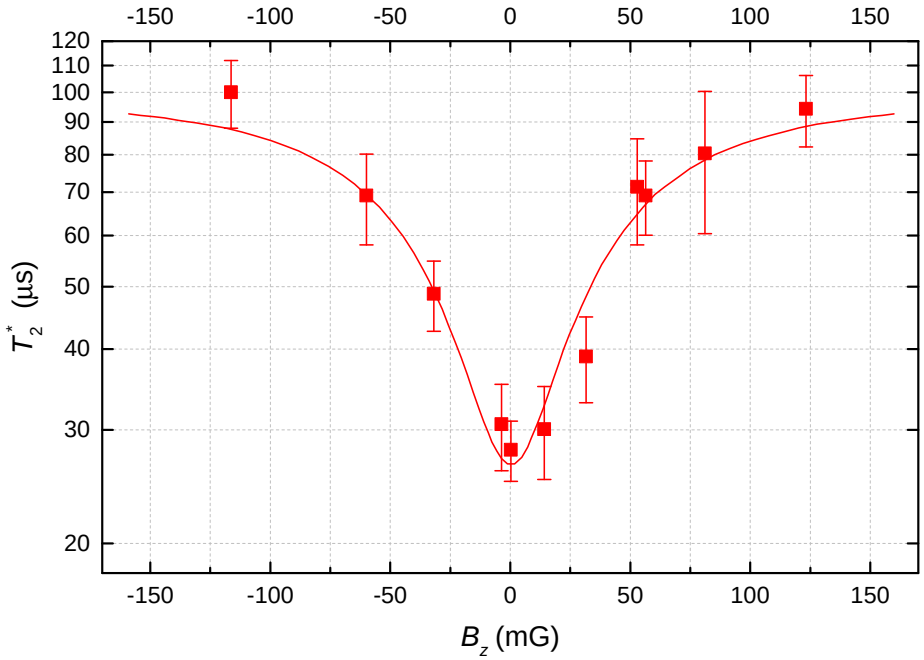

Figure 6.1.6: Suppression of dephasing from transverse electric fields and strain. For the single NV$^-$ center measured in Ref. [94], the dephasing time $T_2^{*\{\text{single}\}}$ at zero magnetic field is limited by electric field fluctuations transverse to the NV$^-$ symmetry axis, E_x and E_y. An applied axial magnetic field suppresses this source of dephasing by decoupling the NV$^-$ center from transverse electric fields and strain. For magnetic fields larger than $\sim$ 100 mG, the value of $T_2^{*\{\text{single}\}}$ is limited by magnetic noise, reaching $\sim$ 100 μs in this isotopically enriched, [^{13}C] = 20 ppm sample. For NV$^-$ ensembles at zero magnetic field, in addition to temporal fluctuations in E_x and E_y that limit $T_2^{*\{\text{single}\}}$, spatial variations in E_x and E_y and in the transverse spin-strain coupling terms $\mathcal{M}_x$ and $\mathcal{M}_y$ may also limit T_2^* for ensembles. Recreated from Ref. [94].

The net frequency shifts of the NV$^-$ ground state spin resonances due to transverse strain and electric fields at zero magnetic field are given by

$$\pm\xi_\perp = \pm\sqrt{\left(\frac{d_\perp E_x}{h} + \mathcal{M}_x\right)^2 + \left(\frac{d_\perp E_y}{h} + \mathcal{M}_y\right)^2}, \tag{6.4}$$

where $d_\perp = 0.17$ Hz/(V/m) [92, 56, 93] is the transverse electric dipole moment of the NV$^-$ ground state spin. Application of an external axial magnetic field $B_{0,z}$ introduces additional magnetic-field-dependent shifts and suppresses the effect of $\pm\xi_\perp$ on the spin resonances. When $\beta_z \equiv (g_e\mu_B/h)B_{0,z} \gg \xi_\perp$, contributions to T_2^* from temporal

fluctuations or spatial variations in $\xi_\perp$ [94, 104] are diminished (see Appendix B). For the nanodiamonds characterized in Ref. [94], with $\xi_\perp = 7$ MHz, $B_{0,z} \sim 30$ G is required to eliminate the contribution to T_2^* from transverse electric fields and strain. For the lower-strain bulk diamonds used in Refs. [104, 94], with $\xi_\perp \sim 10$ kHz, $B_{0,z} \lesssim 100$ mG is sufficient.

6.2 Strategies to improve readout fidelity

6.2.1 Spin-to-charge conversion readout

Spin-to-charge conversion (SCC) readout is an alternative to conventional fluorescence-based readout of the NV^- spin state. The technique has been demonstrated for single NVs [101, 105, 106, 122] and for small ensembles in nanodiamonds [306] and bulk diamond [307]. In SCC readout, the NV^- center's spin state is mapped optically onto the NV's neutral and negative charge states (NV^0 and NV^-). The charge state, and thus the original NV^- spin information, can then be accurately read out by exploiting differences in the NV^0 and NV^- wavelength-dependent excitation and associated fluorescence [308, 309]. Key advantages of SCC readout over conventional spin-state-dependent fluorescence readout are: (i), a slightly increased spin contrast [106]; and (ii), the ability to read out the charge state for extended durations and thus collect more photons per readout, leading to high-fidelity charge-state determination. Larger photon-numbers per readout reduce the relative contribution of shot noise to the measurement, allowing for readout fidelities within order unity of the spin-projection limit $\sigma_R = 1$ (see definition in Section 1.5).

Successful spin-to-charge conversion requires control of the NV charge state. Characterization of charge dynamics under optical excitation [308, 310, 311, 312] indicate power- and wavelength-selective photo-ionization processes, which allow for controlled switching between NV^- and NV^0. For example, green $\sim$532 nm light transfers single NV centers preferentially to NV^- with $70-75\%$ probability [309, 310, 308]; strong yellow $\sim$589 nm [306] or red $\sim$637 nm [101, 106] light can selectively ionize NV^- to NV^0 via absorption of two photons by an electron in the triplet ground state; and near-infrared $\sim$ 900 -1000 nm [105] can similarly ionize NV^- via absorption of two photons by an electron in the singlet metastable state. Readout of the NV^- charge state is commonly performed by applying weak yellow laser light at $\sim$594 nm. At intensities well below the NV^- saturation intensity $I_{\text{sat}} \sim 1$ - 3 mW/μm^2 [112], yellow light efficiently excites the NV^- electronic spin transition with zero phonon line (ZPL) at 637 nm without inducing ionization, while hardly exciting the NV^0 transition (with

ZPL at 575 nm) [309, 310, 308]. Through introduction of a photon-detection threshold combined with appropriate spectral filtering, NV^- (which fluoresces under the yellow excitation) may thus be distinguished from NV^0 (which produces little if any fluorescence). Figure 6.2.1a displays a photon-count histogram characteristic of single-NV charge readout reproduced from Ref. [313]. The clear separation of photon distributions from NV^0 and NV^- at low excitation powers allows charge-state determination with fidelity $> 99\%$ [123].

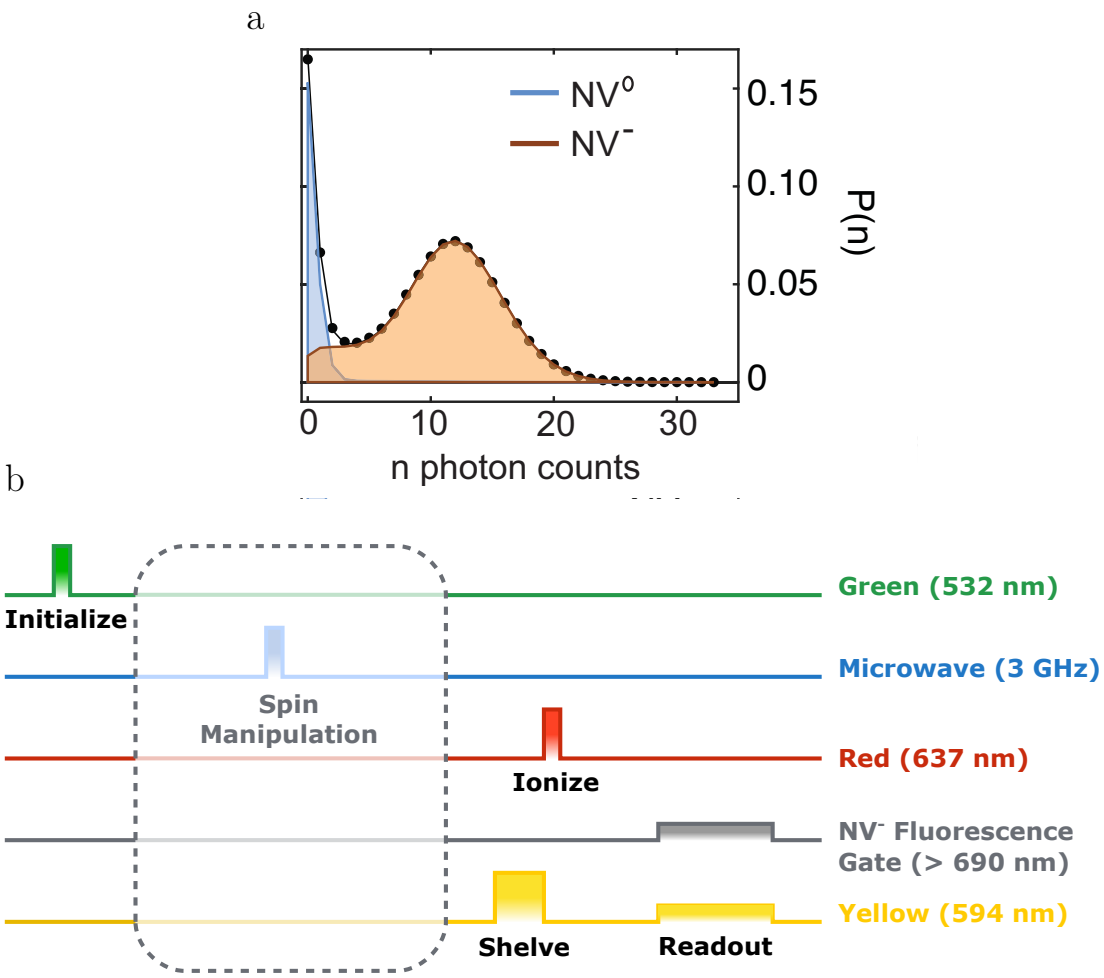

Figure 6.2.1: NV charge state readout and spin-to-charge conversion protocol. a) Probability histogram depicting photon emission from NV^0 and NV^- under weak yellow excitation. The striking difference in photon emission rate between NV^0 and NV^- allows the NV charge state to be determined with fidelity $\gtrsim 99\%$. Adapted from Ref. [313]. b) Schematic of the SCC readout protocol used by Shields *et al.* [101]. Adapted from Ref. [106]

.

The original work by Ref. [101] demonstrates SCC readout on a single NV center in Type IIa diamond nanobeams (see Appendix of Ref. [80] for an overview of diamond types). First, utilizing green laser light (see Figure 6.2.1b) and appropriate MWs, the NV center is prepared in the $m_s = 0$ or one of the $m_s = \pm 1$ spin states of the NV^- triplet electronic ground state. A moderate power, 594 nm yellow "shelving" pulse (145 μW, ~ 0.9 mW/μm^2) then excites the spin population to the triplet excited state. Due to the spin-dependent intersystem crossing from the triplet excited state, the $m_s = 0$ population is more likely to decay back to the ground state, whereas the $m_s = \pm 1$ population is more likely to be shelved into the metastable singlet states. The spin-to-charge conversion is then realized with a $\sim$10 ns high intensity resonant 637-nm pulse (22.5 mW, $\sim$140 mW/μm^2), which ionizes (i.e., converts NV^- to NV^0) the triplet ground state population, corresponding to $m_s = 0$, but leaves the shelved population corresponding to $m_s = \pm 1$ unaffected. Last, the NV charge state is read out by applying weak $\sim$594 nm light. The $\sim$594 nm light with lower energy than the NV^0 ZPL at 575 nm, ensures that only NV^- is excited while the weak intensity ($\sim 1 - 10$ μW, $\sim 6 - 60$ μW/μm^2, Figure 6.2.1a) ensures that NV^- is not ionized during readout.

The single-NV SCC result by Ref. [101] achieves a factor over spin projection noise $\sigma_R = 2.76$ ($\mathcal{F} = 1/\sigma_R = 0.36$, see comparison in Tab. 1.5.1). As the fidelity of the charge readout process itself approaches unity ($\mathcal{F}^{\mathrm{CR}} = 0.975$), the dominant inefficiency is attributed to the imperfect spin-to-charge conversion step ($\mathcal{F}^{\mathrm{SCC}} = 0.37$). Several alternative SCC readout variants have been demonstrated, providing similar sensitivity gains while offering reduced experimental complexity [306], or utilizing the singlet state for ionization [105]. For all SCC readout implementations, however, the improved values of σ_R come at the cost of substantially prolonged spin readout times t_R, which increase the sequence's overhead time and diminish the overall sensitivity improvement (see Section 1.5). For example, the best reported readout fidelity ($\mathcal{F} = 0.36$) [101] is achieved for readout times $t_R = 700$ μs, which exceed conventional fluorescence-based readout times ($t_R \sim 300$ ns) by $\sim 1000\times$. SCC readout is therefore most advantageous for measurement modalities with long sensing intervals (e.g.,

T_1 relaxometry and AC field sensing), where the penalty due to additional readout overhead is less severe. To date, the best SCC readout demonstrations improve field sensitivity only when interrogation times exceed ~ 10 μs [101, 306], which further motivates improvement of spin ensemble properties to achieve sufficiently long dephasing times (see Section 2.1.1).

Given the clear success of SCC readout with single NVs, application to NV^--rich ensembles is a logical progression, especially given the low conventional readout fidelities achieved for NV^--rich ensembles ($\mathcal{F} \lesssim 0.015$, see Tab. 1.5.1). However, the prospect for SCC readout to substantially improve $\mathcal{F}$ in NV^- ensembles likely hinges on whether the additional complex charge dynamics present in NV-rich diamonds can be mitigated [306]. Promising SCC readout results on small NV ensembles in Type Ib nanodiamonds demonstrate $\sigma_R = 20$, compared to $\sigma_R = 70$ with conventional readout in the same setup, allowing the authors to observe improved sensing performance for interrogations times > 6 μs [306]. However, this and other studies [47, 312] report intricate NV^- and NV^0 charge dynamics absent in single NV experiments. The effectiveness of SCC readout in the complex charge environment inherent to NV-rich ensembles (e.g., due to ionization and charge dynamics of substitutional nitrogen and other impurity defects) warrants further investigation (see Section 7.2). Nevertheless, SCC readout overcomes one sensing disadvantage specific to ensembles, namely that NV^- orientations not being used for sensing can be preferentially transferred to NV^0 during the ionization step. This results in reduced background fluorescence and potentially allows for an additional $\sim 2\times$ sensitivity improvement relative to conventional NV^- readout. Overall, beyond the long overhead times already discussed, SCC readout's demanding power requirements are expected to further hamper ensemble-based implementation. In particular, high required optical intensities ($\gtrsim 150$ mW/μm^2) [101, 105, 306] suggest scaling of SCC readout to larger bulk sample sizes ($\gtrsim 100 \times 100$ μm^2) will be challenging.

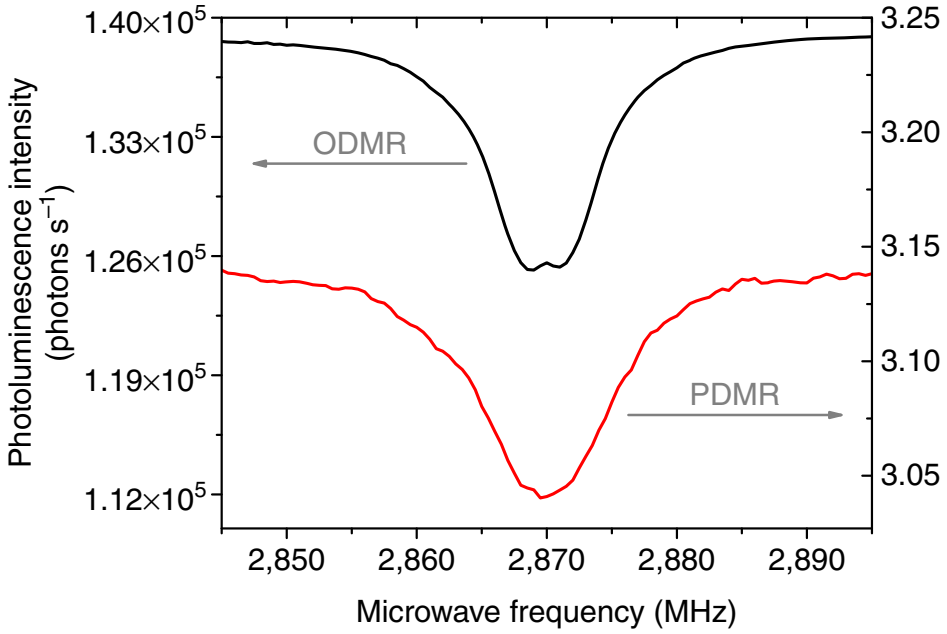

Figure 6.2.2: Photoelectrically detected magnetic resonance (PDMR) of NV^- centers. Spectra are simultaneously measured by ODMR (—) and PDMR (—) in the absence of an external magnetic field. From Ref. [314].

6.2.2 Photoelectric readout

Another method to interrogate the NV^- spin state is photoelectric (PE) readout, which relies on measuring a current of charge carriers resulting from NV^- photo-ionization [314, 315, 316, 317]. Since NV^- photo-ionization is spin-state dependent, (see Sections 6.2.1 and 7.2) [101], the spin state can be inferred from the photocurrent signal in analogy to fluorescence-based readout. Figure 6.2.2 shows a photoelectrically detected magnetic resonance (PDMR) spectrum measured simultaneously with an ODMR spectrum, from Ref. [314]. One promised benefit of PE readout is that the photoelectron collection efficiency can approach unity [314].

In PE readout, a bias voltage is applied across electrodes fabricated on the diamond surface. An excitation laser induces NV^- photo-ionization, and the ejected electrons generate a current, which is collected at the electrodes. NV^- photo-ionization may occur via single- or two-photon excitation. Single-photon ionization of the NV^- $^3A_2$ electronic ground state requires photon energies of 2.7 ± 0.1 eV or higher (wavelength $\lesssim$ 460 nm) [308, 316, 318, 319]. PE readout implementations employing lower

photon energies, such as from 532 nm (2.33 eV) light common for spin-state initialization, ionize the NV^- centers via a two-photon process, namely $^3A_2 \rightarrow {}^3E \rightarrow$ conduction band (see Figure 7.2.1) [320, 314, 315, 316]. Whereas the rate of single-photon ionization scales linearly with optical intensity [311], two-photon ionization depends quadratically on intensity [308].

Optically illuminating the diamond for PE readout may also induce background photocurrent from ionization of other defects present in the sample. Most unfortunately, 532 nm green light ionizes substitutional nitrogen N_S^0 defects in a single-photon process [320]. The background N_S^0 photocurrent may exceed the signal NV^- photocurrent, resulting in poor NV^- measurement contrast. This problem is exacerbated for excitation intensities well below the NV^- saturation intensity, where two-photon NV^- ionization may be weak compared to single-photon ionization of N_S^0, and at elevated nitrogen concentrations $[N_S^0] \gg [NV^-]$ [316, 318].

Multiple approaches can partially mitigate the unwanted photocurrent associated with N_S^0 ionization. For example, lock-in techniques can remove the DC background from the nitrogen photocurrent [315]. Additionally, a shorter-wavelength laser can be employed to induce single-photon ionization from the NV^- $^3A_2$ state, thereby improving the NV^- ionization rate relative to that of N_S^0. However, the authors of Ref. [316] observe that under optimized experimental conditions, single-photon ionization using 450 nm light provides no contrast improvement compared to two-photon ionization with 532 nm light.

A variety of challenges accompany implementation of PE readout, both for small NV^- ensembles [315, 314, 316, 317] and for envisioned extensions to larger detection volumes $\gtrsim (100\ \mu m)^3$ using NV-rich diamonds. In addition to background photocurrent from ionization of nitrogen and other defects, another expected obstacles to PE readout is electrical cross-talk between MW-delivery electrodes (used to manipulate the NV^- spin states) and photocurrent-detection electrodes [315]. Fluctuations in the applied electric field could also add additional measurement noise by coupling to fluctuations in photoelectric collection efficiency.

Scaling PE readout implementations to larger NV^- ensembles may introduce ad-

ditional challenges. Because the electrodes reside on the diamond surface, collecting photocurrent from NV^- centers located $\gtrsim$ 100 μm deep may prove difficult [314]. Achieving the necessary bias electric field strength and uniformity over $\gtrsim (100\ \mu m)^3$ volumes may also be challenging; bias electric field gradients across large detection volumes could reduce NV^- ensemble T_2^* values. Moreover, the presence of charge traps in NV-rich diamonds might hinder photoelectric collection efficiency (see Section 7.6), especially from deeper NV^- centers. In addition, Johnson noise in the readout electrodes may induce magnetic field fluctuations that could limit the achievable sensitivity [321].

In certain PE readout implementations, the detected signal amplitude may be increased by photoelectric gain, an intrinsic charge-carrier amplification arising from the diamond's charge dynamics and the electrode boundary conditions [314, 317, 322]. However, photoelectric gain is expected to be diminished in NV-rich diamonds due to charge traps, non-uniform electric fields, and space-charge limitations [314, 323, 322]. The applicability of photoelectric gain to improving PE readout fidelity in ensemble-based extensions remains to be shown. Although PE readout may prove beneficial for certain applications such as integrated quantum devices [324], this technique's utility for ensemble magnetometry in NV-rich diamonds remains uncertain.

6.2.3 Ancilla-assisted repetitive readout

In conventional readout, the fast ~ 500 ns repolarization of the NV^- electronic spin limits the number of photons an NV^- emits before all initial spin state information is lost (See Figure 1.5.2). Even when implementing conventional readout with the best present collection efficiencies, the average number of collected photons per NV^- center n_{avg} is less than 1, and for many implementations $n_{\mathrm{avg}} \ll 1$, making photon shot noise the dominant contributor to the parameter σ_R (see Equation 1.42, Tab. 1.5.1, Section 6.2.5). An alternative method to increase the readout fidelity $\mathcal{F} = 1/\sigma_R$ circumvents this problem by instead first mapping the initial NV^- electronic spin state information onto an ancilla nuclear spin. In the second step, the ancilla nuclear spin state is mapped back onto the electron spin, which is then detected using conven-

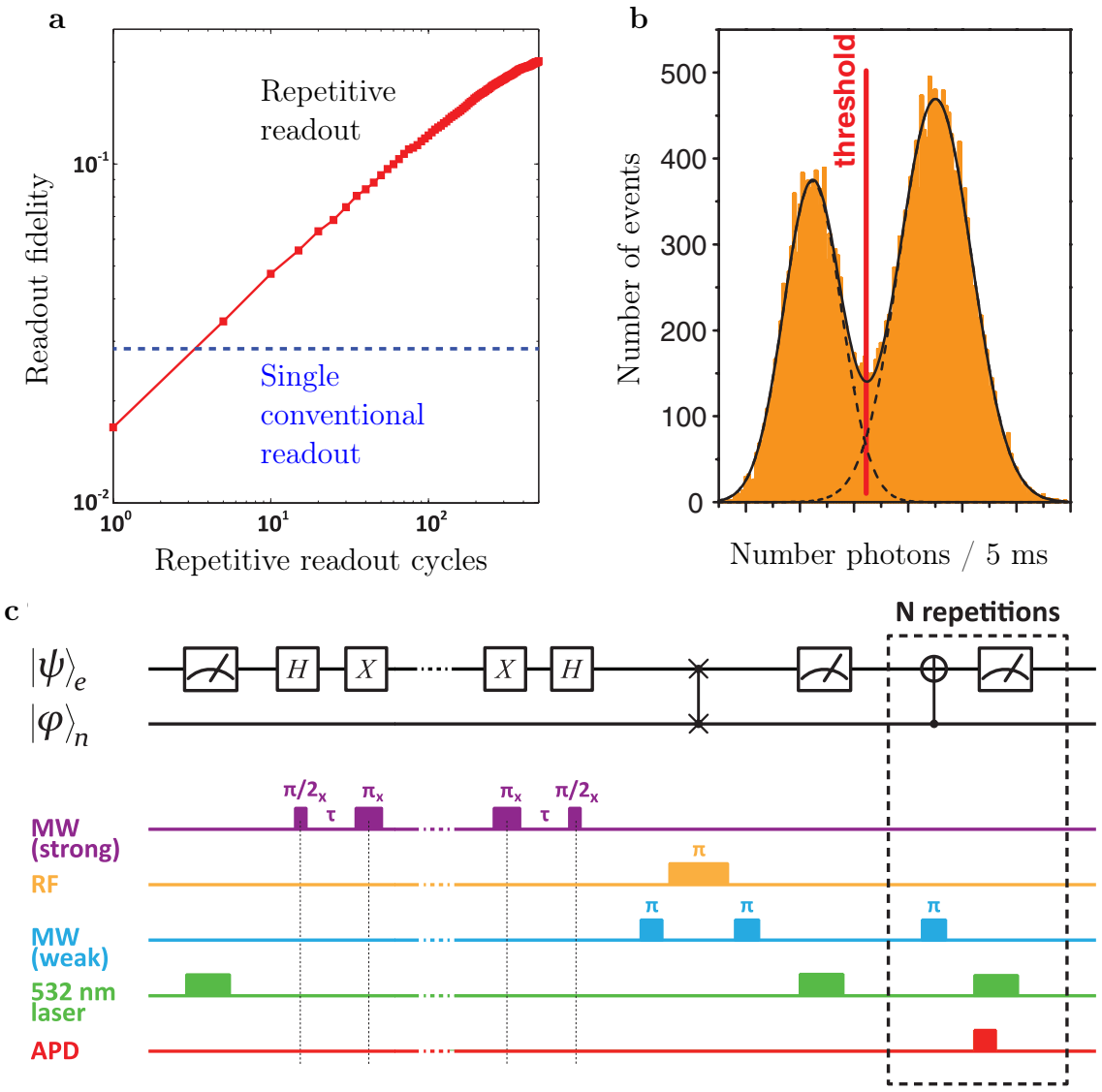

Figure 6.2.3: Overview of ancilla-assisted repetitive readout. a) Readout fidelity $\mathcal{F}$ is improved with the number of repetitive readout cycles. Fidelity for repetitive readout (red) is plotted relative to a single conventional readout (blue, dashed). From Ref. [32]. b) The clear difference in total number of collected photons associated with the initial m_s states allows determination of m_s with fidelity approaching 1 in some implementations. Here $\mathcal{F} \approx 0.92$ in Ref. [107]. From Ref. [107]. c) Quantum circuit diagram and magnetometry pulse sequence with detection via ancilla-assisted repetitive readout. Application of an RF π-pulse between two weak MW π-pulses maps the NV^- electronic spin superposition onto the ancilla nuclear spin. Subsequently the superposition state may be repeatedly mapped back onto the electronic spin via a weak MW π-pulse and optically read out without destroying the ancilla spin's quantum state. Adapted from Ref. [32].

tional fluorescence-based readout. This second step may be repeated many times with each marginal readout improving the aggregate readout fidelity, as shown in Figure 6.2.3a,b. While first demonstrated with a nearby ^{13}C nuclear spin as the ancilla [131], the technique was later realized using the NV$^-$ center's ^{14}N [107] and ^{15}N nuclear spin [32]. In the ^{13}C realization [131, 325], the coupling to the ancilla spin depends on the distance between the NV$^-$ defect and the nearby ^{13}C atom, making the technique difficult to implement for NV$^-$ ensembles where this distance varies. This discussion instead focuses on the more scalable realization using the NV$^-$ nitrogen nuclear spin as the ancilla, which ensures the electron spin to ancilla spin coupling remains fixed over the NV$^-$ ensemble.

Figure 6.2.3c shows a quantum circuit diagram from Ref. [32] depicting the repetitive readout scheme. After the final MW pulse in an NV$^-$ sensing protocol, the NV$^-$ electronic spin state (denoted by subscript e) is mapped onto the nitrogen nuclear spin state (subscript n). In Ref. [32], this mapping is achieved using a SWAP gate ($\mathrm{CNOT}_{e|n} - \mathrm{CNOT}_{n|e} - \mathrm{CNOT}_{e|n}$), where CNOT denotes a controlled NOT gate. The SWAP gate consists of a MW π-pulse, then an RF π-pulse, then another MW π-pulse, where the MW pulses flip the electronic spin and the RF pulse flips the nuclear spin. This procedure swaps the electronic and nuclear spin states, importantly, storing the electronic spin state information in the ancilla nuclear spin. Then an optical pulse re-polarizes the electronic spin to $m_s = 0$. Next, a set of repetitive readouts is performed. In each readout, the nuclear spin state is copied back onto the electronic spin with a MW pulse, (a $\mathrm{CNOT}_{e|n}$ gate), and then the electronic spin is optically read out without affecting the nuclear spin state. This process can be repeated many times ($\gtrsim 10^2$), and is limited in principle by the nuclear spin lifetime $T_{1,n}$. In Ref. [32], while the initial RF pulse used in the SWAP gate requires $\sim$ 50-60 µs, each readout cycle requires only $\sim$1 µs. The large number of readouts allow the aggregate readout fidelity $\mathcal{F} = 1/\sigma_R$ to approach 1; notably, Ref. [107] achieves $\mathcal{F} = 0.92$ ($\sigma_R = 1.1$) as depicted in Figure 6.2.3b.

Extending ancilla-assisted repetitive readout to ensembles is expected to be fruitful but necessitates overcoming further challenges. The scheme requires a large mag-

netic field to minimize coupling between the NV$^-$ nuclear and electronic spins, with Refs. [107, 32] employing fields of 2500 gauss and 6500 gauss respectively. Further, the bias magnetic field must be precisely aligned along a single NV$^-$ symmetry axis, presently precluding its use for sensing from more than one NV$^-$ orientation [25]. Even slight angular misalignments introduce measurement back action on the nuclear spin I_z, which spoils $T_{1,n}$ [107]. The reduction in $T_{1,n}$ limits the available readout duration. Ensemble implementations would therefore require highly uniform bias magnetic fields over ensemble sensing volumes, conceivably on the $\sim$ (100 μm)^3 scale. Engineering such fields is within current technical capability but difficult nevertheless, see 2.2 and Ref. [116]. Additionally, the MW and RF control pulses would ideally manipulate the entire ensemble uniformly; spatial inhomogeneities of the control pulses are likely to result in reduced readout fidelity unless mitigated [116]. Assuming sufficiently strong and homogeneous B_0 fields and MW driving can be realized, and that the additional overhead time is acceptable, repetitive readout appears to be a promising but technically demanding method to improve $\mathcal{F}$ for ensembles.

6.2.4 Level-anticrossing-assisted readout

In conventional readout [8], the readout fidelity $\mathcal{F} = 1/\sigma_R$ depends on the number of photons n_{avg} collected per measurement sequence (see Equation 1.42). The value of n_{avg} is limited by the time the spin population originally in the $m_s = \pm 1$ states spends shelved in the singlet state before decaying to the triplet $m_s = 0$ state. Steiner *et al.* engineer the NV$^-$ spin to pass through the singlet state multiple times before repolarization, extending the readout duration per sequence to increase n_{avg} [326], as depicted in Figure 6.2.4. Using NV$^-$ centers with ^{14}N, which has nuclear spin $I = 1$, three cycles through the singlet state occur during readout, yielding a $\sim 3\times$ increase in n_{avg} and thus a $\sim \sqrt{3}\times$ improvement in the fidelity $\mathcal{F}$. For NV$^-$ centers with ^{15}N with $I = 1/2$, the spin only passes twice through the singlet state before repolarization, yielding only a $\sim \sqrt{2}\times$ improvement in $\mathcal{F}$.

The technique is implemented as follows: the bias field B_0 is tuned to the excited-state level anticrossing at $B_{\text{LAC}} \approx 500$ G [113, 107] to allow resonant flip-flops between

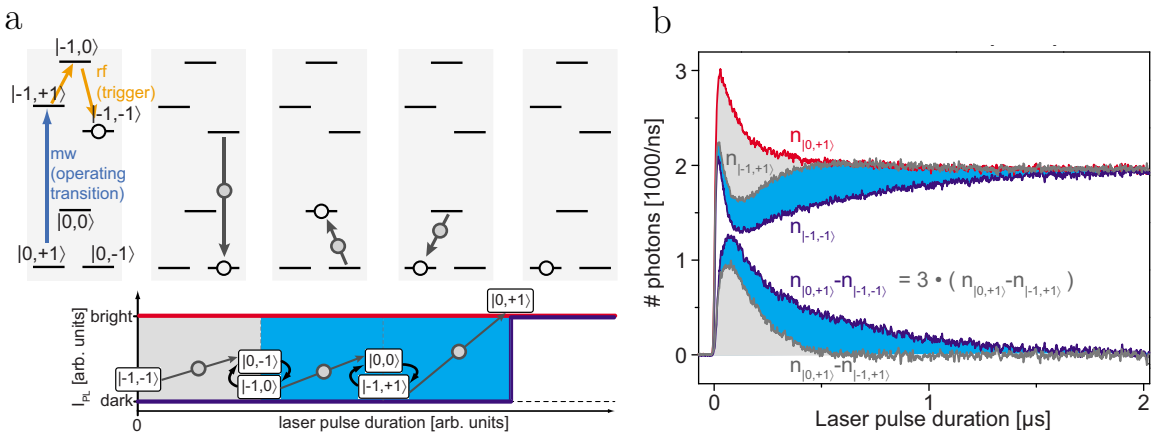

Figure 6.2.4: Level-anticrossing-assisted readout as demonstrated in Ref. [326]. At the excited-state level anticrossing near $B = 500$ G, green optical excitation polarizes NV$^-$ into the spin state $|m_s = 0, m_I = +1\rangle$. a) Upon completion of a sensing sequence, two RF pulses transfer population in the electronic spin state $|m_s = -1\rangle$ from the nuclear spin state $|m_I = +1\rangle$ to $|m_I = -1\rangle$ without affecting the $|m_s = 0\rangle$ state. During optical readout, this population passes three times through the singlet states before being repolarized to $|m_s = 0, m_I = +1\rangle$, increasing the time over which the state-dependent fluorescence contrast persists. b) Time-resolved photon detection comparing conventional readout (gray) and LAC-assisted readout (blue). The optimal readout duration is extended by 3× and the difference in detected photon number between the two spin states is increased by 3×. From Ref. [326].

the NV$^-$ center's electronic spin and its ^{14}N nuclear spin ($I = 1$). Operation at the level anticrossing polarizes the nuclear spin into the state $|m_I = +1\rangle$ [327]. At completion of a sensing sequence, immediately prior to readout, the NV$^-$ electronic spin occupies a superposition of the states $|m_s = 0, m_I = +1\rangle$ and $|m_s = -1, m_I = +1\rangle$. Before the NV$^-$ electronic spin state is read out using a conventional green laser pulse, two sequential RF π-pulses flip the nuclear spin into the $m_I = -1$ state, conditional on the electronic spin occupying the $m_s = -1$ state. This CNOT gate relies on the RF drive being resonant with the nuclear transitions between the m_I states for population in the $m_s = -1$ state and off-resonant for population in the $m_s = 0$ state. During readout, the population in $|m_s = -1, m_I = -1\rangle$ cycles through the long-lived singlet state three times before the information stored in the NV$^-$ electronic spin is lost, allowing more signal photons to be collected. After the first and second pass through the singlet to the $m_s = 0$ state, an electron-nuclear spin flip-flop returns the electronic spin state to $m_s = -1$, as shown in Figure 3a of Ref. [326], enabling another cycle

through the singlet state. The third pass repolarizes the NV$^-$ spin into the stable $|m_s = 0, m_I = +1\rangle$ state.

This technique's utility for magnetic sensing depends on whether the $\leqslant \sqrt{3}\times$ increase in fidelity $\mathcal{F}$ outweighs the cost of additional overhead time (see Equation 1.43) introduced by the RF pulses. Although the authors of Ref. [326] assert that microsecond-scale RF nuclear spin π-pulses are attainable, achieving such nuclear Rabi frequencies over large ensemble volumes $\sim (100\ \mu\text{m})^3$ may prove very difficult, making this method impractical for NV$^-$ ensembles with $T_2^* \lesssim 1\ \mu\text{s}$. Additional challenges for implementation with NV$^-$ ensembles include realizing the requisite uniformity in the MW/RF fields and in the 500 G bias magnetic field over ensemble volumes. Finally, the scheme presently precludes sensing from more than one NV orientation [25].

6.2.5 Improved photon collection methods

In the limit of low contrast, the readout fidelity $\mathcal{F}$ is proportional to the square root of the average number of photons collected per NV$^-$ per measurement, i.e., $\mathcal{F} \propto \sqrt{\mathcal{N}/N} = \sqrt{n_{\text{avg}}}$ (see Equation 1.42). Under these conditions, sensitivity can be enhanced by increasing the geometric collection efficiency η_{geo}, defined as $\mathcal{N}/\mathcal{N}_{\text{max}}$, where $\mathcal{N}$ and $\mathcal{N}_{\text{max}}$ are the number of photons collected and emitted respectively by the NV$^-$ ensemble per measurement.

Efficient photon collection in diamond is hindered by total-internal-reflection confinement resulting from diamond's high refractive index of approximately 2.41. For example, air and oil immersion objectives, with numerical apertures of 0.95 and 1.49 respectively, provide calculated collection efficiencies of only 3.7% and 10.4% respectively for photons emitted directly through the {100} diamond surface [108], as depicted in Figure 6.2.5. Although anti-reflection coatings can allow for higher collection efficiencies, present implementations demonstrate only modest improvement [328]. While great effort has resulted in high values of η_{geo} for single NV$^-$ centers through use of various nano-fabrication approaches [329, 330, 331, 332, 333, 328, 334, 335, 336, 337, 338, 101, 339], such methods do not easily translate to large ensembles.

Successful approaches for bulk ensemble magnetometers have so far focused on collecting NV^- fluorescence that has undergone total internal reflection in the diamond [108, 109]. While absorption of NV^- fluorescence by various defects may limit η_{geo} [340, 171] for some diamonds, nitrogen [341] and NV^- centers [342] are expected to hardly absorb in the NV^- PL band $\sim$600 - 850 nm. A collection efficiency of 39% is demonstrated in Ref. [108] by detecting fluorescence from the four sides of a rectangular diamond chip surrounded by four photodiodes (see Figure 6.2.6). However, the increased experimental complexity associated with employing four detectors in contact with the diamond may be problematic for certain applications. In another approach, Wolf *et al.* employ a trapezoidally-cut diamond chip and a parabolic concentrator to improve collection efficiency [109]. Although the authors calculate η_{geo} to be between 60% and 65%, this result is not confirmed experimentally. Ma *et al.* [343] demonstrate a collection efficiency of 40% by eliminating all air interfaces between the diamond and detector, in conjunction with coupling prisms which direct light exiting the diamond's four side faces to the detector.

In the future, collection efficiency in bulk NV-diamond magnetometers is expected to improve to near 100%, limited only by losses due to absorption. For example, light lost from the top and sides of the diamond in Ref. [109] could be redirected to the detector by coating these sides of the diamond with a metallic [332] or dielectric reflector [344]. The authors of Ref. [109] might also see an improvement in collection efficiency by designing an optimized parabolic concentrator rather than using a commercially available part. Hypothetical geometries for light collection using parabolic or ellipsoidal reflectors are discussed in Ref. [344]. Whereas multiple-reflection methods are suitable for bulk magnetometers, increasing η_{geo} by collecting light undergoing multiple reflections in the diamond may substantially complicate accurate image reconstruction for NV^- magnetic imaging microscopes [326, 49, 50].

6.2.6 Near-infrared absorption readout

The sensitivity of conventional fluorescence-based readout is limited by shot noise on the collected photons due to low fluorescence contrast C (see Equation 1.41). As an

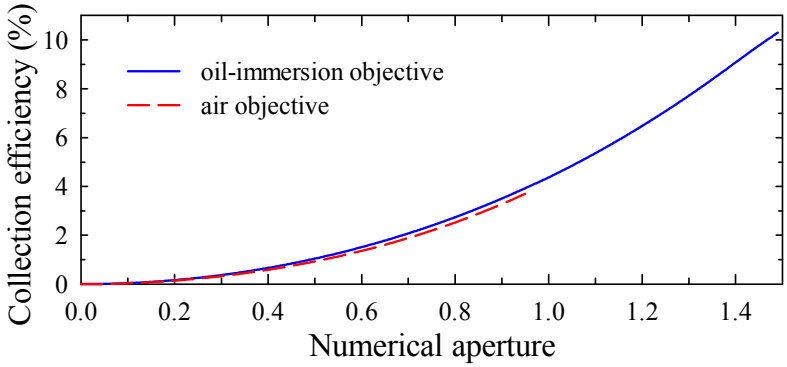

Figure 6.2.5: Calculated collection efficiencies of NV$^-$ fluorescence by oil-immersion or air microscope objectives through the {100} surface of a diamond chip, as a function of numerical aperture. From Ref. [108].

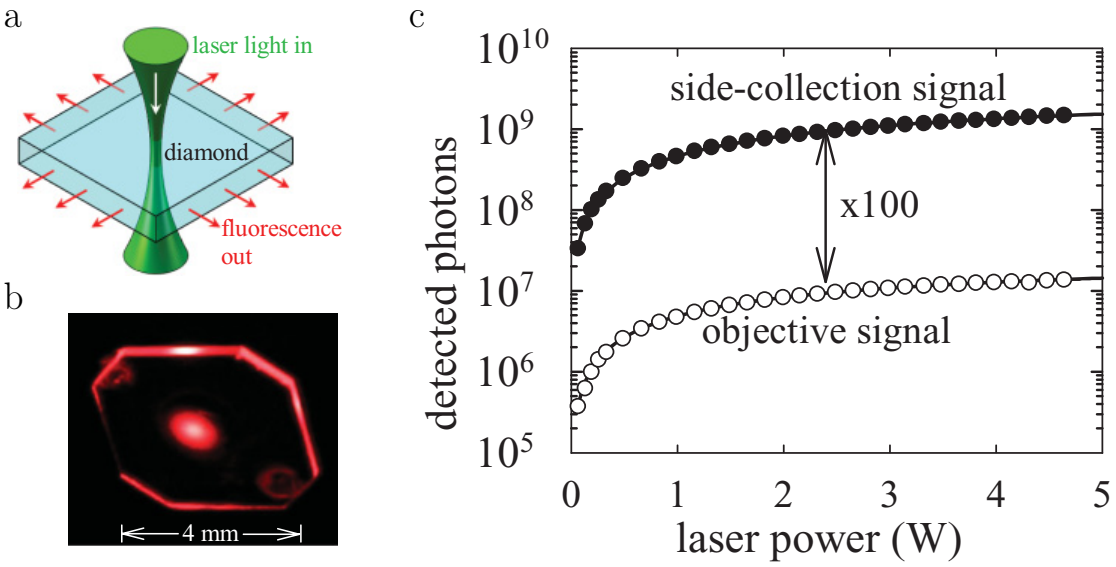

Figure 6.2.6: NV$^-$ PL side-collection method [108]. a) Green optical excitation is applied normal to the large face of the diamond chip, and red fluorescence is collected from the sides. b) Red fluorescence from actual diamond chip. c) The depicted implementation results in a 100× increase in detected photons relative to a 0.4 numerical aperture air objective. From Ref. [108].

alternative to fluorescence-based readout, population in one or both NV^- singlet states may be directly probed via absorption, giving a probabilistic measure of the initial m_s spin state prior to readout. While the upper singlet state $^1A_1$ lifetime of $\lesssim 1$ ns at room temperature [23] is likely too short for such an approach to be effective, the lower singlet state ^1E lifetime $\sim 140-220$ ns at room temperature [98, 99, 23] makes measuring the ^1E population via absorption on the $^1E \leftrightarrow {}^1A_1$ transition at 1042 nm viable.

Near-infrared (NIR) absorption has attractive benefits for certain applications: a) Contrast (and therefore sensitivity) is not reduced by background fluorescence from non-NV^- defects (such as NV^0). b) The directional nature of the 1042 nm probe light allows maximal collection efficiency (ignoring absorptive losses) to be obtained more easily than in a fluorescence-based measurement; for example, this benefit was exploited in the first demonstration of microwave-free magnetometry with NV^- centers [345]. c) Owing to the upper singlet $^1A_1$ lifetime of $\lesssim 1$ ns [23], the saturation intensity of the $^1E \leftrightarrow {}^1A_1$ transition is unusually large ($I_{1042}^{\text{sat}} \sim 50$ megawatts/cm^2 [346]), allowing high intensity 1042 nm probe radiation to be used, so that fractional shot noise is reduced to well below that of an equivalent fluorescence-based measurement [347]. d) NIR absorption readout is nondestructive, allowing for a single NV^- center in the ^1E singlet state to absorb multiple 1042 nm photons before eventual decay to the $^3A_2$ triplet. In principle such absorption by a single NV^- center can allow readout fidelity near the spin-projection limit, even in the presence of non-negligible optical losses.

NIR absorption readout has been successfully implemented in several proof-of-principle magnetometers. In the first demonstration [348], a diamond containing $[NV^-] \sim 16$ ppm is continuously illuminated with 532 nm radiation (driving the $^3A_2 \leftrightarrow {}^3E$ transition to optically polarize the NV^- spin state) and 1042 nm NIR radiation (resonantly addressing the $^1E \leftrightarrow {}^1A_1$ transition), as shown in Figure 6.2.7a. MW radiation transfers population between the ground state Zeeman sublevels. In this first demonstration [348], a single pass of the 1042 nm radiation through the diamond sample resulted in a peak-to-peak contrast of ~ 0.003 at room temperature.

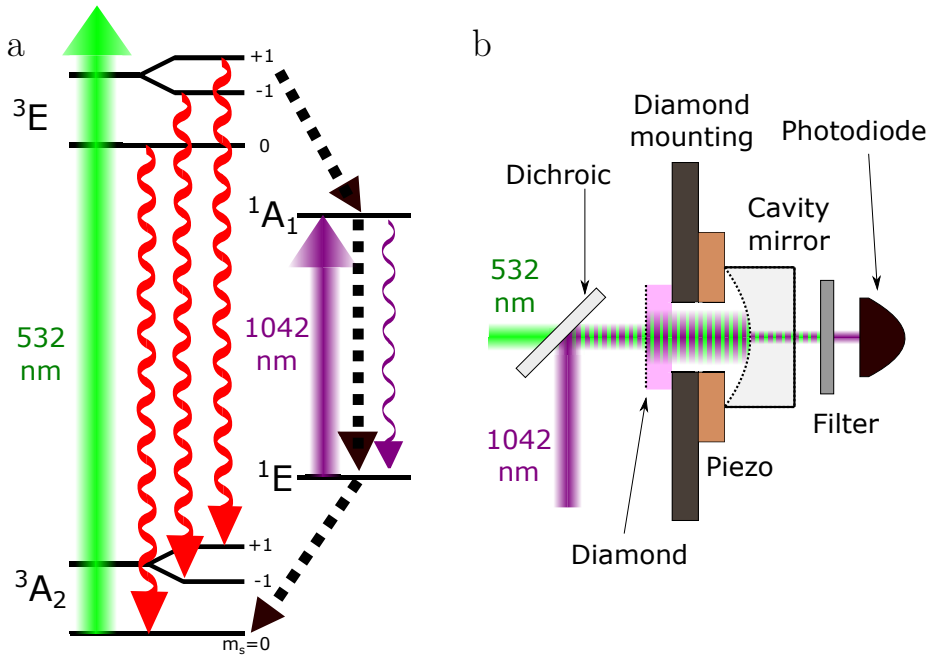

Figure 6.2.7: Near-infrared (NIR) absorption readout. a) Level diagram for the NV$^-$ center. Population accumulating in the ^{1}E singlet state is probed via absorption of 1042 nm radiation resonantly addressing the ^{1}E $\leftrightarrow$^{1}A$_1$ transition. b) Miniature NIR cavity-enhanced diamond magnetometer as described in Ref. [110]. Dashed black lines depict surfaces forming the dual-wavelength optical cavity. Components pertaining to MW delivery are omitted for clarity.

The contrast can be enhanced by increasing the number of NV^- defects interacting with each 1042 nm photon, such as by employing a higher NV^- density or a larger diamond. Alternatively, for a fixed number of NV^- centers, the 1042 nm radiation can be recirculated through the diamond. An NIR absorption magnetometer employing an optical cavity to increase the 1042 nm interaction length is analyzed in Ref. [346] and experimentally realizes a peak-to-peak contrast of 7.1% in Ref. [200] when the bias magnetic field is directed along the [100] crystallographic direction (making the magnetic resonances of all four NV^- orientations degenerate). For this demonstration, the diamond is anti-reflection coated [328] and placed in the center of a dual-wavelength optical cavity, which allows recirculation of both 1042 nm and 532 nm radiation. The more efficient use of the 532 nm light enabled by the cavity allows both a larger NV^- ensemble to be addressed and a higher degree of spin initialization into the $m_s = 0$ state. Ultimately the device in Ref. [200] achieves a sensitivity of 2.5 $\mathrm{nT}/\sqrt{\mathrm{Hz}}$, well above the shot-noise limit of 70 $\mathrm{pT}/\sqrt{\mathrm{Hz}}$.

A notable recent implementation of NIR absorption [110] is depicted in Figure 6.2.7b. One diamond face forms a reflector while the addition of a dual-wavelength concave mirror results in an optical cavity with a finesse of 160 and a cylindrical sensing volume of $\sim$ 76 μm diameter and $\sim$ 390 μm length [110]. With 500 mW of 532 nm radiation and 80 mW of 1042 nm radiation, a DC magnetic field sensitivity of 28 $\mathrm{pT}/\sqrt{\mathrm{Hz}}$ is achieved with this compact setup, with a bandwidth of about 530 Hz. The shot-noise-limited sensitivity is 22 $\mathrm{pT}/\sqrt{\mathrm{Hz}}$ and the spin-projection-noise-limited sensitivity is 0.43 $\mathrm{pT}/\sqrt{\mathrm{Hz}}$.

The NIR absorption approach is hindered, however, by several non-idealities, which so far limit readout fidelity to values far from the spin projection noise limit, similar to conventional optical readout (i.e., $\sigma_R = 65$ for the NIR absorption approach in Ref. [110] versus $\sigma_R \approx 67$ for conventional readout in Ref. [108]). First, the predominantly non-radiative decay of the $^1\mathrm{A}_1$ singlet greatly reduces the absorption cross section σ_{1042} of the $^1\mathrm{E} \leftrightarrow {}^1\mathrm{A}_1$ transition compared to a radiative-decay-only transition [86, 23]. Estimates suggest $\sigma_{1042} = 3^{+3}_{-1} \times 10^{-18}$ cm^2 [349, 346, 200], whereas the purely radiative $^3\mathrm{A}_2 \leftrightarrow {}^3\mathrm{E}$ transition is measured to have a much larger absorption

cross section $\sigma_{532} = (3.1 \pm 0.8) \times 10^{-17}$ cm^2 for 532 nm excitation [112]. Realizing the full potential of this method requires 1042 nm laser intensities of order $I_{1042}^{\text{sat}} \sim 50$ MW/cm^2 [200]. This saturation intensity appears to limit interrogation cross sections to $\lesssim$100 μm^2 for ∼100 mW-scale 1042 nm radiation powers, assuming a cavity finesse of ∼160. Laser intensities of this magnitude may lead to undesirable ionization dynamics (see Section 7.2). Second, as described in Ref. [346], non-resonant losses for 1042 nm radiation compromise sensitivity by reducing the effective achievable collection efficiency. For example, in Ref. [110], 80 mW of 1042 nm radiation input to the dual-wavelength cavity results in 4.2 mW transmitted to the detector. Third, the NIR absorption has only been demonstrated for dense ensembles with [NV$^{\text{T}}$] ∼ 10 ppm to ensure appreciable 1042 nm absorption; the performance of this method for diamonds with more dilute NV$^-$ concentrations and longer T_2^* values remains unknown, and will likely depend on the scaling of cavity finesse with [N$^{\text{T}}$] or [NV$^{\text{T}}$] density.

While NIR absorption readout is effective and may find preference for certain applications [345, 110], without further advances enabling readout fidelity enhancement, (e.g., reduced 1042 nm non-resonant absorption or reduced non-radiative ^{1}A$_1$ singlet decay rate), this method will remain approximately on par with conventional fluorescence readout while requiring the non-trivial overhead of an NIR single frequency laser and an optical cavity.

6.2.7 Green absorption readout

Alternatively, NV$^-$ readout may be achieved by monitoring absorption of green probe laser radiation, which off-resonantly drives the triplet ^{3}A$_2 \leftrightarrow {}^3$E transition [350, 351]. When resonant MWs drive the $m_s = 0 \leftrightarrow m_s = -1$ or $m_s = 0 \leftrightarrow m_s = +1$ ground state spin transitions and facilitate population transfer to the NV$^-$ singlet states, it is expected that the ^{3}A$_2$ state will be depleted, resulting in *increased* green probe transmission and *decreased* red fluorescence. For absorption measurements (both NIR and green), the change in transmitted light upon resonant MW drive is expected to mirror the change in fluorescence light up to a scaling constant, since transmission is minimal when fluorescence is maximal and vice versa [350]. Data consistent with

this understanding is shown in Figure 6.2.8 for NV^- centers illuminated with 514 nm light.

The absorption contrast, denoted C_{absorb}, may differ substantially in magnitude from the fluorescence contrast C_{fluor} (see Figure 6.2.8). Because absorption measurements monitor transmitted light, the detected signal (and thus C_{absorb}) depends on the optical depth of the absorbing material. For example, even for the idealized case where $C_{\text{fluor}} = 1$, if only a small fraction of the incident light is absorbed in the absence of MWs, the change in transmission upon application of resonant MWs will necessarily also be small, yielding a low absorption contrast C_{absorb}. Additionally, the absorption contrast may be further decreased due to the presence of non-radiative decay pathways.

Observed magnitudes of C_{absorb} in the literature are lower than C_{fluor} by $\sim 3\times$ [350, 352] or more. For example, the authors of Refs. [353, 354, 355] use a CW-ODMR-based magnetometer employing a resonant optical cavity to recycle the green excitation light through the diamond multiple times, and observe $C_{\text{fluor}} \sim 0.01$, (which is typical), while measuring $C_{\text{absorb}} \sim 10^{-6}$. In Ref. [355] the same experimental setup performs magnetometry simultaneously using both green absorption and red fluorescence, as shown in Figure 6.2.9. The green absorption yields $\sim$100 nT/$\sqrt{\text{Hz}}$ sensitivity while the conventional readout based on red fluorescence reaches $\sim$ 400pT/$\sqrt{\text{Hz}}$, about 250$\times$ better. As with NIR absorption readout (see Section 6.2.6), recycling the green excitation light via a resonant optical cavity can increase the absorption signal by (i) addressing a larger NV^- population, (ii) improving initialization into the $m_s = 0$ state, or (iii) enhancing C_{absorb}. Although effectively implemented absorption readout may achieve higher optical collection efficiency than fluorescence detection, the low realized absorption contrasts are a current major drawback.

Furthermore, absorption behavior for 532 nm probe radiation can result in *increased* probe laser transmission under resonant MW application [350, 352], leading to an anomalous inversion of the green absorption signal. This deviation from expected behavior has been independently observed in multiple research groups [350, 352]. The anomalous C_{absorb} reveals a strong wavelength and power dependence [350], which

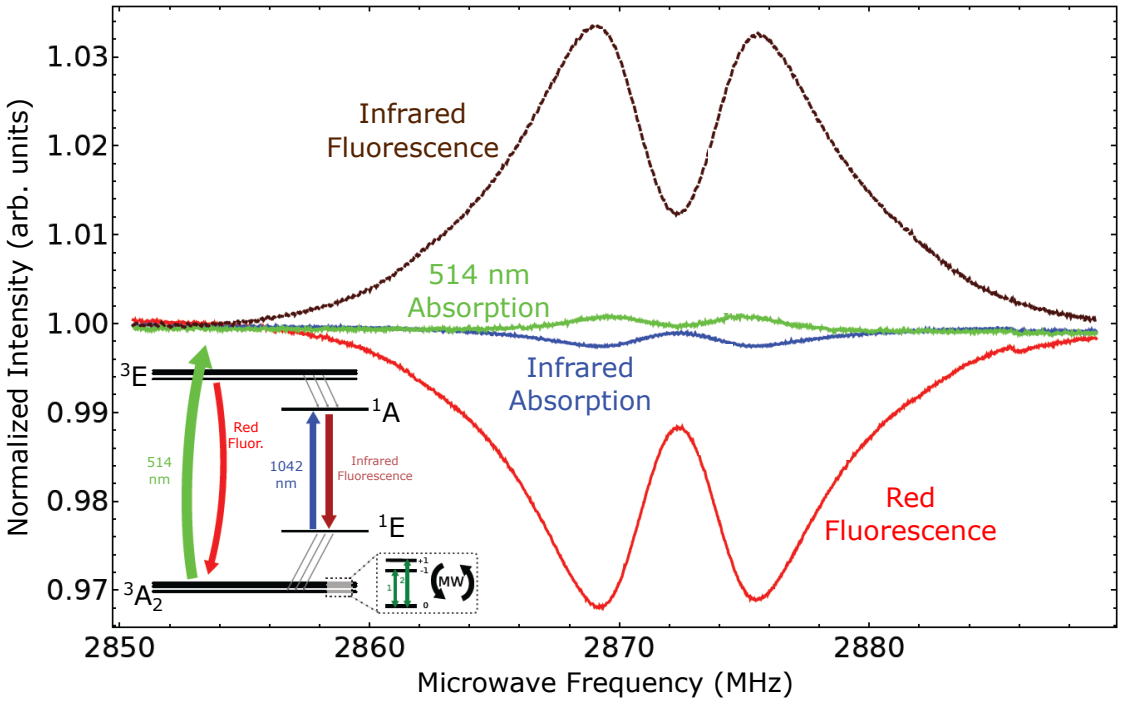

Figure 6.2.8: Simultaneous measurement of absorption and fluorescence on both the triplet and singlet NV$^-$ electronic transitions (see inset lower left). For both transitions, the absorption and fluorescence features have opposite signs and mirror one another up to a scaling factor. Adapted from Ref. [350].

suggests that green absorption readout is hindered by an unknown effect competing with and sometimes dominating otherwise expected behavior. The wavelength and power dependence of this effect suggests NV^0/NV$^-$ charge dynamics could play a role. Further investigation of this behavior might reveal presently unknown NV dynamics. Overall, given the low absorption contrast C_{absorb}, and yet unknown mechanism of anomalous absorption behavior, the utility of green absorption readout remains questionable.

6.2.8 Laser threshold magnetometry

Another approach for bulk NV$^-$ magnetometry is the creation of a NV-diamond-based laser threshold magnetometer, as suggested by Ref. [356]. Lasing is induced on the NV$^-$ $^3\mathrm{E}\,(v = 0) \leftrightarrow^3 \mathrm{A}_2\,(v' \geqslant 1)$ transition; then, when a magnetic-field-dependent population accumulates in the singlet state, the lasing threshold increases,

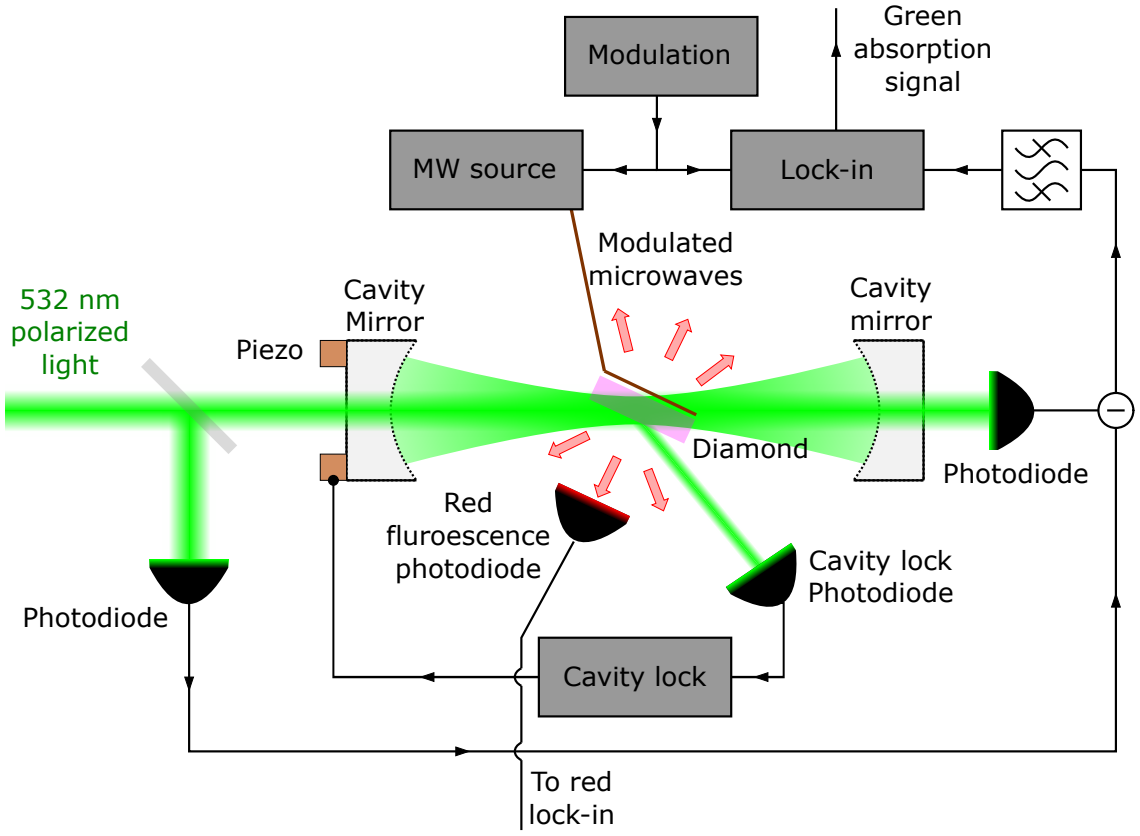

Figure 6.2.9: Cavity-enhanced magnetometry based on green absorption as demonstrated in Refs. [354, 355]. A power build-up cavity allows green excitation light to pass through the diamond sample multiple times, increasing the effective path length. The red fluorescence is measured simultaneously along with the green absorption. Adapted from Ref. [354].

and the laser's output power is reduced. As theoretically outlined [357, 358], the laser threshold approach has a number of benefits relative to generic CW-ODMR methods (Section 1.6.1): (i), effective contrast is enhanced near the lasing threshold due to competition between stimulated and spontaneous emission, (ii) collection efficiency is substantially improved by virtue of the lasing process. Although the emission cross sections for NV^- and NV^0 have been measured [342], and stimulated emission from NV^- was recently demonstrated [357], substantial work remains to address potential problems. For example, absorption by substitutional nitrogen or other defects may obstruct the lasing process [359], and it will need to be shown that other sources of noise affecting the lasing threshold or output power can be either controlled or normalized out [356]. More concerning, however, is that both theory [360] and experiment [361] find large laser field fluctuations in the vicinity of the lasing threshold.

6.3 Miscellaneous sensing techniques

6.3.1 Rotary echo magnetometry

Broadband magnetometry can also be performed using a MW pulse scheme called rotary echo [362, 363, 364]. In this technique pioneered by Aiello *et al.* [362], rotary echoes are produced by periodic reversals of the driving field. The simplest protocol inverts the phase of the driving field to reverse the sign of the Rabi oscillations. The rotary echo technique may have utility for certain niche applications such as event detection [362], but the method so far yields worse sensitivity than a Ramsey protocol. Like other dynamical-decoupling-type methods, rotary echo can be tailored to reject noise at certain frequencies and also has applications for certain narrowband AC sensing, such as detection of individual nuclear spins [364].

6.3.2 Geometric phase magnetometry

In the presence of particular DC and RF magnetic fields, an NV^- spin may accumulate a measurable geometric phase [365] in addition to a dynamical phase. Following demonstrations of control and readout of an NV^- center's geometric phase [366, 367, 368, 369, 370], the authors of Ref. [371] implemented geometric phase measurements for DC magnetometry. In their protocol, depicted in Figure 6.3.1, the phase of a MW Rabi drive is swept adiabatically around a closed phase-space loop during two intervals separated by a central π-pulse. Whereas the π-pulse cancels the dynamic phase accumulated during the sequences, the acquired geometric phase depends on the strength of the DC magnetic field. While this technique enables wide-dynamic-range field sensing by avoiding a 2π phase ambiguity inherent to Ramsey magnetometry, it is unlikely to enhance sensitivity with respect to optimized Ramsey.

6.3.3 Ancilla-assisted upconversion magnetometry

A clever and novel magnetometry scheme pioneered by Liu *et al.* in Ref. [372] utilizes frequency upconversion via an ancilla nuclear spin to make broadband measurements

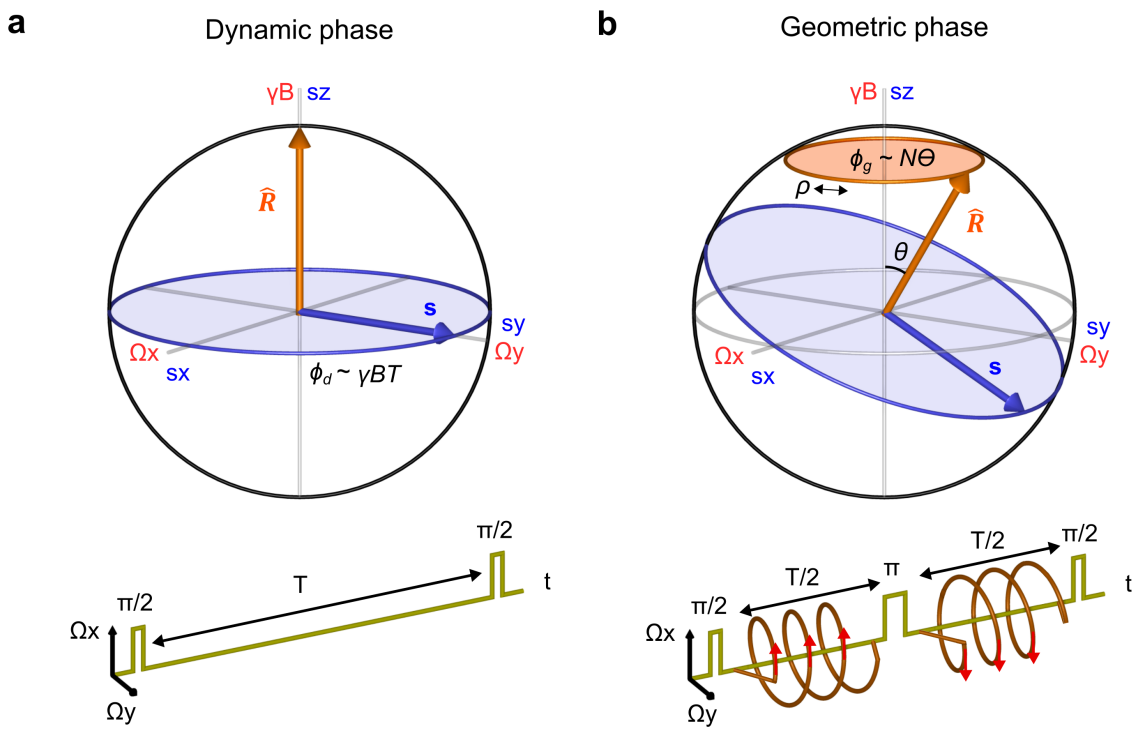

Figure 6.3.1: Comparison of dynamic and geometric phase magnetometry. For dynamic phase magnetometry (i.e., Ramsey), the Bloch vector (blue arrow), is optically prepared and then rotated by a $\pi/2$-pulse to the equator. The Bloch vector then precesses about the fixed Larmor vector (orange arrow) before being mapped into a population difference by a second $\pi/2$-pulse and read out optically. b) For geometric-phase magnetometry, the Bloch vector is optically prepared and then rotated to the equator. Additional off-resonant driving then rotates the Larmor vector about the z-axis. As the spins precess, a geometric phase proportional to the product of the solid angle (orange disk) and the number of Larmor vector rotations is acquired in addition to the dynamic phase. To cancel the dynamic phase while continuing geometric phase accrual, a π-pulse and a reversal of the off-resonant drive are inserted at the sequence midpoint. Lastly, the Bloch vector is mapped onto a population difference by a second $\pi/2$-pulse and read out optically. From Ref. [371].

of an external magnetic field. The method works as follows: A large magnetic field is aligned along the NV$^-$ internuclear axis and tuned to near the ground state level anti-crossing (GSLAC) at ≈ 1024 gauss, allowing the relative strengths of the Zeeman term and the hyperfine coupling of the NV$^-$ electronic spin to the ancilla nuclear spin to be precisely tuned. In this regime, the NV$^-$ electronic spin is first-order insensitive to magnetic fields perpendicular to the NV$^-$ symmetry axis. However, an applied transverse magnetic field $B_\perp$ modulates the strength of the hyperfine interaction, resulting in amplitude modulation of the electronic spin energy level at the nuclear spin precession frequency. The modulation deviation is proportional to $B_\perp$. Thus, by performing standard AC magnetometry at the nuclear spin precession frequency, the magnitude of the perpendicular magnetic field $B_\perp$ can be detected.

The technique is intriguing because (i), it allows the effective gyromagnetic ratio of the sensor to be tuned and (ii), it enables the use of AC magnetometry techniques including dynamical-decoupling protocols to sense DC fields for durations on the order of T_2 or longer (see Section 6.1.1). However, the method is expected (and observed) to upmodulate both magnetic signals and magnetic noise, including spin bath noise, to the AC measurement band. Further, the improved dephasing times are achieved primarily by decreasing the effective gyromagnetic ratio (i.e., the ratio relating $B_\perp$ to an energy level shift) relative to the native NV$^-$ electronic gyromagnetic ratio. Although the scheme enables vector sensing from a single NV$^-$ center and may be compatible with NV$^-$ spin ensembles, the method presently precludes sensing from multiple NV$^-$ orientations. So far there has been no experimental demonstration of improved sensitivity using this method relative to that of an optimized Ramsey-type equivalent. The requirement for ≈ 1000 gauss axial fields is also disadvantageous and likely prevents utilization of off-axis NV$^-$ centers for sensing.

6.3.4 Techniques for the strong NV$^-$-NV$^-$ interaction regime

Dipolar interactions among NV$^-$ spins contribute to ensemble-NV$^-$ dephasing, as described in Section 2.7. When NV$^-$ centers comprise the majority of spin defects in diamond, or when a different majority spin species is decoupled from the NV$^-$ centers

via spin bath driving, NV$^-$-NV$^-$ interactions may degrade relaxation times T_2^*, T_2, and T_1 [47], limiting the sensitivity of both DC and AC magnetometers. Measurement protocols that decouple or leverage these like-spin interactions while retaining sensitivity to magnetic signals offer an avenue to surpass this sensitivity limit.

Proposed techniques to improve sensitivity in the limit of strong NV$^-$-NV$^-$ interactions may be separated into two categories. Protocols in the first category mitigate dipolar interactions between like spins to extend either the dephasing time T_2^* [170] for DC sensing or the coherence time T_2 [187] for AC sensing. However, these techniques partially decouple the spins from the fields to be sensed, which may counteract the sensitivity enhancement from T_2^* or T_2 extension. Protocols in the second category harness like-spin interactions to generate entangled many-body states. Measurements of an entangled spin state comprising N spins can beat the standard quantum limit for spin projection noise ($\eta \propto 1/\sqrt{N}$, see Equation 1.3), and may approach the Heisenberg limit ($\eta \propto 1/N$) [120].

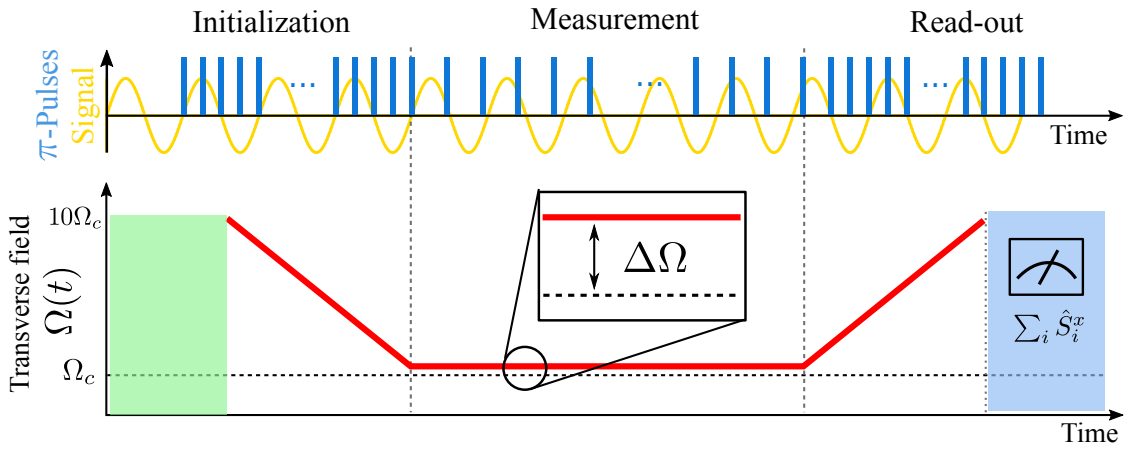

Figure 6.3.2: Schematic diagram of entanglement-enhanced sensing protocol proposed in Ref. [120]. During the initialization, measurement, and readout steps, the amplitude of a transverse magnetic field Ω and the repetition frequency of additional transverse-magnetic-field π-pulses are tuned. In the initialization stage, a correlated many-body spin state is generated as Ω is decreased toward a quantum critical point at Ω_C. At the end of the measurement period, an axial AC magnetic field signal is mapped onto the total magnetization of the ensemble, which for NV$^-$ centers can be detected using conventional readout. From Ref. [120].

To illuminate the promise and challenges associated with entanglement-enhanced techniques, we focus on the specific protocol proposed in Ref. [120]. The technique, which is expected to be applicable to NV^- centers, utilizes strong like-spin interactions to create quantum correlated states sensitive to AC magnetic fields. The proposed scheme, outlined schematically in Figure 6.3.2 generates entanglement within a 2D array of spins by first polarizing the individual spins along a transverse magnetic field (which for NV^- centers may be a MW-frequency field) and then adiabatically decreasing the field toward a quantum critical point. For the measurement to be compatible with global NV^- ensemble readout, the system approaches the quantum critical point, generating entanglement, without crossing over the quantum phase transition to a Greenberger-Horne-Zeilinger (GHZ) state. In the measurement step, periodic transverse-magnetic-field π-pulses are applied to the ensemble, allowing axial AC magnetic fields to excite the many-body system. The number of excitations detected after the transverse field is increased to its original value provides a measure of the strength of the AC magnetic field.

Importantly, the entangled state's coherence time, denoted $\overline{T}_2$, is no longer limited by like-spin interactions, but by external noise. That is, if the coherence time T_2 is separated into contributions from NV^--NV^- dipolar interactions and from other noise (including spin-lattice relaxation) as

$$\frac{1}{T_2} = \frac{1}{T_2\{\text{NV}^-\text{-NV}^-\}} + \frac{1}{T_2\{\text{other}\}}, \tag{6.5}$$

then the entangled state's coherence time $\overline{T}_2$ is only a function of $T_2\{\text{other}\}$. Therefore, when NV^--NV^- interactions dominate, $\overline{T}_2$ may be comparable to or exceed T_2, yielding improved AC magnetic field sensitivity via both the increased coherence time and reduced readout noise.

However, when the noise on each spin in the entangled ensemble is independent, $\overline{T}_2$ is expected to diminish linearly with the number of entangled spins N (i.e., $\overline{T}_2 \propto 1/N$), which at best cancels the sensitivity enhancement obtained from the $1/\sqrt{N}$ reduction in spin projection noise compared to the standard quantum limit. Even without

improved AC magnetic sensitivity, the scheme is expected to provide an increased measurement bandwidth by enabling faster field sampling than conventional sensing. When the dominant noise limiting the NV^- ensemble's spin coherence time is instead set by spatially-correlated noise, such as dipolar interactions with nearby magnetic dipoles of a different species [120], enhanced AC magnetic field sensitivity from reduced spin projection noise may again be possible. Although the protocol may also be compatible with broadband DC magnetometry, the scaling of the correlated ensemble's effective T_2^* with entangled number of spins N remains unclear. Further investigation is required to determine if this protocol could yield a sensitivity improvement over conventional DC magnetometry.

While the approach proposed in Ref. [120] represents an important milestone towards magnetometry enhanced by NV^--NV^- dipolar interactions, the protocol is expected to be challenging to execute. First, the mean NV^--NV^- separation distance $\langle r_{NV^-,NV^-} \rangle$ must be small compared to the average distance to the nearest paramagnetic defect $\langle r_{NV^-,other} \rangle$, but large compared to the thickness L of any (quasi) two-dimensional NV^- layer, i.e., $\langle r_{NV^-,other} \rangle > \langle r_{NV^-,NV^-} \rangle > L$. This hierarchy indicates that for a typical NV^--rich diamond with $\langle r_{NV^-,NV^-} \rangle \sim 10$ nm, the NV^- layer thickness L should be less than a few nanometers. Shallow nitrogen implantation into diamond [49, 13] or nitrogen delta-doping during CVD growth [373, 374] can yield layers that approach the appropriate thickness. Crucially, this 2D requirement restricts the practical NV^- ensemble size, which may limit achievable sensitivity (see Section 1.7.5) when considering wide-field imaging and bulk magnetometry applications. Second, since the preparation and readout steps require a slow adiabatic field ramp, the practical requirement that these steps occur within time $\overline{T}_2$ limits the degree of achievable entanglement. Consequently, the protocol will mostly likely entangle sub-ensembles much smaller than the total ensemble size. Disorder (i.e., static field inhomogeneity) in the ensemble, e.g., from the random positioning of NV^- centers, also restricts the maximum entangled sub-ensemble size. Both of these mechanisms are expected to increase the measurement's spin projection noise above the Heisenberg limit, further restricting the parameter regime where sensitivity enhancements are possible.

In spite of the serious challenges and limitations, the proposed technique remains a promising first step toward practical schemes harnessing the full quantum nature of NV$^-$ ensembles for sensitivity enhancement. While ensemble-NV$^-$ sensing at the standard quantum limit is expected to outperform entanglement-enhanced schemes in the near future, further development of these techniques remains an important endeavor toward enabling long-term sensitivity improvements approaching fundamental limits.

6.4 Conclusion

This chapter outlines a series of methods to increase the spin dephasing time T_2^* and improve spin readout fidelity $\mathcal{F} = 1/\sigma_R$. As discussed in Chapter 2, factors limiting T_2^* include magnetic-field, electric-field, and strain gradients. External bias-magnetic-field gradients may be mitigated through experimental design. Whereas internal strain and electric-field gradients can be more difficult to eliminate outright, the NV$^-$ ensemble can be made insensitive to such gradients through operation at sufficiently strong bias magnetic fields (Section 6.1.4) and employment of double-quantum coherence magnetometry (Section 6.1.2). Ensemble-NV$^-$ T_2^* values may also be limited by dipolar interactions with the diamond's inhomogeneous paramagnetic spin bath. These limitations can be partially mitigated by reducing the unwanted bath-spin concentrations through (i) diamond growth using isotopically-purified ^{12}C (Section 2.2.3), and (ii) diamond treatment via optimized electron irradiation and annealing procedures (discussed in Chapter 7). In addition, here we identify spin bath driving using strong, resonant RF fields as an effective measure to decouple N_S^0 and other impurity spins from the NV$^-$ ensemble (Section 6.1.3). Recent work implementing spin bath driving combined with double-quantum coherence magnetometry in NV$^-$ ensembles demonstrates T_2^* extension by more than 16$\times$ [81]. We expect continued progress on this front; one avenue opened up when T_2^* is increased to the NV$^-$-NV$^-$ dipolar interaction limit is the exploration of enhanced sensing techniques harnessing quantum entanglement [120] (Section 6.3.4).

In Section 6.2 we survey existing techniques to improve ensemble-NV$^-$ readout

fidelity $\mathcal{F} = 1/\sigma_R$, which, for conventional fluorescence-based readout, is currently limited to ~ 0.015 (see Table 1.5.1). We analyze methods that allow readout fidelities for single NV^- centers and small ensembles in nanodiamonds to approach the spin projection limit, including spin-to-charge conversion readout (Section 6.2.1) and ancilla-assisted repetitive readout (Section 6.2.3). However, no demonstrated method has substantially outperformed conventional fluorescence-based readout for large NV^- ensembles (Table 1.5.1). Nonetheless, we anticipate that with careful experimental design and advances in diamond-sample engineering, fidelity-enhancement methods so far limited to single spins or small ensembles may be extended to large NV^- ensembles. Additionally, given that any method employing optical readout benefits from increased collection efficiency, such optimizations (Section 6.2.5) also remain worthwhile for improving magnetometer sensitivity.

Chapter 7

Diamond material engineering for magnetometer sensitivity

Up until this chapter, we have assumed the diamond material to be a magnetometer design constraint. Given that most scientific diamonds are fabricated by a few companies such as Element Six, quantum sensing researchers typically do not control diamond material engineering. However, as the NV-diamond field grows, and desire for high-quality scientific diamonds becomes increasingly widespread, more research centers and groups are developing their own diamond fabrication and treatment capabilities. As a guide for future NV-diamond engineers, here we investigate strategies to optimize the fabrication and treatment of host diamond material for high-sensitivity ensemble-based magnetometry. We recount the development of well-accepted methods for diamond growth and treatment, we identify the most important parameters to be optimized, and we identify areas in diamond engineering and diamond materials science requiring where further study. The majority of this chapter is reproduced with modifications from Ref. [80].

7.1 Conversion efficiency

In an idealized case in which all other parameters are held constant, increasing the NV^- density in a fixed detection volume will result in enhanced sensitivity. Since the

NV^- density is limited by the density of nitrogen introduced into the diamond, the N-to-NV^- conversion efficiency

$$E_{conv} \equiv \frac{[NV^-]}{[N^T]} \tag{7.1}$$

must be increased in order to achieve a high density of NV^- spins while minimizing the concentration of residual paramagnetic substitutional nitrogen. Converting a substitutional nitrogen N_S into a NV^- defect requires both introducing a vacancy to a lattice site adjacent to a substitutional nitrogen (to create the NV), and capturing an electron (to change the NV center's charge state to NV^-). We denote the efficiency with which nitrogen atoms in the diamond are converted to NVs as

$$\chi = \frac{[NV^T]}{[N^T]}, \tag{7.2}$$

where $[N^T] = [N_S^0] + [N_S^+] + [NV^-] + [NV^0] + [NV^+] + [N^{other}]$ accounts for the concentration of substitutional nitrogen N_S in the neutral and ionized charge states, NV centers in all three charge states, and other nitrogen-containing defects in the diamond, such as NVH (see Section 7.6). We define the fraction of NV centers residing in the negative charge state as the charge state efficiency ζ,

$$\zeta = \frac{[NV^-]}{[NV^T]} = \frac{[NV^-]}{[NV^-] + [NV^0] + [NV^+]}, \tag{7.3}$$

so that $E_{conv} = \chi \cdot \zeta$. Although Refs. [375, 376] show evidence for NV^+, this state has so far required application of external voltages for observation. The rest of this section therefore assumes $[NV^+]$ is negligible and can be ignored.

As the N-to-NV^T conversion efficiency χ is determined by the physical location of nitrogen and vacancies in the diamond lattice, the value of χ is expected to be invariant under ambient conditions. Modification of χ requires conditions severe enough to rearrange atoms within the diamond lattice, such as irradiation, implantation, high temperature, or high pressure. With suitable electron irradiation and subsequent annealing, N-to-NV^T conversion efficiencies approaching 1 can be achieved, although

such high values are not necessarily desirable (see Sections 7.4.1 and 7.5).

In contrast, the charge state efficiency ζ depends on local conditions in the diamond and can be affected by external fields and optical illumination. Increasing ζ benefits sensitivity in two ways: first, by increasing the NV^- concentration and thus the number of collected photons $\mathcal{N}$ from the NV^- ensemble; and second, by decreasing the concentration of NV^0 and the associated background fluorescence, which improves measurement contrast. In the following section we discuss factors contributing to the charge state efficiency and methods to optimize it for sensing.

7.2 NV charge state efficiency

The charge state efficiency ζ from Equation 7.3, depends on many factors both internal and external to the diamond. For both native NVs [377] and NVs created by irradiation and annealing of nitrogen-rich diamonds [378], the NV^- and NV^0 charge states can coexist in a single sample. In general, for a given sample and experimental procedure, the steady-state charge state efficiency is difficult to predict. Contributing factors include the concentration of substitutional nitrogen and other defects serving as charge donors or acceptors [379] and their microscopic distributions [380, 381]; the wavelength, intensity, and duty cycle of optical illumination [381, 382, 308, 383]; the application of a bias voltage [384, 385, 386, 387]; and, for near-surface NVs, the diamond surface termination [388, 389, 390, 391, 379, 392, 393, 394, 374, 395, 396]. The charge state efficiency is likely affected by the conditions of diamond growth, as well as the irradiation dose [378] (see Section 7.4.1), the annealing duration and temperature, and possibly the operation temperature [382]. Moreover, the value of the charge state efficiency ζ during an NV^- sensing procedure can be difficult to measure. NVs may be reversibly converted between NV^- and NV^0 by various optical and non-optical processes [171, 308, 316]. Because ζ is strongly affected by the illumination laser intensity and wavelength [308, 316], characterization of ζ by methods such as Fourier-transform infrared spectroscopy (FTIR), ultraviolet-visible (UV-Vis) spectroscopy, and electron paramagnetic resonance (EPR) may be misrepresentative

of NV charge state behavior under the optical illumination employed in most NV-diamond sensing devices.

7.2.1 Non-optical effects on NV charge state efficiency

Here we discuss the charge state efficiency ζ in nitrogen-rich diamond in the absence of optical illumination. For shallow NVs, the charge state is strongly affected by the surface chemical termination [388, 389, 390, 391, 379]. Based on the work in Ref. [379], surface termination should provide enhanced charge state stability to a depth of at least 60 nm and possibly farther [396, 397]. The charge state efficiency ζ can also be controlled electrically [384, 385, 386, 387, 398, 376, 399, 400, 401]. Because diamond is an approximately 5.47 eV wide band gap insulator [402], Ref. [380] contends that an NV center's charge state depends less on the position of the Fermi level and more on the distance to the nearest charge donor. In nitrogen-rich diamonds, these donors are mainly substitutional nitrogen defects N_S, and the charge state efficiency ζ is seen to increase with the concentration $[N_S]$ [380, 382]. Other defects in the diamond lattice can alter ζ as well; for example, in Ref. [379], the NVs in separate implanted regions containing phosphorus (an electron donor) and boron (an electron acceptor), were seen to have increased, and respectively decreased, NV charge state efficiencies.

Introduction of electron donors other than nitrogen into diamond might appear to be a promising avenue for increasing the NV charge state efficiency. For example, phosphorus [379, 381, 399], with donor level 0.6 eV below the conduction band [403], is a shallower donor than nitrogen, which lies 1.7 eV below the conduction band [404, 402]. However, creating n-doped diamond through introduction of phosphorus has proven difficult [405], likely due to an unidentified acceptor introduced along with the phosphorus [406]. Moreover, irradiation and annealing to create NV centers is expected to also create phosphorus-vacancies (PVs), which are predicted to be deep acceptors [406]. PVs in diamond will compete with NVs for electrons, undermining the benefit of the phosphorus donors to the charge state efficiency. Additionally, PL emission at wavelengths overlapping the NV^- PL spectrum was observed in phosphorus-doped diamond [407], further complicating the use of

phosphorus in NV-diamond sensing.

The irradiation and annealing procedures applied to increase the N-to-NV^T conversion efficiency χ can also affect the charge state efficiency ζ. In Type Ib diamonds grown by high-pressure-high-temperature (HPHT) synthesis (see Section 7.3), with $[N_S] \gtrsim 50$ ppm, ζ approaching 1 is seen after low- and moderate-dose irradiation and annealing [382, 378]. As discussed in Section 7.4.1, at higher irradiation doses, the NV^0 concentration is seen to abruptly increase [378], which can be attributed to the combination of an insufficient concentration of nitrogen defects N_S available to donate electrons to the increasing overall NV population, and an increase in deep acceptor states such as multi-vacancy defects [159, 408].

7.2.2 Optical effects on NV charge state efficiency

Optical illumination of diamond may also change the NV charge state efficiency ζ through ionization of NV^- to NV^0 and also recombination of NV^0 back to NV^- [382, 308, 309, 105, 306]. The steady-state value of ζ is seen to depend on the illumination intensity and wavelength, although most of the reported measurements have been taken on single NV centers [308, 309, 105]. For example, an excitation wavelength band from 510 nm to 540 nm was found to produce the most favorable single-NV charge state efficiency in steady state compared to longer and shorter wavelengths [308]. In particular, when single NVs were illuminated by 532 nm light at intensities typical for pulsed sensing protocols [105, 309] or similar wavelength light at lower intensities [308], a charge state efficiency $\zeta \sim 70\text{-}75\%$ was observed. However, the value of ζ under these conditions is likely to differ for dense NV ensembles [382, 409]. For example, measurements in Ref. [382] on an NV ensemble in a diamond with $[N_S^T] \sim 70$ ppm and $[NV^T] \sim 1$ ppm show the charge state efficiency dropping to $\sim 50\%$ as the 532 nm power approaches the saturation power of the NV^- optical transition. More study is required to determine the relative contributions to the NV ensemble ζ of optical charge-state switching, the presence of nearby charge donors/acceptors, and other effects.

Recently, several studies on single NV centers have shown improved optical ini-

tialization to NV^- by applying near-infrared radiation (NIR) in combination with the 532 nm green excitation light [105, 383, 410]. This enhanced charge-state initialization has been demonstrated with 780 nm CW radiation [410], 1064 nm CW radiation [383], and 900 nm - 1000 nm pulsed radiation, achieving in the third case $\zeta > 90\%$ [105]. The effect is theoretically explained as follows: after absorption of a green photon to enter the electronically excited state, an NV^0 absorbs an NIR photon, which promotes a hole to the valence band and forms NV^- [383, 105]. The mechanism, visualized schematically in Figure 7.2.1, is the same as the two-photon ionization and recombination of NV^- and NV^0 by 532 nm radiation, but with the second absorbed photon being an NIR photon. In Ref. [105] the NV^0-to-NV^- recombination process is found to occur with up to a $\sim 7\times$ higher likelihood than the analogous ionization process converting NV^- to NV^0, wherein the excited-state NV^- absorbs an NIR photon, promoting an electron to the conduction band.

NIR-enhancement of charge state efficiency is expected to be compatible with pulsed initialization and readout. However, when employing 532 nm intensities $I \approx I_{\text{sat}} \approx 2.7\,\text{mW}/\mu\text{m}^2$ [112] typical for pulsed experiments, Ref. [105] finds enhancements in ζ to be lessened compared to operation at lower green intensity. Furthermore, if the charge switching rate under green-plus-NIR illumination approaches or exceeds the optical spin polarization rate, spin readout fidelity could be degraded by the increased photoionization during the readout pulse. Refs. [383] and [410] report charge switching rates near $\sim 1\ \mu\text{s}^{-1}$, approaching the singlet state decay rate of $4\ \mu\text{s}^{-1}$ [23]. Nonetheless, Hopper *et al.* achieve enhanced charge state initialization with much lower charge switching rates of $\sim 10\ \text{ms}^{-1}$.

Further work is required to determine if this technique can be extended to increase the charge state efficiency ζ in NV ensembles. Ref. [409] observes no enhancement in the NV^- PL from NIR-plus-green illumination compared to green-only excitation for NV centers in bulk diamond. Moreover, even if NIR-plus-green illumination can enhance the ensemble value of ζ, the power requirements may limit the technique's application to large ensembles. Although the required NIR power for confocal setups addressing single NV^- centers or small ensembles is modest ($\sim$ mW), the NIR intensity

is $\gtrsim 10\times$ higher than the typical 532 nm intensities used for NV$^-$ spin initialization ($I_{\mathrm{NIR}} \approx 23\, I_{\mathrm{sat}}^{532\ \mathrm{nm}}$ in Ref. [105]). Thus, when applying the technique to macroscopic ensemble volumes, the maximum addressable ensemble size will quickly be limited by the available laser power. For example, a (50 μm)^2 spot would require $\gtrsim$ 100 W of NIR [112]. At present, NIR-enhancement of charge state efficiency appears unlikely to yield substantial improvements to ensemble-NV$^-$ magnetometer sensitivities.

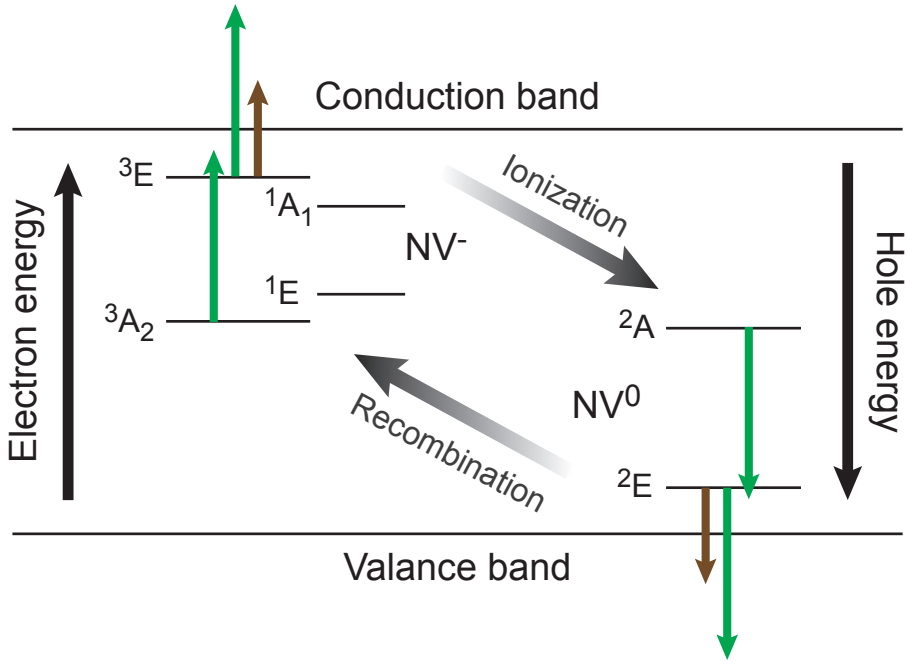

Figure 7.2.1: Energy level diagrams for NV$^-$ and NV^0, representing optical ionization and recombination processes through either absorption of two 532 nm photons (green arrows) or a 532 nm photon and an NIR photon (brown arrows)

7.3 Diamond synthesis and high pressure high temperature treatment

Fabricated bulk diamonds are commonly synthesized using one of two methods. In high pressure high temperature (HPHT) synthesis, a process mimicking natural diamond formation, a carbon source material is mechanically compressed (pressure $>$ 5 GPa) and heated (temperatures $\gtrsim$ 1250 °C) to create conditions where diamond is

the thermodynamically favored carbon allotrope. Dissolving the carbon source (typically graphite) in a metal "solvent-catalyst" can increase the growth rate, decrease the required temperature and pressure, and allow for better composition control. Consequently, solvent-catalysts are nearly always employed. A small seed diamond facilitates the growth; the dissolved carbon precipitates out of the metal catalyst solution and crystallizes onto the seed diamond, growing the size. Nitrogen easily incorporates into the diamond lattice, and is historically the primary impurity element in HPHT diamonds. However, nitrogen content in HPHT-synthesized diamonds can be reduced by varying the atomic composition of the metal solvent catalyst to "getter" the nitrogen, and recent advances in getter technology have allowed direct creation of electronic grade HPHT diamond with $[N_S^0] \lesssim 5$ ppb [411, 412]. References [413, 414, 415] discuss HPHT synthesis in detail.

Plasma-enhanced chemical vapor deposition (PE-CVD) diamond synthesis [416] is a popular alternative to HPHT synthesis, and can leverage established semiconductor fabrication techniques. In the most widespread variant of this method, employing homo-epitaxial growth, a diamond seed is exposed to a hydrocarbon plasma consisting of approximately 95 - 99% hydrogen, with the balance composed of carbon and possibly other species such as oxygen or argon. Methane is the most popular carbon source. Radicalized carbon atoms bond with the growth surface, forming a mixture of sp^2 and sp^3 bonded orbitals. Although hydrogen etches both sp^2 and sp^3 bonded carbon, the etch rate for sp^2 bonded carbon is much greater [417] and, if the hydrogen etching and carbon deposition rates are carefully tuned, diamond synthesis can be achieved [416]. Unlike HPHT synthesis, PE-CVD (alternatively simply called CVD) synthesis can easily allow the production of thin or delta doped layers from nanometer to micron scale [373, 418], masked synthesis of diamond structures [419], or layered epitaxial growth required for PIN [385] or NIN structures [399].

In the past 15 years, the majority of NV-diamond literature has employed diamonds grown by PE-CVD. First, much early work focused on single NV^- centers; and most HPHT-synthesized diamonds were not available at that time with the requisite low nitrogen concentration ($\lesssim 100$ ppb), as HPHT impurity control can be challeng-

ing [420, 167]. Second, the layered deposition inherent to CVD allows straightforward growth of epitaxial layers (as would be required for magnetic imaging devices) and the application of semi-conductor techniques to control diamond composition. Third, the PE-CVD method was historically more popular with commercial collaborators (such as Element Six and Apollo Diamond) responsible for producing the majority of scientific diamonds containing NV^- centers.

In addition, several challenges accompany direct HPHT synthesis of high-quality NV-diamonds. For one, solvent-catalyst incorporation into the diamond lattice may result in metal inclusions with size visible to the naked eye. Such inclusions could be particularly problematic for magnetic sensing applications, since the common materials employed in the solvent catalyst alloys are the ferromagnetic elements Fe, Co, and Ni [415]. The purity of HPHT-synthesized diamonds may be limited by the solid precursor materials, which may not be available with as high chemical or isotopic purity as the gas-phase precursor elements employed for CVD synthesis. Finally, the HPHT process is not intrinsically amenable to fabrication of NV^--rich layers, as are needed for imaging applications. In spite of these challenges, HPHT-fabricated diamonds with good characteristics for ensemble-NV^- DC magnetometry - including long T_2^* ($\gtrsim$ 2 μs), high E_{conv} ($\sim$ 30%), and $[N^T]$ $\sim$ 1-4 ppm - have been recently reported in the literature [109, 421, 422] (see Table 7.3.1).

While the exact motivation for HPHT diamond synthesis is not always explicitly stated [165], HPHT synthesis may circumvent undesired characteristics inherent to CVD-synthesized diamonds [157, 424]. A serious disadvantage of CVD synthesis is the incorporation of unwanted impurities and charge traps into the lattice (see Section 7.6). In addition, CVD-grown diamonds may display undesirable strain non-uniformities or contain a high dislocation density. For example, CVD-grown diamonds sometimes exhibit a brown coloration, which is attributed to vacancy cluster incorporation during synthesis [425, 340]. As vacancy clusters, chains, and rings are typically paramagnetic [160, 426, 427, 428], these clusters can increase NV^- ensemble dephasing, reducing T_2^*. Additionally, since such vacancy chains and clusters are deeper electron acceptors than NV^- [171, 161], their presence may decrease measure-

Reference	T_2^*	T_2	E_{conv}	[NV^-]	[NV^0]	[N^T]	[^{13}C]	Synthesis
[421]	$\sim 2.6\,\mu s$	$84\,\mu s$	29%	0.4 ppm	0.4 ppm	1.4 ppm	300 ppm	HPHT
[109]	-	$\sim 50\,\mu s$	30%	0.9 ppm	-	3 ppm	-	HPHT
[423]	$\geqslant 1.4\,\mu s$	-	-	~ 0.9 ppm	-	> 2.9 ppm	300 ppm	HPHT
[157]	-	-	28%	1.2 ppm	0.7 ppm	4.1 ppm	10700 ppm	CVD+HPHT
This work	$1.55\,\mu s$	$15.7\,\mu s$	$\sim 30\%$	~ 3 ppm	-	~ 10 ppm	100 ppm	CVD
[24]	580 ns	$5.1\,\mu s$	6.3%	~ 1.7 ppm	-	27 ppm	10 ppm	CVD
[25]	450 ns	$7\,\mu s$	$\sim 14\%$	3.8 ppm	2.0 ppm	~ 28 ppm	10700 ppm	CVD

Table 7.3.1: Partial literature survey of diamonds with properties well-suited to ensemble-NV^- magnetometry. Diamonds with long T_2^*, high N-to-NV^- conversion efficiency E_{conv}, and [NV^-] $\gtrsim$ 1 ppm, are expected to be particularly favorable for high sensitivity magnetometry applications. Dashed lines (-) indicate values not reported or unknown.

ment contrast [429]. Naturally occurring diamond that has not undergone irradiation rarely contains vacancies [430], suggesting that vacancies and vacancy clusters should be uncommon in well-synthesized HPHT diamond. As point defects, dislocations, and other extended defects are believed to be the dominant sources of strain in Type IIa diamonds [431], HPHT-synthesized diamonds may also exhibit lower strain than their CVD-grown counterparts. While dislocation densities of $\approx 10^4$ - 10^6 cm^{-2} are typical in CVD-grown diamonds [432], certain HPHT-synthesized diamonds can demonstrate dislocation densities of $\approx$ 100 - 1000 cm^{-2} [420, 412] and substantially lower strain [433, 411].

Although more research is needed, it is observed that the high quantity of hydrogen present during CVD growth can result in hydrogen incorporation into the diamond lattice [424, 434], (see Section 7.6). In contrast, diamonds synthesized directly by HPHT are unlikely to have hydrogen defects, as only one hydrogen-related defect has been found to incorporate into HPHT-synthesized diamond [157].

Alternatively, mixed-synthesis approaches can combine the strengths of CVD and HPHT. One popular method is HPHT treatment, where an existing CVD diamond is heated and subjected to high pressure, resulting in atomic-scale reconfigurations of atoms in the lattice while leaving the macro-scale diamond largely unchanged

[414]. HPHT treatment effectively removes single vacancies [435, 414] and causes vacancy clusters to dissociate [435, 414] or aggregate [436]. Thus, this method is effective to treat CVD-grown diamonds, which can exhibit vacancies and vacancy clusters [424, 157, 340]. The approach of applying HPHT treatment to CVD diamonds was proposed in Ref. [437] and realized by the author of Ref. [157], wherein a CVD-grown diamond was HPHT treated after synthesis but prior to irradiation and subsequent annealing (see Sections 7.4.1 and 7.5). The diamond produced in Ref. [157] exhibits a notably high conversion efficiency $E_{conv} \equiv [NV^-]/[N^T] = 30\%$] as shown in Table 7.3.2. A similar process pioneered by Lucent Diamonds employs HPHT treatment of diamonds prior to irradiation and annealing [438]. This process results in a final material with an intense red hue and photoluminescence dominated by NV^- emission [439, 414], suggesting that HPHT treatment can be effective to increase the charge state efficiency ζ, likely by eliminating charge traps.

Defect	As-grown	1500 °C anneal	Irradiation	800 °C anneal
$[N_S^0]$ (ppb)	1620 (160)	1100 (100)	200 (20)	120 (15)
$[N_S^+]$ (ppb)	1500 (150)	2200 (250)	3000 (300)	1000 (100)
$[NV^0]$ (ppb)	$\leqslant 10$	$\leqslant 10$	$\leqslant 10$	695 (70)
$[NV^-]$ (ppb)	60 (5)	40 (5)	35 (5)	1160 (120)
$[NVH^0]$ (ppb)	500 (50)	310 (30)	380 (40)	290 (30)
$[NVH^-]$ (ppb)	405 (40)	200 (20)	obscured	20 (5)
$[N_2VH^0]$ (ppb)	< 0.1	22 (3)	obscured	24 (5)
$[V_nH^-]$ (ppb)	3.1 (1)	$\leqslant 0.1$	25 (3)	41 (4)

Table 7.3.2: Concentrations of quantifiable defects in sample GG1 in the as-grown state and after each treatment stage. From Ref. [157].

However, HPHT treatment cannot address all diamond deficiencies, CVD-related or otherwise. For example, should a CVD-synthesized diamond incorporate high concentrations of hydrogen or other elemental impurities into the diamond lattice during growth, HPHT treatment is ineffective to remove these impurities [424]. Such treatment is also limited to diamonds with balanced aspect ratios, as thin plates or rods will likely crack under the high applied pressure.

In addition to HPHT treatment of existing diamonds, other mixed-synthesis approaches have also been pursued. For example, utilizing type IIa HPHT seeds for CVD growth rather than CVD-grown seeds can yield material with lower strain and reduced densities of dislocations and other unwanted defects [420, 412, 167, 168]. Another mixed-synthesis method exploits the fine composition control and high chemical purities available with CVD synthesis to create the carbon precursor for HPHT synthesis [165]. The diamond composition can thus be carefully controlled, and HPHT synthesis can take advantage of high-purity or isotopically enriched gaseous sources (e.g., methane or $^{15}N_2$).

Given the prominent role lattice defects and elemental impurities play in determining the charge state efficiency and coherence times for NV^-, additional research focused on synthesizing sensing-optimized diamonds is warranted.

7.4 Electron irradiation

7.4.1 Irradiation overview

For unmodified as-grown CVD diamond, realized conversion efficiency values E_{conv} can be far less than unity, as shown in Table 7.4.1, where the majority of substitutional nitrogen is not converted to NV^- [161, 157]. In fact, for some CVD diamonds (see Table 7.4.2) the concentration of grown-in monovacancies is insufficient to achieve good E_{conv} for total nitrogen concentration $[N^T] \gtrsim 1$ ppm regardless of location; even if every monovacancy were adjacent to a substitutional nitrogen, the conversion efficiency E_{conv} would still be low [430, 319]. However, the monovacancy concentration can be augmented after growth by irradiating the diamond with energetic particles. The high-energy irradiating particles knock carbon atoms out of the diamond lattice, creating both interstitial carbon atoms and monovacancies [440, 441]. Although theoretical calculations have not yet completely converged with experimental observations [319, 442], the widely accepted model posits that upon subsequent annealing (discussed in Section 7.5), diffusing vacancies are captured by substitutional nitrogen

atoms, forming NV centers [7]. Primary considerations in the irradiation process are the particle type, energy, and dose.

E_{conv}	$[N^T]$	Growth location	Reference
$0.0007 - 0.005$	$0.3 - 30$ ppm	Element Six	[161]
$0.0006 - 0.03$	$0.35 - 2.4$ ppm	Apollo Diamond Inc.	[161]
$0.02 - 0.03$	4 ppm	Warwick University	[157]

Table 7.4.1: Native N-to-NV^- conversion efficiencies E_{conv} and total nitrogen concentrations $[N^T]$ in unmodified bulk CVD diamond

$[V^0 + V^-]$	Reference
60 ppb	[443]
$\lesssim$ 20 ppb	[437]
$\lesssim$ 0.03 ppb	[430]

Table 7.4.2: Native monovacancy concentrations in unmodified bulk CVD diamond

The irradiation of diamond has been performed using a variety of particles: protons, ionized deuterium atoms, neutrons, and electrons [444]. Gamma ray irradiation from ^{60}Co has also been used [444, 445]. Many of these particles are suboptimal for NV creation, however, where only single monovacancies V^0 are desired, and other created defects are likely deleterious. A particular problem for certain irradiation methods is the production of "knock-on-atoms" [445, 446], where the irradiating particle has sufficient energy not only to displace an initial carbon atom from the lattice, but to impart enough kinetic energy to that carbon that it displaces additional carbon atoms, resulting in localized lattice damage [447]. Although annealing (see Section 7.5) can partially alleviate such damage, the lattice damage can never be completely repaired [448, 437, 449, 450, 451] and may result in unwanted paramagnetic defects or charge traps. For irradiation with protons, neutrons, or ionized deuterium atoms, damage from such knock-on-atoms can be severe. Similar lattice damage occurs from ion implantation of various species such as nitrogen [451, 426, 452], carbon [452, 453], and helium nuclei [454, 453, 455, 456, 173]. Electrons, with their lower

mass, transfer less kinetic energy to the carbon atoms and are therefore better suited to creating isolated monovacancies. Electron irradiation is favored over gamma ray irradiation because the former can be accomplished in hours whereas the latter, when implemented using ^{60}Co, can take weeks [457]. In summary, electron irradiation is preferred to create NV^- ensembles optimized for sensing applications [458, 459, 437], as this method allows for evenly distributed monovacancies to be created throughout the diamond in a timely manner, with less lattice damage than alternative methods.

Theoretical calculations predict monovacancy creation requires electron energies $\gtrsim$ 165 keV [459], which is consistent with experimental data wherein vacancy creation is observed for electron irradiation along the [100] direction at 180 keV but not 170 keV [460]. Crude estimates suggest electron irradiation energies between 0.5 and 0.8 MeV will create mainly single vacancies [156, 461] and avoid producing multivacancy complexes. While this estimate is consistent with Ref. [462] where divacancies are detected after irradiation with 3.5 MeV electrons, Ref. [437], however, finds no evidence of vacancy pairs after irradiation with 4.6 MeV electrons, suggesting that several-MeV irradiation energies may be safe. The optimal irradiation energy may also depend on sample geometries; thicker diamonds should require higher energies to ensure vacancies are created uniformly through the entire thickness [437, 445]. For small ensembles close to the diamond surface, an electron microscope can provide the needed irradiation [463, 464, 465, 418]. More study is required to resolve remaining discrepancies between experimental data and detailed simulations of the electron irradiation process [445, 459]. For example, recent measurements of monovacancy density profiles versus depth, as judged by GR1 intensities in 1 MeV electron irradiated diamonds [442], are inconsistent with Monte Carlo simulations in Refs. [445, 459].

The irradiation dose should also be approximately matched to the diamond's total nitrogen concentration [N^T] as suggested in Section 7.1; if too many vacancies are created, then $>$ 50% of N_s will be converted to NV^0, and the number of electrons donated by the remaining N_s will be insufficient to convert every NV^0 to NV^-. Figure 2 in Ref. [378] illustrates the importance of matching the irradiation dose to [N^T] to achieve maximal E_{conv}. When determining irradiation dose, in-situ recombination

between a vacancy and an interstitial carbon should be accounted for [446, 445]. Current estimates suggest approximately 30% [445] to 50% [446] of initially created vacancies are immediately lost to spontaneous recombination. For example, using 1 MeV electrons (generating $\sim 2\times10^{-4}$ vacancies/electron/μm according to Ref. [445], and assuming 40% of vacancies recombine immediately and two nitrogens are required to make a single NV^- center, we expect a sample with $[N^T] \sim 1$ ppm to require a dose of 7.3×10^{16} cm^{-2}. However, fine-tuning of the irradiation dose is often done empirically, suggesting either the presence of dynamics more complicated than those included in the simple model presented here (i.e., the presence of other vacancy traps, the formulation of divacancies, loss at surfaces, etc.) or errors in the measured electron flux or substrate temperature [445]. For example, while the production rate of neutral monovacancies from irradiation with 2 MeV electrons is found to be temperature-independent from room temperature to $\sim$ 300 °C, the rate decreases notably for higher temperatures [441].

7.4.2 Irradiation studies in the literature

This section is reproduced with modifications from the appendix of Ref. [82]. Here we review prior literature studies reporting monovacancy creation rates by electron irradiation. Figure 7.4.1 displays vacancies measured in the diamond literature via UV-vis absorption spectrophotometry for varying irradiation doses [466, 467, 468, 440, 441, 469, 470, 342, 437], alongside simulated vacancy creation rates from Ref. [445]. In type IIa diamonds with low concentrations of electron donors, irradiation primarily creates neutral monovacancies (V^0, GR1), whereas in diamonds with a moderate to high concentration of electron donors, such as type Ib diamonds, negative monovacancies (V^-, ND1) are created at similar or greater rates than neutral monovacancies [469]. Figure 7.4.1 depicts only the V^0 concentration for the former sample type and the total vacancy concentration ($V^0 + V^-$) for the latter type.

The GR1 center displays a zero-phonon absorption doublet at 740.9 nm and 744.4 nm [471], while the ND1 center displays a zero-phonon line at 393.6 nm [472]. For the data depicted in Fig. 7.4.1, vacancy concentration is calculated by integrating

under the absorption features to obtain A_{GR1} and A_{ND1}, the absorption strengths in meV cm^{-1}, and then solving the equations $A_{GR1} = f_{GR1}[V^0]$ and $A_{ND1} = f_{ND1}[V^-]$, where f represents the transition's oscillator strength [467, 473]. The authors of Ref. [474] measured the ratio $f_{ND1}/f_{GR1} = 4.0$ using detailed balance arguments applied to an annealing study. Later, the authors of Ref. [467] determined that $f_{ND1} = 4.8(2) \times 10^{-16}$ meV cm^2 by correlating ND1 absorption measurements with well-calibrated EPR measurements of $[V^-]$. Although V^0 is spinless and thus EPR inactive, f_{GR1} is determined to be $1.2(3) \times 10^{-16}$ meV cm^2 by dividing f_{ND1} by $f_{ND1}/f_{GR1} = 4.0$. All vacancy concentrations reported in Fig. 7.4.1 use these calibration constants.

Large variation is apparent between data sets from different publications, and, more specifically, between different irradiation facilities. The diamonds from Refs. [440, 441, 468] were all irradiated at Reading University in the UK and all show significantly higher vacancy creation rates than diamonds irradiated at other facilities. Strikingly, Refs. [440] and [467], published by the same group within the same year using approximately the same electron energy (≈ 2 MeV), report vacancy creation rates of 0.50 cm^{-1} and 1.53 cm^{-1} respectively, a difference of 3×. This discrepancy leaves open the possibility of a calibration error in the applied dosage at one or more irradiation facilities, or a variable which is not controlled for.

Included in this data set are our own vacancy concentration measurements made on six standard grade ($[N] \lesssim 150$ ppb) diamonds from Element Six irradiated with 1 MeV electrons at Prism Gem (the ⋈ symbols in Figure 7.4.1. Excluding the point at 3×10^{18} e$^-$/cm^2), these measurements suggest a V^0 creation rate of 0.30 ± 0.05 cm^{-1} and no production of V^- above the device's detection limit of $[V^-] \sim 100$ ppb. Details of the cryo-UV-vis apparatus and measurements are described in Appendix E.1.

Although Ref. [441] observed the vacancy creation rate to be independent of temperature up to 600 K, such temperatures could be exceeded depending on the irradiation setup; inadequate heat sinking combined with high beam current could cause diamonds to be heated above the temperature at which vacancies become mobile and recombine with interstitials, thereby reducing the measured post-irradiation vacancy

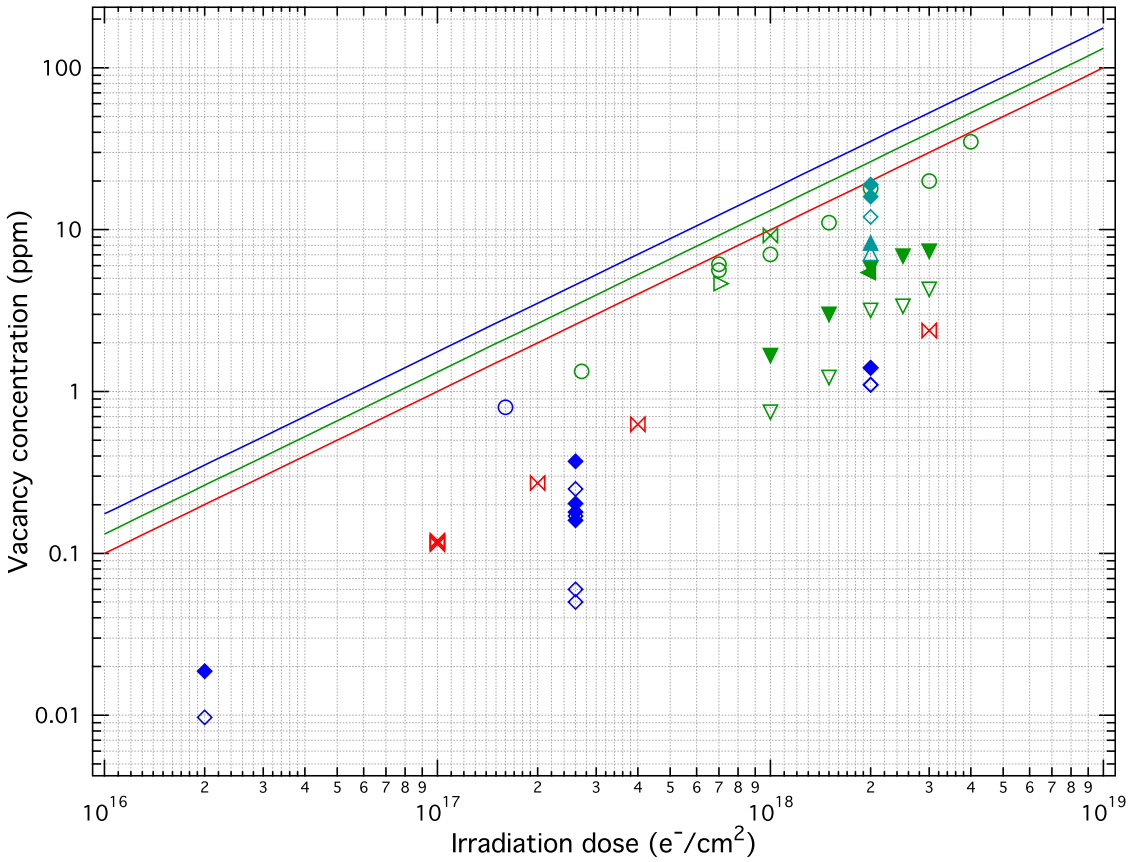

Figure 7.4.1: Reported values of monovacancy concentrations in ppm generated by electron irradiation at 1 MeV (—), 1.9-2 MeV (—), 3 MeV (—), and 4.5-5 MeV (—) from the diamond literature, measured by 77 K UV-vis spectrophotometry using the oscillator strengths f_{GR1} and f_{ND1} reported in Ref. [467]. Solid lines represent the calculated dependence of vacancy creation on irradiation dose from SRIM calculations [475] in Ref. [445], neglecting vacancy-interstitial recombination for electron irradiation at 1 MeV (—), 2 MeV (—), and 5 MeV (—). Filled markers denote measurements of the total monovacancy concentration $V^0 + V^-$ while open markers denote measurements of only V^0. All diamond samples included here contain nitrogen concentrations $\lesssim 10$ ppm. The following markers denote measurements reported in the following references: ⋈ = this work at 1 MeV, ◀ = Ref. [466] at 1.9 MeV recalculated using f_{GR1} and f_{ND1} from Ref. [467], ▽ and ▼ = Ref. [467] at 1.9 MeV, ⋈ = Ref. [468] at 2 MeV recalculated using f_{GR1} and f_{ND1} from Ref. [467], ○ = Ref. [440] at 2 MeV, ▷ = Ref. [441] at 2 MeV, ▲ and △ = Ref. [469] at 3 MeV, ◆ and ◇ = Ref. [470] at 3 MeV, ◆ and ◇ = Ref. [437] at 4.5 MeV, and ○ = Ref. [342] at 4.5 MeV.

concentration for a given dose. The diamonds represented in Fig. 7.4.1 are irradiated with beam currents ranging ranging from μA [467, 440, 468] to tens of mA [476, 477]. In Ref. [437], the vacancies created per dose is seen to vary by more than 2$\times$ between different diamonds. It is unclear whether this variation arises from differences in the samples [474], or inconsistency in the irradiation conditions (such as electron beam inhomogeneity). It is possible that more than one of these surmised explanations combine to describe the variation depicted in Fig. 7.4.1. Moreover, as pointed out in Ref. [478], there exists disagreement in the literature on the value of $f_{\mathrm{ND1}}/f_{\mathrm{GR1}}$. In particular, absorption measurements employing reversible charge interconversion between GR1 and ND1 find the ratio of oscillator strengths $f_{\mathrm{ND1}}/f_{\mathrm{GR1}}$ to range from 2 to 10 [479, 480, 472]. This variation suggests a possible uncertainty in the y-axis of Fig. 7.4.1 of up to $\sim 5\times$. Such uncertainty complicates the determination of the required irradiation dose to create a fixed vacancy concentration, and thus generate a desired NV concentration after annealing.

We further note that all measured data points lie below the predicted relationship between dose and vacancy concentration from Ref. [445], which uses SRIM (Stopping and Range of Ions in Matter) calculations [475]. These simulations ignore spontaneous recombination, which is crudely estimated to occur $30\% - 50\%$ of the time for diamonds irradiated with $\sim$2 MeV electrons [445, 446] and may occur at a higher rate for lower-energy electrons, where the vacancy-interstitial distance is reduced [446]. Uncertainty in the value of $f_{\mathrm{ND1}}/f_{\mathrm{GR1}}$ [457, 479] could help account for the discrepancy between the simulations and much of reported data. The variation in vacancy creation rate reported in the literature demonstrates the need for additional detailed studies to reduce uncertainty and resolve the aforementioned discrepancies.

7.5 Low pressure high temperature annealing

For the successful creation of NV^- centers, substitutional nitrogen and monovacancies must be relocated to occupy adjacent sites in the diamond lattice. This process can be accomplished via diffusion at elevated temperature, i.e., annealing. Since mono-

vacancies migrate in the neutral charge state V^0 [481] with an activation energy of $E_a = 2.3 \pm 0.3$ eV [474, 430], compared to measured values of $E_a = 4.8 - 6.2$ eV for substitutional nitrogen [482, 319, 414], neutral monovacancies diffuse throughout the lattice during annealing until they reach the more immobile nitrogens. The negatively charged monovacancy's higher activation energy [481] ensures that monovacancy diffusion occurs predominantly in the neutral charge state [481], although a negative monovacancy can convert to a neutral monovacancy in a reversible charge transfer process [474]. The diffusion constant D of the neutral monovacancy is [483, 484]

$$D = D_0 e^{-E_a/k_B T}, \tag{7.4}$$

where k_B is the Boltzmann constant, T is the temperature, and D_0 is a diffusion prefactor. The diffusion constant D has been measured to be ~ 1.1 nm^2/s [485, 158, 486] at 750 °C, suggesting D_0 is in good agreement with theoretical calculations [487] and with an independently measured upper bound [7]. Other sources, however find or employ different values for D_0 or E_a [483, 484, 488], suggesting that further measurements are warranted. Once an NV center is formed, the deeper binding energy of the nitrogen-vacancy bond relative to the neutral vacancy ensures that the bound vacancy does not diffuse away [489, 157].

The procedure described here is commonly termed low pressure high temperature (LPHT) annealing to distinguish it from high pressure high temperature (HPHT) annealing (discussed in Section 7.3). Given the role of diffusion in LPHT treatment, the annealing temperature and annealing duration are important control parameters. A temperature of ~800 °C is usually employed [490], given that monovacancies become mobile around 600 °C [474, 491, 458, 492], and annealing times of several hours are typical, e.g., 2 hours in Ref. [7], 4 hours in Ref. [466], 8 hours in Ref. [437], 12 hours in Ref. [24], and 16 hours in Ref. [342]. Diamonds with lower values of $[N^T]$ are expected to require longer annealing times due to the greater initial distances between vacancies and substitutional nitrogens. A study by Element Six found no observable deleterious changes in diamond properties between samples that were annealed at

$\sim$ 800 °C for $\sim$ 8 hours and samples that were annealed at the same temperature for longer periods [437]. This $\sim$ 800 °C annealing step is typically performed under vacuum or in a non-oxidizing, inert gaseous environment to avoid graphitization [414]. Under vacuum, present understanding is that diamond graphitization begins roughly around 1500 °C [493].

Although the 800 °C LPHT treatment is effective to create NVs, unwanted defects may form as well. For example, diffusing monovacancies can combine to form divacancies [159], which are immobile at 800 °C. As deeper electron acceptors than NVs [319, 494], the presence of divacancies reduces E_{conv}. To mitigate divacancy formation, electron irradiation with in-situ (i.e., simultaneous) annealing has been proposed [495]. Under such conditions, single vacancies are continuously created in an environment consisting primarily of substitutional nitrogen (and, as the process progresses, NVs), thereby reducing divacancy formation. Although preliminary work in Ref. [495] finds electron irradiation with in-situ annealing increases T_2^*, no increase in E_{conv} is observed, and further investigation is warranted.

Following NV formation, further LPHT annealing above 800 °C may reduce strain or paramagnetic impurities resulting from lattice damage. For example, divacancies can combine into other defects at $\sim$900 °C [159]. Reduction of a given defect species may be effected by consolidation into other larger defect species, which may be paramagnetic [426, 157, 427, 428]. Annealing to temperatures of 1000 °C to 1200 °C is shown to extend the T_2 of both single NV^- centers [452, 426] and ensembles [496] created by ion implantation. As this increase is attributed to a reduction in paramagnetic multi-vacancy defects [426, 496], improvement in T_2^* is expected as well, though this expectation has not been systematically confirmed in experiment. Practically, this additional LPHT treatment is limited by the temperature at which NVs anneal out, which is typically around 1400 °C to 1500 °C [471, 157, 497] and can vary depending on the presence of other defect species within the diamond [471]. While a systematic study of annealing temperatures and durations is warranted for engineering optimal samples for ensemble-NV^- sensing, a standard recipe for samples is at least several hours at $\sim$800 °C followed by several more hours at $\sim$1200 °C [342, 392, 498].

Diamond defect	Ground state spin
N_S^0	$S = 1/2$
N_S^+	$S = 0$
NV^+	$S = 0$
NV^0	$S = 1/2$
NV^-	$S = 1$
NVH^-	$S = 1/2$
NVH^0	$S = 0$
N_2V^-	$S = 1/2$
N_3V^0	$S = 1/2$
N_2VH^0	$S = 1/2$
VH^0	$S = 1/2$
VH^-	$S = 1$
V_nH^-	$S = 1$
V^+	$S = 1/2$ [158]
V^0	$S = 0$ [158]
V^-	$S = 3/2$ [158]
VV^-	$S = 3/2$ [500]
VV^0	$S = 1$ [159]

Table 7.6.1: Common defects in diamond and their ground state electronic spin

7.6 Other common impurities in synthetic or treated single crystal diamond

Unwanted species in the diamond lattice can degrade magnetometer performance by decreasing the NV charge state efficiency $\zeta = [NV^-]/[NV^T]$, creating local magnetic noise, or reducing the fraction of substitutional nitrogen N_S converted to NV^-. This section restricts detailed discussion to multivacancy clusters and NVH [340], species present in diamond at sufficient concentrations to likely affect NV spin and charge dynamics. Extended discussion of other defects can be found in Refs. [499, 319]; see also Table 7.6.1 for relevant defects commonly found in diamond.

Multivacancy clusters are common in some diamonds grown by chemical vapor

deposition (CVD) [501, 425], and are believed to cause the brown coloration in CVD-grown diamond [425, 502]. During CVD synthesis, the diamond surface can become rough and stepped. When these steps are rapidly covered with additional deposited material, small voids, i.e., clusters of vacancies, can be left in the diamond [425, 340]. Multivacancy cluster incorporation has been observed to increase at high growth rates [425], and may be correlated with nitrogen content [501]. Using positron annihilation, the authors of Ref. [503] found the density of multivacancy clusters was found to be roughly $10^{17}-10^{18}$ cm^{-3} for their growth conditions. Such vacancy clusters can trap electrons [459, 504, 161, 319], reducing the ratio of NV^- to NV^0 and also generating magnetic noise resulting from their trapped unpolarized electron spins. The neutral divacancy V_2^0 [505, 159, 319, 506] and neutral multivacancy chains (V_n^0, $n \geqslant 3$) are paramagnetic [160, 427, 428], and increase environmental magnetic noise. Irradiation or implantation followed by annealing can also produce such defects [452, 426]. Low pressure high temperature annealing is effective to remove certain multivacancy clusters. However, as the removal of multivacancy clusters is effected by aggregating these species together or combining them with other defects, the reduction of smaller multivacancy defects may be accompanied by an increase in larger multivacancy clusters or other defects. High pressure high temperature (HPHT) treatment effectively removes single vacancies [414] and causes some vacancy clusters to dissociate [414], which may aggregate to form different multivacancy clusters [436]. See Section 7.3.

Another common impurity in diamond is hydrogen, which gives rise to many defects [414, 471, 434]. For typical CVD diamond growth, the plasma is composed predominantly of hydrogen ($\gtrsim 95\%$) [507], which can incorporate into single crystal diamond at concentrations as high as 1000 ppm [508]. The hydrogen incorporation rate into the lattice is partially dependent upon the diamond growth recipe [509], and further investigation into the hydrogen quantity incorporated and methods to mitigate hydrogen incorporation is warranted. Hydrogen-related defects may influence the NV charge state [510, 390]. Additionally, at high enough concentrations the nuclear spin of hydrogen may result in non-negligible dephasing or decoherence. At present we are unaware of any published method to effectively remove hydrogen from the bulk

diamond lattice [424, 157].

The presence of hydrogen in the diamond lattice can enable formation of the NVH defect [511], wherein the hydrogen occupies the vacancy of an NV. In as-grown nitrogen-enriched CVD diamond, the ratio of ($[N_S^+]$+$[N_S^0]$):$[NVH^-]$:$[NV^-]$ was found to be approximately 300:30:1 in Ref. [161] and 52:7:1 in Ref. [157]. The NVH species is undesirable because: (i) it lowers the conversion efficiency of incorporated nitrogen to NV centers; (ii) it reduces the concentration of substitutional nitrogen N_S available to donate electrons to turn NV^0 defects into NV^-; (iii) NVH competes with NV as an electron acceptor; (iv) NVH^- is paramagnetic, causing magnetic noise; and (v) the hydrogen in NVH may rapidly tunnel among the three adjacent carbon atoms at GHz frequencies, resulting in high-frequency magnetic or electric noise [512].

No known treatment can transform existing NVH defects into NV defects. The NVH complex is stable against annealing up to approximately 1600 °C but anneals out completely by 1800 °C [340, 157]. However, removal of NVH via annealing is not associated with increased NV concentration; rather, further isochronal annealing to 2000 °C and 2200 °C is accompanied by increases in N_2VH^0 and N_3VH^0 species [157], suggesting the NVH concentration is reduced via aggregation of NVH with one or more nitrogen atoms. NVH^0 exhibits absorption at 3123 cm^{-1} [513] but is otherwise not known to be optically active.

Diamonds subject to temperatures at which substitutional nitrogen or interstitial nitrogen become mobile may exhibit defects consisting of aggregated nitrogen, such as N_2 [514, 515, 516], N_2V [517], N_2VH [157], N_3V [518], N_3VH [519, 157], N_4V [520], or other aggregated nitrogen defects [521]. The presence of aggregated nitrogen defects reduces the quantity of nitrogen available to form NV centers or donate electrons to NV^0 to form NV^-, and can cause additional paramagnetic noise. Other defects such as VH [522, 523], V_2H [524, 525], and OV [513, 157] have been identified in synthetic diamond and may act as charge acceptors or create additional paramagnetic noise. However most defects discussed in this paragraph are observed at concentrations low enough to be neglected for diamonds fabricated for NV^- magnetometry, as shown in Table 7.3.2, reproduced from Ref. [157]. Additional defect species are inferred to

exist from charge conservation arguments but have not been directly observed [171]. More research is needed to better understand defects in synthetic diamond grown for magnetometry applications.

7.7 Preferential orientation

In naturally occurring and many fabricated diamonds, NV^- centers are distributed evenly among all four crystallographic orientations. However, under certain circumstances, CVD-grown diamond can exhibit preferential orientation of NV^- centers along certain crystallographic axes [161, 96]. Several research groups have achieved almost perfect alignment of all NV^- centers along the a single [111] axis. Michl *et al.* demonstrated 94% alignment [526], Lesik *et al.* demonstrated 97% alignment [527], and Fukui *et al.* demonstrated 99% alignment [528]. The mechanism for preferential orientation is explained in Ref. [494].

An ensemble-NV^- magnetometer utilizing a single NV^- orientation in a diamond with no preferential orientation suffers from reduced measurement contrast due to unwanted PL from NV^- centers of other orientations. A diamond with 100% preferential orientation may allow a 4× increase in contrast. In practice, though, the enhancement is typically somewhat less than 4×, since polarized excitation light can already be used to selectively address particular NV^- orientations [527], and high bias fields can suppress fluorescence from off-axis NV^- centers [529, 111].

Diamonds grown with preferential orientation have at least two main drawbacks. First, NV^- concentrations for preferentially grown diamonds in the literature are currently relatively low [526, 527, 528], typically around 10^{12} cm^{-3} although concentrations up to 10^{15} cm^{-3} have been achieved [530]. Second, it appears that the N-to-NV^- conversion efficiency cannot be increased through irradiation and subsequent annealing without destroying the preferential alignment, although conflicting evidence on this topic has been reported [528]. Since electron irradiation followed by annealing can increase the N-to-NV conversion efficiency by $\sim 10\times$ to $100\times$, preferential orientation is not currently believed to be a viable method to achieve better ensemble magnetom-

etry sensitivity. However it is possible that future technical advances or treatment could alter this understanding. Additionally, preferential orientation precludes the implementation of vector magnetometry [25].

7.8 Conclusion

As optimal sensing techniques require co-development with diamond samples tailored to these techniques, this chapter reviews diamond fabrication and relevant material properties. In particular, we focus on methods to engineer lab-grown diamond samples optimized for ensemble-NV^- magnetometry. We analyze growth via chemical vapor deposition, high-pressure-high-temperature synthesis, and mixed-synthesis methods (Section 7.3). We examine how diamond synthesis and treatment can be used to engineer high N-to-NV^- conversion efficiencies E_{conv}, and we investigate methods to improve and stabilize the charge state efficiency $\zeta = [NV^-]/[NV^T]$ (Section 7.2). We also investigate undesired defects commonly found in NV-rich diamond samples (Section 7.6). These defects, including multi-vacancy clusters and hydrogen-related impurities, may both trap charges in the diamond and contribute to the dipolar spin bath, reducing both E_{conv} and T_2^*.

Although present understanding of diamond synthesis, treatment, and characterization is extensive and spans multiple decades, further work is needed to reproducibly create NV^--rich diamond samples with low strain, low concentrations of unwanted impurities, and high NV^- concentrations. In particular, advancing diamond materials science to enable longer native T_2^* values is a worthwhile pursuit; e.g., although the NV^- center's sensitivity to strain can be reduced (Sections 6.1.2 and 6.1.4), employing low-strain host diamonds is preferable regardless. Importantly, a robust and optimized protocol for diamond irradiation and annealing that takes nitrogen concentration into account should be established (Sections 7.4 and 7.5). Furthermore, widespread access to high-quality scientific diamonds is imperative and would greatly accelerate advances in NV-diamond-related research. Presently, diamonds with natural carbon isotopic abundance, suboptimal nitrogen concentrations, and undesired

strain and surface characteristics are widely employed by the community solely because most research groups lack access to optimized diamond samples.

Chapter 8

Conclusion

The common thread running through all chapters of this dissertation is the endeavor to design and implement optimized magnetic sensors and imagers using ensembles of NV^- centers. We present three experiments, each geared toward optimizing a different variant of the DC magnetic field sensitivity - the vector projection sensitivity, the full vector sensitivity, and the volume-normalized sensitivity. The first two experiments (Chapters 3 and 4) employ CW-ODMR magnetometry, as it is technically simpler than pulsed Ramsey magnetometry and can yield high sensitivity for fixed optical and microwave (MW) power in combination with high [NV^-] and large interrogation volume. The third experiment (Chapter 5) employs double-quantum Ramsey magnetometry to allow imaging with uniform, high volume-normalized sensitivity.

In Chapter 3 we present a first optical magnetic detection of action potentials (APs) from single firing neurons. We demonstrate a record magnetic field sensitivity among ensemble NV^- broadband magnetometers of 15 pt/$\sqrt{\text{Hz}}$ from 80 Hz to $\sim$ 3 kHz. With this device, we measure time-resolved magnetic fields produced by single-neuron APs from marine worm and squid. Chapter 4 optimizes the sensitivity to all three Cartesian components of a dynamic vector magnetic field using multi-frequency MW modulation and lock-in detection. The simultaneous vector magnetometer achieves $\sim$ 50 pT/$\sqrt{\text{Hz}}$ sensitivity for each Cartesian magnetic field component simultaneously, a record among full vector magnetometers employing solid-state spins. In Chapter 5 we implement a double-quantum Ramsey magnetic imager based on NV^- ensembles.

We demonstrate a novel phase alternation protocol that mitigates the effects of pulse errors associated with strain gradients over the imaging region. We reconstruct time-resolved magnetic signals from a fabricated neuron-like phantom from DC to $\sim$ kHz over a $\sim$ 300-μm field of view. We discuss ongoing efforts toward improving the volume-normalized magnetic-field sensitivity to allow for biocurrent mapping in living electrically active cells.

The remaining chapters of this dissertation focus on the observation that the best demonstrated DC and broadband magnetometers based on NV^- ensembles exhibit sensitivities orders of magnitude away from theoretical limits. These chapters explore strategies to approach these limits, both through identifying key parameters and evaluating proposed methods to improve these parameters. In Chapter 1 we argue that pulsed Ramsey-type magnetometry protocols are preferable to CW- and pulsed ODMR for pushing sensitivity toward fundamental limits. While CW-ODMR sensitivity is mainly improved through increasing the interrogation volume, which does not improve volume-normalized sensitivity, Ramsey magnetometry can take advantage of additional methods to improve both volume-normalized sensitivity and overall sensitivity. Ramsey sensitivity can benefit from T_2^* extension directly and from readout-fidelity-enhancement techniques that require long T_2^* for sensitivity improvement. Therefore, Chapters 2, 6, and 7 focus on understanding and improving the spin dephasing time T_2^*, the spin readout fidelity $\mathcal{F} = 1/\sigma_R$, and the host diamond material properties to inform efforts to improve ensemble-NV^- Ramsey magnetometers.

Table 8 summarizes our analysis of present and proposed techniques to optimize ensemble-NV^- magnetic field sensitivity. Table 8.0.2 summarizes our review of engineering methods for producing optimized diamond samples for high-sensitivity ensemble-NV^- magnetometry. We determine that spin-to-charge conversion readout (Section 6.2.1) and ancilla-assisted repetitive readout (Section 6.2.3) presently offer the most promise for enabling σ_R to approach the spin-projection limit, yet both techniques introduce long experimental overhead times and thus require $T_2^* \gtrsim 10$ μs to yield sensitivity enhancements. Therefore, a combination of strategies to extend

T_2^* should first be implemented. As many disparate factors limit T_2^*, we recommend a joint approach, combining double-quantum coherence magnetometry (Section 6.1.2), spin bath driving (Section 6.1.3), isotopic engineering (Section 2.2.3), bias magnetic field engineering (Section 6.1.4, reduction of external magnetic field noise and gradients, and optimized diamond growth and treatment to increase the conversion efficiency to NV^- and reduce the concentration of unwanted paramagnetic defects (Chapter 7).

Sensitivity optimization		
Parameter optimized	Method	Method description and evaluation
	Double-quantum coherence magnetometry (Section 6.1.2)	Doubles effective gyromagnetic ratio. Removes dephasing from mechanisms inducing shifts common mode to the $\|m_s = \pm 1\rangle$ states, such as longitudinal strain and temperature. Minor additional MW hardware usually required. Generally recommended.
	Bias magnetic field (Section 6.1.4)	Operation in a bias magnetic field of several gauss or higher suppresses dephasing from transverse electric fields and strain. Generally recommended.
	Spin bath driving (Section 6.1.3)	Mitigates or eliminates dephasing from paramagnetic impurities in diamond. Each impurity's spin resonance must be addressed, often with an individual RF frequency. Additional RF hardware is required. Recommended for many applications.
Dephasing time T_2^*	Dynamical decoupling (Section 6.1.1)	Refocuses spin dephasing using one or more MW π-pulses, extending the relevant relaxation time from T_2^* to T_2, with fundamental limit set by $2T_1$. Recommended for narrowband AC sensing; generally precludes DC or broadband magnetic sensing.
	Rotary echo magnetometry (Section 6.3.1)	MW pulse scheme extends measurement time but offers reduced sensitivity relative to Ramsey. Not recommended outside niche applications.
	Geometric phase magnetometry (Section 6.3.2)	MW spin manipulation method offers increased dynamic range but reduced sensitivity relative to Ramsey. Not recommended outside niche applications.
	Ancilla-assisted upconversion magnetometry (Section 6.3.3)	Method employs NV^- hyperfine interaction to convert DC magnetic fields to AC fields to be sensed using dynamical decoupling. Operates near ground-state level anticrossing (10^3 gauss) and offers similar or reduced sensitivity relative to Ramsey. Not generally recommended.

Continued on next page

Sensitivity optimization – *Continued from previous page*

Parameter optimized	Method	Method description and evaluation
	Spin-to-charge conversion readout (Section 6.2.1)	Maps spin state to charge state of NV, increasing number of photons collected per measurement. Allows $\sigma_R \approx 3$, and initial results show improvement over conventional readout for ensembles. Substantially increased readout time likely precludes application when $T_2^* \lesssim 3$ µs. Requires increased laser complexity. Technique is envisioned as promising; hence, further investigation is warranted.
	Ancilla-assisted repetitive readout (Section 6.2.3)	Maps NV^- electronic spin state to nuclear spin state, enabling repetitive readout and increased photon collection. Allows σ_R to approach 1 for single NVs; no fundamental barriers to ensemble application. Substantially increased readout time likely precludes application when $T_2^* \lesssim 3$ µs. Requires high magnetic field strength and homogeneity. Technique is envisioned as promising, although further investigation is warranted.
Readout fidelity $\mathcal{F} = 1/\sigma_R$	Improved photon collection (Section 6.2.5)	Improves σ_R by reducing fractional shot noise contribution, subject to unity collection and projection noise limits. Near-100% collection efficiency is possible in principle, making this mainly an engineering endeavor. While many schemes are incompatible with wide-field imagers, the method is generally recommended for optical-based readout of single-channel bulk sensors.
	NIR absorption readout (Section 6.2.6)	Probabilistic readout of initial spin population using optical absorption on the $^1E \leftrightarrow {}^1A_1$ singlet transition. Demonstrated σ_R values are on par with conventional ensemble readout, and prospects for further improvement are unknown. Technique is best paired with dense ensembles and an optical cavity but is hindered by non-NV^- absorption and non-radiative NV^- singlet decay. Further investigation is warranted.
	Photoelectric readout (Section 6.2.2)	Spin-dependent photoionization current is detected. Best for small 2D ensembles; has not yet demonstrated sensitivity improvement with respect to optimized conventional readout.

Continued on next page

Sensitivity optimization – *Continued from previous page*		
Parameter optimized	Method	Method description and evaluation
	Level-anticrossing-assisted readout (Section 6.2.4)	Universal technique increases number of spin-dependent photons collected per readout by operation at the excited-state level anticrossing. At best offers a $\sqrt{3}$ improvement in σ_R. Not recommended outside niche applications.
	Green absorption readout (Section 6.2.7)	Probabilistic readout of initial spin state using optical absorption on the $^3A_2 \leftrightarrow ^3E$ triplet transition. Performs best with order unity optical depth. Demonstrations exhibit contrast below that of conventional readout by 3× or more. Prospects are not envisioned as promising.
Readout fidelity $\mathcal{F} = 1/\sigma_R$	Laser threshold magnetometry (Section 6.2.8)	Probes magnetic field by measuring lasing threshold, which depends on NV^- singlet state population. Moderately improved collection efficiency and contrast are predicted compared to conventional readout. Challenges include non-NV^- absorption and system instability near lasing threshold. Prospects are not envisioned as promising.
	Entanglement-assisted magnetometry (Section 6.3.4)	Proposed techniques harness strong NV^- dipolar interactions to improve readout fidelity beyond the standard quantum limit. Existing proposals require 2D ensembles, impose long overhead times, and exhibit unfavorable coherence time scaling with number of entangled spins. While existing protocols are not envisioned as promising, further investigation toward developing improved protocols is warranted.

Table 8.0.1: Summary analysis of approaches to optimize ensemble-NV-diamond magnetic sensitivity

Nonetheless, there remain many areas where future study is warranted to allow for ensemble NV^- magnetic field sensitivity improvements. First, many aspects of NV physics, and charge dynamics for ensembles in particular, remain poorly understood. We anticipate that additional knowledge could be harnessed to improve sensor perfor-

Diamond material optimization		
Parameter optimized	Method	Method description and evaluation
N-to-NV conversion efficiency χ (Section 7.1) NV-to-NV$^-$ charge state efficiency ζ (Section 7.1) Unwanted spin impurities (Section 7.6) Strain (Section 2.2) Nuclear spins (Section 2.2.3)	CVD synthesis (Section 7.3)	Common synthesis method that can produce high-quality NV$^-$-rich bulk and layer diamonds. Relatively easy to control dimensions and electronic/nuclear spin concentrations. May introduce strain and unwanted impurities, which can limit achievable ζ, χ, and T_2^*.
	HPHT synthesis (Section 7.3)	Common synthesis method that can produce high-quality NV$^-$-rich bulk diamonds with lower strain and fewer lattice defects than CVD. Not intrinsically amenable to NV$^-$-rich layer diamonds. Control over doping and impurity concentration may be more difficult than CVD. May incorporate ferromagnetic metals into diamond.
	Irradiation (Section 7.4.1)	Diamond treatment method that, combined with subsequent annealing, converts substitutional nitrogen to NV centers. Electrons are preferred source. Dose should be optimized for diamond's nitrogen concentration for high ζ without degraded χ. Recommended with annealing for producing NV$^-$-rich diamonds.
	LPHT annealing (Section 7.5)	Low-pressure annealing that, combined with prior irradiation, converts substitutional nitrogen to NV centers. Heals some diamond lattice damage. Creates NV$^-$ centers effectively at $\sim$ 800 °C; further treatment at $\sim$ 1200 °C removes certain unwanted impurities. Recommended with irradiation for producing NV$^-$-rich diamonds.
	HPHT treatment (Section 7.3)	High-pressure annealing may reduce strain and eliminate some unwanted impurities. May enable increases in ζ and χ. Recommended for diamonds with balanced aspect ratios.
	Isotopic enrichment (Section 2.2.3)	Diamond synthesis with isotopically enriched source (gas for CVD, typically solid for HPHT) allows reduction of nuclear spin concentration (e.g., ^{13}C) and selection of nitrogen isotope incorporated into NV$^-$ (^{14}N or ^{15}N). CVD diamonds with [^{13}C] $\approx$ 20 ppm have been synthesized. Recommended for extending T_2^*.
	Surface treatment (Section 7.1)	Surface termination can stabilize the desired NV charge state near the surface and extend relaxation times. Generally recommended.
	Preferential orientation (Section 7.7)	CVD diamond synthesis with NV centers preferentially oriented along a single axis. Only maintained in unirradiated diamonds at present, largely hindering its capability to produce NV$^-$-rich diamonds. Not generally recommended.

Table 8.0.2: Summary analysis of diamond engineering parameters and methods for high-sensitivity ensemble-NV$^-$ magnetometry. Colored lines indicate methods that may be employed to optimize each parameter.

mance, similar to how the study of NV^- and NV^0 ionization characteristics under low optical intensity by Aslam *et al.* [308] prompted the development of spin-to-charge conversion readout (Section 6.2.1. Further examination of charge dynamics under magnetometer operating conditions (e.g., high optical intensity) is expected to yield fruitful insights. For NV-rich diamonds, systematic studies of (i) NV^- ionization (both from the singlet and triplet excited states), and (ii) recombination from the NV^0 excited state versus optical wavelength and intensity, would be particularly useful. Such studies would address present knowledge gaps and could inform diamond-engineering protocols to better stabilize the NV^- charge state in ensemble-based devices. These investigations could also lay the groundwork for new sensitivity-enhancement techniques tailored to ensembles. In addition, continued basic research into the NV^- center is warranted. For example, while four electronic states of NV^- have been observed, two additional predicted states have not yet been experimentally confirmed [531].

We also expect unanticipated creative ideas to emerge that further enhance readout fidelity, dephasing time T_2^*, and overall magnetic field sensitivity. Ensemble-NV^- magnetometers are already relevant in wide-varying sensing applications, thanks to key advances made over the past decade, which we have summarized here. Moreover, NV-diamond quantum sensing is a quickly developing platform, well positioned to continue improving, with significant advancements possible before fundamental limits are reached. We hope that this dissertation may serve as both a foundation and a road map for those seeking to implement quantum sensors based on NV^- ensembles in diamond. By combining the knowledge presented here with likely future advances, we expect further expansion of this system's diverse set of applications.

Appendix A

Frequently used symbols and abbreviations

Acronym	Description
AP	Action potential
CPMG	Carr-Purcell-Meiboom-Gill (pulse sequences)
CW	Continuous wave
CVD	Chemical vapor deposition
DEER	Double electron-electron resonance
DQ	Double quantum
EPR	Electron paramagnetic resonance
ESLAC	Excited-state level anti-crossing
ESR	Electron spin resonance
FID	Free induction decay
FM	Frequency modulation
I	In-phase
GSLAC	Ground state level anti-crossing
HPHT	High pressure high temperature
LAC	Level anti-crossing
LIA	Lock-in amplifier
LPHT	Low pressure high temperature
MEG	Magnetoencephalography
MW	Microwave
NIR	Near-infrared
NMR	Nuclear magnetic resonance
NQR	Nuclear quadrupole resonance
ODMR	Optically detected magnetic resonance
PDMR	Photoelectrically detected magnetic resonance
PE	Photoelectric (readout)
PL	Photoluminescence
Q	Quadrature
QND	Quantum non-demolition
RF	Radiofrequency
SCC	Spin-to-charge conversion
SNR	Signal-to-noise ratio
s.d.	Standard deviation
SQ	Single quantum (standard basis)
SQUID	Superconducting quantum interference device

Table A.0.1: Frequently used acronyms

Quantity	Symbol	Units
Longitudinal (spin-lattice) relaxation time	T_1	s
Coherence time (transverse relaxation time)	T_2	s
Dephasing time (free induction decay time)	T_2^*	s
Single-NV$^-$ dephasing time	$T_2^{*\{\text{single}\}}$	s
Magnetic field sensitivity	η	$\text{T}/\sqrt{\text{Hz}}$
Volume-normalized magnetic field sensitivity	$\eta^V \equiv \eta\sqrt{V}$	$\text{T}/\sqrt{\text{Hz}}$
Interrogation time (free-precession time for Ramsey)	τ	s
Initialization, readout, and total overhead time	t_I, t_R, t_O	s
Stretched exponential parameter	p	-
Static (bias) & microwave magnetic field	B_0 & B_1	T
Electronic spin gyromagnetic ratio	$\gamma_e \equiv g_e\mu_B/\hbar$	s^{-1}/T
Readout fidelity	$\mathcal{F} \equiv 1/\sigma_R$	-
Factor above spin projection noise	$\sigma_R \equiv 1/\mathcal{F}$	-
Rabi frequency	Ω_R	s^{-1}
ODMR center frequency & linewidth	ν & $\Delta\nu$	Hz
Dephasing or decay rate	Γ	s^{-1}
Measurement contrast (fringe visibility)	C	-
CW-ODMR contrast, pulsed ODMR contrast	C_{CW}, C_{pulsed}	-
Number of sensors (NV$^-$ centers in ensemble)	N	-
Average collected photons per readout per NV$^-$	n_{avg}	-
Average collected photons per readout from an NV$^-$ ensemble	$\mathcal{N}$	-
Concentration of species X	[X]	cm^{-3} or ppm
Negative, neutral & total NV concentration	[NV$^-$], [NV^0], [NV$^{\text{T}}$]	cm^{-3} or ppm
Total nitrogen concentration in the lattice	[N$^{\text{T}}$]	cm^{-3} or ppm
Neutral, positive, total substitutional nitrogen concentration	[N_S^0], [N_S^+], [$\text{N}_\text{S}^{\text{T}}$]	cm^{-3} or ppm
Contribution to T_2^* from mechanism X	$T_2^*\{\text{X}\}$	s
Dipolar interaction strength between N_S^0 and NV$^-$	$A_{\text{N}_\text{S}^0}$	s^{-1}/ppm

Continued on next page

Continued from previous page

Quantity	Symbol	Units
Dipolar interaction strength between ^{13}C and NV$^-$	$A_{^{13}\mathrm{C}}$	s^{-1}/ppm
Dipolar interaction strength between NV$^-$ spins in the same group (same resonance frequency)	$A_{\mathrm{NV}^-_{\parallel}}$	s^{-1}/ppm
Dipolar interaction strength between NV$^-$ spins in different groups (different resonance frequencies)	$A_{\mathrm{NV}^-_{\nparallel}}$	s^{-1}/ppm
Proportionality factor for $\mathrm{N}^0_{\mathrm{S}}$ contribution to T_2	$B_{\mathrm{N}^0_{\mathrm{S}}}$	s^{-1}/ppm
Hamiltonian	H	J
Electronic spin, electronic spin projection	S, m_s	-
Nuclear spin, nuclear spin projection	I, m_I	-
NV$^-$ ground state spin eigenstates	$\{\|0\rangle, \|-1\rangle, \|+1\rangle\}$	-
NV$^-$ double-quantum superposition states	$\|\pm_{\mathrm{DQ}}\rangle \equiv (\|+1\rangle \pm \|-1\rangle)/\sqrt{2}$	-
Zero field splitting parameter	$D \approx 2.87$ GHz	Hz
Spin-strain coupling parameters	$\mathcal{M}_z$, $\mathcal{M}_x$, $\mathcal{M}_y$, $\mathcal{N}_x$, $\mathcal{N}_y$	Hz
Electric field components	E_x, E_y, E_z	V/m
NV$^-$ transverse, axial (longitudinal) electric dipole moment	$d_\perp$, $d_\parallel$	Hz/(V/m)
Transverse strain and electric field coupling parameter	$\xi_\perp$	Hz
Axial magnetic field coupling parameter	β_z	Hz
Total N-to-NV$^-$ conversion efficiency	$\mathrm{E}_{\mathrm{conv}} \equiv [\mathrm{NV}^-]/[\mathrm{N}^{\mathrm{T}}]$	-
N-to-NV conversion efficiency	$\chi \equiv [\mathrm{NV}^{\mathrm{T}}]/[\mathrm{N}^{\mathrm{T}}]$	-
NV-to-NV$^-$ charge state efficiency	$\zeta \equiv [\mathrm{NV}^-]/[\mathrm{NV}^{\mathrm{T}}]$	-

Table A.0.2: Frequently used symbols

Appendix B

NV$^-$ spin Hamiltonian in limiting regimes

Here we describe coupling of electric fields, strain, and magnetic fields to the NV$^-$ spin resonances in the regimes of both low and high axial bias magnetic field $B_{0,z}$. This treatment draws heavily on equations and analysis in Ref. [94]. While understanding of strain's effect on the NV$^-$ spin continues to evolve [8, 57, 90, 532], we take the NV$^-$ ground state spin Hamiltonian in the presence of a bias magnetic field $\vec{B}_0$, an electric field $\vec{E}$, and intrinsic crystal strain to be [90, 8]

$$\begin{aligned} H/h = &\left(D + \mathcal{M}_z + d_\parallel E_z\right) S_z^2 \\ &+ \frac{g_e \mu_B}{h} \left(B_{0,z} S_z + B_{0,x} S_x + B_{0,y} S_y\right) \\ &+ \left(\frac{d_\perp E_x}{h} + \mathcal{M}_x\right) \left(S_y^2 - S_x^2\right) \\ &+ \left(\frac{d_\perp E_y}{h} + \mathcal{M}_y\right) \left(S_x S_y + S_y S_x\right) \\ &+ \mathcal{N}_x \left(S_x S_z + S_z S_x\right) + \mathcal{N}_y \left(S_y S_z + S_z S_y\right). \end{aligned} \tag{B.1}$$

Here S_i with $i = x, y, z$ are the dimensionless spin-1 projection operators; D is the NV$^-$ zero field splitting (≈ 2.87 GHz at room temperature); $d_\parallel = 3.5 \times 10^{-3}$ Hz/(V/m) and $d_\perp = 0.17$ Hz/(V/m) are the axial and transverse electric dipole moments [92, 56, 93]; and $\mathcal{M}_z$, $\mathcal{M}_x$, $\mathcal{M}_y$, $\mathcal{N}_x$, and $\mathcal{N}_y$ are spin-strain coupling parameters.

The Hamiltonian can be simplified when D is large compared to all other coupling terms, i.e., in the regime of low magnetic field, electric field, and strain. In particular, energy level shifts associated with transverse magnetic field components $B_{0,x}$ and $B_{0,y}$ [94], and with spin-strain coupling parameters $\mathcal{N}_x$ and $\mathcal{N}_y$, are suppressed by D and thus may be neglected from the Hamiltonian [85]. This low-field Hamiltonian H_{LF} is given by

$$\begin{aligned} H_{\mathrm{LF}}/h = &\left(D + \mathcal{M}_z + d_{\parallel}E_z\right) S_z^2 + \frac{g_e\mu_B}{h} B_{0,z} S_z \\ &+ \left(\frac{d_{\perp}E_x}{h} + \mathcal{M}_x\right)\left(S_y^2 - S_x^2\right) \\ &+ \left(\frac{d_{\perp}E_y}{h} + \mathcal{M}_y\right)\left(S_x S_y + S_y S_x\right). \end{aligned} \tag{B.2}$$

We focus on the interplay between different terms in H_{LF} that shift the NV$^-$ spin resonance frequencies in opposite directions, including $B_{0,z}$, E_x, E_y, $\mathcal{M}_x$, and $\mathcal{M}_y$. In contrast, dephasing associated with variations in terms that shift the resonance frequencies in common-mode (D, E_z, and $\mathcal{M}_z$), can be mitigated by employing double-quantum coherence magnetometry (see Section 6.1.2) and are ignored herein. In addition to shifting the spin resonance frequencies, transverse electric fields, E_x and E_y, and transverse spin-strain coupling terms, $\mathcal{M}_x$ and $\mathcal{M}_y$, mix the $m_s = \pm 1$ spin states into

$$|+\rangle = \cos\left(\frac{\theta}{2}\right)|+1\rangle + e^{i\phi}\sin\left(\frac{\theta}{2}\right)|-1\rangle, \tag{B.3}$$

$$|-\rangle = \sin\left(\frac{\theta}{2}\right)|+1\rangle - e^{i\phi}\cos\left(\frac{\theta}{2}\right)|-1\rangle, \tag{B.4}$$

where $\tan(\phi) = (d_{\perp}E_y + \mathcal{M}_y)/(d_{\perp}E_x + \mathcal{M}_x)$ and $\tan(\theta) = \xi_{\perp}/\beta_z$. Here $\beta_z = (g_e\mu_B/h)B_{0,z}$ represents the magnetic field coupling to the NV$^-$ spin and

$$\xi_{\perp} = \sqrt{(d_{\perp}E_x/h + \mathcal{M}_x)^2 + (d_{\perp}E_y/h + \mathcal{M}_y)^2} \tag{B.5}$$

combines the effects of transverse strain and electric fields. The transition frequencies

$|0\rangle \leftrightarrow |+\rangle$ and $|0\rangle \leftrightarrow |-\rangle$ are

$$\nu_{\pm} = D + \mathcal{M}_z + d_{\parallel} E_z \pm \sqrt{\xi_{\perp}^2 + \beta_z^2}, \tag{B.6}$$

and the coupling strength of transverse strain and electric fields to the NV$^-$ spin resonance frequencies is given by

$$\frac{\partial \nu_{\pm}}{\partial \xi_{\perp}} = \frac{\pm 1}{\sqrt{1 + \left(\frac{\beta_z}{\xi_{\perp}}\right)^2}}. \tag{B.7}$$

In the linear Stark regime, characterized by $\beta_z \ll \xi_{\perp}$, the spin eigenstates become, approximately, equal superpositions of $|+1\rangle$ and $|-1\rangle$, and the transition frequencies exhibit maximal sensitivity to variations in $\xi_{\perp}$:

$$\left|\frac{\partial \nu_{\pm}}{\partial \xi_{\perp}}\right|_{\beta_z \ll \xi_{\perp}} = 1 - \frac{1}{2}\left(\frac{\beta_z}{\xi_{\perp}}\right)^2 + \mathcal{O}\left[\left(\frac{\beta_z}{\xi_{\perp}}\right)^4\right]. \tag{B.8}$$

In contrast, in the linear Zeeman regime, characterized by $\beta_z \gg \xi_{\perp}$, the spin eigenstates become, approximately, $|+1\rangle$ and $|-1\rangle$, and sensitivity to strain/electric fields is suppressed by the ratio $\frac{\xi_{\perp}}{\beta_z}$:

$$\left|\frac{\partial \nu_{\pm}}{\partial \xi_{\perp}}\right|_{\beta_z \gg \xi_{\perp}} = \frac{\xi_{\perp}}{\beta_z} - \frac{1}{2}\left(\frac{\xi_{\perp}}{\beta_z}\right)^3 + \mathcal{O}\left[\left(\frac{\xi_{\perp}}{\beta_z}\right)^5\right]. \tag{B.9}$$

By performing magnetic sensing in the linear Zeeman regime, spatial and temporal variations in transverse electric fields and strain couple less strongly to the NV$^-$ spin, and thus their contribution to T_2^* is diminished. The linear Zeeman regime is best suited for high-sensitivity magnetometry not only because of the T_2^* extension from suppressed sensitivity to variations in $\xi_{\perp}$, but also because magnetic field changes couple most strongly to $\nu\pm$ in this regime:

$$\left|\frac{\partial \nu_{\pm}}{\partial \beta_z}\right|_{\beta_z \gg \xi_{\perp}} = 1 - \frac{1}{2}\left(\frac{\xi_{\perp}}{\beta_z}\right)^2 + \mathcal{O}\left[\left(\frac{\xi_{\perp}}{\beta_z}\right)^4\right]. \tag{B.10}$$

Experiments that must operate at near-zero $\vec{B}_0$ for other reasons, such as to protect ferromagnetic samples, should use low-strain diamonds to avoid operating in the unfavorable regime where $\beta_z \ll \xi_\perp$ [13, 68, 251, 423]. In this linear Stark regime, not only is sensitivity to magnetic signals suppressed by the ratio $\frac{\beta_z}{\xi_\perp}$,

$$\left|\frac{\partial \nu_\pm}{\partial \beta_z}\right|_{\beta_z \ll \xi_\perp} = \frac{\beta_z}{\xi_\perp} - \frac{1}{2}\left(\frac{\beta_z}{\xi_\perp}\right)^3 + \mathcal{O}\left[\left(\frac{\beta_z}{\xi_\perp}\right)^5\right], \tag{B.11}$$

but also T_2^* may be shortened by electric field and strain variations.

Appendix C

Considerations for the NV-diamond single-neuron magnetometer

C.1 Diamond surface metalization

We coat the top surface of the NV-diamond employed in Chapter 3 with a thin metallic reflective layer for two purposes: to reflect the NV^- fluorescence down toward the objective in order to increase light collection by the optics below the diamond; and to enable uniform microwave delivery in close proximity to the NV^- sensing layer of the diamond.

The layer shown in Figure C.1.1 is fabricated via metal evaporation.

Platinum, a common metal used in electrophysiology, is fabricated on the very top to provide a nonreactive, biocompatible barrier to the axonÂăand the salt water perfusion liquid. The titanium layers are to adhere the silver to the diamond and the platinum to the silver. Titanium and chromium are both good options for this. In addition to both being good for adhesion, they have similar reflectivity (0.56 for Cr and 0.63 for Ti) and transmittance (0.83 for a 3 nm layer of Cr and 0.81 for a 3 nm layer of Ti) of 700nm light. Here we choose titanium, following Ref. [332]. A thin ahdesion layer is desirable so that very little fluorescence is absorbed. In Ref. [332] a 2 nm Ti layer is deposited. To be slightly more conservative we choose a 3 nm layer, since thicker layers provide more adhesion. The layer above the silver does not need

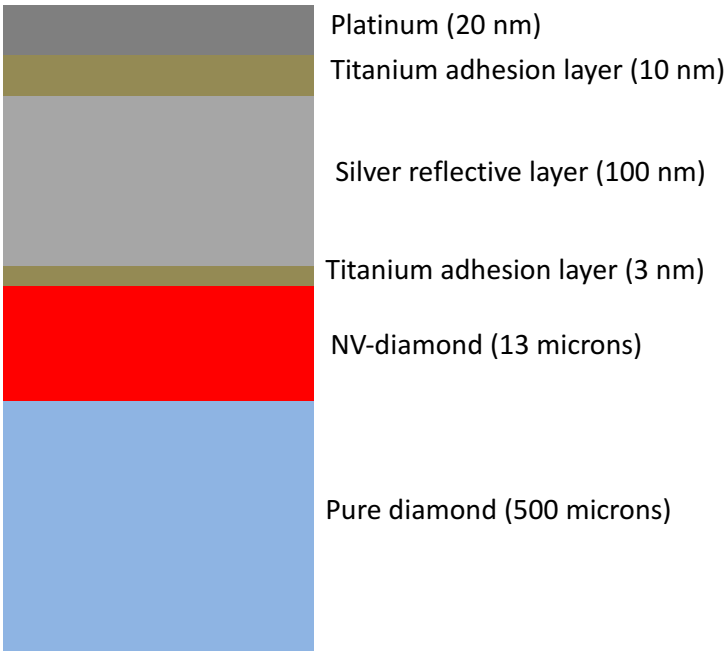

Figure C.1.1: Metalization of the top surface of the NV-diamond employed for optical magnetic detection of single-neuron action potentials (not to scale). The silver layer serves to reflect NV^- fluorescence down toward the objective; the platinum layer provides a nonreactive, biocompatible barrier to the axonÂăand the salt water perfusion liquid; and the titanium layers serve for adhesion.

to be transmissive, so we deposit a thicker 10 nm layer.

Other recipes we considered before settling on the recipe depicted in Figure C.1.1 are examined below. We considered replacing the top platinum layer with a different material or spin-coating an additional layer on top of the platinum, in order to reduce the chance of delamination. Gold is another metal that is straightforward to evaporate and biocompatible, but it is very soft and may delaminate more easily than platinum.

SiO_2 could be spin-coated above the platinum; it is biocompatible and is commonly used to coat commercial protected silver mirrors [533]. However, because it is an insulator, it would complicate microwave delivery to the silver by making it more difficult to ensure good electrical contact without additional fabrication steps. We also considered tungsten, which is much harder and might be less likely to delaminate, but would be more difficult to evaporate (as the crucible in the evaporator is made from tungsten) and may be less biocompatible. Alumina is insulating and would make it difficult to form electrical to deliver MWs to the silver layer. TiO_2, which would form from near-immediate oxidation of a top layer of titanium, is not biocompatible. Silicon, germanium, and silver are not biocompatible; silicon reacts with calcium, making it a neurotoxin, and silver and germanium are also toxic to neurons. Palladium is very similar to platinum but slightly harder. It is inert and not likely to ionize, meaning it is generally biocompatible, although it becomes toxic if ionized.

In practice, we found that the metal layer did not delaminate easily upon agitation in common solvents but was corroded by the salt water perfusion liquid. In order to avoid this problem in the future, we could consider spin coating material on top of the silver or platinum layer after the leads are attached. Poly(methyl methacrylate) (PMMA) is an inexpensive and shelf-stable option, but it dissolves in acetone, a common solvent we use to clean the diamond mount. Hydrogen silsesquioxane (HSQ) or flowable oxide (FOX) resists are expensive, have short shelf life, and could be very easily scratched off if not exposed to e-beam lithography within 12 hours. However, after e-beam exposure these resists would be insoluble in acetone, which is a more favorable property. Ultimately, we resolved to try spin-coating a PMMA layer if needed in the future.

C.2 Microwave design considerations

C.2.1 Introduction

A key challenge to achieving a high-sensitivity magnetic imager is the delivery of high-MW-Rabi-frequencies with a high degree of spatial uniformity and operation over a sufficiently broad frequency spectrum to enable operation at various bias fields or in a vector sensing configuration. This task is tricky in part because some of these goal conflict with one another. For example, resonator structures can enable high Rabi frequencies at the cost of bandwidth [534]. Nonetheless, it is worth investigating whether low-quality factor MW resonators could be engineered to fit without our other design constraints. Here we document a partial list of challenges associated with building a MW resonator at ~ 3 GHz for high-sensitivity NV-diamond magnetic sensing and imaging.

C.2.2 Microwave engineering background and transmission line theory

Design of MW circuits at ~ 3 GHz is complicated by the intermediate wavelength regime ($\lambda \sim 10$ cm in vacuum or ~ 7 cm in 50 Ω coaxial cable). As a general rule of thumb, to design a resonant circuit using lumped elements and obtain performance that agrees with the design, the lumped elements must be smaller than $\lambda/10$. When in a shorter wavelength regimes, capacitors, inductors, transformers, and matching networks in general may be designed and fabricated out of stubs of transmission line. Here we discuss the basics of transmission line theory.

A transmission line is often modeled as an infinite set of parallel capacitors and series inductors of infinitesimal capacitance and inductance. In textbooks, transmission lines are often modeled as lossless. In practice, there is loss: dielectric loss (parallel conductance) and conductor loss (series resistance). The characteristic impedance (Z_0) of a transmission line is the ratio of the amplitudes of voltage and current of a single wave propagating along the line, determined by the geometry and materials of

the transmission line. The impedance Z_0 of a lossless transmission line is purely real, with no reactive (imaginary) component. A transmission line of finite length (lossless or lossy) that is terminated at one end with a load impedance equal to Z_0 appears to the source like an infinitely long transmission line and produces no reflections. For example, the input impedance of a 50 Ω line terminated by a 50 Ω resistor is 50 Ω, regardless of the length of line. Meanwhile, an unmatched load will cause some of the incident wave to be reflected, which sets up a standing wave. The impedance measured at the input will then be a function of cable length as well as the load impedance and the characteristic impedance of the line. At the other extreme, a purely reactive load causes a 100% reflection, with phase shift depending on the load impedance. Important cases are: (i) an open circuit reflects with 0° phase shift, and (ii) a short circuit reflects with 180° phase shift.

The wavelength of electromagnetic radiation traveling in a transmission line is given by $\lambda = v_p/f$ where v_p is the phase velocity in the material and f is the frequency. In 50 Ω coax $v_p = 0.66c$, and in 300 Ω parallel line $v_p = 0.8c$. A transmission line segment that is $\lambda/2$ in length has an input impedance equal to the load impedance, regardless of its own characteristic impedance. A $\lambda/4$ transmission line segment with an open circuit at the end looks like a short circuit at its input, and vice versa. A $\lambda/8$ transmission line with either an open or closed circuit at the end will have the same ratio of current to voltage as if it were terminated with a load matched to its characteristic impedance - that is, the magnitude of the input impedance will be the same as the magnitude of the characteristic impedance, but the phase will be shifted by 90° to look like a purely reactive impedance.

With this basic understanding, we seek to design a matching network to efficiently deliver MWs to the diamond. Note that our goal is not to make an antenna and radiate away our MW power, but rather to create high B_1 fields at the position of the NVs using inductive components.

C.2.3 Resonant circuits

For any circuit that operates at RF or MW frequencies, including MW resonators, impedance matching is important. Impedance matching from a feedline to a resonator is often called coupling to the resonator. There are three coupling regimes: undercoupled, overcoupled, and critically coupled. Undercoupled denotes when $Z_{\text{feedline}} < Z_{\text{resonator}}$, overcoupled denotes when $Z_{\text{feedline}} > Z_{\text{resonator}}$, and critically coupled denotes the case where when $Z_{\text{feedline}} = Z_{\text{resonator}}$, corresponding to a matched impedance and full power transfer.

A resonance condition occurs when the imaginary part of the impedance disappears. If this resonance condition is met, critical coupling then occurs when the real impedances of the feedline and the resonator are matched. The simplest way to achieve critical coupling to a 50 Ω feedline is to make the resistance of the resonator 50 Ω.

The quality factor (Q) of a series resonant RLC circuit is given by the ratio of stored power to dissipated power: For the silvered diamond design for MW delivery to the diamond (see Section C.1), the load inductance is estimated to be $L \sim 4$ nH. To critically couple from a 50 Ω feedline directly to the silver layer requires a load resistance $R = 50$ Ω. This results in $Q = 2\pi \cdot 3 \cdot 4/50 =\sim 1.5$, which is clearly not a very good resonator. Thus, it is clear why we might want our resonant circuit to have a lower resistance. But then we are in the regime of undercoupling. To still obtain critical coupling from a 50 Ω feedline for a low Z_{load}, we need a type of transformer.

At MW frequencies, where the wavelength is often too short to allow use of lumped inductive transformers, a length of transmission line of characteristic impedance Z_0 can serve as a narrow-band transformer from a feedline to a real impedance load of different input impedance. The necessary conditions for this simple matching network, called a *quarter wave transformer* are $Z_0^2 = Z_{\text{feedline}} \cdot Z_{\text{load}}$ and length $= \lambda/4$. Once this quarter wave transformer is in place to match the resistive part of the load impedance, we must solve the remaining challenge of achieving the resonance condition. This turns out to be a difficult task for the silvered diamond design outlined in Section C.1,

where the silver layer on diamond is expected to exhibit a load inductance of $L \sim 4$ nH. For a resonant RLC circuit, we need the resonance frequency $f = \omega/(2\pi)$ to meet the condition $\omega^2 = 1/(LC)$. At $f = 3$ GHz, we require $C = 1/(\omega^2 L) = 1/(4\pi^2 \cdot 3^2 \cdot 4 \times 10^9) = 0.7$ pF, which is practically speaking a tiny capacitance. This illustrates why designing MW resonant circuits at 3 GHz using lumped RLC circuit equations is tricky. For lumped RLC resonant circuits, the resonance frequency needed is so large that even tiny capacitances and tiny inductances are already too high to meet the resonance condition $\omega^2 = 1/(LC)$. Therefore, transmission line theory may be a better fit for understanding and designing MW delivery structures. Therefore, a combination of analytical matching-network design using transmission line theory with finite element modeling of MW delivery structures should allow for a satisfactory solution to the problem of efficient generation of high Rabi frequency at the NV-diamond.

However, given the use of liquids, and in particular salt water, in future envisioned experiments with an enhanced-sensitivity diamond magnetic imager, a resonant circuit might not actually be a desirable solution. Even if we can meet the resonance condition $\omega^2 = 1/(LC)$ and implement a suitable quarter wave transformer to obtain critical coupling for low R_{load} and therefore achieve a high-Q resonator with large, uniform B_1 fields, any resonator operating near 3 GHz is susceptible to the effects of stray capacitances. In a system that involves water, which has a dielectric constant of 80, (not to mention conductive salt water and living organisms), the resonance frequency and coupling condition may be shifted due to parasitic capacitances. The shifts may likely be unpredictable and could change over relevant experimental timescales (minutes to days). For example, we tested the split ring resonator design from Ref. [534] on a network analyzer and found the resonance near 3 GHz disappeared when the resonator was placed in close proximity to a water bath. Nonresonant MW structures such as coplanar waveguides may exhibit higher robustness to stray capacitances than resonant circuits, as the transmission is designed to be frequency independent over a broad frequency range.

Appendix D

Additional details from the simultaneous vector magnetometer

D.1 ODMR hyperfine features

Figure D.1.1 displays an ODMR spectrum from the diamond sensor crystal employed in Chapter 4 at the bias field $\vec{B}_0$, for various MW drive strengths. Each of the eight main ODMR features exhibits subfeatures corresponding to splittings from the NV^- electric quadrupole moment and the hyperfine interaction between the NV^- electronic spin and the ^{14}N nuclear spin ($I = 1$) [169]. The three principal subfeatures correspond to allowed M1 magnetic dipole transitions $\Delta m_I = 0$ [7], and the two smaller outer subfeatures (along with a third unresolved subfeature) correspond to forbidden transitions with $\Delta m_I = \pm 1$. These forbidden spin transitions have been previously observed [243] and arise from state mixing mediated by the significant off-axis components of the bias magnetic field $\vec{B}_0$. As shown in Figure D.1.1, the locations of these subfeatures are in good agreement with theoretical calculations of the forbidden transition frequencies [169, 7]. The relative intensity of the forbidden-transition subfeatures is observed to increase with applied MW power.

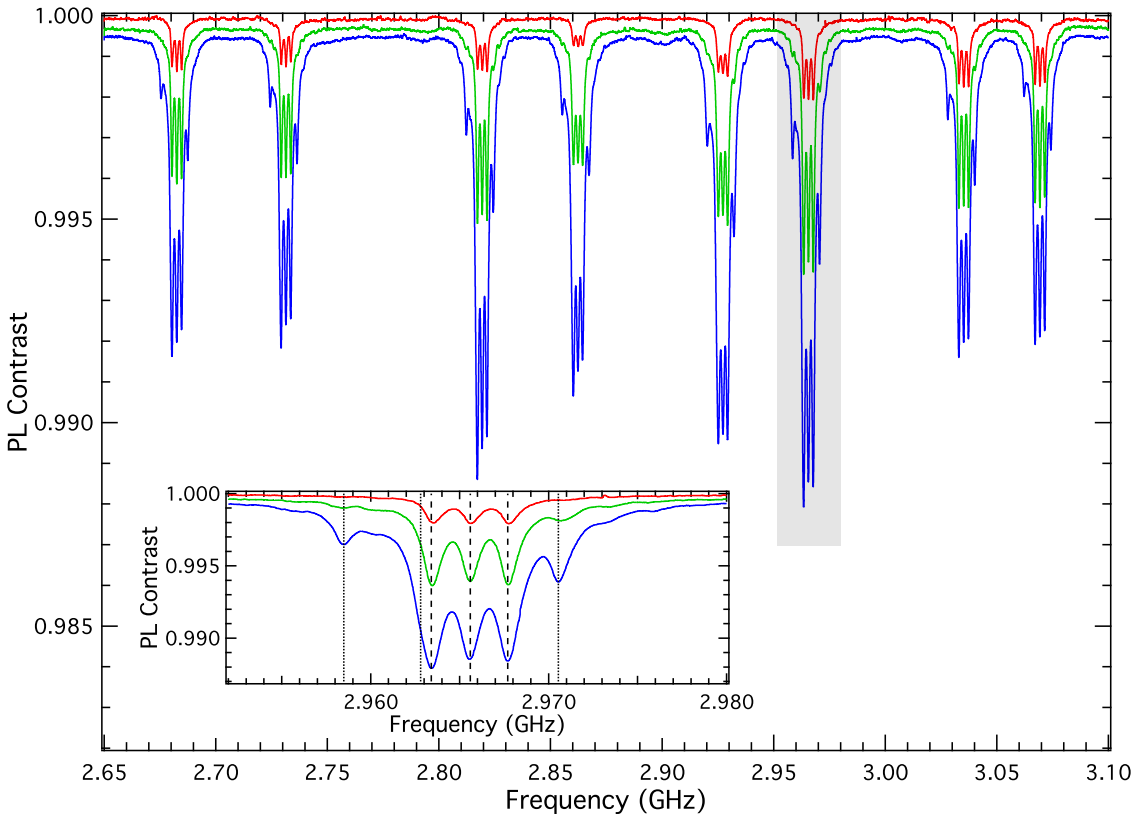

Figure D.1.1: ODMR spectrum of an NV$^-$ ensemble in applied bias field $|\vec{B}_0| = 7.99\,\mathrm{mT}$, $\vec{B}_0 = (3.54, 1.73, 6.95)\,\mathrm{mT}$ for various MW drive strengths. The blue (highest contrast) trace depicts the spectrum with MW power typical of operating conditions, while the green (middle) and red (lowest contrast) traces depict the same spectrum with MW power reduced by 12 and 24 dB, respectively. The subfeatures within the eight main ODMR features correspond to splittings associated with the NV$^-$ center's electric quadrupole moment and the hyperfine interaction between the NV$^-$ electronic spin and ^{14}N nuclear spin ($I = 1$) [169]. The three principal subfeatures correspond to allowed M1 magnetic dipole transitions with $\Delta m_I = 0$, and the two smaller subfeatures correspond to forbidden transitions with $\Delta m_I = \pm 1$, which appear due to state mixing mediated by the significant off-axis magnetic field [243] and are more pronounced for stronger MW drive. Inset shows the ODMR feature enclosed in the gray box. Dashed lines mark the allowed hyperfine transitions [169, 7]; dotted lines mark the frequencies associated with forbidden hyperfine transitions between states of different m_I [243, 7]. Traces are slightly offset for clarity in both main figure and inset.

D.2 Radia simulations of magnetized optical table

In this section we discuss numerical simulations, using the Radia package in *Mathematica* [265, 266], of the effect of a magnetizable optical table on the magnetic fields produced at the diamond sensor by the coils oriented along the x-, y-, and z-axis in Chapter 4.

Prior to nulling the off-axis fields as described in Section 4.7.1, the reconstructed magnetic field components along x, y, and z appear as shown in Figure D.2.1. Here the x coil applies a field at 67 Hz, the y coil applies a field at 32 Hz, and the z coil applies a field at 18 Hz. The black circles mark the expected RMS field amplitude at that frequency for each direction. There appear to be components of the fields produced by the x and z coils in the y-direction. These off-axis fields are ~ 20 - 30% of the on-axis components of the x- and z-coil fields.

In the absence of magnetic materials in the vicinity of the coils and the diamond, the x-component of the detected dynamic magnetic field would only contain signal from the coil oriented along the x-axis, and likewise for the y and z coils. However, we observe that the two horizontal coils (x and z in the frame defined in Chapter 4) produce non-negligible fields in the vertical direction. In contrast, the vertical coils are not observed to produce horizontal fields, nor do the horizontal coils produce fields in their respective orthogonal horizontal directions. The observed distortion cannot not be accounted for by coil misalignment. Based on symmetry arguments, we hypothesize that the magnetizable steel optical table (400 series, likely 430) employed in the present experiment distorts the amplitude and direction of the coil magnetic fields at the diamond sensor.

To investigate this hypothesis, we employed the Radia package in *Mathematica* [265, 266] to simulate the response of ferromagnetic materials to external magnetic fields. We simulated a current-carrying coil - with dimensions and position matching the z coil employed in the present experiment - placed directly above a steel surface, as shown in Figure D.2.2a. The diamond location is taken to be above the center of the surface at a height $y = h = 4.75$". The coil is 9.75" in diameter and is centered at a

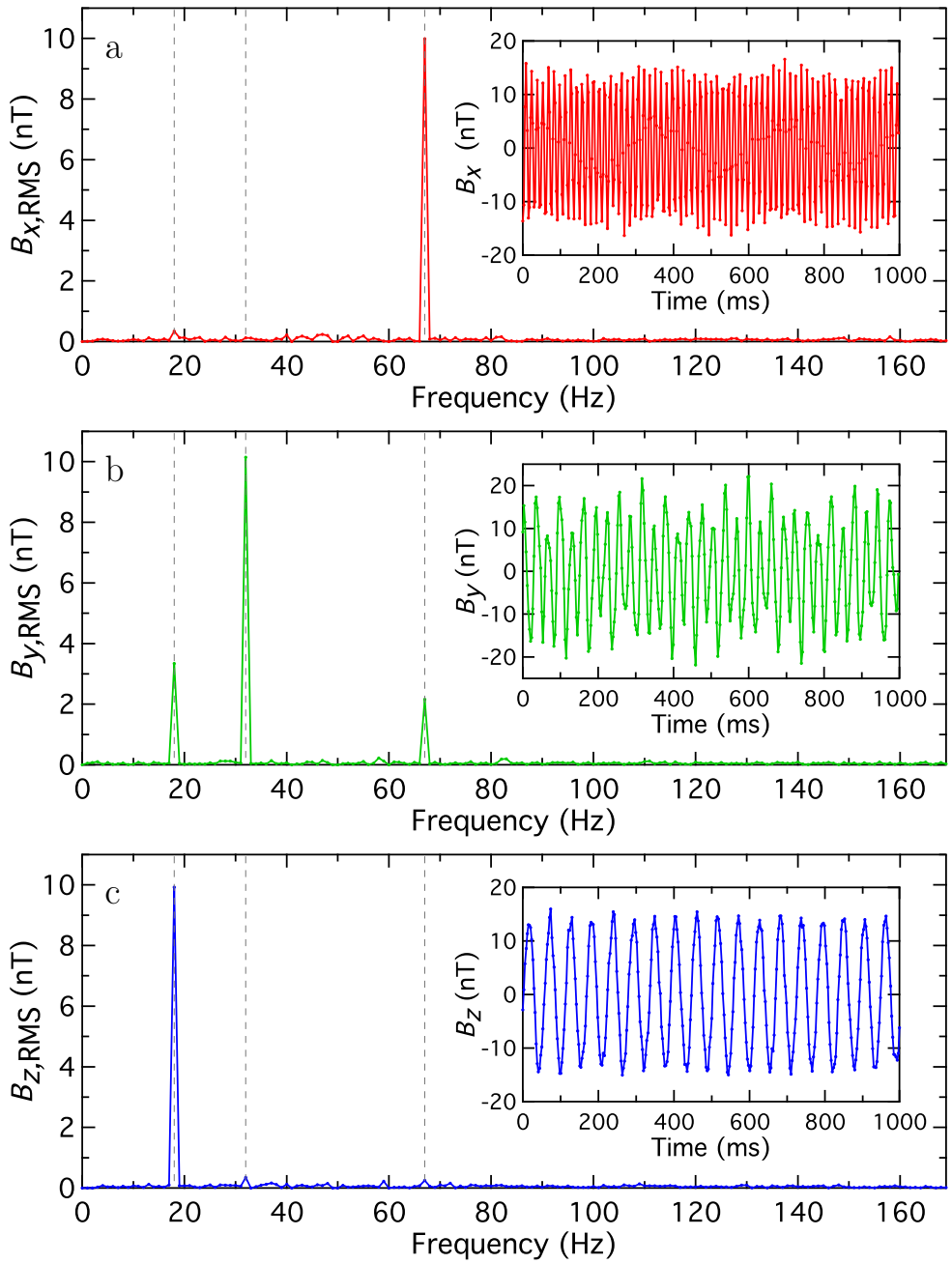

Figure D.2.1: Detected magnetic fields using simultaneous vector magnetometer without off-axis field nulling. a) B_x time trace (inset) and spectral density showing detected signal at $f_x = 67\,\text{Hz}$. b) B_y time trace (inset) and spectral density showing detected signal at $f_y = 32\,\text{Hz}$. c) B_z time trace (inset) and spectral density showing detected signal at $f_z = 18\,\text{Hz}$. Dashed lines mark applied signal frequencies f_x, f_y, f_z, and circles center on expected applied field amplitudes determined by sequential NV$^-$ vector magnetometry. Cartoon recreations of Figure 4.6.1a illustrate isolated detected components of dynamic vector magnetic field $B_x(t)$, $B_y(t)$, $B_z(t)$.

height $y = h_{\text{coil}} = 5$" and a horizontal distance away from the diamond $z = z_{\text{coil}} = 11$" inches.

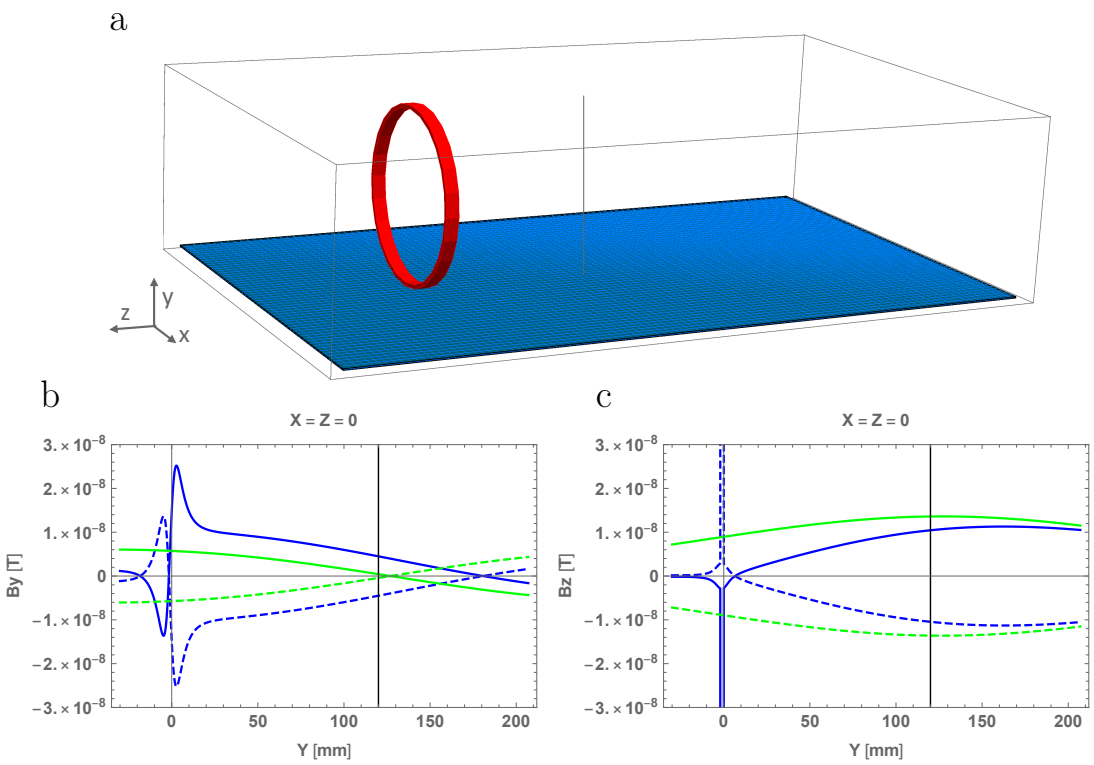

Figure D.2.2: Simulated coil magnetic field distortion due to magnetized optical table. Radia model of z coil employed in simultaneous vector magnetometry demonstration above ferromagnetic steel optical table assumed to have uniform magnetizability of $\chi_m = 1403$ (see text). Diamond is positioned at height $h = 4.75$" above the table $x = z = 0$, and the 9.75"-diameter coil is centered at height $h_{\text{coil}} = 5$" and positioned away at distance $z_{\text{coil}} = 11$". Gray line marks y-cut along which simulated field projections are plotted in b and c. b) Magnetic field projection B_y for positive (solid lines) and negative (dashed lines) currents applied to coils. Green lines depict B_y due to the coils alone and blue lines depict B_y due to coils and the magnetizable optical table. c) Magnetic field projection B_z for positive (solid lines) and negative (dashed lines) currents applied to coils. Green lines depict B_y due to the coils alone and blue lines depict B_z due to coils and the magnetizable optical table. The table results in a reduced B_z and increase B_y with ratio $B_y/B_z = 0.43$, which is consistent with experimental findings up to the uncertainty in χ_m.

The surface represents the top plate of the optical table, which is 2 mm thick. Simulations that also included the 2-mm-thick bottom plate of the optical table 4" below, as well as simulations involving the entire 4"-thick optical table as a monolithic steel block yielded results that agreed qualitatively with the results involving only the

table's top surface. The chosen geometry is both simple, enabling simulations to run quickly, and likely realistic, as the optical table core is a honeycomb, with much lower density than a solid block of steel.

The surface is divided into $n_{\text{div}} = \{55, 1, 101\}$ divisions along $\{x, y, z\}$. The following parameters are assumed for the stainless steel optical table [535]: $\chi_m = 2100$ is the magnetic susceptibility at zero field, $m_{\text{sat}} = 1.6\ T$ is the saturation magnetization, and the magnetization is given in tesla by $M[H] = m_{\text{sat}} \tanh(\chi_m H / m_{\text{sat}}]$. To approximately account for the reduced susceptibility due to partial magnetization induced by the bias magnetic field ($\sim 5\,\text{gauss}$ at the table surface directly below the diamond), we replace χ_m in the simulation by $\chi_m(5\,\text{gauss}) = 1403$.

Figure D.2.2b,c show the simulated B_y and B_z fields plotted vs. vertical position y due to both the optical table and the coil (blue), just the table (red), and just the coil (green). The black line marks the height of the diamond $h = 121$ mm. It is apparent that $B_\perp$ (in this case B_y) must be continuous over boundaries, where $B_\parallel$ (B_z and B_x) can have discontinuities. The presence of the magnetized table raises the position where B_y is zero from the center of the coil by ~ 50 mm. As a result, a non-negligible y-field is present at the position of the diamond. Furthermore, the z-field is somewhat reduced. The ratio of the B_y field to the B_z field at the diamond is 0.43, similar to but slightly higher than the ~ 20 - 30% distortion observed experimentally.

However, there is substantial uncertainty to the quoted value of the steel table's susceptibility. For example, series 400 stainless steels heat treated for maximum hardness may exhibit susceptibilities less than 100 [535]. Repeating the simulation with a susceptibility of ~ 100 yields qualitatively similar behavior and a ratio of B_y to B_z at the diamond of 0.17, much closer to the ratio observed experimentally. Furthermore, as expected from the symmetry, the table is found to negligibly change the B_x field due to the coil at the diamond, also in agreement with experiments.

In conclusion, in spite of uncertainty in χ_m and simplifying assumptions made (such as anisotropic magnetizability), these simulations are consistent with the hypothesis that table magnetization accounts for the observed field distortions. We note that this distortion is particularly noticeable in the present experiment, where

large coils are placed in close proximity to the table. For magnetic signals from local sources at the diamond such as neurons (see Chapter 2), this effect is expected to be substantially reduced. In future implementations, a nonmagnetic optical table will be used, and the use of magnetizable screws and other materials near the diamond will be avoided.

D.3 NV^--NV^- interactions in CW-ODMR

In the process of calibrating and characterizing the simultaneous vector magnetometer described in Chapter 4, we observed that the CW-ODMR signal from a given NV^- orientation is changed by simultaneous driving of ODMR lines from other NV^- orientations. The ODMR linewidth is increased and the depth of the resonance features is increased. The linewidth change appears to be consistent with NV^--NV^- dipolar interactions, whereas the increased depth remain unexplained.

D.3.1 Background

Accurate field reconstruction using the simultaneous vector magnetometry method described in Chapter 4 requires that that signals from the multiple probed axes are independent, i.e., that driving one orientation does not affect the signal from other orientations. One possible source of cross talk occurs from off-resonant MW drive, such as a response from one NV^- orientation to MWs resonant with another orientation's spin resonance. As described in Section 4.7.2, this source of crosstalk is confirmed to be negligible at the 8 mT applied bias field, where the minimum detuning between ODMR lines is 30 MHz.

However, an alternative form of crosstalk is observed experimentally, where the response of one NV^- orientation depends on whether other orientations are being driven on resonance. A series of checks rule out off-resonant MW excitation as well as technical effects such as the MW sources, the MW loop response, or other electronics in the apparatus. A remaining hypothesis consistent with measurements is that this form of crosstalk arises from diamond itself, in particular from NV^--NV^- dipolar

interactions in the [NV$^-$] $\sim$ 3 ppm diamond.

D.3.2 Observed effect

The change in slope of the simultaneous vector magnetometry signal with respect to magnetic field is detected by monitoring a 20 Hz magnetic field signal applied by a coil using a single NV$^-$ orientation and measuring the change in detected field amplitude when the other NV$^-$ orientations are resonantly addressed. The observed change in magnetometry slope is found to be consistent with observed changes in the ODMR lineshapes measured by sweeping MW tones across one NV$^-$ orientation's resonance features while applying additional modulated MW drives either resonant or far-off-resonant with the other NV$^-$ orientation, described herein.

Figure D.3.1a shows the ODMR spectrum from Chapter 4. Three MW tones separated by the ^{14}N hyperfine splitting of 2.16 MHz are swept in frequency from 2.725 to 2.74 GHz over the $m_s = 0 \leftrightarrow m_s = -1$ resonance for the NV$^-$ orientation termed NV$_\lambda$ in Chapter 4. Meanwhile, three additional sets of three MW tones (nine tones total) are applied to the MW-delivery loop. Two cases are compared: (i) where the additional MW tones resonantly address spin transitions for the three other NV$^-$ orientations (NV$_\chi$, NV$_\varphi$, and NV$_\kappa$) and (ii) where the additional MW frequencies are $\gtrsim$ 15 MHz away from any NV$^-$ resonance. A third case, wherein no modulated MWs are applied, is observed to yield PL signals that are indistinguishable in resonance depth and linewidth from the case (ii) in which the additional MW tones are applied off-resonantly. The detected PL signal plotted vs. the center frequency of the three-tone MW drive is shown in Figure D.3.1b,c. Here 15 sweeps of duration 0.9 seconds are averaged together to enhanced the SNR.

We fit these signals to five inverted Lorentzian functions with equal linewidth, fixed separation, and variable height. Based on the fits, the resonant drive the PL trace from case (i) with resonant drive of the other NV$^-$ orientations is found to exhibit contrast increased by 4.5%, and linewidth increased by 2%, or 29 kHz. A 7 kHz ODMR line shift is also observed, but this shift is not repeatable over multiple iterations of the same experiment and can be attributed to slow temperature drifts.

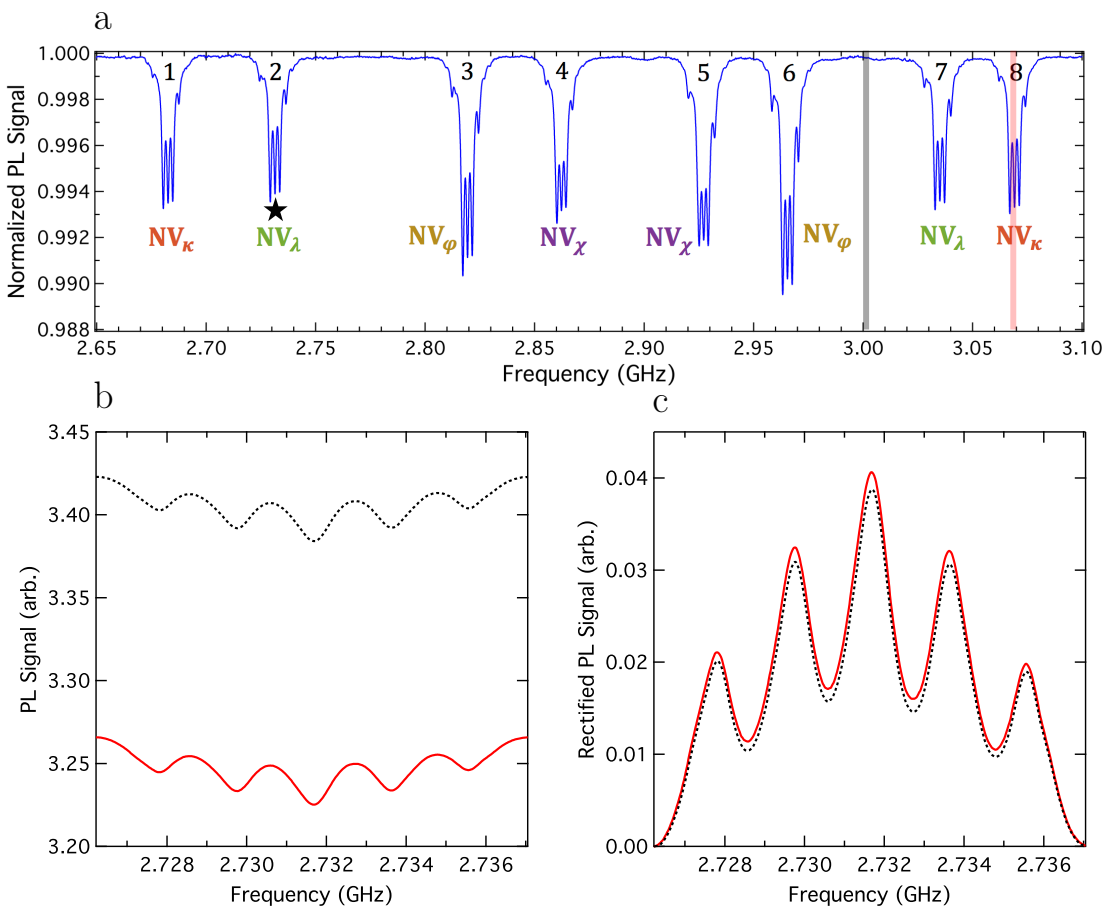

Figure D.3.1: Evidence of possible NV$^-$-NV$^-$ interactions in CW-ODMR. a) ODMR spectrum from Chapter 4. Three-tone MW drive with 2.16 MHz spacing is frequency-swept across $m_s = 0 \leftrightarrow m_s = -1$ resonance NV$_\lambda$, marked by star. Sweep is performed with simultaneous three-tone MW drive applied to m_s transitions for the three other orientations, NV$_\chi$, NV$_\varphi$, and NV$_\kappa$, (pink vertical lines) and compared against same sweep with single-tone MW drives applied away from any resonance (gray vertical lines). b) Raw PL signals from three-tone MW sweep over NV$_\lambda$ resonance with resonant MW drive of other three NV$^-$ orientations (—) and off-resonant drive (···). PL signal with resonant drive is reduced due to reduced background fluorescence from increased population of other NV$^-$ orientations in dimmer $m_s = \pm 1$ states. c) PL signal traces from (b) shifted to 0 and rectified to allow clear comparison of the ODMR linewidth and depth for the two cases. Resonant drive of other NV$^-$ orientations causes increased ODMR depth and increased linewidth. The same qualitative effect is observed for single-tone and modulated MW drive of other NV$^-$ orientations and for single-tone MW sweep over NV$_\lambda$. Increase in NV$_\lambda$ ODMR linewidth is consistent with increase in average dipolar coupling between NV$_\lambda$ and NV$_\kappa$ orientations when NV$_\kappa$ is driven out of the non-interacting $m_s = 0$ state into the interacting $m_s = +1$ state.

D.3.3 Physical explanation

The observed linewidth increase is consistent with increased NV^--NV^- dipolar interactions upon MW drive. Resonant MW drive of other NV^- orientations causes increased population from those orientations in the $m_s = \pm 1$ states compared to the case of no or off-resonant MW drive, where the CW optical excitation selectively populates the $m_s = 0$ state. Dipolar interactions between NV^- centers being probed and NV centers from other orientations do not occur when the other-orientation NV^- centers are in the $m_s = 0$ state [144], they do occur other-orientation NV^- centers are in the $m_s = \pm 1$ state. Therefore, by increasing the population of interacting NV^- centers, resonant driving of the other NV^- orientation classes can broaden the ODMR lines of the NV^- orientation being probed (i.e., decrease T_2^* see Chapter 4).

The diamond sample investigated here has a high concentration of NV^- centers: $[NV^-] \sim 3$ ppm. To estimate the change in ODMR linewidth ($\approx 1/(\pi T_2^*)$ for Lorentzian lineshapes - see Section 2.1.4) of one NV^- orientation in this sample upon resonant drive of the other three NV^- orientation, we employ Equation 2.15 from Chapter 4:

$$\begin{aligned} \frac{1}{T_2^*\{NV^-_{\nparallel}\}} &= \varsigma_{\nparallel} A_{NV^-_{\nparallel}} [NV^-_{\nparallel}] \\ &\sim \varsigma_{\nparallel} \sqrt{\frac{8}{3}} A_{N^0_S} [NV^-_{\nparallel}], \end{aligned} \tag{D.1}$$

with $A_{N^0_S} = 101 \pm 12$ $ms^{-1}ppm^{-1}$ (Section 2.2.1). Here $NV^-_{\nparallel}$ represents NV^- centers of different orientations from the orientation being probed and $\varsigma_{\nparallel}$ represents the fraction of those NV^- centers of not in $m_s = 0$.

We assume $[NV^-_{\nparallel}] \sim 2.25$ ppm, $\varsigma_{\nparallel} = \varsigma_{\kappa} \sim 0.2$ when NV_{κ} is not driven by resonant MWs [536], and $\varsigma_{\kappa} \sim 0.5$ when NV_{κ} is driven by resonant MWs. With these estimates we expect the increase in ODMR linewidth Γ upon resonant drive of the other three orientations is given by

$$\Delta\Gamma = \Delta \frac{1}{\pi T_2^*} \sim 35 \text{ kHz}. \tag{D.2}$$

This estimate is in good agreement with the 29 kHz we measure.

More tests are required, to determine if the effect does in fact arise from NV^--NV^- dipolar interactions, such as repeating the experiment in diamonds of different NV^- concentrations and with pulsed protocols. Nonetheless, the observation that MW drive off-resonant MW drive of the same power as the resonant drive has no effect on the ODMR linewidth or depth rules out many possible technical explanations for this effect.

While the increase in linewidth can be explained by NV^--NV^- interactions, we do not currently have a satisfactory explanation for the increase in resonance depth. Here we discuss two possible explanations that were ruled out: First, we investigated if line-broadening itself in CW-ODMR could be sufficient to increase the ODMR contrast. Based on the simple model for NV^- spin dynamics under continuous optical and MW excitation from Ref. [163], ODMR line broadening decreases the ODMR contrast for all optical intensities, and only marginally so. Therefore, line broadening itself cannot yield an increase in contrast.

Second, we determined that changes in absorption of the green light correlated with MW drive could not be sufficient to explain the observed increase in ODMR depth. If the other three NV^- orientations are driven with resonant MWs such that under optical excitation they spend more time shelved in the singlet states, optical absorption by those NV^- centers may decrease, increasing the optical intensity available for the probed NV^- orientation to absorb. If we assume the $m_s = \pm 1$ state for each NV^- orientation class absorbs $\sim 2\%$ less than the $m_s = 0$ state (a likely overestimate - see Section 6.2.7), and that absorption by NV^- centers accounts for 50% of the total absorption (since substitutional nitrogen N_S^0 also absorbs green light), then the available green light incident on the probed NV^- orientation class changes by at most 1% when the other three axes are driven resonantly. However, from the model in Ref. [163], the CW-ODMR contrast increases at best sublinearly with optical power. Therefore, a 1% change in the available light should cause less than a 1% change in the contrast. So even in a most optimistic view, changing absorption due to resonantly driving the other NV^- classes cannot explain a 4.5% change in ODMR depth. Other possible causes that could be investigated in more detail include MW-dependent NV

ionization, such as that described in Ref. [83]. As with the linewidth increase, pulsed magnetometry protocols could enable better isolation and characterization of this effect.

Although the change in ODMR linewidth and depth can degrade the accuracy of a simultaneous vector magnetometry measurement, they also hint at rich many-body physics of interacting spins in NV^--rich diamond, which is an increasingly popular topic of study [537, 187, 120, 184].

Appendix E

Diamond characterization

E.1 UV-vis spectrophotometry

Essential to diamond material engineering is the ability to accurately and reproducibly characterize the material. Here we implement 77 K ultraviolet-visible (UV-vis) spectrophotometry on bulk diamonds. We use this technique for two characterization purposes: (i) to measure the concentration of monovacancies produced by electron irradiation prior to annealing as a way to calibrate and standardize the appropriate irradiation dose for a desired NV^- concentration, and (ii) to determine the concentrations of NV^- and NV^0 in diamonds with known nitrogen concentrations to determine the nitrogen-to-NV conversion efficiency and NV charge state efficiency after irradiation and annealing. Here we describe our measurements of monovacancy concentrations for electron irradiation dose calibration (Section 7.4.2). These measurements enable systematic studies to be performed to optimize diamond treatment protocols for optimizing NV^--rich diamond material for ensemble magnetometry. One such study employing these UV-vis measurements is documented in a recently submitted manuscript [82].

At 77 K, a forest of absorption features in diamond become resolved [471]. Integrated absorption intensities can be related to concentrations of various defects if calibrated through correlation with a quantitative measurement scheme such as electron paramagnetic resonance (EPR) [467]. We measure the GR1 (neutral mono-

vacancy V^0) and ND1 (negative monovacancy V^-) absorption lines in samples that have received a range of electron irradiation doses, prior to annealing. These measurements aid in fine-tuning irradiation doses to optimize nitrogen-to-NV^- conversion efficiency E_{conv} in future diamond samples. We employ an Agilent Cary 60 UV-vis spectrophotometer at Harvard's Center for Nanoscale Systems, combined with a cryostat mounted to the spectrophotometer via a custom-built adapter. The spectrophotometer covers a wavelength range from 190 nm to 1100 nm and focuses to a $\sim$ 1 mm spot size.

The sample holder in the cryostat consists of two pieces of copper that can be screwed together with a $\sim 1/2''$ aperture. As diamond samples are typically 5 mm $\times$ 5 mm or smaller, the diamond is mounted within the aperture using two pieces of copper tape. As shown in Figure E.1.1a, a few-mm-wide square-shaped hole in both copper sheets allows the diamond to be held in place while allowing an aperture for the beam to pass through to the detector. The copper sheets are clamped together between the copper cryostat holder pieces. Mounting via pressure is preferable as samples are kept from shifting or delaminating when cooled down. The copper tape provides a sufficiently rigid and thermally conductive sample holder, which ensures diamonds are efficiently cooled to 77 K when liquid nitrogen is transferred to the cryostat (see Figure E.1.1b).

Neutral vacancies (GR1 centers) exhibit a zero-phonon absorption doublet at 740.9 nm and 744.4 nm [471], while negative vacancies (ND1 centers) exhibit a zero-phonon line (ZPL) at 393.6 nm [472]. Baselined absorption spectra are recorded at 77 K, yielding the absorbance $A(\lambda) = -\log(I(\lambda)/I_0)$, where $I(\lambda)$ and I_0 are the transmitted and incident intensities. For a known sample thickness t, we convert absorbance to absorption coefficient $a(\lambda) = \frac{\ln(10)}{t} A(lambda)$, and then recast the absorption coefficient as a function of energy in meV. We integrate under the neutral and negative monovacancy (V^0 and V^-) to obtain $\mathcal{A}_{GR1}$ and $\mathcal{A}_{ND1}$, the integrated absorption strengths in meV cm^{-1}. We find the concentrations $[V^0]$ and $[V^-]$ in ppm (using 1 ppm = 1.76×10^{17} cm^{-3}) by solving the equations $A_{GR1} = f_{GR1}[V^0]$ and $A_{ND1} = f_{ND1}[V^-]$, where f represents the transition's oscillator strength [467, 473].

a

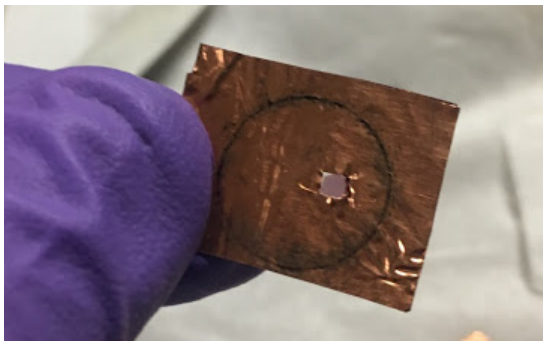

b

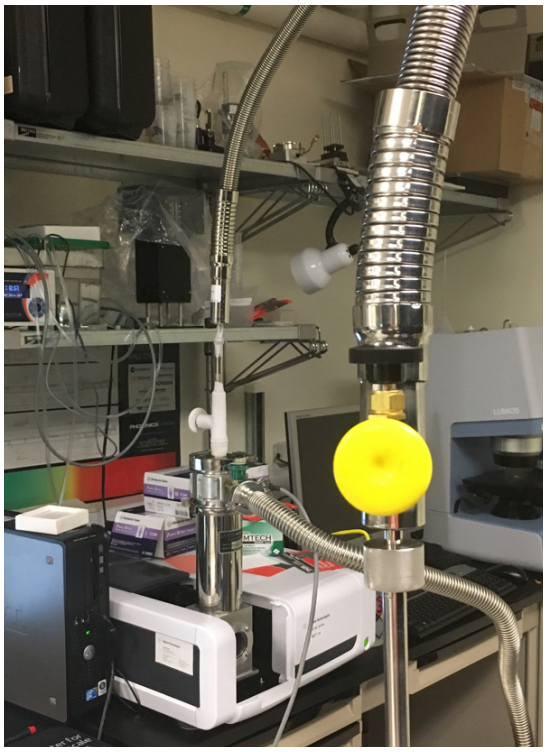

Figure E.1.1: Cryo-UV-vis sample mounting and 77 K operation. a) Diamond samples are mounted between two sheets of copper tape, which are pressed between two copper pieces comprising the cryostat's sample holder. b) Spectrophotometer operation at 77 K utilizing a liquid nitrogen dewar and transfer line at Harvard's Center for Nanoscale Systems.

The authors of Ref. [474] measured the ratio $f_{\mathrm{ND1}}/f_{\mathrm{GR1}} = 4.0$ using detailed balance arguments applied to an annealing study. Later, the authors of Ref. [467] determined that $f_{\mathrm{ND1}} = 4.8(2) \times 10^{-16}$ meV cm^2 by correlating ND1 absorption measurements with well-calibrated EPR measurements of [V^-]. Although V^0 is spinless and thus EPR inactive, f_{GR1} is determined to be $1.2(3) \times 10^{-16}$ meV cm^2 by dividing f_{ND1} by $f_{\mathrm{ND1}}/f_{\mathrm{GR1}} = 4.0$.

The diamonds measured in this study are irradiated by 1 MeV electrons at the company Prism Gem. We perform UV-vis spectrophotmetry on "witness samples," low-nitrogen ([N] $\lesssim$ 150 ppb) standard-grade CVD diamonds from Element Six irradiated alongside the nitrogen-rich diamonds for NV^- magnetometry. The witnesses are intended solely for measuring concentrations of vacancies produced by irradiation, and, because of their low electron donor concentration, they exhibit monovacancies primarily in the neutral state [469]. As such, we observe a small ND1 absorption feature near the device's detection limit of [V^-] $\sim$ 100 ppb, which does not increase in intensity with irradiation dose. We thus determine the vacancies production rate by correlating [V^0] measured by UV-vis against the reported irradiation dose.

Figure E.1.2 shows the measured [V^0] in ppm in six witness samples irradiated with four doses ranging from 10^{17} e^-/cm^2 to 3×10^{18} e^-/cm^2 at 1 MeV. At the highest dose we observe the vacancy concentration has rolled over, whereas the three lower doses exhibit a linear scaling of produced vacancy concentration. Based on the five samples measured at the three lower doses, we extract a V^0 creation rate of 0.30 ± 0.05 cm^{-1}. This calibration allows us to select irradiation doses to produce vacancy concentrations roughly matched to the nitrogen concentration in samples for ensemble-NV^- magnetometry (see Section 7.4.1). However, substantial variation in vacancy creation rate is reported in the literature (see Section 7.4.2), emphasizing the need for more systematic studies to improve accuracy of this and other calibration methods.

.

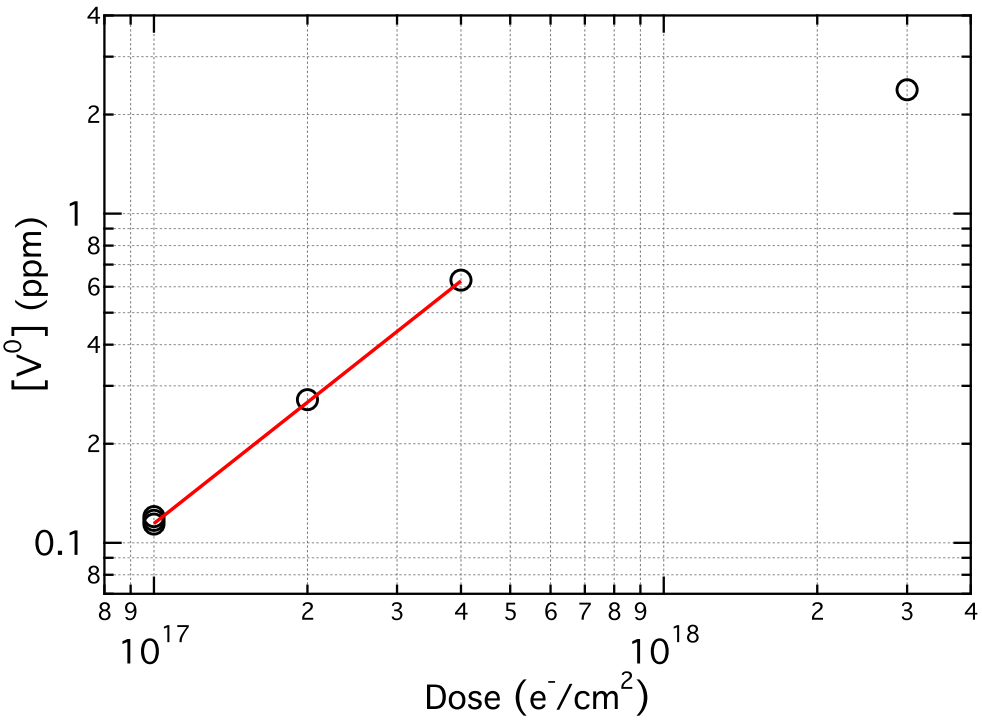

Figure E.1.2: Neutral monovacancy (V^0) concentration versus irradiation dose at 1 MeV, measured by UV-vis spectrophotometry. Red line depicts linear fit to data, with creation rate 0.30 ± 0.05 cm^{-1}, where the measurement at 3×10^{18} e$^-$/cm^2 is excluded from the fit.

Bibliography

[1] D. Budker and M. Romalis, "Optical magnetometry," *Nat. Phys.*, vol. 3, no. 4, pp. 227–234, 04 2007. [Online]. Available: http://dx.doi.org/10.1038/nphys566

[2] C. L. Degen, F. Reinhard, and P. Cappellaro, "Quantum sensing," *Rev. Mod. Phys.*, vol. 89, p. 035002, Jul 2017. [Online]. Available: https://link.aps.org/doi/10.1103/RevModPhys.89.035002

[3] J. M. Taylor, P. Cappellaro, L. Childress, L. Jiang, D. Budker, P. R. Hemmer, A. Yacoby, R. Walsworth, and M. D. Lukin, "High-sensitivity diamond magnetometer with nanoscale resolution," *Nat. Phys.*, vol. 4, no. 10, pp. 810–816, 10 2008. [Online]. Available: http://dx.doi.org/10.1038/nphys1075

[4] C. L. Degen, "Scanning magnetic field microscope with a diamond single-spin sensor," *Appl. Phys. Lett.*, vol. 92, no. 24, p. 243111, 2008. [Online]. Available: https://doi.org/10.1063/1.2943282

[5] J. R. Maze, P. L. Stanwix, J. S. Hodges, S. Hong, J. M. Taylor, P. Cappellaro, L. Jiang, M. V. G. Dutt, E. Togan, A. S. Zibrov, A. Yacoby, R. L. Walsworth, and M. D. Lukin, "Nanoscale magnetic sensing with an individual electronic spin in diamond," *Nature*, vol. 455, no. 7213, pp. 644–647, 10 2008. [Online]. Available: http://dx.doi.org/10.1038/nature07279

[6] G. Balasubramanian, I. Y. Chan, R. Kolesov, M. Al-Hmoud, J. Tisler, C. Shin, C. Kim, A. Wojcik, P. R. Hemmer, A. Krueger, T. Hanke, A. Leitenstorfer, R. Bratschitsch, F. Jelezko, and J. Wrachtrup, "Nanoscale imaging magnetometry with diamond spins under ambient conditions," *Nature*, vol. 455, p. 648, 10 2008. [Online]. Available: http://dx.doi.org/10.1038/nature07278

[7] V. M. Acosta, E. Bauch, M. P. Ledbetter, C. Santori, K.-M. C. Fu, P. E. Barclay, R. G. Beausoleil, H. Linget, J. F. Roch, F. Treussart, S. Chemerisov, W. Gawlik, and D. Budker, "Diamonds with a high density of nitrogen-vacancy centers for magnetometry applications," *Phys. Rev. B*, vol. 80, p. 115202, Sep 2009. [Online]. Available: http://link.aps.org/doi/10.1103/PhysRevB.80.115202

[8] M. W. Doherty, N. B. Manson, P. Delaney, F. Jelezko, J. Wrachtrup, and L. C. Hollenberg, "The nitrogen-vacancy colour centre in diamond," *Phys. Rep.*, vol. 528, no. 1, pp. 1–45, 2013. [Online]. Available: http://www.sciencedirect.com/science/article/pii/S0370157313000562

[9] L. Rondin, J.-P. Tetienne, T. Hingant, J.-F. Roch, P. Maletinsky, and V. Jacques, "Magnetometry with nitrogen-vacancy defects in diamond," *Rep. Prog. Phys.*, vol. 77, no. 5, p. 056503, 2014. [Online]. Available: http://stacks.iop.org/0034-4885/77/i=5/a=056503

[10] F. Casola, T. van der Sar, and A. Yacoby, "Probing condensed matter physics with magnetometry based on nitrogen-vacancy centres in diamond," *Nat. Rev. Mater.*, vol. 3, p. 17088, 01 2018. [Online]. Available: https://doi.org/10.1038/natrevmats.2017.88

[11] R. Schirhagl, K. Chang, M. Loretz, and C. L. Degen, "Nitrogen-vacancy centers in diamond: Nanoscale sensors for physics and biology," *Annu. Rev. Phys. Chem.*, vol. 65, no. 1, pp. 83–105, 2014. [Online]. Available: https://doi.org/10.1146/annurev-physchem-040513-103659

[12] Y. Wu, F. Jelezko, M. B. Plenio, and T. Weil, "Diamond quantum devices in biology," *Angew. Chem. Int. Ed.*, vol. 55, no. 23, pp. 6586–6598, 2016. [Online]. Available: https://onlinelibrary.wiley.com/doi/abs/10.1002/anie.201506556

[13] D. R. Glenn, R. R. Fu, P. Kehayias, D. Le Sage, E. A. Lima, B. P. Weiss, and R. L. Walsworth, "Micrometer-scale magnetic imaging of geological samples using a quantum diamond microscope," *Geochem. Geophys. Geosyst.*, vol. 18, no. 8, pp. 3254–3267, 2017. [Online]. Available: https://agupubs.onlinelibrary.wiley.com/doi/abs/10.1002/2017GC006946

[14] A. Grosz, M. J. Haji-Sheikh, and S. C. Mukhopadhyay, *High Sensitivity Magnetometers*. Springer, 2017. [Online]. Available: https://link.springer.com/book/10.1007/978-3-319-34070-8

[15] A. Jarmola, V. M. Acosta, K. Jensen, S. Chemerisov, and D. Budker, "Temperature- and magnetic-field-dependent longitudinal spin relaxation in nitrogen-vacancy ensembles in diamond," *Phys. Rev. Lett.*, vol. 108, p. 197601, May 2012. [Online]. Available: https://link.aps.org/doi/10.1103/PhysRevLett.108.197601

[16] T. Rosskopf, A. Dussaux, K. Ohashi, M. Loretz, R. Schirhagl, H. Watanabe, S. Shikata, K. M. Itoh, and C. L. Degen, "Investigation of surface magnetic noise by shallow spins in diamond," *Phys. Rev. Lett.*, vol. 112, p. 147602, Apr 2014. [Online]. Available: https://link.aps.org/doi/10.1103/PhysRevLett.112.147602

[17] G. Balasubramanian, P. Neumann, D. Twitchen, M. Markham, R. Kolesov, N. Mizuochi, J. Isoya, J. Achard, J. Beck, J. Tissler, V. Jacques, P. R. Hemmer, F. Jelezko, and J. Wrachtrup, "Ultralong spin coherence time in isotopically engineered diamond," *Nat. Mater.*, vol. 8, no. 5, pp. 383–387, May 2009. [Online]. Available: http://dx.doi.org/10.1038/nmat2420

[18] M. L. Goldman, M. W. Doherty, A. Sipahigil, N. Y. Yao, S. D. Bennett, N. B. Manson, A. Kubanek, and M. D. Lukin, "State-selective intersystem crossing

in nitrogen-vacancy centers," *Phys. Rev. B*, vol. 91, p. 165201, Apr 2015. [Online]. Available: http://link.aps.org/doi/10.1103/PhysRevB.91.165201

[19] M. L. Goldman, A. Sipahigil, M. W. Doherty, N. Y. Yao, S. D. Bennett, M. Markham, D. J. Twitchen, N. B. Manson, A. Kubanek, and M. D. Lukin, "Phonon-induced population dynamics and intersystem crossing in nitrogen-vacancy centers," *Phys. Rev. Lett.*, vol. 114, p. 145502, Apr 2015. [Online]. Available: https://link.aps.org/doi/10.1103/PhysRevLett.114.145502

[20] M. S. Grinolds, M. Warner, K. De Greve, Y. Dovzhenko, L. Thiel, R. L. Walsworth, S. Hong, P. Maletinsky, and A. Yacoby, "Subnanometre resolution in three-dimensional magnetic resonance imaging of individual dark spins," *Nat. Nanotechnol.*, vol. 9, pp. 279 –, 03 2014. [Online]. Available: https://doi.org/10.1038/nnano.2014.30

[21] K. Arai, C. Belthangady, H. Zhang, N. Bar-Gill, S. J. DeVience, P. Cappellaro, A. Yacoby, and R. L. Walsworth, "Fourier magnetic imaging with nanoscale resolution and compressed sensing speed-up using electronic spins in diamond," *Nat. Nanotechnol.*, vol. 10, no. 10, pp. 859–864, Oct 2015. [Online]. Available: http://dx.doi.org/10.1038/nnano.2015.171

[22] J.-C. Jaskula, E. Bauch, S. Arroyo-Camejo, M. D. Lukin, S. W. Hell, A. S. Trifonov, and R. L. Walsworth, "Superresolution optical magnetic imaging and spectroscopy using individual electronic spins in diamond," *Optics Express*, vol. 25, no. 10, pp. 11 048–11 064, 2017. [Online]. Available: http://www.opticsexpress.org/abstract.cfm?URI=oe-25-10-11048

[23] V. M. Acosta, A. Jarmola, E. Bauch, and D. Budker, "Optical properties of the nitrogen-vacancy singlet levels in diamond," *Phys. Rev. B*, vol. 82, no. 20, p. 201202, 11 2010. [Online]. Available: http://link.aps.org/doi/10.1103/PhysRevB.82.201202

[24] J. F. Barry, M. J. Turner, J. M. Schloss, D. R. Glenn, Y. Song, M. D. Lukin, H. Park, and R. L. Walsworth, "Optical magnetic detection of single-neuron action potentials using quantum defects in diamond," *Proc. Natl. Acad. Sci.*, vol. 113, no. 49, pp. 14 133–14 138, 2016. [Online]. Available: http://www.pnas.org/content/113/49/14133.abstract

[25] J. M. Schloss, J. F. Barry, M. J. Turner, and R. L. Walsworth, "Simultaneous broadband vector magnetometry using solid-state spins," *Phys. Rev. Applied*, vol. 10, p. 034044, Sep 2018. [Online]. Available: https://link.aps.org/doi/10.1103/PhysRevApplied.10.034044

[26] C. S. Shin, C. E. Avalos, M. C. Butler, D. R. Trease, S. J. Seltzer, J. Peter Mustonen, D. J. Kennedy, V. M. Acosta, D. Budker, A. Pines, and V. S. Bajaj, "Room-temperature operation of a radiofrequency diamond magnetometer near the shot-noise limit," *J. Appl. Phys.*, vol. 112, no. 12,

p. 124519, 2012. [Online]. Available: https://aip.scitation.org/doi/10.1063/1.4771924

[27] M. Loretz, T. Rosskopf, and C. L. Degen, "Radio-frequency magnetometry using a single electron spin," *Phys. Rev. Lett.*, vol. 110, p. 017602, Jan 2013. [Online]. Available: https://link.aps.org/doi/10.1103/PhysRevLett.110.017602

[28] J. M. Boss, K. Chang, J. Armijo, K. Cujia, T. Rosskopf, J. R. Maze, and C. L. Degen, "One- and two-dimensional nuclear magnetic resonance spectroscopy with a diamond quantum sensor," *Phys. Rev. Lett.*, vol. 116, p. 197601, May 2016. [Online]. Available: https://link.aps.org/doi/10.1103/PhysRevLett.116.197601

[29] J. D. A. Wood, D. A. Broadway, L. T. Hall, A. Stacey, D. A. Simpson, J.-P. Tetienne, and L. C. L. Hollenberg, "Wide-band nanoscale magnetic resonance spectroscopy using quantum relaxation of a single spin in diamond," *Phys. Rev. B*, vol. 94, p. 155402, Oct 2016. [Online]. Available: https://link.aps.org/doi/10.1103/PhysRevB.94.155402

[30] J. Cai, F. Jelezko, M. B. Plenio, and A. Retzker, "Diamond-based single-molecule magnetic resonance spectroscopy," *New J. Phys.*, vol. 15, no. 1, p. 013020, Jan 2013. [Online]. Available: http://doi.org/10.1088/1367-2630/15/1/013020

[31] S. Steinert, F. Ziem, L. T. Hall, A. Zappe, M. Schweikert, N. Götz, A. Aird, G. Balasubramanian, L. Hollenberg, and J. Wrachtrup, "Magnetic spin imaging under ambient conditions with sub-cellular resolution," *Nat. Commun.*, vol. 4, pp. 1607 –, 03 2013. [Online]. Available: https://doi.org/10.1038/ncomms2588

[32] I. Lovchinsky, A. O. Sushkov, E. Urbach, N. P. de Leon, S. Choi, K. De Greve, R. Evans, R. Gertner, E. Bersin, C. Müller, L. McGuinness, F. Jelezko, R. L. Walsworth, H. Park, and M. D. Lukin, "Nuclear magnetic resonance detection and spectroscopy of single proteins using quantum logic," *Science*, vol. 351, no. 6275, pp. 836–841, 2016. [Online]. Available: http://science.sciencemag.org/content/351/6275/836

[33] L. M. Pham, S. J. DeVience, F. Casola, I. Lovchinsky, A. O. Sushkov, E. Bersin, J. Lee, E. Urbach, P. Cappellaro, H. Park, A. Yacoby, M. Lukin, and R. L. Walsworth, "NMR technique for determining the depth of shallow nitrogen-vacancy centers in diamond," *Phys. Rev. B*, vol. 93, p. 045425, Jan 2016. [Online]. Available: https://link.aps.org/doi/10.1103/PhysRevB.93.045425

[34] L. Shao, M. Zhang, M. Markham, A. M. Edmonds, and M. Loncar, "Diamond radio receiver: Nitrogen-vacancy centers as fluorescent transducers of microwave signals," *Phys. Rev. Applied*, vol. 6, p. 064008, Dec 2016. [Online]. Available: https://link.aps.org/doi/10.1103/PhysRevApplied.6.064008

[35] J. M. Boss, K. S. Cujia, J. Zopes, and C. L. Degen, "Quantum sensing with arbitrary frequency resolution," *Science*, vol. 356, no. 6340, pp. 837–840, 2017. [Online]. Available: http://science.sciencemag.org/content/356/6340/837

[36] S. Schmitt, T. Gefen, F. M. Stürner, T. Unden, G. Wolff, C. Müller, J. Scheuer, B. Naydenov, M. Markham, S. Pezzagna, J. Meijer, I. Schwarz, M. Plenio, A. Retzker, L. P. McGuinness, and F. Jelezko, "Submillihertz magnetic spectroscopy performed with a nanoscale quantum sensor," *Science*, vol. 356, no. 6340, pp. 832–837, 2017. [Online]. Available: http://science.sciencemag.org/content/356/6340/832

[37] N. Aslam, M. Pfender, P. Neumann, R. Reuter, A. Zappe, F. Fávaro de Oliveira, A. Denisenko, H. Sumiya, S. Onoda, J. Isoya, and J. Wrachtrup, "Nanoscale nuclear magnetic resonance with chemical resolution," *Science*, vol. 357, no. 6346, pp. 67–71, 2017. [Online]. Available: http://science.sciencemag.org/content/357/6346/67

[38] J.-P. Tetienne, T. Hingant, L. Rondin, A. Cavaillès, L. Mayer, G. Dantelle, T. Gacoin, J. Wrachtrup, J.-F. Roch, and V. Jacques, "Spin relaxometry of single nitrogen-vacancy defects in diamond nanocrystals for magnetic noise sensing," *Phys. Rev. B*, vol. 87, p. 235436, Jun 2013. [Online]. Available: https://link.aps.org/doi/10.1103/PhysRevB.87.235436

[39] M. Pelliccione, B. A. Myers, L. M. A. Pascal, A. Das, and A. C. Bleszynski Jayich, "Two-dimensional nanoscale imaging of gadolinium spins via scanning probe relaxometry with a single spin in diamond," *Phys. Rev. Applied*, vol. 2, p. 054014, Nov 2014. [Online]. Available: https://link.aps.org/doi/10.1103/PhysRevApplied.2.054014

[40] L. T. Hall, P. Kehayias, D. A. Simpson, A. Jarmola, A. Stacey, D. Budker, and L. C. L. Hollenberg, "Detection of nanoscale electron spin resonance spectra demonstrated using nitrogen-vacancy centre probes in diamond," *Nat. Commun.*, vol. 7, p. 10211, Jan 2016. [Online]. Available: https://doi.org/10.1038/ncomms10211

[41] V. Ivády, T. Simon, J. R. Maze, I. A. Abrikosov, and A. Gali, "Pressure and temperature dependence of the zero-field splitting in the ground state of NV centers in diamond: A first-principles study," *Phys. Rev. B*, vol. 90, p. 235205, Dec 2014. [Online]. Available: https://link.aps.org/doi/10.1103/PhysRevB.90.235205

[42] M. W. Doherty, V. V. Struzhkin, D. A. Simpson, L. P. McGuinness, Y. Meng, A. Stacey, T. J. Karle, R. J. Hemley, N. B. Manson, L. C. L. Hollenberg, and S. Prawer, "Electronic properties and metrology applications of the diamond NV^- center under pressure," *Phys. Rev. Lett.*, vol. 112, p. 047601, Jan 2014. [Online]. Available: https://link.aps.org/doi/10.1103/PhysRevLett.112.047601

[43] S. Hsieh, P. Bhattacharyya, C. Zu, T. Mittiga, T. J. Smart, F. Machado, B. Kobrin, T. O. Höhn, N. Z. Rui, M. Kamrani, S. Chatterjee, S. Choi, M. Zaletel, V. V. Struzhkin, J. E. Moore, V. I. Levitas, R. Jeanloz, and N. Y. Yao, "Imaging stress and magnetism at high pressures using a nanoscale quantum sensor," *ArXiv e-prints*, Dec. 2018. [Online]. Available: https://arxiv.org/abs/1812.08796

[44] D. M. Toyli, D. J. Christle, A. Alkauskas, B. B. Buckley, C. G. Van de Walle, and D. D. Awschalom, "Measurement and control of single nitrogen-vacancy center spins above 600 k," *Phys. Rev. X*, vol. 2, p. 031001, Jul 2012. [Online]. Available: https://link.aps.org/doi/10.1103/PhysRevX.2.031001

[45] D. M. Toyli, C. F. de las Casas, D. J. Christle, V. V. Dobrovitski, and D. D. Awschalom, "Fluorescence thermometry enhanced by the quantum coherence of single spins in diamond," *Proc. Natl. Acad. Sci.*, vol. 110, no. 21, pp. 8417–8421, 2013. [Online]. Available: http://www.pnas.org/content/110/21/8417.abstract

[46] T. Plakhotnik, M. W. Doherty, J. H. Cole, R. Chapman, and N. B. Manson, "All-optical thermometry and thermal properties of the optically detected spin resonances of the NV^- center in nanodiamond," *Nano Lett.*, vol. 14, no. 9, pp. 4989–4996, 2014. [Online]. Available: https://doi.org/10.1021/nl501841d

[47] J. Choi, S. Choi, G. Kucsko, P. C. Maurer, B. J. Shields, H. Sumiya, S. Onoda, J. Isoya, E. Demler, F. Jelezko, N. Y. Yao, and M. D. Lukin, "Depolarization dynamics in a strongly interacting solid-state spin ensemble," *Phys. Rev. Lett.*, vol. 118, p. 093601, Mar 2017. [Online]. Available: https://link.aps.org/doi/10.1103/PhysRevLett.118.093601

[48] S. Steinert, F. Dolde, P. Neumann, A. Aird, B. Naydenov, G. Balasubramanian, F. Jelezko, and J. Wrachtrup, "High sensitivity magnetic imaging using an array of spins in diamond," *Rev. Sci. Instrum.*, vol. 81, no. 4, p. 043705, 2010. [Online]. Available: http://dx.doi.org/10.1063/1.3385689

[49] L. M. Pham, D. L. Sage, P. L. Stanwix, T. K. Yeung, D. Glenn, A. Trifonov, P. Cappellaro, P. R. Hemmer, M. D. Lukin, H. Park, A. Yacoby, and R. L. Walsworth, "Magnetic field imaging with nitrogen-vacancy ensembles," *New J. Phys.*, vol. 13, no. 4, p. 045021, 2011. [Online]. Available: http://stacks.iop.org/1367-2630/13/i=4/a=045021

[50] D. Le Sage, K. Arai, D. R. Glenn, S. J. DeVience, L. M. Pham, L. Rahn-Lee, M. D. Lukin, A. Yacoby, A. Komeili, and R. L. Walsworth, "Optical magnetic imaging of living cells," *Nature*, vol. 496, no. 7446, pp. 486–489, 2013. [Online]. Available: http://www.nature.com/nature/journal/v496/n7446/full/nature12072.html

[51] D. R. Glenn, K. Lee, H. Park, R. Weissleder, A. Yacoby, M. D. Lukin, H. Lee, R. L. Walsworth, and C. B. Connolly, "Single-cell magnetic imaging using a

quantum diamond microscope," *Nat. Methods*, vol. 12, no. 8, pp. 736–738, Aug 2015. [Online]. Available: http://dx.doi.org/10.1038/nmeth.3449

[52] H. C. Davis, P. Ramesh, A. Bhatnagar, A. Lee-Gosselin, J. F. Barry, D. R. Glenn, R. L. Walsworth, and M. G. Shapiro, "Mapping the microscale origins of magnetic resonance image contrast with subcellular diamond magnetometry," *Nat. Commun.*, vol. 9, no. 1, p. 131, 2018. [Online]. Available: https://doi.org/10.1038/s41467-017-02471-7

[53] I. Fescenko, A. Laraoui, J. Smits, N. Mosavian, P. Kehayias, J. Seto, L. Bougas, A. Jarmola, and V. M. Acosta, "Diamond magnetic microscopy of malarial hemozoin nanocrystals," *Phys. Rev. Applied*, vol. 11, p. 034029, Mar 2019. [Online]. Available: https://link.aps.org/doi/10.1103/PhysRevApplied.11.034029

[54] B. J. Maertz, A. P. Wijnheijmer, G. D. Fuchs, M. E. Nowakowski, and D. D. Awschalom, "Vector magnetic field microscopy using nitrogen vacancy centers in diamond," *Appl. Phys. Lett.*, vol. 96, no. 9, p. 092504, 2010. [Online]. Available: http://dx.doi.org/10.1063/1.3337096

[55] G. Kucsko, P. C. Maurer, N. Y. Yao, M. Kubo, H. J. Noh, P. K. Lo, H. Park, and M. D. Lukin, "Nanometre-scale thermometry in a living cell," *Nature*, vol. 500, no. 7460, pp. 54–58, 2013. [Online]. Available: http://www.nature.com/nature/journal/v500/n7460/full/nature12373.html

[56] F. Dolde, H. Fedder, M. W. Doherty, T. Nobauer, F. Rempp, G. Balasubramanian, T. Wolf, F. Reinhard, L. C. L. Hollenberg, F. Jelezko, and J. Wrachtrup, "Electric-field sensing using single diamond spins," *Nat. Phys.*, vol. 7, no. 6, pp. 459–463, 06 2011. [Online]. Available: http://dx.doi.org/10.1038/nphys1969

[57] M. S. J. Barson, P. Peddibhotla, P. Ovartchaiyapong, K. Ganesan, R. L. Taylor, M. Gebert, Z. Mielens, B. Koslowski, D. A. Simpson, L. P. McGuinness, J. McCallum, S. Prawer, S. Onoda, T. Ohshima, A. C. Bleszynski Jayich, F. Jelezko, N. B. Manson, and M. W. Doherty, "Nanomechanical sensing using spins in diamond," *Nano Lett.*, vol. 17, no. 3, pp. 1496–1503, 2017. [Online]. Available: http://dx.doi.org/10.1021/acs.nanolett.6b04544

[58] P. Neumann, I. Jakobi, F. Dolde, C. Burk, R. Reuter, G. Waldherr, J. Honert, T. Wolf, A. Brunner, J. H. Shim, D. Suter, H. Sumiya, J. Isoya, and J. Wrachtrup, "High-precision nanoscale temperature sensing using single defects in diamond," *Nano Lett.*, vol. 13, no. 6, pp. 2738–2742, 2013. [Online]. Available: https://doi.org/10.1021/nl401216y

[59] F. Shi, Q. Zhang, P. Wang, H. Sun, J. Wang, X. Rong, M. Chen, C. Ju, F. Reinhard, H. Chen, J. Wrachtrup, J. Wang, and J. Du, "Single-protein spin resonance spectroscopy under ambient conditions," *Science*, vol. 347, no. 6226, pp. 1135–1138, 2015. [Online]. Available: http://science.sciencemag.org/content/347/6226/1135

[60] T. Staudacher, F. Shi, S. Pezzagna, J. Meijer, J. Du, C. A. Meriles, F. Reinhard, and J. Wrachtrup, "Nuclear magnetic resonance spectroscopy on a (5-nanometer)3 sample volume," *Science*, vol. 339, no. 6119, pp. 561–563, 2013. [Online]. Available: http://science.sciencemag.org/content/339/6119/561

[61] D. R. Glenn, D. B. Bucher, J. Lee, M. D. Lukin, H. Park, and R. L. Walsworth, "High-resolution magnetic resonance spectroscopy using a solid-state spin sensor," *Nature*, vol. 555, no. 7696, p. 351, 2018. [Online]. Available: https://www.nature.com/articles/nature2578

[62] S. J. DeVience, L. M. Pham, I. Lovchinsky, A. O. Sushkov, N. Bar-Gill, C. Belthangady, F. Casola, M. Corbett, H. Zhang, M. Lukin, H. Park, A. Yacoby, and R. L. Walsworth, "Nanoscale NMR spectroscopy and imaging of multiple nuclear species," *Nat. Nanotechnol.*, vol. 10, pp. 129 –, 2015. [Online]. Available: https://doi.org/10.1038/nnano.2014.313

[63] P. Kehayias, A. Jarmola, N. Mosavian, I. Fescenko, F. M. Benito, A. Laraoui, J. Smits, L. Bougas, D. Budker, A. Neumann, S. R. J. Brueck, and V. M. Acosta, "Solution nuclear magnetic resonance spectroscopy on a nanostructured diamond chip," *Nat. Commun.*, vol. 8, no. 1, p. 188, 2017. [Online]. Available: https://doi.org/10.1038/s41467-017-00266-4

[64] M. Loretz, S. Pezzagna, J. Meijer, and C. L. Degen, "Nanoscale nuclear magnetic resonance with a 1.9-nm-deep nitrogen-vacancy sensor," *Appl. Phys. Lett.*, vol. 104, no. 3, p. 033102, 2014. [Online]. Available: https://doi.org/10.1063/1.4862749

[65] D. B. Bucher, D. R. Glenn, H. Park, M. D. Lukin, and R. L. Walsworth, "Hyperpolarization-enhanced NMR spectroscopy with femtomole sensitivity using quantum defects in diamond," *ArXiv e-prints*, Oct. 2018. [Online]. Available: https://arxiv.org/abs/1810.02408

[66] D. Rugar, H. J. Mamin, M. H. Sherwood, M. Kim, C. T. Rettner, K. Ohno, and D. D. Awschalom, "Proton magnetic resonance imaging using a nitrogen-vacancy spin sensor," *Nat. Nanotechnol.*, vol. 10, pp. 120–124, Feb. 2015. [Online]. Available: https://doi.org/10.1038/nnano.2014.288

[67] A. O. Sushkov, N. Chisholm, I. Lovchinsky, M. Kubo, P. K. Lo, S. D. Bennett, D. Hunger, A. Akimov, R. L. Walsworth, H. Park, and M. D. Lukin, "All-optical sensing of a single-molecule electron spin," *Nano Lett.*, vol. 14, no. 11, pp. 6443–6448, 2014. [Online]. Available: https://doi.org/10.1021/nl502988n

[68] R. R. Fu, B. P. Weiss, E. A. Lima, R. J. Harrison, X.-N. Bai, S. J. Desch, D. S. Ebel, C. Suavet, H. Wang, D. Glenn, D. Le Sage, T. Kasama, R. L. Walsworth, and A. T. Kuan, "Solar nebula magnetic fields recorded in the semarkona meteorite," *Science*, vol. 346, no. 6213, pp. 1089–1092, 2014. [Online]. Available: http://www.sciencemag.org/content/346/6213/1089.abstract

[69] E. Farchi, Y. Ebert, D. Farfurnik, G. Haim, R. Shaar, and N. Bar-Gill, "Quantitative vectorial magnetic imaging of multi-domain rock forming minerals using nitrogen-vacancy centers in diamond," *Spin*, vol. 07, no. 03, p. 1740015, 2017. [Online]. Available: https://doi.org/10.1142/S201032471740015X

[70] W. M. Itano, J. C. Bergquist, J. J. Bollinger, J. M. Gilligan, D. J. Heinzen, F. L. Moore, M. G. Raizen, and D. J. Wineland, "Quantum projection noise: Population fluctuations in two-level systems," *Phys. Rev. A*, vol. 47, pp. 3554–3570, May 1993. [Online]. Available: https://link.aps.org/doi/10.1103/PhysRevA.47.3554

[71] M. H. Levitt, *Spin Dynamics: Basics of Nuclear Magnetic Resonance*, 2nd ed. John Wiley & Sons, 2008. [Online]. Available: https://books.google.com/books/about/Spin_Dynamics.html?id=bysFAa4MPQcC&printsec=frontcover&source=kp_read_button#v=onepage&q&f=false

[72] B. A. Myers, A. Ariyaratne, and A. C. B. Jayich, "Double-quantum spin-relaxation limits to coherence of near-surface nitrogen-vacancy centers," *Phys. Rev. Lett.*, vol. 118, p. 197201, May 2017. [Online]. Available: https://link.aps.org/doi/10.1103/PhysRevLett.118.197201

[73] J. Kitching, "Chip-scale atomic devices," *Appl. Phys. Rev.*, vol. 5, no. 3, p. 031302, 2018. [Online]. Available: https://doi.org/10.1063/1.5026238

[74] A. Marblestone, B. Zamft, Y. Maguire, M. Shapiro, T. Cybulski, J. Glaser, D. Amodei, P. B. Stranges, R. Kalhor, D. Dalrymple, D. Seo, E. Alon, M. Maharbiz, J. Carmena, J. Rabaey, E. Boyden, G. Church, and K. Kording, "Physical principles for scalable neural recording," *Front. Comput. Neurosci.*, vol. 7, p. 137, 2013. [Online]. Available: https://www.frontiersin.org/article/10.3389/fncom.2013.00137

[75] J. Smits, J. Damron, P. Kehayias, A. F. McDowell, N. Mosavian, I. Fescenko, N. Ristoff, A. Laraoui, A. Jarmola, and V. M. Acosta, "Two-dimensional nuclear magnetic resonance spectroscopy with a microfluidic diamond quantum sensor," *ArXiv e-prints*, Jan. 2019. [Online]. Available: https://arxiv.org/abs/1901.02952

[76] I. Lovchinsky, J. D. Sanchez-Yamagishi, E. K. Urbach, S. Choi, S. Fang, T. I. Andersen, K. Watanabe, T. Taniguchi, A. Bylinskii, E. Kaxiras, P. Kim, H. Park, and M. D. Lukin, "Magnetic resonance spectroscopy of an atomically thin material using a single-spin qubit," *Science*, vol. 355, no. 6324, pp. 503–507, 2017. [Online]. Available: http://science.sciencemag.org/content/355/6324/503

[77] M. Hämäläinen, R. Hari, R. J. Ilmoniemi, J. Knuutila, and O. V. Lounasmaa, "Magnetoencephalography–theory, instrumentation, and applications to noninvasive studies of the working human brain," *Rev. Mod. Phys.*, vol. 65, no. 2, pp. 413–497, 04 1993. [Online]. Available: http://link.aps.org/doi/10.1103/RevModPhys.65.413

[78] F. K. K. Kirschner, F. Flicker, A. Yacoby, N. Y. Yao, and S. J. Blundell, "Proposal for the detection of magnetic monopoles in spin ice via nanoscale magnetometry," *Phys. Rev. B*, vol. 97, p. 140402, Apr 2018. [Online]. Available: https://link.aps.org/doi/10.1103/PhysRevB.97.140402

[79] S. Rajendran, N. Zobrist, A. O. Sushkov, R. Walsworth, and M. Lukin, "A method for directional detection of dark matter using spectroscopy of crystal defects," *Phys. Rev. D*, vol. 96, p. 035009, Aug 2017. [Online]. Available: https://link.aps.org/doi/10.1103/PhysRevD.96.035009

[80] J. F. Barry, J. M. Schloss, E. Bauch, M. J. Turner, C. A. Hart, L. M. Pham, and R. L. Walsworth, "Sensitivity optimization for NV-diamond magnetometry," *ArXiv e-prints*, Mar 2019. [Online]. Available: https://arxiv.org/abs/1903.08176

[81] E. Bauch, C. A. Hart, J. M. Schloss, M. J. Turner, J. F. Barry, P. Kehayias, S. Singh, and R. L. Walsworth, "Ultralong dephasing times in solid-state spin ensembles via quantum control," *Phys. Rev. X*, vol. 8, p. 031025, Jul 2018. [Online]. Available: https://link.aps.org/doi/10.1103/PhysRevX.8.031025

[82] S. T. Alsid, J. F. Barry, L. M. Pham, J. M. Schloss, M. F. O'Keeffe, P. Cappellaro, and D. A. Braje, "Photoluminescence decomposition analysis: A technique to characterize N-V creation in diamond," *Submitted to Phys. Rev. Applied*, 2019.

[83] D. P. L. Aude Craik, P. Kehayias, A. S. Greenspon, X. Zhang, M. J. Turner, J. M. Schloss, E. Bauch, C. A. Hart, E. L. Hu, and R. L. Walsworth, "A microwave-assisted spectroscopy technique for determining charge state in nitrogen-vacancy ensembles in diamond," *ArXiv e-prints*, Nov. 2018. [Online]. Available: https://arxiv.org/abs/1811.01972

[84] E. Bauch, S. Singh, J. Lee, C. A. Hart, J. M. Schloss, M. J. Turner, J. F. Barry, L. Pham, N. Bar-Gill, S. F. Yelin, and R. L. Walsworth, "Decoherence of dipolar spin ensembles in diamond," *ArXiv e-prints*, Apr 2019. [Online]. Available: https://arxiv.org/abs/1904.08763

[85] P. K. Kehayias, M. J. Turner, R. Trubko, J. M. Schloss, C. A. Hart, D. Glenn, M. Wesson, and R. L. R. Walsworth, "Imaging stress in diamond using ensembles of nitrogen vacancy centers," *in prep*, 2019.

[86] L. J. Rogers, S. Armstrong, M. J. Sellars, and N. B. Manson, "Infrared emission of the NV centre in diamond: Zeeman and uniaxial stress studies," *New J. Phys.*, vol. 10, no. 10, p. 103024, 2008. [Online]. Available: http://stacks.iop.org/1367-2630/10/i=10/a=103024

[87] G. Thiering and A. Gali, "Theory of the optical spin-polarization loop of the nitrogen-vacancy center in diamond," *Phys. Rev. B*, vol. 98, p. 085207,

Aug 2018. [Online]. Available: https://link.aps.org/doi/10.1103/PhysRevB.98.085207

[88] N. B. Manson, X.-F. He, and P. T. H. Fisk, "Raman heterodyne detected electron-nuclear-double-resonance measurements of the nitrogen-vacancy center in diamond," *Opt. Lett.*, vol. 15, no. 19, pp. 1094–1096, Oct 1990. [Online]. Available: http://ol.osa.org/abstract.cfm?URI=ol-15-19-1094

[89] N. B. Manson, X.-F. He, and P. T. Fisk, "Raman heterodyne studies of the nitrogen-vacancy centre in diamond," *J. Lumin*, vol. 53, no. 1, pp. 49 – 54, 1992. [Online]. Available: http://www.sciencedirect.com/science/article/pii/002223139290104H

[90] P. Udvarhelyi, V. O. Shkolnikov, A. Gali, G. Burkard, and A. Pályi, "Spin-strain interaction in nitrogen-vacancy centers in diamond," *Phys. Rev. B*, vol. 98, p. 075201, Aug 2018. [Online]. Available: https://link.aps.org/doi/10.1103/PhysRevB.98.075201

[91] V. M. Acosta, E. Bauch, M. P. Ledbetter, A. Waxman, L.-S. Bouchard, and D. Budker, "Temperature dependence of the nitrogen-vacancy magnetic resonance in diamond," *Phys. Rev. Lett.*, vol. 104, p. 070801, Feb 2010. [Online]. Available: http://link.aps.org/doi/10.1103/PhysRevLett.104.070801

[92] E. Van Oort and M. Glasbeek, "Electric-field-induced modulation of spin echoes of N-V centers in diamond," *Chem. Phys. Lett.*, vol. 168, no. 6, pp. 529–532, 5 1990. [Online]. Available: http://www.sciencedirect.com/science/article/pii/000926149085665Y

[93] J. Michl, J. Steiner, A. Denisenko, A. Buelau, A. Zimmermann, K. Nakamura, H. Sumiya, S. Onoda, P. Neumann, J. Isoya, and J. Wrachtrup, "Robust and accurate electric field sensing with solid state spin ensembles," *ArXiv e-prints*, Jan. 2019. [Online]. Available: https://arxiv.org/abs/1901.01614

[94] P. Jamonneau, M. Lesik, J. P. Tetienne, I. Alvizu, L. Mayer, A. Dréau, S. Kosen, J.-F. Roch, S. Pezzagna, J. Meijer, T. Teraji, Y. Kubo, P. Bertet, J. R. Maze, and V. Jacques, "Competition between electric field and magnetic field noise in the decoherence of a single spin in diamond," *Phys. Rev. B*, vol. 93, p. 024305, 2016. [Online]. Available: https://journals.aps.org/prb/abstract/10.1103/PhysRevB.93.024305

[95] G. de Lange, Z. H. Wang, D. Ristè, V. V. Dobrovitski, and R. Hanson, "Universal dynamical decoupling of a single solid-state spin from a spin bath," *Science*, vol. 330, no. 6000, pp. 60–63, 2010. [Online]. Available: http://science.sciencemag.org/content/330/6000/60

[96] L. M. Pham, N. Bar-Gill, D. Le Sage, C. Belthangady, A. Stacey, M. Markham, D. J. Twitchen, M. D. Lukin, and R. L. Walsworth, "Enhanced metrology using preferential orientation of nitrogen-vacancy centers in diamond,"

Phys. Rev. B, vol. 86, no. 12, pp. 121 202–, 09 2012. [Online]. Available: http://link.aps.org/doi/10.1103/PhysRevB.86.121202

[97] N. F. Ramsey, "A molecular beam resonance method with separated oscillating fields," *Phys. Rev.*, vol. 78, pp. 695–699, Jun 1950. [Online]. Available: https://link.aps.org/doi/10.1103/PhysRev.78.695

[98] A. Gupta, L. Hacquebard, and L. Childress, "Efficient signal processing for time-resolved fluorescence detection of nitrogen-vacancy spins in diamond," *J. Opt. Soc. Am. B*, vol. 33, no. 3, pp. B28–B34, Mar 2016. [Online]. Available: http://josab.osa.org/abstract.cfm?URI=josab-33-3-B28

[99] L. Robledo, H. Bernien, T. v. d. Sar, and R. Hanson, "Spin dynamics in the optical cycle of single nitrogen-vacancy centres in diamond," *New J. Phys.*, vol. 13, no. 2, p. 025013, 2011. [Online]. Available: http://dx.doi.org/10.1088/1367-2630/13/2/025013

[100] A. Dréau, M. Lesik, L. Rondin, P. Spinicelli, O. Arcizet, J.-F. Roch, and V. Jacques, "Avoiding power broadening in optically detected magnetic resonance of single NV defects for enhanced dc magnetic field sensitivity," *Phys. Rev. B*, vol. 84, no. 19, pp. 195–204, Nov 2011. [Online]. Available: http://link.aps.org/doi/10.1103/PhysRevB.84.195204

[101] B. J. Shields, Q. P. Unterreithmeier, N. P. de Leon, H. Park, and M. D. Lukin, "Efficient readout of a single spin state in diamond via spin-to-charge conversion," *Phys. Rev. Lett.*, vol. 114, no. 13, p. 136402, 03 2015. [Online]. Available: http://link.aps.org/doi/10.1103/PhysRevLett.114.136402

[102] I. Popa, T. Gaebel, M. Domhan, C. Wittmann, F. Jelezko, and J. Wrachtrup, "Energy levels and decoherence properties of single electron and nuclear spins in a defect center in diamond," *Phys. Rev. B*, vol. 70, no. 20, pp. 201 203–, 11 2004. [Online]. Available: http://link.aps.org/doi/10.1103/PhysRevB.70.201203

[103] L. M. Pham, "Magnetic field sensing with nitrogen-vacancy color centers in diamond," Ph.D. dissertation, Harvard University, 2013. [Online]. Available: http://nrs.harvard.edu/urn-3:HUL.InstRepos:11051173

[104] K. Fang, V. M. Acosta, C. Santori, Z. Huang, K. M. Itoh, H. Watanabe, S. Shikata, and R. G. Beausoleil, "High-sensitivity magnetometry based on quantum beats in diamond nitrogen-vacancy centers," *Phys. Rev. Lett.*, vol. 110, p. 130802, Mar 2013. [Online]. Available: http://link.aps.org/doi/10.1103/PhysRevLett.110.130802

[105] D. A. Hopper, R. R. Grote, A. L. Exarhos, and L. C. Bassett, "Near-infrared-assisted charge control and spin readout of the nitrogen-vacancy center in diamond," *Phys. Rev. B*, vol. 94, p. 241201, Dec 2016. [Online]. Available: https://link.aps.org/doi/10.1103/PhysRevB.94.241201

[106] J.-C. Jaskula, B. J. Shields, E. Bauch, M. D. Lukin, A. S. Trifonov, and R. L. Walsworth, "Improved quantum sensing with a single solid-state spin via spin-to-charge conversion," *ArXiv e-prints*, Nov. 2017. [Online]. Available: https://arxiv.org/abs/1711.02023

[107] P. Neumann, J. Beck, M. Steiner, F. Rempp, H. Fedder, P. R. Hemmer, J. Wrachtrup, and F. Jelezko, "Single-shot readout of a single nuclear spin," *Science*, vol. 329, no. 5991, pp. 542–544, 2010. [Online]. Available: http://science.sciencemag.org/content/329/5991/542

[108] D. Le Sage, L. M. Pham, N. Bar-Gill, C. Belthangady, M. D. Lukin, A. Yacoby, and R. L. Walsworth, "Efficient photon detection from color centers in a diamond optical waveguide," *Phys. Rev. B*, vol. 85, p. 121202, Mar 2012. [Online]. Available: https://link.aps.org/doi/10.1103/PhysRevB.85.121202

[109] T. Wolf, P. Neumann, K. Nakamura, H. Sumiya, T. Ohshima, J. Isoya, and J. Wrachtrup, "Subpicotesla diamond magnetometry," *Phys. Rev. X*, vol. 5, p. 041001, Oct. 2015. [Online]. Available: http://link.aps.org/doi/10.1103/PhysRevX.5.041001

[110] G. Chatzidrosos, A. Wickenbrock, L. Bougas, N. Leefer, T. Wu, K. Jensen, Y. Dumeige, and D. Budker, "Miniature cavity-enhanced diamond magnetometer," *Phys. Rev. Applied*, vol. 8, p. 044019, Oct 2017. [Online]. Available: https://link.aps.org/doi/10.1103/PhysRevApplied.8.044019

[111] J.-P. Tetienne, L. Rondin, P. Spinicelli, M. Chipaux, T. Debuisschert, J.-F. Roch, and V. Jacques, "Magnetic-field-dependent photodynamics of single NV defects in diamond: an application to qualitative all-optical magnetic imaging," *New J. Phys.*, vol. 14, no. 10, p. 103033, 2012. [Online]. Available: http://stacks.iop.org/1367-2630/14/i=10/a=103033

[112] T.-L. Wee, Y.-K. Tzeng, C.-C. Han, H.-C. Chang, W. Fann, J.-H. Hsu, K.-M. Chen, and Y.-C. Yu, "Two-photon excited fluorescence of nitrogen-vacancy centers in proton-irradiated type ib diamond," *J. Phys. Chem. A*, vol. 111, no. 38, pp. 9379–9386, 2007. [Online]. Available: http://dx.doi.org/10.1021/jp073938o

[113] G. D. Fuchs, V. V. Dobrovitski, R. Hanson, A. Batra, C. D. Weis, T. Schenkel, and D. D. Awschalom, "Excited-state spectroscopy using single spin manipulation in diamond," *Phys. Rev. Lett.*, vol. 101, p. 117601, Sep 2008. [Online]. Available: http://link.aps.org/doi/10.1103/PhysRevLett.101.117601

[114] R. S. Schoenfeld and W. Harneit, "Real time magnetic field sensing and imaging using a single spin in diamond," *Phys. Rev. Lett.*, vol. 106, no. 3, pp. 030 802–, 01 2011. [Online]. Available: http://link.aps.org/doi/10.1103/PhysRevLett.106.030802

[115] J. Vanier and C. Audoin, *The Quantum Physics of Atomic Frequency Standards*. A. Hilger, 1989. [Online]. Available: https://books.google.com/books?id=DVFLAQAAIAAJ

[116] L. M. K. Vandersypen and I. L. Chuang, "NMR techniques for quantum control and computation," *Rev. Mod. Phys.*, vol. 76, pp. 1037–1069, Jan 2005. [Online]. Available: https://link.aps.org/doi/10.1103/RevModPhys.76.1037

[117] H. A. R. El-Ella, S. Ahmadi, A. M. Wojciechowski, A. Huck, and U. L. Andersen, "Optimised frequency modulation for continuous-wave optical magnetic resonance sensing using nitrogen-vacancy ensembles," *Opt. Express*, vol. 25, no. 13, pp. 14 809–14 821, Jun 2017. [Online]. Available: http://www.opticsexpress.org/abstract.cfm?URI=oe-25-13-14809

[118] I. I. Rabi, "Space quantization in a gyrating magnetic field," *Phys. Rev.*, vol. 51, pp. 652–654, Apr 1937. [Online]. Available: https://link.aps.org/doi/10.1103/PhysRev.51.652

[119] H. Fedder, F. Dolde, F. Rempp, T. Wolf, P. Hemmer, F. Jelezko, and J. Wrachtrup, "Towards t1-limited magnetic resonance imaging using rabi beats," *Appl. Phys. B*, vol. 102, no. 3, pp. 497–502, Mar 2011. [Online]. Available: https://doi.org/10.1007/s00340-011-4408-4

[120] S. Choi, N. Y. Yao, and M. D. Lukin, "Quantum metrology based on strongly correlated matter," *ArXiv e-prints*, Dec. 2017. [Online]. Available: https://arxiv.org/abs/1801.00042

[121] H. Clevenson, M. E. Trusheim, C. Teale, T. Schroder, D. Braje, and D. Englund, "Broadband magnetometry and temperature sensing with a light-trapping diamond waveguide," *Nat. Phys.*, vol. 11, no. 5, pp. 393–397, 05 2015. [Online]. Available: http://dx.doi.org/10.1038/nphys3291

[122] A. Ariyaratne, D. Bluvstein, B. A. Myers, and A. C. B. Jayich, "Nanoscale electrical conductivity imaging using a nitrogen-vacancy center in diamond," *Nat. Commun.*, vol. 9, no. 1, p. 2406, 2018. [Online]. Available: https://doi.org/10.1038/s41467-018-04798-1

[123] D. A. Hopper, H. J. Shulevitz, and L. C. Bassett, "Spin readout techniques of the nitrogen-vacancy center in diamond," *Micromachines*, vol. 9, no. 9, 2018. [Online]. Available: http://www.mdpi.com/2072-666X/9/9/437

[124] E. Abe and K. Sasaki, "Tutorial: Magnetic resonance with nitrogen-vacancy centers in diamond - microwave engineering, materials science, and magnetometry," *J. Appl. Phys.*, vol. 123, no. 16, p. 161101, 2018. [Online]. Available: https://doi.org/10.1063/1.5011231

[125] E. R. Eisenach, J. F. Barry, L. M. Pham, R. G. Rojas, D. R. Englund, and D. A. Braje, "Broadband loop gap resonator for nitrogen vacancy centers

in diamond," *Rev. Sci. Instrum.*, vol. 89, no. 9, p. 094705, 2018. [Online]. Available: https://doi.org/10.1063/1.5037465

[126] D. A. Simpson, J.-P. Tetienne, J. M. McCoey, K. Ganesan, L. T. Hall, S. Petrou, R. E. Scholten, and L. C. L. Hollenberg, "Magneto-optical imaging of thin magnetic films using spins in diamond," *Sci. Rep.*, vol. 6, p. 22797, Mar 2016. [Online]. Available: http://dx.doi.org/10.1038/srep22797

[127] J.-P. Tetienne, N. Dontschuk, D. A. Broadway, A. Stacey, D. A. Simpson, and L. C. L. Hollenberg, "Quantum imaging of current flow in graphene," *Sci. Adv.*, vol. 3, no. 4, 2017. [Online]. Available: http://advances.sciencemag.org/content/3/4/e1602429

[128] P. C. Hobbs, *Building electro-optical systems: making it all work.* Wiley, 2011. [Online]. Available: https://onlinelibrary.wiley.com/doi/book/10.1002/9780470466339

[129] A. Angerer, T. Nöbauer, G. Wachter, M. Markham, A. Stacey, J. Majer, J. Schmiedmayer, and M. Trupke, "Subnanotesla quantum-interference magnetometry with a single spin in diamond," *ArXiv e-prints*, Sep. 2015. [Online]. Available: https://arxiv.org/abs/1509.01637

[130] T. Nöbauer, A. Angerer, B. Bartels, M. Trupke, S. Rotter, J. Schmiedmayer, F. Mintert, and J. Majer, "Smooth optimal quantum control for robust solid-state spin magnetometry," *Phys. Rev. Lett.*, vol. 115, p. 190801, Nov 2015. [Online]. Available: https://link.aps.org/doi/10.1103/PhysRevLett.115.190801

[131] L. Jiang, J. S. Hodges, J. R. Maze, P. Maurer, J. M. Taylor, D. G. Cory, P. R. Hemmer, R. L. Walsworth, A. Yacoby, A. S. Zibrov, and M. D. Lukin, "Repetitive readout of a single electronic spin via quantum logic with nuclear spin ancillae," *Science*, vol. 326, no. 5950, pp. 267–272, 2009. [Online]. Available: http://science.sciencemag.org/content/326/5950/267

[132] G. de Lange, T. van der Sar, M. Blok, Z.-H. Wang, V. Dobrovitski, and R. Hanson, "Controlling the quantum dynamics of a mesoscopic spin bath in diamond," *Sci. Rep.*, vol. 2, pp. 382 –, Apr 2012. [Online]. Available: http://dx.doi.org/10.1038/srep00382

[133] P. Neumann, R. Kolesov, V. Jacques, J. Beck, J. Tisler, A. Batalov, L. Rogers, N. B. Manson, G. Balasubramanian, F. Jelezko, and J. Wrachtrup, "Excited-state spectroscopy of single NV defects in diamond using optically detected magnetic resonance," *New J. Phys.*, vol. 11, no. 1, p. 013017, 2009. [Online]. Available: http://stacks.iop.org/1367-2630/11/i=1/a=013017

[134] M. Mrózek, D. Rudnicki, P. Kehayias, A. Jarmola, D. Budker, and W. Gawlik, "Longitudinal spin relaxation in nitrogen-vacancy ensembles in diamond," *EPJ Quantum Technology*, vol. 2, no. 1, p. 22, Oct 2015. [Online]. Available: https://doi.org/10.1140/epjqt/s40507-015-0035-z

[135] E. L. Hahn, "Spin echoes," *Phys. Rev.*, vol. 80, pp. 580–594, Nov 1950. [Online]. Available: http://link.aps.org/doi/10.1103/PhysRev.80.580

[136] S. Meiboom and D. Gill, "Modified spin-echo method for measuring nuclear relaxation times," *Rev. Sci. Instrum.*, vol. 29, no. 8, pp. 688–691, 1958. [Online]. Available: https://doi.org/10.1063/1.1716296

[137] T. Gullion, D. B. Baker, and M. S. Conradi, "New, compensated carr-purcell sequences," *J. Magn. Reson.*, vol. 89, no. 3, pp. 479–484, 1990. [Online]. Available: http://www.sciencedirect.com/science/article/pii/0022236490903313

[138] Z.-H. Wang, G. de Lange, D. Ristè, R. Hanson, and V. V. Dobrovitski, "Comparison of dynamical decoupling protocols for a nitrogen-vacancy center in diamond," *Phys. Rev. B*, vol. 85, p. 155204, Apr 2012. [Online]. Available: https://link.aps.org/doi/10.1103/PhysRevB.85.155204

[139] R. de Sousa, *Electron Spin as a Spectrometer of Nuclear-Spin Noise and Other Fluctuations*. Springer Berlin Heidelberg, 2009, pp. 183–220. [Online]. Available: https://link.springer.com/chapter/10.1007/978-3-540-79365-6_10

[140] T. Ishikawa, K.-M. C. Fu, C. Santori, V. M. Acosta, R. G. Beausoleil, H. Watanabe, S. Shikata, and K. M. Itoh, "Optical and spin coherence properties of nitrogen-vacancy centers placed in a 100 nm thick isotopically purified diamond layer," *Nano Lett.*, vol. 12, no. 4, pp. 2083–2087, 2012. [Online]. Available: http://dx.doi.org/10.1021/nl300350r

[141] V. V. Dobrovitski, A. E. Feiguin, D. D. Awschalom, and R. Hanson, "Decoherence dynamics of a single spin versus spin ensemble," *Phys. Rev. B*, vol. 77, no. 24, pp. 245 212–, 06 2008. [Online]. Available: http://link.aps.org/doi/10.1103/PhysRevB.77.245212

[142] R. Hanson, F. M. Mendoza, R. J. Epstein, and D. D. Awschalom, "Polarization and readout of coupled single spins in diamond," *Phys. Rev. Lett.*, vol. 97, p. 087601, Aug 2006. [Online]. Available: http://link.aps.org/doi/10.1103/PhysRevLett.97.087601

[143] R. Hanson, V. V. Dobrovitski, A. E. Feiguin, O. Gywat, and D. D. Awschalom, "Coherent dynamics of a single spin interacting with an adjustable spin bath," *Science*, vol. 320, no. 5874, pp. 352–355, 2008. [Online]. Available: http://science.sciencemag.org/content/320/5874/352

[144] L. T. Hall, J. H. Cole, and L. C. L. Hollenberg, "Analytic solutions to the central-spin problem for nitrogen-vacancy centers in diamond," *Phys. Rev. B*, vol. 90, p. 075201, Aug 2014. [Online]. Available: http://link.aps.org/doi/10.1103/PhysRevB.90.075201

[145] J. R. Maze, A. Dréau, V. Waselowski, H. Duarte, J.-F. Roch, and V. Jacques, "Free induction decay of single spins in diamond," *New J. Phys.*, vol. 14, no. 10, p. 103041, 2012. [Online]. Available: http://stacks.iop.org/1367-2630/14/i=10/a=103041

[146] A. Abragam, *The Principles of Nuclear Magnetism.* Oxford: Clarendon Press, October 1983. [Online]. Available: https://books.google.com/books/about/The_Principles_of_Nuclear_Magnetism.html?id=9M8U_JK7K54C

[147] C. L. Kwan and T. F. Yen, "Electron spin resonance study of coal by line width and line shape analysis," *Anal. Chem.*, vol. 51, no. 8, pp. 1225–1229, 07 1979. [Online]. Available: http://dx.doi.org/10.1021/ac50044a028

[148] J. A. van Wyk, E. C. Reynhardt, G. L. High, and I. Kiflawi, "The dependences of esr line widths and spin - spin relaxation times of single nitrogen defects on the concentration of nitrogen defects in diamond," *J. Phys. D: Appl. Phys.*, vol. 30, no. 12, p. 1790, 1997. [Online]. Available: http://stacks.iop.org/0022-3727/30/i=12/a=016

[149] C. P. Poole, *Electron Spin Resonance: A Comprehensive Treatise on Experimental Techniques*, 2nd, Ed. Courier Corporation, 1996. [Online]. Available: https://books.google.com/books/about/Electron_Spin_Resonance.html?id=P-4PIoi7Z7IC

[150] C. Kittel and E. Abrahams, "Dipolar broadening of magnetic resonance lines in magnetically diluted crystals," *Phys. Rev.*, vol. 90, pp. 238–239, Apr 1953. [Online]. Available: http://link.aps.org/doi/10.1103/PhysRev.90.238

[151] E. R. MacQuarrie, T. A. Gosavi, A. M. Moehle, N. R. Jungwirth, S. A. Bhave, and G. D. Fuchs, "Coherent control of a nitrogen-vacancy center spin ensemble with a diamond mechanical resonator," *Optica*, vol. 2, no. 3, pp. 233–238, Mar 2015. [Online]. Available: http://www.osapublishing.org/optica/abstract.cfm?URI=optica-2-3-233

[152] J. Cao, "A weight-averaged NMR spin-spin relaxation time constant and its determination," *J. Magn. Reson., Ser B*, vol. 103, no. 3, pp. 296–298, 1994. [Online]. Available: http://www.sciencedirect.com/science/article/pii/S1064186684710454

[153] P. L. Stanwix, L. M. Pham, J. R. Maze, D. Le Sage, T. K. Yeung, P. Cappellaro, P. R. Hemmer, A. Yacoby, M. D. Lukin, and R. L. Walsworth, "Coherence of nitrogen-vacancy electronic spin ensembles in diamond," *Phys. Rev. B*, vol. 82, no. 20, pp. 201 201–, 11 2010. [Online]. Available: http://link.aps.org/doi/10.1103/PhysRevB.82.201201

[154] W. V. Smith, P. P. Sorokin, I. L. Gelles, and G. J. Lasher, "Electron-spin resonance of nitrogen donors in diamond," *Phys. Rev.*, vol. 115, no. 6, pp. 1546–1552, 1959. [Online]. Available: http://doi.org/10.1103/PhysRev.115.1546

[155] R. J. Cook and D. H. Whiffen, "Electron nuclear double resonance study of a nitrogen centre in diamond," *Proc. R. Soc. London, Ser. A*, vol. 295, no. 1441, pp. 99–106, 1966. [Online]. Available: http://rspa.royalsocietypublishing.org/content/295/1441/99

[156] J. H. N. Loubser and J. A. van Wyk, "Electron spin resonance in the study of diamond," *Rep. Prog. Phys.*, vol. 41, no. 8, p. 1201, 1978. [Online]. Available: http://stacks.iop.org/0034-4885/41/i=8/a=002

[157] C. B. Hartland, "A study of point defects in cvd diamond using electron paramagnetic resonance and optical spectroscopy," Ph.D. dissertation, University of Warwick, 2014. [Online]. Available: http://wrap.warwick.ac.uk/67156/1/WRAP_THESIS_Hartland_2014.pdf

[158] P. G. Baranov, H. J. von Bardeleben, F. Jelezko, and J. Wrachtrup, *Retrospectives: Magnetic Resonance Studies of Intrinsic Defects in Semiconductors*. Vienna: Springer, 2017, pp. 179–211.

[159] D. J. Twitchen, M. E. Newton, J. M. Baker, T. R. Anthony, and W. F. Banholzer, "Electron-paramagnetic-resonance measurements on the divacancy defect center $R4/W6$ in diamond," *Phys. Rev. B*, vol. 59, pp. 12 900–12 910, May 1999. [Online]. Available: http://link.aps.org/doi/10.1103/PhysRevB.59.12900

[160] K. Iakoubovskii and A. Stesmans, "Dominant paramagnetic centers in ^{17}O-implanted diamond," *Phys. Rev. B*, vol. 66, no. 4, p. 045406, 2002. [Online]. Available: https://journals.aps.org/prb/abstract/10.1103/PhysRevB.66.045406

[161] A. M. Edmonds, U. F. S. D'Haenens-Johansson, R. J. Cruddace, M. E. Newton, K.-M. C. Fu, C. Santori, R. G. Beausoleil, D. J. Twitchen, and M. L. Markham, "Production of oriented nitrogen-vacancy color centers in synthetic diamond," *Phys. Rev. B*, vol. 86, p. 035201, Jul 2012. [Online]. Available: https://link.aps.org/doi/10.1103/PhysRevB.86.035201

[162] M. E. Wieser, N. Holden, T. B. Coplen, J. K. Böhlke, M. Berglund, W. A. Brand, P. De Bièvre, M. Gröning, R. D. Loss, J. Meija, T. Hirata, T. Prohaska, R. Schoenberg, G. O Connor, T. Walczyk, S. Yoneda, and X.-K. Zhu, "Atomic weights of the elements 2011 (iupac technical report)," *Pure Appl. Chem.*, vol. 85, no. 5, pp. 1047–1078, 2013. [Online]. Available: http://pdg.lbl.gov/2016/AtomicNuclearProperties/PurApplChem85_1047.pdf

[163] A. Dréau, J.-R. Maze, M. Lesik, J.-F. Roch, and V. Jacques, "High-resolution spectroscopy of single NV defects coupled with nearby ^{13}C nuclear spins in diamond," *Phys. Rev. B*, vol. 85, p. 134107, Apr 2012. [Online]. Available: https://link.aps.org/doi/10.1103/PhysRevB.85.134107

[164] N. Zhao, S.-W. Ho, and R.-B. Liu, "Decoherence and dynamical decoupling control of nitrogen vacancy center electron spins in nuclear spin

baths," *Phys. Rev. B*, vol. 85, p. 115303, Mar 2012. [Online]. Available: https://link.aps.org/doi/10.1103/PhysRevB.85.115303

[165] T. Teraji, T. Taniguchi, S. Koizumi, Y. Koide, and J. Isoya, "Effective use of source gas for diamond growth with isotopic enrichment," *Appl. Phys. Express*, vol. 6, no. 5, p. 055601, 2013. [Online]. Available: http://stacks.iop.org/1882-0786/6/i=5/a=055601

[166] M. E. Trusheim and D. Englund, "Wide-field strain imaging with preferentially aligned nitrogen-vacancy centers in polycrystalline diamond," *New J. Phys.*, vol. 18, no. 12, p. 123023, 2016. [Online]. Available: http://stacks.iop.org/1367-2630/18/i=12/a=123023

[167] M. Gaukroger, P. Martineau, M. Crowder, I. Friel, S. Williams, and D. Twitchen, "X-ray topography studies of dislocations in single crystal CVD diamond," *Diam. Relat. Mater.*, vol. 17, no. 3, pp. 262–269, 2008. [Online]. Available: https://www.sciencedirect.com/science/article/pii/S0925963507005377

[168] L. T. M. Hoa, T. Ouisse, D. Chaussende, M. Naamoun, A. Tallaire, and J. Achard, "Birefringence microscopy of unit dislocations in diamond," *Cryst. Growth Des.*, vol. 14, no. 11, pp. 5761–5766, 2014. [Online]. Available: https://pubs.acs.org/doi/abs/10.1021/cg501019

[169] M. W. Doherty, F. Dolde, H. Fedder, F. Jelezko, J. Wrachtrup, N. B. Manson, and L. C. L. Hollenberg, "Theory of the ground-state spin of the NV^- center in diamond," *Phys. Rev. B*, vol. 85, p. 205203, May 2012. [Online]. Available: https://link.aps.org/doi/10.1103/PhysRevB.85.205203

[170] M. F. O'Keeffe, L. Horesh, J. F. Barry, D. A. Braje, and I. L. Chuang, "Hamiltonian engineering with constrained optimization for quantum sensing and control," *New J. Phys*, vol. 21, no. 2, p. 023015, Feb 2019. [Online]. Available: https://iopscience.iop.org/article/10.1088/1367-2630/ab00be/meta

[171] R. U. A. Khan, P. M. Martineau, B. L. Cann, M. E. Newton, and D. J. Twitchen, "Charge transfer effects, thermo and photochromism in single crystal cvd synthetic diamond," *J. Phys.: Condens. Matter*, vol. 21, no. 36, p. 364214, 2009. [Online]. Available: http://dx.doi.org/10.1088/0953-8984/21/36/364214

[172] Z.-H. Wang and S. Takahashi, "Spin decoherence and electron spin bath noise of a nitrogen-vacancy center in diamond," *Phys. Rev. B*, vol. 87, p. 115122, Mar 2013. [Online]. Available: https://link.aps.org/doi/10.1103/PhysRevB.87.115122

[173] E. E. Kleinsasser, M. M. Stanfield, J. K. Q. Banks, Z. Zhu, W.-D. Li, V. M. Acosta, H. Watanabe, K. M. Itoh, and K.-M. C. Fu, "High density nitrogen-vacancy sensing surface created via he+ ion implantation of 12c

diamond," *Appl. Phys. Lett.*, vol. 108, no. 20, p. 202401, 2016. [Online]. Available: https://doi.org/10.1063/1.4949357

[174] N. Bar-Gill, L. M. Pham, C. Belthangady, D. Le Sage, P. Cappellaro, J. R. Maze, M. D. Lukin, A. Yacoby, and R. Walsworth, "Suppression of spin-bath dynamics for improved coherence of multi-spin-qubit systems," *Nat. Commun.*, vol. 3, p. 858, 05 2012. [Online]. Available: http://dx.doi.org/10.1038/ncomms1856

[175] V. Stepanov and S. Takahashi, "Determination of nitrogen spin concentration in diamond using double electron-electron resonance," *Phys. Rev. B*, vol. 94, no. 2, pp. 024 421–, 07 2016. [Online]. Available: http://link.aps.org/doi/10.1103/PhysRevB.94.024421

[176] E. Abe, A. M. Tyryshkin, S. Tojo, J. J. L. Morton, W. M. Witzel, A. Fujimoto, J. W. Ager, E. E. Haller, J. Isoya, S. A. Lyon, M. L. W. Thewalt, and K. M. Itoh, "Electron spin coherence of phosphorus donors in silicon: Effect of environmental nuclei," *Phys. Rev. B*, vol. 82, p. 121201, Sep 2010. [Online]. Available: https://link.aps.org/doi/10.1103/PhysRevB.82.121201

[177] W. M. Witzel, M. S. Carroll, A. Morello, Ł. Cywiński, and S. Das Sarma, "Electron spin decoherence in isotope-enriched silicon," *Phys. Rev. Lett.*, vol. 105, no. 18, pp. 187 602–, 10 2010. [Online]. Available: https://link.aps.org/doi/10.1103/PhysRevLett.105.187602

[178] K. M. Itoh and H. Watanabe, "Isotope engineering of silicon and diamond for quantum computing and sensing applications," *MRS Commun.*, vol. 4, no. 4, pp. 143–157, 12 2014. [Online]. Available: http://dx.doi.org/10.1557/mrc.2014.32

[179] N. Mizuochi, P. Neumann, F. Rempp, J. Beck, V. Jacques, P. Siyushev, K. Nakamura, D. J. Twitchen, H. Watanabe, S. Yamasaki, F. Jelezko, and J. Wrachtrup, "Coherence of single spins coupled to a nuclear spin bath of varying density," *Phys. Rev. B*, vol. 80, p. 041201, Jul 2009. [Online]. Available: https://link.aps.org/doi/10.1103/PhysRevB.80.041201

[180] H. Morishita, E. Abe, W. Akhtar, L. S. Vlasenko, A. Fujimoto, K. Sawano, Y. Shiraki, L. Dreher, H. Riemann, N. V. Abrosimov, P. Becker, H.-J. Pohl, M. L. W. Thewalt, M. S. Brandt, and K. M. Itoh, "Linewidth of low-field electrically detected magnetic resonance of phosphorus in isotopically controlled silicon," *Appl. Phys. Express*, vol. 4, no. 2, p. 021302, 2011. [Online]. Available: http://stacks.iop.org/1882-0786/4/i=2/a=021302

[181] M. Markham, J. Dodson, G. Scarsbrook, D. Twitchen, G. Balasubramanian, F. Jelezko, and J. Wrachtrup, "{CVD} diamond for spintronics," *Diam. Relat. Mater.*, vol. 20, no. 2, pp. 134–139, 2011. [Online]. Available: http://www.sciencedirect.com/science/article/pii/S0925963510003274

[182] K. J. Dwyer, J. M. Pomeroy, and D. S. Simons, "99.996 % 12c films isotopically enriched and deposited in situ," *Appl. Phys. Lett.*, vol. 102, no. 25, p. 254104, 2013. [Online]. Available: http://dx.doi.org/10.1063/1.4812745

[183] T. Teraji, T. Yamamoto, K. Watanabe, Y. Koide, J. Isoya, S. Onoda, T. Ohshima, L. J. Rogers, F. Jelezko, P. Neumann, J. Wrachtrup, and S. Koizumi, "Homoepitaxial diamond film growth: High purity, high crystalline quality, isotopic enrichment, and single color center formation," *Phys. Status Solidi A*, vol. 212, no. 11, pp. 2365–2384, 2015. [Online]. Available: http://dx.doi.org/10.1002/pssa.201532449

[184] G. Kucsko, S. Choi, J. Choi, P. C. Maurer, H. Zhou, R. Landig, H. Sumiya, S. Onoda, J. Isoya, F. Jelezko, E. Demler, N. Y. Yao, and M. D. Lukin, "Critical thermalization of a disordered dipolar spin system in diamond," *Phys. Rev. Lett.*, vol. 121, p. 023601, Jul 2018. [Online]. Available: https://link.aps.org/doi/10.1103/PhysRevLett.121.023601

[185] S. Felton, B. L. Cann, A. M. Edmonds, S. Liggins, R. J. Cruddace, M. E. Newton, D. Fisher, and J. M. Baker, "Electron paramagnetic resonance studies of nitrogen interstitial defects in diamond," *J. Phys.: Condens. Matter*, vol. 21, p. 364212, Sep. 2009. [Online]. Available: https://doi.org/10.1088/0953-8984/21/36/364212

[186] S. Felton, A. M. Edmonds, M. E. Newton, P. M. Martineau, D. Fisher, and D. J. Twitchen, "Electron paramagnetic resonance studies of the neutral nitrogen vacancy in diamond," *Phys. Rev. B*, vol. 77, p. 081201, Feb 2008. [Online]. Available: https://link.aps.org/doi/10.1103/PhysRevB.77.081201

[187] S. Choi, N. Y. Yao, and M. D. Lukin, "Dynamical engineering of interactions in qudit ensembles," *Phys. Rev. Lett.*, vol. 119, p. 183603, Nov 2017. [Online]. Available: https://link.aps.org/doi/10.1103/PhysRevLett.119.183603

[188] P. Neumann, R. Kolesov, B. Naydenov, J. Beck, F. Rempp, M. Steiner, V. Jacques, G. Balasubramanian, M. L. Markham, D. J. Twitchen, S. Pezzagna, J. Meijer, J. Twamley, F. Jelezko, and J. Wrachtrup, "Quantum register based on coupled electron spins in a room-temperature solid," *Nat. Phys.*, vol. 6, no. 4, pp. 249–253, 04 2010. [Online]. Available: http://dx.doi.org/10.1038/nphys1536

[189] F. Dolde, I. Jakobi, B. Naydenov, N. Zhao, S. Pezzagna, C. Trautmann, J. Meijer, P. Neumann, F. Jelezko, and J. Wrachtrup, "Room-temperature entanglement between single defect spins in diamond," *Nat. Phys.*, vol. 9, no. 3, pp. 139–143, 03 2013. [Online]. Available: http://dx.doi.org/10.1038/nphys2545

[190] T. Yamamoto, C. Müller, L. P. McGuinness, T. Teraji, B. Naydenov, S. Onoda, T. Ohshima, J. Wrachtrup, F. Jelezko, and J. Isoya, "Strongly coupled diamond spin qubits by molecular nitrogen implantation," *Phys.*

Rev. B, vol. 88, no. 20, pp. 201 201–, 11 2013. [Online]. Available: http://link.aps.org/doi/10.1103/PhysRevB.88.201201

[191] I. Jakobi, S. A. Momenzadeh, F. F. de Oliveira, J. Michl, F. Ziem, M. Schreck, P. Neumann, A. Denisenko, and J. Wrachtrup, "Efficient creation of dipolar coupled nitrogen-vacancy spin qubits in diamond," *J. Phys.: Conf. Ser.*, vol. 752, no. 1, p. 012001, 2016. [Online]. Available: http://stacks.iop.org/1742-6596/752/i=1/a=012001

[192] H. Bernien, B. Hensen, W. Pfaff, G. Koolstra, M. S. Blok, L. Robledo, T. H. Taminiau, M. Markham, D. J. Twitchen, L. Childress, and R. Hanson, "Heralded entanglement between solid-state qubits separated by three metres," *Nature*, vol. 497, p. 86, 04 2013. [Online]. Available: http://dx.doi.org/10.1038/nature12016

[193] B. Hensen, H. Bernien, A. E. Dréau, A. Reiserer, N. Kalb, M. S. Blok, J. Ruitenberg, R. F. L. Vermeulen, R. N. Schouten, C. Abellán, W. Amaya, V. Pruneri, M. W. Mitchell, M. Markham, D. J. Twitchen, D. Elkouss, S. Wehner, T. H. Taminiau, and R. Hanson, "Loophole-free bell inequality violation using electron spins separated by 1.3 kilometres," *Nature*, vol. 526, p. 682, 10 2015. [Online]. Available: http://dx.doi.org/10.1038/nature15759

[194] J. Wikswo, J. Barach, and J. Freeman, "Magnetic field of a nerve impulse: first measurements," *Science*, vol. 208, no. 4439, pp. 53–55, 1980. [Online]. Available: http://science.sciencemag.org/content/208/4439/53

[195] P. Sundaram, A. Nummenmaa, W. Wells, D. Orbach, D. Orringer, R. V. Mulkern, and Y. Okada, "Direct neural current imaging in an intact cerebellum with magnetic resonance imaging," *NeuroImage*, vol. 132, pp. 477–490, 2016. [Online]. Available: https://doi.org/10.1016/j.neuroimage.2016.01.059

[196] Z. Wang, R. van Dorp, A. Weidema, and D. Ypey, "No evidence for effects of mild microwave irradiation on electrophysiological and morphological properties of cultured embryonic rat dorsal root ganglion cells," *Eur. J. Morphol.*, vol. 29, no. 3, pp. 198—206, 1991. [Online]. Available: http://europepmc.org/abstract/MED/1823575

[197] M. G. Shapiro, M. F. Priest, P. H. Siegel, and F. Bezanilla, "Thermal mechanisms of millimeter wave stimulation of excitable cells." *Biophys. J.*, vol. 104 12, pp. 2622–8, 2013. [Online]. Available: https://doi.org/10.1016/j.bpj.2013.05.014

[198] J. A. C. Nicol, "The giant nerve-fibres in the central nervous system of Myxicola (Polychaeta, Sabellidae)," *Q. J. Microsc. Sci.*, vol. 89, no. 1, pp. 1–45, 1948. [Online]. Available: http://jcs.biologists.org/content/s3-89/5/1

[199] ——, "The giant axons of annelids." *Q. Rev. Biol.*, vol. 23, no. 4, pp. 291–323, 1948. [Online]. Available: http://dx.doi.org/10.1086/396594

[200] K. Jensen, N. Leefer, A. Jarmola, Y. Dumeige, V. M. Acosta, P. Kehayias, B. Patton, and D. Budker, "Cavity-enhanced room-temperature magnetometry using absorption by nitrogen-vacancy centers in diamond," *Phys. Rev. Lett.*, vol. 112, no. 16, p. 160802, 04 2014. [Online]. Available: http://link.aps.org/doi/10.1103/PhysRevLett.112.160802

[201] K. R. Swinney and J. Wikswo, J P, "A calculation of the magnetic field of a nerve action potential," *Biophysical journal*, vol. 32, no. 2, pp. 719–731, 11 1980. [Online]. Available: https://www.ncbi.nlm.nih.gov/pubmed/7260298

[202] B. J. Roth and J. P. Wikswo, "The magnetic field of a single axon. a comparison of theory and experiment." *Biophys. J.*, vol. 48, no. 1, pp. 93–109, Jul 1985. [Online]. Available: http://www.ncbi.nlm.nih.gov/pmc/articles/PMC1329380/

[203] J. P. Wikswo and B. J. Roth, "Magnetic determination of the spatial extent of a single cortical current source: a theoretical analysis," *Electroencephalography and Clinical Neurophysiology*, vol. 69, no. 3, pp. 266 – 276, 1988. [Online]. Available: http://www.sciencedirect.com/science/article/pii/0013469488901356

[204] M. L. Hines and N. T. Carnevale, "The neuron simulation environment," *Neural Comput.*, vol. 9, no. 6, pp. 1179–1209, 1997.

[205] M. B. V. Roberts, "The rapid response of *Myxicola infundibulum*," *J. Mar. Biol. Assoc. U K*, vol. 42, no. 3, pp. 527–539, 1962. [Online]. Available: http://doi.org/10.1017/S0025315400054242

[206] K. Kim, S. Begus, H. Xia, S.-K. Lee, V. Jazbinsek, Z. Trontelj, and M. V. Romalis, "Multi-channel atomic magnetometer for magnetoencephalography: A configuration study," *NeuroImage*, vol. 89, pp. 143–151, 2014. [Online]. Available: http://www.sciencedirect.com/science/article/pii/S105381191301063X

[207] D. Drung, C. Abmann, J. Beyer, A. Kirste, M. Peters, F. Ruede, and T. Schurig, "Highly sensitive and easy-to-use squid sensors," *IEEE T. Appl. Supercon.*, vol. 17, no. 2, pp. 699–704, June 2007. [Online]. Available: https://doi.org/10.1109/TASC.2007.897403

[208] S. Tan, B. J. Roth, and J. P. Wikswo, "The magnetic field of cortical current sources: the application of a spatial filtering model to the forward and inverse problems," *Electroencephalography and Clinical Neurophysiology*, vol. 76, no. 1, pp. 73 – 85, 1990. [Online]. Available: https://doi.org/10.1016/0013-4694(90)90059-S

[209] C. Cotman and J. McGaugh, *Behavioral neuroscience: an introduction*. Academic Press, 1980. [Online]. Available: https://books.google.com/books?id=kN1qAAAAMAAJ

[210] J. K. Woosley, B. J. Roth, and J. P. Wikswo, "The magnetic field of a single axon: A volume conductor model," *Math. Biosci.*, vol. 76, no. 1, pp. 1 – 36, 1985. [Online]. Available: http://www.sciencedirect.com/science/article/pii/0025556485900446

[211] J. Sarvas, "Basic mathematical and electromagnetic concepts of the biomagnetic inverse problem," *Phys. Med. Biol.*, vol. 32, no. 1, p. 11, 1987. [Online]. Available: http://stacks.iop.org/0031-9155/32/i=1/a=004

[212] A. I. Ahonen, M. S. Hamalainen, R. J. Ilmoniemi, M. J. Kajola, J. E. T. Knuutila, J. T. Simola, and V. A. Vilkman, "Sampling theory for neuromagnetic detector arrays," *IEEE Transactions on Biomedical Engineering*, vol. 40, no. 9, pp. 859–869, Sep. 1993. [Online]. Available: https://doi.org/10.1109/10.245606

[213] B. J. Roth, N. G. Sepulveda, and J. P. Wikswo, "Using a magnetometer to image a two-dimensional current distribution," *J. Appl. Phys.*, vol. 65, no. 1, pp. 361–372, 1989. [Online]. Available: https://doi.org/10.1063/1.342549

[214] R. L. Parker, "Understanding inverse theory," *Annual Review of Earth and Planetary Sciences*, vol. 5, no. 1, pp. 35–64, 1977. [Online]. Available: https://doi.org/10.1146/annurev.ea.05.050177.000343

[215] H. J. Mamin, M. H. Sherwood, M. Kim, C. T. Rettner, K. Ohno, D. D. Awschalom, and D. Rugar, "Multipulse double-quantum magnetometry with near-surface nitrogen-vacancy centers," *Phys. Rev. Lett.*, vol. 113, no. 3, pp. 030 803–, 07 2014. [Online]. Available: http://link.aps.org/doi/10.1103/PhysRevLett.113.030803

[216] H. Zhang, I. Aharonovich, D. R. Glenn, R. Schalek, A. P. Magyar, J. W. Lichtman, E. L. Hu, and R. L. Walsworth, "Silicon-vacancy color centers in nanodiamonds: cathodoluminescence imaging markers in the near infrared," *Small*, vol. 10, no. 10, pp. 1908–1913, 2014. [Online]. Available: http://dx.doi.org/10.1002/smll.201303582

[217] D. Carpenter, M. Hovey, and A. Bak, "Resistivity of axoplasm. ii. internal resistivity of giant axons of squid and myxicola," *J. Gen. Physiol.*, vol. 66, no. 2, pp. 139–148, 08 1975. [Online]. Available: http://www.ncbi.nlm.nih.gov/pmc/articles/PMC2226202/

[218] S. Murakami and Y. Okada, "Invariance in current dipole moment density across brain structures and species: Physiological constraint for neuroimaging," *NeuroImage*, vol. 111, pp. 49–58, 2015. [Online]. Available: http://www.sciencedirect.com/science/article/pii/S1053811915000956

[219] D. R. Hochbaum, Y. Zhao, S. L. Farhi, N. Klapoetke, C. A. Werley, V. Kapoor, P. Zou, J. M. Kralj, D. Maclaurin, N. Smedemark-Margulies, J. L. Saulnier, G. L. Boulting, C. Straub, Y. K. Cho, M. Melkonian, G. K.-S. Wong, D. J. Harrison, V. N. Murthy, B. L. Sabatini, E. S.

Boyden, R. E. Campbell, and A. E. Cohen, "All-optical electrophysiology in mammalian neurons using engineered microbial rhodopsins," *Nat. Methods*, vol. 11, no. 8, pp. 825–833, 08 2014. [Online]. Available: http://www.nature.com/nmeth/journal/v11/n8/full/nmeth.3000.html

[220] I. Chandrasekar, J. E. Huettner, S. G. Turney, and P. C. Bridgman, "Myosin ii regulates activity dependent compensatory endocytosis at central synapses," *J. Neurosci.*, vol. 33, no. 41, pp. 16 131–16 145, 10 2013. [Online]. Available: http://www.ncbi.nlm.nih.gov/pmc/articles/PMC3792455/

[221] S. G. Turney, M. Ahmed, I. Chandrasekar, R. B. Wysolmerski, Z. M. Goeckeler, R. M. Rioux, G. M. Whitesides, and P. C. Bridgman, "Nerve growth factor stimulates axon outgrowth through negative regulation of growth cone actomyosin restraint of microtubule advance," *Mol. Biol. Cell*, vol. 26, no. 24, 2015. [Online]. Available: http://www.molbiolcell.org/content/early/2015/11/29/mbc.E15-09-0636.abstract

[222] W. L. Webb, "Aircraft navigation instruments," *Electrical Engineering*, vol. 70, no. 5, pp. 384–389, May 1951. [Online]. Available: https://doi.org/10.1109/EE.1951.6432396

[223] J. E. Lenz, "A review of magnetic sensors," *Proceedings of the IEEE*, vol. 78, no. 6, pp. 973–989, Jun 1990.

[224] J. Lenz and S. Edelstein, "Magnetic sensors and their applications," *IEEE Sensors Journal*, vol. 6, no. 3, pp. 631–649, June 2006. [Online]. Available: https://doi.org/10.1109/JSEN.2006.874493

[225] C. J. Cochrane, J. Blacksberg, M. A. Anders, and P. M. Lenahan, "Vectorized magnetometer for space applications using electrical readout of atomic scale defects in silicon carbide," *Scientific Reports*, vol. 6, p. 37077, 11 2016. [Online]. Available: http://dx.doi.org/10.1038/srep37077

[226] D. T. Germain-Jones, "Post-war developments in geophysical instrumentation for oil prospecting," *J. Sci. Instrum.*, vol. 34, no. 1, p. 1, 1957. [Online]. Available: http://stacks.iop.org/0950-7671/34/i=1/a=302

[227] A. Grosz, M. J. Haji-Sheikh, and S. C. Mukhopadhyay, *High Sensitivity Magnetometers*, ser. Smart Sensors, Measurement and Instrumentation. Springer International Publishing, 2016.

[228] T. H. Sander, J. Preusser, R. Mhaskar, J. Kitching, L. Trahms, and S. Knappe, "Magnetoencephalography with a chip-scale atomic magnetometer," *Biomed. Opt. Express*, vol. 3, no. 5, pp. 981–990, May 2012. [Online]. Available: http://www.osapublishing.org/boe/abstract.cfm?URI=boe-3-5-981

[229] T. Wang, Y. Zhou, C. Lei, J. Luo, S. Xie, and H. Pu, "Magnetic impedance biosensor: A review," *Biosensors and Bioelectronics*, vol. 90, pp. 418–435,

2017. [Online]. Available: http://www.sciencedirect.com/science/article/pii/S0956566316310478

[230] F. Camps, S. Harasse, and A. Monin, "Numerical calibration for 3-axis accelerometers and magnetometers," in *2009 IEEE International Conference on Electro/Information Technology*, June 2009, pp. 217–221. [Online]. Available: https://doi.org/10.1109/EIT.2009.5189614

[231] Y. X. Liu, X. S. Li, X. J. Zhang, and Y. B. Feng, "Novel calibration algorithm for a three-axis strapdown magnetometer," *Sensors*, vol. 14, no. 5, pp. 8485–8504, 2014. [Online]. Available: http://www.mdpi.com/1424-8220/14/5/8485

[232] T. C. Richards and C. E. Lucas, "A robust calibration and alignment procedure for collocated magnetometer and accelerometer sensors," Tech. Rep. 009, 6 2015. [Online]. Available: http://cradpdf.drdc-rddc.gc.ca/PDFS/unc188/p801728_A1b.pdf

[233] S.-Y. Lee, M. Niethammer, and J. Wrachtrup, "Vector magnetometry based on $S = \frac{3}{2}$ electronic spins," *Phys. Rev. B*, vol. 92, p. 115201, Sep 2015. [Online]. Available: https://link.aps.org/doi/10.1103/PhysRevB.92.115201

[234] M. Niethammer, M. Widmann, S.-Y. Lee, P. Stenberg, O. Kordina, T. Ohshima, N. T. Son, E. Janzén, and J. Wrachtrup, "Vector magnetometry using silicon vacancies in 4H-sic under ambient conditions," *Phys. Rev. Applied*, vol. 6, p. 034001, Sep 2016. [Online]. Available: https://link.aps.org/doi/10.1103/PhysRevApplied.6.034001

[235] A. Nowodzinski, M. Chipaux, L. Toraille, V. Jacques, J.-F. Roch, and T. Debuisschert, "Nitrogen-vacancy centers in diamond for current imaging at the redistributive layer level of integrated circuits," *Microelectronics Reliability*, vol. 55, no. 9, pp. 1549 – 1553, 2015. [Online]. Available: http://www.sciencedirect.com/science/article/pii/S0026271415001614

[236] P. Wang, Z. Yuan, P. Huang, X. Rong, M. Wang, X. Xu, C. Duan, C. Ju, F. Shi, and J. Du, "High-resolution vector microwave magnetometry based on solid-state spins in diamond," *Nat. Commun.*, vol. 6, p. 6631, 03 2015. [Online]. Available: http://dx.doi.org/10.1038/ncomms7631

[237] A. K. Dmitriev and A. K. Vershovskii, "Concept of a microscale vector magnetic field sensor based on nitrogen-vacancy centers in diamond," *J. Opt. Soc. Am. B*, vol. 33, no. 3, pp. B1–B4, Mar 2016. [Online]. Available: http://josab.osa.org/abstract.cfm?URI=josab-33-3-B1

[238] S. M. Blakley, I. V. Fedotov, L. V. Amitonova, E. E. Serebryannikov, H. Perez, S. Y. Kilin, and A. M. Zheltikov, "Fiber-optic vectorial magnetic-field gradiometry by a spatiotemporal differential optical detection of magnetic resonance in nitrogen–vacancy centers in diamond," *Opt.*

Lett., vol. 41, no. 9, pp. 2057–2060, May 2016. [Online]. Available: http://ol.osa.org/abstract.cfm?URI=ol-41-9-2057

[239] S. Kitazawa, Y. Matsuzaki, S. Saijo, K. Kakuyanagi, S. Saito, and J. Ishi-Hayase, "Vector-magnetic-field sensing via multifrequency control of nitrogen-vacancy centers in diamond," *Phys. Rev. A*, vol. 96, p. 042115, Oct 2017. [Online]. Available: https://link.aps.org/doi/10.1103/PhysRevA.96.042115

[240] C. Zhang, H. Yuan, N. Zhang, L. Xu, J. Zhang, B. Li, and J. Fang, "Vector magnetometer based on synchronous manipulation of nitrogen-vacancy centers in all crystal directions," *J. Phys. D: Appl. Phys.*, vol. 51, no. 15, p. 155102, 2018. [Online]. Available: http://stacks.iop.org/0022-3727/51/i=15/a=155102

[241] H. Clevenson, L. M. Pham, C. Teale, K. Johnson, D. Englund, and D. Braje, "Robust high-dynamic-range vector magnetometry with nitrogen-vacancy centers in diamond," *Applied Physics Letters*, vol. 112, no. 25, p. 252406, 2018. [Online]. Available: https://doi.org/10.1063/1.5034216

[242] L. P. McGuinness, Y. Yan, A. Stacey, D. A. Simpson, L. T. Hall, D. Maclaurin, S. Prawer, P. Mulvaney, J. Wrachtrup, F. Caruso, R. E. Scholten, and L. C. L. Hollenberg, "Quantum measurement and orientation tracking of fluorescent nanodiamonds inside living cells," *Nat. Nanotechnol.*, vol. 6, p. 358, 05 2011. [Online]. Available: http://dx.doi.org/10.1038/nnano.2011.64

[243] S. Felton, A. M. Edmonds, M. E. Newton, P. M. Martineau, D. Fisher, D. J. Twitchen, and J. M. Baker, "Hyperfine interaction in the ground state of the negatively charged nitrogen vacancy center in diamond," *Phys. Rev. B*, vol. 79, p. 075203, Feb 2009. [Online]. Available: https://link.aps.org/doi/10.1103/PhysRevB.79.075203

[244] H. A. R. El-Ella, S. Ahmadi, A. M. Wojciechowski, A. Huck, and U. L. Andersen, "Optimised frequency modulation for continuous-wave optical magnetic resonance sensing using nitrogen-vacancy ensembles," *Opt. Express*, vol. 25, no. 13, pp. 14 809–14 821, Jun 2017. [Online]. Available: http://www.opticsexpress.org/abstract.cfm?URI=oe-25-13-14809

[245] N. Bar-Gill, L. M. Pham, A. Jarmola, D. Budker, and R. L. Walsworth, "Solid-state electronic spin coherence time approaching one second," *Nat. Commun.*, vol. 4, p. 1743, 04 2013. [Online]. Available: http://dx.doi.org/10.1038/ncomms2771

[246] D. Gabor, "Theory of communication. part 1: The analysis of information," *J. I. El. Eng. - Part III: Radio and Communication Engineering*, vol. 93, pp. 429–441(12), November 1946. [Online]. Available: http://digital-library.theiet.org/content/journals/10.1049/ji-3-2.1946.0074

[247] A. Dandridge, A. Tveten, A. Kersey, and A. Yurek, "Multiplexing of interferometric sensors using phase carrier techniques," *J. Light. Technol.*,

vol. 5, no. 7, pp. 947–952, 1987. [Online]. Available: http://dx.doi.org/10.1109/JLT.1987.1075587

[248] D. A. Jackson, A. B. Lobo Ribeiro, L. Reekie, and J. L. Archambault, "Simple multiplexing scheme for a fiber-optic grating sensor network," *Opt. Lett.*, vol. 18, no. 14, pp. 1192–1194, Jul 1993. [Online]. Available: http://ol.osa.org/abstract.cfm?URI=ol-18-14-1192

[249] T. H. Oosterkamp, M. Poggio, C. L. Degen, H. J. Mamin, and D. Rugar, "Frequency domain multiplexing of force signals with application to magnetic resonance force microscopy," *Applied Physics Letters*, vol. 96, no. 8, p. 083107, 2010. [Online]. Available: https://doi.org/10.1063/1.3304788

[250] M. Bal, C. Deng, J.-L. Orgiazzi, F. R. Ong, and A. Lupascu, "Ultrasensitive magnetic field detection using a single artificial atom," *Nat. Commun.*, vol. 3, p. 1324, 12 2012. [Online]. Available: http://dx.doi.org/10.1038/ncomms2332

[251] M. P. Backlund, P. Kehayias, and R. L. Walsworth, "Diamond-based magnetic imaging with fourier optical processing," *Phys. Rev. Applied*, vol. 8, p. 054003, Nov 2017. [Online]. Available: https://link.aps.org/doi/10.1103/PhysRevApplied.8.054003

[252] C. A. Klein and G. F. Cardinale, "Young's modulus and poisson's ratio of cvd diamond," *Diam. Relat. Mater.*, vol. 2, no. 5, pp. 918 – 923, 1993. [Online]. Available: http://www.sciencedirect.com/science/article/pii/0925963593902506

[253] P. Ovartchaiyapong, K. W. Lee, B. A. Myers, and A. C. B. Jayich, "Dynamic strain-mediated coupling of a single diamond spin to a mechanical resonator," *Nat. Commun.*, vol. 5, p. 4429, 07 2014. [Online]. Available: http://dx.doi.org/10.1038/ncomms5429

[254] J. Teissier, A. Barfuss, P. Appel, E. Neu, and P. Maletinsky, "Strain coupling of a nitrogen-vacancy center spin to a diamond mechanical oscillator," *Phys. Rev. Lett.*, vol. 113, p. 020503, Jul 2014. [Online]. Available: https://link.aps.org/doi/10.1103/PhysRevLett.113.020503

[255] C. P. Slichter, *Principles of Magnetic Resonance*. Berlin, Heidelberg: Springer, 1990. [Online]. Available: http://link.springer.com/10.1007/978-3-662-09441-9

[256] J. Herrmann, M. A. Appleton, K. Sasaki, Y. Monnai, T. Teraji, K. M. Itoh, and E. Abe, "Polarization- and frequency-tunable microwave circuit for selective excitation of nitrogen-vacancy spins in diamond," *Applied Physics Letters*, vol. 109, no. 18, p. 183111, 2016. [Online]. Available: https://doi.org/10.1063/1.4967378

[257] R. Shelton and A. Adkins, "Noise bandwidth of common filters," *IEEE Transactions on Communication Technology*, vol. 18, no. 6, pp. 828–830,

December 1970. [Online]. Available: http://doi.org/10.1109/TCOM.1970.1090431

[258] S. Winder, *Analog and Digital Filter Design*, 2nd ed., ser. EDN Series for Design Engineers. Newnes, 2002.

[259] S.-Y. Lee, S. Paik, D. R. McCamey, and C. Boehme, "Modulation frequency dependence of continuous-wave optically/electrically detected magnetic resonance," *Phys. Rev. B*, vol. 86, p. 115204, Sep 2012. [Online]. Available: https://link.aps.org/doi/10.1103/PhysRevB.86.115204

[260] E. T. Jaynes, *Probability Theory: The Logic of Science*, 1st ed., G. L. Bretthorst, Ed. Cambridge University Press, 2003.

[261] J. S. Bendat and A. G. Piersol, *Random Data: Analysis and Measurement Procedures*, 4th ed., ser. Wiley Series in Probability and Statistics. Wiley, 2010.

[262] J. Goodman, *Statistical Optics*, 2nd ed., ser. Wiley Series in Pure and Applied Optics. Wiley, 2015.

[263] S. Eckel, A. O. Sushkov, and S. K. Lamoreaux, "Magnetic susceptibility and magnetization fluctuation measurements of mixed gadolinium-yttrium iron garnets," *Phys. Rev. B*, vol. 79, p. 014422, Jan 2009. [Online]. Available: https://link.aps.org/doi/10.1103/PhysRevB.79.014422

[264] T. W. Kornack, S. J. Smullin, S.-K. Lee, and M. V. Romalis, "A low-noise ferrite magnetic shield," *Appl. Phys. Lett.*, vol. 90, no. 22, p. 223501, 2007. [Online]. Available: https://doi.org/10.1063/1.2737357

[265] P. Elleaume, O. Chubar, and J. Chavanne, "Computing 3d magnetic fields from insertion devices," in *Proceedings of the 1997 Particle Accelerator Conference, Vancouver, BC, Canada*, vol. 3. IEEE, May 1997, pp. 3509–3511. [Online]. Available: https://doi.org/10.1109/PAC.1997.753258

[266] O. Chubar, P. Elleaume, and J. Chavanne, "A three-dimensional magnetostatics computer code for insertion devices," *J. Synchrotron Radiat.*, vol. 5, no. 3, pp. 481–484, May 1998. [Online]. Available: https://doi.org/10.1107/S0909049597013502

[267] E. van Oort, N. B. Manson, and M. Glasbeek, "Optically detected spin coherence of the diamond N-V centre in its triplet ground state," *J. Phys. C: Solid State Phys.*, vol. 21, no. 23, p. 4385, 1988. [Online]. Available: http://stacks.iop.org/0022-3719/21/i=23/a=020

[268] J. L. Walsh, "A closed set of normal orthogonal functions," *Am. J. Math.*, vol. 45, no. 1, pp. 5–24, 1923. [Online]. Available: http://www.jstor.org/stable/2387224

[269] R. Gold, "Optimal binary sequences for spread spectrum multiplexing (corresp.)," *IEEE Transactions on Information Theory*, vol. 13, no. 4, pp. 619–621, October 1967. [Online]. Available: https://doi.org/10.1109/TIT.1967.1054048

[270] K. G. Beauchamp, *Applications of Walsh and related functions: With an introduction to sequence theory*, ser. Microelectronics and Signal Processing. Academic Press, 1984.

[271] B. P. Lathi, *Modern analog and digital communication systems*, 3rd ed. USA: Oxford University Press, 1998.

[272] A. Cooper, E. Magesan, H. N. Yum, and P. Cappellaro, "Time-resolved magnetic sensing with electronic spins in diamond," *Nat. Commun.*, vol. 5, p. 3141, 01 2014. [Online]. Available: http://dx.doi.org/10.1038/ncomms4141

[273] E. H. Chen, O. Gaathon, M. E. Trusheim, and D. Englund, "Wide-field multispectral super-resolution imaging using spin-dependent fluorescence in nanodiamonds," *Nano Letters*, vol. 13, no. 5, pp. 2073–2077, 2013. [Online]. Available: https://doi.org/10.1021/nl400346k

[274] S. K. Sarkar, A. Bumb, X. Wu, K. A. Sochacki, P. Kellman, M. W. Brechbiel, and K. C. Neuman, "Wide-field in vivo background free imaging by selective magnetic modulation of nanodiamond fluorescence," *Biomed. Opt. Express*, vol. 5, no. 4, pp. 1190–1202, Apr 2014. [Online]. Available: http://www.osapublishing.org/boe/abstract.cfm?URI=boe-5-4-1190

[275] M. Chipaux, A. Tallaire, J. Achard, S. Pezzagna, J. Meijer, V. Jacques, J.-F. Roch, and T. Debuisschert, "Magnetic imaging with an ensemble of nitrogen-vacancy centers in diamond," *The European Physical Journal D*, vol. 69, no. 7, p. 166, Jul 2015. [Online]. Available: https://doi.org/10.1140/epjd/e2015-60080-1

[276] A. Jenkins, M. Pelliccione, G. Yu, X. Ma, X. Li, K. L. Wang, and A. C. Bleszynski Jayich, "Single spin sensing of domain wall structure and dynamics in a thin film skyrmion host," *ArXiv e-prints*, p. arXiv:1812.01764, Dec 2018. [Online]. Available: https://arxiv.org/abs/1812.01764

[277] S. Beer and P. Seitz, "Real-time tomographic imaging without x-rays: a smart pixel array with massively parallel signal processing for real-time optical coherence tomography performing close to the physical limits," in *Research in Microelectronics and Electronics, 2005 PhD*, vol. 2, July 2005, pp. 135–138. [Online]. Available: https://ieeexplore.ieee.org/document/1542955

[278] S. Beer, "Real-time photon-noise limited optical coherence tomography based on pixel-level analog signal processing," Ph.D. dissertation, Université de Neuchâtel, 2006.

[279] Heliotis AG, "Specifications for the heliSense^{TM} S3.1." [Online]. Available: https://www.heliotis.ch/html/pOCT3_specification.htm

[280] A. Dubois, Ed., *Handbook of Full-Field Optical Coherence Microscopy: Technology and Applications*, 1st ed. Pan Stanford, 2016. [Online]. Available: https://www.amazon.com/Handbook-Full-Field-Optical-Coherence-Microscopy/dp/9814669164

[281] S. Bourquin, R. P. Prasankumar, F. X. Kärtner, J. G. Fujimoto, T. Lasser, and R. P. Salathé, "High-speed femtosecond pump probe spectroscopy with a smart pixel detector array," *Opt. Lett.*, vol. 28, no. 17, pp. 1588–1590, Sep 2003. [Online]. Available: http://ol.osa.org/abstract.cfm?URI=ol-28-17-1588

[282] L. C. Sinclair, K. C. Cossel, T. Coffey, J. Ye, and E. A. Cornell, "Frequency comb velocity-modulation spectroscopy," *Phys. Rev. Lett.*, vol. 107, p. 093002, Aug 2011. [Online]. Available: https://link.aps.org/doi/10.1103/PhysRevLett.107.093002

[283] M. M. Balaji, P. Rangarajan, D. MacFarlane, A. Corliano, and M. P. Christensen, "Single-shot holography using scattering surfaces," in *Imaging and Applied Optics 2017 (3D, AIO, COSI, IS, MATH, pcAOP)*. Optical Society of America, 2017, p. CTu2B.1. [Online]. Available: http://www.osapublishing.org/abstract.cfm?URI=COSI-2017-CTu2B.1

[284] A. H. Meier and T. Roesgen, "Heterodyne doppler global velocimetry," *Experiments in Fluids*, vol. 47, no. 4, p. 665, Mar 2009. [Online]. Available: https://doi.org/10.1007/s00348-009-0647-0

[285] A. M. Wojciechowski, M. Karadas, A. Huck, C. Osterkamp, S. Jankuhn, J. Meijer, F. Jelezko, and U. L. Andersen, "Contributed review: Camera-limits for wide-field magnetic resonance imaging with a nitrogen-vacancy spin sensor," *Review of Scientific Instruments*, vol. 89, no. 3, p. 031501, 2018. [Online]. Available: https://doi.org/10.1063/1.5010282

[286] Heliotis AG, Personal communication, 2015.

[287] Nikon Instuments Inc., "Coverslip Correction | MicroscopyU." [Online]. Available: https://www.microscopyu.com/microscopy-basics/coverslip-correction

[288] Y. Aratyn-Schaus, F. S. Pasqualini, H. Yuan, M. L. McCain, G. J. Ye, S. P. Sheehy, P. H. Campbell, and K. K. Parker, "Coupling primary and stem cell–derived cardiomyocytes in an in vitro model of cardiac cell therapy," *J. Cell Biol.*, vol. 212, no. 4, pp. 389–397, 2016. [Online]. Available: http://jcb.rupress.org/content/212/4/389

[289] M. L. McCain, A. Agarwal, H. W. Nesmith, A. P. Nesmith, and K. K. Parker, "Micromolded gelatin hydrogels for extended culture of engineered cardiac tissues," *Biomaterials*, vol. 35, no. 21, pp. 5462 – 5471, 2014. [Online]. Available: http://www.sciencedirect.com/science/article/pii/S0142961214003123

[290] J. R. Holzer, L. E. Fong, V. Y. Sidorov, J. Wikswo, John P., and F. Baudenbacher, "High resolution magnetic images of planar wave fronts reveal bidomain properties of cardiac tissue," *Biophysical Journal*, vol. 87, no. 6, pp. 4326–4332, 2019/04/18 2004. [Online]. Available: https://doi.org/10.1529/biophysj.104.049163

[291] A. Irimia, K. R. Swinney, and J. P. Wikswo, "Partial independence of bioelectric and biomagnetic fields and its implications for encephalography and cardiography," *Phys. Rev. E*, vol. 79, p. 051908, May 2009. [Online]. Available: https://link.aps.org/doi/10.1103/PhysRevE.79.051908

[292] L. M. Pham, N. Bar-Gill, C. Belthangady, D. Le Sage, P. Cappellaro, M. D. Lukin, A. Yacoby, and R. L. Walsworth, "Enhanced solid-state multispin metrology using dynamical decoupling," *Phys. Rev. B*, vol. 86, p. 045214, Jul 2012. [Online]. Available: https://link.aps.org/doi/10.1103/PhysRevB.86.045214

[293] L. Cywiński, R. M. Lutchyn, C. P. Nave, and S. Das Sarma, "How to enhance dephasing time in superconducting qubits," *Phys. Rev. B*, vol. 77, p. 174509, May 2008. [Online]. Available: https://link.aps.org/doi/10.1103/PhysRevB.77.174509

[294] L. Childress, M. V. Gurudev Dutt, J. M. Taylor, A. S. Zibrov, F. Jelezko, J. Wrachtrup, P. R. Hemmer, and M. D. Lukin, "Coherent dynamics of coupled electron and nuclear spin qubits in diamond," *Science*, vol. 314, no. 5797, pp. 281–285, 2006. [Online]. Available: http://science.sciencemag.org/content/314/5797/281

[295] P. C. Maurer, J. R. Maze, P. L. Stanwix, L. Jiang, A. V. Gorshkov, A. A. Zibrov, B. Harke, J. S. Hodges, A. S. Zibrov, A. Yacoby, D. Twitchen, S. W. Hell, R. L. Walsworth, and M. D. Lukin, "Far-field optical imaging and manipulation of individual spins with nanoscale resolution," *Nat. Phys.*, vol. 6, pp. 912 –, 2010. [Online]. Available: https://doi.org/10.1038/nphys1774

[296] D. Farfurnik, A. Jarmola, L. M. Pham, Z. H. Wang, V. V. Dobrovitski, R. L. Walsworth, D. Budker, and N. Bar-Gill, "Optimizing a dynamical decoupling protocol for solid-state electronic spin ensembles in diamond," *Phys. Rev. B*, vol. 92, p. 060301, Aug 2015. [Online]. Available: https://link.aps.org/doi/10.1103/PhysRevB.92.060301

[297] G. H. Low, T. J. Yoder, and I. L. Chuang, "Optimal arbitrarily accurate composite pulse sequences," *Phys. Rev. A*, vol. 89, p. 022341, Feb 2014. [Online]. Available: https://link.aps.org/doi/10.1103/PhysRevA.89.022341

[298] X. Rong, J. Geng, F. Shi, Y. Liu, K. Xu, W. Ma, F. Kong, Z. Jiang, Y. Wu, and J. Du, "Experimental fault-tolerant universal quantum gates with solid-state spins under ambient conditions," *Nat. Commun.*, vol. 6, p. 8748, 11 2015. [Online]. Available: http://dx.doi.org/10.1038/ncomms9748

[299] M. Kim, H. J. Mamin, M. H. Sherwood, K. Ohno, D. D. Awschalom, and D. Rugar, "Decoherence of near-surface nitrogen-vacancy centers due to electric field noise," *Phys. Rev. Lett.*, vol. 115, p. 087602, Aug 2015. [Online]. Available: http://link.aps.org/doi/10.1103/PhysRevLett.115.087602

[300] H. S. Knowles, D. M. Kara, and M. Atatüre, "Observing bulk diamond spin coherence in high-purity nanodiamonds," *Nat. Mater.*, vol. 13, p. 21, 2013. [Online]. Available: https://doi.org/10.1038/nmat3805

[301] G. Davies, "Dynamic Jahn-Teller distortions at trigonal optical centres in diamond," *J. Phys. C: Solid State Phys.*, vol. 12, no. 13, pp. 2551–2566, 1979. [Online]. Available: http://stacks.iop.org/0022-3719/12/i=13/a=019

[302] ——, "The jahn-teller effect and vibronic coupling at deep levels in diamond," *Rep. Prog. Phys.*, vol. 44, no. 7, p. 787, 1981. [Online]. Available: http://stacks.iop.org/0034-4885/44/i=7/a=003

[303] C. A. J. Ammerlaan and E. A. Burgemeister, "Reorientation of Nitrogen in Type-Ib Diamond by Thermal Excitation and Tunneling," *Phys. Rev. Lett.*, vol. 47, no. 13, pp. 954–957, Sep 1981. [Online]. Available: http://link.aps.org/doi/10.1103/PhysRevLett.47.954

[304] C. Belthangady, N. Bar-Gill, L. M. Pham, K. Arai, D. Le Sage, P. Cappellaro, and R. L. Walsworth, "Dressed-state resonant coupling between bright and dark spins in diamond," *Phys. Rev. Lett.*, vol. 110, p. 157601, Apr 2013. [Online]. Available: http://link.aps.org/doi/10.1103/PhysRevLett.110.157601

[305] M. Drake, E. Scott, and J. A. Reimer, "Influence of magnetic field alignment and defect concentration on nitrogen-vacancy polarization in diamond," *New J. Phys.*, vol. 18, no. 1, p. 13011, 2016. [Online]. Available: http://dx.doi.org/10.1088/1367-2630/18/1/013011

[306] D. A. Hopper, R. R. Grote, S. M. Parks, and L. C. Bassett, "Amplified sensitivity of nitrogen-vacancy spins in nanodiamonds using all-optical charge readout," *ACS Nano*, vol. 12, no. 5, pp. 4678–4686, 05 2018. [Online]. Available: https://doi.org/10.1021/acsnano.8b01265

[307] H. Jayakumar, S. Dhomkar, J. Henshaw, and C. A. Meriles, "Spin readout via spin-to-charge conversion in bulk diamond nitrogen-vacancy ensembles," *Appl. Phys. Lett.*, vol. 113, no. 12, p. 122404, 2018. [Online]. Available: https://doi.org/10.1063/1.5040261

[308] N. Aslam, G. Waldherr, P. Neumann, F. Jelezko, and J. Wrachtrup, "Photo-induced ionization dynamics of the nitrogen vacancy defect in diamond investigated by single-shot charge state detection," *New J. Phys.*, vol. 15, no. 1, p. 013064, 2013. [Online]. Available: http://stacks.iop.org/1367-2630/15/i=1/a=013064

[309] G. Waldherr, J. Beck, M. Steiner, P. Neumann, A. Gali, T. Frauenheim, F. Jelezko, and J. Wrachtrup, "Dark states of single nitrogen-vacancy centers in diamond unraveled by single shot NMR," *Phys. Rev. Lett.*, vol. 106, p. 157601, Apr 2011. [Online]. Available: http://link.aps.org/doi/10.1103/PhysRevLett.106.157601

[310] K. Beha, A. Batalov, N. B. Manson, R. Bratschitsch, and A. Leitenstorfer, "Optimum photoluminescence excitation and recharging cycle of single nitrogen-vacancy centers in ultrapure diamond," *Phys. Rev. Lett.*, vol. 109, p. 097404, Aug 2012. [Online]. Available: https://link.aps.org/doi/10.1103/PhysRevLett.109.097404

[311] L. Hacquebard and L. Childress, "Charge-state dynamics during excitation and depletion of the nitrogen-vacancy center in diamond," *Phys. Rev. A*, vol. 97, p. 063408, Jun 2018. [Online]. Available: https://link.aps.org/doi/10.1103/PhysRevA.97.063408

[312] N. B. Manson, M. Hedges, M. S. J. Barson, R. Ahlefeldt, M. W. Doherty, H. Abe, T. Ohshima, and M. J. Sellars, "$NV^- - N^+$ pair centre in 1b diamond," *New J. Phys.*, vol. 20, no. 11, p. 113037, 2018. [Online]. Available: http://dx.doi.org/10.1088/1367-2630/aaec58

[313] D. Bluvstein, Z. Zhang, and A. C. B. Jayich, "Identifying and mitigating charge instabilities in shallow diamond nitrogen-vacancy centers," *Phys. Rev. Lett.*, vol. 122, p. 076101, Feb 2019. [Online]. Available: https://link.aps.org/doi/10.1103/PhysRevLett.122.076101

[314] E. Bourgeois, A. Jarmola, P. Siyushev, M. Gulka, J. Hruby, F. Jelezko, D. Budker, and M. Nesladek, "Photoelectric detection of electron spin resonance of nitrogen-vacancy centres in diamond," *Nat. Commun.*, vol. 6, p. 8577, 10 2015. [Online]. Available: https://www.nature.com/articles/ncomms9577

[315] M. Gulka, E. Bourgeois, J. Hruby, P. Siyushev, G. Wachter, F. Aumayr, P. R. Hemmer, A. Gali, F. Jelezko, M. Trupke, and M. Nesladek, "Pulsed photoelectric coherent manipulation and detection of $N-V$ center spins in diamond," *Phys. Rev. Applied*, vol. 7, p. 044032, Apr 2017. [Online]. Available: https://link.aps.org/doi/10.1103/PhysRevApplied.7.044032

[316] E. Bourgeois, E. Londero, K. Buczak, J. Hruby, M. Gulka, Y. Balasubramaniam, G. Wachter, J. Stursa, K. Dobes, F. Aumayr, M. Trupke, A. Gali, and M. Nesladek, "Enhanced photoelectric detection of NV magnetic resonances in diamond under dual-beam excitation," *Phys. Rev. B*, vol. 95, p. 041402, Jan 2017. [Online]. Available: http://link.aps.org/doi/10.1103/PhysRevB.95.041402

[317] F. M. Hrubesch, G. Braunbeck, M. Stutzmann, F. Reinhard, and M. S. Brandt, "Efficient electrical spin readout of NV^- centers in diamond,"

Phys. Rev. Lett., vol. 118, p. 037601, Jan 2017. [Online]. Available: http://link.aps.org/doi/10.1103/PhysRevLett.118.037601

[318] E. Londero, E. Bourgeois, M. Nesladek, and A. Gali, "Identification of nickel-vacancy defects by combining experimental and ab initio simulated photocurrent spectra," *Phys. Rev. B*, vol. 97, p. 241202, Jun 2018. [Online]. Available: https://link.aps.org/doi/10.1103/PhysRevB.97.241202

[319] P. Deák, B. Aradi, M. Kaviani, T. Frauenheim, and A. Gali, "Formation of NV centers in diamond: A theoretical study based on calculated transitions and migration of nitrogen and vacancy related defects," *Phys. Rev. B*, vol. 89, p. 075203, Feb 2014. [Online]. Available: http://link.aps.org/doi/10.1103/PhysRevB.89.075203

[320] F. J. Heremans, G. D. Fuchs, C. F. Wang, R. Hanson, and D. D. Awschalom, "Generation and transport of photoexcited electrons in single-crystal diamond," *Appl. Phys. Lett.*, vol. 94, no. 15, p. 152102, 2009. [Online]. Available: http://dx.doi.org/10.1063/1.3120225

[321] S. Kolkowitz, A. Safira, A. A. High, R. C. Devlin, S. Choi, Q. P. Unterreithmeier, D. Patterson, A. S. Zibrov, V. E. Manucharyan, H. Park, and M. D. Lukin, "Probing johnson noise and ballistic transport in normal metals with a single-spin qubit," *Science*, vol. 347, no. 6226, pp. 1129–1132, 2015. [Online]. Available: http://science.sciencemag.org/content/347/6226/1129

[322] A. Rose, *Concepts in photoconductivity and allied problems*. Interscience Publishers, 1963. [Online]. Available: https://books.google.com/books?id=rzFRAAAAMAAJ

[323] R. Bube, *Photoconductivity of solids*. Wiley, 1960. [Online]. Available: https://books.google.com/books?id=dZg8AAAAIAAJ

[324] H. Morishita, S. Kobayashi, M. Fujiwara Hiromitsu Kato Toshiharu Makino Satoshi Yamasaki, and N. Mizuochi, "Room Temperature Electrically Detected Nuclear Spin Coherence of NV centers in Diamond," *ArXiv e-prints*, Mar. 2018. [Online]. Available: https://arxiv.org/abs/1803.01161

[325] P. C. Maurer, G. Kucsko, C. Latta, L. Jiang, N. Y. Yao, S. D. Bennett, F. Pastawski, D. Hunger, N. Chisholm, M. Markham, D. J. Twitchen, J. I. Cirac, and M. D. Lukin, "Room-temperature quantum bit memory exceeding one second," *Science*, vol. 336, no. 6086, pp. 1283–1286, 2012. [Online]. Available: http://science.sciencemag.org/content/336/6086/1283

[326] M. Steiner, P. Neumann, J. Beck, F. Jelezko, and J. Wrachtrup, "Universal enhancement of the optical readout fidelity of single electron spins at nitrogen-vacancy centers in diamond," *Phys. Rev. B*, vol. 81, p. 035205, Jan 2010. [Online]. Available: http://link.aps.org/doi/10.1103/PhysRevB.81.035205

[327] V. Jacques, P. Neumann, J. Beck, M. Markham, D. Twitchen, J. Meijer, F. Kaiser, G. Balasubramanian, F. Jelezko, and J. Wrachtrup, "Dynamic polarization of single nuclear spins by optical pumping of nitrogen-vacancy color centers in diamond at room temperature," *Phys. Rev. Lett.*, vol. 102, p. 057403, Feb 2009. [Online]. Available: http://link.aps.org/doi/10.1103/PhysRevLett.102.057403

[328] T. K. Yeung, D. L. Sage, L. M. Pham, P. L. Stanwix, and R. L. Walsworth, "Anti-reflection coating for nitrogen-vacancy optical measurements in diamond," *Appl. Phys. Lett.*, vol. 100, no. 25, p. 251111, 2012. [Online]. Available: http://dx.doi.org/10.1063/1.4730401

[329] J. P. Hadden, J. P. Harrison, A. C. Stanley-Clarke, L. Marseglia, Y. L. D. Ho, B. R. Patton, J. L. O'Brien, and J. G. Rarity, "Strongly enhanced photon collection from diamond defect centers under microfabricated integrated solid immersion lenses," *Appl. Phys. Lett.*, vol. 97, no. 24, p. 241901, 2019/01/26 2010. [Online]. Available: https://doi.org/10.1063/1.3519847

[330] T. M. Babinec, H. J. M., M. Khan, Y. Zhang, J. R. Maze, P. R. Hemmer, and M. Loncar, "A diamond nanowire single-photon source," *Nat. Nanotechnol.*, vol. 5, no. 3, pp. 195–199, Mar 2010. [Online]. Available: http://dx.doi.org/10.1038/nnano.2010.6

[331] L. Marseglia, J. P. Hadden, A. C. Stanley-Clarke, J. P. Harrison, B. Patton, Y. L. D. Ho, B. Naydenov, F. Jelezko, J. Meijer, P. R. Dolan, J. M. Smith, J. G. Rarity, and J. L. O'Brien, "Nanofabricated solid immersion lenses registered to single emitters in diamond," *Appl. Phys. Lett.*, vol. 98, no. 13, p. 133107, 2011. [Online]. Available: https://doi.org/10.1063/1.3573870

[332] J. T. Choy, B. J. M. Hausmann, T. M. Babinec, I. Bulu, M. Khan, P. Maletinsky, A. Yacoby, and M. Loncar, "Enhanced single-photon emission from a diamond-silver aperture," *Nat. Photonics*, vol. 5, no. 12, pp. 738–743, 12 2011. [Online]. Available: http://dx.doi.org/10.1038/nphoton.2011.249

[333] T. Schröder, F. Gädeke, M. J. Banholzer, and O. Benson, "Ultrabright and efficient single-photon generation based on nitrogen-vacancy centres in nanodiamonds on a solid immersion lens," *New J. Phys.*, vol. 13, no. 5, p. 055017, 2011. [Online]. Available: http://stacks.iop.org/1367-2630/13/i=5/a=055017

[334] J. T. Choy, I. Bulu, B. J. M. Hausmann, E. Janitz, I.-C. Huang, and M. Loncar, "Spontaneous emission and collection efficiency enhancement of single emitters in diamond via plasmonic cavities and gratings," *Appl. Phys. Lett.*, vol. 103, no. 16, p. 161101, 2013. [Online]. Available: http://dx.doi.org/10.1063/1.4817397

[335] D. Riedel, D. Rohner, M. Ganzhorn, T. Kaldewey, P. Appel, E. Neu, R. J. Warburton, and P. Maletinsky, "Low-loss broadband antenna for

efficient photon collection from a coherent spin in diamond," *Phys. Rev. Applied*, vol. 2, p. 064011, Dec 2014. [Online]. Available: http://link.aps.org/doi/10.1103/PhysRevApplied.2.064011

[336] E. Neu, P. Appel, M. Ganzhorn, J. Miguel-Sánchez, M. Lesik, V. Mille, V. Jacques, A. Tallaire, J. Achard, and P. Maletinsky, "Photonic nano-structures on (111)-oriented diamond," *Appl. Phys. Lett.*, vol. 104, no. 15, p. 153108, 2014. [Online]. Available: https://aip.scitation.org/doi/10.1063/1.4871580

[337] S. A. Momenzadeh, R. J. Stöhr, F. F. de Oliveira, A. Brunner, A. Denisenko, S. Yang, F. Reinhard, and J. Wrachtrup, "Nanoengineered diamond waveguide as a robust bright platform for nanomagnetometry using shallow nitrogen vacancy centers," *Nano Lett.*, vol. 15, no. 1, pp. 165–169, 2015. [Online]. Available: http://dx.doi.org/10.1021/nl503326t

[338] L. Li, E. H. Chen, J. Zheng, S. L. Mouradian, F. Dolde, T. Schröder, S. Karaveli, M. L. Markham, D. J. Twitchen, and D. Englund, "Efficient photon collection from a nitrogen vacancy center in a circular bullseye grating," *Nano Lett.*, vol. 15, no. 3, pp. 1493–1497, 2015. [Online]. Available: http://dx.doi.org/10.1021/nl503451j

[339] T. Häberle, T. Oeckinghaus, D. Schmid-Lorch, M. Pfender, F. F. de Oliveira, S. A. Momenzadeh, A. Finkler, and J. Wrachtrup, "Nuclear quantum-assisted magnetometer," *Rev. Sci. Instrum.*, vol. 88, no. 1, p. 013702, 2019/01/26 2017. [Online]. Available: https://doi.org/10.1063/1.4973449

[340] R. U. A. Khan, B. L. Cann, P. M. Martineau, J. Samartseva, J. J. P. Freeth, S. J. Sibley, C. B. Hartland, M. E. Newton, H. K. Dhillon, and D. J. Twitchen, "Colour-causing defects and their related optoelectronic transitions in single crystal cvd diamond," *J. Phys.: Condens. Matter*, vol. 25, no. 27, p. 275801, 2013. [Online]. Available: http://stacks.iop.org/0953-8984/25/i=27/a=275801

[341] F. D. Weerdt and A. Collins, "Determination of the c defect concentration in hpht annealed type iaa diamonds from uv-vis absorption spectra," *Diam. Relat. Mater.*, vol. 17, no. 2, pp. 171–173, 2008. [Online]. Available: http://www.sciencedirect.com/science/article/pii/S0925963507005122

[342] E. Fraczek, V. G. Savitski, M. Dale, B. G. Breeze, P. Diggle, M. Markham, A. Bennett, H. Dhillon, M. E. Newton, and A. J. Kemp, "Laser spectroscopy of NV- and NV0 colour centres in synthetic diamond," *Opt. Mater. Express*, vol. 7, no. 7, pp. 2571–2585, Jul 2017. [Online]. Available: http://www.osapublishing.org/ome/abstract.cfm?URI=ome-7-7-2571

[343] Z. Ma, S. Zhang, Y. Fu, H. Yuan, Y. Shi, J. Gao, L. Qin, J. Tang, J. Liu, and Y. Li, "Magnetometry for precision measurement using frequency-modulation microwave combined efficient photon-collection technique on an ensemble of nitrogen-vacancy centers in diamond," *Opt.*

Express, vol. 26, no. 1, pp. 382–390, Jan 2018. [Online]. Available: http://www.opticsexpress.org/abstract.cfm?URI=oe-26-1-382

[344] B. P. Boesch, G. S. Bruce, J. D. Cammerata, D. N. Coar, L. N. Egan, B. N. Fisk, W. Lew, A. Manickam, S. M. Sekelsky, J. B. Stetson, P. G. Kaup, J. L. Miller, J. C. Russo, and E. S. Stockman, "DNV magnetic field detector," Patent 118 791, 12 21, 2016, wO Patent 2016/118791 Al. [Online]. Available: http://www.freshpatents.com/-dt20160728ptan20160216341.php

[345] A. Wickenbrock, H. Zheng, L. Bougas, N. Leefer, S. Afach, A. Jarmola, V. M. Acosta, and D. Budker, "Microwave-free magnetometry with nitrogen-vacancy centers in diamond," *Appl. Phys. Lett.*, vol. 109, no. 5, p. 053505, 2016. [Online]. Available: https://aip.scitation.org/doi/10.1063/1.4960171

[346] Y. Dumeige, M. Chipaux, V. Jacques, F. Treussart, J.-F. Roch, T. Debuisschert, V. M. Acosta, A. Jarmola, K. Jensen, P. Kehayias, and D. Budker, "Magnetometry with nitrogen-vacancy ensembles in diamond based on infrared absorption in a doubly resonant optical cavity," *Phys. Rev. B*, vol. 87, p. 155202, Apr 2013. [Online]. Available: https://link.aps.org/doi/10.1103/PhysRevB.87.155202

[347] V. M. Acosta, "Optical magnetometry with nitrogen-vacancy centers in diamond," Ph.D. dissertation, University of California Berkeley, May 2011. [Online]. Available: http://digitalassets.lib.berkeley.edu/etd/ucb/text/Acosta_berkeley_0028E_11215.pdf

[348] V. M. Acosta, E. Bauch, A. Jarmola, L. J. Zipp, M. P. Ledbetter, and D. Budker, "Broadband magnetometry by infrared-absorption detection of nitrogen-vacancy ensembles in diamond," *Appl. Phys. Lett.*, vol. 97, no. 17, p. 174104, Oct. 2010. [Online]. Available: https://doi.org/10.1063/1.3507884

[349] P. Kehayias, M. W. Doherty, D. English, R. Fischer, A. Jarmola, K. Jensen, N. Leefer, P. Hemmer, N. B. Manson, and D. Budker, "Infrared absorption band and vibronic structure of the nitrogen-vacancy center in diamond," *Phys. Rev. B*, vol. 88, p. 165202, Oct 2013. [Online]. Available: https://link.aps.org/doi/10.1103/PhysRevB.88.165202

[350] E. Bauch, "Nitrogen-vacancy defects in diamond for sub-millimeter magnetometry," Master's thesis, Technische Universität Berlin and University of California Berkeley, June 2010.

[351] R. Walsworth, "Absorption-based detection of spin impurities in solid-state spin systems," Patent, May, 2017, u.S. Patent 9,658,301 B2. [Online]. Available: https://www.google.com/patents/US9658301

[352] D. Le Sage and K. Arai, Personal communication, 2011.

[353] S. Ahmadi, H. A. R. El-Ella, J. O. B. Hansen, A. Huck, and U. L. Andersen, "Pump-enhanced continuous-wave magnetometry using nitrogen-vacancy ensembles," *Phys. Rev. Applied*, vol. 8, p. 034001, Sep 2017. [Online]. Available: https://link.aps.org/doi/10.1103/PhysRevApplied.8.034001

[354] S. Ahmadi, H. A. R. El-Ella, A. M. Wojciechowski, T. Gehring, J. O. B. Hansen, A. Huck, and U. L. Andersen, "Nitrogen-vacancy ensemble magnetometry based on pump absorption," *Phys. Rev. B*, vol. 97, p. 024105, Jan 2018. [Online]. Available: https://link.aps.org/doi/10.1103/PhysRevB.97.024105

[355] ——, "Cavity-enhanced nitrogen-vacancy ensemble magnetometry," in *Conference on Lasers and Electro-Optics*. Optical Society of America, 2018, p. JF3B.2. [Online]. Available: http://www.osapublishing.org/abstract.cfm?URI=CLEO_AT-2018-JF3B.2

[356] J. Jeske, J. H. Cole, and A. D. Greentree, "Laser threshold magnetometry," *New J. Phys.*, vol. 18, no. 1, p. 013015, 2016. [Online]. Available: http://stacks.iop.org/1367-2630/18/i=1/a=013015

[357] J. Jeske, D. W. M. Lau, X. Vidal, L. P. McGuinness, P. Reineck, B. C. Johnson, M. W. Doherty, J. C. McCallum, S. Onoda, F. Jelezko, T. Ohshima, T. Volz, J. H. Cole, B. C. Gibson, and A. D. Greentree, "Stimulated emission from nitrogen-vacancy centres in diamond," *Nat. Commun.*, vol. 8, p. 14000, Jan 2017. [Online]. Available: http://dx.doi.org/10.1038/ncomms14000

[358] V. G. Savitski, "Optical gain in NV-colour centres for highly-sensitive magnetometry: a theoretical study," *J. Phys. D: Appl. Phys.*, vol. 50, no. 47, p. 475602, 2017. [Online]. Available: http://stacks.iop.org/0022-3727/50/i=47/a=475602

[359] J. Dodson, J. R Brandon, H. Dhillon, I. Friel, S. L Geoghegan, T. Mollart, P. Santini, G. Scarsbrook, D. Twitchen, A. J Whitehead, J. J Wilman, and H. de Wit, "Single crystal and polycrystalline CVD diamond for demanding optical applications," *Proc. of SPIE*, vol. 8016, pp. 80 160L–1, 05 2011. [Online]. Available: https://doi.org/10.1117/12.885188

[360] V. DeGiorgio and M. O. Scully, "Analogy between the laser threshold region and a second-order phase transition," *Phys. Rev. A*, vol. 2, pp. 1170–1177, Oct 1970. [Online]. Available: https://link.aps.org/doi/10.1103/PhysRevA.2.1170

[361] T.-S. Lim, J.-L. Chern, and K. Otsuka, "Relative intensity fluctuations of single-mode class b lasers," *Opt. Lett.*, vol. 27, no. 12, pp. 1037–1039, Jun 2002. [Online]. Available: http://ol.osa.org/abstract.cfm?URI=ol-27-12-1037

[362] C. D. Aiello, M. Hirose, and P. Cappellaro, "Composite-pulse magnetometry with a solid-state quantum sensor," *Nat. Commun.*, vol. 4, p. 1419, 01 2013. [Online]. Available: https://doi.org/10.1038/ncomms2375

[363] V. V. Mkhitaryan and V. V. Dobrovitski, "Decay of the rotary echoes for the spin of a nitrogen-vacancy center in diamond," *Phys. Rev. B*, vol. 89, p. 224402, Jun 2014. [Online]. Available: https://link.aps.org/doi/10.1103/PhysRevB.89.224402

[364] V. V. Mkhitaryan, F. Jelezko, and V. V. Dobrovitski, "Highly selective detection of individual nuclear spins with rotary echo on an electron spin probe," *Sci. Rep.*, vol. 5, p. 15402, 10 2015. [Online]. Available: https://doi.org/10.1038/srep15402

[365] M. V. Berry, "Quantal phase factors accompanying adiabatic changes," *Proc. R. Soc. London, Ser. A*, vol. 392, no. 1802, pp. 45–57, 1984. [Online]. Available: https://royalsocietypublishing.org/doi/abs/10.1098/rspa.1984.0023

[366] D. Maclaurin, M. W. Doherty, L. C. L. Hollenberg, and A. M. Martin, "Measurable quantum geometric phase from a rotating single spin," *Phys. Rev. Lett.*, vol. 108, p. 240403, Jun 2012. [Online]. Available: https://link.aps.org/doi/10.1103/PhysRevLett.108.240403

[367] C. Zu, W. B. Wang, L. He, W. G. Zhang, C. Y. Dai, F. Wang, and L. M. Duan, "Experimental realization of universal geometric quantum gates with solid-state spins," *Nature*, vol. 514, p. 72, 10 2014. [Online]. Available: https://doi.org/10.1038/nature13729

[368] S. Arroyo-Camejo, A. Lazariev, S. W. Hell, and G. Balasubramanian, "Room temperature high-fidelity holonomic single-qubit gate on a solid-state spin," *Nat. Commun.*, vol. 5, p. 4870, 09 2014. [Online]. Available: https://doi.org/10.1038/ncomms5870

[369] C. G. Yale, F. J. Heremans, B. B. Zhou, A. Auer, G. Burkard, and D. D. Awschalom, "Optical manipulation of the berry phase in a solid-state spin qubit," *Nat. Photonics*, vol. 10, p. 184, 02 2016. [Online]. Available: https://doi.org/10.1038/nphoton.2015.278

[370] B. B. Zhou, P. C. Jerger, V. O. Shkolnikov, F. J. Heremans, G. Burkard, and D. D. Awschalom, "Holonomic quantum control by coherent optical excitation in diamond," *Phys. Rev. Lett.*, vol. 119, p. 140503, Oct 2017. [Online]. Available: https://link.aps.org/doi/10.1103/PhysRevLett.119.140503

[371] K. Arai, J. Lee, C. Belthangady, D. R. Glenn, H. Zhang, and R. L. Walsworth, "Geometric phase magnetometry using a solid-state spin," *Nat. Commun.*, vol. 9, no. 1, p. 4996, 2018. [Online]. Available: https://doi.org/10.1038/s41467-018-07489-z

[372] Y.-X. Liu, A. Ajoy, and P. Cappellaro, "Nanoscale vector dc magnetometry via ancilla-assisted frequency up-conversion," *Phys. Rev. Lett.*, vol. 122, p. 100501, Mar 2019. [Online]. Available: https://link.aps.org/doi/10.1103/PhysRevLett.122.100501

[373] K. Ohno, F. Joseph Heremans, L. C. Bassett, B. A. Myers, D. M. Toyli, A. C. Bleszynski Jayich, C. J. Palmstrøm, and D. D. Awschalom, "Engineering shallow spins in diamond with nitrogen delta-doping," *Appl. Phys. Lett.*, vol. 101, no. 8, p. 082413, 2012. [Online]. Available: https://doi.org/10.1063/1.4748280

[374] C. Osterkamp, J. Lang, J. Scharpf, C. Müller, L. P. McGuinness, T. Diemant, R. J. Behm, B. Naydenov, and F. Jelezko, "Stabilizing shallow color centers in diamond created by nitrogen delta-doping using sf6 plasma treatment," *Appl. Phys. Lett.*, vol. 106, no. 11, p. 113109, 2015. [Online]. Available: https://doi.org/10.1063/1.4915305

[375] M. Pfender, N. Aslam, P. Simon, D. Antonov, G. Thiering, S. Burk, F. Fávaro de Oliveira, A. Denisenko, H. Fedder, J. Meijer, J. A. Garrido, A. Gali, T. Teraji, J. Isoya, M. W. Doherty, A. Alkauskas, A. Gallo, A. Grüneis, P. Neumann, and J. Wrachtrup, "Protecting a diamond quantum memory by charge state control," *Nano Lett.*, vol. 17, no. 10, pp. 5931–5937, 10 2017. [Online]. Available: https://doi.org/10.1021/acs.nanolett.7b01796

[376] M. V. Hauf, P. Simon, N. Aslam, M. Pfender, P. Neumann, S. Pezzagna, J. Meijer, J. Wrachtrup, M. Stutzmann, F. Reinhard, and J. Garrido, "Addressing single nitrogen-vacancy centers in diamond with transparent in-plane gate structures," *Nano Lett.*, vol. 14, no. 5, pp. 2359–2364, 05 2014. [Online]. Available: https://pubs.acs.org/doi/10.1021/nl4047619

[377] K. Iakoubovskii, G. J. Adriaenssens, and M. Nesladek, "Photochromism of vacancy-related centres in diamond," *J. Phys.: Condens. Matter*, vol. 12, no. 2, p. 189, 2000. [Online]. Available: http://stacks.iop.org/0953-8984/12/i=2/a=308

[378] Y. Mita, "Change of absorption spectra in type-i b diamond with heavy neutron irradiation," *Phys. Rev. B*, vol. 53, pp. 11 360–11 364, May 1996. [Online]. Available: http://link.aps.org/doi/10.1103/PhysRevB.53.11360

[379] K. Groot-Berning, N. Raatz, I. Dobrinets, M. Lesik, P. Spinicelli, A. Tallaire, J. Achard, V. Jacques, J.-F. Roch, A. M. Zaitsev, J. Meijer, and S. Pezzagna, "Passive charge state control of nitrogen-vacancy centres in diamond using phosphorous and boron doping," *Phys. Status Solidi A*, vol. 211, no. 10, pp. 2268–2273, 2014. [Online]. Available: http://dx.doi.org/10.1002/pssa.201431308

[380] A. T. Collins, "The fermi level in diamond," *J. Phys.: Condens. Matter*, vol. 14, no. 14, p. 3743, 2002. [Online]. Available: http://stacks.iop.org/0953-8984/14/i=14/a=307

[381] Y. Doi, T. Fukui, H. Kato, T. Makino, S. Yamasaki, T. Tashima, H. Morishita, S. Miwa, F. Jelezko, Y. Suzuki, and N. Mizuochi, "Pure negatively charged state of the NV center in n-type diamond," *Phys. Rev. B*, vol. 93, p. 081203, Feb 2016. [Online]. Available: http://link.aps.org/doi/10.1103/PhysRevB.93.081203

[382] N. B. Manson and J. P. Harrison, "Photoionization of the nitrogen-vacancy center in diamond," *Diam. Relat. Mater.*, vol. 14, pp. 1705–1710, 10 2005. [Online]. Available: https://www.sciencedirect.com/science/article/pii/S0925963505002402

[383] P. Ji and M. V. G. Dutt, "Charge state dynamics of the nitrogen vacancy center in diamond under 1064-nm laser excitation," *Phys. Rev. B*, vol. 94, p. 024101, Jul 2016. [Online]. Available: http://link.aps.org/doi/10.1103/PhysRevB.94.024101

[384] B. Grotz, M. V. Hauf, M. Dankerl, B. Naydenov, S. Pezzagna, J. Meijer, F. Jelezko, J. Wrachtrup, M. Stutzmann, F. Reinhard, and J. A. Garrido, "Charge state manipulation of qubits in diamond," *Nat. Commun.*, vol. 3, p. 729, 03 2012. [Online]. Available: http://dx.doi.org/10.1038/ncomms1729

[385] H. Kato, M. Wolfer, C. Schreyvogel, M. Kunzer, W. Müller-Sebert, H. Obloh, S. Yamasaki, and C. Nebel, "Tunable light emission from nitrogen-vacancy centers in single crystal diamond pin diodes," *Appl. Phys. Lett.*, vol. 102, no. 15, p. 151101, 2013. [Online]. Available: http://dx.doi.org/10.1063/1.4801871

[386] C. Schreyvogel, M. Wolfer, H. Kato, M. Schreck, and C. E. Nebel, "Tuned NV emission by in-plane al-schottky junctions on hydrogen terminated diamond," *Sci. Rep.*, vol. 4, p. 3634, 01 2014. [Online]. Available: http://dx.doi.org/10.1038/srep03634

[387] Y. Doi, T. Makino, H. Kato, D. Takeuchi, M. Ogura, H. Okushi, H. Morishita, T. Tashima, S. Miwa, S. Yamasaki, P. Neumann, J. Wrachtrup, Y. Suzuki, and N. Mizuochi, "Deterministic electrical charge-state initialization of single nitrogen-vacancy center in diamond," *Phys. Rev. X*, vol. 4, p. 011057, Mar 2014. [Online]. Available: http://link.aps.org/doi/10.1103/PhysRevX.4.011057

[388] L. Rondin, G. Dantelle, A. Slablab, F. Grosshans, F. Treussart, P. Bergonzo, S. Perruchas, T. Gacoin, M. Chaigneau, H.-C. Chang, V. Jacques, and J.-F. Roch, "Surface-induced charge state conversion of nitrogen-vacancy defects in nanodiamonds," *Phys. Rev. B*, vol. 82, p. 115449, Sep 2010. [Online]. Available: http://link.aps.org/doi/10.1103/PhysRevB.82.115449

[389] K.-M. C. Fu, C. Santori, P. E. Barclay, and R. G. Beausoleil, "Conversion of neutral nitrogen-vacancy centers to negatively charged nitrogen-vacancy centers through selective oxidation," *Appl. Phys. Lett.*, vol. 96, no. 12, p. 121907, 2010. [Online]. Available: http://dx.doi.org/10.1063/1.3364135

[390] M. V. Hauf, B. Grotz, B. Naydenov, M. Dankerl, S. Pezzagna, J. Meijer, F. Jelezko, J. Wrachtrup, M. Stutzmann, F. Reinhard, and J. A. Garrido, "Chemical control of the charge state of nitrogen-vacancy centers in diamond," *Phys. Rev. B*, vol. 83, p. 081304, Feb 2011. [Online]. Available: http://link.aps.org/doi/10.1103/PhysRevB.83.081304

[391] S. Cui and E. L. Hu, "Increased negatively charged nitrogen-vacancy centers in fluorinated diamond," *Appl. Phys. Lett.*, vol. 103, no. 5, p. 051603, 2013. [Online]. Available: http://dx.doi.org/10.1063/1.4817651

[392] Y. Chu, N. de Leon, B. Shields, B. Hausmann, R. Evans, E. Togan, M. J. Burek, M. Markham, A. Stacey, A. Zibrov, A. Yacoby, D. Twitchen, M. Loncar, H. Park, P. Maletinsky, and M. Lukin, "Coherent optical transitions in implanted nitrogen vacancy centers," *Nano Lett.*, vol. 14, no. 4, pp. 1982–1986, 2014. [Online]. Available: http://dx.doi.org/10.1021/nl404836p

[393] H. Yamano, S. Kawai, K. Kato, T. Kageura, M. Inaba, T. Okada, I. Higashimata, M. Haruyama, T. Tanii, K. Yamada, S. Onoda, W. Kada, O. Hanaizumi, T. Teraji, J. Isoya, and H. Kawarada, "Charge state stabilization of shallow nitrogen vacancy centers in diamond by oxygen surface modification," *Jpn. J. Appl. Phys.*, vol. 56, no. 4S, p. 04CK08, 2017. [Online]. Available: http://stacks.iop.org/1347-4065/56/i=4S/a=04CK08

[394] T. Kageura, K. Kato, H. Yamano, E. Suaebah, M. Kajiya, S. Kawai, M. Inaba, T. Tanii, M. Haruyama, K. Yamada, S. Onoda, W. Kada, O. Hanaizumi, T. Teraji, J. Isoya, S. Kono, and H. Kawarada, "Effect of a radical exposure nitridation surface on the charge stability of shallow nitrogen-vacancy centers in diamond," *Appl. Phys. Express*, vol. 10, no. 5, p. 055503, 2017. [Online]. Available: http://stacks.iop.org/1882-0786/10/i=5/a=055503

[395] A. N. Newell, D. A. Dowdell, and D. H. Santamore, "Surface effects on nitrogen vacancy centers neutralization in diamond," *J. Appl. Phys.*, vol. 120, no. 18, p. 185104, 2016. [Online]. Available: https://doi.org/10.1063/1.4967735

[396] C. Santori, P. E. Barclay, K.-M. C. Fu, and R. G. Beausoleil, "Vertical distribution of nitrogen-vacancy centers in diamond formed by ion implantation and annealing," *Phys. Rev. B*, vol. 79, p. 125313, Mar 2009. [Online]. Available: https://link.aps.org/doi/10.1103/PhysRevB.79.125313

[397] T. Malinauskas, K. Jarasiunas, E. Ivakin, V. Ralchenko, A. Gontar, and S. Ivakhnenko, "Optical evaluation of carrier lifetime and diffusion length in synthetic diamonds," *Diam. Relat. Mater.*, vol. 17, no. 7, pp. 1212–1215, 2008. [Online]. Available: http://www.sciencedirect.com/science/article/pii/S0925963508000241

[398] C. Schreyvogel, V. Polyakov, R. Wunderlich, J. Meijer, and C. E. Nebel, "Active charge state control of single NV centres in diamond by in-plane al-schottky junctions," *Sci. Rep.*, vol. 5, pp. 12 160 –, Jul 2015. [Online]. Available: http://dx.doi.org/10.1038/srep12160

[399] T. Murai, T. Makino, H. Kato, M. Shimizu, T. Murooka, E. D. Herbschleb, Y. Doi, H. Morishita, M. Fujiwara, M. Hatano, S. Yamasaki, and N. Mizuochi, "Engineering of fermi level by nin diamond junction for control of charge states

of NV centers," *Appl. Phys. Lett.*, vol. 112, no. 11, p. 111903, 2018. [Online]. Available: https://doi.org/10.1063/1.5010956

[400] J. Forneris, S. Ditalia Tchernij, A. Tengattini, E. Enrico, V. Grilj, N. Skukan, G. Amato, L. Boarino, M. Jakšić, and P. Olivero, "Electrical control of deep NV centers in diamond by means of sub-superficial graphitic micro-electrodes," *Carbon*, vol. 113, pp. 76–86, 2017. [Online]. Available: http://www.sciencedirect.com/science/article/pii/S0008622316310053

[401] S. Karaveli, O. Gaathon, A. Wolcott, R. Sakakibara, O. A. Shemesh, D. S. Peterka, E. S. Boyden, J. S. Owen, R. Yuste, and D. Englund, "Modulation of nitrogen vacancy charge state and fluorescence in nanodiamonds using electrochemical potential," *Proc. Natl. Acad. Sci.*, vol. 113, no. 15, pp. 3938–3943, 2016. [Online]. Available: http://www.pnas.org/content/113/15/3938

[402] C. J. Wort and R. S. Balmer, "Diamond as an electronic material," *Mater. Today*, vol. 11, no. 1, pp. 22–28, 2008. [Online]. Available: http://www.sciencedirect.com/science/article/pii/S1369702107703498

[403] M. Katagiri, J. Isoya, S. Koizumi, and H. Kanda, "Lightly phosphorus-doped homoepitaxial diamond films grown by chemical vapor deposition," *Appl. Phys. Lett.*, vol. 85, no. 26, pp. 6365–6367, 2004. [Online]. Available: https://doi.org/10.1063/1.1840119

[404] R. Farrer, "On the substitutional nitrogen donor in diamond," *Solid State Commun.*, vol. 7, no. 9, pp. 685–688, 1969. [Online]. Available: http://www.sciencedirect.com/science/article/pii/0038109869905936

[405] R. Kalish, "Doping of diamond," *Carbon*, vol. 37, no. 5, pp. 781–785, 1999. [Online]. Available: http://www.sciencedirect.com/science/article/pii/S000862239800270X

[406] R. Jones, J. E. Lowther, and J. Goss, "Limitations to n-type doping in diamond: The phosphorus-vacancy complex," *Appl. Phys. Lett.*, vol. 69, pp. 2489–2491, Oct. 1996. [Online]. Available: https://doi.org/10.1063/1.117715

[407] G. Z. Cao, F. A. J. M. Driessen, G. J. Bauhuis, L. J. Giling, and P. F. A. Alkemade, "Homoepitaxial diamond films codoped with phosphorus and nitrogen by chemical-vapor deposition," *J. Appl. Phys.*, vol. 78, no. 5, pp. 3125–3131, 1995. [Online]. Available: https://doi.org/10.1063/1.359998

[408] A. Pu, V. Avalos, and S. Dannefaer, "Negative charging of mono- and divacancies in iia diamonds by monochromatic illumination," *Diam. Relat. Mater.*, vol. 10, no. 3, pp. 585–587, 2001. [Online]. Available: http://www.sciencedirect.com/science/article/pii/S0925963500004416

[409] I. Meirzada, Y. Hovav, S. A. Wolf, and N. Bar-Gill, "Negative charge enhancement of near-surface nitrogen vacancy centers by multicolor

excitation," *Phys. Rev. B*, vol. 98, p. 245411, Dec 2018. [Online]. Available: https://link.aps.org/doi/10.1103/PhysRevB.98.245411

[410] X.-D. Chen, S. Li, A. Shen, Y. Dong, C.-H. Dong, G.-C. Guo, and F.-W. Sun, "Near-infrared-enhanced charge-state conversion for low-power optical nanoscopy with nitrogen-vacancy centers in diamond," *Phys. Rev. Applied*, vol. 7, p. 014008, Jan 2017. [Online]. Available: http://link.aps.org/doi/10.1103/PhysRevApplied.7.014008

[411] U. F. D'Haenens-Johansson, A. Katrusha, P. Johnson, W. Wang *et al.*, "Large colorless hpht-grown synthetic gem diamonds from new diamond technology, russia." *Gems Gemol.*, vol. 51, no. 3, 2015. [Online]. Available: https://www.gia.edu/gems-gemology/fall-2015-large-colorless-hpht-grown-synthetic-gem-diamond-technology-russia

[412] A. Tallaire, V. Mille, O. Brinza, T. N. T. Thi, J. Brom, Y. Loguinov, A. Katrusha, A. Koliadin, and J. Achard, "Thick CVD diamond films grown on high-quality type iia hpht diamond substrates from new diamond technology," *Diam. Relat. Mater.*, vol. 77, pp. 146–152, 2017. [Online]. Available: http://www.sciencedirect.com/science/article/pii/S092596351730287X

[413] H. Kanda, "Large diamonds grown at high pressure conditions," *Braz. J. Phys.*, vol. 30, pp. 482–489, 00 2000. [Online]. Available: http://www.scielo.br/scielo.php?script=sci_arttext&pid=S0103-97332000000300003&nrm=iso

[414] I. A. Dobrinets, V. G. Vins, and A. M. Zaitsev, *HPHT-Treated Diamonds: Diamonds Forever*. Springer, 06 2013. [Online]. Available: http://www.springer.com/us/book/9783642374890

[415] Y. N. Palyanov, I. N. Kupriyanov, A. F. Khokhryakov, and V. G. Ralchenko, *Crystal Growth of Diamond*. Elsevier, 12 2015, vol. 2, pp. 671–713. [Online]. Available: http://www.sciencedirect.com/science/article/pii/B9780444633033000171

[416] J. C. Angus, H. A. Will, and W. S. Stanko, "Growth of diamond seed crystals by vapor deposition," *J. Appl. Phys.*, vol. 39, no. 6, pp. 2915–2922, 1968. [Online]. Available: https://doi.org/10.1063/1.1656693

[417] M. Schwander and K. Partes, "A review of diamond synthesis by CVD processes," *Diam. Relat. Mater.*, vol. 20, no. 9, pp. 1287–1301, 2011. [Online]. Available: http://www.sciencedirect.com/science/article/pii/S0925963511002913

[418] C. A. McLellan, B. A. Myers, S. Kraemer, K. Ohno, D. D. Awschalom, and A. C. Bleszynski Jayich, "Patterned formation of highly coherent nitrogen-vacancy centers using a focused electron irradiation technique," *Nano Lett.*, vol. 16, no. 4, pp. 2450–2454, 2016. [Online]. Available: http://dx.doi.org/10.1021/acs.nanolett.5b05304

[419] X. Zhang and E. L. Hu, "Templated growth of diamond optical resonators via plasma-enhanced chemical vapor deposition," *Appl. Phys. Lett.*, vol. 109, no. 8, p. 081101, 2016. [Online]. Available: https://doi.org/10.1063/1.4961536

[420] P. M. Martineau, M. P. Gaukroger, K. B. Guy, S. C. Lawson, D. J. Twitchen, I. Friel, J. O. Hansen, G. C. Summerton, T. P. G. Addison, and R. Burns, "High crystalline quality single crystal chemical vapour deposition diamond," *J. Phys.: Condens. Matter*, vol. 21, no. 36, p. 364205, 2009. [Online]. Available: http://stacks.iop.org/0953-8984/21/i=36/a=364205

[421] C. Grezes, B. Julsgaard, Y. Kubo, W. L. Ma, M. Stern, A. Bienfait, K. Nakamura, J. Isoya, S. Onoda, T. Ohshima, V. Jacques, D. Vion, D. Esteve, R. B. Liu, K. Mølmer, and P. Bertet, "Storage and retrieval of microwave fields at the single-photon level in a spin ensemble," *Phys. Rev. A*, vol. 92, p. 020301, Aug 2015. [Online]. Available: https://link.aps.org/doi/10.1103/PhysRevA.92.020301

[422] F. M. Stürner, A. Brenneis, J. Kassel, U. Wostradowski, R. Rölver, T. Fuchs, K. Nakamura, H. Sumiya, S. Onoda, J. Isoya, and F. Jelezko, "Compact integrated magnetometer based on nitrogen-vacancy centres in diamond," *Diam. Relat. Mater.*, vol. 93, p. 59, 2019. [Online]. Available: http://www.sciencedirect.com/science/article/pii/S092596351830760X

[423] H. Zheng, J. Xu, G. Iwata, T. Lenz, J. Michl, B. Yavkin, K. Nakamura, H. Sumiya, T. Ohshima, J. Isoya, J. Wrachtrup, A. Wickenbrock, and D. Budker, "Zero-field magnetometry based on nitrogen-vacancy ensembles in diamond," *ArXiv e-prints*, Nov. 2018. [Online]. Available: https://arxiv.org/abs/1811.11498

[424] S. J. Charles, J. E. Butler, B. N. Feygelson, M. E. Newton, D. L. Carroll, J. W. Steeds, H. Darwish, C.-S. Yan, H. K. Mao, and R. J. Hemley, "Characterization of nitrogen doped chemical vapor deposited single crystal diamond before and after high pressure, high temperature annealing," *Phys. Status Solidi A*, vol. 201, no. 11, pp. 2473–2485, 2004. [Online]. Available: http://dx.doi.org/10.1002/pssa.200405175

[425] L. S. Hounsome, R. Jones, P. M. Martineau, D. Fisher, M. J. Shaw, P. R. Briddon, and S. Öberg, "Origin of brown coloration in diamond," *Phys. Rev. B*, vol. 73, p. 125203, Mar 2006. [Online]. Available: http://link.aps.org/doi/10.1103/PhysRevB.73.125203

[426] T. Yamamoto, T. Umeda, K. Watanabe, S. Onoda, M. L. Markham, D. J. Twitchen, B. Naydenov, L. P. McGuinness, T. Teraji, S. Koizumi, F. Dolde, H. Fedder, J. Honert, J. Wrachtrup, T. Ohshima, F. Jelezko, and J. Isoya, "Extending spin coherence times of diamond qubits by high-temperature annealing," *Phys. Rev. B*, vol. 88, p. 075206, Aug 2013. [Online]. Available: https://link.aps.org/doi/10.1103/PhysRevB.88.075206

[427] J. N. Lomer and A. M. A. Wild, "Electron spin resonance in electron irradiated diamond annealed to high temperatures," *Radiat. Eff.*, vol. 17, no. 1-2, pp. 37–44, 1973. [Online]. Available: http://dx.doi.org/10.1080/00337577308232595

[428] J. Baker, "Deducing atomic models for point defects in diamond: The relevance of their mechanism of formation," *Diam. Relat. Mater.*, vol. 16, no. 2, pp. 216–219, 2007. [Online]. Available: http://www.sciencedirect.com/science/article/pii/S0925963506001671

[429] A. Tallaire, L. Mayer, O. Brinza, M. A. Pinault-Thaury, T. Debuisschert, and J. Achard, "Highly photostable NV centre ensembles in CVD diamond produced by using N_2O as the doping gas," *Appl. Phys. Lett.*, vol. 111, no. 14, p. 143101, 2017. [Online]. Available: https://doi.org/10.1063/1.5004106

[430] A. Mainwood, "Point defects in natural and synthetic diamond: What they can tell us about CVD diamond," *Phys. Status Solidi A*, vol. 172, no. 1, pp. 25–35, 1999. [Online]. Available: http://adsabs.harvard.edu/abs/1999PSSAR.172...25M

[431] D. Fisher, D. J. F. Evans, C. Glover, C. J. Kelly, M. J. Sheehy, and G. C. Summerton, "The vacancy as a probe of the strain in type IIa diamonds," *Diam. Relat. Mater.*, vol. 15, pp. 1636–1642, Oct. 2006. [Online]. Available: https://www.sciencedirect.com/science/article/pii/S0925963506000276

[432] J. Achard, A. Tallaire, V. Mille, M. Naamoun, O. Brinza, A. Boussadi, L. William, and A. Gicquel, "Improvement of dislocation density in thick CVD single crystal diamond films by coupling h2/o2 plasma etching and chemo-mechanical or icp treatment of hpht substrates," *Phys. Status Solidi A*, vol. 211, no. 10, pp. 2264–2267, 2014. [Online]. Available: http://dx.doi.org/10.1002/pssa.201431181

[433] U. F. D'Haenens-Johansson, K. S. Moe, P. Johnson, S. Y. Wong, R. Lu, and W. Wang, "Near-colorless hpht synthetic diamonds from aotc group," *Gems Gemol.*, vol. 50, no. 1, 2014. [Online]. Available: http://www.gia.edu/gems-gemology/spring-2014-ulrika-hpht-synthetic-diamonds

[434] J. P. Goss, P. R. Briddon, V. Hill, R. Jones, and M. J. Rayson, "Identification of the structure of the 3107cm -1 h-related defect in diamond," *J. Phys.: Condens. Matter*, vol. 26, no. 14, p. 145801, 2014. [Online]. Available: http://stacks.iop.org/0953-8984/26/i=14/a=145801

[435] A. T. Collins, H. Kanda, and H. Kitawaki, "Colour changes produced in natural brown diamonds by high-pressure, high-temperature treatment," *Diam. Relat. Mater.*, vol. 9, no. 2, pp. 113–122, 2000. [Online]. Available: http://www.sciencedirect.com/science/article/pii/S0925963500002491

[436] U. Bangert, R. Barnes, M. H. Gass, A. L. Bleloch, and I. S. Godfrey, "Vacancy clusters, dislocations and brown colouration in diamond," *J. Phys.:*

Condens. Matter, vol. 21, no. 36, p. 364208, 2009. [Online]. Available: http://stacks.iop.org/0953-8984/21/i=36/a=364208

[437] D. J. Twitchen, S. L. Geoghegan, and N. Perkins, "Method for treating single crystal CVD diamond and product obtained," Patent WO 149 775, 12 29, 2010, wO Patent 2010/149775 Al. [Online]. Available: https://www.google.com/patents/WO2010149775A1

[438] V. Vins, "Technique of production of fancy red diamonds," Patent, Mar, 2007, u.S. Patent 2007/0053823 A1. [Online]. Available: https://www.google.ch/patents/US20070053823

[439] Q. Wang, C. P. Smith, M. S. Hall, C. M. Breeding, and T. M. Moses, "Treated-color pink-to-red diamonds from lucent diamonds inc." *Gems Gemol.*, vol. 41, no. 1, 2005. [Online]. Available: https://lucent.diamonds/pages/in-the-media

[440] D. Twitchen, D. Hunt, M. Newton, J. Baker, T. Anthony, and W. Banholzer, "Electron paramagnetic resonance (epr) and optical absorption studies of defects created in diamond by electron irradiation damage at 100 and 350 k," *Physica B: Condens. Matter*, vol. 273–274, pp. 628–631, 1999. [Online]. Available: http://www.sciencedirect.com/science/article/pii/S0921452699005906

[441] M. Newton, B. Campbell, D. Twitchen, J. Baker, and T. Anthony, "Recombination-enhanced diffusion of self-interstitial atoms and vacancy-interstitial recombination in diamond," *Diam. Relat. Mater.*, vol. 11, no. 3-6, pp. 618–622, 2002. [Online]. Available: http://www.sciencedirect.com/science/article/pii/S0925963501006239

[442] A. Zaitsev, K. Moe, and W. Wang, "Optical centers and their depth distribution in electron irradiated {CVD} diamond," *Diam. Relat. Mater.*, vol. 71, pp. 38–52, 2017. [Online]. Available: http://www.sciencedirect.com/science/article/pii/S0925963516305040

[443] K. M. Rutledge and K. K. Gleason, *Characterization Methods*. CRC Press, 1998, ch. 9. [Online]. Available: https://books.google.com/books?id=nsuCDwAAQBAJ

[444] C. E. Ashbaugh III, "Gemstone irradiation and radioactivity," *Gems Gemol.*, vol. 24, no. 4, 1988. [Online]. Available: http://www.gia.edu/gems-gemology/winter-1988-irradiation-radioactivity-ashbaugh

[445] B. Campbell and A. Mainwood, "Radiation damage of diamond by electron and gamma irradiation," *Phys. Status Solidi A*, vol. 181, no. 1, pp. 99–107, 2000. [Online]. Available: https://halldweb.jlab.org/wiki/images/8/8c/Campbell_et_al-2000_rad_damage.pdf

[446] G. Davies, B. Campbell, A. Mainwood, M. Newton, M. Watkins, H. Kanda, and T. Anthony, "Interstitials, vacancies and impurities in diamond," *Phys.*

Status Solidi A, vol. 186, no. 2, pp. 187–198, 2001. [Online]. Available: http://discovery.ucl.ac.uk/1376120/

[447] J. T. Buchan, M. Robinson, H. J. Christie, D. L. Roach, D. K. Ross, and N. A. Marks, "Molecular dynamics simulation of radiation damage cascades in diamond," *J. Appl. Phys.*, vol. 117, no. 24, p. 245901, 2015. [Online]. Available: http://dx.doi.org/10.1063/1.4922457

[448] R. S. Balmer, J. R. Brandon, S. L. Clewes, H. K. Dhillon, J. M. Dodson, I. Friel, P. N. Inglis, T. D. Madgwick, M. L. Markham, T. P. Mollart, N. Perkins, G. A. Scarsbrook, D. J. Twitchen, A. J. Whitehead, J. J. Wilman, and S. M. Woollard, "Chemical vapour deposition synthetic diamond: materials, technology and applications," *J. Phys.: Condens. Matter*, vol. 21, no. 36, p. 364221, 2009. [Online]. Available: http://stacks.iop.org/0953-8984/21/i=36/a=364221

[449] M. Lobaev, A. Gorbachev, S. Bogdanov, A. Vikharev, D. Radishev, V. Isaev, V. Chernov, and M. Drozdov, "Influence of {CVD} diamond growth conditions on nitrogen incorporation," *Diam. Relat. Mater.*, vol. 72, pp. 1–6, 2017. [Online]. Available: http://www.sciencedirect.com/science/article/pii/S0925963516305908

[450] F. Fávaro de Oliveira, S. A. Momenzadeh, D. Antonov, J. Scharpf, C. Osterkamp, B. Naydenov, F. Jelezko, A. Denisenko, and J. Wrachtrup, "Toward optimized surface δ-profiles of nitrogen-vacancy centers activated by helium irradiation in diamond," *Nano Lett.*, vol. 16, no. 4, pp. 2228–2233, 04 2016. [Online]. Available: https://doi.org/10.1021/acs.nanolett.5b04511

[451] F. Fávaro de Oliveira, D. Antonov, Y. Wang, P. Neumann, S. A. Momenzadeh, T. Häußermann, A. Pasquarelli, A. Denisenko, and J. Wrachtrup, "Tailoring spin defects in diamond by lattice charging," *Nat. Commun.*, vol. 8, p. 15409, 05 2017. [Online]. Available: https://doi.org/10.1038/ncomms15409

[452] B. Naydenov, F. Reinhard, A. Lämmle, V. Richter, R. Kalish, U. F. S. D'Haenens-Johansson, M. Newton, F. Jelezko, and J. Wrachtrup, "Increasing the coherence time of single electron spins in diamond by high temperature annealing," *Appl. Phys. Lett.*, vol. 97, no. 24, p. 242511, 2010. [Online]. Available: https://doi.org/10.1063/1.3527975

[453] J. Schwartz, P. Michaelides, C. D. Weis, and T. Schenkel, "In situ optimization of co-implantation and substrate temperature conditions for nitrogen-vacancy center formation in single-crystal diamonds," *New J. Phys.*, vol. 13, no. 3, p. 035022, 2011. [Online]. Available: http://stacks.iop.org/1367-2630/13/i=3/a=035022

[454] F. Waldermann, P. Olivero, J. Nunn, K. Surmacz, Z. Wang, D. Jaksch, R. Taylor, I. Walmsley, M. Draganski, P. Reichart, A. Greentree, D. Jamieson, and S. Prawer, "Creating diamond color centers for quantum

optical applications," *Diam. Relat. Mater.*, vol. 16, no. 11, pp. 1887–1895, 2007. [Online]. Available: http://www.sciencedirect.com/science/article/pii/S0925963507003834

[455] L. Himics, S. Tóth, M. Veres, Z. Balogh, and M. Koós, "Creation of deep blue light emitting nitrogen-vacancy center in nanosized diamond," *Appl. Phys. Lett.*, vol. 104, no. 9, p. 093101, 2014. [Online]. Available: https://doi.org/10.1063/1.4867463

[456] D. McCloskey, D. Fox, N. O'Hara, V. Usov, D. Scanlan, N. McEvoy, G. S. Duesberg, G. L. W. Cross, H. Z. Zhang, and J. F. Donegan, "Helium ion microscope generated nitrogen-vacancy centres in type ib diamond," *Appl. Phys. Lett.*, vol. 104, no. 3, p. 031109, 2014. [Online]. Available: http://dx.doi.org/10.1063/1.4862331

[457] A. T. Collins, "Optical centres produced in diamond by radiation damage," *New. Diam. Front. C. Tec.*, vol. 17, no. 2, pp. 47–61, 2007. [Online]. Available: http://myukk.xsrv.jp/free_journal/download.php?fn=NDFCT532_full.pdf

[458] A. Uedono, K. Mori, N. Morishita, H. Itoh, S. Tanigawa, S. Fujii, and S. Shikata, "Annealing behaviours of defects in electron-irradiated diamond probed by positron annihilation," *J. Phys.: Condens. Matter*, vol. 11, no. 25, p. 4925, 1999. [Online]. Available: http://stacks.iop.org/0953-8984/11/i=25/a=311

[459] B. Campbell, W. Choudhury, A. Mainwood, M. Newton, and G. Davies, "Lattice damage caused by the irradiation of diamond," *Nucl. Instrum. Methods Phys. Res., Sect. A*, vol. 476, no. 3, pp. 680–685, 2002. [Online]. Available: http://www.sciencedirect.com/science/article/pii/S0168900201016643

[460] J. Koike, D. M. Parkin, and T. E. Mitchell, "Displacement threshold energy for type iia diamond," *Appl. Phys. Lett.*, vol. 60, no. 12, pp. 1450–1452, 1992. [Online]. Available: http://scitation.aip.org/content/aip/journal/apl/60/12/10.1063/1.107267

[461] E. W. J. Mitchell, *Radiation Damage in Diamond*. Oxford: Clarendon Press, 1965. [Online]. Available: https://www.amazon.com/Physical-Properties-Diamond-R-Berman/dp/B0000CMSS6

[462] S. Dannefaer, P. Mascher, and D. Kerr, "Defect characterization in diamonds by means of positron annihilation," *Diam. Relat. Mater.*, vol. 1, no. 5, pp. 407–410, 1992. [Online]. Available: http://www.sciencedirect.com/science/article/pii/092596359290138E

[463] E. Kim, V. M. Acosta, E. Bauch, D. Budker, and P. R. Hemmer, "Electron spin resonance shift and linewidth broadening of nitrogen-vacancy centers in diamond as a function of electron irradiation dose," *Appl. Phys. Lett.*, vol. 101, no. 8, p. 082410, 2012. [Online]. Available: http://dx.doi.org/10.1063/1.4747211

[464] D. Farfurnik, N. Alfasi, S. Masis, Y. Kauffmann, E. Farchi, Y. Romach, Y. Hovav, E. Buks, and N. Bar-Gill, "Enhanced concentrations of nitrogen-vacancy centers in diamond through tem irradiation," *Appl. Phys. Lett.*, vol. 111, no. 12, p. 123101, 2017. [Online]. Available: https://doi.org/10.1063/1.4993257

[465] J. Schwartz, S. Aloni, D. F. Ogletree, and T. Schenkel, "Effects of low-energy electron irradiation on formation of nitrogen–vacancy centers in single-crystal diamond," *New J. Phys.*, vol. 14, no. 4, p. 043024, 2012. [Online]. Available: http://dx.doi.org/10.1088/1367-2630/14/4/043024

[466] S. C. Lawson, D. Fisher, D. C. Hunt, and M. E. Newton, "On the existence of positively charged single-substitutional nitrogen in diamond," *J. Phys.: Condens. Matter*, vol. 10, no. 27, p. 6171, 1998. [Online]. Available: http://stacks.iop.org/0953-8984/10/i=27/a=016

[467] D. J. Twitchen, D. C. Hunt, V. Smart, M. E. Newton, and J. M. Baker, "Correlation between nd1 optical absorption and the concentration of negative vacancies determined by electron paramagnetic resonance (epr)," *Diam. Relat. Mater.*, vol. 8, no. 8, pp. 1572–1575, 1999. [Online]. Available: http://www.sciencedirect.com/science/article/pii/S0925963599000382

[468] L. Allers, A. T. Collins, and J. Hiscock, "The annealing of interstitial-related optical centres in type ii natural and cvd diamond," *Diam. Relat. Mater.*, vol. 7, no. 2, pp. 228 – 232, 1998. [Online]. Available: http://www.sciencedirect.com/science/article/pii/S0925963597001611

[469] A. T. Collins and A. Dahwich, "The production of vacancies in type ib diamond," *J. Phys.: Condens. Matter*, vol. 15, no. 37, pp. L591–L596, Sep 2003. [Online]. Available: https://doi.org/10.1088%2F0953-8984%2F15%2F37%2Fl06

[470] K. Iakoubovskii, S. Dannefaer, and A. Stesmans, "Evidence for vacancy-interstitial pairs in ib-type diamond," *Phys. Rev. B*, vol. 71, p. 233201, Jun 2005. [Online]. Available: https://link.aps.org/doi/10.1103/PhysRevB.71.233201

[471] A. M. Zaitsev, *Optical Properties of Diamond*. Berlin: Springer, 2001. [Online]. Available: http://www.springer.com/us/book/9783540665823

[472] H. B. Dyer and L. du Preez, "Irradiation damage in type i diamond," *J. Chem. Phys.*, vol. 42, no. 6, pp. 1898–1906, 1965. [Online]. Available: https://doi.org/10.1063/1.1696224

[473] G. Davies, "Current problems in diamond: towards a quantitative understanding," *Physica B: Condens. Matter*, vol. 273-274, pp. 15–23, 1999. [Online]. Available: http://www.sciencedirect.com/science/article/pii/S0921452699003981

[474] G. Davies, S. C. Lawson, A. T. Collins, A. Mainwood, and S. J. Sharp, "Vacancy-related centers in diamond," *Phys. Rev. B*, vol. 46, pp. 13 157–13 170, Nov 1992. [Online]. Available: http://link.aps.org/doi/10.1103/PhysRevB.46.13157

[475] J. F. Ziegler, M. D. Ziegler, and J. P. Biersack, "Srim–the stopping and range of ions in matter (2010)," *Nuclear Instruments and Methods in Physics Research Section B: Beam Interactions with Materials and Atoms*, vol. 268, no. 11-12, pp. 1818–1823, 2010. [Online]. Available: http://www.sciencedirect.com/science/article/pii/S0168583X10001862

[476] Element Six Ltd., Personal communication, 2016.

[477] Prism Gem LLC, Personal communication, 2016.

[478] A. T. Collins and I. Kiflawi, "The annealing of radiation damage in type ia diamond," *J. Phys.: Condens. Matter*, vol. 21, no. 36, p. 364209, 2009. [Online]. Available: http://stacks.iop.org/0953-8984/21/i=36/a=364209

[479] K. Iakoubovskii, I. Kiflawi, K. Johnston, A. Collins, G. Davies, and A. Stesmans, "Annealing of vacancies and interstitials in diamond," *Physica B: Condensed Matter*, vol. 340, pp. 67–75, 2003. [Online]. Available: http://www.sciencedirect.com/science/article/pii/S0921452603006586

[480] F. De Weerdt, "Spectroscopic studies of defects in diamond including their formation and dissociation," Ph.D. dissertation, King's College London, University of London, 2007. [Online]. Available: https://ethos.bl.uk/OrderDetails.do?uin=uk.bl.ethos.441385

[481] S. J. Breuer and P. R. Briddon, "Ab initio," *Phys. Rev. B*, vol. 51, pp. 6984–6994, Mar 1995. [Online]. Available: https://link.aps.org/doi/10.1103/PhysRevB.51.6984

[482] R. Jones, J. Goss, H. Pinto, and D. Palmer, "Diffusion of nitrogen in diamond and the formation of a-centres," *Diam. Relat. Mater.*, vol. 53, pp. 35–39, 2015. [Online]. Available: http://www.sciencedirect.com/science/article/pii/S092596351500014X

[483] J. Orwa, K. Ganesan, J. Newnham, C. Santori, P. Barclay, K. Fu, R. Beausoleil, I. Aharonovich, B. Fairchild, P. Olivero, A. Greentree, and S. Prawer, "An upper limit on the lateral vacancy diffusion length in diamond," *Diam. Relat. Mater.*, vol. 24, pp. 6–10, 2012. [Online]. Available: http://www.sciencedirect.com/science/article/pii/S0925963512000647

[484] X. Hu, Y. Dai, R. Li, H. Shen, and X. He, "The diffusion of vacancies near a diamond (001) surface," *Solid State Commun.*, vol. 122, no. 1, pp. 45–48, 2002. [Online]. Available: http://www.sciencedirect.com/science/article/pii/S0038109802000698

[485] J. Martin, R. Wannemacher, J. Teichert, L. Bischoff, and B. Köhler, "Generation and detection of fluorescent color centers in diamond with submicron resolution," *Appl. Phys. Lett.*, vol. 75, no. 20, pp. 3096–3098, 1999. [Online]. Available: http://dx.doi.org/10.1063/1.125242

[486] F. Jelezko and J. Wrachtrup, *Single Defect Centers in Diamond.* Wiley, 2008, pp. 257–281. [Online]. Available: http://dx.doi.org/10.1002/9783527623174.ch10

[487] R. C. Fletcher and W. L. Brown, "Annealing of bombardment damage in a diamond-type lattice: Theoretical," *Phys. Rev.*, vol. 92, pp. 585–590, Nov 1953. [Online]. Available: https://link.aps.org/doi/10.1103/PhysRev.92.585

[488] S. Onoda, K. Tatsumi, M. Haruyama, T. Teraji, J. Isoya, W. Kada, T. Ohshima, and O. Hanaizumi, "Diffusion of vacancies created by high-energy heavy ion strike into diamond," *Phys. Status Solidi A*, vol. 214, no. 11, p. 1700160, 2017. [Online]. Available: https://onlinelibrary.wiley.com/doi/abs/10.1002/pssa.201700160

[489] J. P. Goss, P. R. Briddon, M. J. Rayson, S. J. Sque, and R. Jones, "Vacancy-impurity complexes and limitations for implantation doping of diamond," *Phys. Rev. B*, vol. 72, p. 035214, Jul 2005. [Online]. Available: https://link.aps.org/doi/10.1103/PhysRevB.72.035214

[490] J. Botsoa, T. Sauvage, M.-P. Adam, P. Desgardin, E. Leoni, B. Courtois, F. Treussart, and M.-F. Barthe, "Optimal conditions for NV^- center formation in type-1b diamond studied using photoluminescence and positron annihilation spectroscopies," *Phys. Rev. B*, vol. 84, p. 125209, Sep 2011. [Online]. Available: http://link.aps.org/doi/10.1103/PhysRevB.84.125209

[491] G. Davies and M. F. Hamer, "Optical studies of the 1.945 ev vibronic band in diamond," *Proc. R. Soc. London, Ser. A*, vol. 348, no. 1653, pp. 285–298, 1976. [Online]. Available: http://rspa.royalsocietypublishing.org/content/348/1653/285

[492] I. Kiflawi, A. T. Collins, K. Iakoubovskii, and D. Fisher, "Electron irradiation and the formation of vacancy-interstitial pairs in diamond," *J. Phys.: Condens. Matter*, vol. 19, no. 4, p. 046216, 2007. [Online]. Available: http://stacks.iop.org/0953-8984/19/i=4/a=046216

[493] G. Davies and T. Evans, "Graphitization of diamond at zero pressure and at a high pressure," *Proc. R. Soc. London, Ser. A*, vol. 328, no. 1574, pp. 413–427, 1972. [Online]. Available: http://www.jstor.org/stable/78141

[494] T. Miyazaki, Y. Miyamoto, T. Makino, H. Kato, S. Yamasaki, T. Fukui, Y. Doi, N. Tokuda, M. Hatano, and N. Mizuochi, "Atomistic mechanism of perfect alignment of nitrogen-vacancy centers in diamond," *Appl. Phys. Lett.*, vol. 105, no. 26, p. 261601, 2014. [Online]. Available: https://doi.org/10.1063/1.4904988

[495] T. Nöbauer, K. Buczak, A. Angerer, S. Putz, G. Steinhauser, J. Akbarzadeh, H. Peterlik, J. Majer, J. Schmiedmayer, and M. Trupke, "Creation of ensembles of nitrogen-vacancy centers in diamond by neutron and electron irradiation," *ArXiv e-prints*, Sep. 2013. [Online]. Available: https://arxiv.org/abs/1309.0453

[496] J.-P. Tetienne, R. W. de Gille, D. A. Broadway, T. Teraji, S. E. Lillie, J. M. McCoey, N. Dontschuk, L. T. Hall, A. Stacey, D. A. Simpson, and L. C. L. Hollenberg, "Spin properties of dense near-surface ensembles of nitrogen-vacancy centers in diamond," *Phys. Rev. B*, vol. 97, p. 085402, Feb 2018. [Online]. Available: https://link.aps.org/doi/10.1103/PhysRevB.97.085402

[497] H. Pinto, R. Jones, D. W. Palmer, J. P. Goss, P. R. Briddon, and S. Öberg, "On the diffusion of NV defects in diamond," *Phys. Status Solidi A*, vol. 209, no. 9, pp. 1765–1768, 2012. [Online]. Available: https://onlinelibrary.wiley.com/doi/abs/10.1002/pssa.201200050

[498] J. D. Breeze, E. Salvadori, J. Sathian, N. M. Alford, and C. W. M. Kay, "Continuous-wave room-temperature diamond maser," *Nature*, vol. 555, p. 493, Mar. 2018. [Online]. Available: https://doi.org/10.1038/nature25970

[499] M. E. Newton, *EPR, ENDOR and EPR Imaging of Defects in Diamond*. Royal Society of Chemistry, 2007. [Online]. Available: https://pubs.rsc.org/en/content/chapter/ep9780854043255-00131/978-0-85404-325-5

[500] J. Kirui, J. van Wyk, and M. Hoch, "Dynamics of negatively charged divacancies in neutron irradiated type ib diamond," *Diam. Relat. Mater.*, vol. 39, pp. 78–81, 2013. [Online]. Available: http://www.sciencedirect.com/science/article/pii/S0925963513001696

[501] A. Pu, T. Bretagnon, D. Kerr, and S. Dannefaer, "Positron annihilation investigation of vacancies in as-grown and electron-irradiated diamonds," *Diam. Relat. Mater.*, vol. 9, no. 8, pp. 1450–1463, 2000. [Online]. Available: http://www.sciencedirect.com/science/article/pii/S0925963500002648

[502] N. Fujita, R. Jones, S. Öberg, and P. Briddon, "Large spherical vacancy clusters in diamond – origin of the brown colouration?" *Diam. Relat. Mater.*, vol. 18, no. 5–8, pp. 843–845, 2009. [Online]. Available: http://www.sciencedirect.com/science/article/pii/S0925963508005347

[503] S. Dannefaer, T. Bretagnon, and D. Kerr, "Positron lifetime investigations of diamond films," *Diam. Relat. Mater.*, vol. 2, no. 12, pp. 1479–1482, 1993. [Online]. Available: http://www.sciencedirect.com/science/article/pii/092596359390016U

[504] R. Jones, L. S. Hounsome, N. Fujita, S. Öberg, and P. R. Briddon, "Electrical and optical properties of multivacancy centres in diamond," *Phys. Status Solidi A*, vol. 204, no. 9, pp. 3059–3064, 2007. [Online]. Available: http://dx.doi.org/10.1002/pssa.200776311

[505] M. A. Lea-wilsonf, J. N. Lomer, and J. A. V. Wyk, "Electron spin resonance of the r4/w6 defect in irradiated diamond," *Philos. Mag. B*, vol. 72, no. 1, pp. 81–89, 1995. [Online]. Available: http://dx.doi.org/10.1080/13642819508239065

[506] B. Slepetz and M. Kertesz, "Divacancies in diamond: a stepwise formation mechanism," *Phys. Chem. Chem. Phys.*, vol. 16, pp. 1515–1521, 2014. [Online]. Available: http://dx.doi.org/10.1039/C3CP53384K

[507] N. Tokuda, *Homoepitaxial Diamond Growth by Plasma-Enhanced Chemical Vapor Deposition*. Cham: Springer International Publishing, 2015, pp. 1–29. [Online]. Available: http://dx.doi.org/10.1007/978-3-319-09834-0_1

[508] I. Sakaguchi, M. Nishitani-Gamo, K. P. Loh, H. Haneda, and T. Ando, "Homoepitaxial growth and hydrogen incorporation on the chemical vapor deposited (111) diamond," *J. Appl. Phys.*, vol. 86, no. 3, pp. 1306–1310, 1999. [Online]. Available: http://scitation.aip.org/content/aip/journal/jap/86/3/10.1063/1.370886

[509] C. Tang, A. Neves, and A. Fernandes, "Study the effect of {O2} addition on hydrogen incorporation in {CVD} diamond," *Diam. Relat. Mater.*, vol. 13, no. 1, pp. 203–208, 2004. [Online]. Available: http://www.sciencedirect.com/science/article/pii/S0925963503004242

[510] J. L. Lyons and C. G. V. de Walle, "Surprising stability of neutral interstitial hydrogen in diamond and cubic BN," *J. Phys.: Condens. Matter*, vol. 28, no. 6, p. 06LT01, Jan 2016. [Online]. Available: https://iopscience.iop.org/article/10.1088/0953-8984/28/6/06LT01/meta

[511] C. Glover, M. E. Newton, P. Martineau, D. J. Twitchen, and J. M. Baker, "Hydrogen incorporation in diamond: The nitrogen-vacancy-hydrogen complex," *Phys. Rev. Lett.*, vol. 90, p. 185507, May 2003. [Online]. Available: http://link.aps.org/doi/10.1103/PhysRevLett.90.185507

[512] A. M. Edmonds, "Magnetic resonance studies of point defects in single crystal diamond," Ph.D. dissertation, University of Warwick, 2008. [Online]. Available: http://wrap.warwick.ac.uk/2968/1/WRAP_THESIS_Edmonds_2008.pdf

[513] B. L. Cann, "Magnetic resonance studies of point defects in diamond," Ph.D. dissertation, University of Warwick, 2009. [Online]. Available: http://wrap.warwick.ac.uk/3125/1/WRAP_THESIS_Cann_2009.pdf

[514] G. Davies, "The a nitrogen aggregate in diamond-its symmetry and possible structure," *J. Phys. C: Solid State Phys.*, vol. 9, no. 19, p. L537, 1976. [Online]. Available: http://stacks.iop.org/0022-3719/9/i=19/a=005

[515] S. R. Boyd, I. Kiflawi, and G. S. Woods, "The relationship between infrared absorption and the a defect concentration in diamond," *Philos. Mag. B*, vol. 69, no. 6, pp. 1149–1153, 1994. [Online]. Available: http://dx.doi.org/10.1080/01418639408240185

[516] O. D. Tucker, M. E. Newton, and J. M. Baker, "Epr and ^{14}N electron-nuclear double-resonance measurements on the ionized nearest-neighbor dinitrogen center in diamond," *Phys. Rev. B*, vol. 50, pp. 15 586–15 596, Dec 1994. [Online]. Available: http://link.aps.org/doi/10.1103/PhysRevB.50.15586

[517] B. L. Green, M. W. Dale, M. E. Newton, and D. Fisher, "Electron paramagnetic resonance of the N_2V^- defect in ^{15}N-doped synthetic diamond," *Phys. Rev. B*, vol. 92, p. 165204, Oct 2015. [Online]. Available: http://link.aps.org/doi/10.1103/PhysRevB.92.165204

[518] B. L. Green, B. G. Breeze, and M. E. Newton, "Electron paramagnetic resonance and photochromism of N_3V^0 in diamond," *J. Phys.: Condens. Matter*, vol. 29, no. 22, p. 225701, Apr 2017. [Online]. Available: https://doi.org/10.1088/1361-648x/aa6c89

[519] S. Liggins, "Identification of point defects in treated single crystal diamond," Ph.D. dissertation, University of Warwick, 2010. [Online]. Available: http://wrap.warwick.ac.uk/35522/1/WRAP_THESIS_Liggins_2010.pdf

[520] L. A. Bursill and R. W. Glaisher, "Aggregation and dissolution of small and extended defect structures in type ia diamond," *Am. Mineral.*, vol. 70, pp. 608–618, 1985. [Online]. Available: http://www.minsocam.org/ammin/AM70/AM70_608.pdf

[521] J. P. Goss, P. R. Briddon, S. Papagiannidis, and R. Jones, "Interstitial nitrogen and its complexes in diamond," *Phys. Rev. B*, vol. 70, p. 235208, Dec 2004. [Online]. Available: http://link.aps.org/doi/10.1103/PhysRevB.70.235208

[522] C. Glover, M. E. Newton, P. M. Martineau, S. Quinn, and D. J. Twitchen, "Hydrogen incorporation in diamond: The vacancy-hydrogen complex," *Phys. Rev. Lett.*, vol. 92, p. 135502, Mar 2004. [Online]. Available: http://link.aps.org/doi/10.1103/PhysRevLett.92.135502

[523] C. Glover, "A study of defects in single crystal CVD diamond," Ph.D. dissertation, University of Warwick, 2003. [Online]. Available: http://wrap.warwick.ac.uk/2962/1/WRAP_THESIS_Glover_2003.pdf

[524] M. J. Shaw, P. R. Briddon, J. P. Goss, M. J. Rayson, A. Kerridge, A. H. Harker, and A. M. Stoneham, "Importance of quantum tunneling in vacancy-hydrogen complexes in diamond," *Phys. Rev. Lett.*, vol. 95, p. 105502, Sep 2005. [Online]. Available: http://link.aps.org/doi/10.1103/PhysRevLett.95.105502

[525] R. Cruddace, "Magnetic resonance and optical studies of point defects in single crystal CVD diamond," Ph.D. dissertation, University of Warwick, 2007. [Online]. Available: http://wrap.warwick.ac.uk/2964/1/WRAP_THESIS_Cruddace_2007.pdf

[526] J. Michl, T. Teraji, S. Zaiser, I. Jakobi, G. Waldherr, F. Dolde, P. Neumann, M. W. Doherty, N. B. Manson, J. Isoya, and J. Wrachtrup, "Perfect alignment and preferential orientation of nitrogen-vacancy centers during chemical vapor deposition diamond growth on (111) surfaces," *Appl. Phys. Lett.*, vol. 104, no. 10, p. 102407, 2014. [Online]. Available: https://doi.org/10.1063/1.4868128

[527] M. Lesik, J.-P. Tetienne, A. Tallaire, J. Achard, V. Mille, A. Gicquel, J.-F. Roch, and V. Jacques, "Perfect preferential orientation of nitrogen-vacancy defects in a synthetic diamond sample," *Appl. Phys. Lett.*, vol. 104, no. 11, p. 113107, 2014. [Online]. Available: https://aip.scitation.org/doi/10.1063/1.4869103

[528] T. Fukui, Y. Doi, T. Miyazaki, Y. Miyamoto, H. Kato, T. Matsumoto, T. Makino, S. Yamasaki, R. Morimoto, N. Tokuda, M. Hatano, Y. Sakagawa, H. Morishita, T. Tashima, S. Miwa, Y. Suzuki, and N. Mizuochi, "Perfect selective alignment of nitrogen-vacancy centers in diamond," *Appl. Phys. Express*, vol. 7, no. 5, p. 055201, 2014. [Online]. Available: http://dx.doi.org/10.7567/APEX.7.055201

[529] R. J. Epstein, F. M. Mendoza, Y. K. Kato, and D. D. Awschalom, "Anisotropic interactions of a single spin and dark-spin spectroscopy in diamond," *Nat. Phys.*, vol. 1, pp. 94–98, 2005. [Online]. Available: https://www.nature.com/articles/nphys141

[530] K. Tahara, H. Ozawa, T. Iwasaki, N. Mizuochi, and M. Hatano, "Quantifying selective alignment of ensemble nitrogen-vacancy centers in (111) diamond," *Appl. Phys. Lett.*, vol. 107, no. 19, p. 193110, 2015. [Online]. Available: https://doi.org/10.1063/1.4935709

[531] K. Jensen, P. Kehayias, and D. Budker, "Magnetometry with nitrogen-vacancy centers in diamond," in *Smart Sensors, Measurement and Instrumentation: High Sensitivity Magnetometers*, 12 2017, vol. 19, pp. 553–576. [Online]. Available: https://link.springer.com/book/10.1007/978-3-319-34070-8

[532] A. Barfuss, M. Kasperczyk, J. Kölbl, and P. Maletinsky, "Spin-stress and spin-strain coupling in diamond-based hybrid spin oscillator systems," *ArXiv e-prints*, Oct. 2018. [Online]. Available: https://arxiv.org/abs/1810.07190

[533] Thorlabs Inc., "Protected Silver Mirrors." [Online]. Available: https://www.thorlabs.com/newgrouppage9.cfm?objectgroup_id=903

[534] K. Bayat, J. Choy, M. Farrokh Baroughi, S. Meesala, and M. Loncar, "Efficient, uniform, and large area microwave magnetic coupling to NV centers in diamond using double split-ring resonators," *Nano Letters*, vol. 14, no. 3, pp. 1208–1213, 03 2014. [Online]. Available: https://doi.org/10.1021/nl404072s

[535] C. T. Corporation, "Magnetic Properties of Stainless Steels." [Online]. Available: https://www.cartech.com/en/alloy-techzone/technical-information/technical-articles/magnetic-properties-of-stainless-steels

[536] J. Harrison, M. Sellars, and N. Manson, "Measurement of the optically induced spin polarisation of N-V centres in diamond," *Diam. Relat. Mater.*, vol. 15, no. 4, pp. 586 – 588, 2006. [Online]. Available: http://www.sciencedirect.com/science/article/pii/S0925963505006266

[537] S. Choi, J. Choi, R. Landig, G. Kucsko, H. Zhou, J. Isoya, F. Jelezko, S. Onoda, H. Sumiya, V. Khemani, C. von Keyserlingk, N. Y. Yao, E. Demler, and M. D. Lukin, "Observation of discrete time-crystalline order in a disordered dipolar many-body system," *Nature*, vol. 543, p. 221, 03 2017. [Online]. Available: https://doi.org/10.1038/nature21426